

2011

Structure and dynamics of membrane peptides from solid-state NMR

Yongchao Su
Iowa State University

Follow this and additional works at: <https://lib.dr.iastate.edu/etd>

 Part of the [Chemistry Commons](#)

Recommended Citation

Su, Yongchao, "Structure and dynamics of membrane peptides from solid-state NMR" (2011). *Graduate Theses and Dissertations*. 10197.
<https://lib.dr.iastate.edu/etd/10197>

This Dissertation is brought to you for free and open access by the Iowa State University Capstones, Theses and Dissertations at Iowa State University Digital Repository. It has been accepted for inclusion in Graduate Theses and Dissertations by an authorized administrator of Iowa State University Digital Repository. For more information, please contact digirep@iastate.edu.

Structure and dynamics of membrane peptides from solid-state NMR

by

Yongchao Su

A dissertation submitted to the graduate faculty
in partial fulfillment of the requirements for the degree of

DOCTOR OF PHILOSOPHY

Major: Chemistry

Program of Study Committee:

Mei Hong, Major Professor

Klaus Schmidt-Rohr

Xueyu Song

Emily Smith

Yan Zhao

Iowa State University

Ames, Iowa

2011

Copyright © Yongchao Su, 2011. All rights reserved.

To my wife, Yun

Table of Contents

Acknowledgements.....	vii
Chapter 1. Introduction to Nuclear Magnetic Resonance Methodology and Membrane Peptides	
1.1 Introduction	1
1.2 Secondary Structure Determination.....	15
1.3 Dipolar-Based Distance Measurement.....	20
1.4 Paramagnetic Resonance Enhancement NMR.....	30
1.5 Measurements of Local and Global Dynamics of Proteins.....	37
1.6 Peptide-Incorporated Lipid Membrane Samples.....	44
1.7 Thesis Organization.....	46
1.8 Copyright Permissions.....	48
1.9 References.....	48
Chapter 2. Structure and Dynamics of Cationic Membrane Peptides and Proteins: Insights from Solid-State NMR – A Review	
2.1 Abstract.....	54
2.2 Introduction.....	56
2.3 SSNMR Techniques for Studying Protein–Membrane Interactions.....	56
2.4 SSNMR Studies of Antimicrobial Peptides.....	60
2.5 Cell-Penetrating Peptides.....	68
2.6 Arg-Rich Voltage-Sensing Helix of a Potassium Channel.....	75
2.7 Concluding Remarks.....	76
2.8 References.....	77
Chapter 3. Reversible Sheet – Turn Conformational Change of a Cell-Penetrating Peptide in Lipid Bilayers Studied by Solid-State NMR	
3.1 Abstract.....	86
3.2 Introduction.....	86
3.3 Results.....	88
3.4 Discussion.....	102
3.5 Materials and Methods.....	106
3.6 Acknowledgments.....	108
3.7 References.....	108
3.8 Supporting Information.....	113
Chapter 4. Asymmetric Insertion of Membrane Proteins in Lipid Bilayers by Sol-	

	id-State NMR Paramagnetic Relaxation Enhancement: a Cell-Penetrating Peptide Example	
4.1	Abstract.....	115
4.2	Introduction.....	115
4.3	Materials and Methods.....	119
4.4	Results.....	122
4.5	Discussion.....	129
4.6	Acknowledgements.....	133
4.7	References.....	133
4.8	Supporting Information.....	138
Chapter 5.	Role of Arginine and Lysine Residues in the Translocation of a Cell-Penetrating Peptide from ^{13}C , ^{31}P and ^{19}F Solid-State NMR	
1.1	Abstract.....	138
1.2	Introduction.....	138
1.3	Materials and Methods.....	142
1.4	Results.....	145
1.5	Discussion.....	154
1.6	Acknowledgements.....	158
1.7	References.....	158
1.8	Supporting Information.....	162
Chapter 6.	Membrane-Bound Dynamic structure of an Arg-Rich Cell-Penetrating Peptide, the Protein Transduction Domain of HIV TAT, from Solid-State NMR Spectroscopy	
6.1	Abstract.....	163
6.2	Introduction.....	164
6.3	Materials and Methods.....	165
6.4	Results.....	171
6.5	Discussion.....	184
6.6	Conclusion.....	189
6.7	Acknowledgements.....	189
6.8	References.....	190
6.9	Supporting Information.....	195
Chapter 7.	Conformational Disorder of Membrane Peptides and Proteins Studied by Solid-State NMR Spectroscopy	
7.1	Abstract.....	197
7.2	Introduction.....	198

7.3	Materials and Methods.....	199
7.4	Results.....	202
7.5	Discussion.....	214
7.6	Conclusion.....	216
7.7	Acknowledgements.....	217
7.8	References.....	217
7.9	Supporting information.....	223
Chapter 8.	Orientation, Dynamics, and Lipid Interaction of an Antimicrobial Arylamide Investigated by ¹⁹ F and ³¹ P Solid-State NMR spectroscopy	
8.1	Abstract.....	227
8.2	Introduction.....	228
8.3	Materials and Methods.....	230
8.4	Results	233
8.5	Discussion.....	242
8.6	Conclusion.....	247
8.7	Acknowledgements.....	247
8.8	References.....	247
8.9	Supporting information.....	252
Chapter 9.	Solid-State NMR Study of β -hairpin Antimicrobial Peptides in Lipopoly-saccharide Incorporated Lipid Membranes: Mechanism of Gram-Selectivity	
9.1	Abstract.....	253
9.2	Introduction.....	254
9.3	Experimental Procedures.....	258
9.4	Results.....	261
9.5	Discussion.....	273
9.6	Acknowledgements.....	276
9.7	References.....	276
9.8	Supporting Information.....	283
Chapter 10.	High-Resolution Orientation and Depth of Insertion of the Voltage-Sensing S4 Helix of a Potassium Channel in Lipid Bilayers	
10.1	Abstract.....	284
10.2	Introduction.....	285
10.3	Results.....	286
10.4	Discussion.....	291
10.5	Materials and methods.....	297
10.6	Acknowledgements.....	301

10.7	References.....	301
10.8	Supporting information.....	306
Chapter 11. General conclusion.....		311
Appendix A. Preparation protocols of oriented lipid membrane samples		
A.1	Glass-plate mechanically-aligned oriented samples.....	313
A.2	Magnetically-aligned bicelle samples.....	315
Appendix B. Paramagnetic Relaxation Enhancement (PRE) membrane-bound peptide sample preparation protocols		
B.1	One-side and two-side Mn(II) membrane sample.....	318
B.2	Cu(II)-bound membrane sample	320
Appendix C. MATLAB codes of separate-local-field (SLF) experiment for orientation		
	Determination of a body-rigid molecule.....	322
Appendix D. Spin diffusion coefficients consolidated from previous research.....		325

Acknowledgements

I've been asking myself 'the meaning of life' question from an early age. Different people will apparently have different answers. The same person may even have different understanding at an older age due to more life experience. Though no satisfactory explanation yet, life could be all about experience, which may be able to come up with an answer after a lifelong attention. In the past five years, I've certainly been enriched by my graduate study and research experience. While completing this thesis, I would like to express my sincere acknowledgement to my professors, colleagues, friends and family.

First of all, I would like to gratefully and sincerely thank my Ph.D. advisor, Dr. Mei Hong. Her solid knowledge and persistent attitude toward scientific research, as well as her unwavering support, has made Mei an excellent advisor to work under. Her deep understanding of NMR theories and broad scientific outlook and knowledge make Mei definitely the one who can well correlate the theory and experiment and teach them to me in both quantitative and qualitative ways. Over the past five years, she has taught me NMR, chemical and biological knowledge as well as a positive attitude towards any scientific activities. Whenever I have a question, Mei is always there with an open door, with an insightful explanation and with a smart and efficient solution. Her enthusiasm and idea of chasing excellence in research encourages me to do my best work and to pursue the highest quality of my graduate projects as well as all of my scientific interests in the future. I also greatly appreciate her strong support for my career development, and sincerely hope our scientific collaboration can continue.

I own many thanks to Dr. Klaus Schmidt-Rohr for his enlightening NMR lectures and lots of helpful discussions on my research. Dr. Xueyu Song, Dr. Emily Smith and Dr. Yan Zhao are ISU professors in my Ph.D. committee. I thank them for guiding my graduate study, providing nice suggestions in POS meetings and offering me help while I'm looking for my future position. Dr. Alan Waring at UCLA and Dr. William F. Degrado at the University of Pennsylvania have provided many high quality samples. I would like to express my deep appreciation to them. Bev, Carlene, Lynette, Renee, Mary and many other staff in the chemistry department have provided me with helpful assistance, which I much appreciate.

I feel so grateful and lucky to have such helpful lab colleagues who provide a constant source of knowledge and inspiration. They are Dr. Rajeswari Mani, Dr. Shenhui Li, Dr. Tim F. Doherty, Dr. Ming Tang, Dr. Sarah D. Cady, Dr. Wenbin Luo, Yuan Zhang, Fanghao Hu, Shuyu (Aaron) Liao, Tuo Wang, Jon Williams in Hong group, and Dr. Jindong Mao, Dr. Xiaowen Fang, Dr. Yanyan Hu, Dr. Xueqian (Sean) Kong, Dr. Evgeny Levine, Dr. Aditya Rawal and Dr. Bosiljka Njegic in Schmidt-Rhor group. I'd like to thank Frank Lange at Martin Luther University Halle-Wittenberg in Germany for our nice collaboration, which inspires many interesting ideas. I also thank Frank and Jon for proof-reading my thesis. I would like to thank all my other friends outside the lab, who I met at ISU, conferences and apartment community in Ames. Their companionship, trust and generous help make my life outside graduate school so colorful.

I would like to extend my thanks to my B.S. and M.S. advisor Dr. Feng Deng, who was the first to bring me into this exciting journey of the SSNMR research. My NMR knowledge and understanding of scientific research have benefited greatly from working with him. His respectable and prudent working attitude and persistence on doing excellent research as a scholar and continued support as a mentor always inspires me to work on SSNMR as my career without any hesitation. It has been a great experience to learn and work with his group members, Dr. Jun Yang, Dr. Shenhui Li, Dr. Guangjin Hou and many others, who are also old good friends in life.

Finally and most importantly, I would like to thank my family, particularly my wife Xiaoyun Zheng (B.A.), who has contribute all of her time to take care of the family in the past years. She is smart, diligent and so talented in mathematics and deserves a promising future in her major. I would also like to thank our son, Rickey Yun Su, for the tremendous joy he brings to us, like the lovely goodbye kiss in the morning and the sincere welcome to Dad's coming home everyday since he can walk. I left home alone at 16 years old to attend the boarding high school. Since then, I've been traveling far away from parents for my study. Now, I find my home wherever my wife and son are. I would like to thank my parents, Maomei Huang and Qiaosong Su, my sister Yonghong Su and my brother-in-law Yaotao Chen, for their unconditional love and support. Although we are not living together, their encouragement and spiritual support through the phone and occasional visits has always been my driving force to take care of my small family.

Chapter 1

Introduction to Nuclear Magnetic Resonance Methodology and Membrane Peptides

1.1 Introduction

Solid-state NMR (SSNMR) spectroscopy is an indispensable way to elucidate the structure and dynamics of membrane peptides and proteins (1-7), most of which have low aqueous solubility for solution NMR and are hopeless to be crystallized for X-ray crystallography. In the following sections, the quantum-mechanical descriptions of the spin state, various NMR interactions and the origin of the NMR signal are introduced. Frequency modulation under MAS is discussed. Examples of multiple-pulse NMR analysis are given to show density operator evolution under dipolar. Various robust SSNMR methods are discussed to show their application in membrane peptide studies. The SSNMR theories and techniques in this chapter will mostly focus on membrane protein studies, specifically about spin 1/2 nuclei including ^1H , ^{13}C , ^{15}N , ^{19}F and ^{31}P . All membrane peptides studied in my graduate research are concisely introduced. Finally, an overview of different types of peptide-containing membrane samples used in my research is given.

1.1.1 Brief quantum-mechanical view of SSNMR (8-13): spin state and interactions

The state of a spin system can be expressed as the density operator, $\hat{\rho}(t)$. It is a quantity defined in statistical quantum mechanics and can be used to calculate the expectation value of a spin system, which reflects the NMR signal or the magnetization, $\bar{M}(t)$:

$$\bar{M}(t) = c \langle \vec{I} \rangle = c \cdot \text{Tr} \langle \vec{\rho} \cdot \vec{I} \rangle \quad (1.1)$$

where $\vec{\rho}$ and \vec{I} are matrix representation of $\hat{\rho}$ and \vec{I} .

NMR interactions are described by nuclear spin Hamiltonian (\hat{H}) (see **Table 1.1**). \hat{H} is an energy operator as can be seen from:

$$\hat{H}|\psi\rangle = E|\psi\rangle \quad (1.2)$$

The time dependence of $\hat{\rho}$ under the effect of \hat{H} can be described by the von Neumann equation:

$$\frac{d\hat{\rho}(t)}{dt} = -\frac{i}{\hbar}[\hat{H}, \hat{\rho}(t)] \quad (1.3)$$

For time-independent \hat{H} , the solution of **equation 1.3** is (8):

$$\hat{\rho}(t) = U(t)\rho(0)U^{-1}(t), \text{ where the propagator } U(t) = e^{-\frac{i}{\hbar}\hat{H}t} \text{ depends only on } \hat{H}.$$

When the following condition is met:

$$[\hat{H}, [\hat{H}, \hat{\rho}(0)]] = \omega^2 \hat{\rho}(0) \dots$$

The solution of the von Newman equation is

$$\hat{\rho}(t) = \rho(0)\cos(\omega t) - \frac{i[\hat{H}, \rho(0)]}{\omega}\sin(\omega t) \quad (1.4)$$

For spin $\frac{1}{2}$ nuclei, NMR interactions (\hat{H}_{total}) include the interactions between a spin system and the external magnetic field (\hat{H}_0) and the applied (\hat{H}_{RF}), and local interactions including chemical shift shielding (\hat{H}_{CS}), dipolar coupling (\hat{H}_D) and scalar coupling (\hat{H}_J) for spin 1/2 nuclei (8-10):

$$\hat{H}_{total} = \underbrace{\hat{H}_0 + \hat{H}_{RF}}_{external} + \underbrace{\hat{H}_{CS} + \hat{H}_D + \hat{H}_J}_{local} \quad (1.5)$$

NMR interactions of spins in solid samples are illustrated in **Figure 1.1**. When nuclear spins are placed in an external magnetic field, the energy level splits due to the different alignments of the spins with respect to B_0 (**Figure 1.1.a**). The population difference between the different energy levels at thermal equilibrium is proportional to the NMR signal. Larger B_0 induces larger energy differences between spin up and down states, giving higher sensitivity. In a classical mechanics view of the Zeeman effect, the spin (or equivalently the magnetization) will precess around B_0 at a frequency, ω_0 . This

so-called Larmor frequency depends on the strength of B_0 and the type of nucleus (γ). The Larmor precession can be demonstrated by quantum mechanics, where ω_0 indicates the strength of Zeeman interaction Hamiltonian (\hat{H}_0).

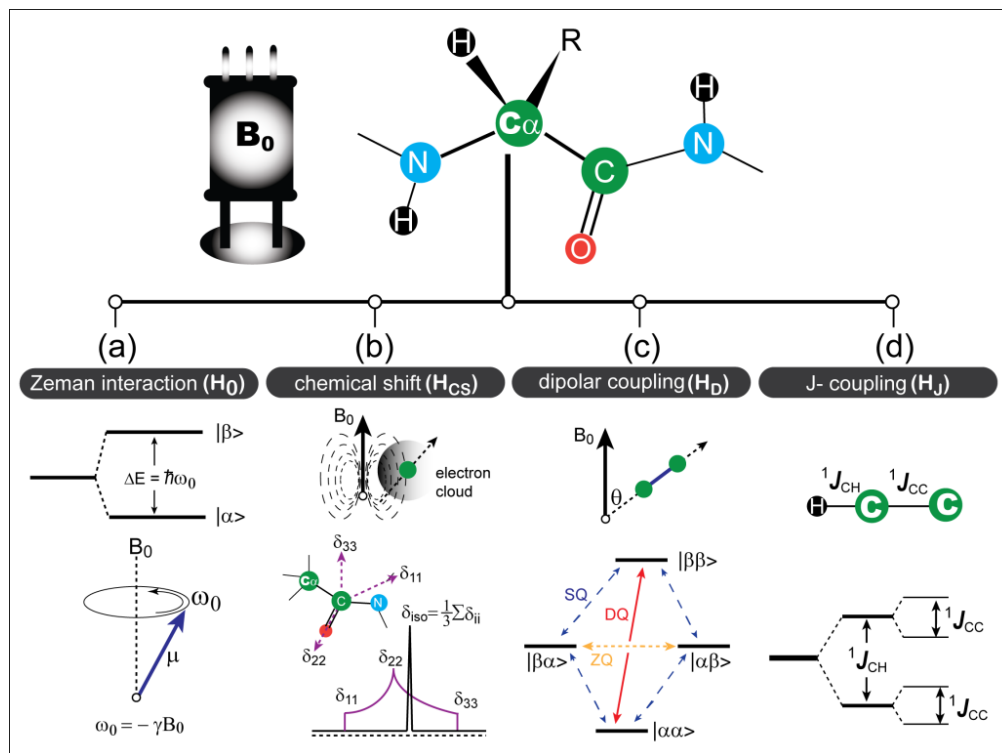


Figure 1.1 SSNMR interactions of spin 1/2 nuclei in a static field. (a) Zeeman interaction (H_0). Top: energy level splitting; Bottom: spin Larmor precession around B_0 . (b) Chemical shift (H_{CS}). Top: interaction between B_0 and local electron current induces an extra magnetic field (B_{local}), which reflects the local magnetic environment and causes perturbation of the Larmor frequency; Bottom: isotropic chemical shifts and three principle values of chemical shift anisotropy. (c) Dipolar coupling (H_D). Top: a dipolar-coupled spin pair in B_0 . Bottom: energy level diagram for a two-spin system and allowed transitions. (d) J-coupling (H_J). J-splittings of an H-C-C coupled system.

An additional magnetic field is generated by electron currents, so each nuclear spin may sense a different effect due to the different electronic environment, causing chemical shift (**Figure 1.1.b**). Chemical shift correlates the atomic magnetic environment with chemical structure, which is why NMR is especially suitable to characterize the atomic-level structure of molecules. Dipolar coupling originates from the direct di-

pole-dipole interaction of the two spins. As illustrated in **Figure 1.1.c**, dipolar coupling causes further splitting of the Zeeman energy states, stimulating zero-quantum (ZQ), single-quantum (SQ), and double-quantum (DQ) transitions, which carry different frequency information and can be directly or indirectly detected. J-coupling is mediated by electrons in the chemical bonds, so it is a through-bond interaction, in contrast to the through-space dipolar interaction (**Figure 1.1.d**). Both J-coupling and dipolar coupling are interactions of coupled spin, so they have similar forms of the spin part in their Hamiltonians (**Table 1.1**)

The Hamiltonian equations, size and field dependence of NMR interactions are summarized in **Table 1.1**. In terms of strength (Hz), the Zeeman interaction is the largest on the scale of a hundred MHz in superconducting magnets. Dipolar coupling and chemical shift anisotropy are smaller, up to tens of kHz. In organic molecules, J-coupling is the weakest interaction with a strength up to hundreds of Hz, which means it can only be observed in high-resolution spectra, e.g. of the isotropic solution sample. While in solid state NMR, it is usually hidden underneath the much stronger dipolar coupling.

Table 1.1. Hamiltonians of NMR spin interactions for spin 1/2 nuclei in solids.

NMR Interactions	Hamiltonian	Size (Hz)	Field dependence
Zeeman interaction	$\hat{H}_0 = -\gamma\hbar\hat{I}_z B_0$	10^7 - 10^8	$\propto B_0$
Chemical shift	$\hat{H}_{CS} = -\gamma\hbar\hat{I}_z \sigma_{zz}^{LF} B_0$	0 - 10^5	$\propto B_0$
Heteronuclear dipolar interaction	$\hat{H}_D^{IS} = -\frac{\hbar\mu_0}{4\pi} \frac{\gamma^I \gamma^S}{r^3} \frac{1}{2} (3\cos^2\theta - 1) 2I_z S_z$	0 - 10^4	independent
Homonuclear dipolar interaction	$\hat{H}_D^{II} = -\frac{\hbar\mu_0}{4\pi} \frac{\gamma^2}{r^3} \frac{1}{2} (3\cos^2\theta - 1) (3I_z J_z - \hat{I} \times \hat{J})$	0 - 10^5	independent
J-coupling	$\hat{H}_J = 2\pi\hbar J_{jk} \hat{I}_j \cdot \hat{I}_k$	0 - 10^3	independent
rf pulse	$\hat{H}_{RF} = -\gamma\hbar B_1 \hat{I}_{x \text{ or } y}$	10^4 - 10^5	$\propto B_1$

In the following part, I will take chemical shift interaction as an example to show truncation of the Hamiltonian, the frequency part (ω_{CS}) and other parameters including the anisotropy parameter (δ_{aniso}), asymmetry parameter (η), isotropic chemical

shift (δ_{iso}), the orientation dependence of anisotropic chemical shift (ω_{cs}^{aniso}) and the time-dependent evolution of the frequency under magic angle spinning (MAS) (8, 12).

The chemical shift interaction can be expressed as: $\hat{H}_{CS} = \gamma \hbar \hat{I} \sigma B_0$, where σ is defined as the second rank chemical shift tensor. The local chemical shielding $\vec{B}_{CS} = -\sigma \vec{B}_0$. This local field interaction is truncated by the strong external B_0 to the non-vanishing parallel term, which is the z -component of \vec{B}_{CS} , $\sigma_{zz}^{LAB} \vec{B}_0^{LAB}$.

$$\text{The truncated chemical shift Hamiltonian is } \hat{H}_{CS} = \omega_{CS} \hat{I}_z = -\omega_0 \sigma_{zz}^{LAB} \hat{I}_z \quad (1.6)$$

In a molecule-fixed principal axis system (PAS) as sketched in **Figure 1.2.b**:

$$\omega_{CS}(\theta, \phi) = -\omega_0 (\sigma_{xx}^{PAS} \sin^2 \theta \cos^2 \phi + \sigma_{yy}^{PAS} \sin^2 \theta \sin^2 \phi + \sigma_{zz}^{PAS} \cos^2 \theta) \quad (1.7)$$

$$\text{The anisotropy parameter, } \delta_{CS} = \sigma_{zz}^{PAS} - \sigma_{iso} \quad (1.8)$$

$$\text{The asymmetry parameter, } \eta = \frac{\sigma_{yy}^{PAS} - \sigma_{xx}^{PAS}}{\sigma_{zz}^{PAS} - \sigma_{iso}} \quad (1.9)$$

$$\text{The isotropic chemical shift, } \sigma_{iso} = \frac{1}{3} (\sigma_{xx}^{PAS} + \sigma_{yy}^{PAS} + \sigma_{zz}^{PAS}) \quad (1.10)$$

Expressed in terms of η and δ , **equation 1.7** can be transformed (8):

$$\omega_{CS}(\theta, \phi) = \omega_{cs}^{iso} + \omega_{cs}^{aniso} = \sigma_{iso} B_0 + \frac{1}{2} \delta_{CS} (3 \cos^2 \theta - 1 - \eta \sin^2 \theta \cos 2\phi) \quad (1.11)$$

Dipolar coupling has a similar expression (12), but $\omega_d^{iso} = 0$ and $\eta = 0$, so

$$\omega_d(\theta) = \delta_d \cdot \frac{1}{2} (3 \cos^2 \theta - 1) \quad (1.12)$$

Thus, the angular dependant components, $\omega_{cs}^{aniso}(\theta, \phi)$ and $\omega_d(\theta)$, indicate the molecular orientation dependence of anisotropic chemical shift and dipolar coupling with respect to B_0 .

As illustrated in **Figure 1.2.a.**, randomly oriented molecules of powder samples have different chemical shift frequencies. The anisotropic chemical shift interaction and dipolar coupling are two dominant line broadening mechanisms in static SSNMR. In or-

der to remove these line broadening factors, a mechanical technique called magic angle spinning (MAS) was developed to spin the sample around an axis tilted by 54.7° from B_0 . Both the anisotropic chemical shift and dipolar coupling frequency is modulated by the second Legendre polynomial, $P_2(\cos\theta) = \frac{1}{2}(3\cos^2\theta - 1)$. When the sample spins at a frequency much larger than the interaction, the anisotropic part disappears and only the isotropic frequency remains. The time-dependent evolution of the NMR frequency under magic angle spinning (MAS) will be discussed below.

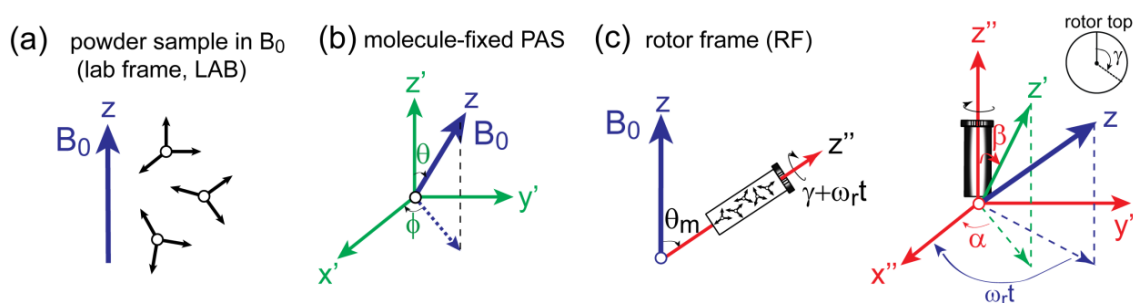


Figure 1.2. (a) Static powder sample in external magnetic field (B_0). Microscopically, molecules have different orientations. (b) The molecule-fixed principle axis system (PAS). (c) Left: macroscopic view of powder sample packed in the rotor, which spins at an angle of θ_m ($\theta_m = \arccos(\sqrt{1/3}) \approx 54.7^\circ$) with respect to B_0 ; Right: conversion from PAS to rotor frame. α , β and γ are the angles between molecule-fixed PAS and rotor frame: α - azimuthal angle, β - polar angle and γ - molecular orientation angle around the rotor axis.

1.1.2 Frequency evolution under magic angle spinning

In the rotor frame as shown in **Figure 1.2.c**, the anisotropic chemical shift frequency (ω_{cs}^{aniso}) can be written in terms of α , β and γ angles as (8):

$$\omega(t) = \delta [C_1 \cos(\gamma + \omega_r t) + C_2 \cos(2\gamma + 2\omega_r t) + S_1 \sin(\gamma + \omega_r t) + S_2 \sin(2\gamma + 2\omega_r t)] \quad (1.13)$$

where $C_1 = -\frac{\sqrt{2}}{2} \sin(2\beta)$, $C_2 = \frac{1}{2} \sin^2 \beta$, $S_1 = S_2 = 0$, for isolated spin pairs, I and S.

The sum of angle γ and $\omega_r t$ can be understood in the sense that both angles are rotational angles around the rotor axis. The periodicity due to MAS creates spinning sidebands (SSB), whose peak envelope at slow MAS represents the CSA powder pattern

(8). To eliminate SSB for spins with large CSA, one can use higher spinning speed or implement the total suppression of sidebands (TOSS) technique (14). **Equation 1.13** also indicates that the frequency becomes time-dependent under MAS. During t_1 , the total phase angle change $\Phi(t)$, which describes the t -dependent precession frequency of magnetization (M_0), is

$$\begin{aligned}\Phi(t_1) &= \int_0^{t_1} \omega(\alpha, \beta, \gamma, t) dt = \int_0^{t_1} \delta [C_1 \cos(\gamma + \omega_r t) + C_2 \cos(2\gamma + 2\omega_r t)] dt \\ &= C_1' [\sin(\gamma + \omega_r t_1) - \sin \gamma] + C_2' [\sin(2\gamma + 2\omega_r t_1) - \sin 2\gamma]\end{aligned}\quad (1.14)$$

After full rotation periods, $t_1 = n\tau_r$ and $n = 0, 1, 2, \dots$,

$$\Phi(n\tau_r) = C_1' [\sin(\gamma + n \cdot 2\pi) - \sin \gamma] + C_2' [\sin(2\gamma + 2n \cdot 2\pi) - \sin 2\gamma] = 0$$

The same derivation applies to the time evolution of dipolar coupling frequency (ω_d). At the end of each rotor period, the chemical shift anisotropy and the dipolar coupling are refocused to zero. Sample spinning is the only way to remove CSA, while dipolar coupling can also be efficiently eliminated by dipolar decoupling pulses. When the spinning frequency is not significantly larger than the dipolar coupling, e.g. rigid C-H bond under 20 kHz MAS, heteronuclear dipolar decoupling by radio-frequency irradiation is absolutely necessary to ensure narrow lines.

Equation 1.14 also shows that the dipolar coupling is not refocused to zero when $t_1 \neq n\tau_r$, which allows the magnetization to evolve under dipolar coupling interaction within one rotor period. This inspires the idea of dipolar coupling measurement using dipolar-chemical shift (DIPSHIFT) experiments (15-16), which will be discussed in **section 1.6**. As an example to show how Hamiltonians of spin interactions and rf pulses manipulate the magnetization under MAS, the density operator derivation of this experiment will be illustrated in the same section. Moreover, if an rf pulse is placed in the middle of the rotor period to interfere with the magnetization evolution, the phase $\Phi(t)$ is no longer equal to zero at the end of each rotor period, causing the so-called dipolar recoupling. This is the original idea of a widely used dipolar recoupling pulse scheme, rotational echo double resonance (REDOR) (17), which will be discussed in **section 1.3**.

1.2.3 NMR sensitivity and its dependence on type of nucleus (γ), static field (B_0) and temperature (T)

NMR signal originates from the population difference of the total spin number at each energy state splitted by the Zeeman interaction (8-13). Taking spin 1/2 nuclei for example, the initial magnetization (M_0) is the magnetization difference between the two states, $|\alpha\rangle$ and $|\beta\rangle$:

$$M_0 = -\frac{1}{2}(N_{|\beta\rangle} - N_{|\alpha\rangle})\gamma\hbar \quad (1.15)$$

$$\text{where } N_{|\alpha\rangle} = Ne^{(-E_{|\alpha\rangle}/zKT)} \text{ and } N_{|\beta\rangle} = Ne^{(-E_{|\beta\rangle}/zKT)}$$

Using (1.2) and applying the high T approximation ($\Delta E \ll KT$, at practical experimental T),

$$\frac{N_{|\beta\rangle}}{N_{|\alpha\rangle}} = \exp\left[\frac{E_{|\beta\rangle} - E_{|\alpha\rangle}}{kT}\right] = \exp\left[\frac{\Delta E}{kT}\right] = \exp\left[\frac{-\hbar\omega_0}{kT}\right] \approx 1 - \frac{\hbar\omega_0}{kT} \quad (1.16)$$

$$\text{where } \Delta E = E_{|\beta\rangle} - E_{|\alpha\rangle} = -\hbar\omega_0.$$

For ^1H , when $T = 300 \text{ K}$ and $B_0 = 9.5 \text{ T}$, $\frac{\hbar\omega_0}{kT} \approx 0.000064$. The calculation shows,

even for a high- γ spin like ^1H , Zeeman interaction causes only $\sim 10^{-5}$ difference between populations of two energy levels. This indicates extremely low sensitivity, which is why NMR is regarded as an insensitive technique compared with other analytical methods. Nevertheless, NMR is still powerful thanks to its ability to detect atomic-level structure and motions in a large range of time scales from ns to s.

To calculate M_0 ,

$$N_{|\beta\rangle} - N_{|\alpha\rangle} = N \frac{E_{|\beta\rangle} - E_{|\alpha\rangle}}{2KT} = N \frac{\Delta E}{2KT} = N \frac{\gamma\hbar B_0}{2KT} \quad (1.17)$$

So, using (1.15) and (1.17),

$$M_0 = -\frac{1}{2}(N_{|\beta\rangle} - N_{|\alpha\rangle})\gamma\hbar B_0 = \frac{N(\gamma\hbar)^2 B_0}{4KT} \quad (1.18)$$

The signal-to-noise ratio,

$$\frac{S}{N} = \sqrt{\omega_0} \cdot M_0 \propto \frac{n \cdot (\gamma)^2 \cdot (B_0)^2}{T}, \text{ considering } noise \propto \sqrt{\omega_0} \quad (1.19)$$

Equation 1.18 and **1.19** implies many routes to improve NMR intensity (M_0) and sensitivity ($\frac{S}{N}$). For example, one can pack more sample to reach a larger spin number (n). One can also reduce the temperature to increase the Boltzmann factor. Higher magnetic field (B_0) can certainly contribute, e.g. a sensitivity increase by 3.4 times from a 400 MHz to a 900 MHz spectrometer. The equations also show that nuclei with high γ (such as electron, ^1H and ^{19}F) have higher intensity and better sensitivity, which can be utilized by direct observation or indirect detection via polarization transfer as shown in **Figure 1.3**.

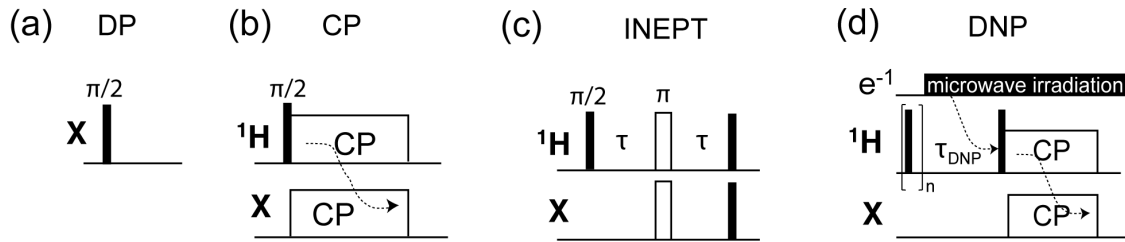


Figure 1.3 Pulse schemes of (a) Direct polarization (DP) and (b-d) signal enhancement techniques via magnetization transfer: (b) Cross polarization (CP). (c) Insensitive nuclei enhanced by polarization transfer (INEPT), which establishes connectivity through J-coupling. The magnetization transfer can be achieved if $\tau = \frac{1}{4 \cdot {}^1J_{HX}}$. (d) Dynamic nuclear polarization (DNP) (18,19).

Magnetization is transferred from electron to ^1H via continuous microwave irradiation. Several 90 degree pulses on ^1H channel are used to destroy ^1H magnetization before DNP.

High- γ and naturally abundant nuclei, such as ^1H and ^{19}F , can be directly excited using a single pulse to yield high intensity sequences (**Figure 1.2.a**). For several other spins like ^{13}C and ^{15}N , their magnetization can be indirectly obtained via magnetization transfer from ^1H (**Figure 1.3.b-d**). For example, ^1H magnetization can be transferred to bonded or nearby X spin via cross polarization when the Hartmann-hahn match condition ($\gamma_S \cdot B_S = \gamma_H \cdot B_H$, for spin $\frac{1}{2}$ S spin) is met. ^1H -X dipolar coupling drives cross polariza-

tion, so the transfer efficiency will largely depend on $^1\text{H-X}$ distance and mobility. A CP contact time of 0.5 ms to 3 ms can be used to gain sensitivity from spacial close protons, but one needs to realize that the magnetization transfer time could not be too long due to $T_{1\rho}$ relaxation. In case of a mobile system, which has a weak $^1\text{H-X}$ dipolar coupling, similar magnetization transfer can be achieved through J-coupling interaction using INEPT (**Figure 1.3c**). Theoretically, both CP and INEPT can enhance the signal of S spins by a factor of $\frac{\gamma_{^1\text{H}}}{\gamma_S}$, which is equal ~ 4 in case of ^1H to ^{13}C transfer. Moreover, the shorter ^1H T_1 allows the use of shorter recycle delays in practical experiments. However, one should realize that CP is not able to give fully quantitative intensities due to the through-space magnetization transfer. Even higher signal enhancement can be achieved if the magnetization is transferred from electrons, which has 658 times larger γ than ^1H . This idea is realized by a revolutionary method called dynamic nuclear polarization, DNP, which has shown as much as ~ 330 times higher ^{13}C intensity enhancement in practice (66,67).

As representatively illustrated in **Figure 1.4.a**, the NMR FID signal is featured as a superposition of sinusoidal oscillations at many frequencies, which decay as time goes on due to relaxation. The time-domain FID is converted to frequency domain signals by Fourier transformation (**Figure 1.4.c**). For example, the simplest NMR signal of a single frequency, ω_0 (8, 11, 13):

$$S(t) = f(t) = e^{i\omega_0 t} \xrightarrow{FT} F(\omega) = \int_{-\infty}^{+\infty} f(t)e^{-i\omega t} dt = 2\pi\delta(\omega - \omega_0) \quad (1.20)$$

In practice, the FID is recorded in terms of discrete digital points, so the numerical discrete FT (DFT) will be applied. Also, a certain period of acquisition time (t_{aq}) rather than infinite time domain is used for signal detection, which behaves like applying a box function and causes signal truncation. The FT of a box function yields a sinc function, which appears as “cut-off wiggles” in the spectrum.

As shown in **Figure 1.4.b**, rotational echoes show up at the end of each rotor period because the orientation of molecules in the rotor goes back to the original position periodically. For a spin system with large CSA under slow MAS, the orientation could be largely different at the beginning of each detection (different γ angles), giving unequal

magnetization. This may cause severe phase distortion. To solve the problem one can spin much faster to shorten the rotor period (τ_r) or to implement a γ -averaging (or γ -integral) period before detection (8).

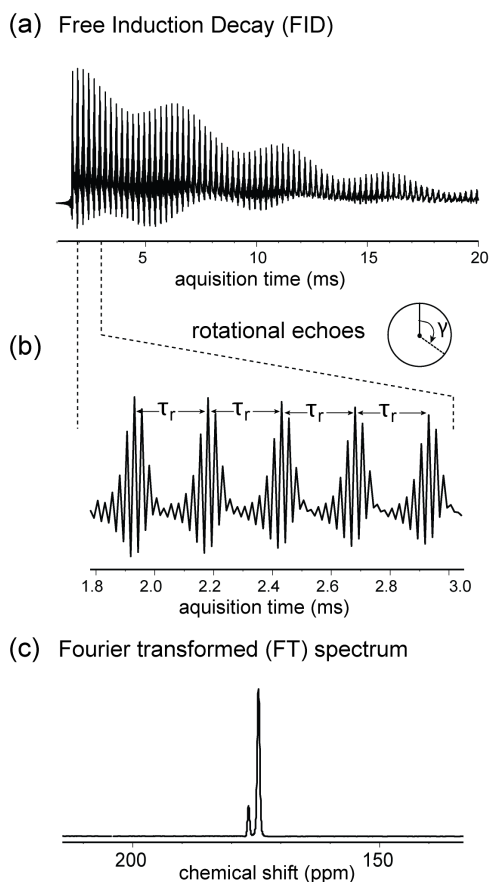


Figure 1.4 (a) Time-domain NMR signal of a 1D NMR experiment. (b) Periodic rotational echoes synchronized with rotor period (τ_r) when a spin rotates back to its original orientation. (c) Frequency-domain (shown in ppm) NMR signal after Fourier transformation. The experiment is a cross polarization experiment of a crystallized ^{13}C O-labeled glycine.

1.1.4 Bio-macromolecules studied in this dissertation.

The goal of membrane peptide and protein studies using SSNMR is to determine atomic- or molecular- level structure and dynamics and elucidate their relation to biological functions. **Figure 1.5.** depicts the rich structural and dynamic features of membrane peptides or proteins. Membrane proteins conduct their biological functions in lipid membranes, which gives rise to many structural features different from globular proteins. For

example, membrane proteins usually have a certain topology, defined as insertion depth and orientation. They interact with lipid through charge-charge interaction or hydrophobic interaction. Moreover, the impact of protein on the lipid membrane can be functionally relevant. This may include membrane disruption, membrane fusion and pore formation.

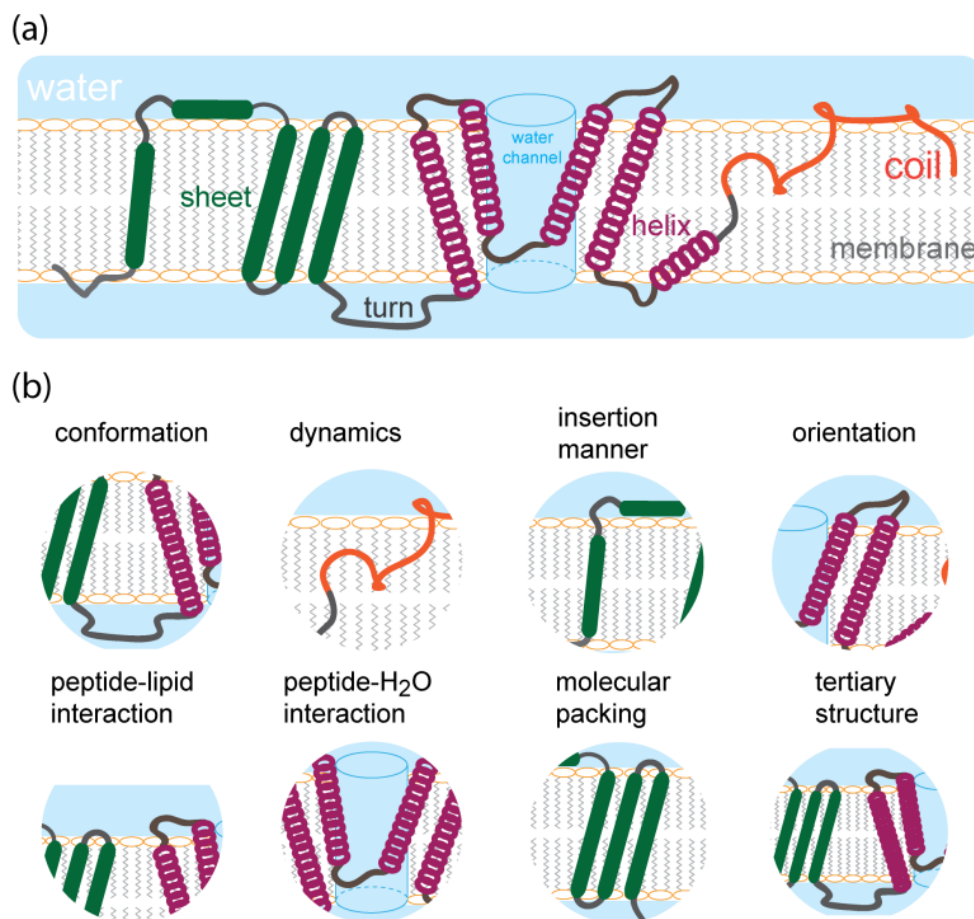


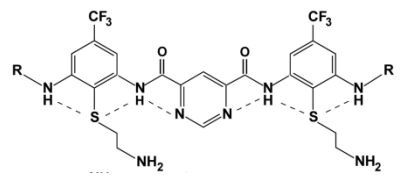
Figure 1.5. (a) A hypothetical membrane protein with domains rich in various conformations, including α -helix, β -sheet, turn and random coil. (b) Biofunctionally related structural and dynamics of NMR interest, using the model protein in (a) as an example.

We have successfully demonstrated the power of SSNMR to study all of these structural and dynamic aspects in many interesting membrane peptides in my PhD research, including two cell-penetrating peptides (CPP) (20, 21), two antimicrobial peptides

(AMP) (22), an antimicrobial drug (23), the gating helix (S4) of a K^+ voltage channel (24) and the transmembrane 1H channel of influenza M2 protein (25). Their origins, biological functions, amino acid sequences and our research motivations are concisely summerized in **Table 1.2**. A detailed discussion of these can be found in a review paper as **chapter 3**.

In the following sections, I'll discuss many NMR methods that have been widely applied and/or improved in my study. In **section 1.2**, I will show how to obtain NMR parameters including chemical shifts and torsion angles and how they are used to determine the protein secondary structure. In **section 1.3**, dipolar-based distance measurement techniques are discussed. Paramagnetic relaxation enhancement NMR, which is used to quantitatively determine long-range distances, is discussed in **section 1.4**. The quantitative distance dependence of PRE is fully derived. In **section 1.5**, I will show how to measure dynamic parameters including dipolar order parameters, CSA and various NMR relaxation times.

Table 1.2. Membrane-active bio-macromolecules studied in my graduate research.

Category	Bio-functions	Bio-macromolecules	Chemical Structure	Research Motivation
Cell-penetrating peptides (CPP)	Delivery of bio-active cargos into cell without disrupting the membrane	Antp(43-58), called penetratin <i>Origin: the 3rd helix of Antennapedia Homeodomain</i>	RQIKIWFQNRRMKWKK	to study the structure basis of membrane translocation, and to study the conformational disorder of membrane proteins
		HIV Tat(48-60), called TAT <i>Origin: the basic domain of Tat protein of HIV-1 virus</i>	GRKKRRQRRRPPQ	
Antimicrobial peptides (AMP)	New generation of antibiotics, with broad spectrum antimicrobial ability and selectivity.	PG-1 <i>Origin: porcine leukocytes</i>	RGGRLCYCRRRFCVVCVGR	to study the antimicrobial mechanism and bacterial gram-selectivity
		IB484 <i>Origin: a charge-reduced PG-1 mutant</i>	HWRLCYCRPKFCVVCV	
Antimicrobial oligomers (AMO)	New generation of antibiotics, with simple and robust organic structure.	PMX30016 <i>Origin: synthesized antimicrobial species</i>		to study the antimicrobial mechanism
Voltage-gated K ⁺ channel (Kv)	K ⁺ transport in eukaryotic cells	KvAP S4 <i>Origin: the 4th helix of the KvAP protein, responsible for voltage gating</i>	LGLFRLVRLLRGLRILLII	to study the orientation and lipid-interaction of the gating helix
Transmembrane proton channel	pH-gated ¹ H channel of influenza virus membrane	M2TM <i>Origin: transmembrane domain of influenza virus M2 protein</i>	SSDPLVVAASIIGILHLILWILDRL	to study Cu ²⁺ -bound structure.

1.2 Secondary Structure Determination

Protein conformation describes the local ribbon structure, defined by the backbone torsion angle (ϕ, ψ). Typical secondary structures are α -helix, β -sheet and random coil, which are distinguished by their hydrogen bonding patterns. For example, α -helix describes a right-handed (natural form) coiled structure, which forms intramolecular hydrogen bonds between backbone N_i-H_i group of the residue i and the backbone $C_{i+4}=O$ group of residue $i+4$. A complete α -helical turn is composed of 3.6 residues. A general backbone-extended conformation is called β -strand. If packed in the manner of parallel or antiparallel through intermolecular hydrogen bonds, another regular conformation called β -sheet is formed. Many peptides and proteins adopt random-coil structure, which is an unstructured conformation without inter- or intra- molecular hydrogen bonds. Protein conformation is a crucial structural property related to the biological function. For example, many diseases, such as Alzheimer's disease, are caused by the protein misfolding and forming highly aggregated β -sheet amyloid fibrils.

As will be discussed in **section 1.3**, chemical shift is induced by the local magnetic field and thus reflects the local structure. Chemical shifts of CO, $C\alpha$, $C\beta$ and $N\alpha$ are very sensitive to the conformation of peptides and proteins. For example, compared with β -sheet conformation, CO/ $C\alpha$ chemical shifts of α -helix are downfield larger by ~ 2 -5 ppm. Thus, protein conformation can be identified by examining the secondary chemical shifts of CO, $C\alpha$, $C\beta$ and $N\alpha$ peaks. The secondary chemical shift is obtained by comparing the experimental value with the database value of random coil conformation (26-28):

$$\delta_{iso}^{secondary} = \delta_{iso}^{experimental} - \delta_{iso, coil}^{database} \quad (1.21)$$

Compared with other conformation determination methods like circular dichroism (CD), the NMR chemical shifts are site-specific and can more accurately reflect protein conformation. Due to peak overlap issue of uniformly ^{13}C , ^{15}N -labeled systems, chemical shifts are obtained using two- or three- dimensional homo- or hetero- nuclear correlation experiments. In the following, I'll discuss many robust two-dimensional correlation techniques. A uniformly ^{13}C ,

^{15}N -labeled model tripeptide (29-30), f-MLF-OH, is used to illustrate the spectra measured by various NMR methods.

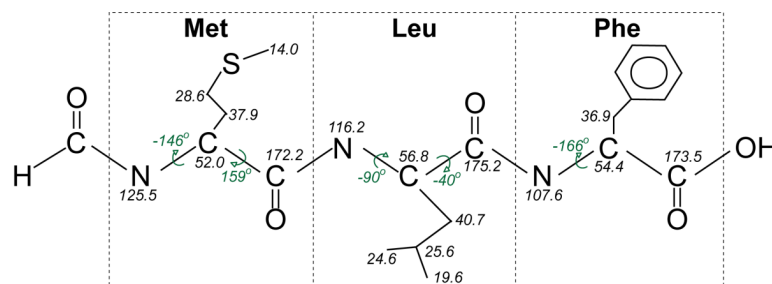


Figure 1.6. Molecular structure of crystalline tripeptide formyl-Met-Leu-Phe-OH (f-MLF-OH). ^{13}C and ^{15}N chemical shifts are indicated in ppm. The backbone torsion angles are shown in green.

1.2.1 Chemical shift assignment from 2D homonuclear correlation NMR

Many 2D ^{13}C - ^{13}C homonuclear correlation techniques have been applied in my thesis research. These includes proton driven spin diffusion (PDS), dipolar-assisted rotational resonance (DARR) (31), double-quantum filtered correlation spectroscopy (COSY), J-based constant time COSY (CT-COSY), incredible natural abundance double quantum transfer experiment (INADEQUATE) (32), most of which are listed in **Figure 1.7**.

In the PDS/DARR experiment (**Figure 1.7.a**), the magnetization is transferred via CP from ^1H and then flipped by a $\pi/2$ pulse to the z -direction to allow ^{13}C - ^{13}C spin diffusion. A mixing time of 20-60 ms can be use to yield intra-residue ^{13}C - ^{13}C correlation. All intra-residue correlations of f-MLF-OH are nicely observed in the spectrum shown on right of **Figure 1.7.a**. For membrane peptides, to eliminate the overlapping lipid signals, double-quantum filtration (e.g. SPC-5 (33)) can be applied during the ^{13}C - ^{13}C polarization transfer period as shown in the DQ-COSY pulse sequence (**Figure 1.7.b**). As shown in the f-MLF-OH DQ-COSY spectrum, this method is different from PDS/DARR and correlates directly bonded carbons since the DQ coherence is excited between two adjacent ^{13}C spins. If t_1 evolution happens in the middle of the DQ period, a correlation of DQ frequency ($\omega_1 + \omega_2$) and SQ frequency (ω_1 or ω_2) can be established as shown in **Figure 1.7.c**. The corresponding spectrum does not have diagonal peaks. As one advantage, this technique can indicate the ^{13}C

connectivity. The enlarged DQ dimension could have better resolution to distinguish close peaks in the indirect dimension of other SQ-SQ correlation methods. These DQ experiments correlate adjacent carbons, e.g. intra-residue $C\alpha$ and $C\beta$, thus are suitable to characterize the conformational disorder of membrane peptides as we studied in **Chapter 7**.

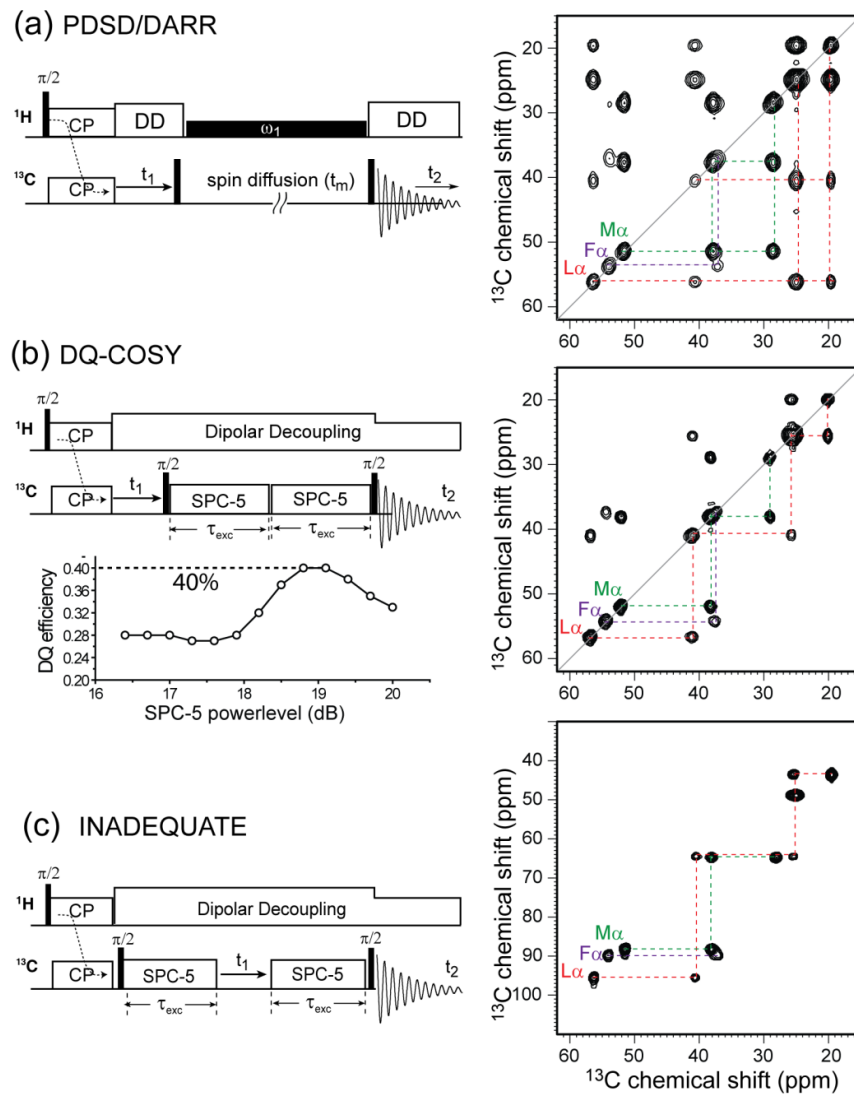


Figure 1.7. Pulse sequences (left) and representative spectra (right) of 2D ^{13}C - ^{13}C homonuclear correlation experiments. (a) Proton-driven spin diffusion (PDS) if ^1H decoupling is off during mixing period, or dipolar assisted rotational resonance (DARR) if ^1H decoupling ($\omega_1 = \omega_r$) is on. (B) Double-quantum COSY experiment. The DQ efficiency dependence on SPC-5 power level is tested under 5.3 kHz MAS and 81 kHz ^1H decoupling. The maximum DQ efficiency is $\sim 40\%$ of CP intensity. (c) Dipolar INADEQUATE experiment. It gives intraresidue carbon connectivity.

1.2.2 Chemical shift assignment from 2D heteronuclear correlation NMR

Heteronuclear correlation (HETCOR) techniques are used to correlate different nuclei in a 2D mode. These methods have their own advantages compared with homonuclear correlation experiments discussed in section 1.2.1. For example, the backbone ^{15}N peaks are heavily overlapped for residues adopting the same conformation. The peak overlap issue may not be well solved in 2D ^{15}N - ^{15}N correlation since most amino acids don't have many ^{15}N groups (other than the backbone ^{15}N) to yield cross peaks. Another issue for is that ^{15}N - ^{15}N dipolar coupling is also much weaker than ^{13}C - ^{13}C spin pairs due to the small γ of ^{15}N spins, so 2D ^{15}N - ^{15}N correlation spectra could not yield high cross peak intensity.

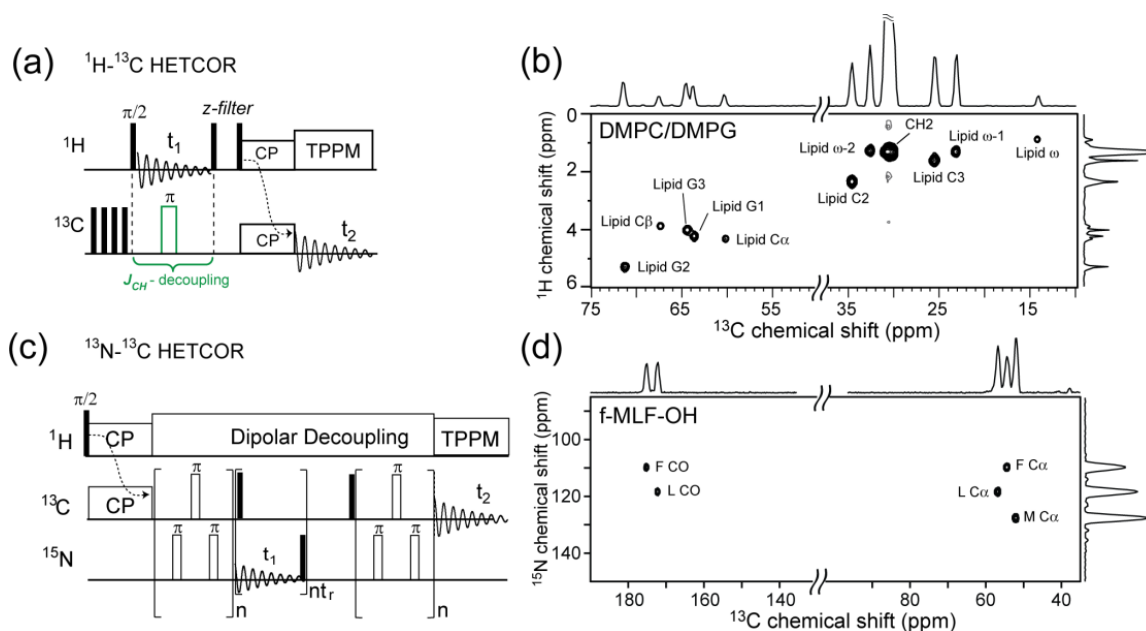


Figure 1.8. 2D ^1H - ^{13}C HETCOR pulse sequence (a) and spectrum (b) of hydrated DMPC/DMPG membrane. 2D ^{15}N - ^{13}C HETCOR pulse sequence (c) and spectrum (d) of f-MLF-OH.

In my thesis research two kinds of heteronuclear dipolar correlation experiments have been applied, including J-decoupled C-H HETCOR (21) and N-C HECTOR (35). The C-H correlation pulse sequence is shown in **Figure 1.8.a**. ^1H and ^{13}C magnetization evolve during t_1 and t_2 period, respectively. We implemented a 180° echo in the t_1 period to refocus the evolution of the C-H scalar coupling. Without J-decoupling, the ^1H peaks in the indirect dimension will suffer from J-splitting by ^{13}C . This technique has helped the chemical shift

assignment of TAT peptide at high temperature as studied in **Chapter 3**. Even without ^1H - ^1H homonuclear decoupling, TAT peaks are well-resolved due to its fast averaging motion as an unstructured peptide. A ^{13}C - ^1H HETCOR spectrum of mobile lipids is shown on the right. ^{15}N and ^{13}C are correlated using N-C HETCOR, which transfer the magnetization between ^{15}N and ^{13}C by using the rotor-synchronized REDOR blocks. As can be seen from the ^{15}N - ^{13}C HECTOR spectrum of f-MLF-OH, all possible one-bond N-C correlations are well established.

1.2.5. Other parameters to identify secondary structure

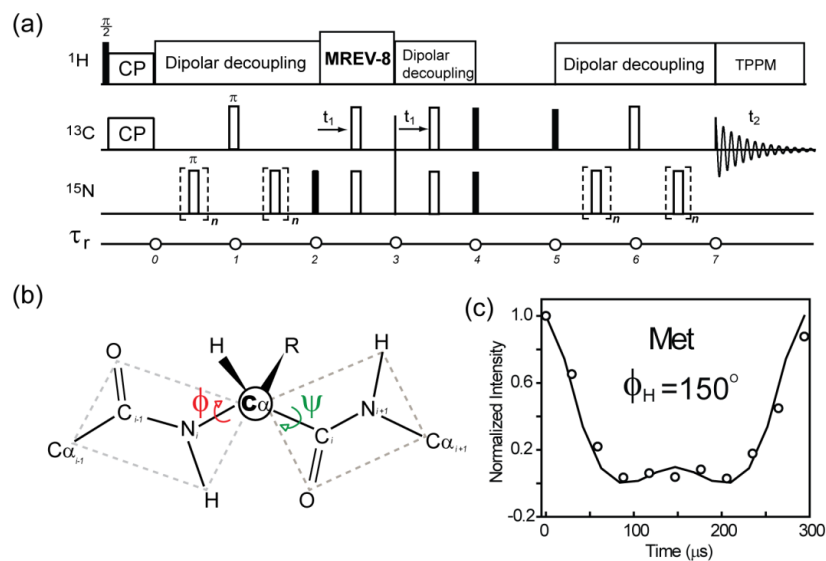


Figure 1.9. (a) HNCH pulse sequence to measure ϕ_H (36), which can be used to calculate ϕ torsion angle by using the equation $\phi = \phi_H + 60^\circ$. (b) Definition of torsion angles of peptide bonds. (c) HNCH curve fitting of Met residue of f-MLF-OH. The data is acquired at 3.4 kHz MAS. Semi-windowless MREV-8 is applied for H-H homonuclear dipolar decoupling. One-bond CH and NH dipolar coupling constants at rigid limit are 22.7 kHz and 10.5 kHz, respectively.

Secondary structure vs. torsion angles. α -helical and β -sheet structure have characteristic backbone torsion angles, ϕ and ψ , which are defined as the dihedral angles of $\text{C}'_{i-1}\text{N}_i^\alpha\text{C}_i^\alpha\text{C}'_i$ and $\text{N}_i^\alpha\text{C}_i^\alpha\text{C}'_i\text{N}_{i+1}^\alpha$, respectively, as shown in **figure 1.9.b**. Representative α -helical torsion angles in the Ramachandran plot are $\phi \in (-40^\circ, -100^\circ)$ and

$\varphi \in (-40^\circ, -65^\circ)$. The β -sheet torsion angles are $\phi \in (-80^\circ, -120^\circ)$ and $\varphi \in (120^\circ, 170^\circ)$ (68). ϕ and ψ angles can be measured using HNCH (36) and NCCN (37), respectively. HNCH correlates the $H_i^{N\alpha} - N_i^\alpha$ and $C_i^\alpha - H_i^{C\alpha}$ dipolar couplings and measure $H_i^{N\alpha} N_i^\alpha C_i^\alpha H_i^{C\alpha}$ angle (ϕ_H), which can be used to calculate the ϕ angle using the following equation:

$$\phi = \phi_H + 60^\circ$$

The HNCH pulse sequence and example of ϕ_H^{Met} measurement of f-MLF-OH are shown in **Figure 1.9.a** and **c**, respectively. Both experiments need to be conducted at low temperature to freeze any backbone motion. Torsion angles are more direct parameters to report secondary structure than chemical shifts. We've applied HNCH method to study TAT in order to see the correlation between the torsion angles and random coil conformation (unpublished data).

Secondary structure vs. dynamics. The secondary structure can also be correlated with different dynamics. For well-defined α -helical and β -sheet structure, the backbone species are usually relatively rigid due to the intra- or inter-molecular hydrogen bonding. For highly dynamic random coil or turn conformation, their backbone groups are expected to be mobile. Motional rates and amplitude can be measured as auxiliary data to identify the conformation.

1.3 Dipolar-Based Distance Measurement

Distance is an important parameter to elucidate the protein structure, domain assembly, and protein-lipid interaction. For example, short and long distance constraints are crucial to establish the tertiary structure after obtaining the secondary structure from chemical shifts or torsion angle measurement. As shown in the \hat{H}_D^{IS} equation in **Table 1.1**, the dipolar coupling constant is distance dependence ($D_{IS} = -\frac{\hbar\mu_0}{4\pi} \frac{\gamma^I \gamma^S}{r^3} \propto r^{-3}$), so many dipolar-coupling based methods are developed to yield distance information, including the direct heteronuclear dipolar coupling measurement by rotor-synchronized heteronuclear dipolar recoupling and dipolar driven spin diffusion among homonuclear spins.

1.3.1 Quantitative heteronuclear distance measurement using REDOR

As shown by **equation 1.14**, dipolar coupling evolution is refocused to zero at the end of each rotor period under relatively fast MAS. To recover dipolar coupling which is averaged by MAS, π pulses are applied at every half rotor period on the S channel (^{31}P in the listed case) as shown in **Figure 1.10**. Consider the first rotor period (17),

$$\Phi(\tau_r) = \int_0^{\tau_r/2} \omega_d(\alpha, \beta, t) dt - \int_{\tau_r/2}^{\tau_r} \omega_d(\alpha, \beta, t) dt = \frac{\sqrt{2}d_{IS}}{\pi} \sin \alpha \sin 2\beta \quad (1.22)$$

The non-zero $\Phi(t)$ indicates the non-vanishing \hat{H}_D^{IS} . So, the evolution of initial magnetization, \hat{I}_x (of ^{13}C spin in the listed case), under \hat{H}_D^{IS} in one rotor period is:

$$\rho(0) = \hat{I}_x \xrightarrow{\hat{H}_D^{IS} = \omega_{IS} 2\hat{I}_z \hat{S}_z} \rho(\tau_r) = \hat{I}_x \cdot \cos(\omega_{IS}^D \tau_r) + 2\hat{I}_y \hat{S}_z \cdot \sin(\omega_{IS}^D \tau_r)$$

The accumulated total phase change after $N\tau_r$ time period is:

$$\Phi(N\tau_r) = \omega_d(\alpha, \beta, t) \cdot N\tau_r = \frac{N\sqrt{2}d_{IS}}{\pi} \sin \alpha \sin 2\beta \quad (1.23)$$

The NMR signal of I spin after applying multiple π pulses on S channel is

$$S(N\tau_r) = \text{tr} \left\{ \rho(N\tau_r) \cdot \hat{I}_x \right\} = \text{tr} \left\{ \hat{I}_x \right\} \cdot \cos(\Phi(N\tau_r)) = S(0) \cdot \cos(\Phi(N\tau_r))$$

$$\text{or, } \frac{S(N\tau_r)}{S(0)} = \cos(\Phi(N\tau_r)) \quad (1.24), \quad \text{where } S(0) \text{ is the NMR signal of I spin}$$

right after CP and without π pulses on S spin.

Apply powder averaging for a solid sample,

$$\frac{S(N\tau_r)}{S(0)} = \frac{1}{2\pi} \cdot \int_0^{2\pi} \int_0^{\pi/2} \cos(\Phi) \sin \beta d\alpha d\beta \quad (1.25)$$

Equation 1.25 shows the dipolar coupling modulated intensity of I spin. By measuring the dephased intensity at various dipolar recoupling time ($N\tau_r$), the dipolar coupling constant (d_{IS} , in **equation 1.22** of $\Phi(N\tau_r)$) can be obtained to extract I-S distance.

The above derivations show how REDOR can measure heteronuclear distance. This dipolar recoupling idea by Gullion and Schaefer should be greatly appreciated (17). Theoret-

ically, these π -trains can also be applied in the observation channel, while in practice they are used to irradiate the spins on the background (or so-called dephasing) channel to avoid too many pulses on the detection channel, as shown in **Figure 1.10.a**. For uniformly labeled proteins, the undecoupled J-coupling of adjacent spin pair will also modulate the intensity of the detection channel. The J-coupling modulation can be deducted in simulation and can also be experimentally suppressed by selective excitation (38,39). For this purpose, a soft Gaussian pulse or rectangular pulse can be applied in the center of the REDOR period as shown in **Figure 1.10.a** and **b**. On the dephasing channel, one needs to ensure the effective rf excitation of spins with a large CSA or spectral window, such as ^{15}N and ^2H .

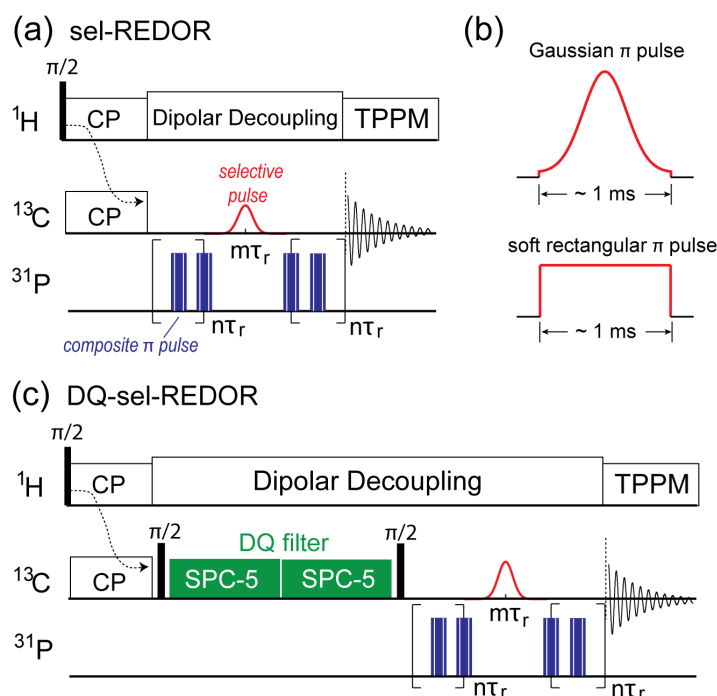


Figure 1.10. Pulse sequence of (a) sel-REDOR (38,39) and (b) DQ-sel-REDOR (40). (c) Selective Gaussian (top) and soft rectangular (bottom) pulse implemented in the middle of the REDOR period on direct detection channel or indirect dephasing channel. Composite π pulses ($90^\circ_{90^\circ}180^\circ_{90^\circ}90^\circ_{90^\circ}$) are used in the π -pulse train to eliminate the pulse imperfection.

The soft π pulse also serves to refocus the isotropic chemical shift evolution. It can also be applied to the dephasing spins to selectively excite the peak of interest. Due to the narrow band excitation, the implementation of a soft Gaussian pulse yield 65% intensity of

CP. For a membrane peptide or protein system, the peak of interest sometimes overlaps with lipid resonance. In order to get rid of the lipid peaks, a DQ-filter is implemented before REDOR period (40). We have shown a successful application of this DQ-sel-REDOR in penetratin study to obtain reliable distance between lipid ^{31}P and Ile $\text{C}\delta 1/\gamma 2$, which completely overlaps with the broad lipid ω peak at ~ 14 ppm at low temperature. One should expect as low as 10 % intensity after DQ excitation and soft pulse selection.

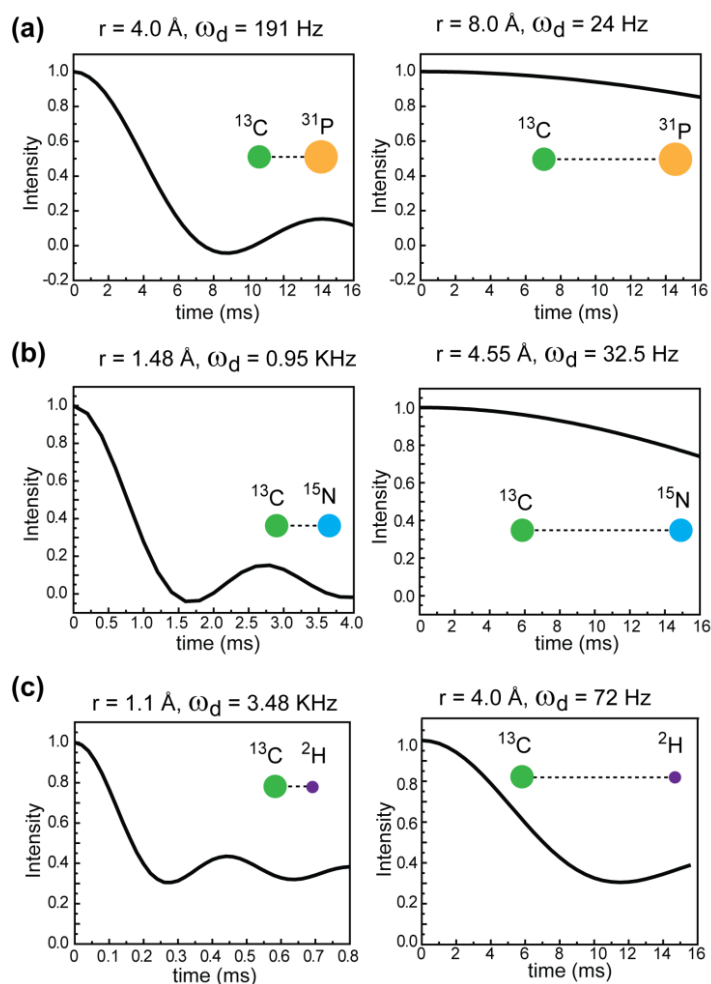


Figure 1.11. REDOR dephasing curves of various dipolar coupled spin pairs at different distances. (a) ^{13}C and ^{31}P . (b) ^{13}C and ^{15}N . (c) ^{13}C and ^2H .

Figure 1.11. shows the REDOR curves of representative dipolar pairs. In (a), a dephasing curve to represent short ^{13}C - ^{31}P distance of 4 \AA is plotted. This short distance has

been observed in many membrane-active peptides in our research, including CPPs, AMPs and a Kv channel. We fit the experimental data using a combination of a short (4 – 5 Å) and long distance (7 – 8 Å). This represents the decay curvature and correlates well with the fact that the guanidinium-phosphate interaction is relatively weak. A ^{13}C - ^{31}P distance of ~ 8 Å usually represents the backbone carbon to phosphate distance. Any ^{13}C - ^{31}P distance longer than ~ 10 Å is not detectable by REDOR due to the very weak dipolar coupling. In (b), ^{13}C - ^{15}N distances of 1.48 Å and 4.55 Å are shown, representing the cases of directly bonded ^{13}C - ^{15}N and backbone carbon to sidechain ^{15}N (e.g. histidine), respectively. In (c), REDOR curves are shown for the directly bonded and a long-distance ^{13}C - ^2H .

1.3.2 Spin diffusion methods to determine homonuclear distance

Homonuclear distances can be qualitatively or semi-quantitatively obtained using spin diffusion methods. NMR spin diffusion is a process of magnetization spreading from one spin to another and is driven by homonuclear dipolar coupling. Thus, the spin diffusion process carries distance information. There are several distance measurement techniques using spin diffusion, including ^{13}C detected ^1H spin diffusion (41,42), homonuclear correlation such as PDS and CHHC experiments (43) and center-band only detection of exchange (CODEX) (44,45). They are distinguished by spin diffusion between different spins, or by different magnetization pre-selections, as summarized in **Table 1.3**.

Table 1.3. Spin diffusion methods to determine homonuclear spin distance

spin diffusion method	X-X spin diffusion	magnetization preselection	spin diffusion time	maximum detectable distance
^{13}C -detected ^1H spin diffusion	^1H - ^1H	mobile groups via T_2 filter	2 - 600 ms	~ 20 Å
PDS	^{13}C - ^{13}C	all groups via CP, with a preference of rigid ones	20-300 ms	~ 6 Å
CHHC	^1H - ^1H	all groups via CP, with a preference of rigid ones	0-200 μs	~ 20 Å
CODEX	^{19}F - ^{19}F		0-3 s	~ 15 Å
	^{13}C - ^{13}C	CSA	0-15 s	~ 6 Å
	^{31}P - ^{31}P		0-6 s	~ 9 Å

Semi-quantitative distance measurement using ^{13}C detected ^1H spin diffusion

The pulse sequence of the ^{13}C -detected ^1H spin diffusion method is shown in **Figure 1.12.a** (41,42). Several consecutive $\pi/2$ pulses on the ^{13}C channel destroy all ^{13}C magnetization. A $\pi/2$ on ^1H channel creates the initial transverse magnetization. The magnetization of the mobile component then selected by a T_2 filter. After the t_1 evolution, the ^1H magnetization is flipped to the z -direction to allow spin diffusion during the mixing time (t_m). After that, the ^1H magnetization is flipped back to the transverse plane and transferred via CP to ^{13}C spins for detection. For a T_2 filter length of 0.5-2.0 ms, protons of the lipid chain and H_2O , which have relatively longer T_2 , can be preferentially selected as the magnetization source for spin diffusion.

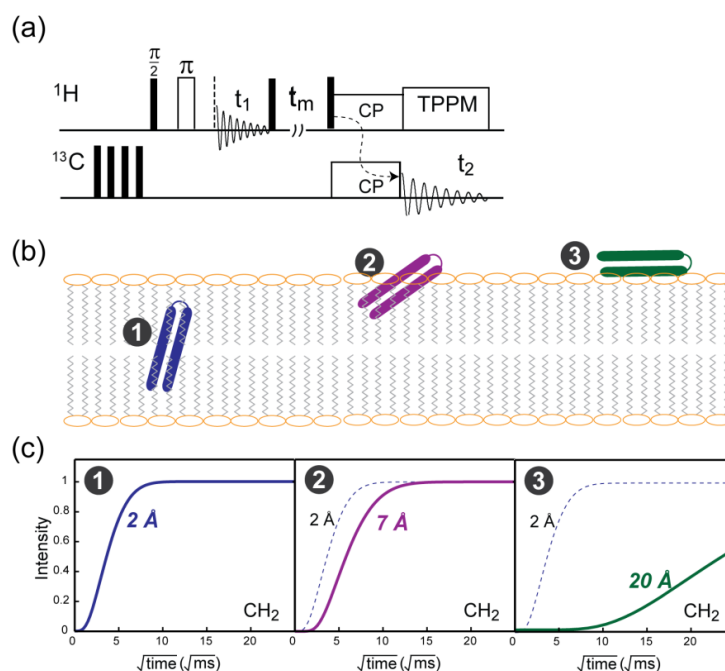


Figure 1.12. ^{13}C detected ^1H spin diffusion method to determine peptide insertion depth in the lipid membrane. (a) Pulse sequence (42). (b) Different insertion manner and (c) corresponding build-up curve of CH_2 intensity: ① full transmembrane (TM), ② partial insertion and ③ in-plane or surface binding.

In practice, one can conduct the experiment in the 1D mode to optimize the T_2 filter

length to make sure all peptide peaks are eliminated under the condition of no spin diffusion. In t_m period, magnetization difference between water/ CH_2 and rigid peptides serves as the driving force of ^1H spin diffusion. The ^1H magnetization reaches equilibrium at a certain mixing time. Different peptide locations and orientations, e.g. on the surface or inside the membrane, will manifest the time to reach equilibrium differently. The spin diffusion rate is determined from the spin diffusion cross peak intensity built-up as a function of time. We have shown that the build-up of the protein-lipid CH_2 cross peak reports the minimal distance from the membrane center (represented by chain-end CH_3 groups) to the peptide (42). Examples of how the spin diffusion method reports the insertion depth is illustrated in **Figure 1.12.b** and **c**. Three representative insertion manners are shown in **(b)** and their corresponding buildup curve of peptide- CH_2 cross peak intensity is shown right below in **(c)**. For the transmembrane case as indicated in ①, the peptide is very close to lipid chains, so the spin diffusion reached equilibrium quickly by ~ 100 ms. If the peptide is partially inserted into the membrane (case ②), the equilibrium is expected at a longer time than ①, at around 250 ms. When the peptide is far from the membrane center as shown in ③, the spin diffusion is very slow. It may take several seconds to reach the intensity plateau, e.g. DNA binding to the membrane surface (42).

The spin diffusion method can be applied to rigid peptides and mobile peptides to yield semi-quantitative and qualitative distance information, respectively. For rigid peptides like the β -hairpin PG-1 (46), the magnetization can be efficiently transferred from the source and then spread quickly within the peptide molecule. The magnetization transfer from CH_2 or water can usually reach equilibrium within a spin diffusion time of 100-625 ms. In the case of a mobile peptide, the spin diffusion from the source is slow due to weak dipolar couplings. This makes it almost impossible to reach spin diffusion equilibrium since the magnetization will be destroyed by the T_1 relaxation during a long mixing time of several seconds. However, qualitative information can be obtained. For example, TAT is an unstructured and highly dynamic peptide and shows a clear peptide- CH_2 cross peak at a relatively short mixing time of 144 ms (21), which strongly indicates the peptide is bound within the membrane, since a surface-bound peptide will take seconds to show clear CH_2 cross peaks. In addition, since magnetization transfer is extremely slow within a very mobile peptide like TAT, the spin dif-

fusion can give site-specific information.

The experimental buildup curve is simulated using a 1D lattice model, which describes the transfer of magnetization from a plane i to the neighboring two planes (plane $i-1$ and plane $i+1$) (41,42). The spin diffusion rate is characterized by the spin diffusion coefficient (D) or interfacial rate (Ω) in the unit of nm^2/ms . Different coefficients, such as D_{peptide} , D_{water} and D_{lipid} , are defined for different groups and spin diffusion medium. The value of diffusion coefficients depends on sample temperature and dynamics of the molecule and are mostly experimentally calibrated. These crucial parameters in the simulation are summarized in **Appendix D**. We have successfully applied the ^{13}C -detected ^1H spin diffusion method to measure the insertion depth of the unstructured TAT in lipid qualitatively (**Chapter 3**) (21) and the β -hairpin IB484 in LPS membrane quantitatively (**Chapter 5**) (22). In the same study, we also experimentally calibrated the interfacial spin diffusion coefficient of lipopolysaccharide-incorporated lipid membrane.

Qualitative distance measurement revealed by PDS and CHHC.

Homonuclear spin diffusion occurs through space and encodes distance information between spins, so correlation of NMR frequencies based on spin diffusion can be used to qualitatively indicate the distance between the correlated spins. This idea is illustrated in **Figure 1.13.a** for ^{13}C - ^{13}C spin diffusion at short and long mixing times. As can be seen from the spectra in **d** and **e**, the ^1H -driven ^{13}C - ^{13}C spin diffusion experiment correlates intra-residue carbons within 20 ms mixing time and inter-residue carbons at 100 ms.

Due to the larger ^1H - ^1H dipolar coupling, long-range distance constraints can be measured at shorter spin diffusion time as shown in **Figure 1.13.b**, compared to ^{13}C - ^{13}C spin diffusion. The CHHC method is used to establish ^{13}C - ^{13}C correlation using ^1H spin diffusion. The CHHC pulse sequence is shown in **Figure 1.13.c** (43). The initial magnetization is from ^1H via CP and is then stored longitudinally in a z -filter. Meanwhile, ^1H magnetization is destroyed by the T_2 relaxation. In the t_1 period, the ^{13}C chemical shifts is encoded and ^{13}C magnetization is then transferred back to ^1H via a short CP. The ^1H - ^1H spin diffusion then happens during t_{mix} . After another short CP, the magnetization is transferred to ^{13}C for detection.

A relatively short ^1H mixing time of less than 200 μs can be used to allow medium-to-long range spin diffusion (up to 20 \AA). Uniformly ^{13}C labeled proteins can provide denser ^{13}C magnetization pool to compensate for the intensity loss due to the 3-step CP transfer. **Figure 1.13.f.** shows the high ^1H spin diffusion efficiency of CHHC, which yields similar correlations at $t_m=0.2$ ms as ^{13}C PDSM with a long mixing time of 200 ms. The CHHC method has been applied to penetratin to obtain reliable chemical shift assignment and long distance constraints.

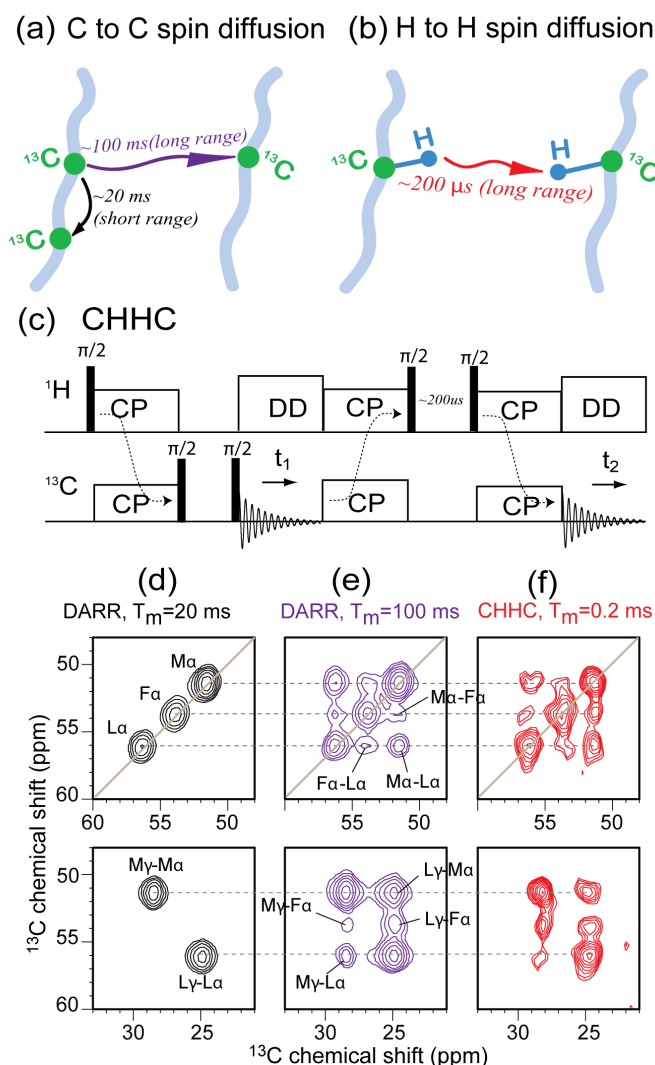


Figure 1.13. Spin diffusion of (a) ^{13}C to ^{13}C spins and (b) ^1H to ^1H spins. (c) CHHC pulse sequence. Representative f-MLF-OH 2D DARR spectra using a 20 ms mixing time (d), and 100 ms mixing time (e), and 2D CHHC spectra using a 0.2 ms mixing time (f).

Oligomeric state and intermolecular distance from ^{19}F CODEX

Similar to ^1H , ^{19}F is another spin 1/2 nucleus with high gyromagnetic ratio (γ) and 100% natural abundance. ^{19}F CODEX is a spin diffusion experiment utilizing large ^{19}F - ^{19}F dipolar coupling to yield long-range distance information (44,45). The ^{19}F CODEX pulse sequence is illustrated in **Figure 1.14 a**. The two π -pulse trains are used to recouple the ^{19}F CSA interaction under MAS. Two z -filters are involved with different time length of t_{mix} and t_z . The desired t_{mix} and short t_z are used for the exchange experiment to give dephased intensity (S). A control experiment (S_0) without exchange uses interchanged t_m and t_z to ensure the same total T_1 relaxation effect as S. This technique is originally designed to study slow dynamics, such as reorientation on a time scale of seconds (44). But, by freezing the molecular motion at low temperature, we use ^{19}F CODEX to detect spin diffusion, which give intermolecular distance and oligomerization information (45,46).

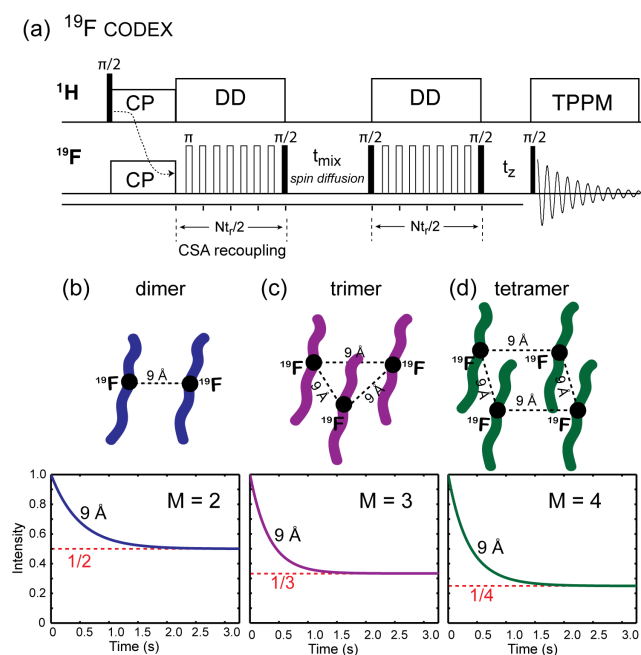


Figure 1.14. (a) ^{19}F CODEX pulse sequence (44) and (b-c) dephasing curves of oligomerized proteins: (b) Dimer with a ^{19}F - ^{19}F distance of 9 Å. (c) Symmetric trimer with ^{19}F - ^{19}F distance of 9 Å to each other. (d) Tetramer with square geometry of four ^{19}F spins. Red dotted lines indicate the equilibrium values, which are 1/2, 1/3 and 1/4 for dimer, trimer and tetramer, respectively. M indicates the oligomeric number.

Figure 1.14 b-d. show the t_m -dependent CODEX dephasing curves of oligomerized peptides with the same intermolecular distances between neighboring monomers. For oligomerized proteins (oligomeric number M), ^{19}F spins at the same site of different monomers are chemically equivalent but magnetically inequivalent due to the different molecular orientation. During t_m , magnetization diffuses among the orientationally inequivalent ^{19}F spins, so the CSA cannot be completely recoupled, showing an intensity drop. Spin diffusion reaches equilibrium when the magnetization distributes equally to all ^{19}F spins, giving a $1/M$ equilibrium intensity. The time to reach equilibrium depends on the distance among all ^{19}F spins. Thus, the time-dependent intensity decay can be used to extract distances. The equilibrium dephasing ratio ($1/M$) indicates the oligomeric number. We applied this method to study the oligomerization of penetratin in **Chapter 3** (40).

An important advantage of ^{19}F CODEX is that ^{19}F spins do not naturally exist in most membrane proteins, so there is no background NMR signal. Many ^{19}F -labeled amino acids are available for ^{19}F -labeling of peptides and proteins, such as 4F-Phe, 3F-Tyr and 5F-Trp. (47, 48)

1.4 Paramagnetic Resonance Enhancement (PRE) NMR for distance determination

As shown in **section 1.3**, the distance dependence of dipolar coupling strength allows us to obtain distance constraints, however, the dipolar couplings become very small for long distances due to $1/r^3$ dependence of the coupling. For example, the homonuclear dipolar coupling strength of ^{13}C spins is 35 Hz when the two spins are 6 Å apart, which is comparable to a one-bond scalar coupling. This results in very low spin diffusion efficiency in ^{13}C - ^{13}C correlation experiments and can also make it difficult to apply the REDOR experiment. Moreover, the dipolar network of uniformly ^{13}C and ^{15}N labeled proteins complicates the quantitative analysis of distances. Thus, long-range distances are usually not easy to measure in protein structure determination. In light of PRE application in solution NMR studies for many years (49, 50), SSNMR spectroscopists have started to use this technique in recent years to establish long-range distance constraints, in both qualitative and quantitative ways (51-55).

Paramagnetic species, which are mostly metal ions with unpaired electrons, will interact with a neighboring nuclear spin via the hyperfine interaction and/or magnetic dipole-dipole interaction (56). These interactions will cause relaxation enhancement (57) or pseudocontact shift (58,59). Several examples of PRE ions showing those effects are given in **Table 1.4**.

Table 1.4. PRE effects of representative paramagnetic ions.

PRE agent	S	T_{1e}	pseudocontact shift (δ^{pc})	NMR relaxation		functional form
				T_1	T_2 or $T_{1\rho}$	
Pr (III)	5/2	< ps	strong	-	weak	Pr ³⁺ (62,63)
Cu (II)	1/2	~1-5 ns	weak	strong	weak	Cu ²⁺ , Cu ²⁺ -EDTA (54), Cu-AA tag (55)
Mn (II)	5/2	~10 ns	no	moderate	strong	Mn ²⁺ (20,60), Mn ²⁺ -EDTA(55)
Gd (III)	1/2	~100 ns	no	strong	weak	nitroxide (61)

Generally, two parameters, the electron g-tensor anisotropy (g_e) and electron spin relaxation time (T_{1e}), determine what kind of effect paramagnetic ions will generate (55). As examples shown in **Table 1.4**, metal ions such as Cu²⁺, Mn²⁺ and Gd³⁺ with ns T_{1e} has large effect on relaxation, while those with subpicosecond T_{1e} (particularly most lanthanide metal ions such as Pr³⁺) show negligible relaxation enhancement but affect chemical shift strongly.

1.4.1 Distance-dependent PRE

The central advantage of PRE for distance determination is the large γ_e compared with regular spin 1/2 nuclei. The large γ_e gives large electron-nucleus dipolar coupling, which depends on the distance. PRE effect is characterized by the enhancement parameters Γ_1 , Γ_2 and $\Gamma_{1\rho}$, which have a unit of s⁻¹. For example:

$$\Gamma_1 = \frac{1}{T_1^{para}} - \frac{1}{T_1^{dia}}, \quad (1.26)$$

where T_1^{dia} and T_1^{para} are the longitudinal relaxation times without and with PRE, both of

which can be experimentally determined. If $T_1^{dia} = 1.0$ s, which should be a reasonable estimation of protein backbone carbons, the dependence of Γ_1 on T_1^{para} is plotted in **Figure 1.15.a**. To obtain a Γ_1 larger than 10 s⁻¹, which corresponds to a ¹³C-Cu²⁺ distance of 8 Å (shown later), the relaxation time has to become ten times shorter ($T_1^{para} = 0.1$ s) under the PRE effect.

The relaxation effect of dipolar coupled electron-nuclei is described by the Solomon-Bloembergen-Morgan equations (64,65):

$$\Gamma_1 = \frac{2}{15} \left(\frac{\mu_0}{4\pi} \right)^2 \frac{\gamma_n^2 g_e^2 \mu_B^2 S(S+1)}{r^6} \cdot \left(\frac{3\tau_{c1}}{1 + \omega_n^2 \tau_{c1}^2} + \frac{7\tau_{c2}}{1 + \omega_e^2 \tau_{c2}^2} \right) \quad (1.27)$$

$$\Gamma_2 = \frac{1}{15} \left(\frac{\mu_0}{4\pi} \right)^2 \frac{\gamma_n^2 g_e^2 \mu_B^2 S(S+1)}{r^6} \cdot \left(4\tau_{c1} + \frac{3\tau_{c1}}{1 + \omega_n^2 \tau_{c1}^2} + \frac{13\tau_{c2}}{1 + \omega_e^2 \tau_{c2}^2} \right) \quad (1.28)$$

where μ_0 is the free space permeability ($\mu_0 = 4\pi \cdot 10^{-7} \text{T} \cdot \text{m/A}$), γ_n is the nuclear gyromagnetic ratio ($\gamma_n = 2\pi \cdot 10.705$ MHz/T for ¹³C), g_e is the value of electron g-tensor anisotropy ($g_e = 2.09$ for Cu²⁺), μ_B is the Bohr magneton ($\mu_B = 9.274 \times 10^{-24} \text{A} \cdot \text{m}^2$), S is the electron spin quantum number ($S = 1/2$ for ¹³C), r is the electron-nucleus distance, and ω_n and ω_e are the Larmor frequencies of the nucleus ($\omega_n = 2\pi \cdot 100.576$ MHz) and electron ($\omega_e = 2\pi \cdot 263$ GHz), respectively. τ_{c1} and τ_{c2} are longitudinal and transverse correlation time, respectively, under the effect of electron spin relaxation (T_{1e} and T_{2e}), rotational molecular motion (τ_r) and chemical exchange (τ_m):

$$\frac{1}{\tau_{c1}} = \frac{1}{T_{1e}} + \frac{1}{\tau_r} + \frac{1}{\tau_M} \quad \text{and}$$

$$\frac{1}{\tau_{c2}} = \frac{1}{T_{2e}} + \frac{1}{\tau_r} + \frac{1}{\tau_M} \quad (1.29)$$

In case of solids, molecular tumbling and chemical exchange are slow and can be

neglected, and $T_{1e} = T_{2e}$, so $\tau_{c1} = \tau_{c2} \approx T_{1e}$. So, for solid samples,

$$\Gamma_1 = \frac{2}{15} \left(\frac{\mu_0}{4\pi} \right)^2 \frac{\gamma_n^2 g_e^2 \mu_B^2 S(S+1)}{r^6} \cdot \left(\frac{3T_{1e}}{1 + \omega_n^2 T_{1e}^2} + \frac{7T_{1e}}{1 + \omega_e^2 T_{1e}^2} \right) \quad (1.30)$$

Taking the example of ^{13}C spins under the Cu^{2+} PRE effect, in **equation 1.30**,

$$\begin{aligned} & \frac{2}{15} \left(\frac{\mu_0}{4\pi} \right)^2 \frac{\gamma_n^2 g_e^2 \mu_B^2 S(S+1)}{r^6} = \\ & = \frac{2}{15} \left(\frac{4\pi \cdot 10^{-7} \text{T} \cdot \text{m/A}}{4\pi} \right)^2 \frac{(2\pi \cdot 10.705 \text{MHz} / T)^2 \cdot 2.09^2 \cdot (9.274 \times 10^{-24} \text{A} \cdot \text{m}^2)^2 \cdot \frac{1}{2} \left(\frac{1}{2} + 1 \right)}{r^6} \\ & = \frac{1.699 \times 10^{-45} (\text{Hz})^2 \cdot \text{m}^6}{r^6} \end{aligned}$$

So, PRE effect

$$\begin{aligned} \Gamma_1 &= \frac{1.699 \times 10^{-45}}{r^6} \left(\frac{3T_{1e}}{1 + \omega_n^2 T_{1e}^2} + \frac{7T_{1e}}{1 + \omega_e^2 T_{1e}^2} \right) \\ &= \frac{1.699 \times 10^{-45}}{r^6} \left(\frac{3T_{1e}}{1 + (2\pi \cdot 100.576 \times 10^6 \text{ Hz})^2 T_{1e}^2} + \frac{7T_{1e}}{1 + (2\pi \cdot 263 \times 10^9 \text{ Hz})^2 T_{1e}^2} \right) \\ &= \frac{1.699 \times 10^{-45} (\text{Hz})^2 \cdot \text{m}^6}{r^6} \cdot \left(\frac{3T_{1e}}{1 + 3.993 \times 10^{17} (\text{Hz})^2 T_{1e}^2} + \frac{7T_{1e}}{1 + 2.731 \times 10^{21} (\text{Hz})^2 T_{1e}^2} \right) \\ &= \frac{1.699 \times 10^{-45} (\text{Hz})^2 \cdot \text{m}^6}{r^6} \cdot \left(\frac{3T_{1e}}{1 + 3.993 \times 10^{17} (\text{Hz})^2 T_{1e}^2} + \frac{7T_{1e}}{1 + 2.731 \times 10^{21} (\text{Hz})^2 T_{1e}^2} \right) \quad (1.31) \end{aligned}$$

A T_{1e} value is required to determine the ^{13}C - Cu^{2+} distance in **equation 1.31**. Cu^{2+} has T_{1e} value of 1 - 5 ns (50). To evaluate how much the T_{1e} value will affect distance determination using PRE, the dependence of r on T_{1e} is shown in **Figure 1.15.b**, at various Γ_1 values of 0.3-200 s^{-1} . At a given Γ_1 , it shows that similar distances are obtained when $T_{1e} > 1\text{ns}$. Taking $\Gamma_1 = 30 \text{ s}^{-1}$ (red curve) for example, a distance of $6.85 \text{ \AA} \pm 0.37 \text{ \AA}$ is obtained for T_{1e} of a 1-5 ns. For smaller Γ_1 of 0.35 s^{-1} as shown by the green curve, a larger but still acceptable uncertainty of $\pm 0.70 \text{ \AA}$ is generated. Thus, a T_{1e} of 2.5 ns should be a reasonable choice to simplify **equation 1.31**.

If $T_{1e} = 2.5$ ns is used, **equation 1.31** can be simplified as:

$$\Gamma_1 = \frac{1.699 \times 10^{-45} (\text{Hz})^2 m^6}{r^6} \cdot 2.147 \times 10^{-9} s = \frac{3.648 \times 10^{-54} \text{ Hz} \cdot m^6}{r^6}$$

$$\text{then, } r = \sqrt[6]{\frac{3.648 \times 10^6}{\Gamma_1}} = \frac{12.407}{\sqrt[6]{\Gamma_1}} \quad (1.32),$$

where r is in ångström and Γ_1 is in second.

Figure 1.15.c is the plot of **equation 1.32**. As can be seen, a Γ_1 of 10 s^{-1} gives a $^{13}\text{C-Cu}^{2+}$ distance of 8 \AA . If Cu^{2+} is as close as 5 \AA to ^{13}C spin, an extremely large Γ_1 of 200 s^{-1} is expected, which converts to a 200-fold decrease of relaxation time (if $T_1^{dia} = 1 \text{ s}$) after adding Cu^{2+} . Moreover, in such a short distance, one should expect moderate T_2 enhancement and small pseudocontact shift. If the relaxation time decreases from 1 s to 0.9 s , a very small Γ_1 of 0.111 s^{-1} is obtained, converting to a $^{13}\text{C-Cu}^{2+}$ distance of $\sim 18 \text{ \AA}$.

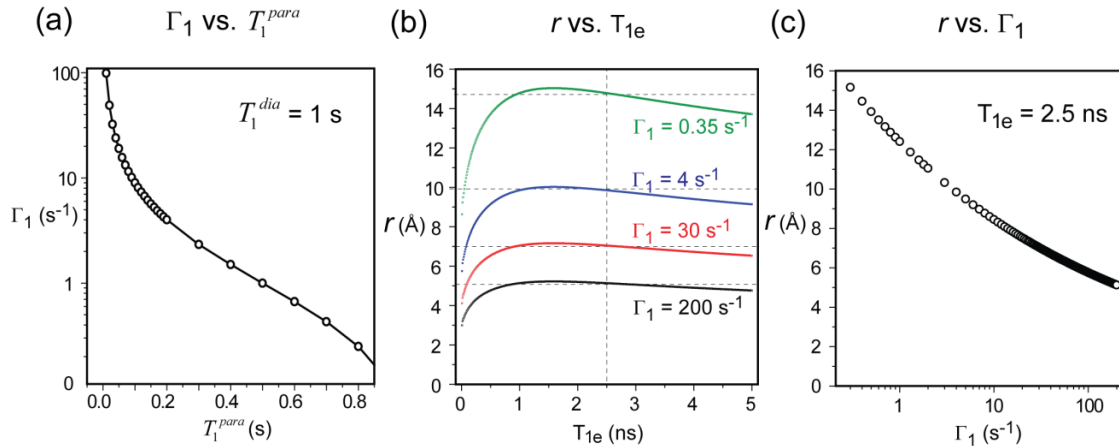


Figure 1.15. (a) Γ_1 dependence on longitudinal relaxation time after adding PRE ions (T_1^{para}). Suppose the constitutional relaxation time without PRE ions (T_1^{dia}) is 1 s . (b) $^{13}\text{C-Cu}^{2+}$ distance (r) dependence on electron spin relaxation time T_{1e} for different Γ_1 . (c) r vs. Γ_1 for $T_{1e} = 2.5 \text{ ns}$.

The above mathematical derivation and discussion show that Cu^{2+} PRE can be used to qualitatively measure distances in the range of $\sim 5 \text{ \AA}$ to $\sim 20 \text{ \AA}$ for ^{13}C spins. Theoretically,

T_2 -dephasing PRE effects can also be used to obtain quantitative distances as shown in **equation 1.28**. In practice, the T_2 effect may cause severe intensity drop, making the T_2 measurement difficult. We have semi-quantitatively determined the penetratin insertion depth using Mn^{2+} T_2 PRE in **Chapter 3**.

1.4.2 Application of PRE method to lipid membrane systems

We applied the PRE method using different paramagnetic ions in our membrane peptide studies to obtain qualitative and quantitative distances. As shown in **Figure 1.16**, PRE ion-bound membrane sample is prepared by binding metal ions (M^{n+} , $M^{n+} = Mn^{2+}$, Cu^{2+} and Pr^{3+}) to the membrane surface. The PRE membrane sample preparation is summarized in **Appendix B**.

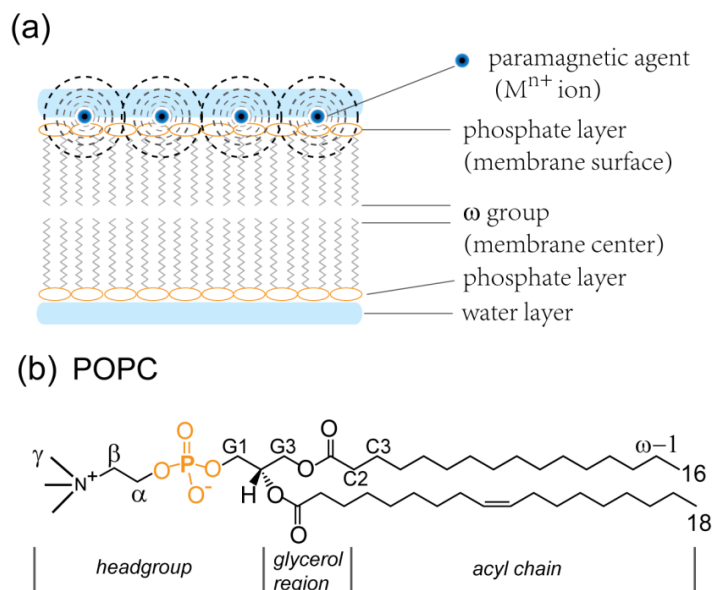


Figure 1.16. (a) One-side PRE agent-bound membrane sample. Binding of PRE ions to both inner and outer surfaces makes it a two-side PRE sample. (b) Molecular structure of POPC, a representative phospholipid with various lipid groups at different membrane depths indicated.

The PRE effects of different paramagnetic ions on lipid groups are shown in **Figure 1.17**. For a Mn^{2+} -bound POPC sample shown in (a), the NMR intensity decreases in a dis-

tance dependent manner: the intensity of headgroup segments drops to half while the bilayer center species remain unchanged, as indicated by the red curve. When converted to a two-side Mn^{2+} sample, all headgroup signals have disappeared. We applied this one-side PRE method to study the binding symmetry of penetratin in the lipid bilayer and also obtained the insertion depth by comparing with the intensity dephasing of lipid peaks (20).

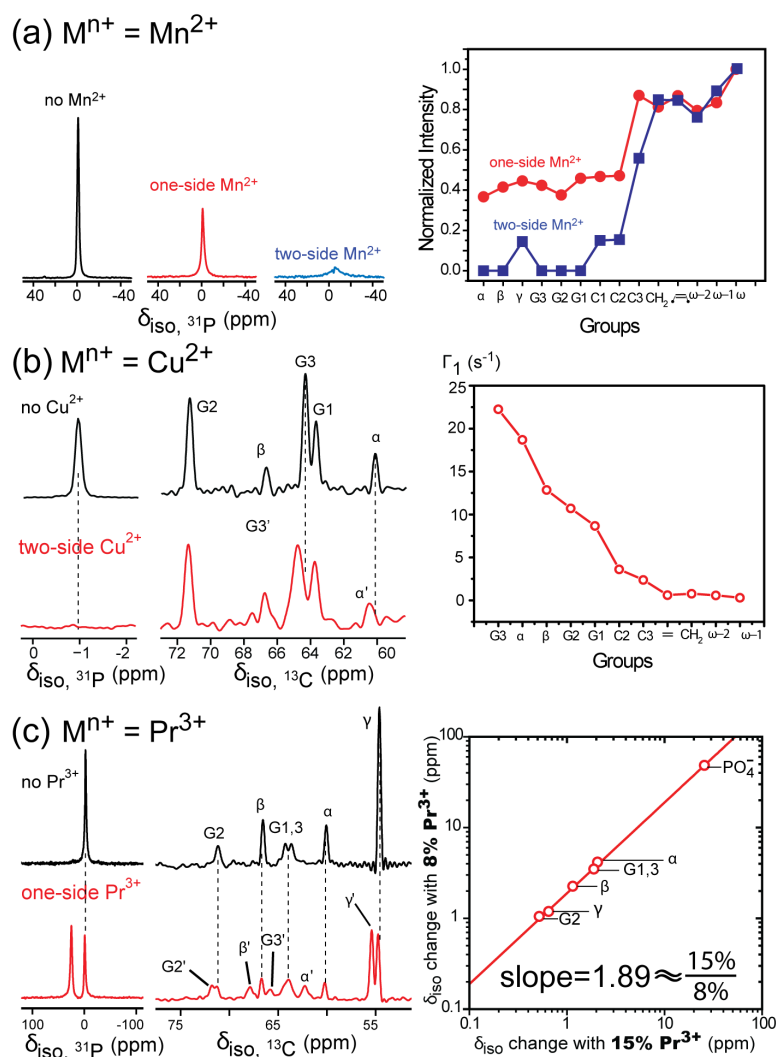


Figure 1.17. PRE effect of paramagnetic-ion-bound lipid membranes. (a) Mn^{2+} ; (b) Pr^{3+} ; (c) Cu^{2+}

Quantitative distances can be obtained by using the Cu^{2+} PRE method as shown in **Figure 1.17.b** (25). The 7% Cu^{2+} containing sample shows no remaining ^{31}P signal, indicat-

ing Cu^{2+} binds most closely to ^{31}P , or more likely the charged oxygen atom of the phosphate group. This is further supported by the fact that the closest carbons, G_3 and α , shows line broadening and small chemical shift change. The PRE effect, Γ_1 values of lipid carbons are obtained by measuring longitudinal relaxation times before and after adding Cu^{2+} ions. The distance dependence of Γ_1 is shown in the curve of **Figure 1.17.b**. Headgroup carbons have larger Γ_1 , indicating stronger PRE. This validates the utility of the Cu^{2+} PRE method for distance determination in lipid membrane systems. Cu(II) is also a metal inhibitor of the transmembrane ^1H channel of the influenza M2 protein. We applied this Cu^{2+} PRE method to study the binding structure of Cu^{2+} in the channel and the results have nicely indicated the binding site and topology of nearby residues (25).

We also observed interesting pseudocontact shift of Pr^{3+} -bound POPC lipids (**Figure 1.17.c**) (unpublished data). After adding 8% Pr^{3+} , all headgroup spins (^{13}C and ^{31}P) show clear chemical shift changes downfield, while carbons in the membrane center are not affected. Interestingly, the chemical shift change is proportional to the Pr^{3+} concentration as indicated by the curve.

1.5 Measurements of Local and Global Dynamics of Proteins

Protein dynamics is a crucial aspect other than the structure that significantly relates to the biological function. Proteins have various motions like segmental reorientation, protein folding, protein domain motion, and protein backbone motion, covering a large range of time scales from second (or Hz) to picosecond (or 10^{12} Hz). Most of these motions can be characterized by SSNMR. For example, fast motion ($< \text{ns}$ or $> 10^7$ Hz) can be characterized by NMR relaxation time (T_1) measurement. Motions occurring on the intermediate time scale ($\sim \text{ms}$ or 10^3 Hz) or sub-microsecond time scale can be revealed by line shape analysis like static ^2H (3) and by measuring scaled dipolar coupling using separate-local-field (SLF) correlation experiments (15). The relaxation time ($T_{1\rho}$) in the rotating frame can also probe motions at $\sim \mu\text{s}$ or tens to hundreds of kHz. Motions slower than tens of ms can be studied by exchange NMR, such as CODEX (46). In the following sections, several robust SSNMR techniques used to obtain dynamic parameters are discussed.

1.5.1 Dipolar coupling measurement using DIPSHIFT and LG-CP

Dipolar-chemical-shift (DIPSHIFT) experiments (32,33) have been extensively applied in my thesis research. It directly measures the motionally averaged dipolar coupling ($\overline{\delta_D}$). The dipolar order parameter (S_{XH}) of a bond X-H is the ratio of the measured dipolar coupling to the rigid-limit value (δ_D). S_{XH} indicates the motional amplitude, represented by the angle θ between the motional axis and the bond of interest.

$$S_{XH} = \frac{\overline{\delta_D}}{\delta_D} = \frac{1}{2}(3 \cos^2 \theta - 1)$$

In the following part, I will show the evolution of both frequency and spin part under heteronuclear dipolar coupling.

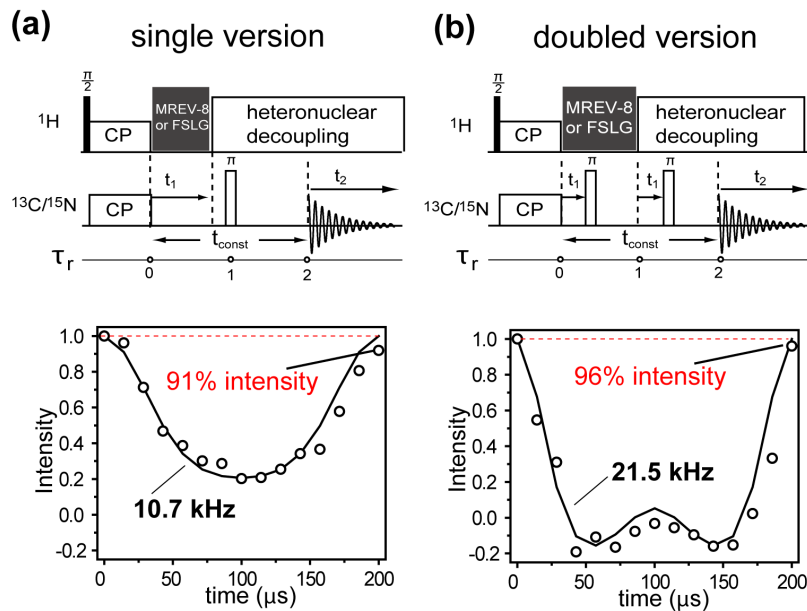


Figure 1.18. Pulse sequences and representative fitting curves of DIPSHIFT: (a) Single version and (b) Doubled version (32,33). The data are measured for f-MLF-OH at 5.0 kHz MAS and MREV-8 pulse scheme (69) for ^1H - ^1H homonuclear dipolar decoupling. Note the minor intensity asymmetry between the first and last data point as guided by the red dotted lines, which is due to T_2 decay.

The NMR signal under MAS is $S(t) = e^{i \int_0^t \omega(t') dt'} = e^{i\Phi(t)}$ (1.33). According to

equation 1.14,

$$(1)S(t) = e^{i\Phi(t)} = 1, \text{ if } t_1 = 0 \text{ and } \tau_r$$

$$(2)S(t) = e^{i\Phi(t)} < 1, \text{ if } t_1 \in (0, \tau_r)$$

So, the NMR signal is modulated by dipolar coupling during one rotor period. Below, I will show how magnetization (M_0) evolves under dipolar coupling interaction (\hat{H}_D) in the single DIPSHIFT experiment (**Figure 1.18a**).

At t_0 , $\hat{\rho}(0) = C\hat{I}_z$, where C is the Boltzmann factor and $C = \frac{\gamma_I \hbar B_0}{KT}$

$$\hat{\rho}(0) \xrightarrow{\frac{\pi}{2} \hat{I}_y} \hat{\rho}(t) = C \cdot \hat{I}_x \xrightarrow{\hat{H}_{CP} = \hbar \omega_{IS} (\hat{I}_z \hat{S}_z + \hat{I}_y \hat{S}_y)} \hat{\rho}(t, \text{ after CP}) =$$

$$C \cdot \left[\hat{I}_x \cdot \frac{1}{2} (1 + \cos \omega_{IS} t) + \hat{S}_x \cdot \frac{1}{2} (1 - \cos \omega_{IS} t) + (\hat{I}_y \hat{S}_z - \hat{I}_z \hat{S}_y) \cdot \sin \omega_{IS} t \right]$$

After CP, consider the evolution of the \hat{S}_x term. During τ_r , $\hat{H}_{total} = \hat{H}_D^H + \hat{H}_D^{IS} + \hat{H}_{CS}^S$, where $\hat{H}_D^H = 0$ under homonuclear dipolar decoupling and \hat{H}_{CS}^S is refocused (averaged to zero) by a π pulse, so only \hat{H}_D^{IS} is retained.

To evaluate whether the conditions to use **equation 1.4** are met:

$$[\hat{H}_D^{IS}, \hat{S}_x] = [\hbar \omega_{IS} 2\hat{I}_z \hat{S}_z, \hat{S}_x] = 2\hbar \omega_{IS} (\hat{I}_z \hat{S}_z \hat{S}_x - \hat{S}_x \hat{I}_z \hat{S}_z) = 2\hbar \omega_{IS} \hat{I}_z [\hat{S}_z, \hat{S}_x] = 2i\hbar \omega_{IS} \hat{I}_z \hat{S}_y$$

$$[\hat{H}_D^{IS}, [\hat{H}_D^{IS}, \hat{S}_x]] = [\hbar \omega_{IS} 2\hat{I}_z \hat{S}_z, 2i\hbar \omega_{IS} \hat{I}_z \hat{S}_y] = 4i\hbar \omega_{IS}^2 \hat{I}_z^2 [\hat{S}_z, \hat{S}_y] = \hbar \omega_{IS}^2 \hat{S}_x = \hbar \omega_{IS}^2 \hat{S}_x$$

Then, use **equation 1.4**:

$$\hat{S}_x \xrightarrow{\hat{H}_D^{IS} = \omega_{IS} 2\hat{I}_z \hat{S}_z t_1} \hat{S}_x \cdot \cos(\omega_{IS}^D t_1) + 2\hat{I}_y \hat{S}_z \cdot \sin(\omega_{IS}^D t_1)$$

Note that $2\hat{I}_y \hat{S}_z \cdot \sin(\omega_{IS} t_1)$ is an antiphase term that can not be detected directly.

During t_2 :

$$\hat{S}_x \cdot \cos(\omega_{IS}^D t_1) \xrightarrow{\hat{H}_{CS}^S = \omega_S^S \hat{S}_z t_2} \hat{S}_x \cdot \cos(\omega_{IS}^D t_1) \cos(\omega_S^{CS} t_2) + \hat{S}_y \cdot \cos(\omega_{IS}^D t_1) \sin(\omega_S^{CS} t_2)$$

$$\text{So, } \hat{\rho}(t_1, t_2) = C \cdot \left[\cos(\omega_{IS}^D t_1) [\hat{S}_x \cdot \cos(\omega_S^{CS} t_2) + \hat{S}_y \cdot \sin(\omega_S^{CS} t_2)] \right]$$

Thus, the complex NMR signal during t_1 and t_2 is,

$$S(t_1, t_2) = C \cdot \text{tr} \{ \hat{\rho}(t_1, t_2) S^+ \} \quad (1.34)$$

After plugging in Pauli matrices for S^+ , $S(t_1, t_2) = C \cdot \cos(\omega_{IS}^D t_1) e^{i\omega_S^{CS} t_2}$

Apply FT in the ω_2 dimension,

$$S(t_1, \omega_2) = C \cdot \cos(\omega_{IS}^D t_1) \int_0^{t_{acq}} dt_2 e^{i\omega_S^{CS} t_2} e^{-i\omega_2 t_2} = C \cdot \cos(\omega_{IS}^D t_1) \cdot 2\pi\delta(\omega_2 - \omega_S^{CS}) \quad (1.35)$$

This shows how the DIPSHIFT experiment correlates dipolar coupling in the indirect dimension and chemical shift in the direct dimension.

To measure weak dipolar coupling, the doubled version of DIPSHIFT (**Figure 1.18.b**) can be used (15). During t_1 , the total phase angle change is:

$$\begin{aligned} \Phi^{2X}(t_1) &= \int_0^{t_1} \omega(t) dt - \int_{t_1}^{\tau_r} \omega(t) dt = \int_0^{t_1} \omega(t) dt - \left[\int_0^{\tau_r} \omega(t) dt - \int_0^{t_1} \omega(t) dt \right] \\ &= 2 \int_0^{t_1} \omega(t) dt = 2\Phi^{1X}(t_1) \end{aligned} \quad (1.36)$$

Equation 1.36 indicates that the dipolar coupling effect is doubled during the t_1 time period, allowing more accurate measurement of mobile systems. Moreover, the homonuclear decoupling time is constant, minimizing the effect of decoupling imperfection and T_2 decay for different t_1 time points. As can be seen from the fitting curve of **Figure 1.18.b**, the peak intensities of the first and last data points are almost the same. MREV-8 is used for homonuclear dipolar decoupling at slow spinning speeds (< 5 kHz) and has a scaling factor of 0.47 (69). For higher spinning speeds, FSLG can be used and has a scaling factor of 0.577 (70).

Another robust technique to measure the dipolar order parameter is LG-CP (71-72), which correlates dipolar splitting and isotropic chemical shift in a 2D manner. As an advantage, one can extract dipolar coupling from the peak splitting in the indirect dimension directly without curve fitting. This experiment can be conducted under fast MAS. Due to the small peak splitting of weak dipolar couplings, LG-CP may not be able to yield accurate readings for highly dynamic systems. It has a scaling factor of 0.577, which is sensitive to the accuracy of the LG-CP setup.

1.5.2 CSA recoupling by ROCSA and SUPER

As shown in previous sections, CSA principle values indicate the molecular orientation with respect to B_0 . When motion exists, CSA interactions, just like dipolar coupling, will be averaged to give a narrower line shape ($\delta_{CS}^{averaged}$) compared with the rigid limit δ_{CS}^{rigid} . The line narrowing scaling factor S , or order parameter, can be obtained and used to characterize the dynamics:

$$S = \delta_{CS}^{averaged} / \delta_{CS}^{rigid} \quad (1.37)$$

Besides the size of CSA, the asymmetry parameter (η) identifies the uniaxiality of motion as $\eta = 0$ for a uniaxial system. For example, the static ^{31}P spectrum of a well-hydrated lipid bilayer corresponding to $\eta = 0$ shows σ_{xx} and σ_{yy} at the same edge ($\sigma_{xx} = \sigma_{yy}$), indicating the nature of uniaxial lipid motion around its molecular axis. For a singly ^{13}C labeled compound, the static spectrum under proper dipolar decoupling gives the CSA lineshape. Under slow MAS spinning, the envelope of sidebands also represents the CSA pattern. The three principal values and the isotropic chemical shift can be obtained from Herzfeld-Berger Analysis (HBA) (73). For uniformly labeled peptides or proteins, the 2D Recoupling of Chemical Shift Anisotropy (ROCSA) experiments can give site-specific CSA information (74).

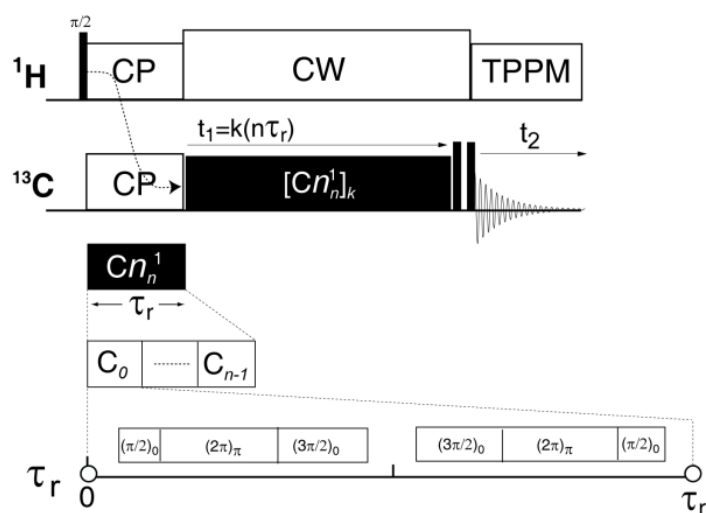


Figure 1.19 Pulse sequence of ROCSA (74).

ROCSA correlates CSA and isotropic chemical shift in the ω_1 and ω_2 dimension, respectively. **Figure 1.19** shows the ROCSA pulse sequence and the CSA recoupling block. The C-symmetry block in n rotor periods, Cn_n^1 , recouples CSA and effectively suppresses the ^{13}C - ^{13}C dipolar coupling. This experiment has a CSA scaling factor of 0.272 and requires the ^{13}C recoupling field strength to be 4.283 times of the MAS frequency (ω_r). High sample spinning speed (~ 7 -20 kHz) is required to allow a reasonably large spectral window in the indirect dimension. In general, it is helpful for obtaining well-defined CSA features if the experiment is carried out at high magnetic fields. Thus, in the experimental setup, several important factors need to be considered together, including the static field strength, MAS frequency and rf field strength of both ^{13}C and ^1H . For example, a ^{13}C rf nutation frequency of 64 kHz is required for 15 kHz MAS. It was found 50 kHz stronger ^1H decoupling than ^{13}C rf field is necessary to yield efficient heteronuclear decoupling (74). So, ^1H decoupling will need to be stronger than 114 kHz.

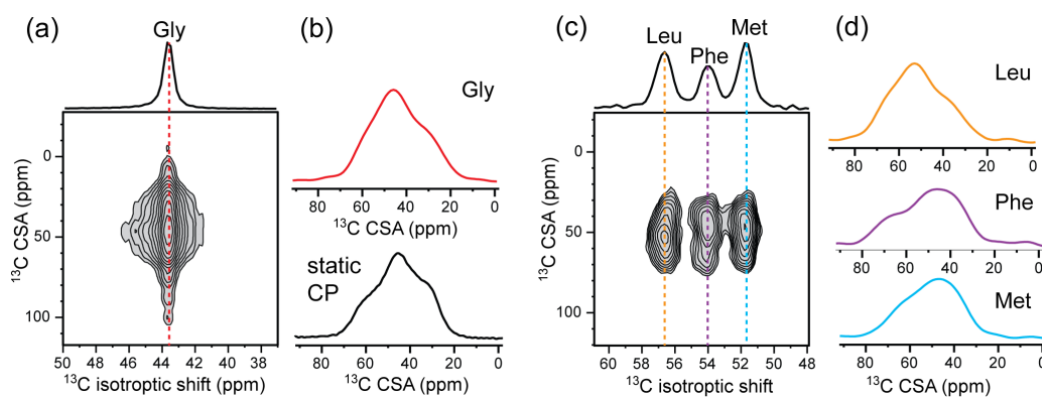


Figure 1.20. $\text{C}\alpha$ CSA measurement of crystalline compounds using ROCSA. (a) 2D ROCSA spectrum of 2- ^{13}C -Gly. (b) Top: ^{13}C CSA line pattern extracted from the cross section at 43.6 ppm in (a); bottom: static cross polarization spectrum of the same compound. (c) 2D ROCSA spectrum of f-MLF-OH and (d) Extracted $\text{C}\alpha$ CSA cross sections. The sample spinning speed is 8-9 kHz for MAS spectra in (a-d). ^1H decoupling of 71-93 kHz is applied during ROCSA period.

Figure 1.20 shows CSA measurement of $\text{C}\alpha$ -labeled glycine and uniformly labeled f-MLF-OH. As can be seen, the red CSA line shape in (b) extracted from the 2D ROCSA

spectra (a) at C α position matches well with the 1D static spectrum. The MLF measurement (c and d) shows the site-specific resolution as an advantage of ROCSA. We have measured the ^{13}C CSA of penetratin and obtained much narrower spans (Chapter 3), indicating fast molecular motion.

2D separation of undistorted powder patterns by effortless recoupling (SUPER) (75), which is designed by Schmidt-Rohr and coworkers, is a robust NMR technique to extract CSA with site resolution. The CSA is recoupled by many rotor-synchronized 2π pulses at desired time points. The scaling factor of SUPER is 0.155. It does not need high MAS ($\omega_r < 4$ kHz). A ^{13}C rf frequency at the strength of $12.12\omega_r$ is required. The fact that the ^{13}C - ^{13}C dipolar coupling and J-coupling are not suppressed during CSA recoupling makes this technique more applicable to the sparsely labeled or natural abundance systems.

1.5.3 Protein dynamics from NMR relaxation times

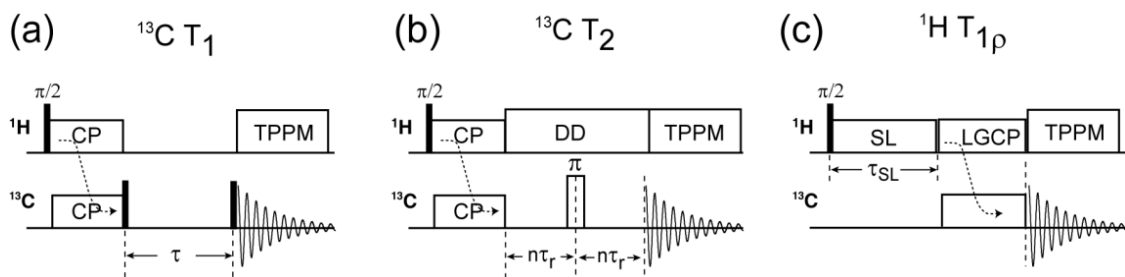


Figure 1.21. Pulse sequences to measure NMR relaxation time. (a) inverse recovery experiment to measure ^{13}C T_1 . (b) CP echo experiment to measure ^{13}C T_2 . (c) LG-CP experiment to measure ^1H $T_{1\rho}$.

NMR relaxation is a process of perturbed magnetization returning to the equilibrium state in a period of time. Longitudinal and transverse relaxation describes the magnetization returning to the z -direction when the equilibrium magnetization $M_z^{eq} = M_0$ and $M_{xy-plane}^{eq} = 0$, respectively. The longitudinal and transverse relaxation times, T_1 and T_2 respectively, describe how fast the corresponding process is. $T_{1\rho}$ relaxation is a relaxation process in a spin locked state. These nuclear spin relaxations are caused by fluctuating local

fields, which are sensitive to motions at a characteristic frequency, e.g. $\omega_0 = -\gamma B_0$ for T_1 relaxation. Different motions can be monitored by different relaxation times. For example, the characteristic frequency of T_1 is the Larmor frequency (ω_0), which is on the order of hundreds of MHz. T_2 under heteronuclear ^1H decoupling and $T_{1\rho}$ under spin-lock frequency are influenced by motions on the decoupling field and spin lock field strengths, which are usually tens of kHz. T_1 , T_2 and $T_{1\rho}$ have been measured in many of my projects using different NMR pulse sequences shown in **Figure 1.21**.

A saturation-recovery experiment is used to measure T_1 . No heteronuclear dipolar decoupling is necessary in the z -filter period since the longitudinal magnetization (\hat{S}_z) commutes with the heteronuclear dipolar coupling Hamiltonian ($\hat{H}_D^{IS} = \omega_{IS} 2\hat{I}_z \hat{S}_z$). So, reasonably long τ can be used. In the CP echo experiment for T_2 measurement, ^1H decoupling is necessary, otherwise magnetization will be destroyed by ^1H - ^{13}C dipolar couplings (76). The echo time ($2n\tau$) needs to be rotor-synchronized to avoid any CSA recoupling. The hard π pulse can be replaced by a Gaussian selective pulse to remove the $^1J_{CC}$ -coupling modulation. To measure $T_{1\rho}$, magnetization is spin locked and magnetization undergoes spin lattice relaxation in the rotating frame. ^1H magnetization is transferred to ^{13}C for detection via LG-CP to give site resolution to the $T_{1\rho}$ (71-72).

1.6 Peptide-Incorporated Lipid Membrane Samples

Hydrated phospholipid membranes are used to mimic the cell membrane in our research. When exposed to water, phospholipids self-assemble into a bilayer with the acyl chain pointing to the center and the polar headgroups pointing to water. Compared to detergents and micelles, the liposome samples used in our SSNMR studies better represent the physiological environment, in terms of the lipid bilayer curvature, membrane thickness, lateral pressure and membrane viscosity.

Figure 1.22 illustrates various hydrated lipid membrane samples and their corresponding orientation-dependent ^{31}P spectra. The orientation of phosphate groups in lipid bilayers is represented by the bilayer normal due to the fast uniaxial motion of the lipid around

the long molecular axis (**Figure 1.22.a**). These samples can be classified into two categories based on whether the bilayer normal has a certain angle with respect to the static field (B_0): oriented samples (**Figure 1.22.b**) and unoriented samples (**Figure 1.22.c**).

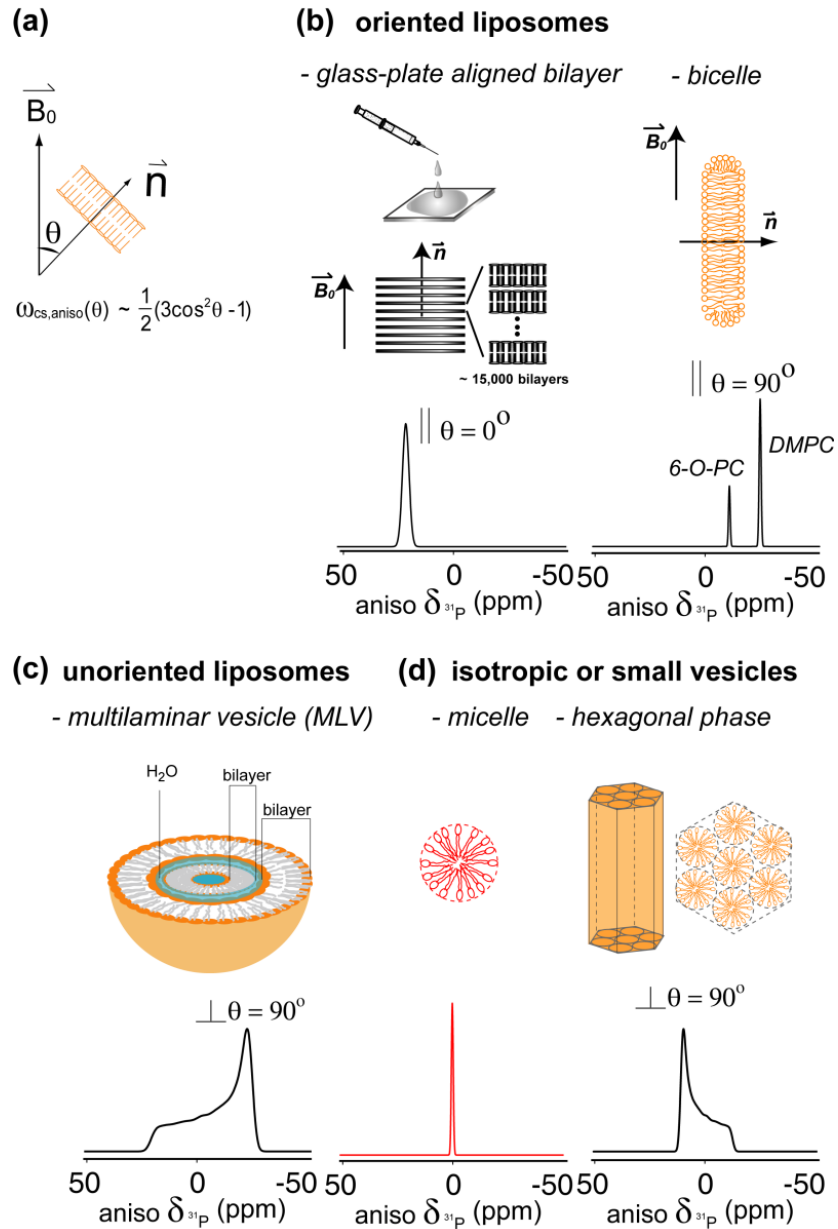


Figure 1.22. Oriented and unoriented lipid membrane samples. (a) Orientational dependence of bilayer normal with respect to static field B_0 . Lipid vesicle curvatures and corresponding ^{31}P spectra of (b) oriented bilayers, (c) multilamellar vesicles, and (d) isotropic or small vesicles.

Oriented samples usually have a unique angle between the bilayer normal and B_0 and are used to measure the orientation of membrane-bound proteins and to examine membrane integrity. There are two kinds of oriented samples, mechanically and magnetically aligned samples. Another category of hydrated membrane samples is the unoriented sample. It is a spherical lipid vesicle and does not have a unique angle between the bilayer normal and B_0 ; instead, the bilayer normal has random orientations, giving a range of ^{31}P resonance frequencies. The frequency distribution results in a broad powder pattern in the spectrum. There are many different kinds of unoriented samples, including small unilamellar vesicle (SUV), giant unilamellar vesicles (GUV), and multilamellar vesicles (MLV). The bilayer structure of these lipid membrane mimics could be disrupted to form isotropic or other small vesicles, such as micelles or hexagonal vesicles, as shown in **Figure 1.23.d**.

Oriented sample preparation protocols can be found in **Appendix A**. Unoriented samples are prepared by aqueous-mixing for water-soluble peptides and detergent-assisted mixing for water-insoluble peptide, as documented in **Appendix B**.

1.7 Thesis Organization

My thesis research focuses on investigating the structure and dynamics of membrane-active peptides in order to elucidate the relation between structure and biological function. Many interesting cationic membrane peptides have been studied and can be classified into different categories including CPP, AMP, transmembrane Kv channel and ^1H channel. The thesis is mainly composed of published papers and organized in order according to the category of the studied peptides.

Chapter 1 introduces and discusses most SSNMR techniques for the membrane peptide studies. Frequency and spin evolution of several robust methods, including REDOR and DIPSHIFT, have been quantitatively derived using quantum mechanics in term of density operators. A full derivation of how PRE NMR determines long-range distances has also been shown. All membrane peptides studied in my graduate research have been concisely introduced. The recent research progress of these cationic membrane peptides are reviewed in **Chapter 2**, where we also took these peptides as examples to introduce various SSNMR

techniques.

Two representative cell-penetrating peptides, penetratin and TAT, were studied in **Chapter 3-7**. Their conformation and dynamics in lipids are investigated in **Chapter 3**. We developed a one-side PRE method and applied it to study the insertion depth of penetratin in **Chapter 4**. In **Chapter 5**, the different roles of two cationic residues, Arg and Lys, have been compared by distance and dynamics measurements. In the same chapter, oligomerization of penetratin in DMPC/DMPG lipids have been studied. To further study the Arg-lipid interaction, highly Arg-rich TAT has been studied in **Chapter 6**, where we found a surprising membrane-bound highly dynamic random-coil structure and correlate it with the translocation function. As a follow-up study in **chapter 7**, we examined the broad linewidth of TAT at low temperature and comprehensively studied the NMR linewidth of several other representative membrane peptides with different conformations. The line broadening mechanisms of membrane peptides have been uncovered.

Chapter 8 and **Chapter 9** are studies of the antimicrobial drug (PMX30016) and antimicrobial peptides (PG-1 and its charge-reduced mutant), respectively. In **Chapter 8**, we successfully applied ^{19}F and ^{31}P SSNMR techniques to study the drug molecule without isotopic labeling and provided various structural and dynamic information. These valuable findings contribute to the understanding of its subtle antimicrobial mechanism. In **Chapter 9**, we have taken PG-1 and IB484 as model peptides to elucidate the antimicrobial mechanism and selectivity in both gram positive and negative lipid membranes.

In **Chapter 10**, the topology and peptide-lipid interaction of the gating helix (S4) of KvAP were determined and compared with the intact Kv protein. These structural data provided valuable insights into the possible gating mechanism of this class of transmembrane potassium channels.

Finally, sample preparation protocols of hydrated peptide-incorporated membrane samples, including glass-plate supported and bicelle oriented samples, unoriented samples, one-side PRE sample and Cu^{2+} -PRE sample, are documented in detail in **Appendix A-B**. The MatLab simulation code for orientation determination of the antimicrobial drug (**Chapter 4**) is included in **Appendix C**. Experimentally calibrated spin diffusion coefficients for spin diffusion simulations (**Chapter 9**) are summarized in **Appendix D**.

Many sample preparation and curve fitting tasks related to my research are not included here, but are well documented in other theses in the group. It is necessary to mention these for future reference. For example, some organic synthesis and protein purification work has been done, including the penetratin peptide purification using HPLC and Fmoc-Proline synthesis and separation using thin-layer chromatography (TLC). Peptide purification using HPLC, desalting using solution exchange, and the protocol of Fmoc-protection are nicely documented in Dr. Tim Doherty's thesis. There, the Fortran codes of SLF experiments to simulate the PISA-wheel pattern of α -helix and 3_{10} helix in **Chapter 10** can also be found. Other home-written curve fitting programs, including dipolar coupling strength simulation for the DIPSHIFT experiment, HNCH experiment, intensity buildup curve of spin diffusion cross peaks to obtain peptide to lipid CH_2 or water distance, can be found in the theses of other group members.

1.8 Copyright Permissions

Chapters 2, 3, 4, 5, 6, 8, 9 and **10** are reprints of published papers. Copyright and printing permissions have been obtained from the following publishing groups:

Chapter 2: *John Wiley and Sons*, license number 2657791346813

Chapter 3: *Elsevier*, license number 2657790911626

Chapter 4: *American Chemical Society*, license number 2657801024110

Chapter 5: *American Chemical Society*, license number 2657800603235

Chapter 6: *American Chemical Society*, license number 2657800805563

Chapter 8: *American Chemical Society*, license number 2657801124766

Chapter 9: *American Chemical Society*, license number 2657800736438

Chapter 10: *Elsevier*, license number 2657791210829

1.9 Reference

1. Renault, M., Cukkemane, A., Baldus, M. (2010) Solid-state NMR spectroscopy on complex biomolecules. *Angew. Chem. Int. Ed. Engl.* 49, 8346-8357.
2. Hong, M and Su, Y. (2011) Structure and Dynamics of Cationic Membrane Peptides and Proteins: Insights from Solid-State NMR, *Protein Sci.*, 20, 641-655

3. Cady, S. D., Schmidt-Rohr, K., Wang, J., Soto, C.S., DeGrado, W.F., Hong, M. (2010) Structure of the amantadine binding site of influenza M2 proton channels In lipid bilayers, *Nature*, 463, 689-692
4. Verardi, R., Shi, L., Traaseth, N.J., Walsh, N., Veglia, G. (2011) Structural topology of phospholamban pentamer in lipid bilayers by a hybrid solution and solid-state NMR method, *Proc. Natl. Acad. Sci. U. S. A.*, 108, 9101-9106
5. Struts, A.V., Salgado, G.F., Brown, M.F. (2011) Solid-state ²H NMR relaxation illuminates functional dynamics of retinal cofactor in membrane activation of rhodopsin, *Proc. Natl. Acad. Sci. U. S. A.*, 108, 8263-8268
6. Schneider, R., Etzkorn, M., Giller, K., Daebel, V., Eisfeld, J., Zweckstetter, M., Griesinger, C., Becker, S., Lange, A. (2010) The native conformation of the human VDAC1 N terminus. *Angew. Chem. Int. Ed. Engl.* 49, 1882-5.
7. Bajaj, V.S., Mak-Jurkauskas, M.L., Belenky, M., Herzfeld, J., Griffin, R.G. (2009) Functional and shunt states of bacteriorhodopsin resolved by 250 GHz dynamic nuclear polarization-enhanced solid-state NMR. *Proc. Natl. Acad. Sci. U. S. A.*, 106, 9244-9249
8. Schmidt-Rohr, K., and Spiess, H. W. (1994) *Multidimensional Solid-State NMR and Polymers*, Academic Press, San Diego, CA.
9. Levitt, M. H. (2001) *Spin Dynamics*, Wiley, West Sussex, England.
10. Harris, R. K. (1986) *Nuclear Magnetic Resonance Spectroscopy*, Longman, Essex, England.
11. Hong, M, (2006) *Lecture notes of Chem 561: fundamental quantum mechanics*, Iowa State University.
12. Hong, M, (2011) *Lecture notes of Chem 564: molecular spectroscopy and structure*, Iowa State University.
13. Schmidt-Rohr, K. (2009), *Lecture notes of Chem 564: molecular spectroscopy and structure*, Iowa State University.
14. Dixon, W. T., Schaefer, J., Sefcik, M. D., Stejskal, E. O., McKay, R. A. (1982) Total Suppression of Sidebands in CPMAS C-13 NMR, *J. Magn. Reson.*, 49, 341
15. Hong, M., Gross, J. D., Rienstra, C. M., Griffin, R. G., Kumashiro, K. K., and Schmidt-Rohr, K. (1997) Coupling Amplification in 2D MAS NMR and Its Application to Torsion Angle Determination in Peptides, *J. Magn. Reson.* 129, 85-92.
16. Munowitz, M. G., Griffin, R. G., Bodenhausen, G., and Huang, T. H. (1981) Two-dimensional rotational spin-echo nuclear magnetic resonance in solids: correlation of chemical shift and dipolar interactions, *J. Am. Chem. Soc.* 103, 2529-2533.
17. Gullion, T. Schaefer, J. (1989) Rotational-echo double-resonance NMR, *J. Magn. Reson.* 81, 196
18. Griffin, R.G. (2010) Spectroscopy: Clear signals from surfaces. *Nature.* 468, 381-382.
19. Hu, K.N., Debelouchina, G.T., Smith, A.A., Griffin, R.G. (2011) Quantum mechanical theory of dynamic nuclear polarization in solid dielectrics. *J. Chem. Phys.* 134, 125105.

20. Su, Y., Mani, R., Hong, M. (2008) Asymmetric Insertion of Membrane Proteins in Lipid Bilayers by Solid-State NMR Paramagnetic Relaxation Enhancement: a Cell-Penetrating Peptide Example, *J. Am. Chem. Soc.* 130, 8856-8864
21. Su, Y., Waring, A. J., Ruchala, P., Hong, M. (2010) Membrane-Bound Dynamic Structure of an Arginine-Rich Cell-Penetrating Peptide, the Protein Transduction Domain of HIV TAT, from Solid-State NMR, *Biochemistry*. 49, 6009–6020
22. Su, Y., Waring, A. J., Ruchala, P., Hong, M. (2010) Solid-State NMR Study of β -hairpin Antimicrobial Protegrin Peptides in Lipopolysaccharide Incorporated Lipid Membranes: Mechanism of Gram Selectivity, *Biochemistry*, 50, 2072-2083
23. Su, Y., DeGrado, W. F., Hong, M. (2010) Orientation, Dynamics, and Lipid Interaction of an Antimicrobial Arylamide Investigated by ^{19}F and ^{31}P Solid-State NMR Spectroscopy, *J. Am. Chem. Soc.* 132, 9197–9205
24. Doherty, T.*, Su, Y.,* (*equal contribution), Hong, M. (2010) High-Resolution Orientation and Depth of Insertion of the Voltage-Sensing S4 Helix of a Potassium Channel in Lipid Bilayers, *J. Mol. Biol.* 401, 642-652
25. Su, Y., Hu, F., Hong, (2011) M. Binding Structure of Cu(II) Inhibition of Influenza A/M2 Proton Channels from Solid-State NMR, in preparation
26. Zhang, H., Neal, S., and Wishart, D. S. (2003) RefDB: A database of uniformly referenced protein chemical shifts, *J. Biomol. NMR*, 25, 173-195
27. Wang, Y., Jardetzky, O., (2002) Probability-based protein secondary structure identification using combined NMR chemical-shift data, *Protein Sci.* 11, 852-861
28. Ye, C., Fu, R., Hu, J., Hou, L., Ding, S. (1993) Carbon-13 chemical shift anisotropies of solid amino acids, *Magn. Reson. in Chem.*, 31, 699-704
29. Rienstra, C. M., Hohwy, M., Hong, M., Griffin, R. G. (2000) 2D and 3D ^{15}N - ^{13}C - ^{13}C NMR chemical shift correlation spectroscopy of solids: Assignment of MAS spectra of peptides, *J. Am. Chem. Soc.* 122, 10979-10990.
30. Rienstra, C. M., Tucker-Kellogg, L.; Jaroniec, C. P.; Hohwy, M., Reif, B., McMahon, M. T., Tidor, B., Lozano-Perez, T., Griffin, R. G. (2002) De novo determination of peptide structure with solid-state magic-angle spinning NMR spectroscopy", *Proc. Natl. Acad. Sci. USA*, 99, 10260-10265
31. Takegoshi, K., Nakamura, S., and Terao, T. (2001) C-13-H-1 dipolar-assisted rotational resonance in magic-angle spinning NMR, *Chem. Phys. Lett.* 344, 631-637.
32. Hong, M. (1999) Solid-State Dipolar INADEQUATE NMR Spectroscopy with a Large Double-Quantum Spectral Width, *J. Magn. Reson.* 136, 86-91.
33. Hohwy, M., Rienstra, C. M., Jaroniec, C. P., and Griffin, R. G. (1999) Fivefold symmetric homonuclear dipolar recoupling in rotating solids: application to double-quantum spectroscopy., *J. Chem. Phys.* 110, 7983-7992.
34. Lesage, A., Bardet, M., and Emsley, L. (1999) Through-Bond Carbon–Carbon Connectivities in Disordered Solids by NMR, *J. Am. Chem. Soc.* 121, 10987-10993

35. Hong, M, Griffin, R.G. (1998) Resonance Assignments for Solid Peptides by Dipolar-Mediated $^{13}\text{C}/^{15}\text{N}$ Correlation Solid-State NMR, *J. Am. Chem. Soc.* 120, 7113-7114
36. Hong, M, Gross, J.D., Griffin, R.G. (1997) Site-resolved Determination of Peptide Torsion Angle Φ from the Relative Orientations of Backbone N-H and C-H Bonds by Solid-State NMR, *J. Phys. Chem.* 101, 5869-5874
37. Costa, P.R., Gross, J.D., Hong, M., Griffin, R.G. (1997) A NCCN 2Q-HLF Experiment for γ Torsion Angle Measurements in Peptides, *Chem. Phys. Lett.* 280, 95-103
38. Jaroniec, C. P., Tounge, B. A., Rienstra, C. M., Herzfeld, J., and Griffin, R. G. (1999) Measurement of ^{13}C - ^{15}N distances in uniformly ^{13}C labeled biomolecules: J-decoupled REDOR., *J. Am. Chem. Soc.* 121, 10237-10238.
39. Jaroniec, C. P., Tounge, B. A., Herzfeld, J., and Griffin, R. G. (2001) Frequency Selective Heteronuclear Dipolar Recoupling in Rotating Solids: Accurate ^{13}C - ^{15}N Distance Measurements in Uniformly ^{13}C , ^{15}N -labeled Peptides., *J. Am. Chem. Soc.* 123, 3507-3519.
40. Su, Y., Doherty, T., Waring, A. J., Ruchala, P., Hong, M (2009) Role of Arginine and Lysine Residues in the Translocation of a Cell-Penetrating Peptide from ^{13}C , ^{31}P and ^{19}F Solid-State NMR, *Biochemistry*, 48, 4587-4595
41. Kumashiro, K.K., Schmidt-Rohr, K., Murphy, O. J. III, Ouellette, K. L., Cramer, W. A., Thompson, L.K., (1998) A Novel Tool for Probing Membrane Protein Structure: Solid-State NMR with Proton Spin Diffusion and X-Nucleus Detection, *J. Am. Chem. Soc.*, 120, 5043-5051
42. Huster, D., Yao, X.L., Hong, M. (2002) Membrane Protein Topology Probed by ^1H Spin Diffusion from Lipids Using Solid-State NMR Spectroscopy, *J. Am. Chem. Soc.* 124, 874-883
43. Lange, A., Luca, S., Baldus, M., (2002) Structural constraints from proton-mediated rare-spin correlation spectroscopy in rotating solids, *J Am Chem Soc.* 124, 9704-5.
44. deAzevedo, E. R., Bonagamba, T. J., Hu, W., and Schmidt-Rohr, K. (1999) Center-band-only detection of exchange: efficient analysis of dynamics in solids by NMR, *J. Am. Chem. Soc.* 121, 8411-8412.
45. Buffy, J. J., Waring, A. J., and Hong, M. (2005) Determination of Peptide Oligomerization in Lipid Membranes with Magic-Angle Spinning Spin Diffusion NMR, *J. Am. Chem. Soc.* 127, 4477-4483.
46. Mani, R., Cady, S. D., Tang, M., Waring, A. J., Lehrer, R. I., and Hong, M. (2006) Membrane-dependent oligomeric structure and pore formation of a beta-hairpin antimicrobial peptide in lipid bilayers from solid-state NMR, *Proc. Natl. Acad. Sci. U S A.* 103, 16242-16247.
47. Dürr, U.H., Grage, S.L., Witter, R., Ulrich, A.S. (2008) Solid state ^{19}F NMR parameters of fluorine-labeled amino acids. Part I: aromatic substituents. *J Magn Reson.* 191, 7-15
48. Grage, S.L., Dürr, U.H., Afonin, S., Mikhailiuk, P.K., Komarov, I.V., Ulrich, A.S. (2008)

- Solid state ^{19}F NMR parameters of fluorine-labeled amino acids. Part II: aliphatic substituents. *J Magn Reson.* 191, 16-23
49. Otting, G., (2010) Protein NMR Using Paramagnetic Ions, *Annu. Rev. Biophys.* 39, 387–405
 50. Bertini, I.; Luchinat, C.; Parigi, G. (2011) *Solution NMR of Paramagnetic Molecules: Applications to Metallobiomolecules and Models*; Elsevier: Amsterdam,
 51. G. A. Webb and R. R. Sharp, (2011) Paramagnetic NMR, *Nuclear Magnetic Resonance*, 30, 477-526
 52. Balayssac, S., Bertini, I., Bhaumik, A., Lelli, M., Luchinat, C. (2008) Paramagnetic shifts in solid-state NMR of proteins to elicit structural information, *Proc Natl Acad Sci U S A.* 105, 17284-17289
 53. Pintacuda, G., Giraud, N., Pierattelli, R., Böckmann, A., Bertini, I., Emsley, L., (2007) Solid-state NMR spectroscopy of a paramagnetic protein: assignment and study of human dimeric oxidized CuII-ZnII superoxide dismutase (SOD), *Angew Chem Int Ed Engl.* 46, 1079-1082.
 54. Parthasarathy, S., Long, F., Miller, Y., Xiao, Y., McElheny, D., Thurber, K., Ma, B., Nussinov, R., Ishii, Y. (2011) Molecular-level examination of Cu^{2+} binding structure for amyloid fibrils of 40-residue Alzheimer's β by solid-state NMR spectroscopy. *J Am Chem Soc.* 133, 3390-3400
 55. Nadaud, P.S., Helmus, J.J., Kall, S.L., Jaroniec, C.P. (2009) Paramagnetic ions enable tuning of nuclear relaxation rates and provide long-range structural restraints in solid-state NMR of proteins. *J Am Chem Soc.* 131, 8108-8120.
 56. La Mar, G. N., Horrocks, W. D., Holm, R. H., (1973) *NMR of paramagnetic molecules; principles and applications*, New York, Academic Press
 57. Satterlee, J.D. (1990) *Fundamental Concepts of NMR in Paramagnetic Systems. Part II: Relaxation Phenomena*, *Concepts in Mag. Res.* 2, 119-129
 58. Lin, I.J., Xia, B., King, D.S., Machonkin, T.E., Westler, W.M., Markley, J.L., (2009) Hyperfine-shifted (^{13}C and (^{15}N) NMR signals from *Clostridium pasteurianum* rubredoxin: extensive assignments and quantum chemical verification, *J Am Chem Soc.* 131, 15555-15563.
 59. Zhang, Y., Sun, H., Oldfield, E., (2005) Solid-state NMR fermi contact and dipolar shifts in organometallic complexes and metalloporphyrins, *J Am Chem Soc.* 127, 3652-3653.
 60. Buffy, J., Hong, T., Waring, A., Lehrer, R.R., Hong, M. (2003) Solid-State NMR Investigation of the Depth of Insertion of PG-1 in DLPC Using Paramagnetic Mn^{2+} , *Biophys. J.* 85, 2363-2373
 61. Nadaud, P. S.; Helmus, J. J.; Hofer, N.; Jaroniec, C. P. (2007) Long-range structural restraints in spin-labeled proteins probed by solid-state nuclear magnetic resonance spectroscopy, *J. Am. Chem. Soc.* 129, 7502–7503.

62. Kumar VV, Malewicz B, Baumann WJ., (1989) Lysophosphatidylcholine stabilizes small unilamellar phosphatidylcholine vesicles. Phosphorus-31 NMR evidence for the "wedge" effect, *Biophys J.* 55, 789-92.
63. Kumar, V.V., Baumann, W.J., (1991) Lanthanide-induced phosphorus-31 NMR down-field chemical shifts of lysophosphatidylcholines are sensitive to lysophospholipid critical micelle concentration, *Biophys J.* 59, 103-107.
64. Solomon, I. (1955) Relaxation process in a system of two spins. *Phys. Rev.* 99, 559-565
65. Bloembergen, N., (1957) Proton relaxation times in paramagnetic solutions. *J. Chem. Phys.* 27, 572-573
66. Joo, C-G., Hu, K-N., Bryant, J. A., and Griffin, R. G. (2006) In situ Temperature Jump-High Frequency DNP Experiments: Enhanced Sensitivity in Liquid State NMR. *J. Am. Chem Soc*, 128, 9428-9432
67. Joo, C-G., Casey, A., Turner, C.J., and Griffin, R.G. (2009) In Situ Temperature Jump Dynamic Nuclear Polarization: Enhanced Sensitivity in Two Dimensional ^{13}C - ^{13}C Correlation Spectroscopy in Solution. *J. Am. Chem. Soc.* 131, 12-13
68. Lovell, S.C., Davis, I.W., Arendall III, W.B., de Bakker, P.I., Word, J.M., Prisant, M.G., Richardson, J.S., Richardson, D.C. (2003) Structure validation by $\text{C}\alpha$ geometry: ϕ , ψ and $\text{C}\beta$ deviation. *Proteins.* 50, 437-450
69. Rhim, W.-K., Elleman, D. D., and Vaughan, R. W. (1973) Analysis of multiple-pulse NMR in solids., *J. Chem. Phys.* 59, 3740-3749.
70. Bielecki, A., Kolbert, A.C., Groot, H.J.M.de, Griffin, R.G., Levitt, M.H. (1990) Frequency-Switched Lee-Goldburg Sequences in Solids", *Adv. Magn. Reson.* 14, 111
71. van Rossum, B.-J., de Groot, C.P., de Groot, H.J.M., Ladizhansky, V., Vega, S. (2000) A method for measuring heteronuclear (^1H ^{13}C) distances in high-speed MAS NMR, *J. Am. Chem. Soc.* 122, 3465-3472.
72. Hong, M., Yao, X.L., Jakes, K., Huster, D., (2002) Investigation of Molecular Motions by Magic-Angle Cross-Polarization NMR Spectroscopy, *J. Phys. Chem.*, 106, 7355-7364
73. Herzfeld, J., Berger, A.E., (1980) Sideband intensities in NMR spectra of samples spinning at the magic angle. *J. Chem. Phys.* 73, 6021-6030
74. Chan, J. C. C., and Tycko, R. (2003) Recoupling of chemical shift anisotropies in solid-state NMR under high-speed magic-angle spinning and in uniformly ^{13}C -labeled systems., *J. Chem. Phys.* 118, 8378-8389.
75. Liu, S.F., Mao, J.D., Schmidt-Rohr, K. (2002) A robust technique for two-dimensional separation of undistorted chemical-shift anisotropy powder patterns in magic-angle-spinning NMR, *J Magn Reson.* 155, 15-28.
76. Hahn, E.L. (1950) Spin echoes, *Phys. Rev.* 80, 580-594

Chapter 2

Structure and dynamics of cationic membrane peptides and proteins: Insights from solid-state NMR

A review paper published in Protein Science

2011, vol. 20, page 641-655

Mei Hong and Yongchao Su

Department of Chemistry, Iowa State University, Ames, IA 50011

2.1 Abstract

Many membrane peptides and protein domains contain functionally important cationic Arg and Lys residues, whose insertion into the hydrophobic interior of the lipid bilayer encounters significant energy barriers. To understand how these cationic molecules overcome the free energy barrier to insert into the lipid membrane, we have used solid-state NMR spectroscopy to determine the membrane-bound topology of these peptides. A versatile array of solid-state NMR experiments now readily yields the conformation, dynamics, orientation, depth of insertion, and site-specific protein–lipid interactions of these molecules. We summarize key findings of several Arg-rich membrane peptides, including β -sheet antimicrobial peptides, unstructured cell-penetrating peptides, and the voltage-sensing helix of voltage-gated potassium channels. Our results indicate the central role of guanidinium-phosphate and guanidinium-water interactions in dictating the structural topology of these cationic molecules in the lipid membrane, which in turn account for the mechanisms of this functionally diverse class of membrane peptides.

2.2 Introduction

In this review we will explore the structure and dynamics of cationic membrane peptides and proteins in lipid bilayers as learned from solid-state NMR. While hydrophobic amino acid residues dominate in large functional membrane proteins, cationic residues such as Arg and Lys are numerous in many membrane peptides, whose biological functions require them to disrupt or cross the lipid membrane (**Table 2.1**). These peptides include the

large family of immune-defense molecules called antimicrobial peptides (AMPs) (1) and the family of delivery molecules called cell-penetrating peptides (CPPs) (2), which contain ~30% to 100% cationic Arg and Lys residues. In larger membrane proteins rich in hydrophobic residues, sparsely distributed cationic residues have also been found to play key roles in function. For example, the voltage-sensing S4 helix of voltage-gated potassium channels contains Arg and Lys residues at every third position, which act as the gating charges that respond to membrane potential changes to open and close the channels (3).

The fascinating fundamental question about these functionally diverse membrane peptides and protein domains is how the cationic residues are imported into and accommodated by the low-dielectric hydrophobic interior of the lipid bilayer against the free energy barrier. The free energy (ΔG) of insertion of the twenty amino acids from aqueous solution to lipid membranes has been measured using an endoplasmic reticulum translocon system (4). While high-resolution details are not provided by this technique, the resulting equilibrium constants of partition are qualitatively consistent with the expectation that hydrophobic residues have favorable (negative) ΔG of transfer into the lipid bilayer while polar and charged residues encounter significant barriers. The ΔG for Arg and Lys was estimated to be +2.5 to +2.7 kcal/mol (4) for transfer to the center of the lipid bilayer where the dielectric constant is the lowest. Thus, for predominantly cationic AMPs and CPPs, where the cationicity is not balanced by many hydrophobic residues, it is puzzling how they overcome the free energy barrier to insert into the center of the membrane, if they indeed do, and moreover how the solvent, the lipid bilayer, adapts to these charges. A second question is how protein insertion into lipid bilayers depends on the secondary structure. While α -helices are stabilized by intramolecular H-bonds, β -strands are stabilized by intermolecular ones. Thus, the membrane insertion of β -sheet-rich peptides, such as some AMPs, would suggest oligomerization (5). Even more unusual is that some highly charged CPPs such as the HIV TAT peptide are unstructured and thus do not possess any peptide-peptide H-bonds (6), yet they are extremely facile in crossing the lipid bilayer. Thus, elucidating the molecular structure and dynamics of these cationic membrane peptides and their interaction with the environment is crucial for understanding their mechanisms of action.

Many molecular dynamics (MD) simulations have been carried out to understand the mode of insertion of Arg-rich peptides (7-10). But solid-state NMR is by far the most direct experimental technique to extract atomic-level structural information about the peptide-membrane interactions of these systems. In this article we will review the solid-state NMR techniques that are now available to determine the structure and dynamics of membrane-bound proteins (11-13), then summarize key findings of several representative AMPs, CPPs, and the voltage-sensing S4 helix of a potassium channel. Finally we will summarize the common principles of membrane interactions of these Arg-rich peptides.

Table 2.1: Examples of Arg-rich membrane peptides and protein domains.

Peptide	Sequence	No. Arg/Lys / Total No. residues
AMP: Protegrin 1	RGRLCYCRRRFCVGVGR	6 Arg / 18
AMP: Tachyplesin I	KWCFRVCYRGICYRRCR	5 Arg, 1 Lys / 18
CPP: HIV TAT(48-60)	GRKKRRQRRRPPQ	6 Arg, 2 Lys / 13
CPP: penetratin	RQIKIWFQNRRMKWKK	3 Arg, 4 Lys / 16
CPP: Arg8	RRRRRRRR	12 Arg / 12
KvAP S4 helix	LGLFRLVRLLRGLRILLII	4 Arg / 19

2.2 Solid-state NMR techniques for studying protein-membrane interactions

Solid-state NMR is a highly versatile and rich spectroscopic technique that can yield atomic-level information about the conformation, dynamics, orientation, depth of insertion of membrane proteins and lipid-protein interactions. Protein conformation, expressed in terms of (ϕ, ψ, χ) torsion angles, can now be determined semi-quantitatively from ^{13}C and ^{15}N chemical shifts, and ever improving computational methods promise more accurate prediction of these protein secondary structure from chemical shifts alone. These chemical shifts can now be measured with multi-dimensional ^{13}C - ^{13}C and ^{13}C - ^{15}N correlation experiments under magic-angle spinning (MAS) (**Fig. 2.1a**) (14, 15). Torsion angles can also be directly quantified by correlating dipolar interactions of the relevant bonds (16, 17) or by measuring internuclear distances. Once the secondary structure is known, the 3D fold of the protein can be obtained by measuring inter-residue ^{13}C - ^{13}C distances using 2D or 3D correlation experi-

ments with long mixing times. This full-structure determination approach has been applied to a human α -defensin, HNP-1 (18, 19).

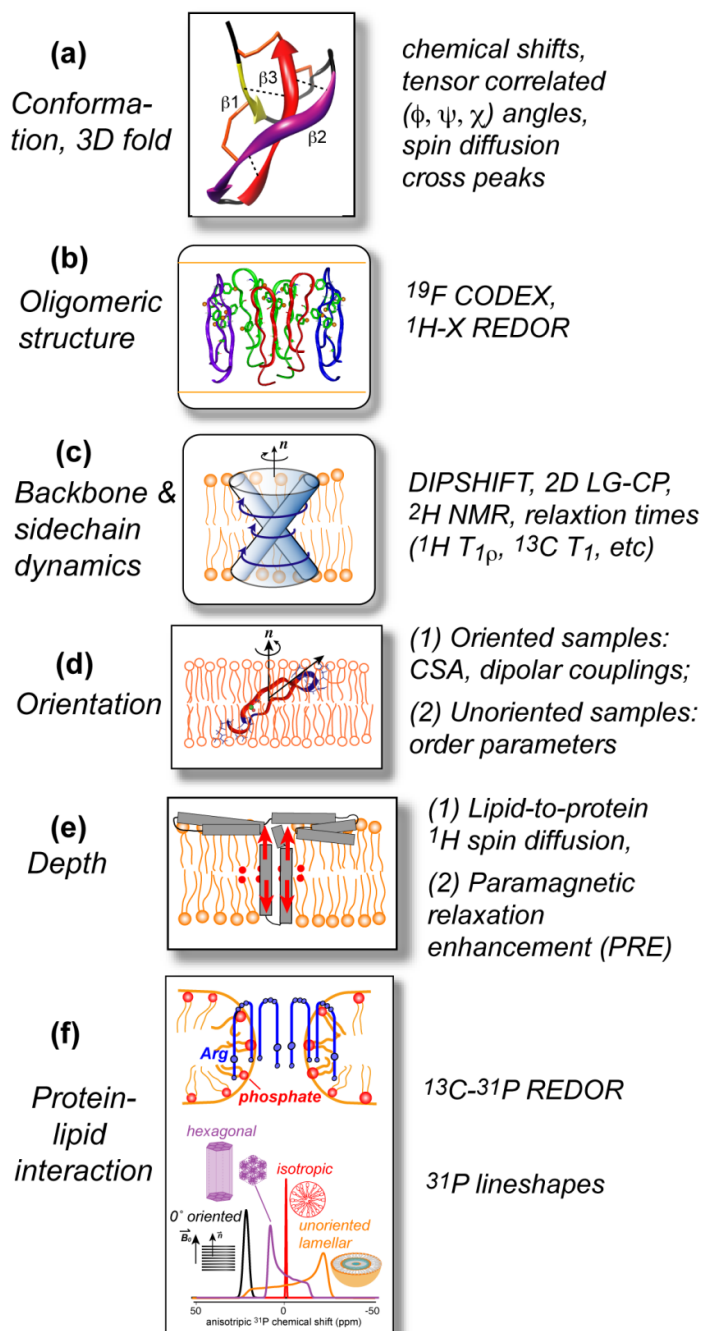


Figure 2.1. Summary of different types of membrane protein structural information that can be obtained from solid-state NMR. (a) Monomer conformation and 3D fold. (b) Oligomeric structure. (c) Protein dynamics. (d) Protein orientation in the membrane. (e) Depth of insertion. (f) Protein-lipid interactions.

The monomer 3D structure forms the basis for determining the oligomeric structure of membrane proteins. To constrain oligomeric packing, one needs to have intermolecular distances well beyond the typical range of 5 Å for NMR. We developed a ^{19}F spin diffusion NMR approach based on the CODEX pulse sequence to measure intermolecular distances up to 15 Å and to determine the oligomeric number of the membrane protein (20-22). We also extended the heteronuclear dipolar-coupling technique, REDOR, to allow measurement of distances from the high-frequency ^1H spin to a low-frequency nucleus, so that distances as long as ~ 8 Å can be detected (23-25) (**Fig. 2.1b**).

Static structure only gives partial insight into membrane protein function. Of equal importance is molecular motion (**Fig. 2.1c**). Both global backbone motion and local segmental motions (6) are common in antimicrobial and cell-penetrating peptides due to the low molecular weights of these peptides and the fluidity of the lipid membrane. With increasing ability to detect motion by NMR, it is now recognized that even larger membrane proteins such as seven transmembrane (TM)-helix proteins can undergo motions of sizeable amplitudes on the NMR timescale. Immobilization of a small polypeptide is usually a sign of its oligomerization in the membrane, while fast uniaxial rotational diffusion is usually associated with monomeric molecules and can disrupt lipid packing in the membrane (28). Motional effects manifest in NMR spectra as line narrowing for fast, sub-microsecond, motions, exchange broadening for intermediate-timescale motions, and cross peaks between conformationally different states for slow millisecond motions. The most robust approach to detect fast motion by NMR is to measure one-bond C-H and N-H dipolar couplings using 2D separated-local-field (SLF) experiments, which resolve the couplings of different sites according to their isotropic chemical shifts. Reduction of the couplings from their rigid-limit values by an order parameter S indicates motion with an amplitude θ where $S \equiv \langle 3\cos^2\theta - 1 \rangle / 2$. To distinguish rigid-body motion from uncorrelated motion, one can measure whether multiple order parameters are correlated according to the protein conformation. For example, α -helices that undergo rigid-body uniaxial rotation around the bilayer normal should exhibit backbone N-H order parameters that fit to a periodic dipolar wave that depends on the tilt angle of the helix axis from the bilayer normal (29, 30). This relationship between orientation and dynamics has been exploited to determine the orientation of several β -sheet AMPs (27, 31).

Local motions of protein sidechains can reveal protein-lipid interactions. For example, the order parameters of the long sidechain of Arg residues in the HIV TAT peptide was found to be the lowest in the middle and higher at the two ends (6), suggesting stabilization of the guanidinium ion by salt bridge interaction with the lipid phosphates.

Membrane proteins differ from globular proteins in that their structure has a topological component, that is, their orientation and depth of insertion in the lipid bilayer. Because of the orientation dependence of nuclear spin interactions, solid-state NMR gives precise information about protein orientation in the membrane. By aligning lipid membranes either mechanically using glass plates or magnetically using lipid bicelles, one can measure orientation-dependent NMR dipolar couplings and anisotropic chemical shifts to report the directions of the bonds from the magnetic field, which in turn reveal the orientation of the molecule from the bilayer normal (**Fig. 2.1d**) (32). Using this approach, and by identifying the so-called PISA wheel patterns in 2D ^{15}N NMR spectra, we have determined the orientation of the voltage-sensing S4 helix of a potassium channel in lipid bicelles (33). While this oriented-sample approach is the mainstay of orientation determination by solid-state NMR, due to the dependence of the order parameters of uniaxially diffusing molecules on molecular orientation, one can now also determine protein orientation using unoriented liposomes (29, 30). In this case more straightforward MAS experiments can be applied and the sample preparation is much simpler. This unoriented sample approach has been demonstrated on a number of membrane peptides and their assemblies (27, 29, 30, 34), due to the prevalence of uniaxial diffusion of small and medium membrane proteins.

To determine how deeply membrane proteins are immersed in the lipid bilayer at physiological temperature, we have adapted both lipid-to-protein spin diffusion (35, 36) and paramagnetic relaxation enhancement (PRE) (37) techniques (**Fig. 2.1e**) (38). The former correlates the ^1H signals of dynamic molecules in the membrane sample with ^{13}C signals of the protein after a ^1H spin diffusion period. The CH_2 and CH_3 signals of the lipid chains are particularly important as the ^1H magnetization source: TM proteins exhibit strong lipid-protein cross peaks in less than 100 ms while surface-bound peptides requires several hundred milliseconds and seconds to develop cross peaks (36). For immobilized membrane proteins, this ^1H spin diffusion technique gives semi-quantitative depth information, since the

diffusion coefficients of the lipid matrix and the lipid-protein interface can be estimated and calibrated (39). For peptides with comparable mobility to the lipids, distance extraction from ^1H spin diffusion is more difficult at ambient temperature, and the PRE technique provides a good alternative. Mn^{2+} or other paramagnetic ions bind to the negatively charged phosphate groups on the membrane surface and cannot freely penetrate into the membrane (38). These paramagnetic ions speed up nuclear spin relaxation in a distance-dependent fashion. Thus, by measuring the PREs of the peptide signals and compare them with those of the lipid carbons, whose depths are well known, one can obtain site-specific depths of the protein residues from the bilayer surface (38). Moreover, lipid vesicles for which only one surface of the bilayer is coated with Mn^{2+} can be prepared to determine the asymmetry of peptide insertion (40). For example, with outer-leaflet Mn^{2+} -bound samples, peptides that insert only into the outer leaflet of the bilayer will exhibit stronger PRE effects (less residual intensity) than peptides that are distributed into both leaflets of the bilayer. Membrane protein depths can also be examined by measuring ^{13}C - ^{31}P distances from the protein backbone to the lipid ^{31}P , provided that the lamellar structure of the bilayer remains intact so that the positions of the ^{31}P atoms represent a well defined membrane surface.

Finally, peptide-induced membrane disorder can be studied using ^{31}P NMR, which is highly sensitive to the membrane morphology (41). Lamellar fluid bilayers exhibit a characteristic uniaxial powder pattern of about 40 ppm wide, while small vesicles or micelles exhibit an isotropic peak at 0 ppm (**Fig. 2.1f**). Hexagonal-phase lipids have a two-fold narrower uniaxial lineshape that is mirror symmetric with the lamellar powder pattern. Site-specific interactions between cationic residues and anionic lipid phosphates can be gleaned from sidechain ^{13}C distances to lipid ^{31}P (**Fig. 2.1f**) (42). Water-protein H-bonding, which may be involved in charge solvation, can be detected using 2D ^{13}C - ^1H and ^{15}N - ^1H correlation experiments (43).

2.3 Solid-state NMR studies of antimicrobial peptides

Antimicrobial peptides are small and predominantly cationic peptides of the innate immune systems of many animals and plants (1, 44, 45). They kill a broad spectrum of microbes, from bacteria to fungi and even viruses, while possessing high selectivity between

eukaryotic cells and microbial cells. AMPs as a family exhibit diverse secondary structures. Well studied α -helical AMPs include LL37 from humans, magainins from frogs, and cecropins from insects (1). β -sheet rich AMPs usually contain 1-4 disulfide bonds. Examples include protegrins from pigs, tachyplesins from horseshoe crabs, and defensins from humans and other mammals (45). AMPs can also adopt random coil or turn conformations, such as indolicidins from cows and histatins from humans.

Based on the similar activities of D- and L-amino acid versions of AMPs, it is known that the principal mechanism of action of many AMPs is the destruction of the lipid-rich microbial cell membranes (46), because enzyme active sites cannot accommodate mirror images of peptides while the dynamic lipid solvent is insensitive to protein chirality. The protective membranes of bacteria vary with the cell type. Gram-positive bacteria are coated by a thick (20-80 nm) but porous peptidoglycan layer (47) and a 4-nm phospholipid bilayer, which is the main permeability barrier of the cell. Gram-negative bacteria are covered by an outer membrane rich in anionic and bulky lipopolysaccharides (LPS) and an inner cytoplasmic phospholipid bilayer. Both the LPS-rich outer membrane and the cytoplasmic membrane must be crossed and disrupted for AMPs to kill Gram-negative bacteria (48, 49). In addition to phospholipid membranes, other targets of bacteria have also been found. These include bacterial cell wall precursors such as lipid II (50, 51) and outer-membrane proteins for cell-wall biogenesis (52).

For AMPs that disrupt phospholipid and LPS membranes, four main structural models have been proposed: barrel stave, toroidal pore, carpet, and in-plane diffusion (44, 53). The barrel-stave model, proposed based on studies of alamethicin (54, 55), posits the formation of TM water-filled pores lined by the amphipathic peptides. Lipid molecules adopt their normal parallel orientation to the bilayer normal, with the acyl chains contacting the hydrophobic part of the amphipathic AMPs. In the carpet model, AMPs aggregate on the membrane surface; at sufficiently high concentrations, they thin the membrane and eventually micellize it. In the toroidal pore model, the peptides change the orientation of some lipid molecules so that the two leaflets merge. The resulting water-filled pore is lined by both peptides and polar lipid headgroups (56, 57). Finally, the in-plane diffusion model posits that

highly dynamic peptides undergo rotational diffusion in the membrane plane, causing transient defects that disrupt the barrier function (58).

These mechanistic models provide readily testable hypotheses because the peptide orientation, depth of insertion and dynamics differ significantly and can be accurately measured using SSNMR techniques described in section 2. Below we summarize the key structural results for several disulfide-bonded β -sheet-rich AMPs, which reveal the mechanistic diversity as well as common structural elements in this class of AMPs.

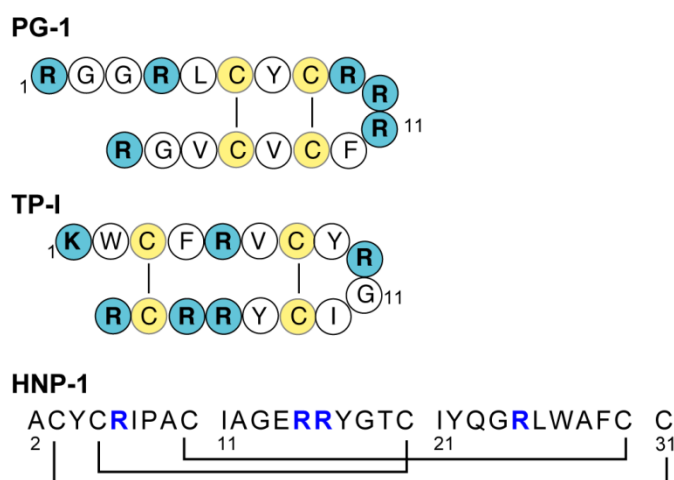


Figure 2.1 Amino acid sequence of three disulfide-stabilized β -sheet AMPs.

2.3.1 *Protegrin-1*

PG-1 is a hexa-Arg 18-residue β -hairpin AMP constrained by two disulfide bonds (**Fig. 2**). It is derived from porcine leukocytes and has broad-spectrum antimicrobial activities (48, 59, 60). The structure-activity relation of PG-1 has been explored extensively (61). ^{13}C and ^{15}N chemical shifts confirmed the β -strand conformation of the peptide in lipid membranes (62, 63) as in solution (64). Dipolar order parameters indicate that except for the short-chain lipid DLPC (12:0), PG-1 is immobilized in lipid membranes with similar thickness as cell membranes, which contain 16- and 18-carbon chains (62). Since a monomeric 18-residue peptide should undergo fast rotational diffusion (65), PG-1 immobilization in the biologically

relevant membrane thickness suggests extensive peptide oligomerization and possible formation of peptide-lipid supramolecular complexes (62).

PG-1 also induces membrane disorder in a thickness-dependent manner: static ^{31}P NMR spectra of both oriented and unoriented samples showed strong isotropic peaks in POPX (X=C, G, E) membranes but not DLPC membranes (63). The non-lamellar intensities increase with the concentrations of the peptide and the anionic lipids and decrease upon the addition of cholesterol (63, 66). These trends correlate well with the selective disruption of anionic bacterial cell membranes. ^{31}P 1D and 2D exchange NMR, which are sensitive to millisecond lipid orientational changes, suggested that PG-1 slowed down the lipid lateral diffusion and reduced the average radius of curvature of POPC vesicles by three fold (67), implying that the membrane is fragmented to smaller vesicles or formed curved morphologies such as toroidal pores within the bilayer.

The depth and orientation of PG-1 were determined in intact DLPC bilayers using Mn^{2+} PRE experiments (38). The two long ends of the elongated molecule experienced stronger T_2 relaxation enhancements, whereas residues in the middle of the hairpin are more shielded from the Mn^{2+} effects. Thus, PG-1 spans both leaflets of the DLPC bilayer (38). Comparison with the lipid PREs further suggested that the DLPC bilayer was thinned by 8-10 Å by PG-1. Since DLPC bilayers are already thinner than POPX bilayers, the result suggests even more severe mismatch with POPX membranes, which may drive the formation of large-scale defects (63, 66). The PG-1 depth was corroborated by orientation measurements. The ^{13}C chemical shift tensor in a β -strand is highly sensitive to the orientations of the β -sheet axis and plane. The ^{13}C and ^{15}N chemical shift anisotropies (CSAs) of glass-plate-aligned PG-1 in DLPC bilayers corresponded to a tilt angle of 55° for the β -strand axis. Thus, the 30 Å-long peptide projects a hydrophobic length of ~ 17 Å onto the bilayer normal, which is comparable with the hydrophobic thickness of the DLPC bilayer. The fact that PG-1 is not more upright may be due to the distribution of the Arg's: a tilted β -sheet would better allow snorkeling of the Arg sidechains to the two membrane surfaces than an upright β -sheet.

In POPX membranes, PG-1 is immobilized, suggesting aggregation. The precise oligomeric structure was examined using ^{19}F spin diffusion and REDOR experiments. In the anionic bacteria-mimetic POPE/POPG membrane, ^1H - ^{13}C and ^{13}C - ^{19}F REDOR data indicated

that the β -hairpins align in parallel with two C-terminal strands in H-bonding distance of each other (68). ^{19}F spin diffusion data confirmed this result, and further showed that the N-terminal strands also pack together, but more loosely. Each ^{19}F label existed in a two-spin cluster within the 15 Å upper limit of the technique (69). Thus, the basic unit of PG-1 assembly is a NCCN dimer, which further associates into a ...NCCNNCCN... oligomer that likely wraps onto itself to form a β -barrel. Leakage assays suggested an inner diameter of about 20 Å for PG-1 formed pores, delineating the size of the β -barrel. Lipid-protein ^1H spin diffusion indicates that the β -barrel is TM, in close contact with the lipid chains (**Fig. 2.3a**).

In eukaryote-mimetic POPC/cholesterol membranes, the topology and oligomeric structure of PG-1 differ dramatically from the anionic membrane situation. The peptide formed at least tetramers, which are no longer inserted into the membrane, as manifested by slow ^1H spin diffusion from the lipid chains (69). Thus, PG-1 is prevented from inserting into the cholesterol-rich host cell membranes due to the membrane rigidity and negative curvature imparted by cholesterol.

The lipid structure around the PG-1 β -barrels in the POPE/POPG membrane was probed using ^{13}C - ^{31}P REDOR experiments (42). For the first time, short Arg C ζ -P distances (4.0 – 5.7 Å) were found, indicating H-bonding of the guanidinium with the phosphates. This short distance was true even for an Arg residue in the middle of the TM β -strand. Combined with the fact that two consecutive residues in the middle of the N-terminal strand have the same short C α -P distances (6.5 Å), these results indicate that the local ^{31}P plane is parallel to the TM β -hairpin, which means that some lipid headgroups are embedded in the hydrophobic part of the membrane, which is precisely the signature of the toroidal pore morphology (57, 70) (**Fig. 2.3a**).

We further probed the nature of the guanidinium-phosphate interaction by mutating the Arg's to dimethylated Arg's (Arg^{mm}), which removed two possible H-bond donors (27). If electrostatic attraction is the only factor causing the Arg-phosphate interaction, then dimethylation should have no effect on PG-1 structure and activity. Instead, Arg^{mm}-PG-1 has three-fold weaker antimicrobial activities, and has significantly altered structure in the membrane (27): it is uniaxially mobile and thus no longer highly oligomerized in the membrane.

Based on backbone order parameters, we determined the orientation of Arg^{mm}-PG-1: it “slices” into the membrane like a knife, with the β -strand axis roughly perpendicular to the bilayer normal (27). This dynamic “molecular knife” motif may explain the partial retention of the antimicrobial activity, and has since been found in other antimicrobial molecules (34). Thus, H-bonding indeed contributes to stabilization of the guanidinium-phosphate complex.

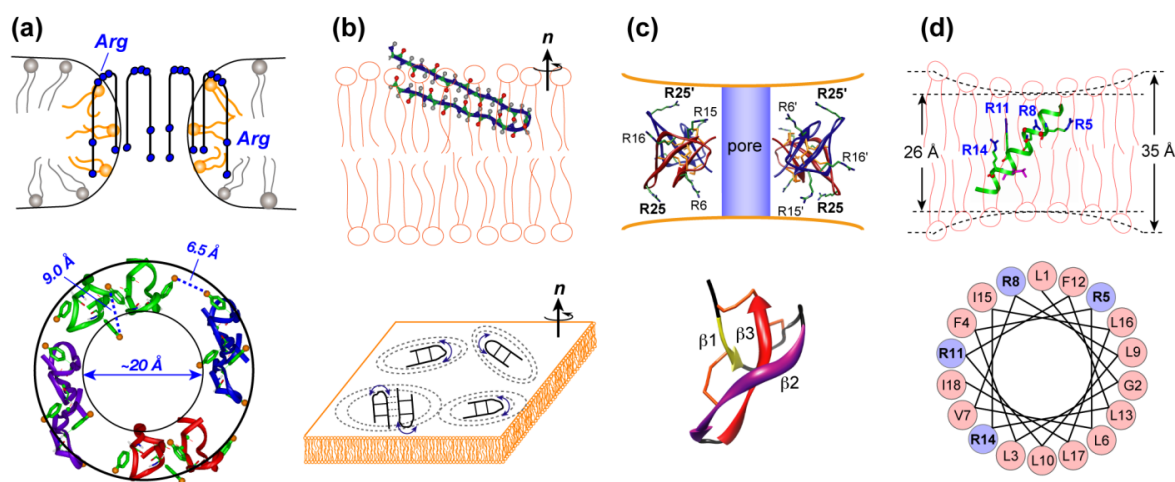


Figure 2.3. The topology of Arg-rich membrane peptides reveals their mechanisms of action. (a) PG-1 forms TM β -barrels that cause toroidal pore defects in POPE/POPG membranes. (b) TP-1 binds to the interface of anionic lipid membranes and undergoes fast uniaxial diffusion to cause membrane defects. (c) HNP-1 forms TM pores with each dimer oriented with the hydrophobic basket bottom facing the lipids and the hydrophilic top facing the pore. R25 is closest among the four Arg's to the membrane surface. (d) The S4 helix of the KvAP voltage-sensing domain is tilted by 40° and thus the membrane to stabilize the gating Arg's.

The sequence dependence of PG-1 structure in the membrane has been examined. The disulfide bonds are important in so far as it maintains the amphipathic structure of the β -hairpin. Removal of the disulfide bonds by Cys-Ala mutations yielded a random coil peptide that no longer disrupted the lipid membrane (71). Decreasing the Arg density weakened the antimicrobial activity (61) and caused a mutant that no longer inserted fully into anionic membranes, in contrast to the wild-type peptide (72).

We recently also investigated the interaction of PG-1 and a charge-reduced mutant with LPS-rich membranes versus regular phospholipid membranes (73). While PG-1 is active against both Gram-positive and Gram-negative bacteria, the charge-reduced mutant is inac-

tive against Gram-negative bacteria, which contain the LPS-rich outer membrane. Depth measurements indicated that PG-1 spans the LPS-rich membrane and causes TM pores without lipid orientational change. These pores may allow a conduit for more peptide to cross into the cytoplasmic membrane to kill the cells. In comparison, the charge-reduced mutant is only partially inserted in the LPS-rich membrane, thus accounting for its inactivity against Gram-negative bacteria.

2.3.2 *Tachyplestin-I*

Tachyplestin I is a horseshoe-crab-derived β -hairpin AMP with an analogous sequence to PG-1 (74). The main difference lies in the distribution of the Arg residues: they are interspersed with the hydrophobic residues in TP-I but segregated from the non-polar ones in PG-1 (**Fig. 2.2**) (12). ^{31}P spectra of glass-plate aligned samples showed sensitive dependence of the TP-I induced disorder on the membrane composition: the peptide caused no disorder to POPC/POPG (3:1) bilayers but both isotropic and powder intensities in POPE/POPG samples (75). Since POPE is the main zwitterionic lipid in bacteria membranes and has a smaller headgroup than POPC, this selective disordering is consistent with the peptide activity and suggests the role of curvature induction in TP-I action.

Unlike PG-1, we directly measured and confirmed the β -hairpin structure of TP-I to address inconsistent prior solution NMR results that showed the N- and C-terminal chains to be straight β -strands at low DPC concentrations but curved in the middle of each strand at high DPC concentrations (76). In DMPC/DMPG bilayers, the (ϕ, ψ) torsion angles of Val6 were measured using dipolar correlation experiments and were found to be $(-133^\circ, 142^\circ)$, while Cys7 (ϕ, ψ) angles were determined through a Val6 ^{13}C O – Phe8 ^{15}N distance to also correspond to the β -strand conformation (77). Thus, the N-terminal chain adopts ideal β -strand conformation without a kink, supporting the low-DPC bound structure. For comparison, the Gly10 ϕ angle was 85° or -85° , confirming its $i+2$ position in the β -turn tip.

How is TP-I inserted into the anionic lipid membrane? The backbone ^{13}C distances to ^{31}P were measured to be $\sim 7 \text{ \AA}$, and peptide cross peaks with lipid CH_2 did not reach plateau within 100 ms but continued to grow at longer mixing times (77). Thus, TP-I is partially

inserted into the anionic lipid membrane (**Fig. 2.3b**), which differs from PG-1 and suggests that the interspersed nature of the basic and hydrophobic residues limits TP-I insertion. In this way, the Arg residues may be stabilized in the intermediate dielectric environment of the membrane-water interface.

To understand how the partially inserted TP-I achieves its antimicrobial activity, we compared its structure and dynamics with two Cys mutants with different activities: TPF4, where all four Cys's were mutated to Phe, was similarly active as TP-I, while TPA4 has much weaker activities. We found that the active TPF4 and the inactive TPA4 both adopt a straight β -strand conformation without a turn, and TPA4 has similar insertion depth as TP-I. Thus, neither conformation nor depth correlates with the activity profile of the three peptides (28). Instead, the mobility profile does: the active TP-I and TPF4 both show fast segmental and global motions in the membrane, whereas TPA4 was immobilized. These dynamic differences were observed from temperature-dependent ^{13}C intensities, motionally averaged couplings, and spin relaxation times. These data suggest that TP-I and TPF4 disrupt the lipid membrane by in-plane diffusion, where the interfacial-located peptides diffuse around the bilayer normal to cause membrane defects (28) (**Fig. 2.3b**). In comparison, TPA4 is immobilized by aggregation and lies on the membrane surface, which is the first stage in the carpet model of antimicrobial activity. The relative activities thus suggest that the in-plane diffusion mechanism is more effective in disrupting lipid membranes than the carpet mechanism, since the latter requires a higher amount of peptides.

2.3.3 Human α -defensin

Defensins are larger disulfide-bonded AMPs than PG-1 and TP-I: they typically contain three β -strands linked by short segments of other secondary structures. Depending on their disulfide linkage patterns, defensins are categorized into α -, β -, and θ -families (45). Humans have six α -defensins, whose crystal structures have been solved in the absence of lipid-mimetic solvents (78, 79). The proteins crystallize into basket-shaped dimers with a polar top and a non-polar base. Based on this structure, several membrane-binding models were proposed, including wedge, dimer pore, general pore (78), and multimeric pore (80). Recently, methods for recombinant expression of correctly folded defensins became availa-

ble (81), facilitating high-resolution structural studies of these proteins in membrane-mimetic environments.

We carried out full structure determination of one of the six human α -defensins, HNP-1, using multidimensional solid-state NMR of uniformly ^{13}C , ^{15}N -labeled protein (18). Experiments on microcrystalline, lipid-free, HNP-1 were conducted to resolve and assign all protein signals. 2D and 3D correlation experiments, now standard in MAS NMR (82, 83), allowed the full assignment of HNP-1 resonances. 3D ^{13}C - ^{13}C - ^{13}C correlation spectra then provided the crucial inter-residue distances to constrain the 3D fold (84) (**Fig. 2.3c**). The NMR structure showed the same disulfide-constrained fold as the crystal structures, but also indicated differences from HNP-3 (78) in the conformation of the rigid loop connecting the first and second β -strands (18). This loop conformation is also variable among different defensin crystal structures, suggesting it may be caused by sequence differences among α -defensins (18).

Upon reconstitution into DMPC/DMPG bilayers, HNP-1 exhibited much broader linewidths, indicating lipid-induced conformational heterogeneity. But the peak positions remain largely unchanged from the microcrystalline state, indicating that the *average* conformation of the protein is unperturbed by lipid binding, which is expected for this disulfide-stabilized protein (19). The main exception is the R25 and I21 in the turn between the second and third β -strands, whose sidechain signals became stronger in the membrane-bound state, suggesting immobilization by membrane binding. In contrast to the smaller PG-1 and TP-I, HNP-1 caused little membrane orientational disorder. ^1H spin diffusion from the lipid chains to the protein is rapid, indicating that HNP-1 inserts across the membrane in a TM fashion, which rules out the wedge model. Analysis of ^{13}C - ^{31}P distances for the four Arg's and the water-protein ^1H spin diffusion profile led to the conclusion that the HNP-1 dimer is oriented with the hydrophobic basket bottom facing the lipids and the polar top facing the aqueous pore, such that R25 is the closest Arg to the membrane surface ^{31}P (19) (**Fig. 2.3c**). This topology explains the R25 immobilization seen in the 2D ^{13}C correlation spectrum. The aqueous pore thus formed by the membrane-spanning protein should depolarize the bacterial cell. Recent reports also suggest that HNP-1 may interact with bacterial cell wall precursors such as lipid II (51) to achieve its antimicrobial function.

2.4 Cell-penetrating peptides

2.4.1 Biological activities

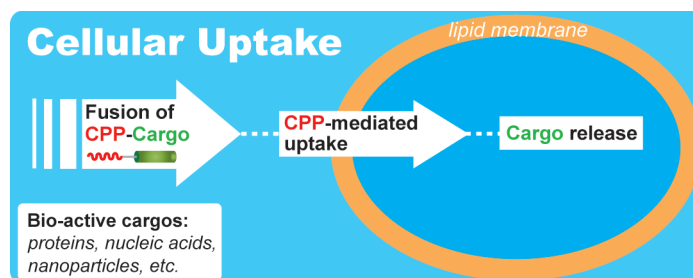


Figure 2.4. CPP-mediated intracellular delivery of therapeutic cargos.

Efficient intracellular delivery of bioactive molecules such as proteins, DNA, and nanoparticles is therapeutically important but difficult to achieve due to the impermeable nature of cell membranes. Cell-penetrating peptides (CPPs), also called protein transduction domains, are a family of small and highly cationic peptides that are readily internalized into cells while tethered to large macromolecular cargos by electrostatic interactions or covalent bonds (**Fig. 2.4**) (2, 85-87). Two of the most studied CPPs are the trans-activating transcriptional activator (TAT) of HIV-1 virus (88, 89) and the penetratin peptide of the *Antennapedia* homeodomain of *Drosophila* (90). Other protein-derived or chemically synthesized CPPs such as polyarginines have also been characterized (91, 92). Because of the highly charged nature of CPPs, the same free-energy question for AMPs is also relevant for CPPs. Structural studies of CPPs when bound to lipid membranes thus provide valuable insights into their mechanism of membrane translocation. We summarize below our SSNMR findings of penetratin and HIV TAT.

2.4.2 Dynamic and unstructured nature of membrane-bound CPPs

In contrast to AMPs, which mostly have well-defined and amphipathic structures, neither penetratin nor HIV TAT exhibit canonical secondary structures in the lipid bilayer. TAT was already known to exist as a random coil in aqueous and organic solutions (93); nevertheless, its random conformation in the lipid bilayer was surprising (6) because many peptides acquire H-bonded secondary structures upon membrane binding (94). The confor-

mation of penetratin was known to depend on the environment: it is random coil in water, α -helical in SDS micelles (95), and α -helical, random coil or β -sheet in lipid-mimetic solvents depending on the thickness and anionic content of the membrane (96-98).

Chemical shifts indicate that in anionic bilayers, penetratin conformation depends on the temperature: in the gel phase the peptide exhibits β -sheet ^{13}C and ^{15}N shifts while at physiological temperature it exhibits coil or turn chemical shifts (99). This unusual sheet-to-coil conformational change occurs in saturated DMPC/DMPG and unsaturated POPC/POPG membranes, is reversible with temperature, and occurs at a range of peptide/lipid molar ratios. Thus it is an intrinsic property of the peptide. Analysis of the peak intensities of the two states indicated that the sheet-to-coil transition is entropically driven: a positive enthalpy change of +0.89 kcal/mol is countered by a positive entropy change of +3.1 cal/(mol·K) (99). At high temperature, the backbone exhibits low order parameters of 0.23-0.52 (99). However, among five examined residues, one residue, Arg10, retained the β -strand torsion angles at high temperature and exhibited a nearly rigid-limit $\text{C}\alpha\text{-H}\alpha$ order parameter ($S_{\text{CH}}=0.92$) (100). This difference suggests that Arg's, due to their interactions with lipid phosphates, may stabilize the conformation of the otherwise coil or turn-rich penetratin.

The dynamic structure is even more pronounced for membrane-bound HIV TAT (6). Not only do TAT chemical shifts correspond to the random coil conformation, but the linewidths are extremely narrow at high temperature (~ 0.3 ppm for ^{13}C) and broadened (~ 4.5 ppm for ^{13}C) to include all secondary shifts at low temperature. This random coil conformation was corroborated by extremely low backbone order parameters (0.14-0.20) and the resolution of $^1\text{J}_{\text{CH}}$ couplings in 2D ^1H - ^{13}C correlation spectra measured without ^1H homonuclear decoupling. Thus, HIV TAT is arguably the first clear documented case of a membrane-bound random coil peptide. The fact that both penetratin and HIV TAT are highly dynamic and unstructured suggests that this state may be relevant for membrane translocation, which is supported by other data summarized below.

2.4.3 Depth of insertion of CPPs and weak membrane perturbation

To understand how the cationic CPPs cross the lipid membrane, we measured the insertion depths using PRE, ^{13}C - ^{31}P REDOR and ^1H spin diffusion experiments. One-side PRE was developed to determine both the depth and symmetry of penetratin insertion in liquid-crystalline membranes (40) (**Fig. 2.5a, b**). An electroporation model had suggested that at low concentrations CPPs bind to the outer leaflet of the bilayer, causing a TM electric field that alters membrane curvature. At sufficiently high concentrations, electroporation-like membrane permeabilization occurs, driving peptide translocation and relieving the curvature stress (101). The T_2 PREs of outer-surface Mn^{2+} indicate that penetratin retains more than 60% of the intensity at P/L=1:40, thus the peptide is distributed in both leaflets of the bilayer already at low concentrations (40). The peptide backbone exhibits ^{13}C - ^{31}P distances 6.9 Å - 8.2 Å, indicating an interfacial location. Therefore, penetratin is inserted into both leaflets of the bilayer but is far from the membrane center (**Fig. 2.5c**). The one-side PRE technique was also recently applied to an antimicrobial arylamide to reveal its interfacial binding (34).

^1H spin diffusion was used to measure the depth of HIV TAT in DMPC/DMPG bilayers (6). Although mobile peptides generally do not lend themselves well to *quantitative* depth extraction using this technique, due to the difficulty of estimating the diffusion coefficients, *qualitative* depth information can still be obtained based on the observation of lipid-peptide cross peaks. TAT exhibited strong water cross peaks and, despite its nearly isotropic mobility and hence inefficient spin diffusion, weak but clear lipid-chain cross peaks with the peptide were observed within a short mixing time of 144 ms. Thus, the peptide is bound inside the membrane, likely in the glycerol backbone region (**Fig. 2.5d**). Indeed, TAT binding enhanced ^1H spin diffusion from water to the lipid headgroups in POPE/POPG membranes, also ruling out an external surface location. All polar residues with exchangeable protons such as Lys4, Gln7 and Arg8 showed strong water cross peaks, indicating stabilization of the charged residues by peptide-water interactions.

Static ^{31}P NMR lineshapes showed that, in contrast to PG-1 and TP-I, penetratin and TAT did not create isotropic or hexagonal phase peaks, but only increased the powder intensities in glass-plate aligned samples (34, 40). Static ^2H spectra showed no changes in the ^2H quadrupolar splittings of the lipid acyl chains upon peptide binding. Therefore, the lamellar

order of the lipid membrane was intact, consistent with the generally non-disruptive nature of CPPs.

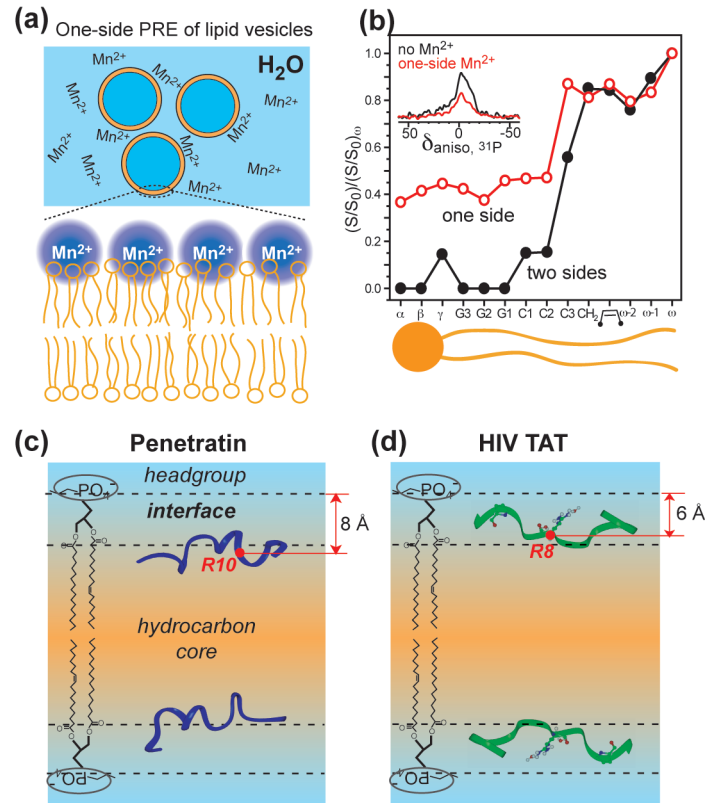


Figure 2.5. Depth of insertion of CPPs. (a) One-side PRE of large unilamellar vesicles. Orange: lipids. Blue: water. Mn²⁺ ions are distributed only on the outer surface of the lipid vesicles. (b) Double normalized intensity of Mn²⁺-bound POPC/POPG membranes. ³¹P intensities are roughly halved in a one-side Mn²⁺ sample (inset) as expected. Carbons more embedded in the membrane experience less T_2 relaxation enhancement and thus exhibit higher intensities. Red: one-side Mn²⁺-bound samples. Black: two-side Mn²⁺-bound samples. (c) Depth of penetratin in POPC/POPG membranes (P/L=1:15) from one-side PRE and ¹³C-³¹P distances. (d) Depth of HIV TAT in DMPC/DMPG membranes (P/L=1:15) from ¹H spin diffusion and ¹³C-³¹P distances.

2.4.4 Different roles of Arg and Lys in membrane translocation

Penetratin and HIV TAT contain 38% and 62% cationic residues, respectively (Table 2.1), and thus are ideal for studying the roles of Arg and Lys in membrane translocation. Fig. 2.6 summarizes key ¹³C-³¹P distances measured in the two peptides (6, 100). Penetratin exhibits short sidechain ¹³C-³¹P distances of 4.2 Å and 4.0 Å from Arg10 C ζ and Lys13 C ϵ , re-

spectively, while the neutral sidechains of Ile3 has much longer distances (*100*). Therefore, short ^{13}C - ^{31}P distances are specific to cationic sidechains due to charge neutralization and H-bonding.

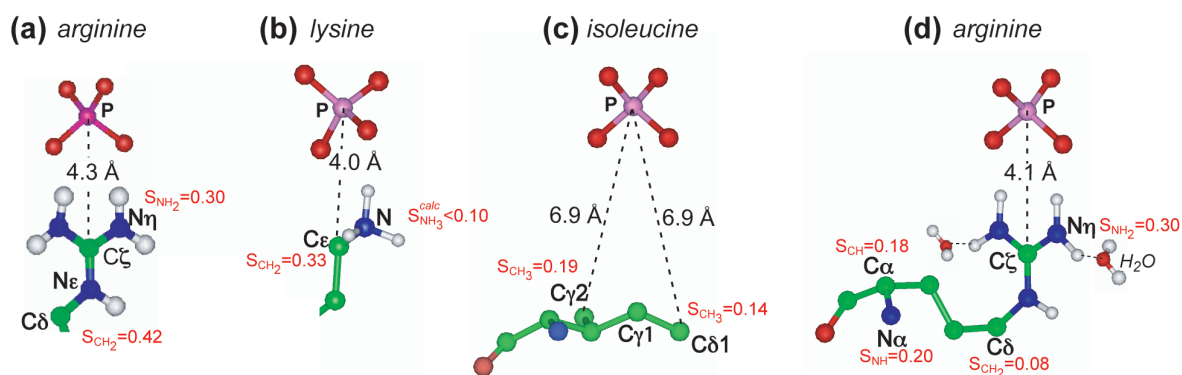


Figure 2.6. ^{13}C - ^{31}P distances and order parameters of several residues in membrane-bound penetratin (a-c) and TAT (d). (a) Arg10 $\text{C}\zeta$ -P distance in DMPC/DMPG-bound penetratin. (b) Lys13-phosphate distance in DMPC/DMPG bound penetratin. (c) Longer Ile3 ^{13}C - ^{31}P distances in penetratin indicate no interaction between neutral residues and lipid headgroups. (d) Guanidinium-phosphate and guanidinium-water interactions of Arg8 in DMPC/DMPG bound TAT. All distances were measured in gel-phase membranes while dipolar order parameters were measured in the liquid-crystalline phase.

It is well documented that CPP analogs where Arg's were replaced by Lys's have lower translocation efficiencies (*102*). For example, the uptake efficiency of an all-Arg analog of penetratin was higher than the wild-type peptide, which contains 3 Arg's and 4 Lys's, whereas an all-Lys analog had lower translocation abilities (*103*). Thus, the similarly short ^{13}C - ^{31}P distances of Arg10 and Lys13 sidechains were at first puzzling. However, these distances were measured in the gel-phase membrane in order to freeze lipid motions. In the fluid phase, Arg10 guanidinium exhibited much higher order parameters ($S_{\text{NH}}=0.3$) than the Lys13 ammonium ($S_{\text{NH}} < 0.1$), indicating that the Lys-phosphate interaction is weaker at physiological temperature where membrane translocation occurs, due to the mobility of the ammonium group and the poorly directed nature of its H-bonds.

Similarly short Arg8 $\text{C}\zeta$ - ^{31}P distance was detected for HIV TAT in DMPC/DMPG bilayers (**Fig. 2.6d**) (6). Interestingly, the guanidinium-phosphate interaction caused a non-monotonic order parameter profile of the sidechain: the order parameters decreased from

$N\alpha$ ($S_{NH} = 0.20$) to $C\delta$ ($S_{CH} = 0.08$) and then increased to $N\eta$ ($S_{NH} = 0.30$), thus confirming the presence of stabilizing salt bridge interactions.

2.4.5. Free energy of CPP insertion into lipid membranes

The classical Wimley-White interfacial scale has been used to estimate the free energy of transferring an amino acid from water to the membrane-water interface (104). Based on this scale, the insertion of TAT from water to the membrane-water interface would require a high energy of ~ 9 kcal/mol. However, the actual energy barrier for TAT binding to anionic membranes is almost certainly much lower, because the Wimley-White interfacial scale was derived for neutral POPC bilayers and thus does not include electrostatic attraction between cationic peptides and anionic lipids. Indeed, calorimetric studies of the binding energy of HIV-TAT to 25% anionic membranes (105, 106) reported a *favorable* free energy of -5.2 kcal/mol, 80% of which was estimated to be due to electrostatic interaction. In addition to electrostatic attraction, H-bonding of the guanidinium ions to the lipid phosphates and water, as detected in the NMR spectra (6), must further contribute to the stabilization of TAT at the membrane-water interface. Each guanidinium ion can form up to five H-bonds with lipid phosphates and water. Thus the hexa-Arg TAT could gain up to -15 kcal/mol favorable free energy (99). We hypothesize that these two contributions overcome the Born repulsion and account for the facile insertion of this highly charged peptide into the lipid membrane.

2.4.6 Mechanism of CPP translocation

Much of the debate about the mechanism of action of CPPs centers on whether cellular uptake proceeds via direct membrane crossing, endocytosis, or other transient vesicle-mediated routes. The endocytosis mechanism was proposed based on the observation that cellular uptake of CPPs in living cells is temperature and energy-dependent (107); however such temperature sensitivity should also occur in membrane-mediated cellular uptake. Even if the endocytotic pathway is operative, a CPP may still need to cross the endosomal membrane in order to enter the cytoplasm. An earlier inverse micelle model (108) can be ruled out by the lack of isotropic signals in static ^{31}P NMR spectra (40). A membrane-crossing mechanism for CPPs was supported by MD simulations (8, 109) and by the solid-state NMR data

summarized here. The CPP interaction with lipids is unique in many ways among membrane peptides. The high cationic density has several consequences. First, it drives CPP binding to the membrane surface (105, 106), after which Arg-phosphate interactions facilitate peptide insertion into the membrane by minimizing the exposure of the charged residues to the hydrophobic interior. Second, the Arg clusters can strongly interact with lipid headgroups on the distal surface of the bilayer to drive translocation. Third, the high charge density removes any amphipathic structure, thus preventing the peptide from forming long-lasting supramolecular complexes with lipids that would prevent its further entry into the cell. The unstructured CPPs stabilize their backbone polar groups by forming transient *intermolecular* H-bonds with the lipid phosphates and water (6). Thus, the much higher conformational dynamics and the unstructured nature of TAT and penetratin compared to most AMPs are likely functionally relevant and distinguish them from AMPs, which seemingly have similar amino acid sequences.

2.5 Arg-rich voltage-sensing helix of a potassium channel

The opening and closing of voltage-gated potassium channels are controlled by several conserved Arg residues at every third position in the S4 helix of the voltage-sensing domain (VSD) (110, 111). The interaction of these Arg's with the lipid membrane has been of strong interest for understanding the atomic mechanisms of voltage-gated ion channels. A paddle model based on the crystal structure suggested that the gating Arg's interact directly with the lipids (3), while the canaliculi model proposed that the Arg's were shielded by acidic residues in other TM helices of the VSD (112).

We determined the orientation and insertion depth of a peptide corresponding to the S4 helix of a potassium channel, KvAP, in lipid bilayers using both oriented-sample and MAS NMR (33). 2D experiments correlating the ^{15}N CSAs with N-H dipolar couplings of magnetically aligned S4 peptide revealed a tilt angle of 40° and one of two possible rotation angles differing by 180° (Fig. 2.3d). Remarkably, this orientation is nearly identical to that in the intact VSD (113), suggesting that interactions between S4 and the other helices of the VSD may not be essential for the membrane topology of the gating domain. ^{13}C - ^{31}P distances from the peptide backbone to lipid ^{31}P suggested that DMPC/DMPG bilayers are thinned by $\sim 9 \text{ \AA}$ at

the peptide binding site, which translates to 2-Å average thinning of the entire membrane when the peptide/lipid ratio was taken into account (33). This result is consistent with neutron diffraction of the KvAP VSD (114). REDOR experiments further indicate that the second Arg has a short C ζ distance of 4.6 Å to the lipid ³¹P, thus the same guanidinium-phosphate interaction seen in AMPs and CPPs also exist in the S4 helix. This topology and lipid-peptide interaction suggest that the S4 amino acid sequence plays a more important role than previously thought for determining the membrane topology of the gating segment, possibly without requiring inter-helical protein-protein interactions. The tilted orientation of the S4 helix is reminiscent of the orientation of PG-1 in DLPC bilayers (63), despite their different secondary structures, and suggests that the need for Arg's to snorkel to the membrane surface may in general disfavor a more upright orientation in the membrane.

2.6 Concluding Remarks

The above survey shows that, while cationic membrane peptides and protein domains encompass a large number of functionally diverse molecules with different mechanisms of action, there do exist common atomic and molecular structural features. One common structural feature is that Arg residues form electrostatically and H-bonded complexes with lipid phosphates. Existence of such guanidinium-phosphate salt bridges has been experimentally identified by both distance and dynamic NMR results. These complexes likely have the stoichiometry of two phosphates per guanidinium ion, although it has not been directly proved. Mutation of the Arg's significantly altered the function of one AMP and is known to be debilitating for voltage-gated potassium channels. Another general interaction, Arg-water H-bonding, has also been experimentally verified, for example for TAT and PG-1, based on 2D ¹H-¹³C and ¹H-¹⁵N correlation NMR (6, 43). These two interactions can effectively make the free energy of insertion of these cationic peptides favorable (negative).

Our solid-state NMR studies also suggest that the strongest membrane perturbation is caused by peptides with intermediate cationic charge densities and with an amphipathic structure (Table 2.1). At higher Arg densities, peptides such as CPPs become less structured and more dynamic, and cause little orientational disorder to the membrane. At lower Arg densities, peptides such as KvAP S4 (Fig. 2.3d) and HNP-1 (Fig. 2.3c) also become less

perturbing to the membrane and instead exhibit local interactions between the charged residues and lipid headgroups. How exactly Arg's and Lys's dictate the topology of this third class of peptides is subtler and future investigations may give more insights into the structural principles behind these systems. Overall, the cationic residues play a significant and possibly central role in dictating the membrane-bound topology of the peptides. Together with the oligomeric structure and dynamics, they underlie the mechanism of action of this large class of membrane peptides and protein domains.

2.7 Acknowledgement

This work is funded by NIH grant GM-066976.

2.8 Reference

1. Zasloff, M. (2002) Antimicrobial peptides of multicellular organisms, *Nature* 415, 389-395.
2. Fischer, R., Fotin-Mleczek, M., Hufnagel, H., and Brock, R. (2005) Break on through to the other side-biophysics and cell biology shed light on cell-penetrating peptides, *ChemBioChem*. 6, 2126-2142.
3. Jiang, Y., Lee, A., Chen, J., Ruta, V., Cadene, M., Chait, B. T., and MacKinnon, R. (2003) X-ray structure of a voltage-dependent K⁺ channel, *Nature* 423, 33-41.
4. Hessa, T., Kim, H., Bihlmaier, K., Lundin, C., Boekel, J., Andersson, H., Nilsson, I., White, S. H., and von Heijne, G. (2005) Recognition of transmembrane helices by the endoplasmic reticulum translocon, *Nature* 433, 377-381.
5. Popot, J. L., and Engelman, D. M. (1990) Membrane protein folding and oligomerization: the two-stage model., *Biochemistry* 29, 4031-4037.
6. Su, Y., Waring, A. J., Ruchala, P., and Hong, M. (2010) Membrane-bound dynamic structure of an arginine-rich cell-penetrating peptide, the protein transduction domain of HIV TAT, from solid-state NMR, *Biochemistry* 49, 6009-6020.
7. Freites, J. A., Tobias, D. J., von Heijne, G., and White, S. H. (2005) Interface connections of a transmembrane voltage sensor, *Proc. Natl. Acad. Sci. U. S. A.* 102, 15059-15064.
8. Herce, H. D., and Garcia, A. E. (2007) Molecular dynamics simulations suggest a mechanism for translocation of the HIV-1 TAT peptide across lipid membranes, *Proceedings of the National Academy of Sciences of the United States of America* 104, 20805-20810.

9. MacCallum, J. L., Bennett, W. F., and Tieleman, D. P. (2008) Distribution of amino acids in a lipid bilayer from computer simulations, *Biophys. J.* 94, 3393-3404.
10. Dorairaj, S., and Allen, T. W. (2007) On the thermodynamic stability of a charged arginine side chain in a transmembrane helix, *Proc. Natl. Acad. Sci. U. S. A.* 104, 4943-4948.
11. Hong, M. (2006) Solid-state NMR studies of the structure, dynamics, and assembly of beta-sheet membrane peptides and alpha-helical membrane proteins with antibiotic activities, *Acc. Chem. Res.* 39, 176-183.
12. Hong, M. (2007) Structure, Topology, and Dynamics of Membrane Peptides and Proteins from Solid-State NMR Spectroscopy, *J. Phys. Chem. B.*, 10340-10351.
13. Hong, M. (2006) Oligomeric structure, dynamics, and orientation of membrane proteins from solid-state NMR, *Structure* 14, 1731-1740.
14. Hong, M. (1999) Resonance Assignment of $^{13}\text{C}/^{15}\text{N}$ Labeled Proteins by Two- and Three-Dimensional Magic-Angle-Spinning NMR, *J. Biomol. NMR* 15, 1-14.
15. Rienstra, C. M., Hohwy, M., Hong, M., and Griffin, R. G. (2000) 2D and 3D ^{15}N - ^{13}C - ^{13}C NMR chemical shift correlation spectroscopy of solids: assignment of MAS spectra of peptides., *J. Am. Chem. Soc.* 122, 10979-10990.
16. Costa, P. R., Gross, J. D., Hong, M., and Griffin, R. G. (1997) Solid-State NMR Measurement of ψ in Peptides: a NCCN 2Q-Heteronuclear Local Field Experiment, *Chem. Phys. Lett.* 280, 95-103.
17. Hong, M., Gross, J. D., and Griffin, R. G. (1997) Site-resolved determination of peptide torsion angle ϕ from the relative orientations of backbone N-H and C-H bonds by solid-state NMR, *J. Phys. Chem. B* 101, 5869-5874.
18. Zhang, Y., Doherty, T., Li, J., Lu, W., Barinka, C., Lubkowski, J., and Hong, M. (2010) Resonance assignment and three-dimensional structure determination of a human α -defensin, HNP-1, by solid-state NMR, *J. Mol. Biol.* 397 408-422.
19. Zhang, Y., Lu, W., and Hong, M. (2010) The Membrane-Bound Structure and Topology of a Human α -Defensin Indicate a Dimer Pore Mechanism for Membrane Disruption, *Biochemistry* 49, 9770-9782.
20. Buffy, J. J., Waring, A. J., and Hong, M. (2005) Determination of peptide oligomerization in lipid bilayers using ^{19}F spin diffusion NMR., *J. Am. Chem. Soc.* 127, 4477-4483.
21. deAzevedo, E. R., Bonagamba, T. J., Hu, W., and Schmidt-Rohr, K. (1999) Centerband-only detection of exchange: efficient analysis of dynamics in solids by NMR, *J. Am. Chem. Soc.* 121, 8411-8412.
22. Luo, W., and Hong, M. (2006) Determination of the oligomeric number and intermolecular distances of membrane protein assemblies by anisotropic ^1H -driven spin diffusion NMR spectroscopy, *J. Am. Chem. Soc.* 128, 7242-7251.

23. Schmidt-Rohr, K., and Hong, M. (2003) Measurements of carbon to amide-proton distances by C-H dipolar recoupling with ^{15}N NMR detection, *J. Am. Chem. Soc.* 125, 5648-5649.
24. Sinha, N., and Hong, M. (2003) X- ^1H Rotational-Echo Double-Resonance NMR For Torsion Angle Determination of Peptides, *Chem. Phys. Lett.* 380, 742-748.
25. Wi, S., Sinha, N., and Hong, M. (2004) Long range ^1H - ^{19}F distance measurement in peptides by Solid-State NMR, *J. Am. Chem. Soc.* 126, 12754-12755.
26. Yamaguchi, S., Huster, D., Waring, A., Lehrer, R. I., Tack, B. F., Kearney, W., and Hong, M. (2001) Orientation and Dynamics of an Antimicrobial Peptide in the Lipid Bilayer by Solid-State NMR, *Biophys. J.* 81, 2203-2214.
27. Tang, M., Waring, A. J., Lehrer, R. I., and Hong, M. (2008) Effects of guanidinium-phosphate hydrogen bonding on the membrane-bound structure and activity of an arginine-rich membrane peptide from solid-state NMR spectroscopy, *Angew, Chem. Int. Ed. Engl.* 47, 3202-3205.
28. Doherty, T., Waring, A. J., and Hong, M. (2008) Dynamic structure of disulfide-removed linear analogs of tachyplesin-I in the lipid bilayer from solid-state NMR, *Biochemistry* 47, 1105-1116.
29. Cady, S. D., Goodman, C., C.Tatko, DeGrado, W. F., and Hong, M. (2007) Determining the orientation of uniaxially rotating membrane proteins using unoriented samples: a ^2H , ^{13}C , and ^{15}N solid-state NMR investigation of the dynamics and orientation of a transmembrane helical bundle, *J. Am. Chem. Soc.* 129, 5719-5729.
30. Hong, M., and Doherty, T. (2006) Orientation determination of membrane-disruptive proteins using powder samples and rotational diffusion: a simple solid-state NMR approach, *Chem. Phys. Lett.* 432, 296-300.
31. Tang, M., and Hong, M. (2009) Structure and mechanism of beta-hairpin antimicrobial peptides in lipid bilayers from solid-state NMR spectroscopy, *Mol. Biosyst.* 5, 317-322.
32. Opella, S. J., and Marassi, F. M. (2004) Structure determination of membrane proteins by NMR spectroscopy, *Chem. Rev.* 104, 3587-3606.
33. Doherty, T., Su, Y., and Hong, M. (2010) High-resolution orientation and depth of insertion of the voltage-sensing S4 helix of a potassium channel in lipid bilayers, *J. Mol. Biol.* 401, 642-652.
34. Su, Y., DeGrado, W. F., and Hong, M. (2010) Orientation, dynamics, and lipid interaction of an antimicrobial arylamide investigated by ^{19}F and ^{31}P solid-state NMR spectroscopy, *J. Am. Chem. Soc.* 132, 9197-9205.
35. Kumashiro, K. K., Schmidt-Rohr, K., Murphy, O. J., Ouellette, K. L., Cramer, W. A., and Thompson, L. K. (1998) A novel tool for probing membrane protein structure: solid-state NMR with proton spin diffusion and X-nucleus detection, *J. Am. Chem. Soc.* 120, 5043-5051.

36. Huster, D., Yao, X. L., and Hong, M. (2002) Membrane Protein Topology Probed by ^1H Spin Diffusion from Lipids Using Solid-State NMR Spectroscopy, *J. Am. Chem. Soc.* 124, 874-883.
37. Solomon, I. (1955) Relaxation processes in a system of two spins., *Phys. Rev.* 99, 559-565.
38. Buffy, J. J., Hong, T., Yamaguchi, S., Waring, A., Lehrer, R. I., and Hong, M. (2003) Solid-State NMR Investigation of the Depth of Insertion of Protegrin-1 in Lipid Bilayers Using Paramagnetic Mn^{2+} , *Biophys. J.* 85, 2363-2373.
39. Mani, R., Waring, A. J., and Hong, M. (2007) Conformation, Dynamics, and Insertion of a Noncysteine-Containing Protegrin-1 Analogue in Lipid Membranes from Solid-State NMR Spectroscopy, *ChemBioChem* 8, 1877-1884.
40. Su, Y., Mani, R., and Hong, M. (2008) Asymmetric insertion of membrane proteins in lipid bilayers by solid-state NMR paramagnetic relaxation enhancement: a cell-penetrating Peptide example, *J. Am. Chem. Soc.* 130, 8856-8864.
41. Seelig, J. (1978) ^{31}P nuclear magnetic resonance and the headgroup structure of phospholipids in membranes, *Biochim. Biophys. Acta* 515, 105-140.
42. Tang, M., Waring, A. J., and Hong, M. (2007) Phosphate-Mediated Arginine Insertion into Lipid Membranes and Pore Formation by a Cationic Membrane Peptide from Solid-State NMR, *J. Am. Chem. Soc.* 129, 11438-11446.
43. Li, S., Su, Y., Luo, W., and Hong, M. (2010) Water-protein interactions of an arginine-rich membrane peptide in lipid bilayers investigated by solid-state nuclear magnetic resonance spectroscopy, *J. Phys. Chem. B* 114, 4063-4069.
44. Brogden, K. A. (2005) Antimicrobial peptides: pore formers or metabolic inhibitors in bacteria?, *Nat. Rev. Microbiol.* 3, 238-250.
45. Ganz, T. (2003) Defensins: antimicrobial peptides of innate immunity, *Nature Reviews Immunology* 3, 710-720.
46. Wade, D., Boman, A., Wahlin, B., Drain, C. M., Andreu, D., Boman, H. G., and Merrifield, R. B. (1990) All D-amino acid containing channel forming antibiotic peptides, *Proc. Natl. Acad. Sci. USA* 87, 4761-4765.
47. Demchick, P., and Koch, A. L. (1996) The permeability of the wall fabric of *Escherichia coli* and *Bacillus subtilis*, *J. Bacteriol.* 178, 768-773.
48. Kagan, B. L., Selsted, M. E., Ganz, T., and Lehrer, R. I. (1990) Antimicrobial defensin peptides form voltage-dependent ion-permeable channels in planar lipid bilayer membranes, *Proc. Natl. Acad. Sci. U.S.A.* 87, 210-214.
49. Lehrer, R. I., Barton, A., and Ganz, T. (1988) Concurrent assessment of inner and outer membrane permeabilization and bacteriolysis in *E. coli* by multiple-wavelength spectrophotometry, *J. Immunol. Methods* 108, 153-158.
50. Schneider, T., Kruse, T., Wimmer, R., Wiedemann, I., Sass, V., Pag, U., Jansen, A., Nielsen, A. K., Mygind, P. H., Raventós, D. S., Neve, S., Ravn, B., Bonvin, A. M., De

- Maria, L., Andersen, A. S., Gammelgaard, L., Sahl, H. G., and Kristensen, H. H. (2010) Plectasin, a fungal defensin, targets the bacterial cell wall precursor Lipid II, *Science* 328, 1168-1172.
51. de Leeuw, E., Li, C., Zeng, P., Li, C., Diepeveen-de Buin, M., Lu, W. Y., Breukink, E., and Lu, W. (2010) Functional interaction of human neutrophil peptide-1 with the cell wall precursor lipid II, *FEBS Lett.* 584, 1543-1548.
 52. Srinivas, N., Jetter, P., Ueberbacher, B. J., Werneburg, M., Zerbe, K., Steinmann, J., Van der Meijden, B., Bernardini, F., Lederer, A., Dias, R. L., Misson, P. E., Henze, H., Zumbunn, J., Gombert, F. O., Obrecht, D., Hunziker, P., Schauer, S., Ziegler, U., Käch, A., Eberl, L., Riedel, K., DeMarco, S. J., and Robinson, J. A. (2010) Peptidomimetic Antibiotics Target Outer-Membrane Biogenesis in *Pseudomonas aeruginosa*, *Science* 327, 1010-1013.
 53. Epanand, R. M., and Vogel, H. J. (1999) Diversity of antimicrobial peptides and their mechanisms of action, *Biochim. Biophys. Acta* 1462, 11-28.
 54. Baumann, G., and Mueller, P. (1974) A molecular model of membrane excitability, *J. Supramol. Struct.* 2, 538-557.
 55. He, K., Ludtke, S. J., Worcester, D. L., and Huang, H. W. (1996) Neutron scattering in the plane of membranes: structure of alamethicin pores, *Biophys. J.* 70, 2659-2666.
 56. Huang, H. W., Chen, F. Y., and Lee, M. T. (2004) Molecular mechanism of peptide-induced pores in membranes, *Phys. Rev. Lett.* 92, 198304.
 57. Matsuzaki, K. (1999) Why and how are peptide-lipid interactions utilized for self-defense? Magainins and tachyplesins as archetypes, *Biochim. Biophys. Acta* 1462, 1-10.
 58. Bechinger, B. (1999) The structure, dynamics, and orientation of antimicrobial peptides in membranes by multidimensional solid-state NMR spectroscopy, *Biochim. Biophys. Acta* 1462, 157-183.
 59. Kokryakov, V. N., Harwig, S. S., Panyutich, E. A., Shevchenko, A. A., Aleshina, G. M., Shamova, O. V., Korneva, H. A., and Lehrer, R. I. (1993) Protegrins: leukocyte antimicrobial peptides that combine features of corticostatic defensins and tachyplesins, *FEBS Lett.* 327, 231-236.
 60. Bellm, L., Lehrer, R. I., and Ganz, T. (2000) Protegrins: new antibiotics of mammalian origin, *Expert Opin. Investig. Drugs.* 9, 1731-1742.
 61. Chen, J., Falla, T. J., Liu, H., Hurst, M. A., Fujii, C. A., Mosca, D. A., Embree, J. R., Loury, D. J., Radel, P. A., Cheng, C. C., Gu, L., and Fiddes, J. C. (2000) Development of protegrins for the treatment and prevention of oral mucositis: structure-activity relationships of synthetic protegrin analogues, *Biopolymers* 55, 88-98.
 62. Buffy, J. J., Waring, A. J., Lehrer, R. I., and Hong, M. (2003) Immobilization and aggregation of the antimicrobial peptide protegrin-1 in lipid bilayers investigated by solid-state NMR, *Biochemistry* 42, 13725-13734.

63. Yamaguchi, S., Hong, T., Waring, A., Lehrer, R. I., and Hong, M. (2002) Solid-state NMR investigations of peptide-lipid interaction and orientation of a beta-sheet antimicrobial peptide, protegrin, *Biochemistry* 41, 9852-9862.
64. Fahrner, R. L., Dieckmann, T., Harwig, S. S., Lehrer, R. I., Eisenberg, D., and Feigon, J. (1996) Solution structure of protegrin-1, a broad-spectrum antimicrobial peptide from porcine leukocytes, *Chem. & Biol.* 3, 543-550.
65. Saffman, P. G., and Delbruck, M. (1975) Brownian motion in biological membranes, *Proc. Natl. Acad. Sci. USA* 72, 3111-3113.
66. Mani, R., Buffy, J. J., Waring, A. J., Lehrer, R. I., and Hong, M. (2004) Solid-state NMR investigation of the selective disruption of lipid membranes by protegrin-1, *Biochemistry* 43, 13839-13848.
67. Marasinghe, P. A. B., Buffy, J. J., Schmidt-Rohr, K., and Hong, M. (2005) Membrane curvature change induced by an antimicrobial peptide detected by ³¹P exchange NMR, *J. Phys. Chem. B* 109, 22036-22044.
68. Mani, R., Tang, M., Wu, X., Buffy, J. J., Waring, A. J., Sherman, M. A., and Hong, M. (2006) Membrane-bound dimer structure of a b-hairpin antimicrobial peptide from rotational-echo double-resonance solid-state NMR, *Biochemistry* 45, 8341-8349.
69. Mani, R., Cady, S. D., Tang, M., Waring, A. J., Lehrer, R. I., and Hong, M. (2006) Membrane-dependent oligomeric structure and pore formation of a beta-hairpin antimicrobial peptide in lipid bilayers from solid-state NMR, *Proc. Natl. Acad. Sci. U S A* 103, 16242-16247.
70. Yang, L., Weiss, T. M., Lehrer, R. I., and Huang, H. W. (2000) Crystallization of antimicrobial pores in membranes: magainin and protegrin, *Biophys. J.* 79, 2002-2009.
71. Mani, R., Waring, A. J., Lehrer, R. I., and Hong, M. (2005) Membrane-disruptive abilities of beta-hairpin antimicrobial peptides correlate with conformation and activity: a ³¹P and ¹H NMR study, *Biochim Biophys Acta.* 1716, 11-18.
72. Tang, M., Waring, A. J., and Hong, M. (2009) Effects of arginine density on the membrane-bound structure of a cationic antimicrobial peptide from solid-state NMR, *Biochim. Biophys. Acta.* 1788, 514-521.
73. Su, Y., Waring, A. J., Ruchala, P., and Hong, M. (2011) Structure of beta-hairpin antimicrobial peptides in lipopolysaccharide membranes: mechanism of gram selectivity obtained from solid-state NMR, *Biochemistry*, submitted.
74. Nakamura, T., Furunaka, H., T, T. M., Tokunaga, F., Muta, T., Iwanaga, S., Niwa, M., Takao, T., and Shimonishi, Y. (1988) Tachyplesin, a class of antimicrobial peptide from the hemocytes of the horseshoe crab (*Tachyplesus tridentatus*). Isolation and chemical structure, *J. Biol. Chem.* 263, 16709-16713.
75. Doherty, T., Waring, A. J., and Hong, M. (2006) Peptide-lipid interactions of the beta-hairpin antimicrobial peptide tachyplesin and its linear derivatives from solid-state NMR, *Biochim. Biophys. Acta* 1758, 1285-1291.

76. Laederach, A., Andreotti, A. H., and Fulton, D. B. (2002) Solution and micelle-bound structures of tachyplesin I and its active aromatic linear derivatives, *Biochemistry* 41, 12359-12368.
77. Doherty, T., Waring, A. J., and Hong, M. (2006) Membrane-bound conformation and topology of the antimicrobial peptide tachyplesin-I by solid-state NMR *Biochemistry* 45, 13323-13330.
78. Hill, C. P., Yee, J., Selsted, M. E., and Eisenberg, D. (1991) Crystal structure of defensin HNP-3, an amphiphilic dimer: mechanisms of membrane permeabilization., *Science* 251, 1481-1485.
79. Szyk, A., Wu, Z., Tucker, K., Yang, D., Lu, W., and Lubkowski, J. (2006) Crystal structures of human alpha-defensins HNP4, HD5, and HD6, *Protein Sci.* 15, 2749-2760.
80. Wimley, W. C., Selsted, M. E., and White, S. H. (1994) Interactions between human defensins and lipid bilayers: evidence for formation of multimeric pores, *Protein Sci.* 3, 1362-1373.
81. Pazgier, M., and Lubkowski, J. (2006) Expression and purification of recombinant human alpha-defensins in *Escherichia coli*, *Protein Expr. Purif.* 49, 1-8.
82. Baldus, M. (2006) Solid-state NMR spectroscopy: molecular structure and organization at the atomic level, *Angew. Chem. Int. Ed. Engl.* 45, 1186-1188.
83. McDermott, A. E. (2009) Structure and dynamics of membrane proteins by magic angle spinning solid-state NMR, *Annu. Rev. Biophys.* 38, 385-403.
84. Li, S., Zhang, Y., and Hong, M. (2010) 3D ¹³C-¹³C-¹³C correlation NMR for de novo distance determination of solid proteins and application to a human alpha defensin, *J. Magn. Reson.* 202, 203-210.
85. Fawell, S., Seery, J., Daikh, Y., Moore, C., Chen, L. L., Pepinsky, B., and Barsoum, J. (1994) Tat-mediated delivery of heterologous proteins into cells, *Proc. Natl. Acad. Sci. U. S. A.* 91, 664-668.
86. Gratton, J. P., Yu, J., Griffith, J. W., Babbitt, R. W., Scotland, R. S., Hickey, R., Giordano, F. J., and Sessa, W. C. (2003) Cell-permeable peptides improve cellular uptake and therapeutic gene delivery of replication-deficient viruses in cells and in vivo, *Nat. Med.* 9, 357-362.
87. Torchilin, V. P., Levchenko, T. S., Rammohan, R., Volodina, N., Papahadjopoulos-Sternberg, B., and D'Souza, G. G. (2003) Cell transfection in vitro and in vivo with nontoxic TAT peptide-liposome-DNA complexes, *Proc. Natl. Acad. Sci. U. S. A.* 100, 1972-1977.
88. Frankel, A. D., and Pabo, C. O. (1988) Cellular Uptake of the Tat Protein from Human Immunodeficiency Virus, *Cell* 55, 1189-1193.
89. Green, M., and Loewenstein, P. M. (1988) Autonomous functional domains of chemically synthesized human immunodeficiency virus tat trans-activator protein, *Cell* 55, 1179-1188.

90. Derossi, D., Joliot, A. H., Chassaing, G., and Prochiantz, A. (1994) The third helix of the Antennapedia homeodomain translocates through biological membranes, *J. Biol. Chem.* 269, 10444-10450.
91. Khafagya, E.-S., Morishitaa, M., Isowab, K., Imaib, J., and Takayamaa, K. (2009) Effect of cell-penetrating peptides on the nasal absorption of insulin, *J. Contolled Release* 133, 103-108.
92. Rothbard, J. B., Jessop, T. C., Lewis, R. S., Murray, B. A., and Wender, P. A. (2004) Role of membrane potential and hydrogen bonding in the mechanism of translocation of guanidinium-rich peptides into cells, *J. Am. Chem. Soc.* 126, 9506-9507.
93. Futaki, S., Suzuki, T., Ohashi, W., Yagami, T., Tanaka, S., Ueda, K., and Sugiura, Y. (2001) Arginine-rich peptides. An abundant source of membrane-permeable peptides having potential as carriers for intracellular protein delivery, *J. Biol. Chem.* 276, 5836-5840.
94. White, S. H., and Wimley, W. C. (1999) Membrane protein folding and stability: physical principles, *Annu. Rev. Biophys. Biomol. Struct.* 28, 319-365.
95. Czajlik, A., Meskó, E., Penke, B., and Perczel, A. (2002) Investigation of penetratin peptides. Part 1. The environment dependent conformational properties of penetratin and two of its derivatives, *J. Pept. Sci.* 8, 151-171.
96. Berlose, J. P., Convert, O., Derossi, D., Brunissen, A., and Chassaing, G. (1996) Conformational and associative behaviours of the third helix of antennapedia homeodomain in membrane-mimetic environments, *Eur. J. Biochem.* 242, 372-386.
97. Clayton, A. H., Atcliffe, B. W., Howlett, G. J., and Sawyer, W. H. (2006) Conformation and orientation of penetratin in phospholipid membranes., *J. Pept. Sci.* 12, 233-238.
98. Lindberg, M., Biverstahl, H., Graslund, A., and Maler, L. (2003) Structure and positioning comparison of two variants of penetratin in two different membrane mimicking systems by NMR, *Eur. J. Biochem.* 270, 3055-3063.
99. Su, Y., Mani, R., Doherty, T., Waring, A. J., and Hong, M. (2008) Reversible sheet-turn conformational change of a cell-penetrating peptide in lipid bilayers studied by solid-state NMR, *J. Mol. Biol.* 381, 1133-1144.
100. Su, Y., Doherty, T., Waring, A. J., Ruchala, P., and Hong, M. (2009) Roles of Arginine and Lysine Residues in the Translocation of a Cell-Penetrating Peptide from ¹³C, ³¹P, and ¹⁹F Solid-State NMR, *Biochemistry* 48, 4587-4595.
101. Binder, H., and Lindblom, G. (2003) Charge-dependent translocation of the Trojan peptide penetratin across lipid membranes, *Biophys. J.* 85, 982-995.
102. Mitchell, D. J., Kim, D. T., Steinman, L., Fathman, C. G., and Rothbard, J. B. (2000) Polyarginine enters cells more efficiently than other polycationic homopolymers, *J. Pept. Res.* 56, 318-325.

103. Amand, H. L., Fant, K., Nordén, B., and Esbjörner, E. K. (2008) Stimulated endocytosis in penetratin uptake: effect of arginine and lysine, *Biochem. Biophys. Res. Commun.* 371, 621-625.
104. Wimley, W. C., and White, S. H. (1996) Experimentally determined hydrophobicity scale for proteins at membrane interfaces, *Nat. Struct. Biol.* 3, 842-848.
105. Torchilin, V. P., Rammohan, R., Weissig, V., and Levchenko, T. S. (2001) TAT peptide on the surface of liposomes affords their efficient intracellular delivery even at low temperature and in the presence of metabolic inhibitors, *Proc. Natl. Acad. Sci. U. S. A.* 98, 8786-8791.
106. Ziegler, A., LiBlatter, X., Seelig, A., and Seelig, J. (2003) Protein Transduction Domains of HIV-1 and SIV TAT Interact with Charged Lipid Vesicles. Binding Mechanism and Thermodynamic Analysis, *Biochemistry* 42, 9185-9194.
107. Richard, J. P., Melikov, K., Vives, E., Ramos, C., Verbeure, B., Gait, M. J., Chernomordik, L. V., and Lebleu, B. (2003) Cell-penetrating peptides. A reevaluation of the mechanism of cellular uptake, *J. Biol. Chem.* 278, 585-590.
108. Derossi, D., Calvet, S., Trembleau, A., Brunissen, A., Chassaing, G., and Prochiantz, A. (1996) Cell internalization of the third helix of the Antennapedia homeodomain is receptor-independent, *J. Biol. Chem.* 271, 18188-18193.
109. Herce, H. D., Garcia, A. E., Litt, J., Kane, R. S., Martin, P., Enrique, N., Rebolledo, A., and Milesi, V. (2009) Arginine-rich peptides destabilize the plasma membrane, consistent with a pore formation translocation mechanism of cell-penetrating peptides, *Biophys. J.* 97, 1917-1925.
110. Seoh, S. A., Sigg, D., Papazian, D. M., and Bezanilla, F. (1996) Voltage-sensing residues in the S2 and S4 segments of the Shaker K⁺ channel, *Neuron* 16, 1159-1167.
111. Swartz, K. J. (2008) Sensing voltage across lipid membranes, *Nature* 456, 891-897.
112. Cuello, L. G., Cortes, D. M., and Perozo, E. (2004) Molecular architecture of the KvAP voltage-dependent K⁺ channel in a lipid bilayer, *Science* 306, 491-495.
113. Long, S. B., Tao, X., Campbell, E. B., and MacKinnon, R. (2007) Atomic Structure of a Voltage-Dependent K⁺ Channel in a Lipid Membrane-Like Environment, *Nature* 450, 376-383.
114. Krepiy, D., Mihailescu, M., Freites, J. A., Schow, E. V., Worcester, D. L., Gawrisch, K., Tobias, D. J., White, S. H., and Swartz, K. J. (2009) Structure and hydration of membranes embedded with voltage-sensing domains, *Nature* 462, 473-479.

Chapter 3

Reversible Sheet – Turn Conformational Change of a Cell-Penetrating Peptide in Lipid Bilayers Studied by Solid-State NMR

A paper published in Journal of Molecular Biology

2008, vol. 381, page 1133-1144

Yongchao Su¹, Rajeswari Mani^{1†}, Tim Doherty¹, Alan J. Waring² and Mei Hong^{1*}

¹Department of Chemistry, Iowa State University, Ames, IA 50011

²Department of Medicine, University of California at Los Angeles School of Medicine, Los Angeles, California 90095

3.1 Abstract

The membrane-bound conformation of a cell-penetrating peptide, penetratin, is investigated using solid-state NMR spectroscopy. The ¹³C chemical shifts of ¹³C, ¹⁵N-labeled residues in the peptide indicate a reversible conformational change from β -sheet at low temperature to coil-like at high temperature. This conformational change occurs for all residues examined between positions 3 and 13, at peptide/lipid molar ratios of 1:15 and 1:30, in membranes with 25-50% anionic lipids, and in both saturated DMPC/DMPG membranes and unsaturated POPC/POPG membranes. Thus it is an intrinsic property of penetratin. The coil state of the peptide has C-H order parameters of 0.23 – 0.52 for C α and C β sites, indicating that the peptide backbone is not unstructured. Moreover, chemical shift anisotropy lineshapes are uniaxially averaged, suggesting that the peptide backbone undergoes uniaxial rotation around the bilayer normal. These observations suggest that the dynamic state of penetratin at high temperature is a structured turn instead of an isotropic random coil. The thermodynamic parameters of this sheet – turn transition are extracted and compared to other membrane peptides reported to exhibit conformational changes. We suggest that the function of this turn conformation may be to reduce hydrophobic interactions with the lipid chains and facilitate penetratin translocation across the bilayer without causing permanent membrane damage.

3.2 Introduction

Cell-penetrating peptides (CPPs) are small cationic peptides that are able to enter cells carrying macromolecular cargos such as DNA and proteins without leaking the cell content or causing permanent damage to the cell membrane (1-3). The promise of these peptides as drug-delivery compounds has made them the objects of many studies to understand their mechanism of cell entry. Earlier investigations using fluorescence microscopy and flow cytometry found that the internalization was independent of both temperature and the D, L-configuration of the amino acids (4, 5), suggesting that these peptides directly translocate across the plasma membrane rather than entering by endocytosis. More recent analysis of HIV Tat (48-60) and (Arg)₉, two commonly studied CPPs, found that the cell fixation procedure used in the microscopy experiments caused artifactual peptide uptake into cells, and that the actual uptake in living cells was temperature-dependent (6), suggesting the involvement of the energy-dependent transport mechanism, endocytosis. However, reduced cell internalization at low temperatures does not rule out direct membrane permeation as another route of entry, since this mechanism is also less efficient at low temperature in the gel-phase membrane, as shown by experiments comparing cell lines with different membrane fluidities (7). Furthermore, even peptides internalized via the endocytotic pathway, as detected by biological readout assays (8), must still cross the endosomal membrane in order to enter the cytosol, and must cross additional membranes if they are internalized in intracellular compartments. A large number of biophysical studies of CPPs in model membranes has shown the strong affinity of CPPs to lipid membranes (9). This raises the fundamental question of how these peptides, whose amino acid sequences contain 40–100% of the cationic residues Arg and Lys, translocate across the hydrophobic part of the lipid membrane against large free energy barriers (10).

CPPs share their cationic sequences with antimicrobial peptides, which are also Arg- or Lys-rich peptides but which cause permanent damages to the cell membranes of microbial organisms to achieve their cell-killing function. Antimicrobial peptides generally have distinct amphipathic structures, which are considered essential to their membrane-disruptive function (11, 12). In comparison, the role of conformation to the translocation of cell-penetrating peptides remains ambiguous. It has been suggested that no specific conformation is required for translocation, since some CPPs such as the HIV Tat peptide show no

distinct secondary structures (13) while other CPPs such as penetratin are structurally plastic depending on the environment (9). MD simulations of Tat(47-58) showed a random coil that crosses the membrane by electrostatic interactions between the Arg sidechains and the lipid phosphate groups (14). For penetratin, there is general consensus that it is a random coil in aqueous solution and becomes significantly α -helical in SDS micelles (15-17). But in lipid vesicles both α -helical and β -sheet conformations have been reported depending on the anionic lipid content and the peptide/lipid molar ratio (P/L) (16, 18-20). Since most conformational studies on membrane-bound CPPs used circular dichroism (CD), which is complicated by light scattering of lipid vesicles and spectral deconvolution uncertainties, the CD structural information has limited accuracy. Thus, the conformation of CPPs in lipid membranes remains to be elucidated to understand the potential role of conformation in membrane translocation and to gain insight into the general mechanism of cationic protein interaction with the lipid membrane.

In this work, we use solid-state NMR spectroscopy to investigate the conformation and dynamics of penetratin in lipid membranes. Penetratin is a 16-residue peptide corresponding to the third helix (residues 43-58) of the Antennapedia homeodomain of *Drosophila*. It is the first discovered CPP (4, 5) and one of the most extensively characterized so far. We studied the penetratin conformation in hydrated multilamellar liposomes, which have no large intra-vesicular aqueous compartments as in real cells. Thus, the peptide is mostly partitioned in the lipid membrane instead of water. This sample condition allows us to capture the structure adopted by the peptide when it interacts transiently with the membranes of real cells. We show chemical shift and dynamic data that indicate a clear temperature-induced reversible sheet \leftrightarrow coil conformational change of the membrane-bound penetratin. The nature of this “coil-like” conformation and its potential relevance to membrane translocation is discussed.

3.3 Results

Temperature-induced penetratin conformational change in the membrane

To determine the conformation of penetratin in the lipid membrane, we measured the ^{13}C chemical shifts and assigned them by 2D ^{13}C - ^{13}C correlation spectra. The main membrane

composition in this study is DMPC/DMPG (8:7). The high anionic lipid content of ~50% is used since it was reported to be necessary for the peptide to bind to both leaflets of the bilayer (21).

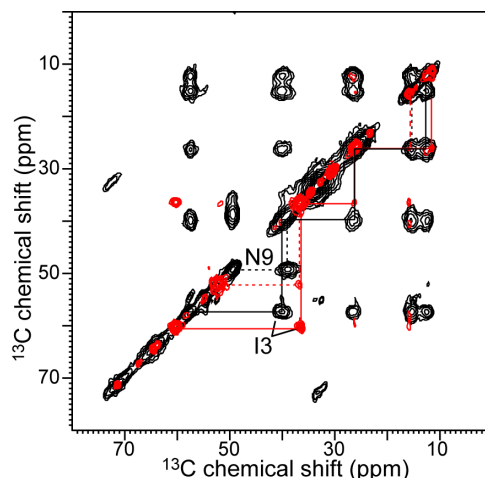


Figure 3.1. 2D ^{13}C - ^{13}C correlation spectra of (I3, N9)-labeled penetratin in DMPC/DMPG (8:7) membranes at P/L = 1:15. Black: 243 K; red: 310 K. Note the frequency changes of the α/β cross peaks, which denote conformational change. The spectra were measured under 6 kHz MAS with a 20 ms DARR mixing time.

Figure 3.1 shows the aliphatic region of the 2D spectra of (I3, N9)-labeled penetratin in DMPC/DMPG (8:7) bilayers. The spectra were obtained with a short mixing time of 20 ms, thus showing mainly intra-residue cross peaks that are relevant for chemical shift assignment. The spectra were measured at two temperatures, 243 K, which corresponds to the gel phase of the membrane, and 310 K, which corresponds to the liquid-crystalline (LC) phase of the membrane. All expected intra-residue cross peaks are observed, with the C' , $\text{C}\alpha$, and $\text{C}\beta$ chemical shifts reflecting the peptide conformation.

Interestingly, both I3 and N9 α/β cross peaks exhibit frequency changes between the two temperatures. At the higher temperature, the $\text{C}\alpha$ chemical shifts increased by 2.8 ppm while the $\text{C}\beta$ chemical shifts decreased by 2.2 and 3.5 ppm compared to the low temperature values. The $\text{C}\alpha$ and $\text{C}\beta$ isotropic shifts depend on the (ϕ, ψ) torsion angles in a counter-directional fashion: the α -helical conformation has larger $\text{C}\alpha$ chemical shifts and smaller $\text{C}\beta$ chemical shifts compared to the random coil, while the β -sheet conformation has negative $\text{C}\alpha$ and positive $\text{C}\beta$ secondary shifts (22, 23). The observed chemical shift changes of I3 and

N9 thus indicate a change from a β -sheet like conformation at low temperature to a helix or coil-like conformation at high temperature.

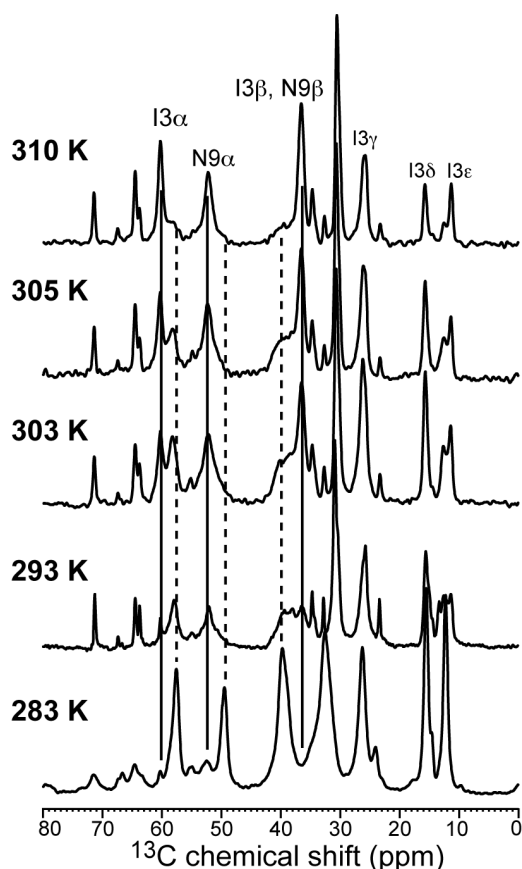


Figure 3.2. ^{13}C CP-MAS spectra of (I3, N9)-labeled penetratin in DMPC/DMPG (8:7) membranes (P/L = 1:15) as a function of temperature. Dashed and solid lines guide the eye for β -sheet and random coil peaks, respectively.

To determine whether the appearance of the second conformation is gradual or sudden, we measured the ^{13}C CP-MAS spectra of the peptide as a function of temperature. Figure 3.2 shows the 283 – 310 K ^{13}C spectra of (I3, N9)-labeled penetratin in the DMPC/DMPG (8:7) membrane. It can be seen that the second conformation grows gradually: as the temperature decreases, the random-coil peaks decrease in intensity while the β -sheet peaks increase in intensity. Around 303 K, both conformations coexist. Below 283 K only β -sheet peaks are present and the spectra no longer change. For each site, only two chemical

shifts are observed, without intermediate values between them. Table S3.1 lists the intensity fractions of the two sets of peaks for I3 and N9 C α sites at the temperatures examined.

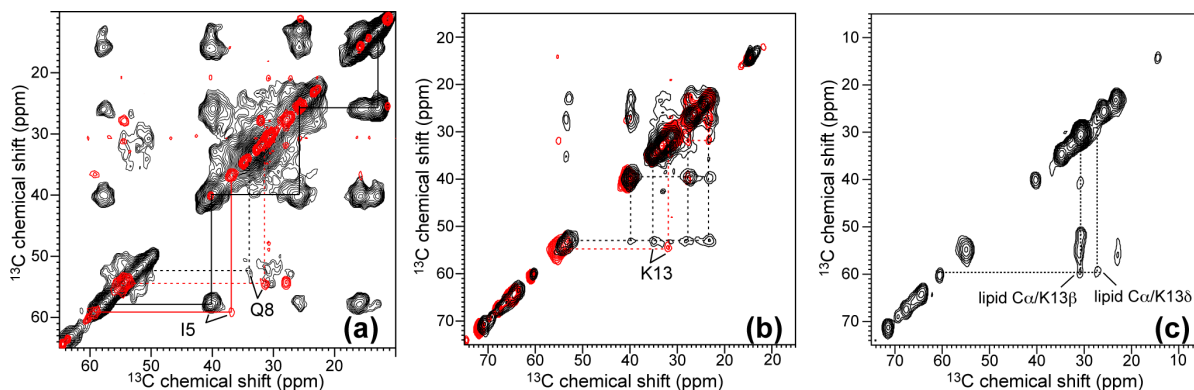


Figure 3.3 2D ^{13}C - ^{13}C correlation spectra of labeled penetratin in DMPC/DMPG membranes (8:7) at P/L = 1:15. (a) (I5, Q8, K13)-labeled penetratin at 249 K with 50 ms PDSM mixing (black) and at 310 K with 100 ms PDSM mixing (red). (b) K13-labeled penetratin at 273 K with 50 ms DARR mixing (black) and at 310 K with 30 ms DARR mixing (red). (c) 2D PDSM spectrum of K13-labeled penetratin at 310 K with 100 ms mixing. Note the lipid/peptide cross peaks.

To assess if the conformational changes occur in multiple residues in the peptide, we measured the ^{13}C chemical shifts of three other sites, I5, Q8, and K13. Figure 3.3 shows the 2D spectra at high and low temperatures for two samples containing the labeled sites. It can be seen that the C α /C β chemical shift changes are present for all three residues, indicating that the sheet-turn conformational change occurs for a large fraction of the peptide. Figure 3.3c shows a long mixing-time 2D spectrum at 310 K, where cross peaks between the lipid headgroup C α and the peptide K13 signals are detected, indicating that the high-temperature state of the peptide is in intimate contact with the lipids. The variable-temperature 1D ^{13}C spectra of (I5, Q8, K13)-labeled penetratin in DMPC/DMPG (8:7) bilayers (Figure 3.4) further illustrate the temperature-induced chemical shift changes.

Table S3.2 tabulates the high- and low-temperature ^{13}C chemical shifts of all measured residues in the DMPC/DMPG membrane. The differences of these chemical shifts from the random coil values give information on the secondary structure of the peptides. Using the random coil values of Zhang et al, (24), we plotted the secondary chemical shifts in Figure

3.5. The low-temperature secondary shifts are negative for $C\alpha$ and CO but positive for $C\beta$, which clearly indicate a β -sheet conformation. In comparison, the high-temperature secondary shifts are near the random coil values and much less than the α -helical secondary shifts. Thus, while the peptide adopts an α -helical conformation in its parent protein, as an independent molecule bound to the liquid-crystalline lipid bilayer, it adopts neither a β -sheet nor an α -helical conformation, but is more like a random coil.

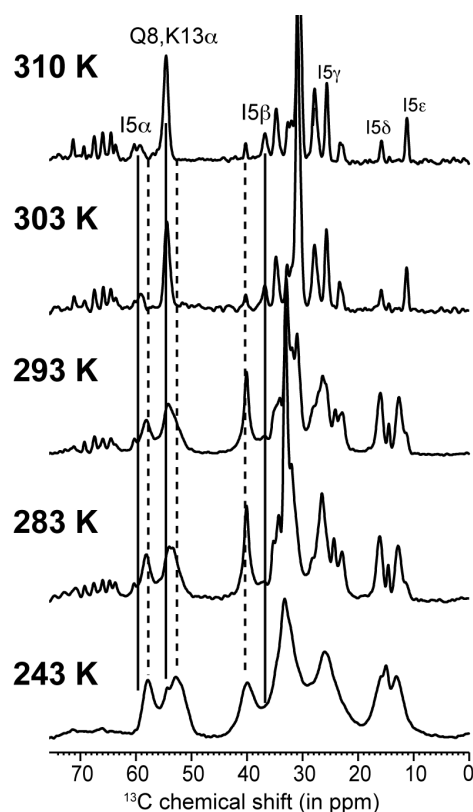


Figure 3.4 Variable-temperature 1D ^{13}C CP-MAS spectra of (I5, Q8, K13)-labeled penetratin in DMPC/DMPG (8:7) membranes at P/L = 1:15. Dashed and solid lines guide the eye for sheet and coil peaks, respectively.

Generality of the sheet \leftrightarrow coil transition of penetratin

We next examine the generality of this conformational change of penetratin in lipid membranes. Does it occur only at high peptide concentrations or also at low P/L ratios? Is it unique to the nearly 50% anionic DMPC/DMPG membrane or is it present also at other

membrane compositions? To address these questions, we prepared a low-concentration sample, with P/L = 1:30, in the DMPC/DMPG (8:7) membrane, a high-concentration P/L = 1:15 sample in 25% anionic DMPC/DMPG (3:1) membrane, and a high-concentration P/L = 1:15 sample in the unsaturated POPC/POPG (8:7) membrane.

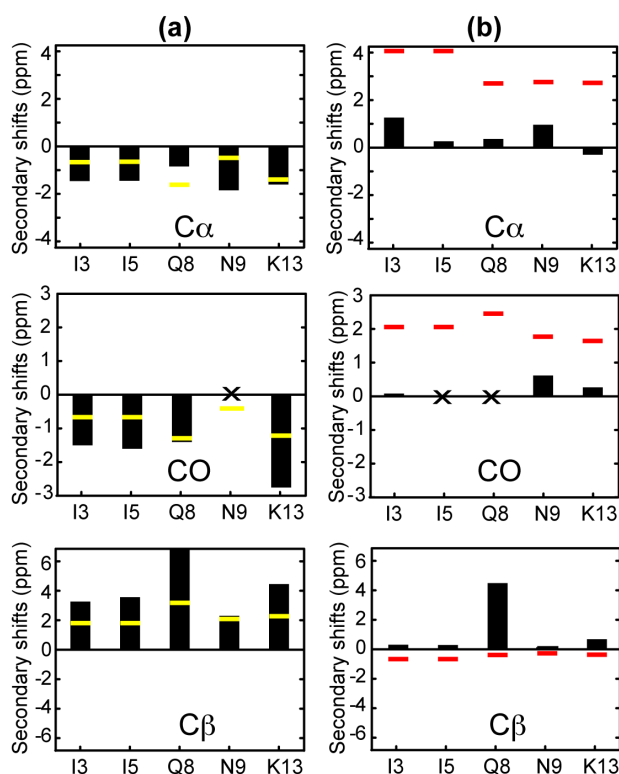


Figure 3.5. Experimental $C\alpha$, CO, and $C\beta$ secondary shifts of all labeled residues in penetratin in DMPC/DMPG (8:7) bilayers at P/L=1:15. (a) 243 K. (b) 310 K. Yellow and red lines in (a) and (b) are database secondary chemical shifts for β -sheet and α -helical conformations, respectively (24).

Figure 3.6 shows the variable-temperature ^{13}C CP-MAS spectra of (I3, N9)-labeled penetratin in DMPC/DMPG (8:7) bilayers at the concentration of P/L = 1:30. The same chemical shift changes are detected, but the relative intensities of the two components at each temperature differ from those of the 1:15 sample (Table S3.1). Figure 3.7 shows the ^{13}C spectra of the peptide in the 25% anionic DMPC/DMPG (3:1) membrane. This sample allows us to assess whether the conformational change is mainly induced by the anionic lipid. Again, the same sheet \leftrightarrow coil chemical shift changes are observed between low and high tempera-

tures. Thus, the conformational change is not a result of the peptide preferentially partitioning into anionic lipid domains, but also occurs in zwitterionic membranes.

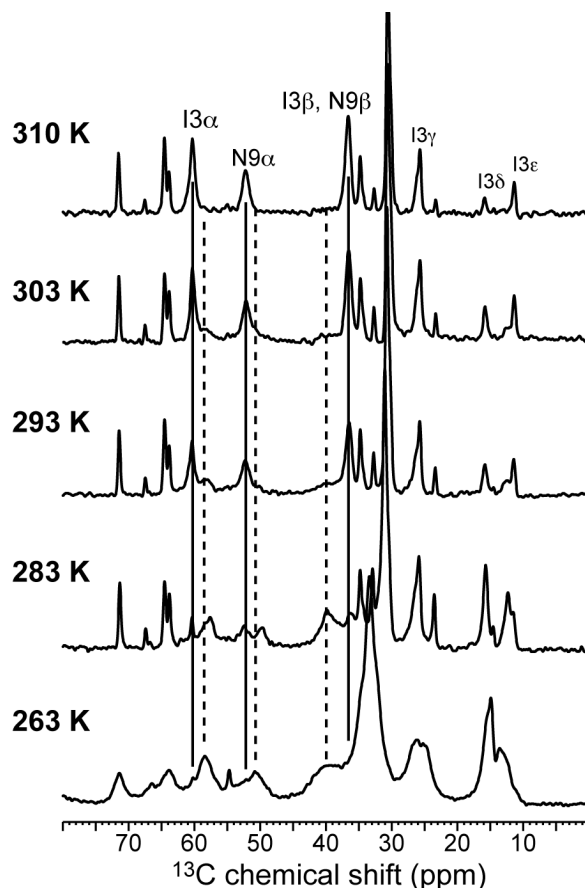


Figure 3.6. Variable-temperature ^{13}C CP-MAS spectra of (I3, N9)-labeled penetratin in DMPC/DMPG (8:7) membranes at P/L = 1:30. Dashed and solid lines guide the eye for the sheet and coil peaks, respectively.

In the unsaturated POPC/POPG (8:7) membrane, we found the same chemical shift changes indicative of a sheet \leftrightarrow coil conformational change (Figure 3.8). However, the spectral linewidths of the POPC/POPG-bound peptide are much broader than the DMPC/DMPG samples near and below the phase transition temperature. This suggests that penetratin exhibits more pronounced intermediate-timescale motion in the POPC/POPG membrane than in the DMPC/DMPG membrane, possibly due to the higher dynamic disorder of the unsaturated chains of POPC and POPG lipids.

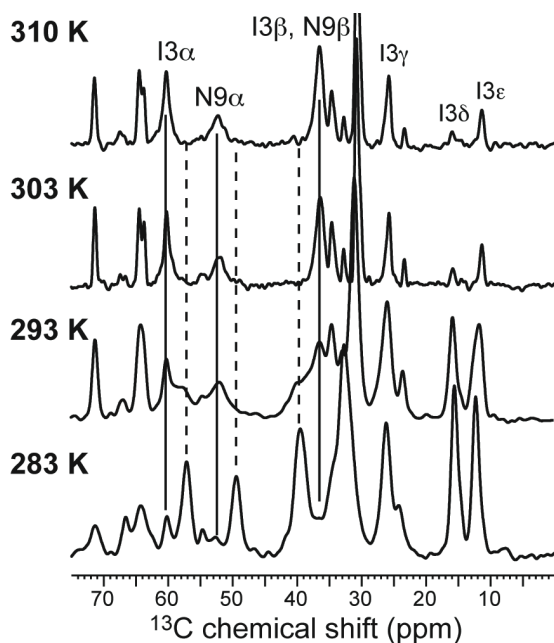


Figure 3.7. Variable-temperature ^{13}C CP-MAS spectra of (I3, N9)-labeled penetratin in DMPC/DMPG (3:1) membranes at P/L = 1:15. Dashed and solid lines guide the eye for the sheet and coil peaks, respectively.

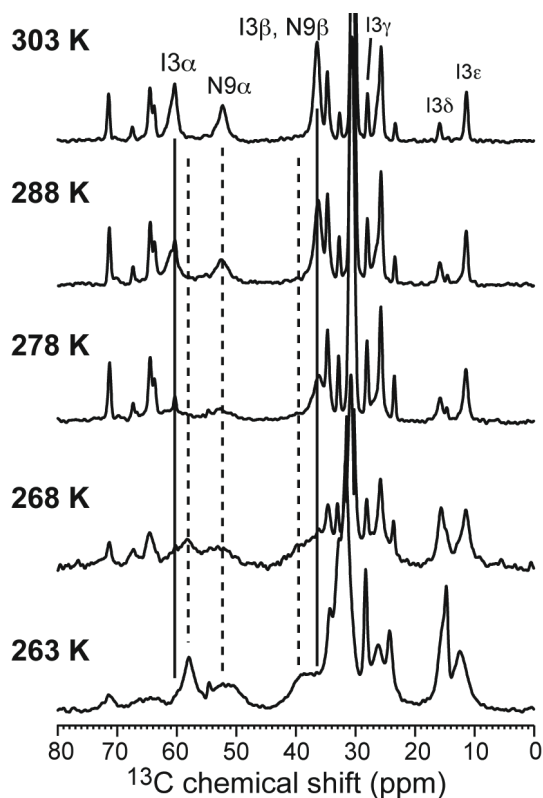


Figure 3.8. Variable-temperature ^{13}C CP-MAS spectra of (I3, N9)-labeled penetratin in POPC/POPG (8:7) membranes at P/L = 1:15. Dashed and solid lines guide the eye for the sheet and coil peaks, respectively.

Nature of the coil-like conformation in the membrane from penetratin dynamics

It has been proposed that random coils, by definition without any fixed structure due to stochastic isotropic motion of the protein segments, are not compatible with the lipid membrane due to the energetically unfavorable exposure of non-hydrogen-bonded backbone polar functional groups to the hydrophobic lipid chains (25). Peptides that are unstructured in solution often adopt helical or sheet structures upon association with the lipid membrane (26). Thus, it is puzzling that penetratin exhibits random coil chemical shifts in the liquid-crystalline lipid membranes.

Table 3.1. C-H order parameters of penetratin in DMPC/DMPG membranes at 303 K and 283 K. Superscripts c and s denote coil and sheet conformations, respectively. Superscript o indicates partial overlap with another peptide peak. Sidechain groups other than C β have no conformational dependence.

Residue	Site	303 K	283 K
I3	C α	0.94 ^s	0.94 ^s
	C β	0.33 ^{c,o} , 0.66 ^{s,o}	0.84 ^{s,o}
	C δ	0.19	0.23
	C ϵ	0.14	0.23
I5	C α	-	0.94 ^s
	C γ	0.33	0.52
	C δ	0.14	0.33
	C ϵ	0.14	0.28
Q8	C α	0.33 ^c	0.89 ^s
N9	C α	0.52 ^c	0.84 ^s
	C β	0.33 ^{c,o} , 0.66 ^{s,o}	0.84 ^{s,o}
K13	C α	0.23 ^c	0.94 ^s
	C ϵ	0.33	0.37

To better understand the nature of the penetratin structure at high temperature, we measured the C-H dipolar couplings of the peptide. A true random coil should exhibit vanishing dipolar couplings, corresponding to C-H order parameters of 0. In contrast, a β -strand conformation is usually only stable in the membrane if inter-strand hydrogen bonds are present (27, 28). Such a multi-strand β -sheet is usually immobilized and should have order parameters near 1 (29). Figure 3.9 shows the C-H DIPSHIFT curves of two backbone C α sites, Q8 and K13, in penetratin in DMPC/DMPG bilayers (P/L=1:15). The coil peaks give clearly

less dipolar dephasing, or weaker dipolar couplings, than the corresponding β -sheet peaks. The $C\alpha$ - $H\alpha$ and $C\beta$ - $H\beta$ order parameters of the β -sheet signals range from 0.84 to 0.94, while the order parameters of the coil signals range from 0.23 to 0.52 (Table 3.1). Thus, the backbone of the coil peptide indeed undergoes large-amplitude motion in the lipid membrane. However, since the $C\alpha$ and $C\beta$ order parameters are much higher than 0, the motion is not isotropic, and the peptide retains significant residual anisotropy.

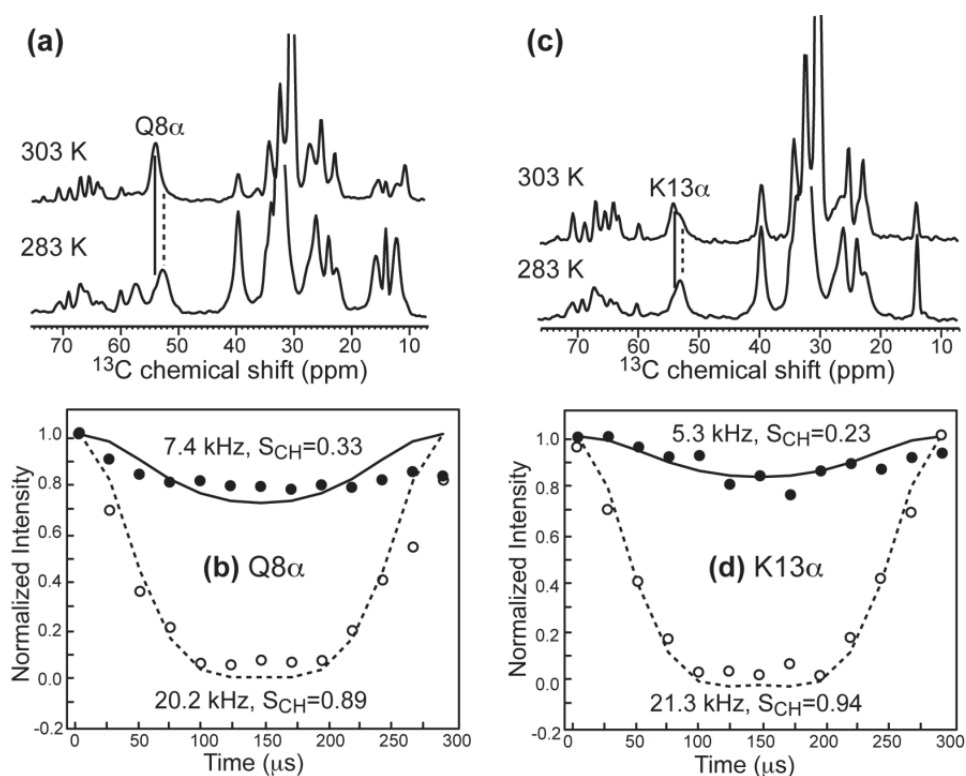


Figure 3.9. C-H dipolar couplings of coil and sheet $C\alpha$ peaks of Q8 and K13 at 303 K and 283 K, respectively. The lipid membrane is DMPC/DMPG (8:7) and P/L = 1:15. (a) ^{13}C dimensions of the 2D DIPSHIFT spectra showing the $Q8\alpha$ chemical shift change. (b) C-H dipolar dephasing of $Q8\alpha$ at 303 K (filled symbols, solid line) and 283 K (open symbols, dashed line). (c) ^{13}C dimensions of the 2D DIPSHIFT spectra showing the $K13\alpha$ chemical shift change. (d) C-H dipolar dephasing of $K13\alpha$ at 303 K (filled symbols, solid line) and 283 K (open symbols, dashed line). Best-fit couplings and the corresponding order parameters are given in (b, d).

Table 3.1 also shows the sidechain order parameters for all resolved sites. Interestingly, while the ends of the long Ile sidechains exhibit the expected small order parameters of 0.14-0.19 at 303 K, the end of the long Lys sidechain, $C\epsilon$, exhibits a much higher order pa-

parameter of 0.33 at 303 K. This suggests that the cationic Lys amino group may form transient associations with the lipid phosphate groups, similar to what has been observed for Arg residues in an antimicrobial peptide (30, 31).

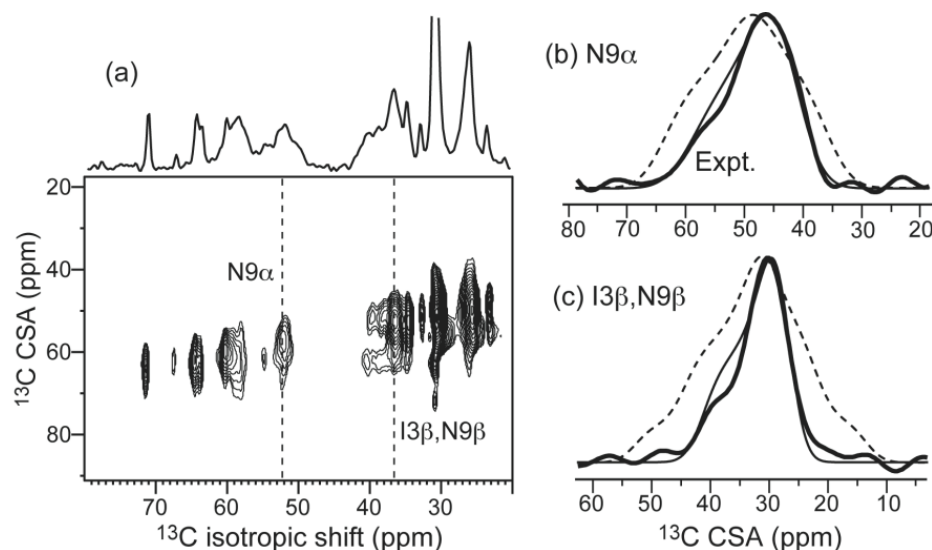


Figure 3.10. 2D ROCSA spectra of (I3, N9)-labeled penetratin in DMPC/DMPG (8:7) membranes at 303 K and P/L = 1;15. (a) 2D spectrum. (b) N9 α cross section at 52.2 ppm. (c) I3 β and N9 β cross section at 36.5 ppm. In the 1D panels (b, c), thick line is the experimental data, thin line is the best fit, and dashed line is the calculated static-limit CSA lineshape based on *ab initio* calculations for the β -sheet conformation of these residues (36).

For protein backbones, bond order parameters may be smaller than 1 for two different types of motion. They may reflect internal segmental motion, which is the case, for example, for a random coil, or they may reflect overall motion of a rigid molecule. If rigid-body motion is axially symmetric around an external axis, which for membrane-bound proteins is typically the bilayer normal, then the different order parameters simply reflect the different orientations of the individual bond vectors with respect to the bilayer normal. Distinguishing segmental motion from rigid-body motion is a complex task requiring the determination of the order tensor for each segment of the molecule (32, 33). Determining each order tensor, which is a traceless and symmetric second-rank tensor, requires five independent NMR couplings (34). In the limiting case of rigid-body uniaxial rotation, the situation is much simpler: all segments have the same order tensor, with a diagonalized unique principal value of 1.

Further, the uniaxiality of the motion imposes an axially symmetric lineshape to all NMR interactions, described by an asymmetry parameter η of 0.

One can assess which motional model is more likely for penetratin backbone in the LC membrane by determining the asymmetry parameter of motion. If the only motion giving rise to the reduced dipolar couplings is uncorrelated segmental motion, then the motionally averaged NMR spectra should in general exhibit $\bar{\eta}$ different from 0. We can measure the asymmetry of the lineshape through chemical shift anisotropy (CSA) spectra, since the static-limit CSAs of $C\alpha$ and $C\beta$ sites of proteins are generally non-uniaxial. We used the ROCSA technique (35) to recouple the ^{13}C CSA while suppressing the ^{13}C - ^{13}C dipolar couplings. Figure 3.10 shows the 2D ROCSA spectrum of (I3, N9)-labeled penetratin in DMPC/DMPG bilayers at 303 K, along with the CSA cross sections of the $N9\alpha$ coil peak and the mixed I3 β and N9 β coil peak. It can be seen that the CSA lineshapes are close to uniaxial and are clearly narrower than the static-limit CSA. The $N9\alpha$ lineshape is well fit by a motionally averaged anisotropy parameter $\bar{\delta}$ of 9.9 ppm and $\bar{\eta} = 0$. This is very different from the static-limit δ of 14.4 ppm and $\eta = 0.90$. The static-limit CSA principal values were taken from *ab initio* calculated shielding values (36) for the β -sheet conformation. For the mixed I3 β and N9 β peak, the predicted rigid-limit β -sheet CSA (δ, η) is (21.1 ppm, 0.82) for Asn $C\beta$ and (11.8 ppm, 0.82) for Ile $C\beta$. Their average gives the dashed line pattern in Figure 3.10c, which is clearly broader than the measured CSA pattern. The experimental pattern is well fit with $(\bar{\delta}, \bar{\eta}) = (9.1 \text{ ppm}, 0)$. For both sites, the measured CSA lineshapes are not only much narrower than the static-limit patterns, but are also axially symmetric within experimental uncertainty (37), indicating that the peptide undergoes fast uniaxial rotation around the bilayer normal. This backbone uniaxial motion suggests that the coil chemical shifts may result from a rigid turn conformation that rotates around the membrane normal rather than an isotropic random coil. The chemical shifts of various β - and γ -turns are intermediate between helix and sheet chemical shifts and are not well distinguished from random coil chemical shifts in protein databases. Since the coil chemical shifts are observed for residues from I3 to K13, the proposed turn structure involves a large segment of the peptide in the fluid membrane.

Thermodynamics of the sheet ↔ turn transition

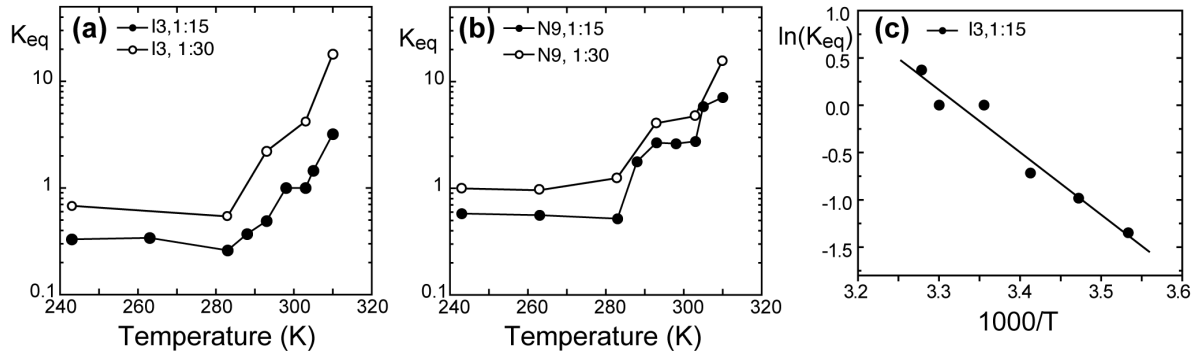


Figure 3.11. Thermodynamics of the sheet ↔ turn conformational change. The turn/sheet intensity ratios, K_{eq} , are plotted as a function of temperature. (a) I3 α . (b) N9 α . (c) $\ln(K_{eq})$ versus $1000/T$ for I3 α at P/L = 1:15. The slope of the linear fit gives the ΔH and the intercept gives the ΔS of the conformational change.

The temperature-induced reversible sheet ↔ turn transition of penetratin is an equilibrium reaction. Assuming a simple two-state model, sheet ↔ turn + ΔH , we can estimate the enthalpy and entropy of the conformational change using the van't Hoff equation:

$$\ln K_{eq} = -\frac{\Delta H}{RT} + \frac{\Delta S}{R}, \text{ where } K_{eq} = \frac{[\text{turn}]}{[\text{sheet}]} \quad (1)$$

The equilibrium constant K_{eq} can be obtained from the intensity ratio between the turn and sheet peaks at each temperature. These K_{eq} values are listed in Table 3.2 for I3 α and N9 α in the DMPC/DMPG (8:7) membrane at both high and low peptide concentrations. Figure 3.11(a-b) plots K_{eq} for the two sites at both concentrations as a function of temperature. All four curves plateau below 283 K, where the β -sheet conformation dominates. The lower concentration curves are shifted up from the high-concentration curves, indicating increased populations of the turn conformation. This is expected since the β -sheet conformation requires intermolecular association and is thus favored by high peptide concentrations.

The turn conformation does not yet exhibit a plateau at the highest temperature measured (310 K) that is still deemed safe for the samples. Figure 3.11(a-b) shows that the conformational change occurs broadly around the DMPC/DMPG phase transition temperature of 296 K.

Table 3.2. Temperature-dependent equilibrium constant $K_{eq} = [\text{turn}]/[\text{sheet}]$ for the sheet \leftrightarrow turn transition of I3 α and N9 α of penetratin in DMPC/DMPG membranes (8:7) at P/L = 1:15 and 1:30.

T (K)	P/L = 1:15		P/L = 1:30	
	I3 α	N9 α	I3 α	N9 α
243	0.33	0.58	0.68	1.00
263	0.34	0.56	0.29	0.96
283	0.26	0.52	0.54	1.25
288	0.37	1.78	-	-
293	0.49	2.68	2.21	4.08
298	1.00	2.62	7.29	32.8
303	1.00	2.76	4.21	4.76
305	1.45	5.85	-	-
310	3.20	7.13	18.0	15.5

Table 3.3. Enthalpy and entropy changes of the sheet \leftrightarrow turn transition of penetratin in DMPC/DMPG (8:7) membranes. The thermodynamic values are for one mole of peptide.

Residue, P/L	$\ln K_{eq}$ vs. $1000/T$		ΔH (kcal/mol K)	ΔS (kcal/mol K)
	slope	intercept		
I3 α , 1:15	-7.52	25.1	14.9	0.050
N9 α , 1:15	-7.07	24.8	14.0	0.049
I3 α , 1:30	-6.79	24.1	13.5	0.048
N9 α , 1:30	-7.20	25.8	14.3	0.051
mean	-	-	14.2	0.050

Figure 3.11c shows a representative plot of $\ln K_{eq}$ versus $1000/T$ for I3 α at P/L = 1:15. For the temperature regime where the transition occurs, the data fits well to a straight line with a negative slope. This linear regime covers 263 – 310 K for I3 α at P/L = 1:30 and 283 – 310 K for the other three conditions. As indicated by eq. 1, the slope of the line gives the enthalpy ΔH of the conformation change, while the intercept gives the entropy change, ΔS . The negative slope indicates a positive enthalpy, or an endothermic sheet \leftrightarrow

turn reaction, consistent with the fact that high temperature induces the turn conformation. The entropy change is also positive, consistent with the higher mobility of the turn state. Table 3.3 lists the enthalpy and entropy changes for the conformational transition. The ΔH and ΔS values are similar between the two residues, suggesting that the conformational change is global rather than local. Assuming that all 16 residues are involved in the conformational change, then ΔH per residue is +0.89 kcal/mol, while ΔS per residue is 3.1 cal/(mol · K).

3.4 Discussion

Plasticity of penetratin conformation

The conformation of penetratin has been studied extensively and has been found to be highly plastic, sensitive to the nature of the solvent (buffer, organic solution, micelles, bicelles, or lipid vesicles), peptide concentration, and membrane composition. Most studies employed CD spectroscopy. In water, the peptide is clearly a random coil. In helix-promoting solvents such as trifluoroethanol (15, 38) the peptide becomes partly α -helical. In SDS micelles the helical content is even higher (~50%) but the random coil fraction remains significant from both CD and ^1H NMR data (15-17, 39). In comparison, in lipid bilayers, CD spectra show that penetratin has significant helicity only in largely zwitterionic membranes at low peptide concentrations (18-20, 40, 41). In zwitterionic membranes at high peptide concentrations, the CD spectra indicate a high percentage of random coil (16, 42). In anionic membranes with high peptide concentrations, penetratin conformation shifts to β -structures, including β -strands as well as β -turns (42).

Since CD spectroscopy of membrane-bound peptides is complicated by light scattering of lipid vesicles and uncertainties in spectral deconvolution, the conformation information is only approximate. In comparison, NMR gives site-specific and accurate information on the peptide conformation in lipid membranes. So far the only NMR study of penetratin in lipid membranes used DMPC/DMPG (10:1) bicelles with a low anionic lipid content and a low peptide concentration (P/L = 1:130). Under these conditions, ^1H chemical shifts and ^1H - ^1H nuclear Overhauser effects (NOEs) indicate that the central 9 residues of the pep-

tide are α -helical but with somewhat irregular geometries (18), reminiscent of the random coils observed under other conditions.

Coil or turn conformation at high temperature?

The current solid-state NMR chemical-shift based conformational constraints are obtained for penetratin bound to 50% and 25% anionic lipid membranes and at P/L ratios of 1:15 and 1:30. We found that in the gel-phase membrane, the peptide is clearly a β -sheet from residue 3 to 13. But in the fluid phase, penetratin changes to a coil-like structure with significant residual anisotropy and uniaxial mobility. The latter two observations suggest that the high-temperature conformation may be a structured turn rather than an unstructured coil. The (ϕ , ψ) torsion angles and three-dimensional fold of this turn-rich conformation are not yet determined, since most existing solid-state NMR techniques for quantitative structure determination require immobilized molecules, which would require freezing penetratin, which would destroy the very structure of interest.

These solid-state NMR results are in qualitative agreement with CD studies done on membranes with similar compositions. CD spectra measured in POPC/POPG (70:30) vesicles at high peptide concentrations of P/L = 1:17 to 1:33 yielded estimates of 40-60% β -structure, 20-25% random coil, and 20-30% helix (42). The β -structure included not only antiparallel and parallel β -strands but also β -turns, thus the result is consistent with the NMR data. The remaining α -helical content estimated from the CD spectra may be attributed to the different vesicle sizes used. The CD experiments were carried out on sonicated small unilamellar vesicles while the solid-state NMR data were measured on large unilamellar vesicles. Since penetratin has large helicity in curved SDS micelles, high curvature of the bilayer should also promote α -helix formation.

We found that the sheet \leftrightarrow turn conformational change of penetratin occurs under a range of peptide concentrations, anionic lipid contents, and lipid chain saturation. Thus it appears to be an intrinsic property of the peptide in lipid bilayers. It is possible that short segments of β -strand residues, not included among the five labeled residues here, connect the turns. Turn-rich proteins with very short β -strand segments have been observed before. For

example, the elastin-mimetic (VPGVG)_n polypeptides consist of repeated β -turns, called β -spirals, centered at Pro and Gly residues in each repeat (43). Turn-rich conformations have also been found in a number of cationic antimicrobial peptides such as indolicidin and tritrypticin (44-46). Solution NMR structures indicate that these turn-rich conformations lead to an amphipathic organization of the peptides, which facilitate their membrane-disruptive activity. For penetratin, whose translocation function leaves the membrane intact, the turn conformation may disfavor an amphipathic three-dimensional fold.

It is important to note that the high-temperature turn state of penetratin is embedded in the membrane rather than floating in the aqueous phase, in contrast to other peptides that undergo coil \leftrightarrow helix or coil \leftrightarrow sheet changes as a result of membrane binding. Evidence for the strong membrane association includes cross peaks between the lipid C α and the coil peptide (Figure 3.3c) and paramagnetic relaxation enhancement data that show that the turn conformation is well shielded from the Mn²⁺ ions on the membrane surface (47).

Energetics of penetratin sheet \leftrightarrow turn transition and comparison with other peptides

Coil \leftrightarrow sheet conformational changes have been reported for several membrane peptides before (26, 48, 49), and are usually triggered by the partitioning of the peptides from aqueous solution to the lipid membrane (25). The thermodynamics of this bilayer-induced secondary structure formation has been studied using CD and isothermal titration calorimetry (50), which yielded quite variable ΔH and ΔS values. For example, the hexapeptide AcWL₅ is a monomeric random coil in solution, aggregates to β -sheets upon membrane binding, and unfolds back to a coil upon heating. The per-residue enthalpy change, $\Delta H_{\text{residue}}$, of the sheet \rightarrow coil unfolding was found to be +1.3 kcal/mol (48). The antimicrobial peptide (KIGAKI)₃ is random coil in solution and becomes a nearly perfect β -sheet upon membrane binding. The $\Delta H_{\text{residue}}$ of the β -sheet formation was measured to be -0.23 kcal/mol (26), which corresponds to +0.23 kcal/mol for the reverse sheet \rightarrow coil transition. The significant ΔH variation among different β -sheet formers has been noted before (26) and contrasts with the relatively uniform helix \leftrightarrow coil enthalpy change of +0.7 – +1.1 kcal/mol. For penetratin, assuming that the sheet \leftrightarrow turn transition occurs for all residues of the peptide,

$\Delta H_{\text{residue}}$ is +0.89 kcal/mol, which is within the range reported in the literature. However, since penetratin is much closer to (KIGAKI)₃ than AcWL₅ in terms of sequence length and the cationic nature, ΔH for penetratin might be expected to be much closer to the value of +0.23 kcal/mol for (KIGAKI)₃. Experimental conditions such as peptide concentration and membrane composition may explain the different ΔH values.

The entropy change per residue, $\Delta S_{\text{residue}}$, of the sheet \leftrightarrow turn transition from the intercept of the linear fit is +3.1 cal/mol·K. Combined with $\Delta H_{\text{residue}}$, it means that the free energy change, $\Delta G_{\text{residue}} = \Delta H_{\text{residue}} - T\Delta S_{\text{residue}}$, is only slightly negative, -0.05 kcal/mol, at 298 K, which is consistent with the coexistence of turn and sheet peaks at this temperature. Increasing the temperature to 310 K makes $\Delta G_{\text{residue}}$ slightly more negative, -0.07 kcal/mol, thus the sheet \leftrightarrow turn transition is an entropically driven process. Overall, the small free energy reduction of penetratin's sheet \leftrightarrow turn transition contrasts with the previously reported $\Delta G_{\text{residue}}$ of about -0.5 kcal/mol for bilayer-induced secondary structure formation (25). This lends further support to our conclusion that the conformational change of penetratin occurs within the membrane, rather than involving a change from the membrane to the aqueous phase.

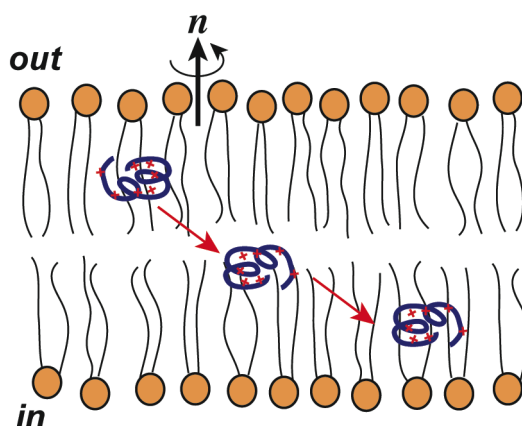


Figure 3.12. Proposed model of membrane translocation by penetratin. A compact turn-rich conformation reduces hydrophobic interactions with the lipid chains and enables the peptide to cross the lipid bilayer without causing long-lasting pores.

What is the significance of this turn conformation to the translocation function of penetratin? The structural polymorphism of penetratin has been suggested to be important for cell internalization by facilitating the peptide's passage through solvents with very different dielectric constants (51). We suggest a more specific hypothesis for the existence of the turn structure in the LC membrane after initial peptide binding. Since the turn structure has a small surface-to-volume ratio and lacks amphipathic organization, it may facilitate the peptide's translocation across the membrane by minimizing hydrophobic interactions with the lipid chains (Figure 3.12). Such hydrophobic interactions are implicated in the stabilization of amphipathic antimicrobial peptides in the membrane, which leads to pores or other permanent damage to the membrane (27, 52). In comparison, penetratin's function requires it to have only transient association with the lipid bilayer, without leaking the cell content, and a compact turn conformation may be better suited than amphipathic β -sheet or α -helical structures for rapid crossing through and eventual dissociation from the membrane. This model suggests that peptide conformation may in fact be important in cell internalization. It does not, however, explain the driving force for passage through the membrane. That driving force has been suggested to be the voltage potential across the cell membrane created by differential intracellular and extracellular ion concentrations (53).

3.5 Materials and Methods

Membrane sample preparation

All lipids, including 1,2-dimyristoyl-*sn*-glycero-3-phosphatidylcholine (d₅₄-DMPC), 1,2-dimyristoyl-*sn*-glycero-3-phosphatidylglycerol (DMPG), 1-palmitoyl-2-oleoyl-*sn*-glycero-3-phosphatidylcholine (POPC), 1-palmitoyl-2-oleoyl-*sn*-glycero-3-phosphatidylglycerol (POPG), were purchased from Avanti Polar Lipids (Alabaster, AL) and used without further purification. Penetratin (RQIKIWFQNR RMKWKK) was synthesized using Fmoc solid-phase protocols (PrimmBiotech, Cambridge, MA) and purified by HPLC to >95% purity. U-¹³C, ¹⁵N-labeled residues were incorporated at positions I3, I5, Q8, N9, and K13 in three different samples.

Hydrated membrane samples were prepared by an aqueous-phase mixing protocol. First, a zwitterionic lipid and an anionic lipid were mixed in chloroform at the desired molar

ratio and dried under N₂ gas. The lipid film was dissolved in cyclohexane and lyophilized overnight. The mixed lipid powder was redissolved in deionized water and vortexed thoroughly, then freeze-thawed eight times. The lipid vesicle solution was then extruded successively through 1.0 μm, 0.4 μm and 0.1 μm polycarbonate filters to obtain large unilamellar vesicles of ~100 nm diameter. The vesicle solution was added to an appropriate amount of peptide-containing aqueous solution. The mixture was incubated overnight, then centrifuged at 55,000 rpm for 3 hours above the lipid phase transition temperature to obtain a pellet. The pellet was center-packed into a 4 mm MAS rotor with Teflon spacer at the bottom to give a hydrated membrane sample for NMR experiments. This study used three membrane compositions – DMPC/DMPG (8:7), POPC/POPG (8:7), and DMPC/DMPG (3:1), and two P/L ratios – 1:15 and 1:30, to examine the environmental dependence of penetratin conformation. Chain-perdeuterated d₅₄-DMPC was used in the membrane mixtures to reduce the intensities of the lipid background signals.

NMR experiments

Solid-state NMR experiments were carried out on a Bruker AVANCE-600 (14.1 T) spectrometer and a DSX-400 (9.4 T) spectrometer (Karlsruhe, Germany) using magic-angle-spinning (MAS) probes. Low temperatures were achieved with a Bruker BCU-Xtreme unit on the AVANCE-600 spectrometer and a Kinetics Thermal Systems XR air-jet sample cooler (Stone Ridge, NY) on the DSX-400 spectrometer. Typical 90° pulse lengths were 5.0 μs for ¹³C and 3.5–4.0 μs for ¹H. The α-glycine C' resonance of 176.49 ppm on the tetramethylsilane scale was used as the external reference for the ¹³C chemical shifts. ¹H-¹³C cross-polarization (CP) experiments were carried out with a contact time of 500 μs and a ¹H decoupling field of 62 kHz. Variable-temperature ¹³C spectra were acquired after stabilizing the sample for at least 25 minutes at each temperature.

2D ¹H-driven ¹³C spin diffusion experiments were carried out without ¹H decoupling (PDSO) or with ¹H decoupling at the spinning frequency (DARR) during the mixing time. Mixing times of 20–100 ms and spinning speeds of 5.0 and 6.0 kHz were used. ¹³C-¹H dipolar couplings were measured using the 2D dipolar chemical-shift correlation (DIPSHIFT) experiment at a spinning speed of 3401 Hz. For ¹H homonuclear decoupling, the MREV-8 se-

quence (54) was used. The t_1 dipolar data were fit using a home-written Fortran program. The fit values were divided by the scaling factor, 0.47, of the MREV-8 sequence to obtain the true C-H dipolar couplings. The ratio of the true coupling with the rigid-limit one-bond C-H dipolar coupling, 22.7 kHz, gives the bond order parameter, S_{CH} . For CH_2 groups, the three-spin system gives rise to an $\eta = 1$ dipolar pattern with principal values of $(-\delta, 0, \delta)$, where δ is the coupling strength. For four-spin CH_3 systems, the 1:3:3:1 multiplet pattern was simulated using a 3:1 mixture of dipolar couplings δ and 3δ .

^{13}C chemical shift anisotropy (CSA) was measured using the 2D ROCSA experiment (35), where the CSA interaction is recoupled by an Cn_n^1 sequence and the ^{13}C - ^{13}C homonuclear dipolar coupling is mostly suppressed. The ^{13}C recoupling spin-lock field strength is 4.283 times the spinning speed. The experiment has a CSA scaling factor of 0.272. The experiments were carried out at 310 K under 8.0 kHz MAS.

3.6 Acknowledgement

This work is funded by an NIH grant GM-066976.

3.7 Reference

1. gSchwarze, S. R., Ho, A., Vocero-Akbani, A., and Dowdy, S. F. (1999) In vivo protein transduction: delivery of a biologically active protein into the mouse, *Science* 285, 1569-1572.
2. Torchilin, V. P., Rammohan, R., Weissig, V., and Levchenko, T. S. (2001) TAT peptide on the surface of liposomes affords their efficient intracellular delivery even at low temperature and in the presence of metabolic inhibitors, *Proc. Natl. Acad. Sci. U. S. A.* 98, 8786-8791.
3. Gratton, J. P., Yu, J., Griffith, J. W., Babbitt, R. W., Scotland, R. S., Hickey, R., Giordano, F. J., and Sessa, W. C. (2003) Cell-permeable peptides improve cellular uptake and therapeutic gene delivery of replication-deficient viruses in cells and in vivo, *Nat. Med.* 9, 357-362.
4. Derossi, D., Joliot, A. H., Chassaing, G., and Prochiantz, A. (1994) The third helix of the Antennapedia homeodomain translocates through biological membranes, *J. Biol. Chem.* 269, 10444-10450.

5. Derossi, D., Calvet, S., Trembleau, A., Brunissen, A., Chassaing, G., and Prochiantz, A. (1996) Cell internalization of the third helix of the Antennapedia homeodomain is receptor-independent, *J. Biol. Chem.* 271, 18188-18193.
6. Richard, J. P., Melikov, K., Vives, E., Ramos, C., Verbeure, B., Gait, M. J., Chernomordik, L. V., and Lebleu, B. (2003) Cell-penetrating peptides. A reevaluation of the mechanism of cellular uptake, *J. Biol. Chem.* 278, 585-590.
7. Letoha, T., Gaál, S., Somlai, C., Czajlik, A., Perczel, A., and Penke, B. (2003) Membrane translocation of penetratin and its derivatives in different cell lines, *J. Mol. Recognit.* 16, 272-279.
8. El Andaloussi, S., Guterstam, P., and Langel, U. (2007) Assessing the delivery efficacy and internalization route of cell-penetrating peptides, *Nat. Protoc.* 2, 2043-2047.
9. Fischer, R., Fotin-Mleczek, M., Hufnagel, H., and Brock, R. (2005) Break on through to the other side-biophysics and cell biology shed light on cell-penetrating peptides, *ChemBioChem.* 6, 2126-2142.
10. Hessa, T., Kim, H., Bihlmaier, K., Lundin, C., Boekel, J., Andersson, H., Nilsson, I., White, S. H., and von Heijne, G. (2005) Recognition of transmembrane helices by the endoplasmic reticulum translocon, *Nature* 433, 377-381.
11. Epanand, R. M., and Vogel, H. J. (1999) Diversity of antimicrobial peptides and their mechanisms of action, *Biochim. Biophys. Acta* 1462, 11-28.
12. Powers, J. P., and Hancock, R. E. (2003) The relationship between peptide structure and antibacterial activity, *Peptides* 24, 1681-1691.
13. Futaki, S., Suzuki, T., Ohashi, W., Yagami, T., Tanaka, S., Ueda, K., and Sugiura, Y. (2001) Arginine-rich peptides. An abundant source of membrane-permeable peptides having potential as carriers for intracellular protein delivery, *J. Biol. Chem.* 276, 5836-5840.
14. Herce, H. D., and Garcia, A. E. (2007) Molecular dynamics simulations suggest a mechanism for translocation of the HIV-1 TAT peptide across lipid membranes, *Proc. Natl. Acad. Sci. U. S. A.* 104, 20805-20810.
15. Berlose, J. P., Convert, O., Derossi, D., Brunissen, A., and Chassaing, G. (1996) Conformational and associative behaviours of the third helix of antennapedia homeodomain in membrane-mimetic environments, *Eur. J. Biochem.* 242, 372-386.
16. Magzoub, M., Kilk, K., Eriksson, L. E., Langel, U., and Graslund, A. (2001) Interaction and structure induction of cell-penetrating peptides in the presence of phospholipid vesicles, *Biochim. Biophys. Acta* 1512, 77-89.
17. Drin, G., Demene, H., Tamsamani, J., and Brasseur, R. (2001) Translocation of the pAntp peptide and its amphipathic analogue AP-2AL, *Biochemistry* 40, 1824-1834.
18. Lindberg, M., Biverstahl, H., Graslund, A., and Maler, L. (2003) Structure and positioning comparison of two variants of penetratin in two different membrane mimicking systems by NMR, *Eur. J. Biochem.* 270, 3055-3063.

19. Persson, D., Thoren, P. E., Herner, M., Lincoln, P., and Norden, B. (2003) Application of a novel analysis to measure the binding of the membrane-translocating peptide penetratin to negatively charged liposomes, *Biochemistry* 42, 421-429.
20. Clayton, A. H., Atcliffe, B. W., Howlett, G. J., and Sawyer, W. H. (2006) Conformation and orientation of penetratin in phospholipid membranes., *J. Pept. Sci.* 12, 233-238.
21. Binder, H., and Lindblom, G. (2003) Charge-dependent translocation of the Trojan peptide penetratin across lipid membranes, *Biophys. J.* 85, 982-995.
22. Spera, S., and Bax, A. (1991) Empirical correlation between protein backbone conformation and Ca and Cb ¹³C NMR chemical shifts, *J. Am. Chem. Soc.* 113, 5490-5492.
23. Wishart, D. S., and Sykes, B. D. (1994) The ¹³C chemical-shift index: a simple method for the identification of protein secondary structure using ¹³C chemical-shift data., *J. Biomol. NMR* 4, 171-180.
24. Zhang, H., Neal, S., and Wishart, D. S. (2003) RefDB: A database of uniformly referenced protein chemical shifts, *J. Biomol. NMR* 25, 173-195.
25. White, S. H., and Wimley, W. C. (1999) Membrane protein folding and stability: physical principles, *Annu. Rev. Biophys. Biomol. Struct.* 28, 319-365.
26. Meier, M., and Seelig, J. (2007) Thermodynamics of the coil \rightleftharpoons beta-sheet transition in a membrane environment, *J. Mol. Biol.* 369, 277-289.
27. Mani, R., Cady, S. D., Tang, M., Waring, A. J., Lehrer, R. I., and Hong, M. (2006) Membrane-dependent oligomeric structure and pore formation of a b-hairpin antimicrobial peptide in lipid bilayers from solid-state NMR, *Proc. Natl. Acad. Sci. USA* 103, 16242-16247.
28. Mani, R., Tang, M., Wu, X., Buffy, J. J., Waring, A. J., Sherman, M. A., and Hong, M. (2006) Membrane-bound dimer structure of a b-hairpin antimicrobial peptide from rotational-echo double-resonance solid-state NMR, *Biochemistry* 45, 8341-8349.
29. Buffy, J. J., Waring, A. J., Lehrer, R. I., and Hong, M. (2003) Immobilization and Aggregation of Antimicrobial Peptide Protegrin in Lipid Bilayers Investigated by Solid-State NMR, *Biochemistry* 42, 13725-13734.
30. Tang, M., Waring, A. J., and Hong, M. (2007) Phosphate-mediated arginine insertion into lipid membranes and pore formation by a cationic membrane peptide from solid-state NMR, *J. Am. Chem. Soc.* 129, 11438 - 11446.
31. Tang, M., Waring, A. J., Lehrer, R. I., and Hong, M. (2008) Effects of Guanidinium-Phosphate Hydrogen Bonding on the Membrane-Bound Structure and Activity of an Arginine-Rich Membrane Peptide from Solid-State NMR, *Angew. Chem. Int. Ed. Engl.*, in press.
32. Zhang, Q., Stelzer, A. C., Fisher, C. K., and Al-Hashimi, H. M. (2007) Visualizing spatially correlated dynamics that directs RNA conformational transitions., *Nature* 450, 1263-1267.

33. Zhang, Q., Sun, X., Watt, E. D., and Al-Hashimi, H. M. (2006) Resolving the motional modes that code for RNA adaptation, *Science* 311, 653-656.
34. Schmidt-Rohr, K., and Hong, M. (1996) Information on bond orientation in lipids and liquid crystals from segmental order parameters., *J. Phys. Chem.* 100, 3861-3866.
35. Chan, J. C. C., and Tycko, R. (2003) Recoupling of chemical shift anisotropies in solid-state NMR under high-speed magic-angle spinning and in uniformly ¹³C-labeled systems., *J. Chem. Phys.* 118, 8378-8389.
36. Sun, H., Sanders, L. K., and Oldfield, E. (2002) Carbon-¹³C NMR shielding in the twenty amino acids: comparisons with experimental results in proteins., *J. Am. Chem. Soc.* 124, 5486-5495.
37. Wylie, B. J., Franks, W. T., and Rienstra, C. M. (2006) Determinations of ¹⁵N chemical shift anisotropy magnitudes in a uniformly ¹⁵N,¹³C-labeled microcrystalline protein by three-dimensional magic-angle spinning nuclear magnetic resonance spectroscopy, *J. Phys. Chem. B.* 110, 10926-10936.
38. Czajlik, A., Meskó, E., Penke, B., and Perczel, A. (2002) Investigation of penetratin peptides. Part 1. The environment dependent conformational properties of penetratin and two of its derivatives, *J. Pept. Sci.* 8, 151-171.
39. Lindberg, M., and Gräslund, A. (2001) The position of the cell penetrating peptide penetratin in SDS micelles determined by NMR, *FEBS Lett.* 497, 39-44.
40. Magzoub, M., Eriksson, L. E., and Gräslund, A. (2003) Comparison of the interaction, positioning, structure induction and membrane perturbation of cell-penetrating peptides and non-translocating variants with phospholipid vesicles, *Biophys. Chem.* 103, 271-288.
41. Thoren, P. E., Persson, D., Karlsson, M., and Norden, B. (2000) The antennapedia peptide penetratin translocates across lipid bilayers - the first direct observation, *FEBS Lett.* 482, 265-268.
42. Magzoub, M., Eriksson, L. E., and Gräslund, A. (2002) Conformational states of the cell-penetrating peptide penetratin when interacting with phospholipid vesicles: effects of surface charge and peptide concentration, *Biochim. Biophys. Acta* 1563, 53-63.
43. Yao, X. L., and Hong, M. (2004) Structural Distribution in an Elastin-Mimetic Peptide (VPGVG)₃ Investigated by Solid-State NMR, *J. Am. Chem. Soc.* 126, 4199-4210.
44. Ladokhin, A. S., Selsted, M. E., and White, S. H. (1999) CD spectra of indolicidin antimicrobial peptides suggest turns, not polyproline helix, *Biochemistry* 38, 12313-12319.
45. Schibli, D. J., Hwang, P. M., and Vogel, H. J. (1999) Structure of the antimicrobial peptide tritrpticin bound to micelles: a distinct membrane-bound peptide fold., *Biochemistry* 38, 16749-16755.
46. Chan, D. I., Prenner, E. J., and Vogel, H. J. (2006) Tryptophan- and arginine-rich antimicrobial peptides: structures and mechanisms of action, *Biochim. Biophys. Acta* 1758, 1184-1202.

47. Su, Y., Mani, R., and Hong, M. (2008) Asymmetric insertion of membrane proteins in lipid bilayers by solid-state NMR paramagnetic relaxation enhancement: a cell-penetrating peptide example., *J. Am. Chem. Soc.*, in press.
48. Wimley, W. C., Hristova, K., Ladokhin, A. S., Silverstro, L., Axelsen, P. H., and White, S. H. (1998) Folding of b-sheet membrane proteins: a hydrophobic hexapeptide model, *J. Mol. Biol.* 277, 1091-1110.
49. Terzi, E., Hölzemann, G., and Seelig, J. (1995) Self-association of beta-amyloid peptide (1-40) in solution and binding to lipid membranes, *J. Mol. Biol.* 252, 633-642.
50. Ladokhin, A. S., and White, S. H. (1999) Folding of amphipathic alpha-helices on membranes: energetics of helix formation by melittin, *J. Mol. Biol.* 285, 1363-1369.
51. Deshayes, S., Decaffmeyer, M., Bresseur, R., and Thomas, A. (2008) Structural polymorphism of two CPP: An important parameter of activity, *Biochim. Biophys. Acta* 1778, 1197-1205.
52. Hong, M. (2007) Structure, topology, and dynamics of membrane peptides and proteins from solid-state NMR spectroscopy, *J. Phys. Chem. B.* 111, 10340-10351.
53. Rothbard, J. B., Jessop, T. C., Lewis, R. S., Murray, B. A., and Wender, P. A. (2004) Role of membrane potential and hydrogen bonding in the mechanism of translocation of guanidinium-rich peptides into cells, *J. Am. Chem. Soc.* 126, 9506-9507.
54. Rhim, W.-K., Elleman, D. D., and Vaughan, R. W. (1973) Analysis of multiple-pulse NMR in solids., *J. Chem. Phys.* 59, 3740-3749.

3.8 Supporting information

Table S3.1. Intensity fractions of sheet and turn peaks of (I3, N9)-labeled penetratin in DMPC/DMPG (8:7) membranes at P/L = 1:15 and 1:30.

T (K)	P/L = 1:15				P/L = 1:30			
	I3 α		N9 α		I3 α		N9 α	
	Sheet	Turn	Sheet	Turn	Sheet	Turn	Sheet	Turn
243	0.75	0.25	0.63	0.37	0.60	0.40	0.50	0.50
263	0.75	0.25	0.64	0.36	0.77	0.23	0.51	0.49
283	0.79	0.21	0.66	0.34	0.65	0.35	0.44	0.56
288	0.73	0.27	0.36	0.64	-	-	-	-
293	0.67	0.33	0.27	0.73	0.31	0.69	0.20	0.80
298	0.50	0.50	0.28	0.72	0.12	0.88	0.03	0.97
303	0.50	0.50	0.27	0.73	0.19	0.81	0.17	0.83
305	0.41	0.59	0.15	0.85	-	-	-	-
310	0.24	0.76	0.12	0.88	0.05	0.95	0.06	0.94

Table S3.2: ^{13}C chemical shifts (ppm) of penetratin in DMPC/DMPG bilayers at 310 K and 243 K.

residue	site	310 K	243 K
I3	CO	173.8	172.3
	C α	60.2	57.4
	C β	36.3	39.8
	C γ	26.2	26.4
	C δ	15.7	15.2
	C ϵ	11.4	12.7
I5	CO	-	172.2
	C α	59.2	57.5
	C β	36.8	40.1
	C γ	25.6	26.5
	C δ	15.7	15.9
	C ϵ	11.3	12.7
Q8	CO	-	172.8
	C α	54.6	53.4
	C β	31.4	33.8
	C γ	27.9	31.6
	C δ	-	177.7
N9	CO	173.9	-
	C α	52.2	49.4
	C β	36.6	38.8
	C γ	175.6	-
K13	CO	174.2	171.7
	C α	54.4	53.1
	C β	31.5	35.3
	C γ	22.7	22.8
	C δ	27.2	27.2
	C ϵ	39.8	39.7

Chapter 4

Asymmetric Insertion of Membrane Proteins in Lipid Bilayers by Solid-State NMR Paramagnetic Relaxation Enhancement: a Cell-Penetrating Peptide Example

A paper published in Journal of American Chemical Society

2008, vol. 130(27), page 8856-8864

Yongchao Su, Rajeswari Mani and Mei Hong

Department of Chemistry, Iowa State University, Ames, IA 50011

4.1 Abstract

A novel solid-state NMR technique for identifying the asymmetric insertion depths of membrane proteins in lipid bilayers is introduced. By applying Mn^{2+} ions on the outer but not the inner leaflet of lipid bilayers, the sidedness of protein residues in the lipid bilayer can be determined through paramagnetic relaxation enhancement (PRE) effects. Protein-free lipid membranes with one side Mn^{2+} -bound surfaces exhibit significant residual ^{31}P and lipid headgroup ^{13}C intensities, in contrast to two side Mn^{2+} -bound membranes, where lipid headgroup signals are mostly dephased. Applying this method to a cell-penetrating peptide, penetratin, we found that at low peptide concentrations, penetratin is distributed in both leaflets of the bilayer, in contrast to the prediction of the electroporation model, which predicts that penetratin binds to only the outer lipid leaflet at low peptide concentrations to cause an electric field that drives subsequent peptide translocation. The invalidation of the electroporation model suggests an alternative mechanism for intracellular import of penetratin, which may involve guanidinium-phosphate complexation between the peptide and the lipids.

4.1 Introduction

The depth of protein residues in lipid bilayers is an important aspect of the three-dimensional (3D) structure of membrane proteins. Even before the complete atomic-level high-resolution structure is determined for a membrane protein, knowledge of the depth of its residues already gives information on the topology of the protein in the mem-

brane (*1*), which is crucial for understanding its function. Solid-state NMR spectroscopy has provided a number of tools to determine the depth of insertion of membrane proteins. For example, ^1H spin diffusion from the lipid chains in the center of the membrane to the protein and from water on the membrane surface to the protein has been exploited (*2-6*). Paramagnetic relaxation enhancement (PRE) (*7, 8*) is another powerful approach to measure the site-specific depths of membrane proteins (*9-12*) or membrane-bound small molecules (*13*). Paramagnetic ions such as Mn^{2+} , Gd^{3+} and Dy^{3+} bound to the membrane surfaces enhance the T_2 relaxation rates of nuclear spins in a distance-dependent fashion, so that nuclear spins closer to the membrane surface manifest larger relaxation enhancement, or lower intensities. Membrane-soluble paramagnetic oxygen has also been used to induce depth-dependent changes in chemical shifts and T_1 and T_2 relaxation rates (*14, 15*). By comparing the protein PRE effects with those of the lipid functional groups whose depths are well known (*16*), one can measure the depths quantitatively (*9*). The ability for depth calibration is a unique feature of membrane protein PRE, as compared to PRE applications to macromolecules in solution (*17, 18*) or to microcrystalline proteins (*19*).

Despite the many advances in determining membrane protein insertion depths, to our best knowledge there is so far no report of the determination of the asymmetric insertion of membrane proteins in the lipid bilayer. Most membrane proteins insert in a unidirectional fashion as required by their function (*1*). It is thus important to determine which leaflet of the bilayer, in addition to the depth, a residue is inserted to. If the paramagnetic ions are distributed on both surfaces of the bilayer, then it is not possible to distinguish the depth in the inner versus the outer leaflet. We demonstrate here a simple modification of the PRE technique that distributes the paramagnetic ions on only one side of the bilayer, thus allowing the determination of the asymmetric insertion depths of membrane proteins. This concept has been shown using lanthanide shift reagents to distinguish outer- and inner-leaflet lipids (*20, 21*), and in a related approach to separate extracellular versus intracellular metabolite signals in solution (*22*). However, to our best knowledge it has not been applied to membrane peptides and proteins.

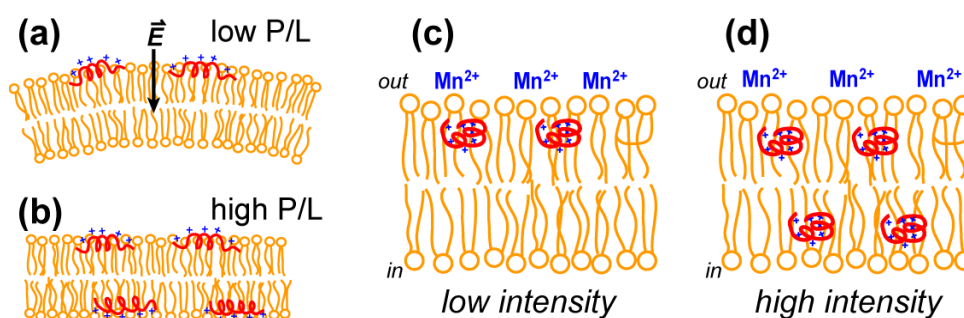


Figure 4.1. One side paramagnetic relaxation enhancement NMR for determining the asymmetric binding of membrane proteins. (a, b) Electroporation model of cell-penetrating peptides. (a) At low P/L, the peptides are bound to the outer leaflet of the membrane, causing an electric field and membrane curvature strain. (b) At high P/L, the peptides distribute to both leaflets of the membrane, releasing the curvature strain. When Mn^{2+} ions are distributed on the outer surface of the membrane: (c) Membrane proteins inserted only to the outer leaflet experience strong PRE and give low intensities. (d) Membrane proteins bound to both leaflets of the bilayer have high intensities due to the negligible PRE experienced by the inner-leaflet molecules.

We demonstrate the one-side PRE technique on a cell-penetrating peptide (CPP), penetratin. CPPs are Arg- and Lys-rich cationic peptides that have the remarkable ability of transporting macromolecular cargos into cells and the cell nucleus without disrupting the cell membrane (23-25). As such, CPPs are promising drug-delivery molecules. A large number of biophysical studies have shown that the intracellular import of CPPs is intimately related to their affinity to and interaction with the lipid bilayer (26). The membrane in question can be the plasma membrane of the cell, for peptides that directly translocate across the cell membrane, or, for peptides that enter cells by endocytosis (27), the endosomal membrane from which the peptides must escape. Given the highly cationic nature of these peptides, their mechanism of translocation across the lipid membrane is intriguing and is the subject of intense study. Penetratin is the first and one of the most extensively studied CPPs, and is a 16-residue peptide corresponding to the third helix of the *Drosophila Antennapedia* homeo-domain (28).

Three models have been proposed to explain the membrane translocation of CPPs. In the electroporation model (29), below a threshold peptide concentration, the peptide binds only to the outer leaflet of the bilayer (Fig. 1a), thus creating a transmembrane electric field that alters the lateral and curvature stress of the membrane. Above the threshold concentration, electroporation-like permeabilization of the membrane occurs, giving rise to transient

membrane defects that allow the peptide to distribute to both leaflets of the bilayer (Fig. 1b), thus relieving the curvature stress. Isothermal titration calorimetry experiments indicated that the threshold peptide/lipid molar ratio (P/L) of penetratin was 1:20; moreover an anionic lipid fraction of at least ~50% was found to be necessary for translocation (29, 30). Recently, ^1H solution NMR NOESY spectra of bicelle-bound penetratin showed that the depth of penetratin increases with the peptide concentration (31), which was interpreted as supporting the electroporation model.

The second model proposes that inverse micelles transiently form in the bilayer to trap the peptide from the outer leaflet and release it to the inner leaflet (32). This model was primarily based on lipid ^{31}P NMR spectra that showed an isotropic peak indicative of micelles in the presence of the peptide (33). However, the peptide-free control sample exhibited a similar isotropic peak, suggesting that the micelles result from sample preparation procedures rather than peptide binding. Sonication, extrusion, and extensive freeze-thawing all create small lipid vesicles that have high isotropic mobility, which give rise to an isotropic peak in the ^{31}P spectra. In addition, no hexagonal-phase peak was detected in these ^{31}P spectra, ruling out the hexagonal-phase model (34).

The third model posits that guanidinium-phosphate complexation neutralizes the Arg residues in CPPs, thus allowing the peptides to cross the membrane without a high free-energy penalty. This model was based on phase transfer experiments of oligoarginines (35) and ^{13}C - ^{31}P distance measurements of an Arg-rich antimicrobial peptide (36). A molecular dynamics simulation of HIV Tat (48-60), another well-studied CPP, showed transient association of the Arg residues with phospholipids in the distal leaflet from the binding side, supporting the guanidinium-phosphate association model for Tat translocation (37).

In this work, we test the electroporation model for penetratin translocation using the one side Mn^{2+} PRE method. By placing the Mn^{2+} ions only on the outer surface of the lipid bilayer, we readily distinguish the asymmetric outer-leaflet-only binding from the symmetric double-leaflet binding of peptides. In the first scenario, the outer-surface Mn^{2+} ions will broaden the signals of most peptides and thus cause low intensity in the spectra (Fig. 1c). In the second scenario, half of the peptide, those in the inner leaflet, will experience minimal PRE, thus much higher intensities will result in the spectra (Fig. 1d). Below, we first demon-

strate the feasibility of one side Mn^{2+} binding by ^{13}C NMR on peptide-free lipid membrane samples, then apply this method to anionic lipid membranes containing penetratin at low and high P/L ratios, where the electroporation model predicts a change from asymmetric to symmetric insertion. We show that penetratin is bound to both leaflets of the bilayer at both low and high peptide concentrations, thus indicating that the electroporation model does not apply.

4.2 Materials and Methods

Lipids and peptides

All lipids, including 1-palmitoyl -2-oleoyl-*sn*-glycero-3-phosphatidylcholine (POPC), 1-palmitoyl-2-oleoyl-*sn*-glycero-3-phosphatidylglycerol (POPG), 1,2-dimyristoyl-*sn*-glycero-3-phosphocholine (DMPC), 1,2-dimyristoyl-*sn*-glycero-3-phosphatidylglycerol (DMPG), were purchased from Avanti Polar Lipids (Alabaster, AL) and used without further purification. Penetratin (RQIKI WFQNR RMKWK K) samples incorporating uniformly ^{13}C , ^{15}N -labeled residues were synthesized by Fmoc solid-phase protocols and purified by HPLC to > 95% purity (38). Three peptide samples, containing labeled residues at I3, I5, Q8, N9 and K13, were used in this work.

Membrane sample preparation

Oriented membrane samples on glass plates were prepared using a naphthalene-incorporated method as described before (39, 40). Unoriented hydrated liposomes for magic-angle spinning (MAS) experiments were prepared by an aqueous-phase mixing protocol (38). POPC/POPG membranes with molar ratios of 8:7 or 13:7 were used for all PRE experiments. The mixed lipids were freeze-thawed eight times and extruded through 100 nm pores to produce large unilamellar vesicles (LUVs) of ~100 nm diameter. Peptide-containing samples used peptide/lipid molar ratios (P/L) of either 1:15 or 1:40. The membrane mixtures were ultracentrifuged above the phase transition temperature to obtain pellets, which are then packed into 4 mm MAS rotors.

Mn^{2+} ions were incorporated into the membrane samples using one of two methods. For pure membrane samples without the peptide, the $MnCl_2$ solution was added to the LUVs after extrusion but before ultracentrifugation (UC). Mn^{2+} ions cannot penetrate the hydrophobic part of the bilayer, which is known from earlier work on Mn^{2+} ions as well as lanthanide ions added to sonicated small unilamellar vesicles (20). Thus, as long as the bilayers do not reassemble, the Mn^{2+} ions are naturally confined to the outer surface of the bilayers (Fig. 2a). ^{31}P and ^{13}C NMR spectra were used to confirm that UC does not perturb the unilamellar nature of the vesicles and retains the one-sided nature of the Mn^{2+} distribution (see below). To create peptide-containing one side Mn^{2+} samples, we added the Mn^{2+} solution to the ultracentrifuged membrane pellet. Adding Mn^{2+} ions to the LUV solution before UC was found to lead to two side Mn^{2+} distribution by ^{31}P NMR, possibly due to transient membrane defects caused by the peptide. In contrast, the dense membrane pellet retains the one-sided nature of the Mn^{2+} distribution, as shown by the ^{31}P spectra and the lipid headgroup ^{13}C MAS intensities (see below) (Fig. 2c). All Mn^{2+} containing samples used a Mn^{2+} concentration of 8 mol% of lipids.

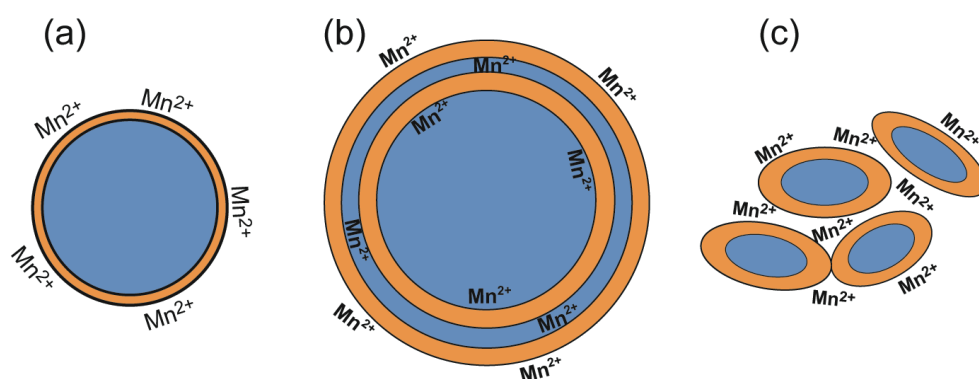


Figure 4.2. One side and two side Mn^{2+} -bound membrane samples. Orange: lipids. Blue: water. (a) One side Mn^{2+} -bound large unilamellar vesicles before ultracentrifugation. Mn^{2+} ions are distributed only on the outer surface of the bilayer. (b) Two side Mn^{2+} -bound membranes after freeze-thawing. Oligolamellar vesicles form where Mn^{2+} ions are distributed on both sides of each bilayer. (c) Mn^{2+} ions added to the membrane pellet after ultracentrifugation. The Mn^{2+} ions diffuse between unilamellar vesicles and remain on the outer surface of the bilayers.

To create two side Mn^{2+} -bound membrane samples, after Mn^{2+} binding, the LUVs were freeze-thawed eight times. The freezing process fragments the LUVs by ice formation

(41) and thawing reassembles the lipids so that Mn^{2+} ions are now distributed on both sides of each bilayer (Fig. 2b) (42). The freeze-thawed vesicles may be oligo-lamellar rather than unilamellar.

For peptide-lipid ^{13}C - ^{31}P REDOR experiments, d_{54} -DMPC/DMPG (8:7) membrane mixtures were used. The saturated lipids have a higher phase transition temperature of $23^{\circ}C$, thus better suppressing undesired peptide and lipid motions.

Solid-state NMR experiments

NMR experiments were carried out on a Bruker AVANCE-600 (14.1 T) and DSX-400 spectrometer (Karlsruhe, Germany). Low temperature was achieved using Kinetics Thermal Systems XR air-jet sample cooler (Stone Ridge, NY) connected to the 400 MHz system. ^{13}C chemical shifts were referenced externally to the ^{13}CO signal of α -glycine at 176.49 ppm on the tetramethylsilane scale. ^{31}P chemical shifts were referenced to the ^{31}P signal of hydroxylapatite at -2.73 ppm on the phosphoric acid scale.

Direct polarization (DP) and cross polarization (CP) magic-angle spinning (MAS) experiments were conducted with 1H decoupling field strengths of ~ 62.5 kHz. Typical radiofrequency (rf) pulse lengths were 5 μs for ^{13}C and 4 μs for 1H . All PRE experiments were carried out at 295 K, which is ~ 25 K above the phase transition temperature (T_m) of the two lipids. 2D ^{13}C - ^{13}C correlation experiments were measured at 303 K using the DARR sequence with a mixing time of 30 ms.

Static ^{31}P DP experiments on oriented membrane samples were carried out in a custom-designed 6 x 12 x 5 mm rectangular coil. The glass plates were inserted into the magnet with the alignment axis parallel to the magnetic field. A typical 5 μs excitation pulse of ^{31}P and a 50 kHz 1H decoupling field were used. Static 2H NMR spectra were measured at 310 K using a quadrupolar echo pulse sequence with a 2H 90° pulse length of 5 μs .

$^{13}C\{^{31}P\}$ REDOR experiments was conducted on a 4 mm $^1H/^{13}C/^{31}P$ triple-resonance MAS probe using a REDOR pulse sequence with a soft Gaussian π pulse on the ^{13}C channel to remove ^{13}C - ^{13}C J-coupling (43, 44). To suppress lipid and peptide motions, all REDOR experiments were carried out at 233 K.

4.3 Results

One side Mn²⁺-bound lipid membranes

When added to lipid bilayers with negatively charged phosphate groups at the surface, the Mn²⁺ ion is naturally confined to the outer surface and cannot cross the bilayer to the inner surface due to its cationic nature (Fig. 2a). Only when the bilayer is disrupted and the lipids reassembled can the phosphate-bound Mn²⁺ ions redistribute to both surfaces of the bilayer. Thus, any processes that cause bilayer reassembly, such as freeze-thaw and sonication, should be avoided when making one side Mn²⁺-bound membranes. Conversely, two side Mn²⁺-bound lipid membranes can be formed by freeze-thawing the Mn²⁺-bound lipid vesicles (Fig. 2b). For our membrane samples, once the Mn²⁺ solution is mixed with the lipid vesicles, the samples are kept above the phase-transition temperature of the lipids so that the lipid bilayers do not undergo reorganization.

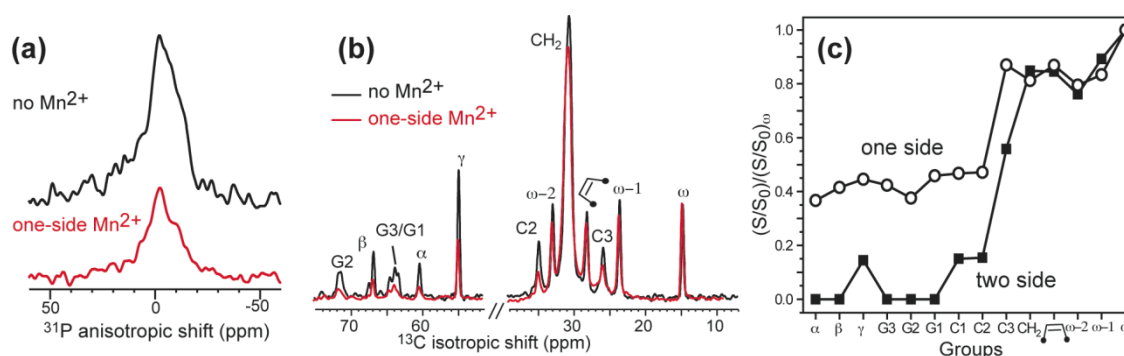


Figure 4.3. ³¹P static and ¹³C MAS spectra of POPC/POPG (3:1) vesicles without any peptide. (a) ³¹P static spectra without Mn²⁺ (top) and with Mn²⁺ on one side (bottom). (b) ¹³C MAS spectra without Mn²⁺ (black) and with (red) one side Mn²⁺. (c) Double-normalized intensity of Mn²⁺-bound POPC/POPG membranes. Open circles: one side Mn²⁺-bound membrane. Filled squares: two side Mn²⁺-bound membrane.

We first verified the one-sided nature of Mn²⁺-binding on POPC/POPG bilayers without any peptide. Fig. 3a shows the ³¹P static spectra of the lipids before and after Mn²⁺ addition. The Mn²⁺-bound sample gave a spectrum with ~30% of the height of the control sample. Since the sample is a pellet obtained after ultracentrifugation, the presence of significant intensity indicates that ultracentrifugation does not disrupt the bilayer.

Fig. 3b shows the ^{13}C DP-MAS spectra of the Mn^{2+} -free and one side Mn^{2+} -bound POPC/POPG bilayers. The site resolution of the ^{13}C MAS spectra and known depths of lipid functional groups allow us to monitor the intensity as a function of depths. The more embedded groups should experience less T_2 relaxation enhancement and thus retain higher intensity. The normalized intensity of each peak, S/S_0 where S corresponds to the Mn^{2+} -bound sample and S_0 corresponds to the control sample, should exhibit a monotonic increase with increasing depth. To facilitate comparison between different samples, we further normalize the S/S_0 of each peak with the S/S_0 of the chain-end methyl carbon ω . Experiments show that the S/S_0 values for the ω group fall within 80-120% in the DP spectra for the 16 and 18-carbon chain lengths of POPC and POPG lipids. Fig. 3c shows the double-normalized intensity, $(S/S_0)/(S/S_0)_\omega$, for all resolved lipid signals. The trend is indeed roughly monotonic. At 8% Mn^{2+} , the headgroup and glycerol signals show dephasing values of 35-45% compared to ω . Importantly, the same sites have vanishing intensities in the two side Mn^{2+} -bound samples, thus confirming the one-sided nature of the non-freeze-thawed samples. The headgroup choline $\text{C}\gamma$ exhibits higher intensity than α and β due to the fast three-site jumps of each methyl group around the $\text{C}\gamma\text{-N}$ axis and the three-site jumps between the methyl groups around the $\text{N-C}\beta$ axis. Compared to the headgroup and glycerol carbons, the acyl chain sites from C3 to the chain termini show higher intensities. The largest slope in the curve occurs at the C2-C3 transition. As we have shown before (9), changing the Mn^{2+} concentration shifts the position of the maximum slope: lower Mn^{2+} concentrations shift the depth-sensitive region towards the surface while higher Mn^{2+} concentrations shift the depth-sensitive region towards the membrane center.

Predicted PRE effects of symmetrically and asymmetrically inserted proteins in lipid bilayers

If a membrane peptide is predominantly distributed in the outer leaflet of the membrane, then its intensities should be low in both the one side and two side Mn^{2+} -bound samples (Fig. 1c). However, if the peptide is symmetrically distributed in both leaflets of the membrane, then the half of the peptide molecules in the inner leaflet should experience

minimal PRE from the outer surface, so that the one side Mn^{2+} -bound sample should have much higher intensity than the two side Mn^{2+} -bound sample (Fig. 1d). Quantitatively, assuming $(S/S_0)_0 = 1$, then the normalized PRE intensity of each lipid functional group is $0.5(S/S_0)_L + 0.5$ in the one side Mn^{2+} bound sample, where the constant 0.5 results from the inner leaflet lipids far from the outer-surface Mn^{2+} ions. The intensity decreases to $(S/S_0)_L$ for the two side Mn^{2+} -bound bilayers, where $(S/S_0)_L \leq 1$. If the peptides are bound only to the outer leaflet, then its PRE intensities are $(S/S_0)_P$ in both the one side and two side Mn^{2+} -bound samples. In contrast, if the peptides are distributed in both leaflets symmetrically, then the PRE intensities are $0.5(S/S_0)_P + 0.5$ in the one side Mn^{2+} -bound sample, which is larger than $(S/S_0)_P$ for the two side Mn^{2+} -bound sample. Thus, a peptide inserted only in the outer leaflet should have little intensity change between the one side and two side Mn^{2+} -bound samples, while a symmetrically bound peptide exhibits intensity decrease from the one side Mn^{2+} -bound sample to the two side Mn^{2+} -bound sample.

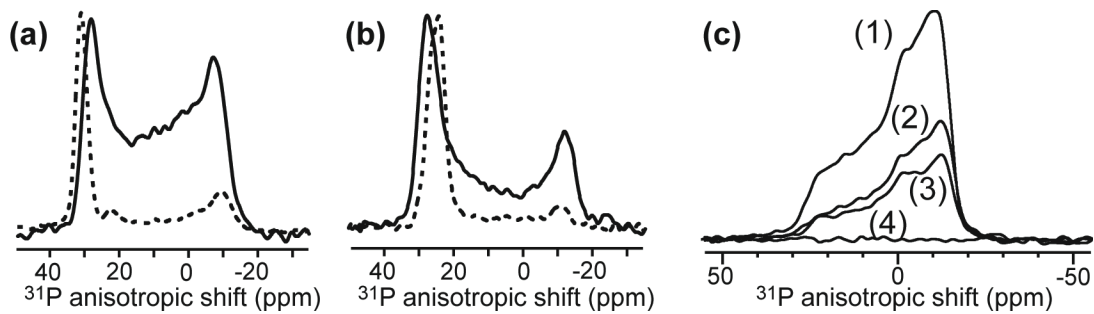


Figure 4.4 Static ^{31}P spectra of lipid membranes showing the effects of penetratin on membrane disorder and of Mn^{2+} on ^{31}P intensity. (a) Oriented ^{31}P spectra of POPC/POPG (8:7) bilayers without (dashed line) and with 4 mol% penetratin (solid line). (b) Oriented ^{31}P spectra of POPC/cholesterol (55:45) bilayers without (dashed line) and with 4 mol% penetratin (solid line). The lipid membranes are oriented on thin glass plates. Note the absence of any isotropic peak. (c) ^{31}P powder spectra of penetratin-containing POPC/POPG (8:7) membrane before and after the addition of Mn^{2+} . Compared to the full control spectrum without Mn^{2+} (1), 15 minutes after addition of Mn^{2+} a roughly two-fold intensity reduction is seen (2). Three days after Mn^{2+} addition the ^{31}P intensity is largely retained (3), indicating that rf pulses do not cause Mn^{2+} scrambling. After freeze-thawing the membrane the ^{31}P intensity is completely suppressed by the strong PRE effect (4).

One side and two side Mn²⁺-bound membranes containing penetratin

Before applying the one side Mn²⁺ PRE method to penetratin, we first tested the effect of penetratin binding to the lipid bilayer, to verify that the peptide does not destroy the lamellar structure by forming pores or micelles, which would scramble the Mn²⁺ ions onto both surfaces of the bilayer. Fig. 4(a, b) shows the static ³¹P spectra of uniaxially aligned POPC/POPG (8:7) membrane and POPC/cholesterol (55:45) membrane without the peptide and with 4 mol% peptide. The membranes are well aligned in the absence of the peptide. The addition of penetratin increased powder intensities indicative of misalignment but did not create sharp isotropic signals indicative of isotropic phases. Thus, the lamellar morphology of the bilayer is retained in the presence of the peptide.

One side and two side Mn²⁺ PRE experiments are carried out at peptide concentrations of P/L=1:40 and 1:15. ³¹P static spectra confirming the one sided and two-sided nature of Mn²⁺ binding are shown in Fig. 4c. As predicted, once the membrane sample is subjected to freeze-thawing, the ³¹P intensity is completely destroyed due to lipid reassembly and Mn²⁺ distribution on both bilayer surfaces. Fig. 5 shows the ¹³C DP-MAS spectra of U-I3, N9-labeled penetratin in POPC/POPG (8:7) membranes at four combinations of P/L ratios and Mn²⁺ sidedness. The Mn²⁺-bound spectra are superimposed with the Mn²⁺-free control spectra. For all resolved sites, the double-normalized intensities are plotted in Fig. 6. The lipid intensities give the expected monotonic increase with depth, unperturbed by Mn²⁺ binding. In comparison, the penetratin PRE intensities at P/L=1:40 cover the range of C2 to the double bond of the acyl chains in the one side Mn²⁺ sample (Fig. 6a). The I3 C α is more shielded from the Mn²⁺ ions than N9 C α , suggesting that the peptide backbone may be tilted relative to the membrane plane. Upon converting the sample to two side Mn²⁺ by freeze-thaws, the peptide intensities decreased to the range of glycerol G3 to acyl chain C2, indicating closer distances to the surface (Fig. 6b). This is consistent with the peptide being distributed in both leaflets of the membrane. Moreover, comparison of the peptide PRE intensities with the lipid intensities shows that the peptide exhibits shallower depths in the one side Mn²⁺-bound samples than in the two side Mn²⁺-bound samples. For example, the I3 C α

PRE corresponds to a depth similar to the lipid C2 and C3 sites for the outer leaflet, but when Mn^{2+} is bound to both bilayer surfaces, the I3 C α PRE shifts to the lipid G1 to chain C2 (Table 4.1).

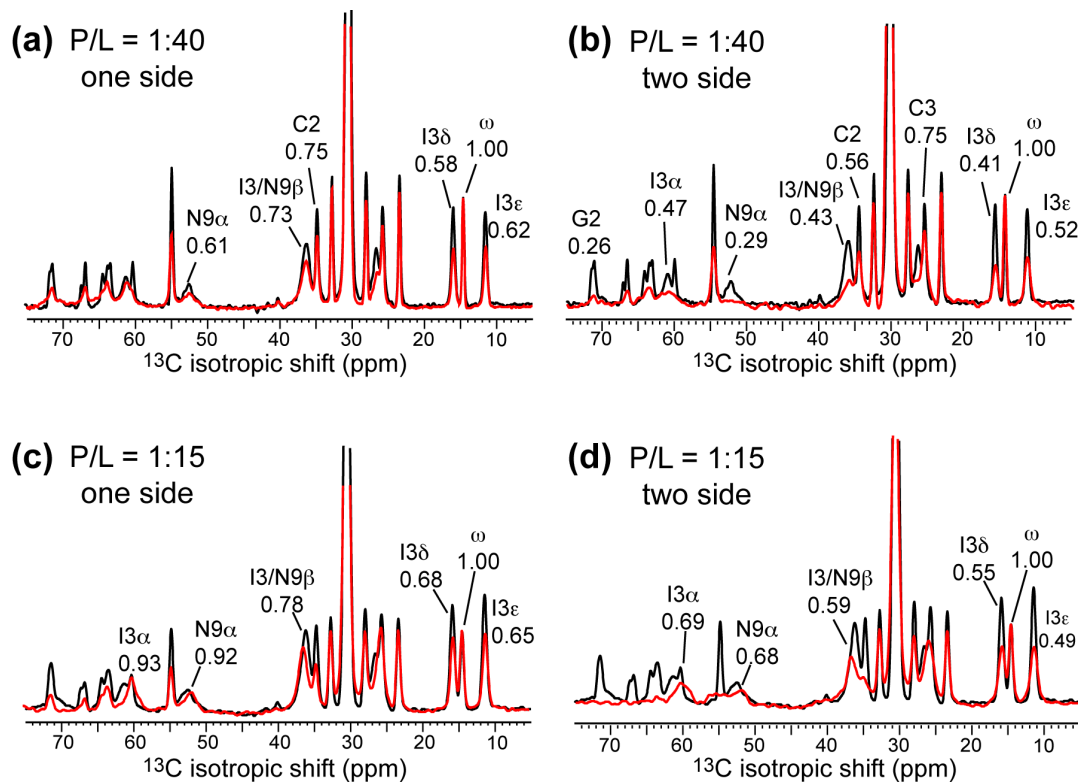


Figure 4.5. ^{13}C DP-MAS spectra of I3, N9-labeled penetratin in POPC/POPG (8:7) membranes under different peptide concentrations and Mn^{2+} binding methods. Red: Mn^{2+} -bound spectra, Black: Mn^{2+} -free control spectra. (a) P/L = 1:40, with one side Mn^{2+} . (b) P/L=1:40, with two side Mn^{2+} . (c) P/L = 1:15, with one side Mn^{2+} . (d) P/L = 1:15, with two side Mn^{2+} . Assignments are shown for key peptide and lipid peaks.

At P/L = 1:15, the peptide signals also show a general decrease from the one side Mn^{2+} -sample to the two side Mn^{2+} sample (Fig. 6c, d). Thus, the peptide is similarly embedded in both leaflets of the membrane. In the one side Mn^{2+} -bound membrane, the peptide has a significant depth distribution between the backbone and the sidechain: the overall depth ranges from C2 to the end of the acyl chains, while the backbone C α depth is much more narrowly defined, between ω -1 and the double bond (Fig. 4.6c, Table 4.1). For the two side Mn^{2+} sample, the backbone and sidechain combined exhibit a depth range from C2 to the

middle of the chains, but the backbone lies between the double bond and C3 (Fig. 6d). Thus, similar to the low-concentration sample, the peptide backbone has a shallower average depth in the two leaflets than in the outer leaflet alone, indicating that penetratin in the inner leaflets lies closer to the inner surface than those in the outer leaflet to the outer surface.

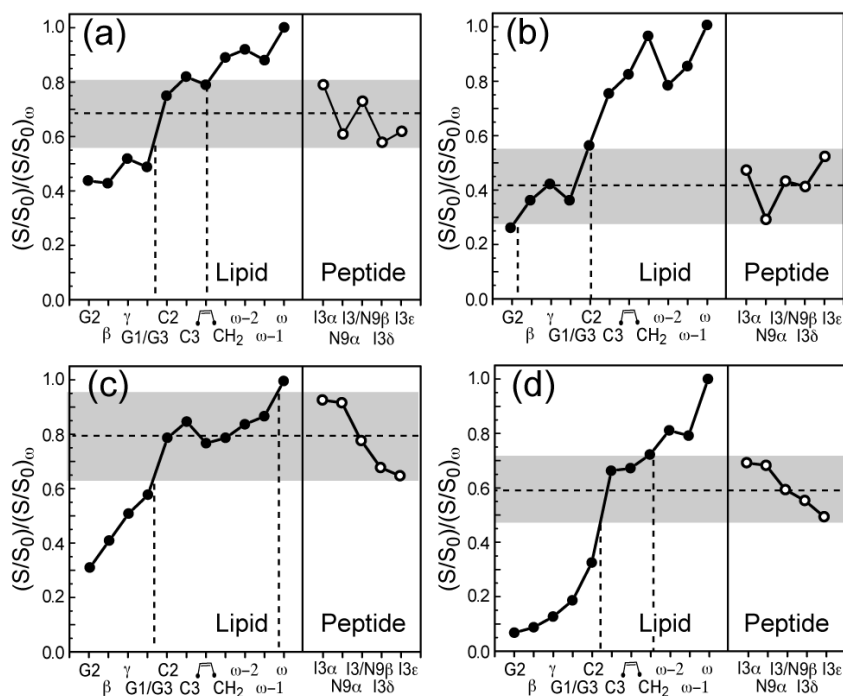


Figure 4.6. Normalized intensities of penetratin in POPC/POPG (8:7) bilayers at 295 K. (a) P/L = 1:40, with one side Mn^{2+} . (b) P/L = 1:40, with two side Mn^{2+} . (c) P/L=1:15, with one side Mn^{2+} . (d) P/L=1:15, with two side Mn^{2+} .

Table 4.1. Depths of penetratin backbone sites in POPC/POPG (8:7) membranes from one side and two side Mn^{2+} PRE.

P/L	Site	Mn^{2+} on outer leaflet	Mn^{2+} on both leaflets
1:40	I3 C α	C2 – C3	G1 – C2
	N9 C α	G1 – C2	G3
	K13 C α	C2 – C3	C3 – (CH ₂) _n
1:15	I3 C α	ω -1 – ω	C9
	N9 C α	ω -1 – ω	C9
	K13 C α	Double bond	C3

¹³C CP-MAS spectra reproduced the trend of the DP based PRE curve; however, the CP depth curve is noisier, as a result of the sensitivity of the intensity of highly mobile lipid

groups to the ^1H - ^{13}C CP matching condition. Table 4.1 summarizes the depths of all measured backbone $\text{C}\alpha$ sites, including I3, N9 and K13.

^{13}C - ^{31}P distances between penetratin and the lipids

We also measured ^{13}C - ^{31}P distances between penetratin and the lipid phosphate groups to determine the quantitative depth of the peptide from the membrane surface without distinguishing the sidedness. To freeze the peptide and lipid motions, the experiments were carried out at 233 K, well into the gel phase of the DMPC/DMPG membrane.

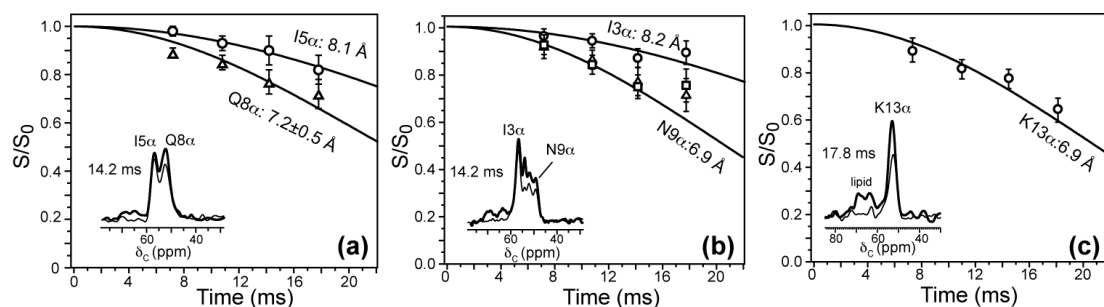


Figure 4.7. ^{13}C - ^{31}P REDOR curves of penetratin in DMPC/DMPG bilayers at 233 K and P/L = 1:15. (a) I5 α and Q8 α . (b) I3 α and N9 α . (c) K13 α .

Table 4.2. ^{13}C - ^{31}P distances (R) of penetratin residues in DMPC/DMPG (8:7) membranes at P/L = 1:15 and 233 K.

Residue	I3 C α	I5 C α	Q8 C α	N9 C α	K13 C α
distance (\AA)	8.2	8.1	7.2	6.9	6.9

Fig. 7 shows the REDOR decay curves of the labeled residues. The distances fall in the range of 6.9 – 8.2 \AA , with the N-terminal residues having slightly longer distances than the C-terminal residues (Table 4.2), in good agreement with the PRE results obtained from the LC phase of the bilayer. We simulated the REDOR curves assuming two-spin systems. As we showed recently, the incorporation of multiple ^{31}P spins into the simulation only lengthens the individual ^{13}C - ^{31}P distances, but the actual vertical distance from the ^{13}C to the ^{31}P plane is actually slightly shorter than the apparent two-spin distance. For example, a REDOR curve that corresponds to a two-spin distance of 8.0 \AA , when simulated assuming a five-spin system, gives a vertical ^{13}C - ^{31}P plane distance of ~ 7.0 \AA (36). A two-spin distance

of 7 Å corresponds to a vertical distance of ~ 5.2 Å in a five-spin simulation. Here, we use only the two-spin distances in considering the relative depths of individual residues from the membrane surface.

4.4 Discussion

Penetratin insertion does not proceed by electroporation

Comparison of the one side and two side Mn^{2+} PRE data clearly indicates that penetratin is inserted into both leaflets of the anionic lipid bilayer even at the low P/L ratio of 1:40, which is well within the concentration regime previously considered to have asymmetric binding (29). The fact that the one side Mn^{2+} samples have high peptide intensities is possible only if 1) the peptide is deeply embedded in the outer leaflet alone, 2) if half of the molecules are embedded in the inner leaflet and experience minimal PRE while the other half of the molecules are inserted in the outer leaflet, or 3) if all the peptides are solely distributed in the inner leaflet. Scenario 3 can be ruled out because it would require higher peptide PRE intensities than even the membrane-center ω group, which is inconsistent with the experimental observation. Scenario 1 is also ruled out since distributing Mn^{2+} ions to both surfaces of the bilayer caused intensity reduction in the ^{13}C spectra. Therefore, in the P/L regimes of 1:40 – 1:15, penetratin is inserted into both leaflets of the lipid bilayer. This result invalidates the electroporation model for penetratin (29).

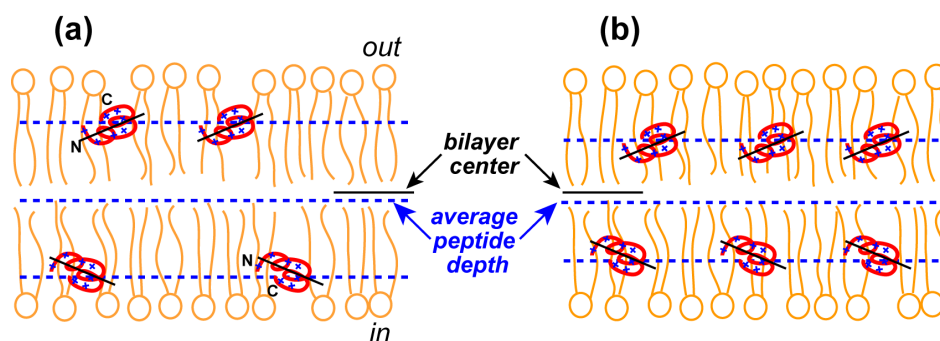


Figure 4.8. Symmetry and depth of insertion of penetratin in the anionic POPC/POPG membranes. (a) P/L = 1:40. (b) P/L = 1:15. In (b) the peptides are more deeply inserted in each leaflet than in (a). However, the common aspects are that the peptide is inserted into both leaflets of the bilayer, the average depth is closer to the inner surface than the outer surface, and the peptide is slightly tilted with respect to the bilayer plane.

Fig. 8 summarizes the depth information obtained from the PRE data in the liquid-crystalline phase, supplemented by the REDOR data from the gel-phase membrane. Penetratin is distributed in both leaflets of the bilayer, with an average depth closer to the inner surface than the outer surface. At P/L = 1:40, the peptide is located near the upper part of the acyl chains, with the backbone slightly tilted with respect to the membrane surface so that the N-terminus is more buried than the C-terminus. At P/L = 1:15, the peptide backbone is more deeply buried and near the middle of the acyl chains (Table 4.1).

We represent the peptide schematically with a turn-rich conformation with no α -helical or β -sheet structures. This information was obtained from extensive ^{13}C chemical shift and dipolar coupling data (38): the peptide conformation falls into the “random coil” regime in the liquid-crystalline phase of the membrane. However, the $\text{C}\alpha$ and $\text{C}\beta$ C-H order parameters are 0.23-0.52 instead of 0, and chemical shift anisotropies are uniaxially averaged, indicating that the peptide undergoes anisotropic, uniaxial motion around the bilayer normal. Thus, we hypothesized that the peptide adopts a turn conformation, which would satisfy both the secondary chemical shift constraints and the dynamics data. The significance of this conformation may be that it minimizes the hydrophobic interaction between the peptide and the lipid chains, which would facilitate passage of the peptide through the bilayer and into the cell.

While the PRE data rule out asymmetric insertion at peptide concentrations of P/L = 1:40 and higher, it does not rule out the possibility that at much lower concentrations the peptide may still be asymmetrically inserted. However, we think this scenario is unlikely as an equilibrium state of the peptide, since at P/L = 1:40 the average peptide depth is already shifted towards the inner surface of the membrane.

Smith and coworkers used ^1H NOESY experiments to characterize the depth of insertion of penetratin in DMPC/DMPG/DHPC (10:3:13) bicelles (31). By observing the lipid-peptide cross peaks in the 2D NOESY spectra, they found that the peptide contact with the lipid chains increased with the peptide concentration. This concentration dependence of cross peak intensity was interpreted as supporting the electroporation model. However, the ^1H NOESY technique, like most NMR techniques, does not distinguish the two sides of the

lipid bilayer. Our current data is consistent with the Smith report in that penetratin shows an increased depth in each leaflet as the peptide concentration increases (Fig. 6). However, the two-sided nature of penetratin binding is already present at the low P/L and remains unchanged at the high P/L. Thus, the most essential feature of the electroporation model, the asymmetric binding, is invalid within the concentration regimes examined here.

The Mn^{2+} PRE data shown here indicate that penetratin sidechains adopt somewhat different depths from the backbone. For example, at P/L = 1:15, the sidechains show clearly lower intensities than the backbone, indicating closer proximity to the membrane surface. This suggests that there may exist possible interactions between the sidechains and the membrane surface phosphate groups, an example of which has been shown recently in a cationic antimicrobial peptide (36).

^2H NMR spectra (Fig. S1, supporting information) of chain-perdeuterated d_{54} -DMPC/DMPG bilayers show very similar quadrupolar couplings in the absence and presence of penetratin. This is consistent with the aligned bicelle ^2H spectra (31) and indicates that penetratin does not perturb the order of the hydrophobic core of the membrane significantly.

Since neither the inverse micelle model nor the electroporation model are consistent with solid-state NMR data, what mechanism explains the translocation of penetratin through lipid membranes? Combining the high-temperature conformation, dynamics, and depth of the peptide (38) we have determined, we propose the following model. Initially penetratin binds to the membrane through electrostatic attraction, then the concentration gradient of the peptide from the extracellular space to the membrane drives insertion into the membrane. Once in contact with the membrane, the compact turn-shaped molecule has minimal hydrophobic interaction with the lipid chains that retains it in the membrane. Moreover the cationic Arg and Lys sidechains preferentially interact with the lipid phosphate groups in the distal membrane leaflet (36, 37). These two factors drive penetratin to cross the lipid bilayer rapidly into the intracellular solution.

Application of the asymmetric PRE technique for studying membrane protein topology

The one side Mn^{2+} PRE approach for lipid bilayers is generally applicable. Most membrane proteins insert into lipid bilayers with a unique orientation and topology (1), thus the site-specific insertion depths are an important component of structure determination. Various extensions of the outer-leaflet Mn^{2+} -PRE technique can be envisioned: for example, inner-leaflet Mn^{2+} PRE is possible with suitable treatment of the lipid vesicles (45), and covalent linkage of Mn^{2+} ions to membrane proteins may also be feasible, similar to what has been shown for DNA-protein complexes in solution (17, 18). In addition to membrane protein topology, functionally important membrane asymmetry between the two leaflets (46) can be readily investigated with this technique by detecting suitable lipid signals.

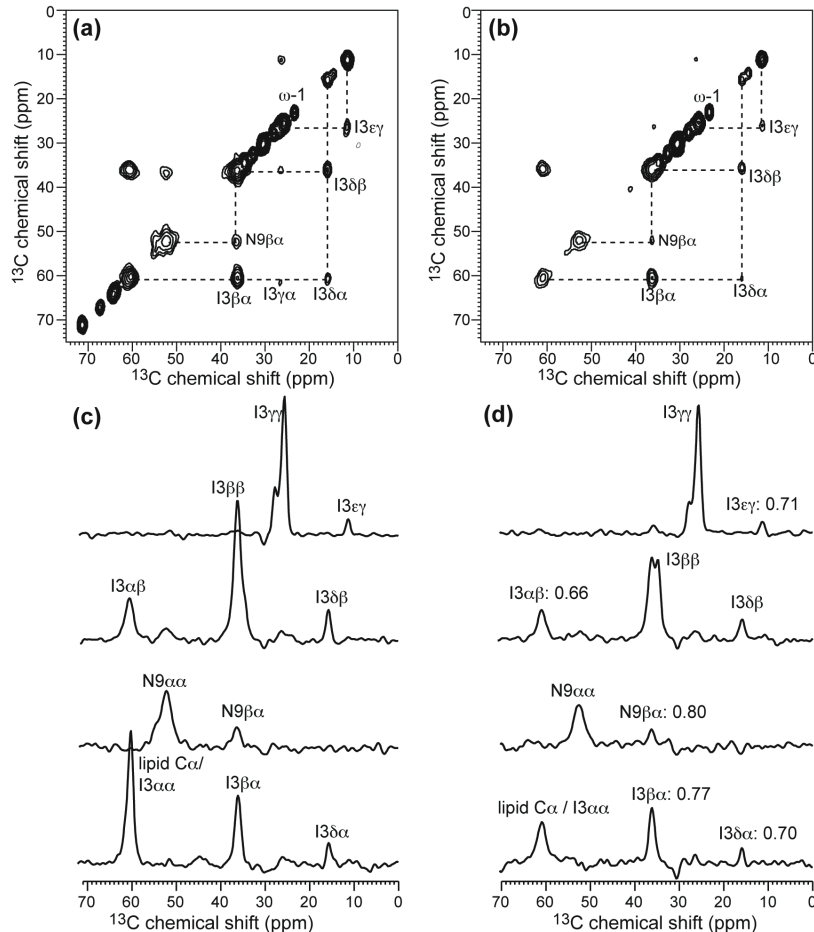


Figure 4.9. 2D ^{13}C - ^{13}C correlation spectra of POPC/POPG membranes containing I3, N9-labeled penetratin. (a) Without Mn^{2+} . P/L = 1:15. (b) With 8% Mn^{2+} on both sides of the membrane. P/L = 1:20. (c, d) Row cross sections at positions indicated by dashed lines in the 2D spectra. (c) Cross sections from (a) give the S_0 intensity. (d) Cross sections from (b) give the S intensity. The double nor-

malized intensity $(S/S_0)/(S/S_0)_{\omega-1}$ of several cross peaks are indicated. The spectra were collected at 303 K under 5.0 kHz MAS using a 30 ms DARR mixing time.

Although we demonstrated this one side PRE approach using only 1D ^{13}C experiments due to the good resolution of the mobile and site-specifically labeled penetratin, two- and three-dimensional experiments can be employed when needed to obtain high resolution for larger membrane proteins. The experiment is also not restricted to only the lipid chain-end ω peak for normalizing the PRE intensities, thus direct ^{13}C excitation is not mandatory. The large $(\text{CH}_2)_n$ peak of the lipid, for example, has reproducible CP intensities, thus for lipids of the same chain lengths, the $(\text{CH}_2)_n$ signal can serve as an intensity reference with a known average depth. As an example, Fig. 9 shows the 2D ^{13}C - ^{13}C DARR (47) correlation spectra of a control and a two side Mn^{2+} -bound sample of POPC/POPG membranes containing I3, N9-labeled penetratin. The dephasing of the cross peaks are readily measured and the separation of the peptide cross peaks from the lipid background ^{13}C signals along the diagonal is a significant advantage of the 2D spectroscopy. For Figure 4.9, the cross peak S/S_0 of the peptide peaks is normalized with respect to the S/S_0 of the lipid $\omega-1$ peak at 23.5 ppm along the diagonal. The cross peak dephasing values reflect the average depths between the two carbons establishing the cross peak. Since the two carbons are spatially close, the average depth does not compromise the depth information.

4.5 Acknowledgement

We thank Professor Alan Waring (UCLA) for providing the (I3, N9)-labeled peptide sample. This work is funded by an NIH grant GM-066976 to M. H.

4.6 Reference

1. von Heijne, G. (2006) Membrane-protein topology, *Nat. Rev. Mol. Cell Biol.* 7, 909-918.
2. Kumashiro, K. K., Schmidt-Rohr, K., Murphy, O. J., Ouellette, K. L., Cramer, W. A., and Thompson, L. K. (1998) A novel tool for probing membrane protein structure: solid-state NMR with proton spin diffusion and X-nucleus detection, *J. Am. Chem. Soc.* 120, 5043-5051.

3. Huster, D., Yao, X. L., and Hong, M. (2002) Membrane Protein Topology Probed by ^1H Spin Diffusion from Lipids Using Solid-State NMR Spectroscopy, *J. Am. Chem. Soc.* 124, 874-883.
4. Luo, W., and Hong, M. (2006) Sensitivity-enhanced ^1H spin diffusion from lipids to protein for determining membrane protein topology, *Solid State NMR* 29, 163-169.
5. Etzkorn, M., Martell, S., Andronesi, O. C., Seidel, K., Engelhard, M., and Baldus, M. (2007) Secondary structure, dynamics, and topology of a seven-helix receptor in native membranes, studied by solid-state NMR spectroscopy, *Angew. Chem. Int. Ed. Engl.* 46, 459-462.
6. Hong, M. (2007) Structure, topology, and dynamics of membrane peptides and proteins from solid-state NMR spectroscopy, *J. Phys. Chem. B.* 111, 10340-10351.
7. Bloembergen, N. (1957) Proton relaxation times in paramagnetic solutions., *J. Chem. Phys.* 27, 572-573.
8. Solomon, I. (1955) Relaxation processes in a system of two spins., *Phys. Rev.* 99, 559-565.
9. Buffy, J. J., Hong, T., Yamaguchi, S., Waring, A., Lehrer, R. I., and Hong, M. (2003) Solid-State NMR Investigation of the Depth of Insertion of Protegin-1 in Lipid Bilayers Using Paramagnetic Mn^{2+} , *Biophys. J.* 85, 2363-2373.
10. Tuzi, S., Hasegawa, J., Kawaminami, R., Naito, A., and Saito, H. (2001) Regio-selective detection of dynamic structure of transmembrane alpha-helices as revealed from (^{13}C) NMR spectra of $[3\text{-}^{13}\text{C}]\text{Ala}$ -labeled bacteriorhodopsin in the presence of Mn^{2+} ion, *Biophys. J.* 81, 425-434.
11. Grobner, G., Glaubitz, C., and Watts, A. (1999) Probing membrane surfaces and the location of membrane-embedded peptides by (^{13}C) MAS NMR using lanthanide ions, *J. Magn. Reson.* 141, 335-339.
12. Prosser, R. S., Evanics, F., Kitevski, J. L., and Patel, S. (2007) The measurement of immersion depth and topology of membrane proteins by solution state NMR, *Biochim. Biophys. Acta* 1768, 3044-3051.
13. Villalain, J. (1996) Location of cholesterol in model membranes by magic-angle-sample-spinning NMR, *Eur. J. Biochem.* 241, 586-593.
14. Prosser, R. S., Luchette, P. A., and Westerman, P. W. (2000) Using O_2 to probe membrane immersion depth by ^{19}F NMR, *Proc. Natl. Acad. Sci. U.S.A.* 97, 9967-9971.
15. Luchette, P. A., Prosser, R. S., and Sanders, C. R. (2002) Oxygen as a paramagnetic probe of membrane protein structure by cysteine mutagenesis and (^{19}F) NMR spectroscopy, *J. Am. Chem. Soc.* 124, 1778-1781.
16. Wiener, M. C., and White, S. H. (1992) Structure of a fluid DOPC bilayer determined by joint refinement of X-ray and neutron diffraction data III Complete structure, *Biophys. J.* 61, 434-447.

17. Iwahara, J., and Clore, G. M. (2006) Detecting transient intermediates in macromolecular binding by paramagnetic NMR, *Nature* 440, 1227-1230.
18. Iwahara, J., Anderson, D. E., Murphy, E. C., and Clore, G. M. (2003) EDTA-derivatized deoxythymidine as a tool for rapid determination of protein binding polarity to DNA by intermolecular paramagnetic relaxation enhancement, *J. Am. Chem. Soc.* 125, 6634-6635.
19. Nadaud, P. S., Helmus, J. J., Höfer, N., and Jaroniec, C. P. (2007) Long-range structural restraints in spin-labeled proteins probed by solid-state nuclear magnetic resonance spectroscopy, *J. Am. Chem. Soc.* 129, 7502-7503.
20. Nolden, P. W., and Ackermann, T. (1976) A high-resolution NMR study (^1H , ^{13}C , ^{31}P) of the interaction of paramagnetic ions with phospholipids in aqueous dispersions, *Biophys. Chem.* 4, 297-304.
21. Kumar, V. V., Malewicz, B., and Baumann, W. J. (1989) Lysophosphatidylcholine stabilizes small unilamellar phosphatidylcholine vesicles. Phosphorus-31 NMR evidence for the "wedge" effect., *Biophys. J.* 55, 789-792.
22. Aime, S., Botta, M., Mainero, V., and Terreno, E. (2002) Separation of intra- and extracellular lactate NMR signals using a lanthanide shift reagent, *Magn. Reson. Med.* 47, 10-13.
23. Eguchi, A., Akuta, T., Okuyama, H., Senda, T., Yokoi, H., Inokuchi, H., Fujita, S., Hayakawa, T., Takeda, K., Hasegawa, M., and Nakanishi, M. (2001) Protein transduction domain of HIV-1 Tat protein promotes efficient delivery of DNA into mammalian cells, *J. Biol. Chem.* 276, 26204-26210.
24. Gratton, J. P., Yu, J., Griffith, J. W., Babbitt, R. W., Scotland, R. S., Hickey, R., Giordano, F. J., and Sessa, W. C. (2003) Cell-permeable peptides improve cellular uptake and therapeutic gene delivery of replication-deficient viruses in cells and in vivo, *Nat. Med.* 9, 357-362.
25. Schwarze, S. R., Ho, A., Vocero-Akbani, A., and Dowdy, S. F. (1999) In vivo protein transduction: delivery of a biologically active protein into the mouse, *Science* 285, 1569-1572.
26. Fischer, R., Fotin-Mleczek, M., Hufnagel, H., and Brock, R. (2005) Break on through to the other side-biophysics and cell biology shed light on cell-penetrating peptides, *ChemBioChem.* 6, 2126-2142.
27. Richard, J. P., Melikov, K., Vives, E., Ramos, C., Verbeure, B., Gait, M. J., Chernomordik, L. V., and Lebleu, B. (2003) Cell-penetrating peptides. A reevaluation of the mechanism of cellular uptake, *J. Biol. Chem.* 278, 585-590.
28. Derossi, D., Joliot, A. H., Chassaing, G., and Prochiantz, A. (1994) The third helix of the Antennapedia homeodomain translocates through biological membranes, *J. Biol. Chem.* 269, 10444-10450.

29. Binder, H., and Lindblom, G. (2003) Charge-dependent translocation of the Trojan peptide penetratin across lipid membranes, *Biophys. J.* 85, 982-995.
30. Drin, G., Cottin, S., Blanc, E., Rees, A. R., and Temsamani, J. (2003) Studies on the internalization mechanism of cationic cell-penetrating peptides, *J. Biol. Chem.* 278, 31192-31201.
31. Zhang, W., and Smith, S. O. (2005) Mechanism of penetration of Antp(43-58) into membrane bilayers, *Biochemistry* 44, 10110-10118.
32. Derossi, D., Calvet, S., Trembleau, A., Brunissen, A., Chassaing, G., and Prochiantz, A. (1996) Cell internalization of the third helix of the Antennapedia homeodomain is receptor-independent, *J. Biol. Chem.* 271, 18188-18193.
33. Berlose, J. P., Convert, O., Derossi, D., Brunissen, A., and Chassaing, G. (1996) Conformational and associative behaviours of the third helix of antennapedia homeodomain in membrane-mimetic environments, *Eur. J. Biochem.* 242, 372-386.
34. Prochiantz, A. (1996) Getting hydrophilic compounds into cells: lessons from homeopeptides, *Curr. Opin. Neurobiol.* 6, 629-634.
35. Rothbard, J. B., Jessop, T. C., Lewis, R. S., Murray, B. A., and Wender, P. A. (2004) Role of membrane potential and hydrogen bonding in the mechanism of translocation of guanidinium-rich peptides into cells, *J. Am. Chem. Soc.* 126, 9506-9507.
36. Tang, M., Waring, A. J., and Hong, M. (2007) Phosphate-mediated arginine insertion into lipid membranes and pore formation by a cationic membrane peptide from solid-state NMR, *J. Am. Chem. Soc.* 129, 11438 - 11446.
37. Herce, H. D., and Garcia, A. E. (2007) Molecular dynamics simulations suggest a mechanism for translocation of the HIV-1 TAT peptide across lipid membranes, *Proc. Natl. Acad. Sci. U. S. A.* 104, 20805-20810.
38. Su, Y., Mani, R., Doherty, T., Waring, A. J., and Hong, M. (2008) Reversible sheet-turn conformational change of a cell-penetrating peptide in lipid bilayers studied by solid-state NMR, submitted.
39. Hallock, K. J., Henzler Wildman, K., Lee, D. K., and Ramamoorthy, A. (2002) An innovative procedure using a sublimable solid to align lipid bilayers for solid-state NMR studies, *Biophys. J.* 82, 2499-2503.
40. Mani, R., Buffy, J. J., Waring, A. J., Lehrer, R. I., and Hong, M. (2004) Solid-State NMR Investigation of the Selective Disruption of Lipid Membranes by Protegrin-1, *Biochemistry* 43, 13839-13848.
41. Traikia, M., Warschawski, D. E., Recouvreur, M., Cartaud, J., and Devaux, P. F. (2000) Formation of unilamellar vesicles by repetitive freeze-thaw cycles: characterization by electron microscopy and ³¹P NMR, *Eur. Biophys. J.* 29, 184-195.
42. Mayer, L. D., Hope, M. J., Cullis, P. R., and Janoff, A. S. (1985) Solute distributions and trapping efficiencies observed in freeze-thawed multilamellar vesicles, *Biochim. Biophys. Acta* 817, 193-196.

43. Jaroniec, C. P., Tounge, B. A., Rienstra, C. M., Herzfeld, J., and Griffin, R. G. (1999) Measurement of ^{13}C - ^{15}N distances in uniformly ^{13}C labeled biomolecules: J-decoupled REDOR., *J. Am. Chem. Soc.* 121, 10237-10238.
44. Jaroniec, C. P., Tounge, B. A., Herzfeld, J., and Griffin, R. G. (2001) Frequency Selective Heteronuclear Dipolar Recoupling in Rotating Solids: Accurate ^{13}C - ^{15}N Distance Measurements in Uniformly ^{13}C , ^{15}N -labeled Peptides., *J. Am. Chem. Soc.* 123, 3507-3519.
45. Oku, N., and MacDonald, R. C. (1983) Differential effects of alkali metal chlorides on formation of giant liposomes by freezing and thawing and by dialysis, *Biochemistry* 22, 855-863.
46. Daleke, D. L. (2003) Regulation of transbilayer plasma membrane phospholipid asymmetry, *J. Lipid Res.* 44, 233-242.
47. Takegoshi, K., Nakamura, S., and Terao, T. (2001) C-13-H-1 dipolar-assisted rotational resonance in magic-angle spinning NMR, *Chem. Phys. Lett.* 344, 631-637.

4.7 Supporting information

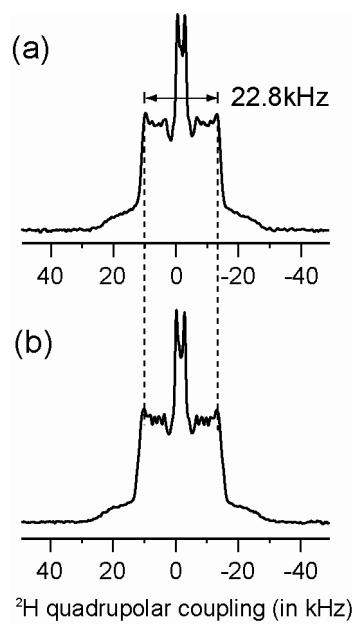


Figure S4.1. Static ^2H powder spectra of d_{54} -DMPC/DMPG membrane without (a) and with (b) penetratin at 310 K.

Chapter 5

Role of Arginine and Lysine Residues in the Translocation of a Cell-Penetrating Peptide from ^{13}C , ^{31}P and ^{19}F Solid-State NMR

*A paper published in **Biochemistry***

2009, vol. 48(21), page 4587-4595

Yongchao Su ¹, Tim Doherty ¹, Alan J. Waring ², Piotr Ruchala ³, and Mei Hong ^{1*}

¹ Department of Chemistry, Iowa State University, Ames, IA 50011

² Department of Medicine, David Geffen School of Medicine, University of California at Los Angeles, Los Angeles, CA 90095

³ David Geffen School of Medicine, University of California at Los Angeles, 10833 Le Conte Avenue, CHS 37-068, Los Angeles, CA 90095

April 11, 2009

5.1 Abstract

Cell-penetrating peptides (CPPs) are small cationic peptides that cross the cell membrane while carrying macromolecular cargoes. We use solid-state NMR to investigate the structure and lipid interaction of two cationic residues, Arg₁₀ and Lys₁₃, in the CPP penetratin. ^{13}C chemical shifts indicate that Arg₁₀ adopts a rigid β -strand conformation in the liquid-crystalline state of anionic lipid membranes. This behavior contrasts with all other residues observed so far in this peptide, which adopt a dynamic β -turn conformation with coil-like chemical shifts at physiological temperature. Low-temperature ^{13}C - ^{31}P distances between the peptide and the lipid phosphates indicate that both the Arg₁₀ guanidinium C ζ and the Lys₁₃ C ϵ lie in close proximity to the lipid ^{31}P (4.0 – 4.2 Å), proving the existence of charge-charge interaction for both Arg₁₀ and Lys₁₃ in the gel-phase membrane. However, since lysine substitution in CPPs are known to reduce their translocation ability, we propose that low temperature stabilizes both lysine and arginine interactions with the phosphates, whereas at high temperature the lysine–phosphate interaction is much weaker than the arginine–phosphate interaction. This is supported by the unusually high rigidity of the Arg₁₀ sidechain and its β -strand conformation at high temperature. The latter is proposed to be important for ion pair formation by allowing close approach of the lipid headgroups to guani-

dinium sidechains. ^{19}F and ^{13}C spin diffusion experiments indicate that penetratin is oligomerized into β -sheets in gel-phase membranes. These solid-state NMR data indicate that guanidinium-phosphate interactions exist in penetratin, and guanidinium groups play a stronger structural role than ammonium groups in the lipid-assisted translocation of CPPs across liquid-crystalline cell membranes.

Abbreviations: DMPC, 1,2-dimyristoyl-*sn*-glycero-3-phosphatidylcholine; DMPG, 1,2-dimyristoyl-*sn*-glycero-3-phosphatidylglycerol; POPC, 1-palmitoyl-2-oleoyl-*sn*-glycero-3-phosphatidylcholine; POPE, 1-palmitoyl-2-oleoyl-*sn*-glycero-3-phosphoethanolamine; POPG, 1-palmitoyl-2-oleoyl-*sn*-glycero-3-phosphatidylglycerol.

5.2 Introduction

Cell-penetrating peptides (CPP) are arginine- and lysine-rich cationic peptides that can readily enter cells not only by themselves but also carrying other macromolecular cargos (1-3). Thus they are promising drug-delivery molecules. Many studies have established that the intracellular entry of CPPs is related to their strong affinity to lipid bilayers (4). The lipid membrane can be the plasma membrane of the cell or the endosomal membrane from which CPPs must escape after endocytosis (5). The fundamental biophysical question of interest is how these highly cationic peptides cross the hydrophobic part of the lipid bilayer against the free energy barrier, and doing so without causing permanent damage to the membrane, in contrast to another family of cationic membrane peptides, antimicrobial peptides (AMPs).

Several models have been proposed to explain the membrane translocation of CPPs. The inverse micelle model proposes that transient inverse micelles form in the membrane to trap the peptides from the outer leaflet and subsequently release them to the inner leaflet (6, 7). However, this model is inconsistent with the lipid ^{31}P spectra (8), and the large rearrangement of lipids is difficult to achieve energetically. The electroporation model (9) posits that at low concentrations CPPs bind only to the outer leaflet of the bilayer, thus causing a transmembrane electric field. Above a threshold peptide concentration, the membrane is permeabilized in an electroporation-like manner, which creates transient defects that enable the peptides to distribute to both leaflets, thus relieving the membrane curvature stress (9-11). The third model posits that the guanidinium ions in these arginine-rich peptides associate

with the lipid phosphate groups to neutralize the arginine residues and thus allow the peptides to cross the membrane without a high energy penalty. This model is supported by phase transfer experiments of oligoarginines (12) and by molecular dynamics simulation of the HIV-1 Tat peptide, which showed transient association of arginine residues with the phosphate groups on both sides of the bilayer (13).

We recently investigated the depth of insertion and conformation of a CPP, penetratin, using solid-state ^{13}C and ^{31}P NMR. Penetratin is the first discovered CPP and is derived from the third helix (residues 43-58) of the *Drosophila Antennapedia* homeodomain (14). Using Mn^{2+} paramagnetic relaxation enhancement (PRE) experiments, we showed that penetratin is bound to both leaflets of the lipid bilayer at both low and high concentrations (peptide-lipid molar ratios of 1:40 and 1:15) (15, 16). This data indicates that the electroporation model is unlikely for penetratin. No ^{31}P peaks at the isotropic frequency or the hexagonal-phase frequency were observed, thus ruling out the inverse micelle model. In addition, we found that penetratin undergoes an interesting conformational change, as manifested by ^{13}C chemical shifts, from a β -sheet structure in the gel-phase membrane to a coil-like conformation in the liquid-crystalline membrane (17). The coil-like conformation at high temperature has non-negligible residual order parameters of 0.23 – 0.52 (17), indicating that the peptide remains structured. We hypothesized that the high-temperature conformation is a β -turn that undergoes uniaxial rotation around the bilayer normal.

Given the above experimental evidence against the electroporation model and the inverse micelle model, we now test the validity of the guanidinium-phosphate complexation model for the membrane translocation of penetratin. For this purpose we measured ^{13}C - ^{31}P distances between several peptide sidechains and lipid ^{31}P atoms. As shown before for an arginine-rich antimicrobial peptide, strong associations with the lipid phosphates manifest as short ^{13}C - ^{31}P distances (18, 19). We show here that the cationic Arg₁₀ in penetratin indeed exhibits shorter distances to phosphate groups than hydrophobic residues. However, another cationic residue, Lys₁₃, also exhibits short ^{13}C - ^{31}P distances, despite the fact that Lys mutants of CPPs have much weaker translocation activities. We show that the answer to this puzzle lies not in the low-temperature structure and distances of the two residues, but in their high-temperature dynamic structures, which differ significantly. And it is the structure in the

liquid-crystalline membrane that accounts for the distinct roles of Arg and Lys in CPP entry into the cell. Finally, we investigate the oligomeric structure of penetratin in gel-phase membranes using ^{19}F and ^{13}C spin diffusion NMR.

5.3 Materials and Methods

All lipids were purchased from Avanti Polar Lipids (Alabaster, AL) and used without further purification. Penetratin (RQIKI WFQNR RMKW KK), which contains three arginines and four lysines, was synthesized using standard Fmoc solid-phase peptide synthesis methods (20). Uniformly ^{13}C , ^{15}N -labeled arginine was purchased from Cambridge Isotope Laboratory and incorporated into Arg₁₀ in the peptide. Ile₃ and Lys₁₃ were labeled in two other peptide samples as described before (17). 4- ^{19}F -Phe₇ labeled penetratin was used for ^{19}F experiments to determine the oligomeric structure. All peptide samples were purified by HPLC to > 95% purity.

Hydrated membrane samples were prepared using an aqueous-phase mixing method. Lipids were first codissolved in chloroform at the desired molar ratios and dried under a stream of N₂ gas. After lyophilization in cyclohexane overnight, the dry lipid powder was suspended in water and freeze-thawed several times before the peptide solution was added. The solution was incubated overnight to facilitate binding, then centrifuged at 55,000 rpm for 3 hours to obtain a hydrated membrane pellet. For the Arg₁₀ experiments, a hydrated DMPC/DMPG (8:7) membrane with a peptide : lipid molar ratio of 1:15 was used in most 2D correlation and distance measurements. The molar ratio was chosen to balance the positive charges of the peptide (+7) by the negatively charged PG lipids (-1). This DMPC/DMPG sample is supplemented by a hydrated POPC/POPG (8:7) sample for the conformation study, and by a trehalose-protected dry POPE/POPG (8:7) sample for the ^{13}C - ^{31}P REDOR experiment. For distance measurements of other residues, several trehalose-protected dry DMPC/DMPG membranes were used to ensure that both the peptide and the lipid head-groups are completely immobilized at low temperature (21). Trehalose is known to protect the lamellar structure of the lipid bilayer in the absence of water (22). Below we refer to the non-trehalose containing membrane samples as hydrated samples to distinguish from the dry trehalose-containing samples.

Solid-state NMR experiments

All experiments were carried out on a Bruker DSX-400 (9.4 Tesla) spectrometer (Karlsruhe, Germany) at a resonance frequency of 100.7 MHz for ^{13}C , 376.8 MHz for ^{19}F and 162.1 MHz for ^{31}P . Magic-angle-spinning (MAS) probes tuned to $^1\text{H}/^{13}\text{C}/^{31}\text{P}$ and $^1\text{H}/^{19}\text{F}/\text{X}$ and equipped with 4 mm spinning modules were used for all experiments. Low temperature was achieved using a Kinetics Thermal System XR air-jet sample cooler (Stone Ridge, NY). The temperature of the sample was read from a thermocouple placed near the rotor and was not further calibrated. Typical 90° pulse lengths are 3.5-5.0 μs . ^1H decoupling fields of 50-80 kHz were used. ^{13}C , ^{31}P and ^{19}F chemical shifts were referenced externally to the $\alpha\text{-Gly } ^{13}\text{C}'$ resonance at 176.49 ppm on the TMS scale, the hydroxyapatite ^{31}P signal at 2.73 ppm and the Teflon ^{19}F signal at -122 ppm, respectively.

^{13}C cross polarization (CP) MAS experiments were conducted with a contact time of 0.5-1.0 ms at a typical Hartman-Hahn field strength of 50 kHz. For variable-temperature experiments, samples were stabilized for at least 20 min at each temperature before data acquisition. 2D ^{13}C - ^{13}C dipolar assisted rotational resonance (DARR) experiments (23) were conducted under 5 kHz MAS and with a mixing time of 20 ms and 30 ms. A ^1H -driven spin diffusion experiment with a longer mixing time of 50 ms was used to detect inter-residue cross peaks of penetratin in DMPC/DMPG membranes.

^{13}C - ^1H and ^{15}N - ^1H dipolar couplings were measured using DIPSHIFT (24, 25) experiments at 303 K under 3.401 and 3.000 kHz MAS, respectively. The MREV-8 sequence was used for ^1H homonuclear decoupling (26), with an 105° ^1H pulse length of 4.0 μs . In the C-H DIPSHIFT experiment, the ^{13}C - ^{13}C dipolar coupling is removed by MAS while the ^{13}C - ^{13}C scalar coupling has no effect on the t_1 -dependent intensity modulation due to the constant time nature of the evolution period. The normalized t_1 intensities were fitted using a home-written Fortran program. The best-fit values were divided by the theoretical scaling factor of 0.47 for the MREV-8 sequence. For the doubled N-H DIPSHIFT experiment, the fit value was further divided by 2 to obtain the true couplings. The ratio between the true coupling and the rigid limit value gives the order parameter S_{XH} . The rigid-limit coupling used

was 22.7 kHz for C-H and 10.6 kHz for N-H dipolar couplings. Simulations took into account the difference between the XH and XH₂ spin systems.

Frequency-selective rotational-echo double-resonance (REDOR) experiments were used to measure distances between peptide ¹³C and lipid ³¹P (27, 28). The experiments were conducted at ~230 K under 4 kHz MAS. A rotor-synchronized soft ¹³C Gaussian 180° pulse of 1000 μs was applied in the middle of the REDOR period to suppress the ¹³C-¹³C *J*-coupling between the on-resonance ¹³C and its directly bonded ¹³C spins. ³¹P 180° pulses of 9 μs were applied every half rotor period. The DMPC/DMPG sample were used to measure the Arg₁₀ sidechain and CO distances to ³¹P, whereas the POPE/POPG sample was used to measure the Cα -³¹P distance, as the DMPC Cγ peak (54 ppm) overlaps with the Arg₁₀ Cα signal.

A double-quantum (DQ) selective REDOR experiment (**Figure 5.5a**) was designed to measure the ¹³C-³¹P distance of Ile₃ sidechains, whose signals overlap extensively with the lipid ¹³C peaks. An SPC-5 pulse train (29) was used to create DQ coherence of the labeled ¹³C sites and suppress the natural abundance lipid ¹³C signals. The efficiency of the DQ-REDOR experiment is about 20% of the single-quantum selective REDOR experiment.

For the ¹³CO-³¹P REDOR experiment, the DQ-REDOR experiment was not used due to the low sensitivity of the CO signal. Thus, the lipid natural-abundance contribution to the ¹³CO signal was corrected using the equation $(S/S_0)_{\text{observed}} = 0.79(S/S_0)_{\text{peptide}} + 0.21(S/S_0)_{\text{lipid}}$, where the weight fractions were obtained from the peptide-lipid molar ratio. At the low temperature used for the REDOR experiments, the lipid and peptide CO groups have very similar CP efficiencies, thus the natural abundance correction is relatively accurate.

All ¹³C-³¹P REDOR data were fit by two-spin simulations. As we showed before, for distances shorter than 5 Å, two-spin simulations are sufficient. For distances larger than 7 Å, the two-spin simulation only slightly overestimates the distances compared to the vertical distance from ¹³C to the ³¹P plane obtained from a multi-spin simulation (18).

The oligomeric structure of penetratin was determined using the ¹⁹F CODEX experiment (30, 31). The experiments were conducted at 233 K on a trehalose-protected DMPC/DMPG sample to freeze potential motion of the peptide. Two experiments were conducted for each mixing time: an exchange experiment (*S*) with the desired mixing time (τ_m)

and a short z -filter (τ_z), and a reference experiment (S_0) with interchanged τ_m and τ_z . The normalized intensity, S/S_0 , was measured as a function of the mixing time until it reached a plateau. The inverse of the equilibrium S/S_0 value gives the minimum oligomeric number. Error bars were propagated from the signal-to-noise ratios of the isotropic peak and its sidebands. The τ_m -dependent CODEX curve was simulated as described before (32) to extract intermolecular distances.

5.4 Results

Arg₁₀ conformation and dynamics in penetratin

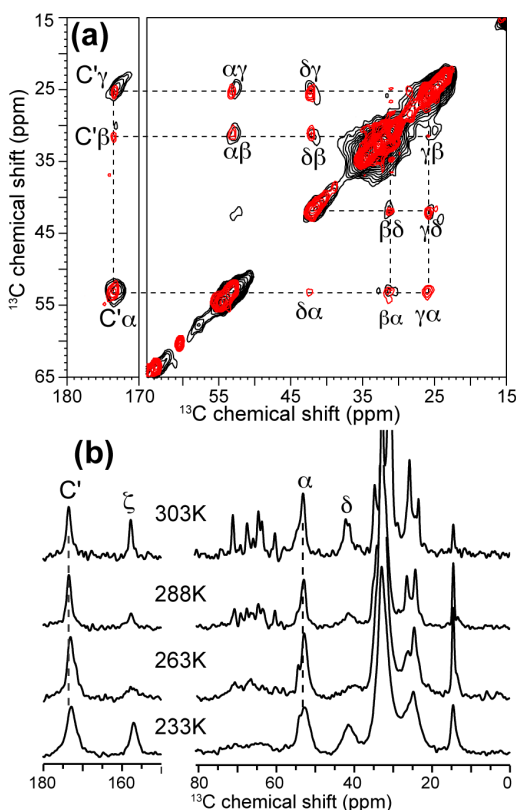


Figure 5.1. (a) 2D ^{13}C - ^{13}C correlation spectra of Arg₁₀ labeled penetratin in DMPC/DMPG (8:7) membranes at 303 K (red) and 234 K (black), with DARR mixing times of 30 ms and 20 ms, respectively. (b) 1D ^{13}C CP-MAS spectra of Arg₁₀-penetratin in the DMPC/DMPG membrane as a function of temperature. Lines guide the eye for Arg₁₀ backbone signals and the lack of temperature-induced chemical shift changes.

In the present study, we focus on Arg₁₀, one of the three arginine residues in penetratin, to understand whether cationic residues in general and arginine residues in particular play a special role in the membrane translocation of the peptide. We first investigate the conformation of Arg₁₀. We recently reported the reversible conformational change of many penetratin residues in the lipid bilayer between a β -turn state at high temperature and a β -strand state at low temperature. This conformational change was manifested as chemical shift changes and was observed at Ile₃, Ile₅, Gln₈, Asn₉ and Lys₁₃. The chemical shift change is independent of the membrane composition (POPC/POPG and DMPC/DMPG), anionic lipid fraction (PC/PG = 8:7 and 3:1), and peptide concentration (P/L = 1:15 and 1:30) (17).

Figure 5.1a shows the 2D ¹³C-¹³C correlation spectra of Arg₁₀-labeled penetratin in DMPC/DMPG bilayers at 303 K and 234 K. Most intra-residue cross peaks are seen, and show no frequency differences between high and low temperatures. Thus, in contrast to all other residues examined, Arg₁₀ does not have temperature-induced conformational change. The difference of the experimental isotropic chemical shifts from the random coil values reflects the secondary structure of the protein (33). Based on the ¹³CO, ¹³C α and ¹³C β ¹³C isotropic shifts (Supporting Information **Table S1**), we find Arg₁₀ adopts β -strand conformation at both high and low temperatures.

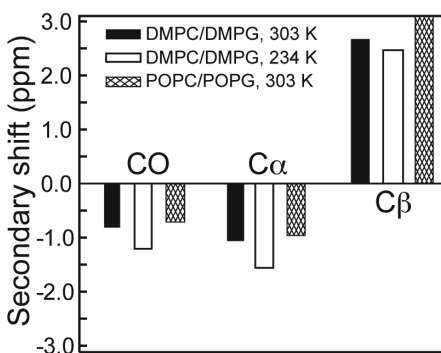


Figure 5.2. ¹³C secondary chemical shifts of CO, C α and C β of Arg₁₀ of penetratin in two lipid membranes and at two temperatures.

One-dimensional ¹³C CP-MAS spectra scanned between 303 K and 233 K (**Figure 5.1b**) confirm the lack of chemical shift changes in DMPC/DMPG bilayers. Moreover, the 1D spectra show that the penetratin ¹³C lines are broader at low temperature. This phenome-

non is common to many membrane peptides (34, 35), and can be attributed to conformational distribution of the peptide in the lipid membrane, which is averaged at high temperature but frozen in at low temperature. For the sidechain C δ signal, the largest line broadening is observed between 288 K and 263 K, below which the lines sharpen again. This is a definitive signature of intermediate-timescale motion, which means that at 303 K the Arg₁₀ sidechain undergoes fast torsional motion. The lack of exchange broadening for the C α and CO signals indicate that the Arg₁₀ backbone is already in the slow motional limit at 303 K.

We also measured the Arg₁₀ chemical shifts in POPC/POPG (8:7) membranes (Supporting Information **Figure S5.1**) and similarly found only β -strand chemical shifts in a wide temperature range. **Figure 5.2** plots the ¹³C secondary chemical shifts of Arg₁₀ at two temperatures in two different lipid membranes. The temperature-independent β -strand conformation of Arg₁₀ differs from all other residues examined so far in penetratin (17).

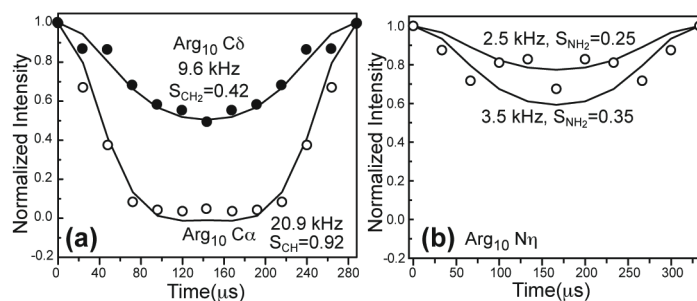


Figure 5.3. X-H DIPSHIFT time evolution of Arg₁₀ sites. (a) C-H dipolar couplings of C α (open circles) and C δ (filled circles) at 303 K, measured under 3.401 kHz MAS. The best-fit true couplings are given along with the corresponding order parameters. (b) N-H dipolar coupling of N η , measured under 3.000 kHz MAS. The scatter in the data is bracketed by two simulated curves, giving an S_{NH} of 0.30 ± 0.05 .

The β -strand conformation is usually more rigid than a coil or turn conformation due to hydrogen bond constraints, and thus should have order parameters close to 1 (17, 36). To verify this, we measured the C-H dipolar couplings of various Arg₁₀ segments in DMPC/DMPG bilayers. **Figure 5.3a** shows the ¹³C-¹H DIPSHIFT curves of C α and C δ at 303 K. The backbone C α -H α dipolar coupling is 20.9 kHz, corresponding to an S_{CH} of 0.92, which translates to a small motional amplitude of 13° (37). This order parameter fits into the S_{CH} range of 0.89-0.94 measured for the other five residues when in the β -strand confor-

mation. In comparison, the sidechain C δ has a S_{CH} of 0.42. While this value is much lower than the backbone due to the many torsional motions of the sidechain, it is actually larger than all other measured sidechain order parameters, which range from 0.23 to 0.37 in the β -sheet conformation (17). For comparison, the Lys₁₃ sidechain C ϵ was previously found to have an S_{CH} order parameter of 0.33 (17). We also measured the N-H dipolar coupling of the guanidinium N η group, and found an N-H dipolar coupling of 3.2 ± 0.5 kHz (Figure 5.3b). This translates to an S_{NH} of 0.30 ± 0.05 , which is significant considering this segment is six bonds away from the backbone C α .

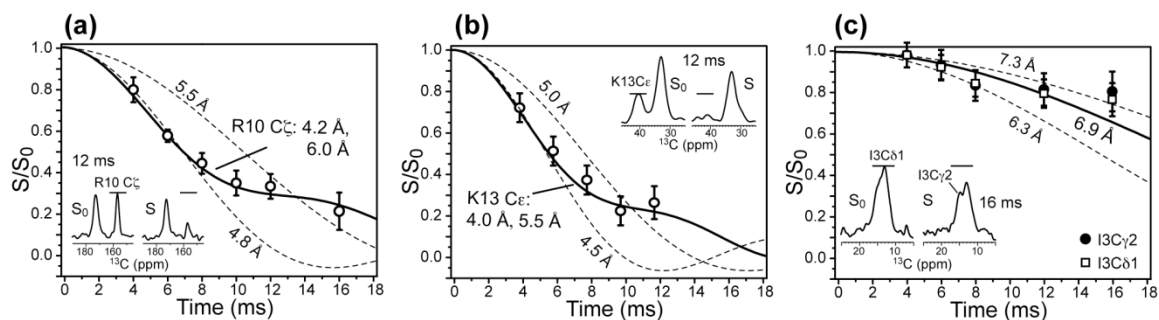


Figure 5.4. ^{13}C - ^{31}P REDOR data of penetratin sidechains in lipid membranes at 233 K. (a) Arg₁₀ C ζ in hydrated DMPC/DMPG (8:7) bilayers. (b) Lys₁₃ C ϵ in dry trehalose-protected DMPC/DMPG (8:7) bilayers. (c) Ile₃ methyl groups in dry trehalose-protected DMPC/DMPG (8:7) bilayers. Representative REDOR S_0 and S spectra are shown in the inset.

^{13}C - ^{31}P distances between penetratin and lipid headgroups

The main goal of the present study is to determine if the cationic residues in penetratin interact strongly with the negatively charged lipid phosphates. ^{13}C - ^{31}P distance measurements can provide this information site-specifically. Figure 5.4 shows the ^{13}C - ^{31}P REDOR data of Arg₁₀, Lys₁₃, and Ile₃ sidechains in DMPC/DMPG membranes. The experiments were carried out at 233 K where the ^{31}P chemical shift span is 195 – 198 ppm, corresponding to fully immobilized headgroups. The arginine C ζ and lysine C ϵ groups directly neighbor the cationic amines and have well resolved chemical shifts of 157.0 ppm and 40.2 ppm, respectively, thus they are ideal reporters of the interaction of these sidechain ends with the lipid headgroups. Arg₁₀ C ζ exhibits significant ^{13}C - ^{31}P REDOR dephasing of $S/S_0 = 0.35$ by 10 ms (Figure 5.4a), indicating relatively short distances to ^{31}P . The time dependence of

the REDOR intensities cannot be fit to a single distance due to the presence of a kink around 12 ms. Instead, a combination of a long distance of 6.0 Å and a short distance of 4.2 Å at a 1:1 ratio is found by a least-squares analysis to fit the data best (RMSD = 0.029). The short distance of 4.2 Å can only be satisfied if the guanidinium N-H groups are within hydrogen bonding distance with the O-P groups (18). Similarly, Lys₁₃ Cε exhibits significant dephasing and the REDOR intensities are best fit by two distances of 4.0 Å and 5.5 Å (1:1) (RMSD = 0.036). Again, the short distance supports hydrogen bonding with the lipid phosphate groups. Details of the two-distance best fit for Arg₁₀ and Lys₁₃ are shown in Supporting Information **Figure S5.2**. Single-distance fitting of the Arg₁₀ REDOR data indicate that the longer distance must be greater than 5.5 Å while the shorter distance must be smaller than 4.8 Å (**Figure 5.4a**). Further, the ¹³C-³¹P distances cannot be shorter than 3.6 Å due to steric constraints. Thus, two-distance REDOR curves were calculated using short distances of 3.6 – 4.8 Å with an increment of 0.2 Å and long distances of 5.4 – 7.2 Å with an increment of 0.3 Å, and the two contributions were averaged at a 1:1 ratio. The Lys₁₃ data was analyzed similarly. The simulations indicate that the experimental uncertainties for these ¹³C-³¹P REDOR data are about ±0.2 Å for distances shorter than 5.5 Å and ±0.4 Å for distances longer than 5.5 Å.

Are the short ¹³C-³¹P distances of Arg₁₀ and Lys₁₃ specific to the cationic sidechains or are they also true for hydrophobic residues in penetratin? To answer this question, we measured the ¹³Cγ2-³¹P and ¹³Cδ1-³¹P distances of the neutral hydrophobic residue Ile₃. Its Cδ1 is three bonds away from Cα, which is similarly separated from the backbone as lysine Cε. To remove the lipid natural abundance ¹³C signals that overlap with the Ile Cγ2 and Cδ1 peaks between 8.9 and 19.0 ppm, we designed a DQ selective REDOR experiment, whose pulse sequence is shown in **Figure 5.5a**. The DQ-selected spectra of Ile₃ Cγ2 and Cδ1 signals are shown in **Figure 5.5b** (middle and bottom spectra). The REDOR dephasing of Ile₃ is shown in **Figure 5.4c**. Much less REDOR decay is observed, with S/S₀ values of ~0.80 at 16 ms. The data is best fit to a distance of 6.9 Å for both Cγ2 and Cδ1, which is 2.7-2.9 Å longer than the Arg₁₀ Cζ and Lys₁₃ Cε. Thus, the short ¹³C-³¹P distances are specific to arginine and lysine sidechains instead of being true for all sidechains.

We also measured the ^{13}C - ^{31}P distances of Arg₁₀ backbone C α and CO, which are 6.8 Å and 7.8 Å, respectively (**Figure 5.6**). These values fall into the range of 6.9-8.2 Å previously measured for other residues (15). The ^{13}CO data was corrected for the lipid natural abundance signals, whose systematic uncertainty is much smaller than the random noise of the data. All ^{13}C - ^{31}P distances are summarized in **Table 5.1**.

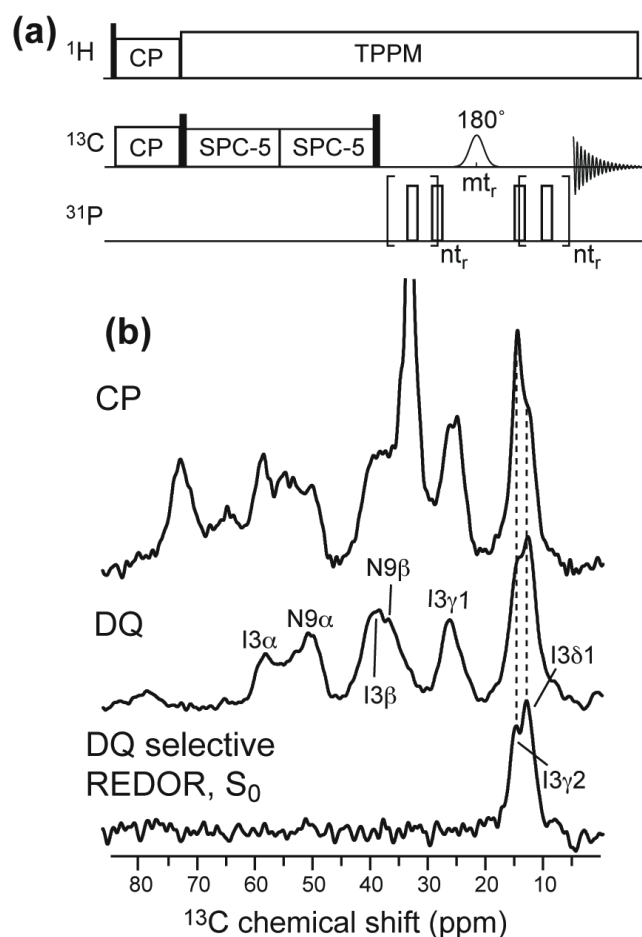


Figure 5.5. (a) Pulse sequence for the DQ selective REDOR experiment. (b) ^{13}C MAS spectra of Ile₃, Asn₉-labeled penetratin in trehalose-protected DMPC/DMPG bilayers. Top: CP spectrum, showing both the lipid and peptide signals. Middle: DQ-filtered spectrum, showing only peptide signals. Bottom: DQ selective REDOR S_0 spectrum, showing only the Ile₃ sidechain C γ 2 and C δ 1 signals.

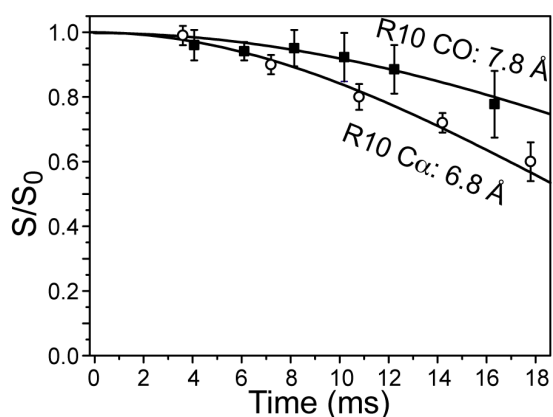


Figure 5.6. ^{13}C - ^{31}P REDOR of Arg₁₀ C α (open circles) and CO (filled squares) at 233 K. The C α data were measured in dry trehalose-protected POPE/POPG (8:7) bilayers. The CO data were measured in frozen hydrated DMPC/DMPG (8:7) membranes.

Table 5.1. ^{13}C - ^{31}P distances of penetratin residues in lipid membranes at P/L = 1:15 and 233 K. C α and Lys₁₃ C α distances are obtained from ref (15).

Residue	^{13}C - ^{31}P distances (Å)		
Ile ₃	C α : 8.2,	C γ 2: 6.9,	C δ 1: 6.9
Arg ₁₀	CO: 7.8,	C α : 6.8,	C ζ : 4.2, 6.0
Lys ₁₃	C α : 6.9,	C ϵ : 4.0, 5.5	

Oligomeric structure of penetratin in the lipid membrane

The ^{19}F CODEX experiment was used to determine the oligomeric number and intermolecular distances of penetratin in gel-phase membranes. **Figure 5.7a** shows the normalized exchange intensities of 4- ^{19}F -Phe₇ penetratin in trehalose-protected DMPC/DMPG bilayers. The CODEX intensities decay to an equilibrium value of 0.35 by 2.5 s, indicating three-spin clusters detectable by the ^{19}F distance ruler. To fit the decay trajectory quantitatively, we first assumed an equilateral triangle geometry for the three ^{19}F spins (**Figure 5.7b**). The best-fit possible under this assumption gives an internuclear distance of 9.0 Å for each side of the triangle; however, the fit curve (dashed line) does not capture the fast initial decay of the experimental data. To better fit the bi-exponential nature of the data, we then used a triangular geometry with one short distance of much less than 9 Å and two distances longer than or comparable to 9 Å. Modeling of penetratin as a trimer of antiparallel β -strands (see

below) yielded one distance of 6.0 Å and two distances of about 10 Å (**Figure 5.7c**), which were found to give excellent fit to the experimental data.

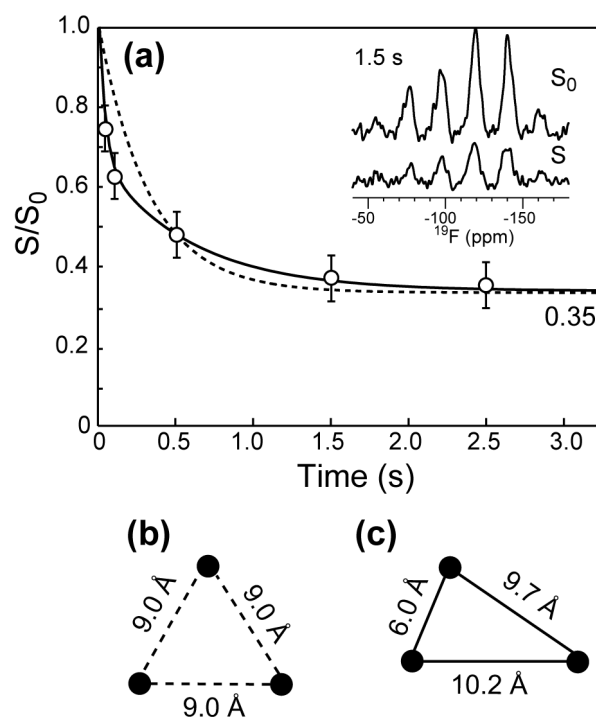


Figure 5.7. (a) Normalized CODEX intensities as a function of mixing time for 4- ^{19}F -Phe $_7$ -penetratin in trehalose-protected DMPC/DMPG (8:7) membrane. The data were collected under 8 kHz MAS and 233 K. Representative S_0 and S spectra are shown. (b) The equilateral triangle geometry used to generate the dashed-line fit curve in (a). (c) The three-spin geometry with unequal distances used to obtain the solid-line best-fit curve in (a).

To further constrain the intermolecular packing of penetratin in the lipid membrane, we measured a 2D ^1H -driven ^{13}C spin diffusion spectrum with a mixing time of 50 ms. **Figure 5.8** shows the 2D spectrum of Ile $_5$, Gln $_8$, Lys $_{13}$ -labeled penetratin in DMPC/DMPG bilayers at 249 K. Two inter-residue cross peaks were observed: I5 α -K13 α and Q8 δ -I5 α . Since the peptide adopts a β -strand conformation at this temperature, the intramolecular distances are ~ 27 Å and 11 Å for I5 α -K13 α and Q8 δ -I5 α , respectively, which are too long to be observed by ^{13}C spin diffusion NMR. Thus, these cross peaks must result from intermolecular contacts, which are most likely less than 6 Å for the 50 ms mixing time used.

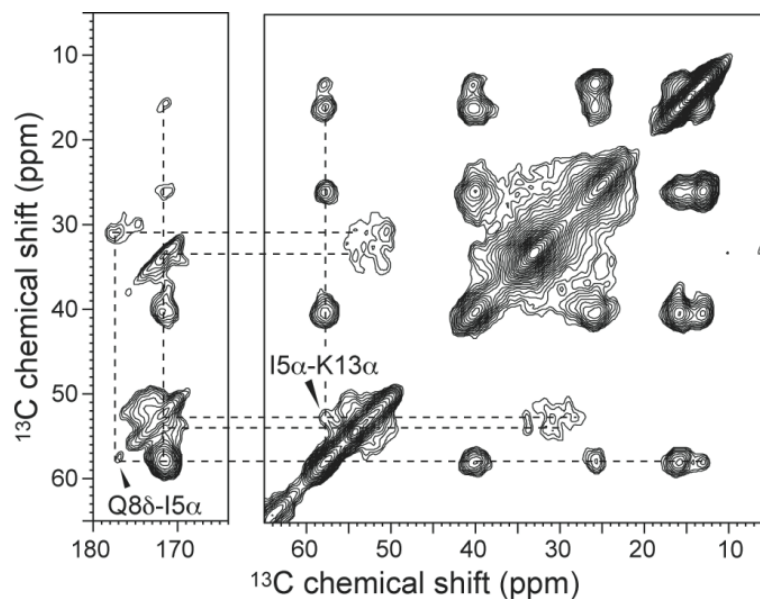


Figure 5.8. 2D ^{13}C - ^{13}C correlation spectrum of Ile₅, Gln₈, and Lys₁₃-labeled penetratin in DMPC/DMPG (8:7) bilayers at 249 K. The spin diffusion mixing time was 50 ms. Two inter-residue cross peaks are detected and assigned.

Using standard geometries for β -sheets, where inter-strand hydrogen bonds have $R_{\text{N-O}}$ distances of 2.8 – 3.4 Å and backbone torsion angles are $\phi = -139^\circ$, $\psi = 135^\circ$, we built a β -sheet model for penetratin at low temperature that is consistent with the ^{19}F and ^{13}C spin diffusion data (38, 39). Three penetratin β -strands are arranged as a trimer, with the middle strand antiparallel to the two outer strands and shifted by one residue (**Figure 5.9a**). This arrangement gives inter-strand I5 α -K13 α distances of 4.4 – 5.8 Å, consistent with the 2D ^{13}C spectrum. The three Phe₇ rings point to the same side of the β -sheet, giving ^{19}F - ^{19}F distances of 6.0 Å, 9.7 Å and 10 Å (**Figure 5.9b**). Short Q8 δ -I5 α distances cannot be satisfied within the same β -sheet, but requires two β -sheets stacked in parallel, with an inter-sheet distance of ~ 10 Å. This gives a Q8 δ -I5 α distance of 5.7 Å (**Figure 5.9a**), where the Q8 χ_1 angle is -177° , which is the dominant rotamer of Gln in the β -sheet conformation (40).

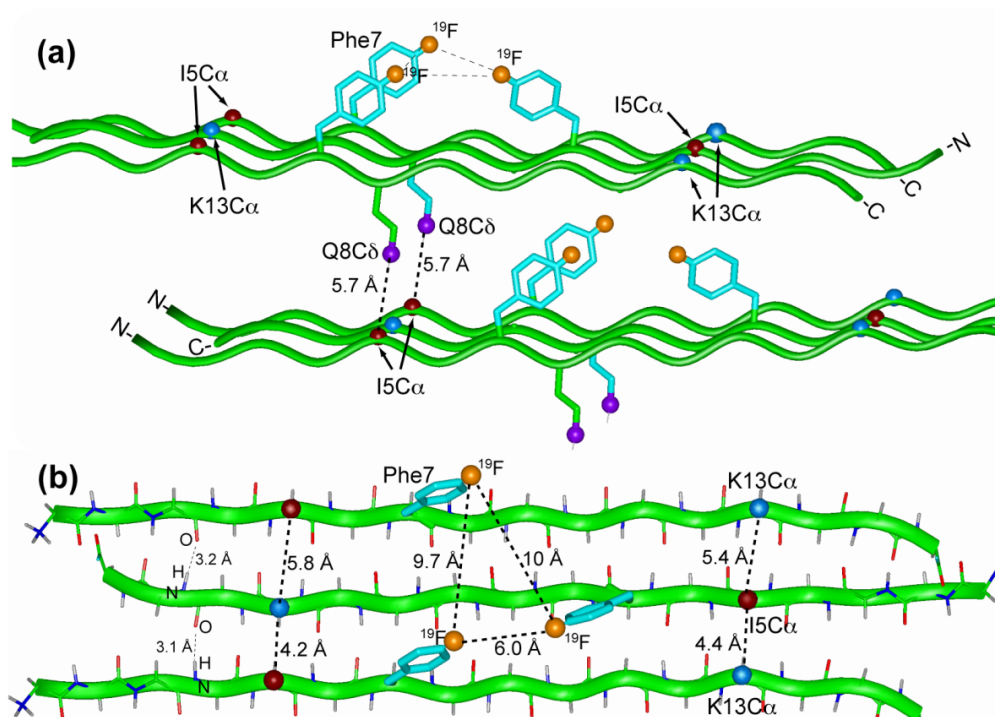


Figure 5.9. Oligomeric structure of penetratin in the gel-phase membrane. (a) Side view. (b) Top view. Constraints used to build the model include Phe₇ ¹⁹F-¹⁹F distances of 6.0, 9.7 and 10 Å, I5α-Q8δ and I5α-K13α distances of less than 6.0 Å, R_N-O hydrogen-bond distances of 2.8 – 3.4 Å, and inter-sheet distances of ~10 Å. The β-strand backbone has uniform (φ, ψ) angles of (-139°, 135°). The χ₁ angle is -177° for both Phe₇ and Gln₈.

5.5 Discussion

Interaction of charged sidechains in penetratin with lipid phosphates

The main finding of the current study is that an arginine and a lysine sidechain in penetratin both form close contacts with the lipid phosphates at low temperature. The Arg₁₀ Cζ-P distance of 4.2 Å and Lys₁₃ Cε-P distance of 4.0 Å both indicate the formation of N-H···O-P hydrogen bonds. **Figure 5.10** shows the sidechain conformations of Arg₁₀ and Lys₁₃ and the spatial arrangements with a phosphate group that satisfy the distances measured here. The N-O distances in both cases must be less than 3.0 Å to satisfy the experimental Cζ and Cε distances to ³¹P.

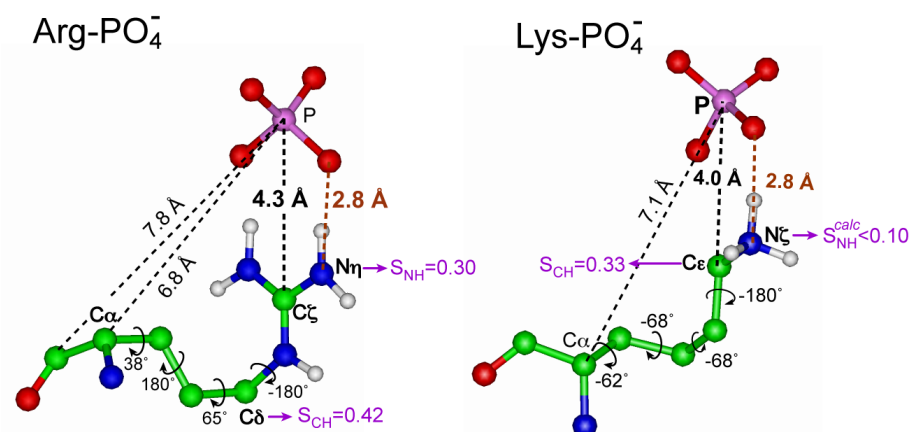


Figure 5.10. Low-temperature sidechain conformation and phosphate-interaction of Arg₁₀ and Lys₁₃ in penetratin. The measured ^{13}C - ^{31}P distances are indicated in black; the implied N-H \cdots O hydrogen bond distances are indicated in brown. Sidechain torsion angles that satisfy both backbone and sidechain ^{13}C - ^{31}P distances are indicated. At physiological temperature, sidechain order parameters of various segments indicate that the lysine-phosphate complex is significantly weakened whereas the arginine-phosphate complex remains.

The short distances of the Arg₁₀ sidechain to the lipid ^{31}P indicates that guanidinium-phosphate complexation occurs not only in antimicrobial peptides but also in cell-penetrating peptides, even though they differ in whether they cause permanent membrane damage. The similarity of lipid-peptide charge-charge attraction and hydrogen-bond formation suggests that penetratin, like some AMPs, also uses this interaction as the main mechanism for its function, which is crossing the lipid membrane. The fundamental driving force for the complex formation is the reduction in the free energy when a neutral species crosses the bilayer. The complexation entails that the peptide drags some lipid headgroups into the hydrophobic region of the membrane, thus causing membrane disorder. However, since no isotropic signal was observed in the ^{31}P spectra of penetratin-containing POPC/POPG (8:7) membranes (15), the disorder is probably transient and not observable on the NMR timescale or under NMR experimental conditions. The ^{13}C - ^{31}P distances must be measured at low temperature in the gel-phase membrane in order to freeze molecular motions that would average the dipolar couplings. At physiological temperature where motion is abundant and the penetratin structure is neither a canonical α -helix nor a β -strand (17), whether the ^{13}C - ^{31}P distances remain short is not possible to determine, but can be inferred from the sidechain dynamics of the residues (see below).

More interestingly, we found that Arg₁₀ and Lys₁₃ sidechains both establish short distances to ³¹P at low temperature. This is at first puzzling, since it is well documented that CPP analogs where arginine residues were replaced by lysine have much weaker translocation abilities (41, 42). For penetratin, which contains three arginines and four lysines, cellular uptake efficiencies have been compared among the wild-type peptide, the all-arginine analog, and the all-lysine analog. The efficiency was found to be the highest for the all-arginine analog and the lowest for the all-lysine analog (43). Since both arginine and lysine bear a positive charge at neutral pH, the higher activity of arginine-rich peptides has been suggested to be due to more diffuse charge distribution of the guanidinium group, or the ability of guanidinium ions to form multiple hydrogen bonds with oxyanions in a spatially directed manner (44).

We propose that the similar ¹³C-³¹P distances of Arg₁₀ and Lys₁₃ is only true at low temperature at which the REDOR experiments are carried out. Low temperature stabilizes charge-charge interactions, and masks different lipid interactions between Arg and Lys at physiological temperature. Indeed, there is good evidence for a much weaker interaction of the lysine sidechain with phosphates at ambient temperature. First, whereas the Arg₁₀ Nη-Hη order parameters could be measured, attempts to determine the Lys₁₃ Nζ order parameter failed due to unstable ¹H-¹⁵N cross polarization, which in itself indicates extensive dynamics of the amino group. Second, Arg₁₀ Cδ and Nη have C-H and N-H order parameters of 0.42 and 0.30±0.05 at 303 K, which are relatively large considering that they are three and six bonds away from the backbone Cα. Further, the similar order parameters indicate that the guanidinium moiety as a whole is relatively rigid at physiological temperature, which should facilitate its complexation with the phosphate groups. In comparison, the Lys₁₃ Nζ-Hζ order parameter, although not directly measurable, can be estimated as the product of the Cε S_{CH} of 0.33 with an additional scaling factor of 0.33 due to the three-site jumps of the amino group. Thus, the maximum Lys₁₃ Nζ-Hζ order parameter should be only 0.10, which is much smaller than the Arg₁₀ Nη order parameter of 0.30. With this small order parameter, the Lys₁₃ amino group is unlikely to form any long-lasting hydrogen bonds with lipid phosphates.

The fact that Arg₁₀ adopts a β -sheet backbone conformation that is independent of the temperature or membrane composition, in contrast to all other residues seen so far in penetratin, further supports the unique interaction of arginine with lipid phosphates. Residues Ile₃, Ile₅, Gln₈, Asn₉, and Lys₁₃ all exhibit coil-like chemical shifts at high temperature, which were assigned to a β -turn conformation (17). These data, together with the Arg₁₀ chemical shifts measured here, suggest that the β -turns connect a short stretch of β -strand encompassing Arg₁₀. β -turn residues separated by short β -strands are present in various naturally occurring proteins. For example, elastins have recurring (VPGVV)_n sequences where the central PG residues adopt a β -turn conformation whereas the flanking Val residues have the β -strand conformation (45).

For penetratin, between the β -turn Asn₉ and Lys₁₃, there are two arginine residues and one Met (RRM). It is very likely that the conformational propensity of Arg₁₀ is not unique to this residue but is also true for Arg₁₁, because the peptide backbone may be forced into an extended structure in order to allow the lipid headgroups to approach the charged guanidinium moieties to form the guanidinium-phosphate complex. In other words, guanidinium-phosphate interactions may be the cause of the persistent β -sheet conformation of Arg₁₀ at high and low temperatures. As a corollary, the fact that Lys₁₃ adopts the β -turn instead of β -strand conformation at high temperature is yet another piece of evidence that the ammonium group has much weaker interactions with the phosphates in the liquid-crystalline membrane.

The β -sheet oligomeric structure of penetratin in the gel-phase membrane is energetically favorable. The establishment of intermolecular C=O \cdots H-N hydrogen bonds reduces the free-energy cost of inserting the peptide into the membrane (46). As discussed above, the extended conformation (**Figure 5.9**) may facilitate the close approach of lipid phosphate groups with the cationic sidechains, thus allowing both arginine and lysine to interact with the phosphates and establish short ¹³C-³¹P distances (**Figure 5.10**).

In conclusion, we have shown that strong guanidinium-phosphate interactions exist in the cell-penetrating peptide penetratin, similar to antimicrobial peptides. Moreover, by considering not only low-temperature ¹³C-³¹P distances of Arg₁₀ and Lys₁₃, but also

high-temperature order parameters of the two sidechains and the unique high-temperature β -strand conformation of Arg₁₀, we deduce that the arginine sidechain interacts more strongly with lipid phosphates than the lysine sidechain at physiological temperature. Therefore, charge- and hydrogen-bond-stabilized guanidinium-phosphate interaction is not only responsible for membrane translocation of this cationic peptide, but also influences the conformation of the peptide.

5.6 Acknowledgment

We thank Professor Klaus Schmidt-Rohr for discussions of the ¹⁹F CODEX results.

5.7 Reference

- (1) Eguchi, A., Akuta, T., Okuyama, H., Senda, T., Yokoi, H., Inokuchi, H., Fujita, S., et al. (2001) Protein transduction domain of HIV-1 Tat protein promotes efficient delivery of DNA into mammalian cells, *J. Biol. Chem.* 276, 26204-26210.
- (2) Gratton, J. P., Yu, J., Griffith, J. W., Babbitt, R. W., Scotland, R. S., Hickey, R., Giordano, F. J., et al. (2003) Cell-permeable peptides improve cellular uptake and therapeutic gene delivery of replication-deficient viruses in cells and in vivo, *Nat. Med.* 9, 357-362.
- (3) Schwarze, S. R., Ho, A., Vocero-Akbani, A., and Dowdy, S. F. (1999) In vivo protein transduction: delivery of a biologically active protein into the mouse, *Science* 285, 1569-1572.
- (4) Fischer, R., Fotin-Mleczek, M., Hufnagel, H., and Brock, R. (2005) Break on through to the other side-biophysics and cell biology shed light on cell-penetrating peptides, *ChemBioChem*. 6, 2126-2142.
- (5) Richard, J. P., Melikov, K., Vives, E., Ramos, C., Verbeure, B., Gait, M. J., Chernomordik, L. V., et al. (2003) Cell-penetrating peptides. A reevaluation of the mechanism of cellular uptake, *J. Biol. Chem.* 278, 585-590.
- (6) Derossi, D., Calvet, S., Trembleau, A., Brunissen, A., Chassaing, G., and Prochiantz, A. (1996) Cell internalization of the third helix of the Antennapedia homeodomain is receptor-independent, *J. Biol. Chem.* 271, 18188-18193.
- (7) Berlose, J. P., Convert, O., Derossi, D., Brunissen, A., and Chassaing, G. (1996) Conformational and associative behaviours of the third helix of antennapedia homeodomain in membrane-mimetic environments, *Eur. J. Biochem.* 242, 372-386.
- (8) Prochiantz, A. (1996) Getting hydrophilic compounds into cells: lessons from homeopeptides, *Curr. Opin. Neurobiol.* 6, 629-634.

- (9) Binder, H., and Lindblom, G. (2003) Charge-dependent translocation of the Trojan peptide penetratin across lipid membranes, *Biophys. J.* 85, 982-995.
- (10) Drin, G., Cottin, S., Blanc, E., Rees, A. R., and Temsamani, J. (2003) Studies on the internalization mechanism of cationic cell-penetrating peptides, *J. Biol. Chem.* 278, 31192-31201.
- (11) Zhang, W., and Smith, S. O. (2005) Mechanism of penetration of Antp(43-58) into membrane bilayers, *Biochemistry* 44, 10110-10118.
- (12) Rothbard, J. B., Jessop, T. C., Lewis, R. S., Murray, B. A., and Wender, P. A. (2004) Role of membrane potential and hydrogen bonding in the mechanism of translocation of guanidinium-rich peptides into cells, *J. Am. Chem. Soc.* 126, 9506-9507.
- (13) Herce, H. D., and Garcia, A. E. (2007) Molecular dynamics simulations suggest a mechanism for translocation of the HIV-1 TAT peptide across lipid membranes, *Proc. Natl. Acad. Sci. U. S. A.* 104, 20805-20810.
- (14) Derossi, D., Joliot, A. H., Chassaing, G., and Prochiantz, A. (1994) The third helix of the Antennapedia homeodomain translocates through biological membranes, *J. Biol. Chem.* 269, 10444-10450.
- (15) Su, Y., Mani, R., and Hong, M. (2008) Asymmetric insertion of membrane proteins in lipid bilayers by solid-state NMR paramagnetic relaxation enhancement: a cell-penetrating Peptide example, *J. Am. Chem. Soc.* 130, 8856-8864.
- (16) Buffy, J. J., Hong, T., Yamaguchi, S., Waring, A., Lehrer, R. I., and Hong, M. (2003) Solid-State NMR Investigation of the Depth of Insertion of Protegrin-1 in Lipid Bilayers Using Paramagnetic Mn²⁺, *Biophys. J.* 85, 2363-2373.
- (17) Su, Y., Mani, R., Doherty, T., Waring, A. J., and Hong, M. (2008) Reversible sheet-turn conformational change of a cell-penetrating peptide in lipid bilayers studied by solid-state NMR, *J. Mol. Biol.* 381, 1133-1144.
- (18) Tang, M., Waring, A. J., and Hong, M. (2007) Phosphate-mediated arginine insertion into lipid membranes and pore formation by a cationic membrane peptide from solid-state NMR, *J. Am. Chem. Soc.* 129, 11438 - 11446.
- (19) Tang, M., Waring, A. J., Lehrer, R. I., and Hong, M. (2008) Effects of guanidinium-phosphate hydrogen bonding on the membrane-bound structure and activity of an arginine-rich membrane peptide from solid-state NMR spectroscopy, *Angew. Chem. Int. Ed. Engl.* 47, 3202-3205.
- (20) Yamaguchi, S., Hong, T., Waring, A., Lehrer, R. I., and Hong, M. (2002) Solid-state NMR investigations of peptide-lipid interaction and orientation of a beta-sheet antimicrobial peptide, protegrin, *Biochemistry* 41, 9852-9862.
- (21) Tang, M., Waring, A. J., and Hong, M. (2007) Trehalose-protected lipid membranes for determining membrane protein structure and insertion, *J. Magn. Reson.* 184, 222-227.
- (22) Crowe, J. H., Carpenter, J. F., and Crowe, L. M. (1998) The role of vitrification in anhydrobiosis, *Annu. Rev. Physiol.* 60, 73-103.

- (23) Takegoshi, K., Nakamura, S., and Terao, T. (2001) C-13-H-1 dipolar-assisted rotational resonance in magic-angle spinning NMR, *Chem. Phys. Lett.* 344, 631-637.
- (24) Munowitz, M. G., Griffin, R. G., Bodenhausen, G., and Huang, T. H. (1981) Two-dimensional rotational spin-echo nuclear magnetic resonance in solids: correlation of chemical shift and dipolar interactions, *J. Am. Chem. Soc.* 103, 2529-2533.
- (25) Hong, M., Gross, J. D., Rienstra, C. M., Griffin, R. G., Kumashiro, K. K., and Schmidt-Rohr, K. (1997) Coupling amplification in 2D MAS NMR and its application to torsion angle determination in peptides, *J. Magn. Reson.* 129, 85-92.
- (26) Rhim, W. K., Elleman, D. D., and Vaughan, R. W. (1973) Analysis of multiple-pulse NMR in solids., *J. Chem. Phys.* 59, 3740-3749.
- (27) Jaroniec, C. P., Tounge, B. A., Rienstra, C. M., Herzfeld, J., and Griffin, R. G. (1999) Measurement of ¹³C-¹⁵N distances in uniformly ¹³C labeled biomolecules: J-decoupled REDOR., *J. Am. Chem. Soc.* 121, 10237-10238.
- (28) Jaroniec, C. P., Tounge, B. A., Herzfeld, J., and Griffin, R. G. (2001) Frequency selective heteronuclear dipolar recoupling in rotating solids: accurate (¹³C)-(¹⁵N) distance measurements in uniformly (¹³C),(¹⁵N)-labeled peptides, *J. Am. Chem. Soc.* 123, 3507-3519.
- (29) Hohwy, M., Rienstra, C. M., Jaroniec, C. P., and Griffin, R. G. (1999) Fivefold symmetric homonuclear dipolar recoupling in rotating solids: application to double-quantum spectroscopy., *J. Chem. Phys.* 110, 7983-7992.
- (30) deAzevedo, E. R., Bonagamba, T. J., Hu, W., and Schmidt-Rohr, K. (1999) Center-band-only detection of exchange: efficient analysis of dynamics in solids by NMR, *J. Am. Chem. Soc.* 121, 8411-8412.
- (31) Buffy, J. J., Waring, A. J., and Hong, M. (2005) Determination of Peptide Oligomerization in Lipid Membranes with Magic-Angle Spinning Spin Diffusion NMR, *J. Am. Chem. Soc.* 127, 4477-4483.
- (32) Luo, W., and Hong, M. (2006) Determination of the oligomeric number and intermolecular distances of membrane protein assemblies by anisotropic ¹H-driven spin diffusion NMR spectroscopy, *J. Am. Chem. Soc.* 128, 7242-7251.
- (33) Zhang, H., Neal, S., and Wishart, D. S. (2003) RefDB: A database of uniformly referenced protein chemical shifts, *J. Biomol. NMR* 25, 173-195.
- (34) Cady, S. D., and Hong, M. (2008) Amantadine-Induced Conformational and Dynamical Changes of the Influenza M2 Transmembrane Proton Channel, *Proc. Natl. Acad. Sci. U.S.A* 105, 1483-1488.
- (35) Tang, M., Waring, A. J., and Hong, M. (2008) Arginine Dynamics in a Membrane-Bound Cationic Beta-Hairpin Peptide from Solid-State NMR, *ChemBioChem* 9, 1487-1492.

- (36) Buffy, J. J., Waring, A. J., Lehrer, R. I., and Hong, M. (2003) Immobilization and aggregation of the antimicrobial peptide protegrin-1 in lipid bilayers investigated by solid-state NMR, *Biochemistry* 42, 13725-13734.
- (37) Huster, D., Xiao, L. S., and Hong, M. (2001) Solid-State NMR Investigation of the dynamics of colicin Ia channel-forming domain, *Biochemistry* 40, 7662-7674.
- (38) Mani, R., Cady, S. D., Tang, M., Waring, A. J., Lehrer, R. I., and Hong, M. (2006) Membrane-dependent oligomeric structure and pore formation of a b-hairpin antimicrobial peptide in lipid bilayers from solid-state NMR, *Proc. Natl. Acad. Sci. USA* 103, 16242-16247.
- (39) Mani, R., Tang, M., Wu, X., Buffy, J. J., Waring, A. J., Sherman, M. A., and Hong, M. (2006) Membrane-bound dimer structure of a b-hairpin antimicrobial peptide from rotational-echo double-resonance solid-state NMR, *Biochemistry* 45, 8341-8349.
- (40) Lovell, S. C., Word, J. M., Richardson, J. S., and Richardson, D. C. (2000) The penultimate rotamer library, *Proteins: Struct., Funct., Genet.* 40, 389-408.
- (41) Wender, P. A., Mitchell, D. J., Pattabiraman, K., Pelkey, E. T., Steinman, L., and Rothbard, J. B. (2000) The design, synthesis, and evaluation of molecules that enable or enhance cellular uptake: peptoid molecular transporters, *Proc. Natl. Acad. Sci. U. S. A.* 97, 13003-13008.
- (42) Mitchell, D. J., Kim, D. T., Steinman, L., Fathman, C. G., and Rothbard, J. B. (2000) Polyarginine enters cells more efficiently than other polycationic homopolymers, *J. Pept. Res.* 56, 318-325.
- (43) Amand, H. L., Fant, K., Nordén, B., and Esbjörner, E. K. (2008) Stimulated endocytosis in penetratin uptake: effect of arginine and lysine, *Biochem. Biophys. Res. Commun.* 371, 621-625.
- (44) Jiang, Y., Ruta, V., Chen, J., Lee, A., and MacKinnon, R. (2003) The principle of gating charge movement in a voltage-dependent K⁺ channel, *Nature* 423, 42-48.
- (45) Yao, X. L., and Hong, M. (2004) Structural Distribution in an Elastin-Mimetic Peptide (VPGVG)₃ Investigated by Solid-State NMR, *J. Am. Chem. Soc.* 126, 4199-4210.
- (46) White, S. H., and Wimley, W. C. (1999) Membrane protein folding and stability: physical principles, *Annu. Rev. Biophys. Biomol. Struct.* 28, 319-365.

5.8 Supporting information

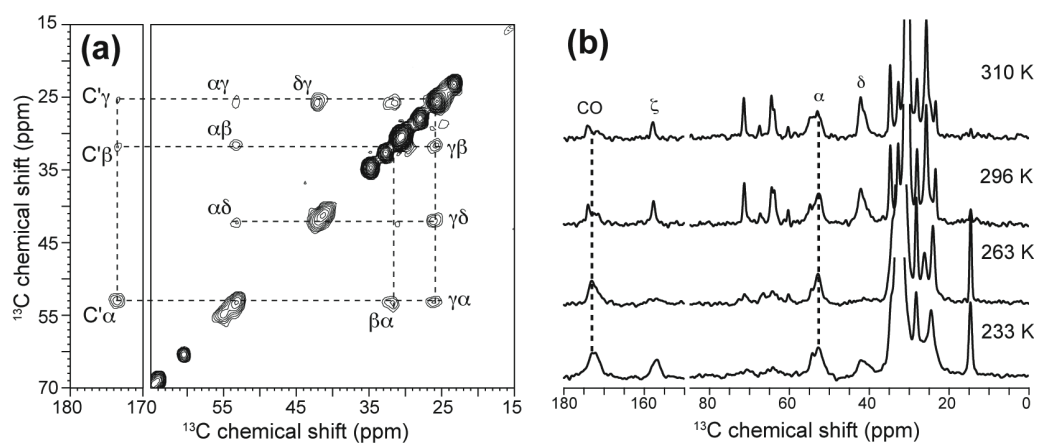


Figure S1. ^{13}C spectra of Arg₁₀-labeled penetratin in POPC/POPG (8:7) membranes. (a) 2D ^{13}C - ^{13}C DARR spectra measured at 303 K. (b) Temperature-dependent 1D ^{13}C CP-MAS spectra.

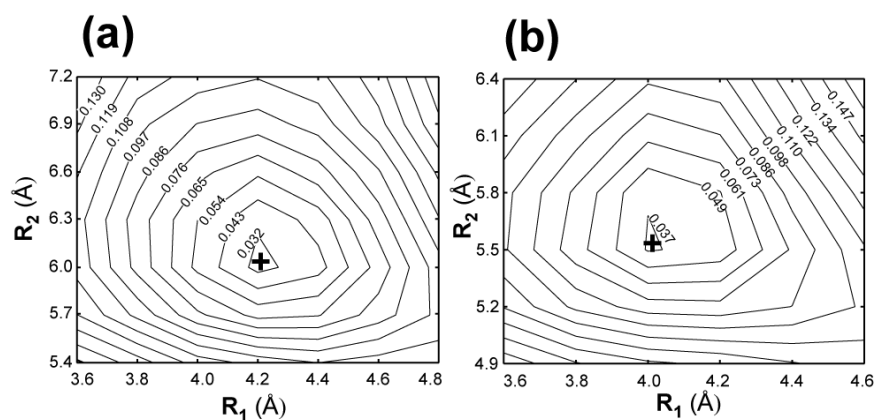


Figure S5.2. Root-mean-square deviations between the calculated and experimental ^{13}C - ^{31}P REDOR intensities. (a) Arg₁₀ C ζ . (b) Lys₁₃ C ϵ . The REDOR curve fitting used a combination of a short distance (R_1) and a long distance (R_2) at a 1:1 ratio. Best-fits are 6.0 Å and 4.2 Å for Arg₁₀ C ζ (minimum RMSD = 0.029), and 5.5 Å and 4.0 Å for Lys₁₃ C ϵ (minimum RMSD = 0.036).

Table S5.1. ^{13}C chemical shifts of penetratin Arg₁₀ in DMPC/DMPG (8:7) at 303 K and 243 K, and in POPC/POPG (8:7) at 303 K.

Site	DMPC/DMPG		POPC/POPG
	303 K	234 K	303 K
CO	173.4	173.0	173.5
C α	53.2	52.7	53.3
C β	31.5	31.3	31.9
C γ	25.8	25.0	25.9
C δ	42.2	41.5	42.1
C ζ	157.8	157.0	157.8

Chapter 6

Membrane-Bound Dynamic Structure of an Arginine-Rich Cell-Penetrating Peptide, the Protein Transduction Domain of HIV TAT, from Solid-State NMR

*A paper published in **Biochemistry***

2010, vol. 49(29), page 6009-6020

Yongchao Su ¹, Alan J. Waring ², Piotr Ruchala ², and Mei Hong ^{1*}

¹ Department of Chemistry, Iowa State University, Ames, IA 50011

² Department of Medicine, David Geffen School of Medicine, University of California at Los Angeles, Los Angeles, CA 90095

6.1 Abstract

The protein transduction domain of HIV-1 TAT, TAT(48-60), is an efficient cell-penetrating peptide (CPP) that diffuses across the lipid membranes of cells despite eight cationic Arg and Lys residues. To understand its mechanism of membrane translocation against the free energy barrier, we have conducted solid-state NMR experiments to determine the site-specific conformation, dynamics, and lipid interaction of the TAT peptide in anionic lipid bilayers. We found that TAT(48-60) is a highly dynamic and nearly random-coil peptide in the lipid bilayer, and inserts into the membrane-water interface near the glycerol backbone region. Arg-phosphate salt bridge interaction was revealed by short guanidinium-phosphate distances and restricted dynamics of the guanidinium. Together with the observation of strong peptide-water cross peaks in ¹H spin diffusion spectra, these results indicate that TAT binding to the membrane-water interface is stabilized not only by electrostatic attraction to the anionic lipids, but also by intermolecular hydrogen bonding with the lipid phosphates and water, which may take the role of intramolecular hydrogen bonds in canonical secondary structures. The random-coil structure of TAT and another CPP, penetratin, suggests that the lack of amphipathic structure is essential for rapid translocation of these Arg-rich CPPs across the lipid membrane without causing permanent damages to the membrane integrity.

Abbreviations: CPP, cell-penetrating peptide; DMPC, 1,2-dimyristoyl-*sn*-glycero-3-phosphatidylcholine; DMPG, 1,2-dimyristoyl-*sn*-glycero-3-phosphatidylglycerol; POPC, 1-palmitoyl-2-oleoyl-*sn*-glycero-3-phosphatidylcholine; POPE, 1-palmitoyl-2-oleoyl-*sn*-glycero-3-phosphoethanolamine; POPG, 1-palmitoyl-2-oleoyl-*sn*-glycero-3-phosphatidylglycerol; MAS, magic-angle spinning; CP, cross-polarization; DARR, dipolar-assisted rotational resonance INADEQUATE, incredible natural abundance double quantum transfer experiment; HETCOR, heteronuclear correlation; DIPSHIFT, dipolar-chemical-shift correlation; REDOR, rotational-echo double-resonance; FWHM, full width at half maximum.

6.2 Introduction

Cell-penetrating peptides (CPPs) are highly cationic and Arg-rich peptides that are able to cross lipid membranes into cells both alone and in conjugation with large macromolecular cargos (1, 2). Therefore, CPPs are potentially important molecules for drug delivery and for studying macromolecular structures inside living cells (3). CPPs have been discovered from diverse origins such as the TAT protein of HIV-1 (4), penetratin from the *Drosophila Antennapedia* homeodomain (5), and synthetic polyarginine peptides (6, 7). In contrast to antimicrobial peptides (AMPs), which are similarly Arg-rich sequences but which kill bacterial cells by disrupting their lipid membranes, CPPs appear to enter eukaryotic cells without causing long-lasting damage to the integrity of the cell membrane.

The physical basis for the membrane translocation of CPPs has been much debated and still not well understood (8). It is well known that the low-dielectric interior of cell membranes presents a high-energy barrier to the direct unassisted diffusion of charged ions and molecules. The free energies of transfer of amino acid residues from the aqueous to a nonpolar solvent have been measured experimentally and are highly positive for Arg and Lys (9). It is thus puzzling how short peptides containing a high density of Arg residues are able to cross the membrane. Two models, an inverse micelle model (10) and an electroporation model (11), had been proposed to account for membrane translocation of CPPs, but neither was supported by recent solid-state NMR studies of penetratin. Specifically, ^{31}P NMR line-shapes indicated the absence of isotropic entities in the membrane, thus ruling out the inverse micelle model (12). Paramagnetic relaxation enhancement experiments using Mn^{2+} ions bound to the outer surface of lipid bilayers versus both surfaces indicated that penetratin was distributed equally in the two leaflets of the membrane even at low peptide concentrations (12). This finding contradicted the electroporation model, which posits that asymmetric asso-

ciation of CPPs with the outer leaflet of the membrane causes an electric field that alters the lateral and curvature stress of the membrane, eventually causing electroporation-like perforation of the membrane (11). Instead, site-specific distances between penetratin and the lipid headgroups indicated tight guanidinium-phosphate associations (13), suggesting that ion pair interaction between the Arg residues and the anionic lipid headgroups may play a significant role in the membrane translocation of CPPs.

Despite many biophysical studies of CPPs in membrane-mimetic environments, little site-specific high-resolution structural information of membrane-bound CPPs is yet available. Our recent studies of membrane-bound penetratin through solid-state NMR ^{13}C chemical shifts suggested an unusual turn-rich conformation at physiological temperature (14), whose functional role is still unclear. Moreover, the penetratin conformation was found to depend on the temperature: in the gel phase of the membrane, penetratin adopts a β -strand conformation, while in the liquid-crystalline phase random-coil chemical shifts were observed for most labeled sites except for an Arg (14). To further elucidate how conformation underlies the mechanism of CPPs, and to examine the diversity of the structure-function relation for this class of peptides, we have now investigated the structure and dynamics of the hexa-Arg CPP domain of the HIV TAT protein (residues 48-60), whose potent CPP activities have been extensively characterized (15-17). Using solid-state NMR, we have determined the conformation, dynamics, depth of insertion, and lipid interaction of TAT(48-60) in anionic lipid membranes, which led us to propose a structural basis for the translocation mechanism of this peptide.

6.3 Materials and Methods

Membrane sample preparation

TAT(48-60) (GRKKR RQRRR PPQ-CONH₂) was synthesized using standard solid phase Fmoc chemistry and purified by HPLC to >95% purity. Uniformly ^{13}C , ^{15}N -labeled Lys, Gln, Arg, and Pro were incorporated at residues 4, 7, 8, and 11 of the peptide, respectively, in singly labeled samples. A ^{13}C , ^{15}N -Ile₃ labeled penetratin sample (RQIKI WFQNR RMKW KK-CONH₂) bound to DMPC/DMPG bilayers (13) was also used for the ^1H $T_{1\rho}$ experiment to compare with the TAT peptide. All lipids, including DMPC, DMPG, POPC, POPE

and POPG, were purchased from Avanti Polar Lipids (Alabaster, AL). Most experiments were conducted on hydrated DMPC/DMPG (8:7 mole ratio) membranes. The high-melting DMPC/DMPG mixture allows the peptide to be immobilized at moderate low temperatures to facilitate distance and chemical shift measurements. The low-melting unsaturated lipids (POPC, POPE and POPG) were used in aligned membrane samples since they are more easily hydrated and aligned at ambient temperature. We chose phosphatidylglycerol (PG) instead of phosphatidylserine (PS), which is the anionic lipid of eukaryotic cell membranes, for our samples in order to facilitate comparison with the large literature of CPP studies in model membranes. Eukaryotic cell membranes contain ~10% anionic lipids (18), which is much less than the ~50% charge density used in this work. However, the cationic TAT is most likely clustered in the anionic-lipid-rich regions of the biological membrane during translocation, so the current model membrane is still relevant for understanding the translocation mechanism.

Hydrated membrane samples were prepared by aqueous phase mixing. DMPC and DMPG (8 : 7 mole ratio) lipids were mixed in chloroform and dried under a stream of N₂ gas. The lipid mixture was further lyophilized overnight to obtain a homogeneous dry powder, which was then suspended in 2 mL phosphate buffer (5.8 mM NaH₂PO₄ and 4.2 mM Na₂HPO₄, pH = 7.0) and freeze-thawed 8 times. The resulting lipid vesicle solution was added to the peptide solution to obtain a peptide : lipid molar ratio of 1 : 15. After incubation overnight, the solution was centrifuged at 55,000 rpm for 4 hrs at 4-6 °C to obtain a wet pellet. The pellet was slowly dried to a hydration level of ~40 wt%, then packed into a 4 mm MAS rotor for NMR experiments. Over 95% of the peptide was bound to the lipids as checked by UV-VIS spectrometry. The POPE/POPG bound TAT sample was prepared similarly.

Oriented membranes were prepared on thin glass plates using an organic-solvent protocol described before (19). The dry lipid/peptide film (~1 mg) on each glass plate was first hydrated by directly dropping 1 µl water on each plate, giving a hydration level of ~50%. The hydrated glass plates were then kept in a 97% humidity chamber containing saturated K₂SO₄ solution at room temperature for 4-5 days before NMR measurements. Samples with TAT concentrations at 1%, 2%, 4% and 8% were prepared to determine the degree of mem-

brane disorder induced by the peptide. Three series of lipid membranes, neutral POPC, anionic POPC/POPG (8:7), and anionic POPE/POPG (8:7), were prepared.

Solid-state NMR experiments

All solid-state NMR experiments were carried out on a Bruker DSX-400 (9.4 T) spectrometer (Karlsruhe, Germany) operating at 400.5 MHz for ^1H , 100.7 MHz for ^{13}C and 162.1 MHz for ^{31}P . A triple-resonance $^1\text{H}/^{13}\text{C}/^{31}\text{P}$ 4 mm magic-angle spinning (MAS) probe was used for ^{13}C - ^{31}P REDOR experiments, while a double-resonance $^1\text{H}/\text{X}$ MAS probe was used for other MAS experiments. Low temperature was achieved using a Kinetics Thermal System XR air-jet sample cooler (Stone Ridge, NY). All experimental temperatures refer to the sample temperature indicated by the probe thermocouple, and are estimated to be within 1° of the actual sample temperature since no fast spinning nor high-salt samples were used in this work. Typical 90° pulse lengths of ^{13}C , ^{15}N and ^{31}P were $5\ \mu\text{s}$ and typical ^1H decoupling field strengths were 75 kHz at low temperature and 50 kHz at ambient temperature. ^{13}C and ^{15}N chemical shifts were calibrated, respectively, to the α -Gly $^{13}\text{C}'$ resonance at 176.49 ppm on the TMS scale and ^{15}N -acetyl-valine (NAV) at 122 ppm on the ammonium scale. ^{31}P chemical shifts were referenced to the hydroxyapatite signal at 2.73 ppm for unoriented samples and to the signal of 98% phosphoric acid at 0 ppm for oriented samples.

^{13}C and ^{15}N cross-polarization (CP) MAS experiments were conducted using CP contact times of 0.5 – 1.5 ms. One-dimensional double-quantum (DQ) filtered ^{13}C MAS spectra were measured at 233 K using SPC-5 for ^{13}C - ^{13}C dipolar recoupling (20). When extracting full widths at half maximum, we took care to use appropriate line broadening that is less than the intrinsic linewidths of the signals at the specific temperatures.

Two 2D ^{13}C - ^{13}C correlation experiments, dipolar-assisted rotational resonance (DARR) (21) and the DQ dipolar INADEQUATE experiment (22), were used to assign the TAT ^{13}C chemical shifts at low temperature. The INADEQUATE experiment suppresses the natural abundance lipid ^{13}C signals and gives relatively well-resolved peptide ^{13}C resonances. The SPC-5 sequence was used for DQ excitation and reconversion. The INADEQUATE spectra were measured at 233 K under 5333 Hz MAS.

2D ^{13}C - ^1H heteronuclear correlation (HETCOR) experiments without ^1H spin diffusion were used to assign ^1H and ^{13}C chemical shifts of TAT at ambient temperatures. No ^1H decoupling was applied during the evolution period, thus only signals of highly dynamic species can survive in the spectra. The experiments were conducted either with or without $^1\text{J}_{\text{CH}}$ decoupling for the t_1 period, by the presence or absence of a ^{13}C 180° pulse in the middle of the t_1 period. The pulse sequence of $^1\text{J}_{\text{CH}}$ -decoupled 2D HETCOR experiment was shown in **Fig. 2a**. The non- $^1\text{J}_{\text{CH}}$ decoupled HECTOR was conducted at 5 kHz MAS while the $^1\text{J}_{\text{CH}}$ decoupled HETCOR experiments were carried out under 7-8 kHz MAS at 303 K, in the liquid-crystalline phase of the DMPC/DMPG membrane. For ^1H spin diffusion experiments probing the interaction of TAT with lipids and water, we used a similar HETCOR sequence but with the addition of a ^1H spin diffusion mixing period after t_1 (23). These experiments were carried out under 5 kHz MAS at 303 K.

^{13}C - ^1H and ^{15}N - ^1H order parameters were measured using the 2D dipolar-chemical-shift correlation (DIPSHIFT) experiment with dipolar doubling (24, 25). The experiments were conducted at 303 K under slow spinning rates of 2800 Hz and 3401 Hz. ^1H homonuclear decoupling was achieved using semi-windowless MREV-8 with a ^1H 105° pulse length of 4.0 μs (26). Small asymmetry in the t_1 curves was fit using an apparent T_2 relaxation factor. The best-fit couplings were divided by the theoretical scaling factor, 0.47, of semi-windowless MREV-8 and a factor of 2 for doubling to give the true X-H dipolar couplings. The order parameters, S_{XH} , were calculated as the ratio of the true coupling with the rigid-limit one-bond X-H dipolar coupling. The rigid-limit value was taken as 22.7 kHz for C-H and 10.6 kHz for N-H dipolar coupling, respectively.

^1H rotating-frame spin-lattice relaxation times ($T_{1\rho}$), which reflect microsecond-timescale motions that are important for biological membranes, were measured using a ^{13}C -detected ^1H Lee-Goldburg spin-lock sequence with an effective ^1H field strength of 61.2 kHz (27). The experiments were conducted at 303 K under 7 kHz MAS.

^{13}C - ^{31}P rotational-echo double-resonance (REDOR) experiments were carried out under 4 kHz MAS at 230 K, where both the lipids and the peptide were immobilized. A ^{31}P 180° pulse length of 9 μs was used to achieve complete inversion of the broad ^{31}P spectral width. A frequency-selective version of REDOR (28) was used to measure the distance of

$C\alpha$ to ^{31}P . A 1 ms ^{13}C Gaussian 180° pulse centered at the ^{13}C resonance of interest was used to remove the J -coupling between the on-resonance $C\alpha$ and its directly bonded ^{13}C spins. Two-spin simulations were used to fit the ^{13}C - ^{31}P REDOR data. Although multiple ^{31}P spins are present on the membrane surface, the average ^{31}P density on the membrane surface (10 Å spacing between ^{31}P atoms) is sufficiently low that when the REDOR dephasing is fast, corresponding to two-spin ^{13}C - ^{31}P distances of ~ 5 Å or less, two-spin simulations report the correct distance of the ^{13}C to a single ^{31}P (29). When the dephasing is slow, comparison of multi-spin and two-spin simulations indicated that the two-spin distance is effectively the vertical distance between the ^{13}C and the ^{31}P plane, thus reporting the depth of the ^{13}C spin (29).

Due to overlap with the lipid ^{13}CO signals, the ^{13}CO - ^{31}P REDOR data were corrected for the natural abundance lipid background (13) using the equation $(S/S_0)_{\text{observed}} = 0.79(S/S_0)_{\text{peptide}} + 0.21(S/S_0)_{\text{lipid}}$, where the weight fractions were calculated based on the peptide/lipid molar ratio of 1 : 15. The lipid ^{13}CO - ^{31}P REDOR dephasing was previously measured using POPC lipids (29). The Pro₁₁ $C\alpha$ REDOR was similarly corrected for the small percentage of overlapping natural abundance lipid $C\alpha$ signal, whose distance to ^{31}P is fixed at 2.9 Å. To fit the Arg C ζ REDOR data, which shows heterogeneous couplings, we used two distances in the simulation, where the long and short distances were each incremented at 0.1 Å steps within physically allowed ranges (13). The best fit was obtained as the lowest RMSD between the data and simulations. **Table S6.1** summarizes the main conditions of all the experiments carried out in this work.

Table 6.1. ^1H , ^{13}C and ^{15}N chemical shifts (ppm) of labeled residues of TAT in DMPC/DMPG bilayers at 303 K and 233 K.

Residue	Site	303 K	233 K	Random coil values (31)
Lys ₄	CO	174.7	174.5	174.5
	$C\alpha$	54.4	54.3	54.7
	$C\beta$	30.9	31.3	30.8
	$C\gamma$	22.8	22.9	-
	$C\delta$	27.2	26.3	-
	$C\epsilon$	40.2	39.7	-

Table 6.1. (Continued) ^1H , ^{13}C and ^{15}N chemical shifts (ppm) of labeled residues of TAT in DMPC/DMPG bilayers at 303 K and 233 K.

Residue	Site	303 K	233 K	Random coil values (31)
Lys ₄	H α	4.29	-	4.28
	H β	1.82	-	-
	H γ	1.45	-	-
	H δ	1.69	-	-
Gln ₇	CO	173.8	174.0	174.2
	C α	53.8	53.8	54.2
	C β	27.8	26.7	27.0
	C γ	32.0	33.3	-
	C δ	178.4	177.9	-
	H α	4.37	-	4.26
	H β	2.01	-	-
	H γ	-	-	-
Arg ₈	N α	123.1	122.2	118.9
	N ϵ	85.4	83.2	-
	N η	73.0	71.3	-
	CO	174.1	174.3	174.2
	C α	54.2	53.4	54.3
	C β	28.9	28.7	28.8
	C γ	25.2	25.4	-
	C δ	41.5	41.0	-
	C ζ	157.7	156.9	-
	H _N	8.40	-	8.17
	H α	4.31	-	4.33
	H β	1.87	-	-
	H γ	1.64	-	-
	H δ	3.22	-	-
Pro ₁₁	N α	138.3	136.9	-
	CO	172.5	172.6	175.2
	C α	59.7	58.6	61.8
	C β	29.0	28.7	30.2
	C γ	25.4	25.5	-
	C δ	48.6	48.3	-
	H α	4.68	-	4.41
	H β	1.92	-	-
	H γ	2.00	-	-
	H δ	3.82	-	-

6.4 Results

Random coil conformation and high mobility of TAT in lipid bilayers

We first examined the conformation of TAT in DMPC/DMPG membranes using ^{13}C and ^{15}N chemical shifts. Four uniformly ^{13}C , ^{15}N -labeled residues, Lys₄, Gln₇, Arg₈ and Pro₁₁, were singly incorporated into the peptide.

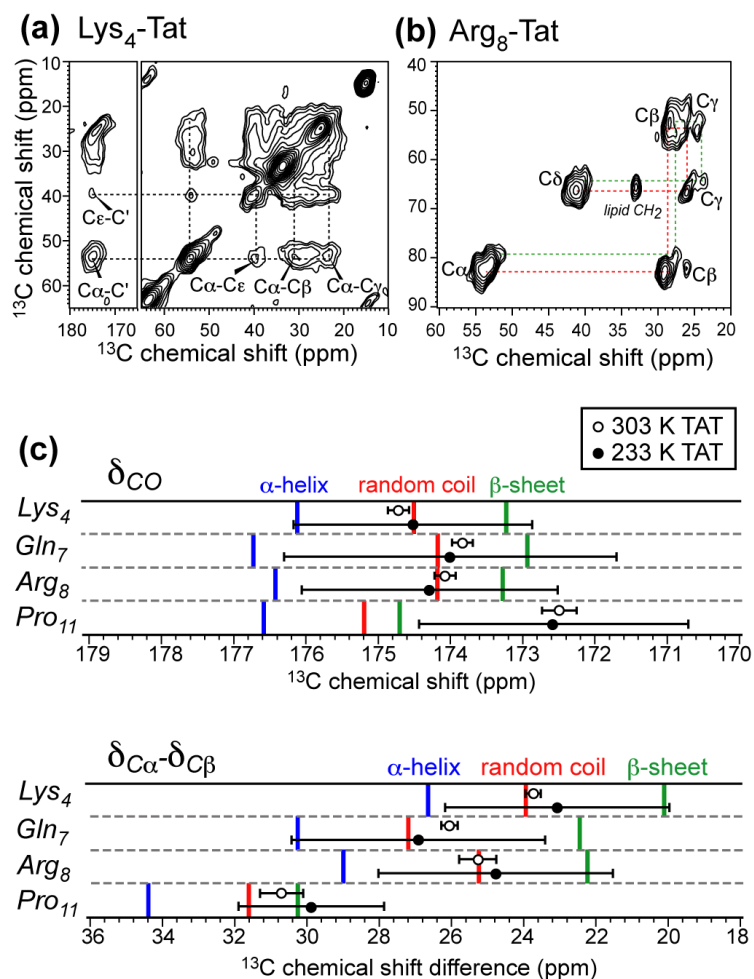


Fig. 6.1. ^{13}C chemical shifts of HIV TAT(48-60) in DMPC/DMPG (8:7) bilayers. (a) 2D ^{13}C - ^{13}C DARR spectrum of Lys₄-TAT at 233 K, measured with a mixing time of 30 ms. (b) 2D INADEQUATE spectrum of Arg₈-TAT at 233 K. (c) TAT ^{13}C chemical shifts at 303 K (open circles) and 233 K (closed circles) compared to database values for various secondary structures (31). The C α -C β chemical shift difference was used as a marker of secondary structure (58).

Fig. 6.1 shows representative 2D ^{13}C - ^{13}C correlation spectra of Lys₄- and Arg₈-labeled TAT in the gel phase of the membrane at 233 K. Broad C α and C β peaks with linewidths of 4.0 – 5.1 ppm were observed, indicating significant conformational heterogeneity. When the lipid ^{13}C signals were removed by a double-quantum (DQ) filter, more than one set of ^{13}C chemical shifts was found for some of the ^{13}C sites in Lys₄, Gln₇, and Arg₈ (**Fig. 6.1b**), suggesting that the conformational distribution may be more complex than a single Gaussian. Chemical shift multiplicity for the same domain in the intact TAT protein was also observed in solution, and was postulated to result from transient folding events of the protein (30). When the chemical shifts of the dominant peaks of membrane-bound TAT were compared with random coil values from protein databases (31), we found most residues to exist in a random-coil state (**Fig. 6.1c**). The only exception is Pro₁₁, which is known to be predisposed to β -strand conformation by the imine sidechain.

To examine if the random coil chemical shifts of TAT at low temperature were caused by the gel-phase disorder of the membrane, we measured the TAT ^{13}C chemical shifts in the liquid-crystalline phase of the membrane at 303 K using 2D ^1H - ^{13}C correlation experiments. Even in the absence of ^1H - ^1H homonuclear decoupling, we observed extremely narrow ^1H and ^{13}C linewidths and resolved $^1J_{\text{CH}}$ splittings in the ^1H dimension (**Fig. 6.2b**): the ^{13}C linewidths were 0.3-0.4 ppm while the undecoupled ^1H linewidths were 0.15-0.30 ppm. Thus, fast isotropic motion largely averaged the ^1H - ^1H dipolar couplings, giving well-resolved ^1H peaks even without homonuclear decoupling. As a comparison, in the HETCOR spectrum (data not shown) of Ile₃-labeled penetratin with $^1J_{\text{CH}}$ -decoupling, no peptide ^1H peaks survived in the spectra, indicating penetratin has slower motion than TAT. Most importantly, the TAT ^{13}C chemical shifts remained at the random coil positions, close to the center of the broad peaks at low temperature (**Fig. 6.1c**). Thus, TAT undergoes near-isotropic motion at high temperature, with an average conformation approaching the random coil. This result is consistent with circular dichroism data of TAT in POPC/POPG vesicles, which also suggested a random-coil structure similar to that in buffer (32).

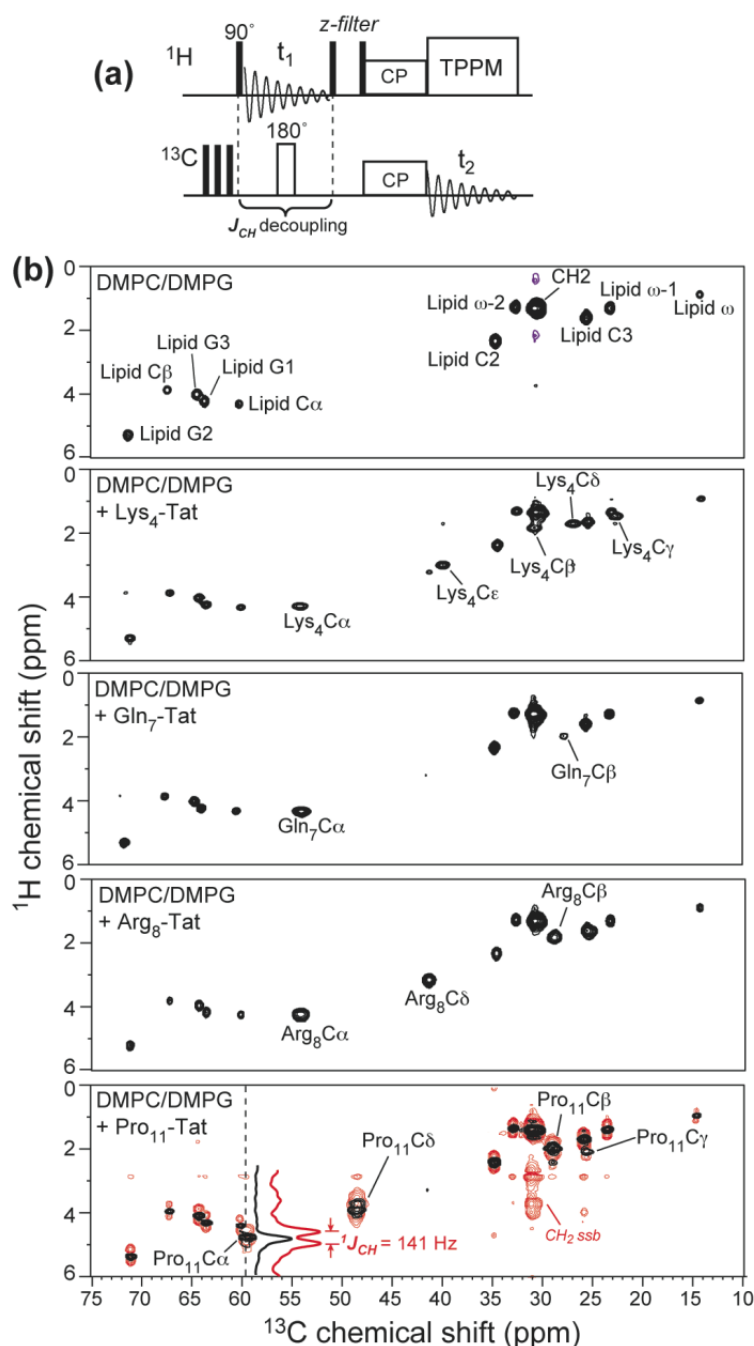


Fig. 6.2. 2D ^1H - ^{13}C HETCOR spectra of TAT in DMPC/DMPG bilayers at 303 K. (a) Pulse sequence of $^1J_{CH}$ -decoupled 2D HETCOR experiment. No ^1H homonuclear decoupling was applied during t_1 , thus only highly dynamic molecules can exhibit ^1H - ^{13}C cross peaks. (b) $^1J_{CH}$ -decoupled HETCOR spectra (black) of the DMPC/DMPG membrane without and with various site-specifically labeled TAT. The spectrum in red in the bottom panel is the HETCOR spectrum of Pro $_{11}$ -TAT without $^1J_{CH}$ decoupling. A 141 Hz $^1J_{CH}$ splitting of Pro $_{11}$ C α peak was observed. The C α ^1H cross section was compared between the $^1J_{CH}$ -decoupled and undecoupled spectra.

To observe how the narrow linewidths of TAT at high temperature transition to broad linewidths at low temperature, we measured the 1D ^{13}C and ^{15}N spectra of TAT as a function of temperature. **Fig. 6.3a, b** shows ^{13}C and ^{15}N spectra of Arg₈-labeled TAT bound to DMPC/DMPG bilayers from 303 K to 233 K. The Arg₈ signals were sharp at 303 K: the limiting ^{13}C linewidths were sufficiently small that ^{13}C - ^{13}C scalar-splittings of ~ 40 Hz were observed for many sites such as C α . The peptide signals became undetectable around 283 K, and became broad and strong at 233 K, with 3.5 – 4.8 ppm linewidths for ^{13}C and a 12 ppm linewidth for N α . Similar trends were observed for the other labeled residues. For the backbone C α , the low-temperature linewidth of Arg₈ covers the entire range of helix to sheet conformations (**Fig. 6.3c**). We further compared the TAT linewidths to several other membrane peptides, including penetratin, the β -sheet antimicrobial peptide PG-1 (29), and the α -helical influenza M2 transmembrane peptide (33). Among these peptides, TAT exhibits the narrowest linewidths at high temperature and the largest linewidths at low temperature (**Fig. 6.3d**), indicating that TAT undergoes faster exchange among a wider range of conformations at high temperature, thus giving rise to sharp signals averaged at the random coil chemical shifts. Lowering the temperature freezes the motion and captures all conformation-dependent chemical shifts.

Thus, the broad low-temperature linewidths reflect the large conformational space sampled by TAT. While it is difficult to quantify the exact conformational distribution, compared to the structurally defined β -sheet PG-1 and α -helical M2, the TAT structure is almost completely random. Comparison with PG-1 and M2 also indicates that the contribution of gel-phase membrane disorder is minor compared the intrinsic disorder of the peptide. Furthermore, the possibility that freezing changed the TAT conformation can be ruled out, since the average chemical shift frequencies were unchanged between high and low temperatures (with the slight exception of Pro₁₁ C α).

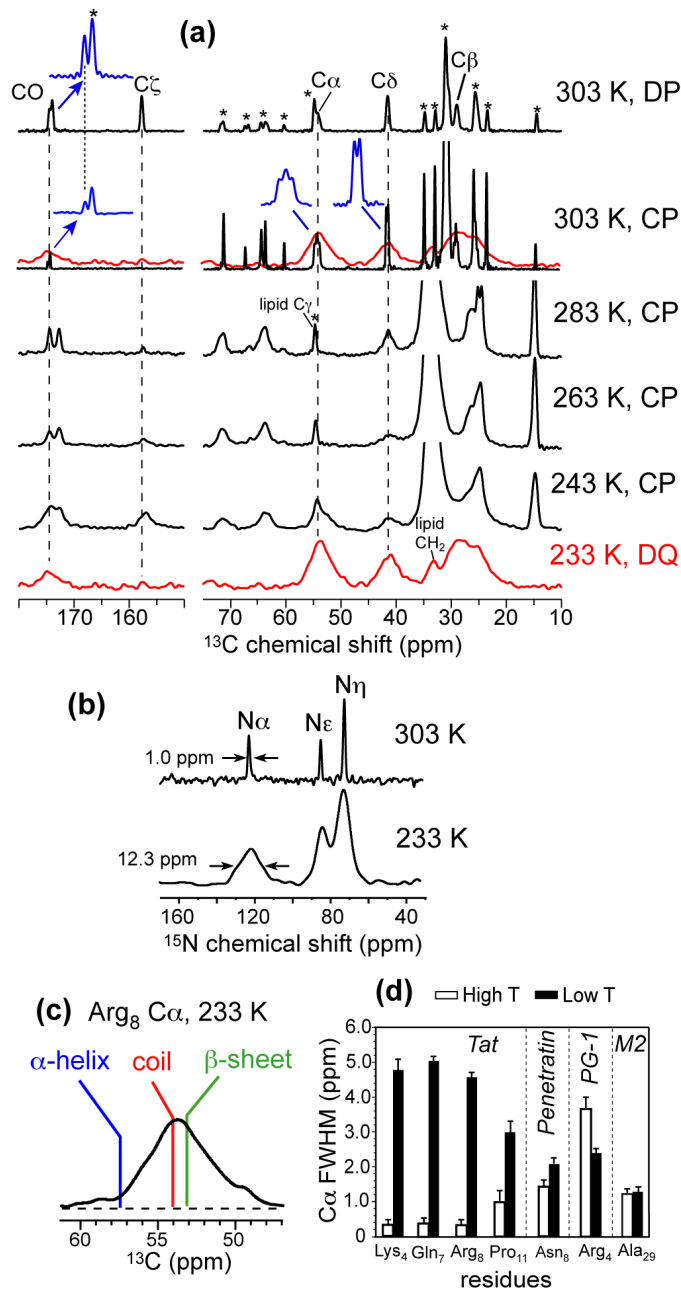


Fig. 6.3. Temperature-dependent TAT linewidths in DMPC/DMPG membranes. (a) ^{13}C MAS spectra from 303 K to 233 K for Arg₈-TAT. Stars denote lipid peaks. Most spectra were measured by cross polarization (CP). A 303 K spectrum was measured by ^{13}C direct polarization (DP). A 233 K ^{13}C DQ-filtered spectrum gives pure peptide peaks and linewidths. ^{13}C - ^{13}C J splittings were resolved for some peaks at 303 K, as shown in expanded regions in blue. (b) ^{15}N spectra of Arg₈-TAT at 303 K (by DP) and 233 K (by CP). (c) The C α peak of Arg₈ at 233 K from the DQ spectrum spans the chemical shift range for canonical secondary structures. (d) Comparison of C α linewidths of TAT, penetratin, PG-1, and the influenza M2 peptide in lipid bilayers at high and low temperatures.

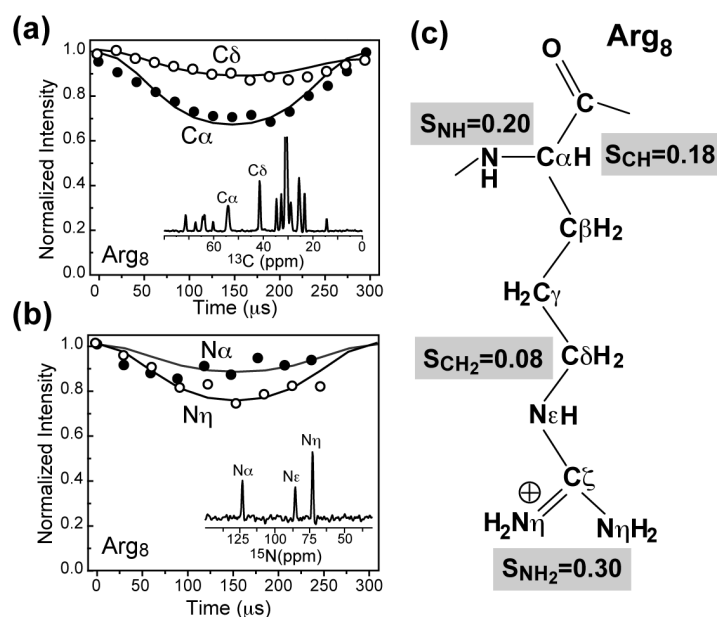


Fig. 6.4. C-H and N-H dipolar couplings of Arg₈-TAT in DMPC/DMPG membranes at 303 K. (a) C α and C δ C-H DIPSHIFT curves. (b) N α and N η N-H DIPSHIFT curves. (c) Arg₈ order parameters from the measured dipolar couplings. The lowest order parameters were observed for the middle of the sidechain, while the guanidinium moiety and the backbone exhibit higher order parameters.

To quantify the dynamics of TAT in the lipid membrane, we measured ^{13}C - ^1H and ^{15}N - ^1H dipolar couplings and the corresponding order parameters at 303 K using 2D DIPSHIFT experiments. Order parameters indicate the amplitude of motion. A maximum order parameter of 1 corresponds to the rigid limit while a minimum order parameter of 0 indicates large-amplitude, isotropic motion. **Fig. 6.4** shows representative dipolar coupling data of the membrane-bound TAT. Low order parameters of 0.14-0.20 were found for the peptide backbone (**Table 6.2**), comparable to the order parameters of the middle portion of the lipid molecules (34), indicating that the peptide undergoes large-amplitude motion. Interestingly, the Arg₈ order parameters decrease from N α ($S_{\text{NH}} = 0.20$) to C δ ($S_{\text{CH}} = 0.08$) but then reverse the trend and increase to N η ($S_{\text{NH}}=0.30$), indicating that two relatively rigid ends of the residue flank a more mobile aliphatic middle (**Fig. 6.4c**). The larger order parameters of the guanidinium moiety immediately suggest stabilizing interactions with the lipid headgroups. TAT also exhibits long ^1H $T_{1\rho}$ relaxation times of 10 – 30 ms (**Table 6.3**), indicating that the large-amplitude motions occur at rates far exceeding 10^6 s^{-1} .

Table 6.2. ^{13}C - ^1H and ^{15}N - ^1H dipolar couplings (kHz) and order parameters of TAT in DMPC/DMPG membranes at 303 K.

Residue	Site	δ (ppm)	XH_n	ω_{XH}^a	S_{XH}
Arg ₈	N α	123.1	NH	2.13	0.20
	N η	73.0	NH ₂	3.19	0.30
	C α	54.2	CH	4.09	0.18
	C β	28.9	CH ₂	3.41	0.15
	C δ	41.4	CH ₂	1.82	0.08
Pro ₁₁	C α	59.7	CH	3.18	0.14
	C β	28.9	CH ₂	3.86	0.17
	C δ	48.7	CH ₂	4.54	0.20
Lipids	C α	60.3	CH ₂	2.72	0.12
	G ₂	71.4	CH	4.31	0.19
	C ₂	34.7	CH ₂	4.77	0.21
	(CH ₂) _n	31.0	CH ₂	5.68	0.25

^a ω_{XH} is the true dipolar couplings after taking into account various scaling factors in the pulse sequence. The rigid-limit couplings used for calculating the order parameters are 10.6 kHz for N-H and 22.7 kHz for C-H dipolar couplings.

Table 6.3. ^1H $T_{1\rho}$ relaxation times (ms) of TAT and penetratin in DMPC/DMPG membranes at 303 K, measured with a ^1H effective spin-lock field of 61.2 kHz.

Peptide	Residue	Site	$T_{1\rho}$ (ms)
TAT (48-60)	Arg ₈	C α	11.6
		C β	11.3
		C δ	29.3
	Pro ₁₁	C α	14.9
		C β	8.8
		C δ	7.0
Penetratin	Ile ₃	C α	3.0
		C δ	4.9
		C ϵ	6.2

Interaction of TAT with lipid membranes

To probe whether TAT binding causes membrane disorder, we measured ^{31}P spectra of oriented lipid bilayers of several compositions in the presence of increasing amounts of the peptide.

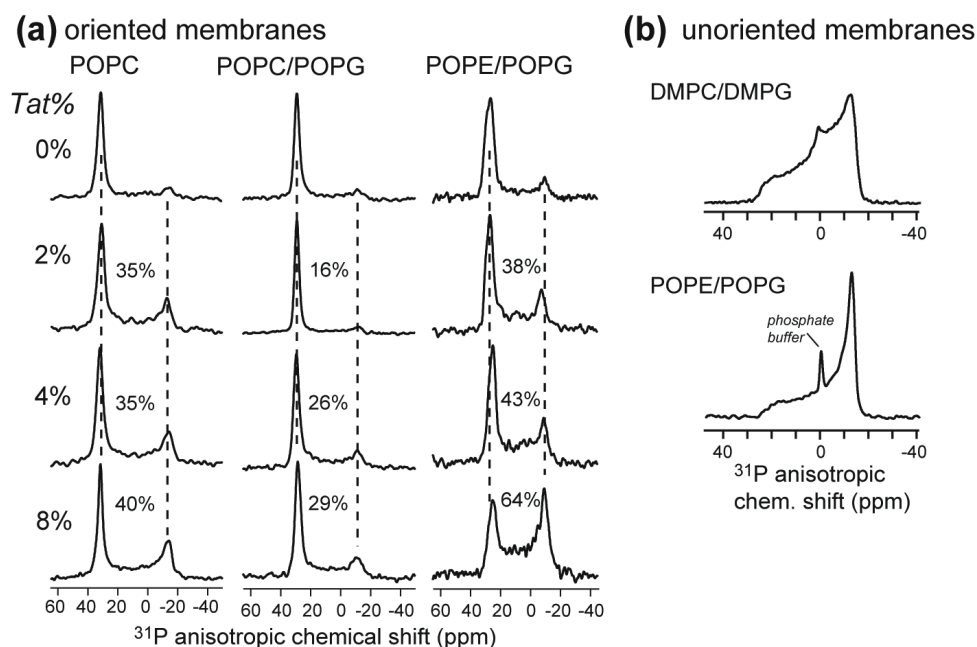


Fig. 6.5. Effects of TAT on the membrane structure. (a) Static ^{31}P spectra of glass-plate oriented lipid membranes with varying mole concentrations of TAT. Three membrane compositions, POPC, POPC/POPG (8:7) and POPE/POPG (8:7), were examined. The percentage of intensity in the 12 to -27 ppm range is indicated for each spectrum to denote the amount of membrane disorder. No isotropic signal near 0 ppm was observed in any spectra. (b) Static ^{31}P spectra of unoriented DMPC/DMPG (8:7) membrane and POPE/POPG (8:7) membranes containing 6 mol% TAT. The isotropic peak at 1.6 ppm is the phosphate buffer peak. All ^{31}P spectra were measured at 296 K.

Fig. 6.5 shows the effects of TAT on both the neutral zwitterionic POPC membrane and two anionic membranes, POPC/POPG (8:7) and POPE/POPG (8:7). Up to 8 mol% peptide, the POPC and POPC/POPG membranes remain largely well ordered, as shown by the high 0° peak at ~ 30 ppm and the low 90° peak of the powder pattern at -15 ppm, which is indicative of misalignment of the membrane. The lack of an isotropic peak at 0 ppm indicates that the membrane remains lamellar and intact. For the POPE/POPG membrane, higher powder intensities were observed compared to the other two membranes, but the isotropic peak is still absent. The lack of membrane disruption was further confirmed by static ^{31}P spectra of unoriented DMPC/DMPG and POPE/POPG membranes containing 6% TAT, where regular uniaxial powder lineshapes were observed (**Fig. 6.5b**). The minor isotropic peaks were attributed to the phosphate buffer. The lack of isotropic disorder is consistent with previously reported ^{31}P NMR spectra of unoriented POPC/POPG (3:1) membranes (32)

containing TAT, and is also consistent with the ability of this cell-penetrating peptide to cross the membrane without damaging its integrity.

Depth of insertion of TAT in lipid bilayers from ^1H spin diffusion

To determine how deeply TAT is inserted into the lipid bilayer, we carried out ^{13}C -detected ^1H spin diffusion experiments from water and lipids to the peptide (23). The distance between the source protons and protein protons determines the intensities of the intermolecular cross peaks. Since TAT is similarly mobile as lipids at ambient temperature, the dipolar-mediated ^1H spin diffusion process is similarly inefficient in the peptide as in the soft lipid matrix. Therefore, spin diffusion cross peak intensities depend on the distances of individual residues from the source protons. The site-specific nature of the depth information for the mobile TAT differs from the case of large immobile membrane proteins, where rapid spin diffusion within the protein largely removes the site-resolution of the depth, and only the shortest distance between the protein and the source protons can be obtained (23).

Fig. 6.6 shows representative ^{13}C -detected ^1H spin diffusion spectra of Arg₈- and Pro₁₁-TAT, measured with a ^1H spin diffusion mixing time of 225 ms and 144 ms, respectively. Weak cross peaks were observed between the lipid chain CH₂ protons at 1.3 ppm and the peptide ^{13}C signals. The mixing time of 100-200 ms is modest for the highly dynamic TAT with low spin diffusion coefficients. For comparison, immobilized DNA bound to the surface of cationic lipid membranes showed no cross peaks with the lipid chain protons until after ~400 ms, even though the spin diffusion coefficient of the rigid DNA rods is much larger than TAT (23). Thus, if TAT were similarly surface-bound as DNA, ~20 Å from the center of the membrane, then it will not exhibit any cross peaks with the lipid chain protons in the short mixing times used here. Therefore, the presence of the lipid-TAT cross peaks within the modest mixing time is strong qualitative evidence that TAT binds inside the lipid bilayer rather than lying on the membrane surface.

Fig. 6.6 shows strong water cross peaks at 4.7 ppm for Arg₈ but not Pro₁₁. **Fig. 6.7** compares the water region of the ^{13}C - ^1H 2D spectra for all sites studied. Interestingly, all polar residues containing labile protons – Lys₄, Gln₇ and Arg₈ - exhibited water cross peaks, while the hydrophobic Pro₁₁ without any exchangeable protons did not. This difference indi-

cates that hydrogen exchange is necessary for water-protein spin diffusion cross peaks to occur, consistent with many recent studies of the mechanism of water-protein magnetization transfer (35-37). Thus, Pro₁₁ is not necessarily further away from water than the other residues. Overall, the strong water cross peaks with the peptide indicate that TAT is not deeply inserted into the bilayer.

The coexistence of water and lipid cross peaks with TAT is most consistent with a location of the peptide in the glycerol backbone and headgroup region of the membrane. This interfacial location inside the membrane is further supported by the fact that TAT enhanced the water-to-lipid spin diffusion of the POPE/POPG membrane. **Fig. 6.8** shows that the lipid headgroup C α and acyl chain C2 have stronger cross peaks with water in the presence of TAT than in its absence, which is not possible if TAT were on the surface of the membrane.

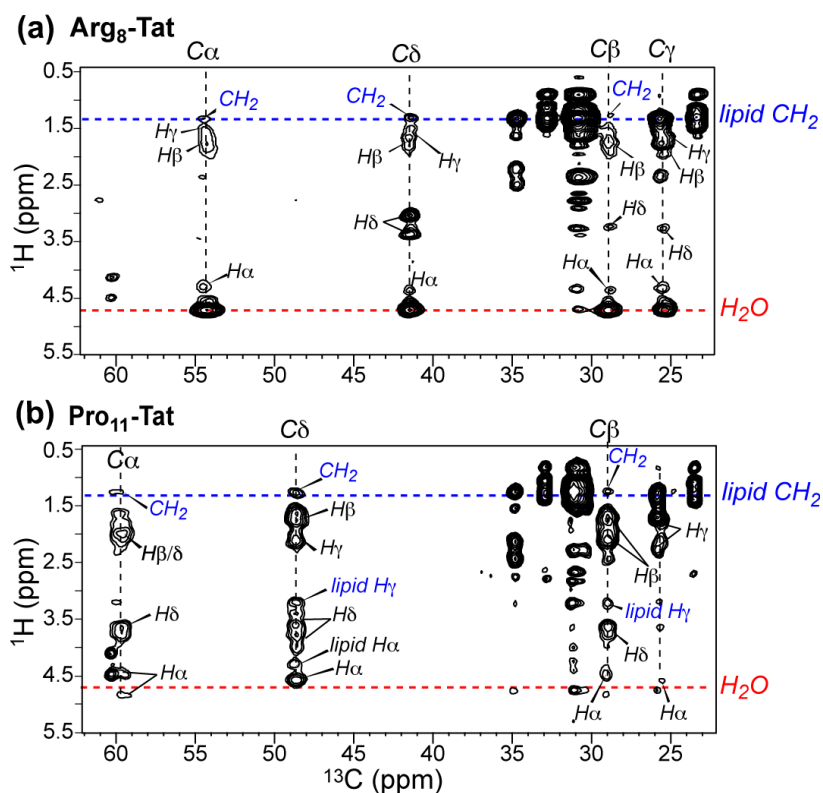


Fig. 6.6. (a) 2D ^{13}C -detected ^1H spin diffusion spectra of DMPC/DMPG-bound TAT at 303 K. (a) Arg₈-TAT spectrum measured with 225 ms spin diffusion. Water and lipid CH_2 cross peaks are colored. (b) Pro₁₁-TAT spectrum with a mixing time of 144 ms. No water cross peaks (37) but clear lipid CH_2 cross peaks were detected.

The exact distance of TAT to the center of the membrane cannot be quantified by observing cross peak buildup intensities as a function of mixing time due to the lack of well-calibrated spin diffusion coefficients for dynamic molecules. Nevertheless, one can obtain some insights based on the relative intensities of the water-peptide and lipid-peptide cross peaks. In ~40% hydrated membrane samples, the number of water protons is about twice the number of lipid CH₂ protons. Previous calibrations of water and lipid-chain spin diffusion coefficients indicated that the water spin diffusion coefficient is about 10-fold larger than the lipid chain diffusion coefficient because of the faster translational motion of water (23, 38). Thus, the water-peptide cross peak should be higher than the lipid-peptide cross peak even if a residue is at comparable distances to the membrane surface water and to the hydrophobic chains. Thus, the presence of a lipid-TAT cross peak at all is a strong indication of the membrane-immersed nature of TAT.

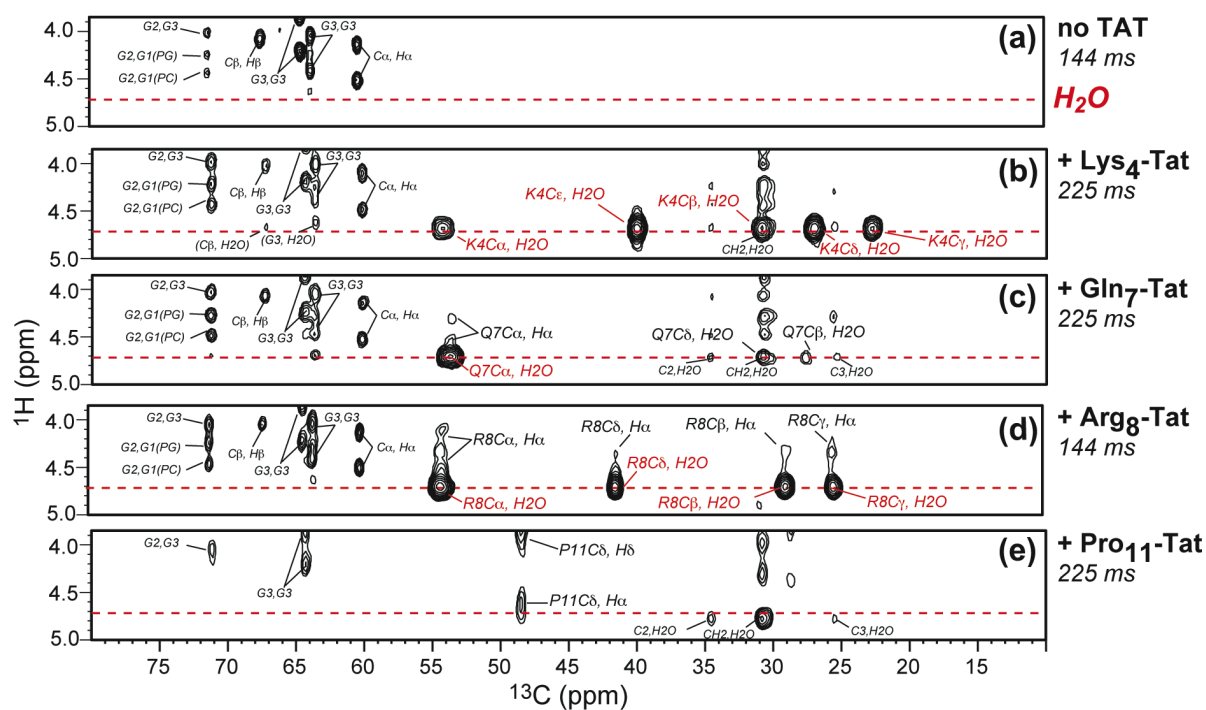


Fig. 6.7. 2D ¹³C-detected ¹H spin diffusion spectra of DMPC/DMPG (8:7) membranes with and without TAT. (a) Without TAT. (b) With Lys₄-labeled TAT. (c) With Gln₇-labeled TAT. (d) With Arg₈-labeled TAT. Water-peptide cross peaks were detected in (b-d). (e) With Pro₁₁-labeled TAT with a mixing time of 225 ms. No Pro₁₁-water cross peaks were observed.

Site-specific distances to the membrane surface from ^{13}C - ^{31}P REDOR

To confirm the interfacial location of TAT, we carried out ^{13}C - ^{31}P distance measurements at low temperature using REDOR. If TAT were inserted into the hydrophobic core of the bilayer, long ^{13}C - ^{31}P distances or slow dipolar dephasing would be expected, as is the case for the lipid chain ^{13}C signal. The REDOR experiments were conducted at ~ 230 K to completely freeze the dynamics of both the DMPC/DMPG membrane and the peptide. The ^{31}P spectra at this temperature give a span of 197 ppm (**Fig. S6.1**), which is the rigid limit for the ^{31}P chemical shift tensor (29).

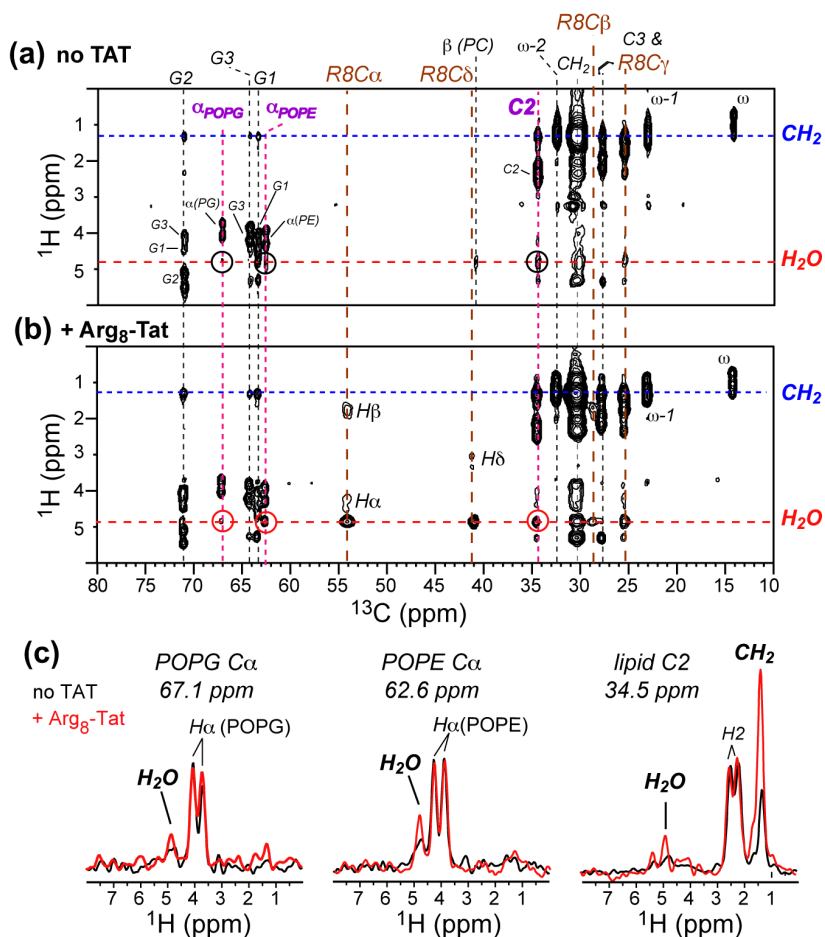


Fig. 6.8. 2D ^{13}C -detected ^1H spin diffusion spectra of POPE/POPG (8:7) membranes with a mixing time of 144 ms. (a) Without TAT. Only very weak water-lipid cross peaks were observed. (b) With Arg_8 -labeled TAT (P/L = 1:15), showing stronger water-lipid cross peaks. (c) ^1H cross sections at several lipid ^{13}C frequencies. The TAT-free spectrum is in black and the TAT-containing spectrum is in red. TAT enhances the water-lipid cross peaks, indicating that the peptide is inserted into the membrane. All spectra were measured at 303 K under 5 kHz MAS.

Fig. 6.9 shows the ^{13}C - ^{31}P REDOR data of the backbone and sidechain sites of Arg₈ and Pro₁₁. Relatively short backbone ^{13}C - ^{31}P distances of 5.7 – 6.6 Å were observed, consistent with the ^1H spin diffusion result that the peptide backbone lies in the glycerol backbone region of the membrane-water interface. Natural abundance lipid signals were corrected for both the Arg₈ CO peak and the Pro₁₁ C α peak. For the guanidinium C ζ of Arg₈, a 1 : 1 combination of 4.1 Å and 5.5 Å distances fit the data well (**Fig. 6.9b**). The former is at the lower limit of the possible distance between the guanidinium and the lipid phosphate, and places the two groups within hydrogen-bonding contact of each other (29, 39).

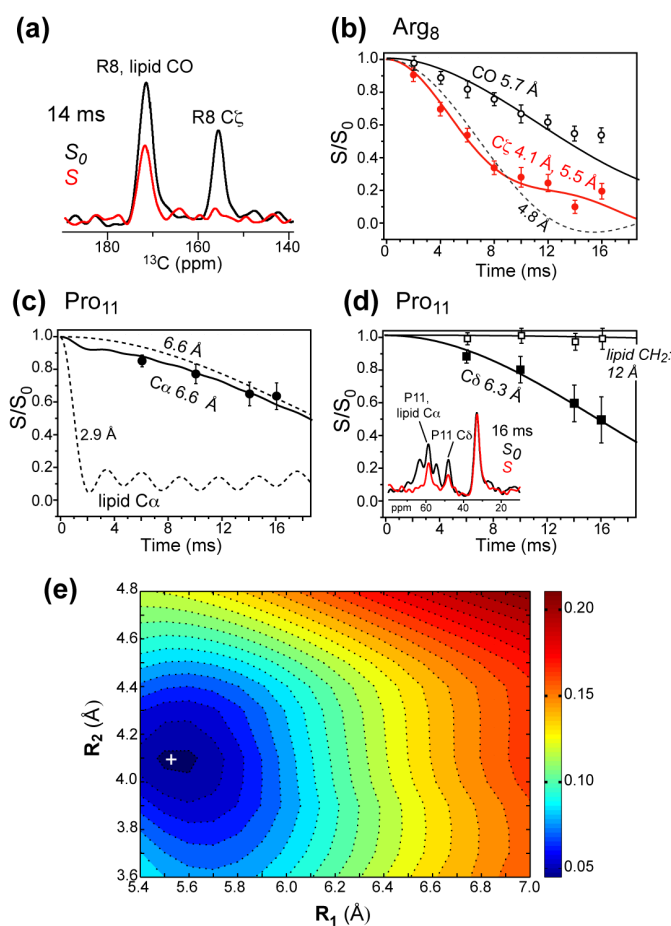


Fig. 6.9. ^{13}C - ^{31}P REDOR data of DMPC/DMPG-bound TAT at 230 K. (a) Representative REDOR control (S_0) and dephased (S) spectra. (b) REDOR data and simulation for Arg₈ CO and C ζ . The C ζ data is best-fit fit by a 1:1 ratio of 4.1 Å and 5.5 Å. (c) REDOR data and best fit for Pro₁₁ C α . The lipid C α contribution (7% of full intensity) was taken into account by a fixed distance of 2.9 Å. (d)

REDOR data and best fit for Pro₁₁ C δ . (e) RMSD between the simulated and experimental REDOR curves of Arg₈ C ζ to obtain the best-fit distances for C ζ in (b).

Thus, the Arg residues in TAT interact with the negatively charged lipid headgroups in a similar fashion to Arg-rich antimicrobial peptides (29, 40). Since the superposition of two distances fits the C ζ data well, there is no sign of a broad distance distribution, suggesting that guanidinium-phosphate ion pair interaction, rather than the peptide backbone conformation, is the determining factor for the Arg sidechain conformation.

6.5 Discussion

Depth and thermodynamics of insertion of TAT into lipid membranes

The ¹H spin diffusion and ¹³C-³¹P distance data indicate that TAT binds inside the DMPC/DMPG (8:7) bilayer in the glycerol backbone and headgroup region of the membrane-water interface (**Fig. 6.10**). This location is consistent with the temperature dependence of the ¹³C and ¹⁵N spectra (**Fig. 6.3**), since exchange broadening of TAT signals coincided with the membrane phase transition. This depth is also consistent with molecular dynamics simulations of TAT and the related CPP penetratin (41, 42).

It is interesting to consider the free energies of TAT insertion into the membrane-water interface. Using the Wimley-White interfacial scale developed for zwitterionic POPC bilayers (43), an energy barrier of about 9 kcal/mol against insertion would be predicted. However, the interfacial scale derived from neutral POPC bilayers does not account for strong electrostatic attraction between cationic peptides and highly anionic membranes as used in this study. Using isothermal titration calorimetry experiments, Seelig and coworkers characterized the thermodynamics of TAT binding to anionic membranes in detail, and found that the free energy of binding of TAT to 25% anionic membranes in 100 mM salt solution was about 80% electrostatic and 20% hydrophobic, with a total Gibbs free energy of -5.2 kcal/mol (32). The NMR samples used here contain less salt (10 mM) and more (~50%) anionic lipids, thus the binding energy should be even more negative or favorable. Similar to TAT, oligoarginine peptides also showed a significant electrostatic component in their binding energies (44).

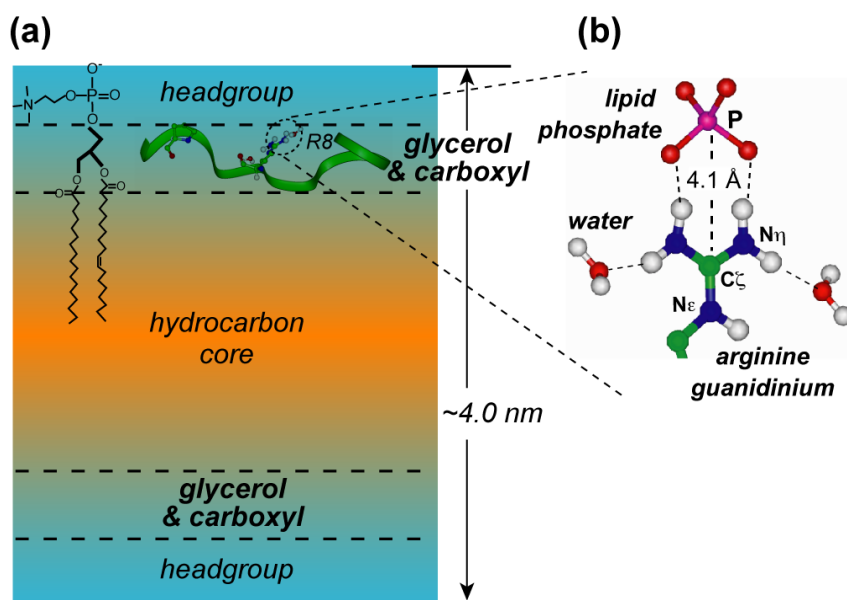


Fig. 6.10. Model of TAT structure and dynamics in DMPC/DMPG bilayers. The random coil peptide is inserted into the bilayer at the glycerol backbone region, outside the hydrophobic core, and is stabilized by intermolecular hydrogen bonds with lipid phosphates and water. The glycerol region has intermediate dielectric constant and accommodates TAT through the polar phosphate and carboxyl groups, which can act as hydrogen bond acceptors for the guanidinium.

In addition to the electrostatic attraction, ^{13}C - ^{31}P REDOR experiments found tight association of the Arg₈ guanidinium group with the lipid phosphates, similar to a number of other Arg-rich CPPs and antimicrobial peptides (12, 29, 40). A C ζ -P distance of 4-5 Å indicates hydrogen bonding between the guanidinium N-H and the lipid P-O groups. The importance of this hydrogen bonding was demonstrated for the antimicrobial peptide PG-1, where mutation of the guanidinium to dimethylated guanidinium weakened the antimicrobial activity by 3-fold and changed the oligomeric structure and orientation of the peptide in the lipid bilayer (40). Each guanidinium ion can form up to five hydrogen bonds with lipid phosphates or water. Thus, the hexa-Arg TAT can form as many as thirty hydrogen bonds from the Arg sidechains. If each hydrogen bond formation gives a favorable free energy change of -0.5 kcal/mol (45), then the total free energy change can be as much as -15 kcal/mol in favor of binding, which would greatly stabilize TAT at the membrane-water interface. Therefore, the combined electrostatic attraction and hydrogen bonding effects should be more than sufficient to overcome Born repulsion and facilitate TAT insertion into the

glycerol backbone region of the membrane-water interface. An increasing number of MD simulations also pointed out the importance of guanidinium-phosphate and guanidinium-water interactions for reducing the free energy cost of inserting Arg residues into the lipid membrane (42, 46-48).

The location of TAT is deeper than polylysine peptides, which was found by monolayer pressure and area measurements to lie on the surface of anionic lipid monolayers (49). Differences in the experimental conditions as well as the intrinsic membrane affinities of the two peptides most likely account for the observed depth difference. The polylysine measurements were carried out in 33% negatively charged membranes in 100 mM salt (49), while the bilayer samples in the present NMR study contained ~50% anionic lipids and only 10 mM salt. A lower fraction of acidic lipids reduces the electrostatic attraction while a higher salt concentration shields the electrostatic attraction between the peptide and the membrane. Thus the polylysine peptides are expected to have weaker membrane binding than the TAT peptide under the conditions of the two studies. The sensitivity of membrane binding to salt concentration is well known, and is exemplified by the fact that the free energies of polylysine binding decreased from -1.5 kcal/mol to -7 kcal/mol from 500 mM to 50 mM salt (49). The polylysine binding study also used lipid monolayers, where the lack of a distal membrane surface, with its concomitant anionic lipid headgroups, may weaken the propensity of the polylysines to insert into the membrane. In addition to these experimental differences, there is also a real difference in the affinity of Arg-rich and Lys-rich cationic peptides for the membrane interior. It is well known that Lys substitution for Arg in cell-penetrating peptides abolishes the membrane translocation ability (50, 51). An increasing number of recent studies of CPPs and antimicrobial peptides suggested that the structural basis for this difference may lie in the ability of guanidinium to form hydrogen-bond-stabilized bidentate complexes with lipid phosphates (12, 29, 40, 52), which cannot be achieved by the mobile amine of the Lys sidechains.

Taken together, the interfacial location of the Arg-rich TAT in the lipid bilayer correlates well with the membrane translocation ability of the peptide, and can be attributed to the strong electrostatic attraction between TAT and the anionic lipid membranes as well as hydrogen-bond stabilization of the Arg residues by the lipid phosphates and water.

TAT perturbation of lipid membranes

³¹P NMR spectra of both neutral and anionic lipid membranes in the presence of TAT showed little isotropic disorder. The observation is reproduced in both aligned membranes and unoriented vesicle samples (**Fig. 6.5**). This finding suggests that TAT binding does not significantly perturb the lamellar structure of the lipid bilayer. Interestingly, a detailed ³¹P NMR characterization of TAT binding as a function of membrane composition showed that the isotropic disorder is a sensitive function of the acyl chain saturation and temperature (53). Low-melting lipids such as DLPC and POPC did not exhibit membrane disruption by TAT, while high-melting DMPC and DPPC bilayers were. Moreover, the non-lamellar disorder was only present in zwitterionic bilayers and not in anionic bilayers. The present use of unsaturated lipids in all three membrane series for the oriented ³¹P NMR experiments thus precluded the observation of any potential isotropic features. Our depth and conformational experiments were conducted in negatively charged lipid membranes, thus similarly precluding the observation of membrane disorder. When we applied two cycles of heating and cooling to the TAT-containing DMPC/DMPG (8:7) membrane sample, we did not observe an isotropic peak (**Fig. S6.2**), which confirmed the lack of significant membrane disorder induced by thermal history.

Interestingly, an MD simulation of HIV TAT in a neutral DOPC bilayer as a function of peptide/lipid molar ratios found transient pores at high peptide concentrations (42). Based on these simulations, Hecce and Garcia proposed that the mechanism of translocation involves membrane thinning, reorientation of the lipids near the peptide, and attraction of TAT to lipid headgroups on the distal (far) side of the membrane. The ¹³C-³¹P distances measured here support the latter two proposals. However, the lack of isotropic ³¹P signals indicates the absence of long-lasting pores, although our data, which describes the equilibrium state of the peptide, does not rule out the existence of transient pores during translocation. One possibility is that the Arg-phosphate salt bridge interaction may slow down the fast lipid lateral diffusion necessary for observing an isotropic signal, so that membrane defects may be present but undetectable in the ³¹P NMR spectra. However, we do not think this scenario is likely, because the salt bridge interaction is too weak (with a guanidinium Nη order parameter of 0.30) to retard the lipid diffusion. Moreover, similar Arg-phosphate salt bridge

interactions were observed in antimicrobial peptides such as PG-1 (29), which caused pronounced ^{31}P isotropic features (39, 54).

Random coil conformation of TAT in lipid bilayers

The temperature-independent random coil chemical shifts of TAT and the temperature-dependent linewidth changes provide a rare example of a truly dynamic random coil peptide in lipid membranes. The 2D INADEQUATE spectra at low temperatures (**Fig. 6.1**) exhibited fine structures for some sidechain peaks. However, the chemical shift differences between the multiple peaks of each site are small compared to the linewidths, thus they do not change the qualitative conclusion that the TAT adopts a random coil conformation in the lipid membrane.

While TAT is known to be unstructured in solution (30), the finding that it remains a random coil in the lipid bilayer is still surprising, since it is generally believed that unstructured peptides in solution acquire hydrogen-bonded canonical conformations upon membrane binding to reduce the number of polar N-H and C=O groups exposed to the membrane (45). In light of the lipid-peptide interaction data here, we propose that TAT remains random coil by substituting intramolecular hydrogen bonds by intermolecular ones with the lipid phosphates and water, and by residing in the membrane-water interface, which has a higher dielectric constant than the hydrocarbon region of the bilayer. The intermolecular Arg-phosphate interaction is not only revealed by the short guanidinium-phosphate distance but also by the fact that the guanidinium exhibits higher order parameters than the rest of the Arg sidechain. This lipid anchoring effect dovetails a recent solution NMR and MD simulation study of Arg sidechains in ribonuclease H, where the dynamics of the guanidinium Ne was found to be primarily governed by salt bridges and was decoupled from the dynamics of the rest of the aliphatic sidechain (55).

The random coil backbone should facilitate TAT interaction with multiple lipid headgroups, whose positions in the fluid bilayer are highly disordered. The completeness of the Arg₈ C ζ - ^{31}P REDOR dephasing (**Fig. 6.9**) confirms that all peptide molecules, instead of just a fraction, experience guanidinium-phosphate interactions. Finally, a random coil backbone reduces the hydrophobic surface of TAT and prevents any defined polar/apolar separa-

tion. In this way, the peptide may rapidly cross the bilayer instead of being retained permanently in the membrane, as is the case for amphipathic antimicrobial peptides. Since the intermolecular lipid-TAT and water-TAT hydrogen bonds can be formed for any phospholipid membranes, TAT is expected to adopt similar random coil structures in any anionic membranes. This prediction is supported by the fact that the same random coil chemical shifts were found in both DMPC/DMPG membranes and POPE/POPG membranes, even though PE membranes appear to permit more efficient translocation of TAT than PC membranes (52).

6.6 Conclusion

In summary, using solid-state NMR we found that HIV TAT(48-60) adopts a random-coil conformation and inserts into the glycerol backbone region of the membrane-water interface in anionic lipid bilayers. This structure is thermodynamically stabilized by electrostatic attraction with the anionic lipids, guanidinium-phosphate salt bridges and guanidinium-water hydrogen bonding. The highly dynamic TAT does not cause permanent damages to the membrane integrity, but may cause transient defects, as suggested by short guanidinium-phosphate distances. These results suggest that TAT translocation is an extremely rapid phenomenon that relies on transient interactions of the Arg sidechains with lipid phosphates of the distal leaflet. The equilibrium structure observed by solid-state NMR, showing the peptide lying at the membrane-water interface of both leaflets, is the structure after translocation. Catching the peptide “in action”, during translocation, may require independent experiments of the kind that has been used to probe transient macromolecular interactions and structural changes in solution (56, 57). We postulate that the role of the random coil conformation is to prevent the peptide from permanently residing in the hydrocarbon core of the lipid bilayer through hydrophobic interactions. The dynamic nature of TAT, together with the previously reported dynamic turn-rich conformation of penetratin, suggests that the Arg-rich CPPs differ from the Arg-rich amphipathic AMPs mainly by the presence or absence of intramolecular hydrogen-bonded conformations (14).

6.7 Acknowledgement

This work was supported by grant GM066976 from the National Institutes of Health (to M.H.).

6.8 Reference

1. Torchilin, V. P. (2008) Tat peptide-mediated intracellular delivery of pharmaceutical nanocarriers, *Adv. Drug Delivery Rev.* 60, 548.
2. Brooks, H., Lebleu, B., and Vives, E. (2005) Tat peptide-mediated cellular delivery: back to basics, *Adv. Drug Delivery Rev.* 57, 559.
3. Inomata, K., Ohno, A., Tochio, H., Isogai, S., Tenno, T., Nakase, I., Takeuchi, T., Futaki, S., Ito, Y., Hiroaki, H., and Shirakawa, M. (2009) High-resolution multi-dimensional NMR spectroscopy of proteins in human cells, *Nature* 485, 106-110.
4. Vives, E., Brodin, P., and Lebleu, B. (1997) A Truncated HIV-1 Tat Protein Basic Domain Rapidly Translocates through the Plasma Membrane and Accumulates in the Cell Nucleus, *J. Biol. Chem.* 272, 16010-16017.
5. Derossi, D., Joliot, A. H., Chassaing, G., and Prochiantz, A. (1994) The third helix of the Antennapedia homeodomain translocates through biological membranes, *J. Biol. Chem.* 269, 10444-10450.
6. Rothbard, J. B., Jessop, T. C., Lewis, R. S., Murray, B. A., and Wender, P. A. (2004) Role of membrane potential and hydrogen bonding in the mechanism of translocation of guanidinium-rich peptides into cells, *J. Am. Chem. Soc.* 126, 9506-9507.
7. Rothbard, J. B., Jessop, T. C., and Wender, P. A. (2005) Adaptive translocation: the role of hydrogen bonding and membrane potential in the uptake of guanidinium-rich transporters into cells, *Adv. Drug Delivery Rev.* 57, 495.
8. Fischer, R., Fotin-Mleczek, M., Hufnagel, H., and Brock, R. (2005) Break on through to the other side-biophysics and cell biology shed light on cell-penetrating peptides, *ChemBioChem.* 6, 2126-2142.
9. Hessa, T., Kim, H., Bihlmaier, K., Lundin, C., Boekel, J., Andersson, H., Nilsson, I., White, S. H., and von Heijne, G. (2005) Recognition of transmembrane helices by the endoplasmic reticulum translocon, *Nature* 433, 377-381.
10. Derossi, D., Calvet, S., Trembleau, A., Brunissen, A., Chassaing, G., and Prochiantz, A. (1996) Cell internalization of the third helix of the Antennapedia homeodomain is receptor-independent, *J. Biol. Chem.* 271, 18188-18193.
11. Binder, H., and Lindblom, G. (2003) Charge-dependent translocation of the Trojan peptide penetratin across lipid membranes, *Biophys. J.* 85, 982-995.
12. Su, Y., Mani, R., and Hong, M. (2008) Asymmetric insertion of membrane proteins in lipid bilayers by solid-state NMR paramagnetic relaxation enhancement: a cell-penetrating Peptide example, *J. Am. Chem. Soc.* 130, 8856-8864.

13. Su, Y., Doherty, T., Waring, A. J., Ruchala, P., and Hong, M. (2009) Roles of Arginine and Lysine Residues in the Translocation of a Cell-Penetrating Peptide from ^{13}C , ^{31}P , and ^{19}F Solid-State NMR, *Biochemistry* 48, 4587-4595.
14. Su, Y., Mani, R., Doherty, T., Waring, A. J., and Hong, M. (2008) Reversible sheet-turn conformational change of a cell-penetrating peptide in lipid bilayers studied by solid-state NMR, *J. Mol. Biol.* 381, 1133-1144.
15. Frankel, A. D., and Pabo, C. O. (1988) Cellular Uptake of the Tat Protein from Human Immunodeficiency Virus, *Cell* 55, 1189-1193.
16. Fawell, S., Seery, J., Daikh, Y., Moore, C., Chen, L. L., Pepinsky, B., and Barsoum, J. (1994) Tat-mediated delivery of heterologous proteins into cells, *Proc. Natl. Acad. Sci. U. S. A.* 91, 664-668.
17. Eguchi, A., Akuta, T., Okuyama, H., Senda, T., Yokoi, H., Inokuchi, H., Fujita, S., Hayakawa, T., Takeda, K., Hasegawa, M., and Nakanishi, M. (2001) Protein transduction domain of HIV-1 Tat protein promotes efficient delivery of DNA into mammalian cells, *J. Biol. Chem.* 276, 26204-26210.
18. Gennis, R. B. (1989) *Biomembranes: Molecular Structure and Function*, Springer, New York.
19. Hallock, K. J., Henzler Wildman, K., Lee, D. K., and Ramamoorthy, A. (2002) An innovative procedure using a sublimable solid to align lipid bilayers for solid-state NMR studies, *Biophys. J.* 82, 2499-2503.
20. Hohwy, M., Rienstra, C. M., Jaroniec, C. P., and Griffin, R. G. (1999) Fivefold symmetric homonuclear dipolar recoupling in rotating solids: application to double-quantum spectroscopy, *J. Chem. Phys.* 110, 7983-7992.
21. Takegoshi, K., Nakamura, S., and Terao, T. (2001) $\text{C-}^{13}\text{-H-}^1$ dipolar-assisted rotational resonance in magic-angle spinning NMR, *Chem. Phys. Lett.* 344, 631-637.
22. Hong, M. (1999) Solid-State Dipolar INADEQUATE NMR Spectroscopy with a Large Double-Quantum Spectral Width, *J. Magn. Reson.* 136, 86-91.
23. Huster, D., Yao, X. L., and Hong, M. (2002) Membrane Protein Topology Probed by ^1H Spin Diffusion from Lipids Using Solid-State NMR Spectroscopy, *J. Am. Chem. Soc.* 124, 874-883.
24. Hong, M., Gross, J. D., Rienstra, C. M., Griffin, R. G., Kumashiro, K. K., and Schmidt-Rohr, K. (1997) Coupling Amplification in 2D MAS NMR and Its Application to Torsion Angle Determination in Peptides, *J. Magn. Reson.* 129, 85-92.
25. Munowitz, M. G., Griffin, R. G., Bodenhausen, G., and Huang, T. H. (1981) Two-dimensional rotational spin-echo nuclear magnetic resonance in solids: correlation of chemical shift and dipolar interactions, *J. Am. Chem. Soc.* 103, 2529-2533.
26. Rhim, W. K., Elleman, D. D., and Vaughan, R. W. (1973) Analysis of multiple pulse NMR in solids, *J. Chem. Phys.* 59, 3740-3749.

27. Huster, D., Xiao, L. S., and Hong, M. (2001) Solid-State NMR Investigation of the dynamics of colicin Ia channel-forming domain, *Biochemistry* 40, 7662-7674.
28. Jaroniec, C. P., Tounge, B. A., Herzfeld, J., and Griffin, R. G. (2001) Frequency selective heteronuclear dipolar recoupling in rotating solids: accurate $(13)\text{C}$ - $(15)\text{N}$ distance measurements in uniformly $(13)\text{C}$, $(15)\text{N}$ -labeled peptides, *J. Am. Chem. Soc.* 123, 3507-3519.
29. Tang, M., Waring, A. J., and Hong, M. (2007) Phosphate-mediated arginine insertion into lipid membranes and pore formation by a cationic membrane peptide from solid-state NMR, *J. Am. Chem. Soc.* 129, 11438-11446.
30. Shojania, S., and O'Neil, J. D. (2006) HIV-1 Tat is a natively unfolded protein: the solution conformation and dynamics of reduced HIV-1 Tat-(1-72) by NMR spectroscopy, *J. Biol. Chem.* 281, 8347-8356.
31. Wang, Y., and Jardetzky, O. (2002) Probability-based protein secondary structure identification using combined NMR chemical-shift data., *Protein Sci.* 11, 852-861.
32. Ziegler, A., LiBlatter, X., Seelig, A., and Seelig, J. (2003) Protein Transduction Domains of HIV-1 and SIV TAT Interact with Charged Lipid Vesicles. Binding Mechanism and Thermodynamic Analysis, *Biochemistry* 42, 9185-9194.
33. Cady, S. D., and Hong, M. (2009) Effects of Amantadine Binding on the Dynamics of Bilayer-Bound Influenza A M2 Transmembrane Peptide Studied by NMR Relaxation, *J. Biomol. NMR* 45, 185-196.
34. Hong, M., Schmidt-Rohr, K., and Pines, A. (1995) Measurement of Signs and Magnitudes of C-H Dipolar Couplings in Lecithin, *J. Am. Chem. Soc.* 117, 3310-3311.
35. Lesage, A., Emsley, L., Penin, F., and Böckmann, A. (2006) Investigation of dipolar-mediated water-protein interactions in microcrystalline Crh by solid-state NMR spectroscopy, *J. Am. Chem. Soc.* 128, 8246-8255.
36. Lesage, A., Gardiennet, C., Loquet, A., Verel, R., Pintacuda, G., Emsley, L., Meier, B. H., and Bockmann, A. (2008) Polarization transfer over the water-protein interface in solids, *Angew. Chem., Int. Ed.* 47, 5851-5854.
37. Doherty, T., and Hong, M. (2009) 2D 1H - 31P solid-state NMR studies of the dependence of inter-bilayer water dynamics on lipid headgroup structure and membrane peptides, *J. Magn. Reson.* 196, 39-47.
38. Mani, R., Cady, S. D., Tang, M., Waring, A. J., Lehrer, R. I., and Hong, M. (2006) Membrane-dependent oligomeric structure and pore formation of a beta-hairpin antimicrobial peptide in lipid bilayers from solid-state NMR, *Proc. Natl. Acad. Sci. USA* 103, 16242-16247.
39. Tang, M., and Hong, M. (2009) Structure and Mechanism of Beta-Hairpin Antimicrobial Peptides in Lipid Bilayers from Solid-State NMR Spectroscopy, *Mol. Biosys.* 5, 317-322.

40. Tang, M., Waring, A. J., Lehrer, R., and Hong, M. (2008) Effects of Guanidinium-Phosphate Hydrogen Bonding on the Membrane-Bound Structure and Activity of an Arginine-Rich Membrane Peptide from Solid-State NMR Spectroscopy, *Angew. Chem. Int. Ed.* 47, 3202-3205.
41. Lensink, M. F., Christiaens, B., Vandekerckhove, J., Prochiantz, A., and Rosseneu, M. (2005) Penetratin-membrane association: W48/R52/W56 shield the peptide from the aqueous phase, *Biophys. J.* 88, 939-952.
42. Herce, H. D., and Garcia, A. E. (2007) Molecular dynamics simulations suggest a mechanism for translocation of the HIV-1 TAT peptide across lipid membranes, *Proc. Natl. Acad. Sci. U. S. A.* 104, 20805-20810.
43. Wimley, W. C., and White, S. H. (1996) Experimentally determined hydrophobicity scale for proteins at membrane interfaces, *Nat. Struct. Biol.* 3, 842-848.
44. Goncalves, E., Kitas, E., and Seelig, J. (2005) Binding of Oligoarginine to Membrane Lipids and Heparan Sulfate: Structural and Thermodynamic Characterization of a Cell-Penetrating Peptide, *Biochemistry* 44, 2692-2702.
45. White, S. H., and Wimley, W. C. (1999) Membrane protein folding and stability: physical principles, *Annu. Rev. Biophys. Biomol. Struct.* 28, 319-365.
46. Freitas, J. A., Tobias, D. J., von Heijne, G., and White, S. H. (2005) Interface connections of a transmembrane voltage sensor, *Proc. Natl. Acad. Sci. U.S.A.* 102, 15059-15064.
47. Li, L., Vorobyov, I., and Allen, T. W. (2008) Potential of mean force and pKa profile calculation for a lipid membrane-exposed arginine side chain, *J. Phys. Chem. B.* 112, 9574-9587.
48. MacCallum, J. L., Bennett, W. F., and Tieleman, D. P. (2008) Distribution of amino acids in a lipid bilayer from computer simulations, *Biophys. J.* 94, 3393-3404.
49. Ben-Tal, N., Honig, B., Peitzsch, R. M., Denisov, G., and McLaughlin, S. (1996) Binding of small basic peptides to membranes containing acidic lipids: theoretical models and experimental results, *Biophys. J.* 71, 561-575.
50. Wender, P. A., Mitchell, D. J., Pattabiraman, K., Pelkey, E. T., Steinman, L., and Rothbard, J. B. (2000) The design, synthesis, and evaluation of molecules that enable or enhance cellular uptake: peptoid molecular transporters, *Proc. Natl. Acad. Sci. U. S. A.* 97, 13003-13008.
51. Mitchell, D. J., Kim, D. T., Steinman, L., Fathman, C. G., and Rothbard, J. B. (2000) Polyarginine enters cells more efficiently than other polycationic homopolymers, *J. Pept. Res.* 56, 318-325.
52. Mishra, A., Gordon, V. D., Yang, L., Coridan, R., and Wong, G. C. L. (2008) HIV TAT Forms Pores in Membranes by Inducing Saddle-Splay Curvature: Potential Role of Bidentate Hydrogen Bonding, *Angew. Chem. Int. Ed. Engl.* 47, 2986-2989.

53. Afonin, S., Frey, A., Bayerl, S., Fischer, D., Wadhvani, P., Weinkauff, S., and Ulrich, A. S. (2006) The cell-penetrating peptide TAT(48-60) induces a non-lamellar phase in DMPC membranes, *ChemPhysChem* 7, 2134-2142.
54. Mani, R., Buffy, J. J., Waring, A. J., Lehrer, R. I., and Hong, M. (2004) Solid-State NMR Investigation of the Selective Disruption of Lipid Membranes by Protegrin-1, *Biochemistry* 43, 13839-13848.
55. Trbovic, N., Cho, J. H., Abel, R., Friesner, R. A., Rance, M., and Palmer, A. G. r. (2009) Protein side-chain dynamics and residual conformational entropy, *J. Am. Chem. Soc.* 131, 615-622.
56. Iwahara, J., and Clore, G. M. (2006) Detecting transient intermediates in macromolecular binding by paramagnetic NMR, *Nature* 440, 1227-1230.
57. Lee, M. K., Gal, M., Frydman, L., and Varani, G. (2010) Real-time multidimensional NMR follows RNA folding with second resolution, *Proc. Natl. Acad. Sci. U. S. A.* 107, 9192-9197.
58. Luca, S., Filippov, D. V., van Boom, J. H., Oschkinat, H., de Groot, H. J., and Baldus, M. (2001) Secondary chemical shifts in immobilized peptides and proteins: a qualitative basis for structure refinement under magic angle spinning, *J. Biomol. NMR* 20, 325-331.

Supporting Information

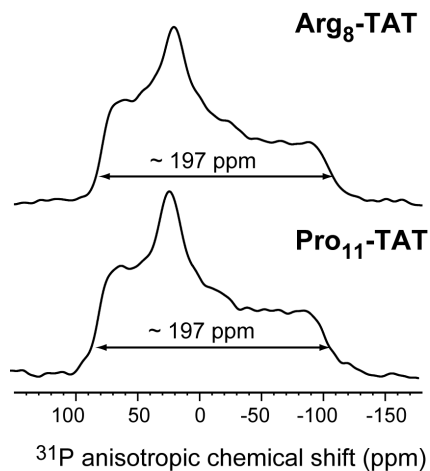


Figure S6.1. Static ^{31}P CP spectra of two TAT-containing DMPC/DMPG (8:7) membrane samples (P/L=1:15) used for ^{13}C - ^{31}P REDOR experiments. The spectra were measured at 230 K. The span of 197 ppm indicates completely immobilized lipid headgroups.

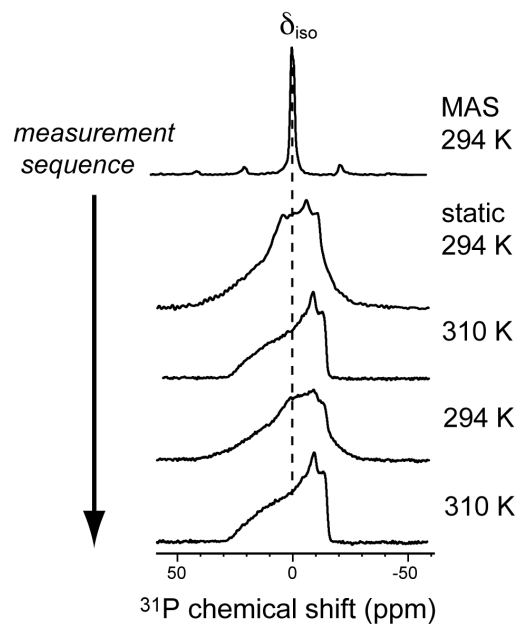


Figure S6.2. ^{31}P spectra of TAT-containing DMPC/DMPG (8:7) membranes at P/L=1:15. Spectra were measured on a 600 MHz NMR spectrometer. After two cycles of heating and cooling, no isotropic peak appeared, indicating that the lipid order is largely preserved independent of the thermal history.

Table S6.1. Different types of solid-state NMR experiments performed in this work.

Motivation	Experiment name	T (K)	MAS rate (kHz)	Sample
Membrane perturbation	Static ^{31}P DP	296	0	Oriented and unoriented membranes
Conformation	1D $^{13}\text{C}/^{15}\text{N}/^1\text{H}$ CP/DP	233-303	4-5	Unoriented membranes
	2D ^{13}C - ^{13}C DARR	233-303	5	
	2D ^{13}C - ^{13}C INADEQUATE	233	5.3	
	1D ^{13}C DQ filtered spectra	233	5.5	
	2D ^{13}C - ^1H HETCOR	303	5-8	
Dynamics	2D $^{13}\text{C}/^{15}\text{N}$ - ^1H DIPSHIFT	303	2.8, 3.4	
	1D ^{13}C -detected ^1H $T_{1\rho}$ (LG-CP)	303	7	
Insertion	2D ^{13}C -detected ^1H spin diffusion	303	5	
	1D ^{13}C - ^{31}P REDOR	233	4	

Chapter 7

Conformational Disorder of Membrane Peptides and Proteins Studied by Solid-State NMR Spectroscopy

A manuscript under review of Journal of Physical Chemistry B

Yongchao Su and Mei Hong

Department of Chemistry, Iowa State University, Ames, IA 50011

7.1 Abstract

A challenge in the application of solid-state NMR spectroscopy to membrane proteins and peptides is the relatively broad linewidths compared to solution NMR spectra. To understand the linewidth contributions to membrane protein spectra, we have measured the inhomogeneous and homogeneous linewidths of several well-studied membrane peptides under immobilized conditions. ^{13}C T_2 relaxation times of uniformly ^{13}C -labeled residues show that the homogeneous linewidths of the peptides are comparable to those of crystalline model compounds under identical ^1H decoupling and magic-angle-spinning conditions, indicating that the homogeneous linewidths are determined by conformation-independent factors, including residual dipolar coupling, J coupling and intrinsic T_2 relaxation. However, the membrane peptides exhibit larger apparent linewidths than the crystalline compounds, indicating conformational disorder. A cationic cell-penetrating peptide, the human immunodeficiency virus TAT, exhibits the largest apparent linewidths, which are about 5-fold larger than the homogeneous linewidths, while the transmembrane helix of the influenza M2 protein and the β -hairpin antimicrobial peptide PG-1 have moderately larger apparent linewidths than the crystalline compounds. These results are consistent with the random coil nature of the TAT peptide, which contrast with the intramolecularly hydrogen-bonded M2 and PG-1. Cross peak lineshapes of 2D double-quantum correlation spectra show that the conformational disorder can occur at the residue level and can result from three origins: lipid-peptide interaction, intrinsic structural disorder encoded in the amino acid sequence, and sidechain rotameric averaging. A particularly important lipid-peptide interaction for cationic membrane peptides is

guanidinium-phosphate salt bridge formation. Thus, NMR linewidths and lineshapes are useful for understanding the conformational disorder of membrane peptides and proteins.

7.2 Introduction

Solid-state NMR (SSNMR) spectroscopy has become a powerful probe of the molecular structure and dynamics of insoluble biological macromolecules such as membrane proteins, amyloid fibrils, and cell walls (1-7). A persistent challenge in high-resolution structure determination of these systems is spectral resolution. While biomolecules in solution have narrow linewidths due to their fast isotropic tumbling, solid systems without the benefit of such motion exhibit broad NMR linewidths. Under this condition strong orientation-dependent nuclear spin interactions such as chemical shift anisotropy (CSA) and dipolar couplings cause significant line broadening. Magic-angle-spinning (MAS) (8) and many hetero- and homo-nuclear dipolar decoupling techniques (9-14) eliminate most of this orientational broadening. Nevertheless, residual dipolar couplings between protons and heteronuclei due to imperfect decoupling still contribute sizeable linewidths, and dipolar couplings between isotopically enriched heteronuclei can broaden lines when MAS rates are insufficient. These coherent dipolar broadening mechanisms are ameliorated by higher magnetic fields (15), which reduce the relative contribution of dipolar coupling to the field-dependent chemical shift frequency. They are also reduced by faster MAS rates (14, 16) and chemical means of reducing the proton density. For example, protein perdeuteration followed by H/D exchange gives rise to much higher-resolution spectra than protonated analogs (17-19).

An incoherent source of line broadening that cannot be removed by radio-frequency (rf) pulses is transverse T_2 relaxation, which results from incoherent fluctuations of local magnetic fields due to molecular motion (20, 21). When motional rates are comparable to the strength of the dipolar decoupling field or the MAS rate, extreme line broadening occurs that abolishes the spectral intensity altogether. This intermediate-rate motional broadening has been studied in both small-molecule compounds (22, 23) and membrane peptides (24-26).

The third line broadening mechanism, which also cannot be refocused by rf pulses, is molecular conformational disorder. The structural distribution in disordered solids gives rise to multiple isotropic chemical shifts for each chemically unique nuclear spin, in the same

way that chemically inequivalent spins have different isotropic chemical shifts. This inhomogeneous line broadening causes characteristic lineshapes in 2D spectra (27, 28) and can be substantial, even if the homogeneous linewidths due to T_2 relaxation and residual dipolar coupling are small. The large difference between inhomogeneous and homogeneous linewidths has been exploited for developing J-coupling based polarization transfer experiments in solids (29, 30).

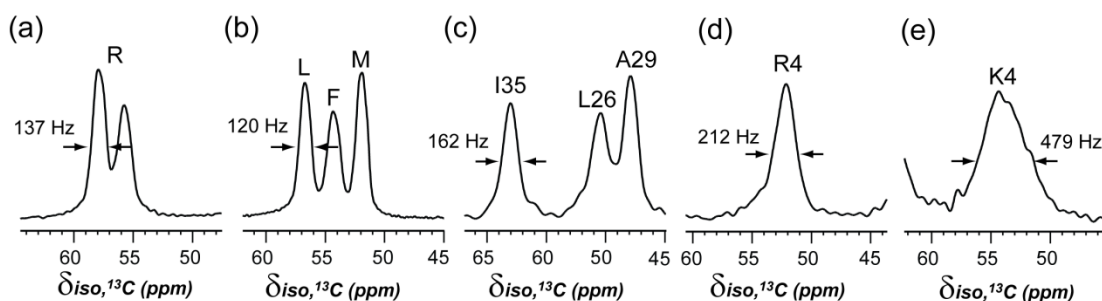


Fig. 7.1. Representative $C\alpha$ peaks from the ^{13}C CP-MAS spectra of (a) Arg · HCl at 296 K, (b) f-MLF-OH at 296 K, (c) LAGI-M2TM in viral membranes at 238 K, (d) Arg4 labeled PG-1 in POPE/POPG lipids at 238 K. (e) Lys4 labeled TAT in POPE/POPG lipids at 238 K.

To date, the line broadening mechanisms of only a few biological solids has been investigated in detail. These include the natural biopolymer wood cellulose (27, 28, 30), elastin (31), and a crystalline tripeptide, formyl-Met-Leu-Phe-OH (f-MLF-OH-OH) (32, 33). No explicit investigation of the linewidth contributions of membrane-bound peptides and proteins has been reported. The amphipathic lipid bilayer surrounding membrane proteins (34) presents a complex anisotropic environment, with a distribution of lateral pressures and dielectric constants across the bilayer normal (35) and tremendous thermal disorder for the lipid chains at physiological temperatures. Therefore, membrane-bound peptides and proteins have additional sources of conformational disorder compared to semi-crystalline molecules, globular proteins, and fibrous biopolymers. **Fig. 7.1** compares the ^{13}C MAS spectra of two crystalline small molecules, arginine hydrochloride (Arg · HCl) and f-MLF-OH-OH, with three membrane-bound peptides: the transmembrane (TM) domain of the influenza M2 protein (M2TM), the disulfide-bonded β -hairpin antimicrobial peptide PG-1, and the Arg-rich cell-penetrating peptide (CPP) HIV TAT. The membrane peptide spectra were recorded at

sufficiently low temperature, 238 K, to immobilize the peptide backbone and thus eliminate dynamic contributions to line broadening. To keep the contribution of coherent dipolar broadening the same among different samples, we applied the same ^1H decoupling field strength (71 kHz) and MAS spinning rate (7 kHz). Arginine hydrochloride and f-MLF-OH exhibit $\text{C}\alpha$ linewidths (full width at half maximum, FWHM) of 137 and 120 Hz, M2TM and PG-1 show modestly larger $\text{C}\alpha$ linewidths of 160 Hz and 212 Hz, but in contrast TAT gives an extremely large linewidth of 480 Hz.

Understanding the different sources of line broadening of membrane peptides is important both for developing new ways to enhance spectral resolution and for harvesting the structural information inherent in the linewidths and lineshapes. In this work, we investigate the line broadening mechanisms of these representative membrane peptides by measuring the apparent and homogeneous linewidths and by analyzing peak lineshapes in 2D correlation spectra (36). We analyze the linewidths at a moderate low temperature of about 240 K, where the backbones of these membrane peptides are immobilized in the gel phase of the membrane. Low-temperature membrane protein linewidths are interesting for both technological and structural reasons, because an increasing number of solid-state NMR experiments now utilize low temperature to enhance the spectral sensitivity (37) and to elucidate protein-folding pathways (38). Our experiments reveal several mechanisms of structural disorder that contribute to the inhomogeneous linewidths, and shed light on the relationship between dynamic conformational exchange at physiological temperature and the structural distribution at low temperature.

7.3 Materials and Methods

Sample Preparation

All phospholipids, including POPE, POPG, DMPC, DPPC, DPPE, and egg sphingomyelin (SPM) and cholesterol were purchased from Avanti Polar Lipids and used without further purification. Uniformly ^{13}C , ^{15}N -labeled Arg · HCl was purchased from Sigma-Aldrich. Fmoc-protected uniformly ^{13}C , ^{15}N -labeled amino acids were either prepared in-house (39) or purchased from Sigma-Aldrich and Cambridge Isotope Laboratories. All peptides, including PG-1 (RGGRLCYCRRRFCVCGR), the CPP domain of the HIV Tat

protein (residues 48-60, GRKKRRQRRRPPQ), and M2TM (residues 22-46, SSDPLVVAASIIGILHLILWILDRL), were synthesized using Fmoc chemistry and purified by HPLC.

Hydrated proteoliposomes were prepared in aqueous solution as described before [Cady, 2008 #40; Mani, 2006 #38]. Lipids were mixed in chloroform and dried under nitrogen gas. The lipid film was redissolved in cyclohexane and lyophilized to remove trace organic solvent. The lipid vesicles were prepared by suspending the dry powder in phosphate buffer and freeze-thawed for six cycles. For the water-soluble PG-1 and TAT, a peptide solution was directly added to the lipid vesicle solution and incubated overnight before ultracentrifugation. For the insoluble M2TM, the peptide was reconstituted into lipid bilayers by dialysis using octyl- β -D-glucopyranoside [Cady, 2008 #104]. All proteoliposomes have peptide/lipid molar ratios of 1: 15 or 1:12.5 and were hydrated to about 40% by mass using a pH 7.0 and 7.5 phosphate buffer.

All peptides contain uniformly ^{13}C and ^{15}N labeled residues. One PG-1 sample contained labeled Gly3 and Leu5 while another PG-1 sample contained labeled Arg4. Both samples were incorporated into POPE/POPG (3:1) membranes. One M2TM sample contained labeled Val27, Ser31, Gly34 and Asp44 (VSGD-M2TM) and was reconstituted into DMPC bilayers. Another M2TM sample contained Leu26, Ala29, Gly34 and Ile35 labels (LAGI-M2TM) and was reconstituted into a virus-mimetic membrane mixture consisting of DPPC, DPPE, SPM and cholesterol (6 : 6 : 4.5 : 6.4). Two TAT samples containing a Lys4 label and an Arg8 label were bound to POPE/POPG (8:7) membranes.

Solid-State NMR experiments

All solid-state NMR experiments were carried out on a Bruker DSX-400 spectrometer (Karlsruhe, Germany) operating at Larmor frequencies of 400.49 MHz for ^1H , 100.70 MHz for ^{13}C , and 40.58 MHz for ^{15}N . A double-resonance MAS probe tuned to $^{13}\text{C}/^1\text{H}$ or $^{15}\text{N}/^1\text{H}$ modes was used. A Kinetics Thermal System XR air-jet sample cooler (Stone Ridge, NY) was used for cooling samples using dry air or nitrogen gas as input. Sample temperatures were direct readings from the thermocouple and were estimated to be within 1°C of the true temperature due to the moderate MAS rates (< 8 kHz) of all experiments. ^{13}C and ^{15}N

chemical shifts were externally referenced to the α -glycine ^{13}C O resonance at 176.49 ppm on the TMS scale and ^{15}N -acetylvaline (NAV) at 122.0 ppm on the NH_3 scale, respectively.

One-dimensional ^{13}C and ^{15}N cross polarization (CP) MAS spectra were measured using CP contact times of 0.5-1.5 ms. T_2 relaxation times were measured using the Hahn-echo experiment (40) under 7 kHz MAS. The temperature was 238 K for membrane peptides and 296 K for crystalline model compounds. ^1H TPPM decoupling (9) at 71.4 kHz was applied during detection. An acquisition time of ~ 17 ms, which was sufficiently long to avoid truncation of the time signal, was used for most membrane peptides at 238 K.

1D CP-MAS or 1D double-quantum (DQ) filtered MAS spectra were measured to extract the apparent ^{13}C linewidth as a function of temperature. The DQ experiment suppresses the natural-abundance lipid ^{13}C signals and gives well-resolved peptide ^{13}C signals. When extracting the full width at half-maximum (FWHM), we did not apply apodization to the time signals. In a few cases where two peaks partially overlap, we obtained the FWHM as twice the half width at half maximum. For 2D correlation spectra shown in **Fig. 5**, modest line broadening was used as indicated in the figure caption. The SPC-5 sequence (41) was used to recouple the ^{13}C - ^{13}C dipolar coupling for DQ excitation and reconversion. All DQ spectra were measured under 5333 Hz MAS. The 2D DQ dipolar INADEQUATE experiment (36) suppresses natural abundance ^{13}C signals and correlates mostly resonances of directly bonded carbons (**Fig. 7.4, 7.5**). It uses a shorter DQ excitation time than the J-coupling analog of the INADEQUATE experiment (30) and thus has higher sensitivity in our experience.

7.4 Results

We chose three membrane peptides with diverse secondary structures and dynamics to gain a comprehensive understanding of the structure dependence of SSNMR linewidths and lineshapes. The TM domain of the influenza M2 protein forms a four-helix bundle in the virus envelope and conducts protons for the virus lifecycle (42). The antimicrobial peptide PG-1 is a disulfide-linked β -hairpin that associates into β -barrels in anionic lipid membranes to kill bacterial cells (43-45). The cell-penetrating peptide, TAT, from HIV crosses the membrane of target cells to transport molecular cargos (46). Both PG-1 and TAT are cationic

due to a large fraction of Arg residues in their amino acid sequences (34) while M2TM is highly hydrophobic (42, 47). We measure the *static* conformational disorder by freezing the membrane peptides at 238 K, which is well into the gel phase of the lipid membranes used.

Immobilized membrane peptides have similar homogeneous linewidths as crystalline compounds

We measured the T_2 relaxation times using the spin-echo experiment. The echo-detected T_2 gives the homogeneous linewidth (Δ) according to $\Delta = 1/\pi T_2$. In this work, we include the effects of both residual dipolar broadening and true T_2 relaxation in the homogeneous linewidths, since the two cannot be completely separated without infinite ^1H decoupling strength. The apparent linewidth (Δ^*) obtained from the FWHM of the peaks includes both inhomogeneous and homogeneous contributions and translates to an apparent T_2 relaxation time (T_2^*) according to $\Delta^* = 1/\pi T_2^*$. We measured all spectra at a magnetic field of 9.4 Tesla and all ^{13}C T_2 relaxation times at a ^1H decoupling field of 71 kHz. Stronger ^1H decoupling will give narrower Δ , while higher magnetic fields will result in larger apparent linewidths Δ^* (in frequency units) due to the field dependence of chemical shift. Since the crystalline compounds and the examined residues in the membrane peptides are all uniformly labeled in ^{13}C , and neither MAS nor the hard-pulse echo experiment removes ^{13}C - ^{13}C J coupling, a fixed contribution of 50-80 Hz due to one-bond ^{13}C J couplings contributes to both the homogeneous and apparent linewidths.

Fig. 7.2a shows the aliphatic region of the ^{13}C CP-MAS spectra of the crystalline model compounds and the immobilized membrane peptides. Only resolved ^{13}C signals were used to report the T_2 values. Arginine hydrochloride shows two peaks for each ^{13}C site due to two inequivalent molecules in the asymmetric unit cell (48, 49). Representative T_2 decays are shown in **Fig. 7.2b**. All data fit to single-exponential decays with time constants of 3-4 ms, indicating that the J-coupled ^{13}C homogeneous linewidths are ~ 100 Hz (1.0 ppm) for both the crystalline compounds and the hydrated membrane peptides under the ^1H decoupling and MAS conditions used here.

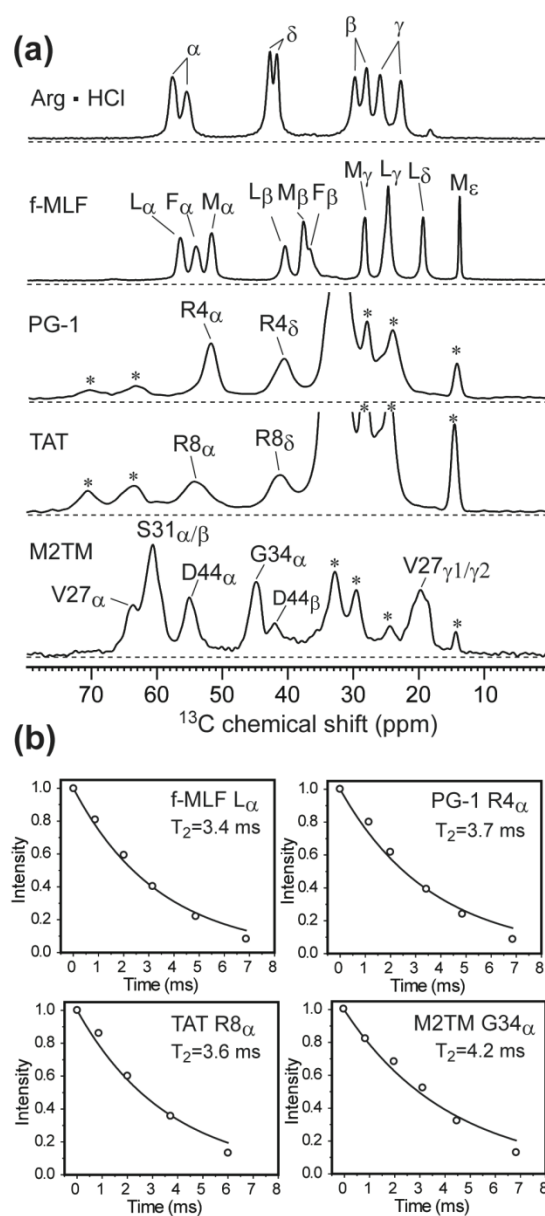


Fig. 7.2. ^{13}C CP-MAS spectra and T_2 relaxation decays. (a) Representative ^{13}C CP spectra of Arg·HCl, f-MLF-OH, Arg8-TAT in POPE/POPG bilayers and VSGD-M2TM in DMPC bilayers. Experiments were conducted at 293 K for the model compounds and at 238 K for the membrane peptides. (b) Representative fittings of exponential T_2 decays, measured under 7 kHz MAS and 71 kHz ^1H TPPM decoupling.

Table 7.1 lists Δ and Δ^* of all measured carbons, distinguished by their numbers of directly bonded protons. For backbone C_α , the homogeneous linewidths (Δ) of all samples range from 75 to 100 Hz (0.75 - 1.0 ppm), irrespective of the crystalline or the mem-

brane-bound nature of the samples. At stronger ^1H decoupling fields the linewidths decrease (16, 30, 50), especially for rigid CH_2 groups, as shown in **Table S7.1**. The membrane peptides exhibit the expected larger Δ^* than the crystalline compounds. For backbone $\text{C}\alpha$, the membrane peptide linewidths ranges from 160 to 500 Hz while the model compound linewidths span 110-140 Hz. The ratio Δ^*/Δ is an indicator of the conformational heterogeneity of the sample (30): larger conformational disorder gives many uncorrelated chemical shift frequencies, whose intrinsic linewidth can be much smaller.

Table 7.1. ^{13}C apparent (Δ^*) and homogeneous (Δ) linewidths of ^{13}C , ^{15}N -labeled compounds obtained from 1D ^{13}C spectra and T_2 measurements, respectively.

Peptide	Site	CH_n	Δ^* (Hz)	Δ (Hz)	Δ^*/Δ
f-MLF-OH	L C α	CH	120	93	1.3
	F C α	CH	140	96	1.5
	M C α	CH	116	78	1.5
	L C γ	CH	90	64	1.4
	L C β	CH_2	112	98	1.1
	M C β	CH_2	106	68	1.6
	M C γ	CH_2	73	43	1.7
	L C $\delta_{1/2}$	$(\text{CH}_3)_2$	64	47	1.4
Arg · HCl	R C ζ	C	75	45	1.7
	R C α	CH	137	102	1.3
	R C δ	CH_2	112	70	1.6
	R C β	CH_2	125	95	1.3
	R C γ	CH_2	125	99	1.3
M2TM	G34 C α	CH	158	75	2.1
	V27 C β	CH	178	116	1.5
	D44 C α	CH	167	89	1.9
	D44 C β	CH_2	180	105	1.7
PG-1	R4 C ζ	C	187	49	3.8
	R4 C α	CH	215	86	2.5
	L5 C α	CH	160	90	1.8
	R4 C δ	CH_2	290	97	3.0
TAT	R8 C ζ	C	212	51	4.3
	K4 C α	CH	479	100	4.8
	R8 C α	CH	506	89	5.7
	R8 C δ	CH_2	358	100	3.6
	K4 C ϵ	CH_2	354	145	2.4

Table 7.1 shows that the two crystalline compounds have $C\alpha \Delta^*/\Delta$ ratios of 1.3–1.5, M2TM and PG-1 have moderately larger $C\alpha \Delta^*/\Delta$ ratios of 1.8–2.5. In contrast, TAT has very large Δ^*/Δ ratios of 5–6, indicating severe conformational disorder. The TAT peptide disorder approaches the reported Δ^*/Δ ratios of 5 – 17 for cellulose in wood, obtained under 10 kHz MAS and 100 kHz ^1H decoupling (30).

Sidechain CH_2 carbons show similar trends of Δ^* among the different samples, with TAT exhibiting the largest Δ^* . **Fig. 7.3** plots the homogeneous (open bars) and apparent (filled bars) linewidths of the different carbons, organized according to CH , CH_2 , CH_3 and quaternary carbons. The average homogeneous linewidth is the smallest for quaternary carbons, 45–51 Hz, as expected for their weak ^1H dipolar coupling. Methine and methylene carbons show similar homogeneous linewidths, averaging ~ 91 Hz. CH_2 carbons are generally expected to have larger Δ due to stronger residual dipolar coupling to protons; however many CH_2 groups examined here are from the amino acid sidechains, whose mobility at the temperatures of the experiments may attenuate the ^1H - ^{13}C dipolar coupling.

The crystalline $\text{Arg} \cdot \text{HCl}$ have smaller Δ^*/Δ (1.3–1.7) ratios than arginines in membrane-bound PG-1 and TAT (2.5–5.7). Arg4 in PG-1 also has 1.4 times larger Δ^*/Δ than its neighboring residue Leu5. Another Arg in PG-1, Arg11, exhibits an even larger $C\alpha$ linewidth Δ^* of 460 Hz (not shown). Thus, Arg in membrane peptides experiences additional line broadening mechanisms that are absent in the crystalline environment. ^{13}C - ^{31}P distance measurements have shown that many Arg-rich membrane peptides form guanidinium-phosphate complexes with lipid headgroups (34, 44–46, 51) to carry out their function. We attribute the larger linewidths of Arg residues in membrane peptides to this specific peptide-lipid interaction.

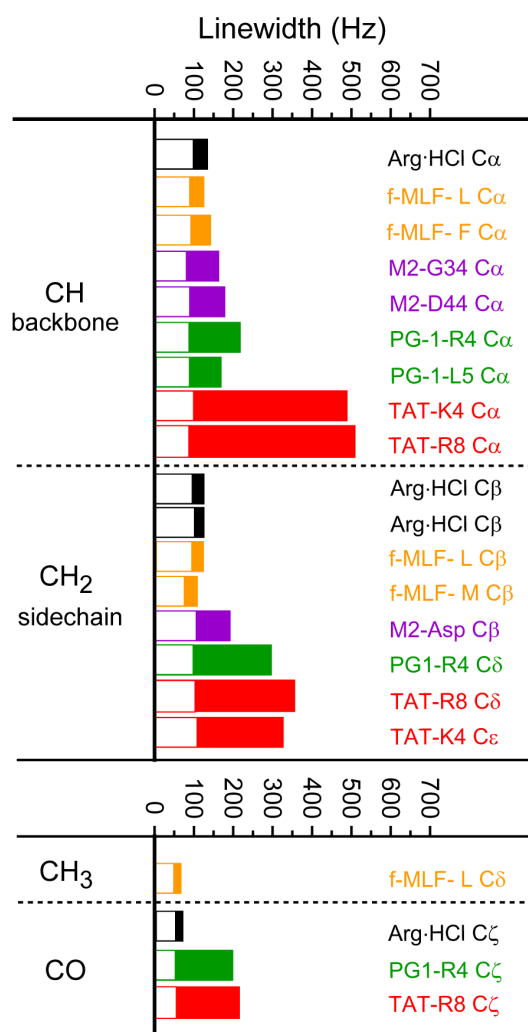


Fig. 7.3. Summary of the ^{13}C apparent linewidths (Δ^* , filled bars) and homogeneous linewidths (Δ , open bars) of CH_n ($n = 0-3$) in crystalline compounds and membrane peptides.

Conformational disorder of membrane peptides from 2D correlation spectra

The 1D ^{13}C spectra above show strong variations in the apparent linewidths (Δ^*) of the three membrane peptides. M2TM has the smallest Δ^* while the cationic residues in PG-1 and TAT have the largest Δ^* . To gain insights into the nature of the conformational disorder represented by these linewidths, we measured the 2D single-quantum (SQ) correlation spectra of these peptides with a double-quantum (DQ) filtered polarization transfer sequence. **Fig. S7.1** shows the aliphatic regions of several representative 2D spectra. Database chemical shift ranges for α -helical, β -sheet and random coil structures are distinguished by color. Peak assignments are based on the connectivity patterns and literature (52, 53). Along

the spectral diagonal, the crystalline compounds exhibit round lineshapes while the membrane peptide lineshapes are elongated. The latter is a sign of the inhomogeneous nature of the line broadening, where the homogeneous linewidth is reflected by the narrower linewidth in the direction perpendicular to the spectral diagonal. The specific conformations of the residues can be gleaned from the chemical shifts spanned by the $C\alpha$ diagonal peaks. One of the two $C\alpha$ peaks of Arg · HCl resonates at a coil/sheet chemical shift while the other $C\alpha$ signal resonates at the α -helical frequency. In f-MLF-OH, the three $C\alpha$ chemical shifts correspond to different conformations that are in agreement with direct (ϕ, ψ) torsion angle measurements (54). For M2TM, the D44 $C\alpha$ peak spans the α -helical and coil chemical shifts when the peptide is bound to DMPC bilayers but becomes only α -helical when the peptide is reconstituted into a virus-mimetic membrane (**Fig. S7.1e, f**). Arg8 $C\alpha$ of TAT shows the largest chemical shift distribution among all sites examined: the linewidth is more than two times larger than M2TM $C\alpha$ sites.

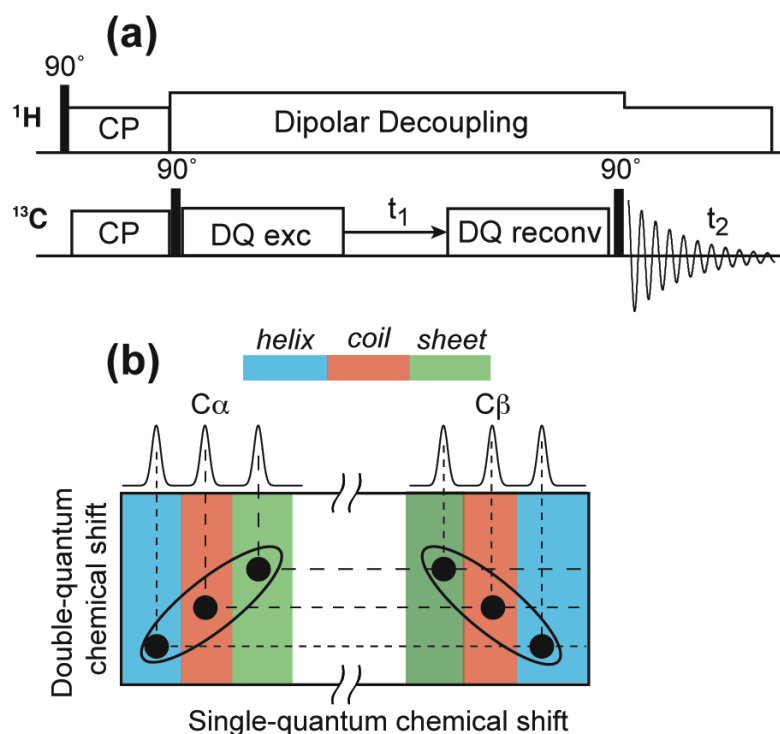


Fig. 7.4. (a) Pulse sequence of the dipolar INADEQUATE experiment (36). (b) Predicted $C\alpha$ - $C\beta$ INADEQUATE $C\alpha$ - $C\beta$ cross peak lineshapes if a residue experiences well defined secondary structures within each molecule, but with the secondary structure varying from one molecule to another.

To examine how the lineshape of one carbon is correlated with the lineshape of its directly bonded carbon, we measured 2D DQ – SQ correlation spectra using the dipolar INADEQUATE experiment (36) (**Fig. 7.4a**). The indirect dimension of the spectrum represents the sum chemical shift of the two coupled ^{13}C spins. Compared to SQ 2D correlation experiments, the INADEQUATE experiment has the advantages that it not only suppresses natural abundance ^{13}C signals but also removes the spectral diagonal so that carbons with similar chemical shifts are well resolved. While ^{13}C - ^{13}C J-coupling can be used to transfer polarization between directly bonded ^{13}C spins, in rigid molecules dipolar-based transfer is similarly selective for one-bond ^{13}C pairs since the one-bond ^{13}C - ^{13}C dipolar coupling is about 5-fold larger than two-bond ^{13}C - ^{13}C dipolar couplings.

Fig. 7.4b depicts the hypothetical lineshapes expected for a $\text{C}\alpha$ - $\text{C}\beta$ spin pair of proteins. For conformationally disordered proteins, multiple cross peaks are expected for each ^{13}C pair. It is well known that $\text{C}\alpha$ and $\text{C}\beta$ have opposite signs for their secondary-structure dependent chemical shifts (55, 56). For example, in α -helices, $\text{C}\alpha$ has larger chemical shifts than random coils while $\text{C}\beta$ has smaller chemical shifts than random coil values. As a result, if each molecule exhibits a well-defined conformation but the structure varies from one molecule to another, then the pair of $\text{C}\alpha$ - $\text{C}\beta$ cross peaks should be elongated and tilted in opposite directions in the INADEQUATE spectrum (**Fig. 7.4b**). On the other hand, if each molecule samples a variety of conformations due to dynamic disorder, then a single $\text{C}\alpha$ chemical shift can correlate with multiple $\text{C}\beta$ chemical shifts and vice versa, leading to round lineshapes for the cross peaks. Finally, a structurally ordered molecular ensemble should exhibit narrow linewidths due only to T_2 relaxation and residual dipolar or J couplings. Approximating the DQ T_2 as the sum of the two SQ T_2 's (57), then the pair of cross peaks should have elliptical lineshapes with the long axis parallel to the ω_1 axis.

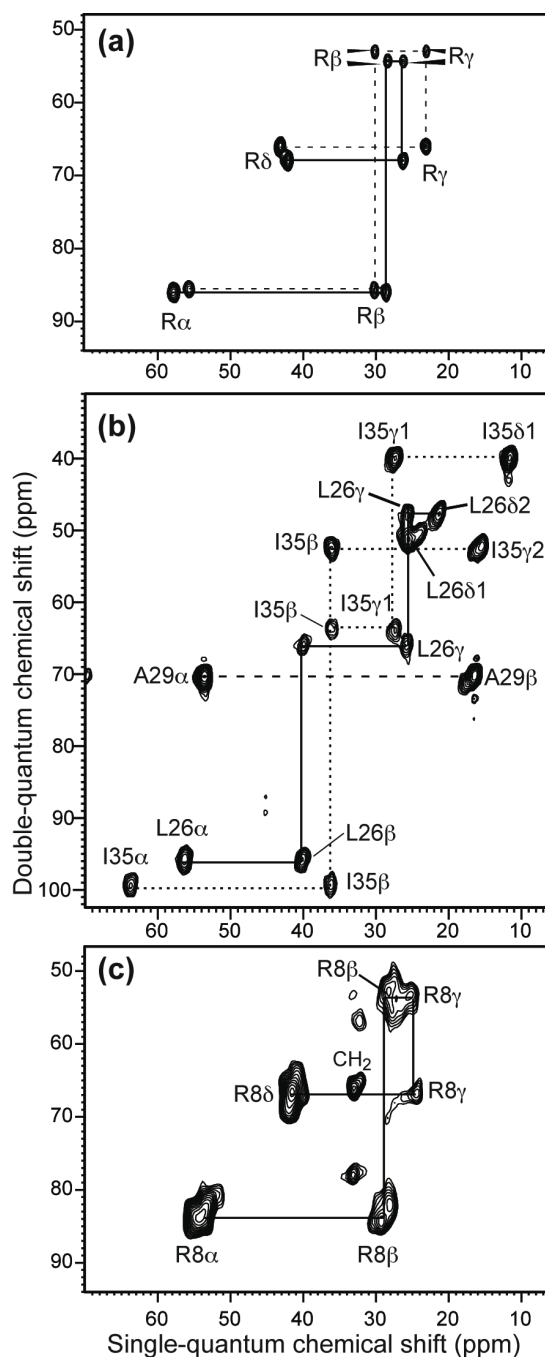


Fig. 7.5. 2D ^{13}C INADEQUATE spectra of (a) Arg · HCl at 296 K, (b) viral-membrane-bound LAGI-M2TM at 238 K, and (c) Arg8-labeled TAT in POPE/POPG membranes at 238 K. All spectra were measured under 5333 Hz MAS and 71 kHz ^1H TPPM decoupling. Gaussian multiplication was applied to both dimensions with LB/GB values of -3/0.1, -7/0.07 and -15/0.04 for (a), (b) and (c), respectively. The single-quantum $\text{C}\alpha$ linewidths of Arg hydrochloride, M2TM Ile35 and TAT Arg8 are 126 Hz, 138 Hz and 360 Hz, respectively.

Fig. 7.5 shows three representative 2D INADEQUATE spectra. The Arg · HCl spectrum resolves two sets of ^{13}C connectivities for the two inequivalent molecules (**Fig. 5a**) and shows parallel oval lineshapes for each pair of cross peaks, consistent with the ordered nature of this crystalline compound. The viral-membrane bound M2TM has modestly larger linewidths than arginine hydrochloride but most pairs of cross peaks exhibit oval lineshapes with the long axis parallel to the ω_1 axis, with the exceptions of the sidechain carbons of Ala29 and Leu26, which show tilted lineshapes indicative of sidechain disorder. Membrane-bound TAT exhibits by far the broadest peaks with ill defined shapes.

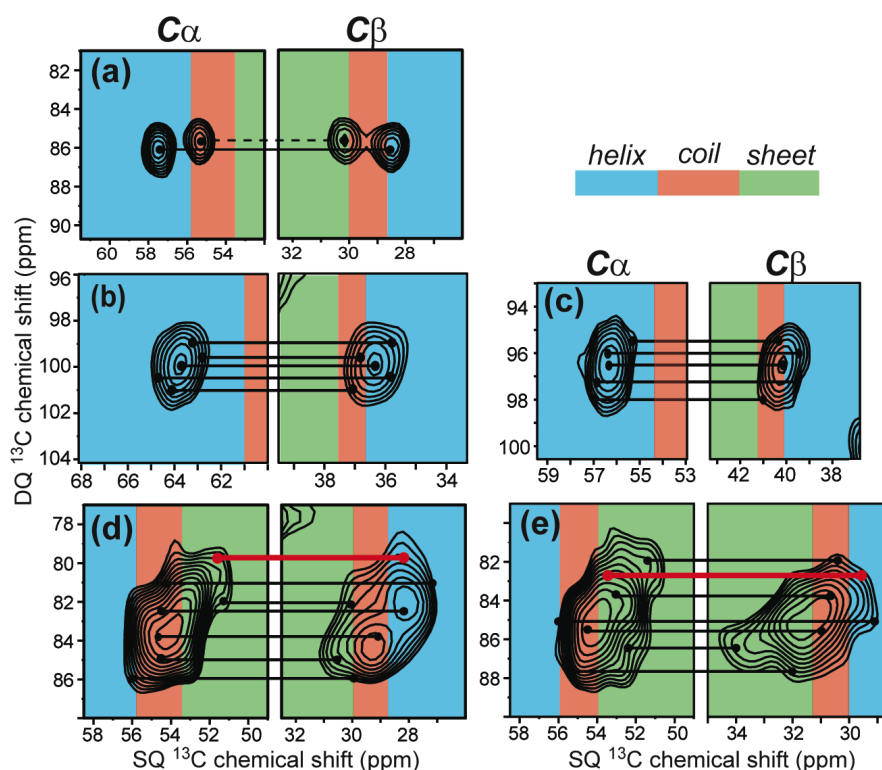


Fig. 7.6. Amplified $\text{C}\alpha$ - $\text{C}\beta$ regions of the INADEQUATE spectra. (a) Arg · HCl at 296 K. (b) Ile35 of viral-membrane bound M2TM at 238 K. (c) Leu26 of viral-membrane bound M2TM at 238 K. (d) Arg8 of TAT in POPE/POPG bilayers at 238 K. (e) Lys4 of TAT in POPE/POPG bilayers at 238 K. Helix, coil and sheet chemical shift regions are shaded in blue, red and green, respectively. Selected correlated $\text{C}\alpha$ - $\text{C}\beta$ positions are connected by lines to guide the eye. Sheet-helix chemical shift correlations are colored by red lines.

Fig. 7.6 zooms in the $\text{C}\alpha$ - $\text{C}\beta$ region of the 2D spectra to examine the backbone conformational distribution. Characteristic chemical shift ranges for α -helix, β -sheet and

random coil (58) are shaded in blue, green, and red, respectively. The two dimensions of the spectra are drawn with the same ppm span per unit length to reflect the relative linewidths of the DQ and SQ dimensions. In Arg · HCl, one pair of C α -C β cross peaks corresponds to the α -helical conformation while the other pair falls in the coil/sheet secondary shift region. This is consistent with the crystal structure, which shows one molecule with (ϕ, ψ) angles of (-50°, -51°), corresponding to a helical backbone, while the other molecule has (ϕ, ψ) angles of (0°, -41°), outside the helix or sheet regions. The apparent linewidths in the DQ dimension are 40-50 Hz smaller than the sum of the SQ linewidths for the two crystalline model compounds, due to the fact that DQ coherence commutes with the ^{13}C - ^{13}C coupling so that the ω_1 dimension should not suffer from ^{13}C - ^{13}C J broadening.

In viral-membrane bound M2TM, the Ile35 and Leu26 lineshapes show moderate conformational disorder: both C α peaks fall well within the α -helical range while the C β chemical shifts are found in both the helix and coil regions (**Fig. 7.5b, c**). In contrast, the Lys4 and Arg8 peaks of TAT span all three secondary structures (**Fig. 7.5d, e**). In addition to the expected coil – coil and sheet – sheet C α -C β correlations, we also observed β -sheet C α frequencies correlated with α -helical C β chemical shifts (red lines). The random correlation at individual frequency components creates tilted lineshapes that differ from the case depicted in **Fig. 7.4b**. Thus, some molecules at these residues adopt (ϕ, ψ) torsion angles far from the canonical secondary structures. This suggests large conformational distributions at the residue level at low temperature, which implies interconverting conformations at physiological temperature.

Sidechain conformational disorder

An inhomogeneously broadened peak can result from a continuous distribution of many frequency components or the overlap of a few discrete peaks. Bajaj et al. studied the temperature-dependent linewidths of the microcrystalline f-MLF-OH and found discrete multiple peaks per carbon between 90 K and 200 K (59), which they attributed to protein glass transition. Specifically, they assigned changes in the Met and Leu sidechain conformation to the slowing down of the phenylene ring motion at low temperature.

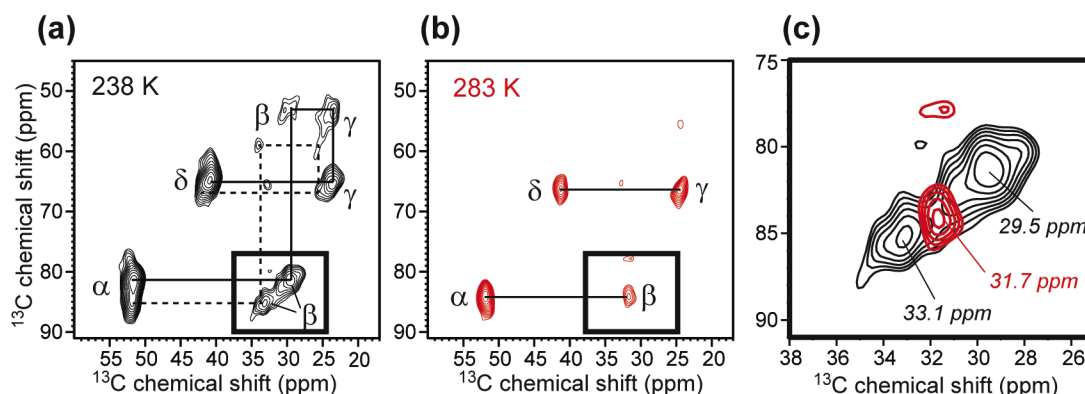


Fig. 7.7. 2D ^{13}C INADEQUATE spectra of POPE/POPG-bound Arg4-labeled PG-1 at (a) 238 K and (b) 283 K. (c) Enlarged region of the $\text{C}\beta$ peak at the two temperatures.

We observed a similar phenomenon of discrete sidechain disorder in PG-1. At 238 K, Arg4 of PG-1 in POPE/POPG membranes shows two $\text{C}\beta$ peaks (29.5 ppm and 33.1 ppm) correlated with the same $\text{C}\alpha$ chemical shift (**Fig. 7.7a**). When the temperature increased to 283 K, a single $\text{C}\beta$ peak at the averaged position (31.7 ppm) of the two low-temperature chemical shifts (**Fig. 7.7b, c**) was observed. Thus, Arg4 undergoes equal-population two-site exchange that is slow at 238 K but fast at 283 K. Since PG-1 backbone is disulfide bonded to be a robust β -hairpin structure, and Arg4 $\text{C}\alpha$ does not display this peak doubling, the nature of the conformational exchange is most likely sidechain rotameric averaging, which is consistent with the low order parameters measured for the sidechain (60). The existence of the sidechain conformational distribution is also consistent with the fact that the $^{13}\text{C}\zeta\text{-}^{31}\text{P}$ distance between Arg4 guanidinium and lipid phosphates shows a distribution in the previously reported REDOR data (45). Assuming a Gaussian distribution, we obtained a best-fit distance of 5.7 Å with a distribution of 1.5 Å. The present observation of two discrete $\text{C}\beta$ peaks suggests that the conformational distribution should be bimodal rather than a single Gaussian distribution. Indeed, **Fig. S7.2** shows that the REDOR dephasing data can be equally well fit by a 1:1 combination of a short distance of 4.8 Å and a long distance of 8.5 Å. This revised two-distance fitting, with one of the two distances being much shorter than the average distance of 5.7 Å from the single-Gaussian fitting, strengthens our model that guanidinium-phosphate interaction is strong for membrane-bound PG-1 (44, 45, 61). Arg4 lies in the

β -strand part of the peptide, far from the tip of the hairpin near the membrane surface. Thus, the fact that Arg4 guanidinium can approach lipid ^{31}P to 4.8 Å means that the guanidinium ions are highly effective in dragging lipid headgroups into the traditionally hydrophobic region of the bilayer, causing toroidal pore defects.

7.5 Discussion

All ^{13}C sites examined for the three membrane peptides exhibit larger apparent linewidths and Δ^*/Δ ratios than the crystalline compounds, indicating larger static disorder. On the other hand, the homogeneous linewidths Δ are similar between the membrane peptides and the crystalline compounds, supporting the notion that Δ is mainly dictated by intrinsic T_2 relaxation and residual dipolar and J broadening.

Both 2D INADEQUATE lineshapes and Δ^*/Δ ratios indicate that the three membrane peptides have different degrees of conformational disorder. M2TM and neutral residues in PG-1 have relatively small disorder, while cationic residues in PG-1 and TAT have much larger inhomogeneous broadening. These differences can be understood based on the oligomeric structure and lipid interactions of these peptides. M2TM forms a water-filled tetrameric helical bundle (1, 62-64) that is immobilized in the virus-mimetic membrane (65). The interhelical interactions stabilize the peptide backbone, and the high viscosity of the cholesterol-rich viral membrane reduces the conformational plasticity of the helices (65). The conformational landscape of M2TM has been investigated extensively. It is known that the peptide adopts several discrete “basis” conformations whose equilibrium depends on the membrane composition, pH and drug binding (66). In the virus-mimetic membrane used here, a single dominant conformation is observed with small distributions in the backbone (ϕ, ψ) angles, consistent with the relatively narrow linewidths seen in the 2D spectra.

PG-1 is constrained by two disulfide bonds to adopt a well-defined β -hairpin structure (67). In addition, it oligomerizes into a transmembrane β -barrel in the POPE/POPG membrane, thus the peptide-peptide interaction should also reduce conformational distribution. Countering this influence is the abundant peptide-lipid interaction due to guanidinium-phosphate ion pairing, which causes larger linewidths, multiplicity of sidechain chemical

shifts, and distributions of ^{13}C - ^{31}P distances. The fact that guanidinium-phosphate interaction is the main contributor to line broadening is reflected by the narrower linewidths of neutral residues in PG-1 (**Table 7.1**).

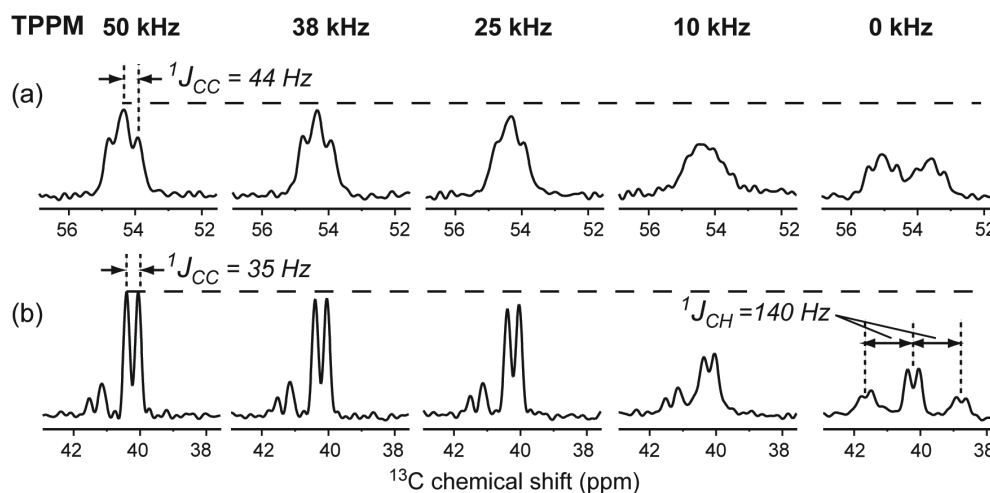


Fig. 7.8. $\text{C}\alpha$ (a) and $\text{C}\epsilon$ (b) peaks of Lys4-labeled TAT in POPE/POPG bilayers at 303 K. The spectra were measured by direct ^{13}C polarization under 5 kHz MAS with varying ^1H decoupling field strengths. (a) $\text{C}\alpha$ peaks. (b) $\text{C}\epsilon$ peaks.

The cationic TAT peptide also suffers large inhomogeneous line broadening for the Arg sidechains, but charge-charge interaction is not the only or the dominant factor. Instead, the amino acid sequence of TAT encodes for an intrinsic lack of conformation. The Tat protein from which the TAT domain is derived is an RNA-binding protein central for HIV replication, and interacts with a variety of intracellular and extracellular molecules. Solution NMR studies showed that Tat does not have a fixed conformation in solution (68), similar to a number of other natively unfolded proteins, which adopt specific structures only upon binding to substrates (69). Our data show that the highly basic cell-penetrating domain of the Tat protein remains unstructured upon binding to the lipid bilayer. The broad low-temperature $\text{C}\alpha/\text{C}\beta$ peaks correlate with extremely narrow high-temperature peaks, both of which resonate at random coil chemical shifts (46) regardless of the membrane composition (**Table S7.2**). This indicates that at high temperature TAT undergoes nearly isotropic conformational fluctuations and samples a large conformational space, which is captured by slow freezing. The nearly isotropic distribution of TAT structure gives rise to resolved

^{13}C - ^{13}C J-splittings in the high-temperature spectra (**Fig. 7.8**), even when the ^1H decoupling strength is weak (50 and 25 kHz). In DMPC/DMPG bilayers the C-H order parameters for $\text{C}\alpha$ and $\text{C}\beta$ sites are as small as 0.15-0.18 (46, 70), further confirming the dynamic nature of this peptide in the lipid bilayer.

We posit that the unstructured nature of the TAT peptide in the membrane is functionally relevant. By not having a fixed conformation stabilized by intramolecular H-bonds, TAT can better form transient intermolecular H-bonds with lipid phosphates and water to facilitate its translocation across the lipid bilayer (46). The lack of a stable amphipathic conformation also prevents TAT from forming long-lasting hydrophobic interactions with the lipid bilayer, which would retard its cell-penetrating activity.

The homogeneous linewidths reported here are specific for the ^1H decoupling field strength of ~ 70 kHz. Stronger ^1H decoupling increases the T_2 and decreases the homogeneous linewidths (71, 72) (**Table S7.2**). As noted above, ^{13}C - ^{13}C J-coupling and residual dipolar coupling also contribute a fixed amount to the homogeneous linewidths of the uniformly ^{13}C -labeled residues. For comparison, the ^{15}N spins, without any J-coupling, show limiting homogeneous linewidths of ~ 10 Hz (0.25 ppm) for crystalline compounds (**Table S7.3**). For singly ^{13}C labeled crystalline model compounds, the ^{13}C homogeneous linewidths are 20-30 Hz for backbone $\text{C}\alpha$ (**Table S7.4**) significantly smaller than the values of uniformly ^{13}C labeled samples.

7.6 Conclusions

We have systematically examined the conformational disorder of several membrane peptides by comparing their homogeneous and apparent linewidths and by examining their 2D spectral lineshapes. At low temperature the membrane peptides exhibit similar homogeneous linewidths as crystalline compounds, consistent with the origins of homogeneous linewidths in residual dipolar and J-coupling and T_2 relaxation. But membrane peptides exhibit larger apparent linewidths than crystalline compounds, the extent of which depends on the peptide structure. The largest apparent linewidths are observed for non-oligomeric and cationic TAT, due to its intrinsic amino acid sequence and extensive peptide-lipid interactions. The main source of disordering peptide-lipid interactions in cationic membrane peptides is

guanidinium-phosphate interaction, which can cause multiple sidechain conformations and distance distributions.

Our study indicates that strong peptide-peptide interactions through oligomerization and intramolecular H-bonding promote relatively homogeneous conformations, while peptide-lipid interactions cause larger linewidths and structural disorder. This insight is useful for freeze trapping experiments for studying protein folding intermediates (73) and protein photoreactions (59, 74). Low-temperature experiments have become increasingly important in biological SSNMR (38, 73, 75-77) due to the maturation of the dynamic nuclear polarization technique (59, 78). Our data suggest that the linewidths of membrane proteins without strong charge interactions with lipids should not be excessively broadened at low temperature, thus DNP should be applicable to a large number of membrane protein systems.

7.7 Acknowledgement

This work is funded by NIH grant GM66976 to M.H.

7.8 Reference

1. Cady, S., D., Schmidt-Rohr, K., Wang, J., Soto, C. S., Degrado, W. F., and Hong, M. (2010) Structure of the amantadine binding site of influenza M2 proton channels in lipid bilayers, *Nature* 463, 689-692.
2. Lange, A., Giller, K., Hornig, S., Martin-Eauclaire, M. F., Pongs, O., Becker, S., and Baldus, M. (2006) Toxin-induced conformational changes in a potassium channel revealed by solid-state NMR, *Nature* 440, 959-962.
3. Petkova, A. T., Ishii, Y., Balbach, J. J., Antzutkin, O. N., Leapman, R. D., Delaglio, F., and Tycko, R. (2002) A structural model for Alzheimer's beta -amyloid fibrils based on experimental constraints from solid state NMR., *Proc. Natl. Acad. Sci. USA* 99, 16742-16747.
4. Wasmer, C., Lange, A., Van Melckebeke, H., Siemer, A. B., Riek, R., and Meier, B. H. (2008) Amyloid fibrils of the HET-s(218-289) prion form a beta solenoid with a triangular hydrophobic core, *Science* 319, 1523-1526.
5. Helmus, J. J., Surewicz, K., Nadaud, P. S., Surewicz, W. K., and Jaroniec, C. P. (2008) Molecular conformation and dynamics of the Y145Stop variant of human prion protein in amyloid fibrils, *Proc. Natl. Acad. Sci. U. S. A.* 105, 6284-6289.
6. Cegelski, L., O'Connor, R. D., Stueber, D., Singh, M., Poliks, B., and Schaefer, J. (2010) Plant Cell-Wall Cross-Links by REDOR NMR Spectroscopy, *J. Am. Chem. Soc.* 132,

- 16052-16057.
7. Dick-Pérez, M., Zhang, Y., Hayes, J., Salazar, A., Zabolina, O. A., and Hong, M. (2011) Structure and interactions of plant cell-wall polysaccharides by two- and three-dimensional magic-angle-spinning solid-state NMR, *Biochemistry* 50, 989-1000.
 8. Maricq, M. M., and Waugh, J. S. (1979) NMR in rotating solids, *J. Chem. Phys.* 70, 3300-3316.
 9. Bennett, A. E., Rienstra, C. M. A., M., Lakshmi, K. V., and Griffin, R. G. (1995) Heteronuclear decoupling in rotating solids, *J. Chem. Phys.* 103, 6951-6958.
 10. Fung, B. M., Khitrin, A. K., and Ermolaev, K. (2000) An improved broadband decoupling sequence for liquid crystals and solids, *J. Magn. Reson.* 142, 97-101.
 11. Detken, A., Hardy, E. H., Ernst, M., and Meier, B. H. (2002) An experimental study of decoupling sequences for multiple-quantum and high-resolution MAS experiments in solid-state NMR, *Chem. Phys. Lett.* 356, 298-304.
 12. Sakellariou, D., Lesage, A., Hodgkinson, P., and Emsley, L. (2000) Homonuclear dipolar decoupling in solid-state NMR using continuous phase modulation, *Chem. Phys. Lett.* 319, 253-260.
 13. De Paëpe, G., Giraud, N., Lesage, A., Hodgkinson, P., Böckmann, A., and Emsley, L. (2003) Transverse dephasing optimized solid-state NMR spectroscopy, *J. Am. Chem. Soc.* 125, 13938-13939.
 14. Hodgkinson, P. (2005) Heteronuclear decoupling in the NMR of solids, *Prog. Nucl. Magn. Reson. Spectrosc.* 46, 197-222.
 15. Sperling, L. J., Nieuwkoop, A. J., Lipton, A. S., Berthold, D. A., and Rienstra, C. M. (2010) High resolution NMR spectroscopy of nanocrystalline proteins at ultra-high magnetic field, *J. Biomol. NMR* 46, 149-155.
 16. Zorin, V. E., Brown, S. P., and Hodgkinson, P. (2006) Origins of linewidth in ^1H magic-angle spinning NMR, *J. Chem. Phys.* 125, 144508.
 17. Akbey, U., Lange, S., Trent Franks, W., Linser, R., Rehbein, K., Diehl, A., van Rossum, B. J., Reif, B., and Oschkinat, H. (2010) Optimum levels of exchangeable protons in perdeuterated proteins for proton detection in MAS solid-state NMR spectroscopy, *J. Biomol. NMR* 46, 67-73.
 18. Hologne, M., Chevelkov, V., and Reif, B. (2006) Deuterated peptides and proteins in MAS solid-state NMR, *Prog. Nucl. Magn. Reson. Spectrosc.* 48.
 19. Morcombe, C. R., Gaponenko, V., Byrd, R. A., and Zilm, K. W. (2005) ^{13}C CPMAS spectroscopy of deuterated proteins: CP dynamics, line shapes, and T_1 relaxation, *J. Am. Chem. Soc.* 127, 397-404.
 20. Mehring, M. (1983) *Principles of High Resolution NMR in Solids*, Springer-Verlag, New York.
 21. Rothwell, W. P., and Waugh, J. S. (1981) Transverse relaxation of dipolar coupled spin systems under rf irradiation: Detecting motions in solids, *J. Chem. Phys.* 74, 2721-2732.

22. Long, J. R., Sun, B. Q., Bowen, A., and Griffin, R. G. (1994) Molecular Dynamics and Magic Angle Spinning NMR, *J. Am. Chem. Soc.* 116, 11950-11956.
23. deAzevedo, E. R., Saalwachter, K., Pascui, O., de Souza, A. A., Bonagamba, T. J., and Reichert, D. (2008) Intermediate motions as studied by solid-state separated local field NMR experiments, *J. Chem. Phys.* 128, 104505.
24. Cady, S. D., Goodman, C., C.Tatko, DeGrado, W. F., and Hong, M. (2007) Determining the orientation of uniaxially rotating membrane proteins using unoriented samples: a ^2H , ^{13}C , and ^{15}N solid-state NMR investigation of the dynamics and orientation of a trans-membrane helical bundle, *J. Am. Chem. Soc.* 129, 5719-5729.
25. Cady, S. D., and Hong, M. (2009) Effects of Amantadine Binding on the Dynamics of Bilayer-Bound Influenza A M2 Transmembrane Peptide Studied by NMR Relaxation, *J. Biomol. NMR* 45, 185-196.
26. Su, Y., Waring, A. J., Ruchala, P., and Hong, M. (2011) Structures of β -Hairpin Antimicrobial Protegrin Peptides in Lipopolysaccharide Membranes: Mechanism of Gram Selectivity Obtained from Solid-State Nuclear Magnetic Resonance, *Biochemistry* 50, 2072-2083.
27. Sakellariou, D., Brown, S. P., Lesage, A., Hediger, S., Bardet, M., Meriles, C. A., Pines, A., and Emsley, L. (2003) High-resolution NMR correlation spectra of disordered solids, *J. Am. Chem. Soc.* 125, 4376-4380.
28. Cadars, S., Lesage, A., and Emsley, L. (2005) Chemical shift correlations in disordered solids, *J. Am. Chem. Soc.* 127, 4466-4476.
29. Duma, L., Hediger, S., Brutscher, B., Böckmann, A., and Emsley, L. (2003) Resolution enhancement in multidimensional solid-state NMR spectroscopy of proteins using spin-state selection, *J Am. Chem. Soc.* 125, 11816-11817.
30. Lesage, A., Bardet, M., and Emsley, L. (1999) Through-Bond Carbon–Carbon Connectivities in Disordered Solids by NMR, *J. Am. Chem. Soc.* 121, 10987-10993.
31. Yao, X. L., and Hong, M. (2004) Structural Distribution in an Elastin-Mimetic Peptide (VPGVG) $_3$ Investigated by Solid–State NMR, *J. Am. Chem. Soc.* 126, 4199-4210.
32. Bajaj, V. S., van der Wel, P. C., and Griffin, R. G. (2009) Observation of a Low-Temperature, Dynamically Driven Structural Transition in a Polypeptide by Solid-State NMR Spectroscopy, *J. Am. Chem. Soc.* 131, 118-128.
33. Hong, M., and Griffin, R. G. (1998) Resonance Assignment for Solid Peptides by Dipolar-Mediated $^{13}\text{C}/^{15}\text{N}$ Correlation Solid-State NMR, *J. Am. Chem. Soc.* 120, 7113-7114.
34. Hong, M., and Su, Y. (2011) Structure and dynamics of cationic membrane peptides and proteins: Insights from solid-state NMR, *Protein Sci.*, Published online.
35. Cross, T. A., Sharma, M., Yi, M., and Zhou, H. X. (2010) Influence of solubilizing environments on membrane protein structures, *Trends Biochem. Sci.* Epub ahead of print.
36. Hong, M. (1999) Solid-state dipolar INADEQUATE NMR spectroscopy with a large

- double-quantum spectral width, *J. Magn. Reson.* 136, 86-91.
37. Maly, T., G.T./, D., Bajaj, V. S., Hu, K. N., Joo, C. G., Mak-Jurkauskas, M. L., Sirigiri, J. R., van der Wel, P. C. A., Herzfeld, J., Temkin, R. J., and Griffin, R. G. (2008) Dynamic nuclear polarization at high magnetic fields, *J. Chem. Phys.* 128, 052211.
 38. Hu, K. N., and Tycko, R. (2010) What can solid state NMR contribute to our understanding of protein folding?, *Biophys. Chem.* 151, 10-21.
 39. Carpino, L. A., and Han, G. Y. (1972) 9-Fluorenylmethoxycarbonyl amino-protecting group, *Org. Chem.* 37, 3404-3409.
 40. Hahn, E. L. (1950) Spin echoes, *Phys. Rev.* 80, 580-594.
 41. Hohwy, M., Rienstra, C. M., Jaroniec, C. P., and Griffin, R. G. (1999) Fivefold symmetric homonuclear dipolar recoupling in rotating solids: Application to double quantum spectroscopy, *J. Chem. Phys.* 110, 7983-7992.
 42. Cady, S. D., Luo, W., Hu, F., and Hong, M. (2009) Structure and function of the influenza M2 proton channel, *Biochemistry* 48, 7356-7364.
 43. Mani, R., Cady, S. D., Tang, M., Waring, A. J., Lehrer, R. I., and Hong, M. (2006) Membrane-dependent oligomeric structure and pore formation of a beta-hairpin antimicrobial peptide in lipid bilayers from solid-state NMR, *Proc. Natl. Acad. Sci. U S A.* 103, 16242-16247.
 44. Tang, M., and Hong, M. (2009) Structure and mechanism of beta-hairpin antimicrobial peptides in lipid bilayers from solid-state NMR spectroscopy, *Mol. Biosyst.* 5, 317-322.
 45. Tang, M., Waring, A. J., and Hong, M. (2007) Phosphate-Mediated Arginine Insertion into Lipid Membranes and Pore Formation by a Cationic Membrane Peptide from Solid-State NMR, *J. Am. Chem. Soc.* 129, 11438-11446.
 46. Su, Y., Waring, A. J., Ruchala, P., and Hong, M. (2010) Membrane-bound dynamic structure of an arginine-rich cell-penetrating peptide, the protein transduction domain of HIV TAT, from solid-state NMR, *Biochemistry* 49, 6009-6020.
 47. Hong, M. (2011) Membrane Protein NMR, *Annual Review of Physical Chemistry*.
 48. Khawas, B. (1971) X-ray Study of L-Arginine HCl, L-Cysteine, DL-Lysine and DL-Phenylalanine, *Acta. Cryst. B*27, 1517-1520.
 49. Mazumdar, S. K., and Venkatesan, K. (1969) The crystal structure of L-arginine hydrochloride, *Zeitschrift für Kristallographie* 130, 328-339.
 50. Cowans, B. A., and Grutzner, J. B. (1993) Examination of Homogeneous Broadening in Solids via Rotationally Synchronized Spin Echo NMR Spectroscopy, *J. Magn. Reson.* 105, 10-18.
 51. Su, Y., Doherty, T., Waring, A. J., Ruchala, P., and Hong, M. (2009) Roles of arginine and lysine residues in the translocation of a cell-penetrating peptide from (^{13}C) , (^{31}P) , and (^{19}F) solid-state NMR, *Biochemistry* 48, 4587-4595.
 52. Petkova, A. T., Hu, J. G., Bizounok, M., Simpson, M., and Griffin, R. G. H., J. (1999) Arginine activity in the proton-motive photocycle of bacteriorhodopsin: solid-state

- NMR studies of the wild-type and D85N proteins, *Biochemistry* 38, 1562-1572.
53. Ladizhansky, V., Jaroniec, C. P., Diehl, A., Oschkinat, H., and Griffin, R. G. (2003) Measurement of multiple psi torsion angles in uniformly $^{13}\text{C},^{15}\text{N}$ -labeled alpha-spectrin SH3 domain using 3D $^{15}\text{N}-^{13}\text{C}-^{13}\text{C}-^{15}\text{N}$ MAS dipolar-chemical shift correlation spectroscopy, *J. Am. Chem. Soc.* 125, 6827-6833.
 54. Rienstra, C. M., Tucker-Kellogg, L., Jaroniec, C. P., Hohwy, M., Reif, B., McMahon, M. T., Tidor, B., Lozano-Pérez, T., and Griffin, R. G. (2002) De novo determination of peptide structure with solid-state magic-angle spinning NMR spectroscopy, *Proc. Natl. Acad. Sci. U. S. A.* 99, 10260-10265.
 55. Spera, S., and Bax, A. (1991) Empirical correlation between protein backbone conformation and Ca and Cb ^{13}C NMR chemical shifts, *J. Am. Chem. Soc.* 113, 5490-5492.
 56. Wishart, D. S., Sykes, B. D., and Richards, F. M. (1991) Relationship between nuclear magnetic resonance chemical shift and protein secondary structure, *J. Mol. Biol.* 222, 311-333.
 57. Levitt, M. H., Raleigh, D. P., Cruzet, F., and Griffin, R. G. (1990) Theory and simulations of homonuclear spin pair systems in rotation solids, *J. Chem. Phys.* 92, 6347-6364.
 58. Wang, Y., and Jardetzky, O. (2002) Probability-based protein secondary structure identification using combined NMR chemical-shift data, *Protein Sci.* 11, 852-861.
 59. Bajaj, V. S., Mak-Jurkauskas, M. L., Belenky, M., Herzfeld, J., and Griffin, R. G. (2009) Functional and shunt states of bacteriorhodopsin resolved by 250 GHz dynamic nuclear polarization-enhanced solid-state NMR, *Proc. Natl. Acad. Sci. U. S. A.* 106, 9244-9249.
 60. Tang, M., Waring, A. J., and Hong, M. (2008) Arginine dynamics in a membrane-bound cationic beta-hairpin peptide from solid-state NMR, *Chembiochem* 9, 1487-1492.
 61. Tang, M., Waring, A. J., Lehrer, R. I., and Hong, M. (2008) Effects of Guanidinium-Phosphate Hydrogen Bonding on the Membrane-Bound Structure and Activity of an Arginine-Rich Membrane Peptide from Solid-State NMR, *Angew. Chem. Int. Ed. Engl.* 47, 3202-3205.
 62. Acharya, A., Carnevale, V., Fiorin, G., Levine, B. G., Polishchuk, A., Balannick, V., Samish, I., Lamb, R. A., Pinto, L. H., DeGrado, W. F., and Klein, M. L. (2010) Structural mechanism of proton transport through the influenza A M2 protein, *Proc. Natl. Acad. Sci. U. S. A.* 107, 15075-15080.
 63. Stouffer, A. L., Acharya, R., Salom, D., Levine, A. S., Di Costanzo, L., Soto, C. S., Terreshko, V., Nanda, V., Stayrook, S., and DeGrado, W. F. (2008) Structural basis for the function and inhibition of an influenza virus proton channel, *Nature* 451, 596-599.
 64. Luo, W., and Hong, M. (2010) Conformational changes of an ion channel membrane protein detected through water-protein interactions using solid-state NMR spectroscopy, *J. Am. Chem. Soc.* 132, 2378-2384.
 65. Luo, W., Cady, S. D., and Hong, M. (2009) Immobilization of the Influenza A M2 Transmembrane Peptide in Virus-Envelope Mimetic Lipid Membranes: A Solid-State

- NMR Investigation, *Biochemistry* 48, 6361-6368.
66. Hu, F., Luo, W., Cady, S. D., and Hong, M. (2011) Conformational plasticity of the influenza A M2 transmembrane peptide in lipid bilayers under varying pH, drug binding and membrane thickness, *Biochim. Biophys. Acta* 1808, 415-423.
 67. Fahrner, R. L., Dieckmann, T., Harwig, S. S., Lehrer, R. I., Eisenberg, D., and Feigon, J. (1996) Solution structure of protegrin-1, a broad-spectrum antimicrobial peptide from porcine leukocytes, *Chem. & Biol.* 3, 543-550.
 68. Shojania, S., and O'Neil, J. D. (2006) HIV-1 Tat is a natively unfolded protein: the solution conformation and dynamics of reduced HIV-1 Tat-(1-72) by NMR spectroscopy, *J. Biol. Chem.* 281, 8347-8356.
 69. Wright, P. E., and Dyson, H. J. (1999) Intrinsically unstructured proteins: re-assessing the protein structure-function paradigm, *J. Mol. Biol.* 293, 321-331.
 70. Hong, M., Gross, J. D., Rienstra, C. M., Griffin, R. G., Kumashiro, K. K., and Schmidt-Rohr, K. (1997) Coupling Amplification in 2D MAS NMR and Its Application to Torsion Angle Determination in Peptides, *J. Magn. Reson.* 129, 85-92.
 71. De Paëpe, G., Lesage, A., and Emsley, L. (2003) The performance of phase modulated heteronuclear dipolar decoupling schemes in fast magic-angle-spinning nuclear magnetic resonance experiments, *J. Chem. Phys.* 119, 4833-4841.
 72. Tang, M., Comellas, G., Mueller, L. J., and Rienstra, C. M. (2010) High resolution ¹³C-detected solid-state NMR spectroscopy of a deuterated protein, *J. Biomol. NMR* 48, 103-111.
 73. Hu, K. N., Yau, W. M., and Tycko, R. (2010) Detection of a transient intermediate in a rapid protein folding process by solid-state nuclear magnetic resonance, *J. Am. Chem. Soc.* 132, 24-25.
 74. Mak-Jurkauskas, M. L., Bajaj, V. S., Hornstein, M. K., Belenky, M., Griffin, R. G., and Herzfeld, J. (2008) Energy transformations early in the bacteriorhodopsin photocycle revealed by DNP-enhanced solid-state NMR, *Proc. Natl. Acad. Sci. U. S. A.* 105, 883-888.
 75. Havlin, R. H., and Tycko, R. (2005) Probing site-specific conformational distributions in protein folding with solid-state NMR, *Proc. Natl. Acad. Sci. U. S. A.* 102, 3284-3289.
 76. Hu, K. N., Havlin, R. H., Yau, W. M., and Tycko, R. (2009) Quantitative determination of site-specific conformational distributions in an unfolded protein by solid-state nuclear magnetic resonance, *J. Mol. Biol.* 292, 1055-1073.
 77. Siemer, A. B., Huang, K. Y., and McDermott A.E. (2010) 107(41), -. (2010) Protein-ice interaction of an antifreeze protein observed with solid-state NMR, *Proc. Natl. Acad. Sci. U. S. A.* 107, 17580-17585.
 78. Griffin, R. G. (2010) Spectroscopy: Clear signals from surfaces, *Nature* 468, 381-382.

7.9 Supporting information

Table S7.1. ^{13}C apparent (Δ^*) and homogeneous (Δ) linewidths of f-MLF and POPE/POPG-bound TAT under different ^1H decoupling fields. The linewidths were measured at 293 K for f-MLF and 238 K for TAT under 7 kHz MAS.

Peptide	site	50 kHz			62.5 kHz			83.3 kHz		
		Δ^*	Δ	Δ^*/Δ	Δ^*	Δ	Δ^*/Δ	Δ^*	Δ	Δ^*/Δ
f-MLF-OH	LC α	138	127	1.1	127	103	1.2	119	89	1.3
	FC α	159	127	1.3	145	106	1.4	141	94	1.5
	MC α	127	100	1.3	118	86	1.4	115	77	1.5
	LC β	199	199	1.0	152	145	1.0	111	98	1.1
	MC γ	94	84	1.1	86	68	1.3	74	38	1.9
	LC δ	78	71	1.1	69	59	1.2	66	51	1.3
TAT	KC α	637	122	5.2	531	106	5.0	455	94	4.8
	KC ϵ	398	245	1.6	354	168	2.1	318	127	2.5

Table S7.2. ^{13}C apparent linewidth Δ (Hz) of labeled residues of DMPC/DMPG-bound TAT at 233 K. The data were from ¹.

Residue	Lys4	Gln7	Arg8	Pro11
C α	460	500	460	290
C β	400	500	480	280

Table S7.3. ^{15}N apparent (Δ^*) and intrinsic (Δ) linewidths measured under 7 kHz MAS and 71 kHz ^1H decoupling.

peptide	site	NH_n	Δ^* (Hz)	Δ (Hz)	Δ^*/Δ
f-MLF-OH	M $\text{N}\alpha$	NH	36	9	4.0
	L $\text{N}\alpha$	NH	40	13	3.0
	F $\text{N}\alpha$	NH	41	11	3.7
Arg-HCl	R $\text{N}\epsilon$	NH	58	24	2.4
	R $\text{N}\epsilon$	NH	47	23	2.1
	R $\text{N}\eta_1$	NH_2	52	21	2.4
	R $\text{N}\eta_1$	NH_2	44	20	2.2
	R $\text{N}\eta_2$	NH_2	48	20	2.4
	R $\text{N}\eta_2$	NH_2	42	16	2.6
	R $\text{N}\alpha$	NH_2	37	31	1.2
M2TM	G34 $\text{N}\alpha$	NH	114	16	6.9
	V27&D44 $\text{N}\alpha$	NH	152	17	8.8
PG-1	L5/R4 $\text{N}\alpha$	NH	212	25	8.6
	G3 $\text{N}\alpha$	NH	202	27	7.5
	L5 $\text{N}\alpha$	NH	180	19	9.5
	R4 $\text{N}\epsilon$	NH	227	47	4.9
	R4 $\text{N}\eta$	NH_2	290	51	5.6
TAT	R8 $\text{N}\alpha$	NH	590	39	16.4
	R8 $\text{N}\epsilon$	NH	265	58	4.6
	R8 $\text{N}\eta$	NH_2	290	64	4.5

Table S7.4. ^{13}C apparent (Δ^*) and homogeneous (Δ) linewidths of singly ^{13}C labeled crystalline amino acids under 71 kHz ^1H TPPM decoupling and 7 kHz MAS.

Amino acid	CH_n	Δ^* (Hz)	Δ (Hz)	Δ^*/Δ
2- ^{13}C -Leu	CH	63	31	2.0
2- ^{13}C -Gly	CH_2	39	20	2.0
3- ^{13}C -Ala	CH_3	27	13	2.1

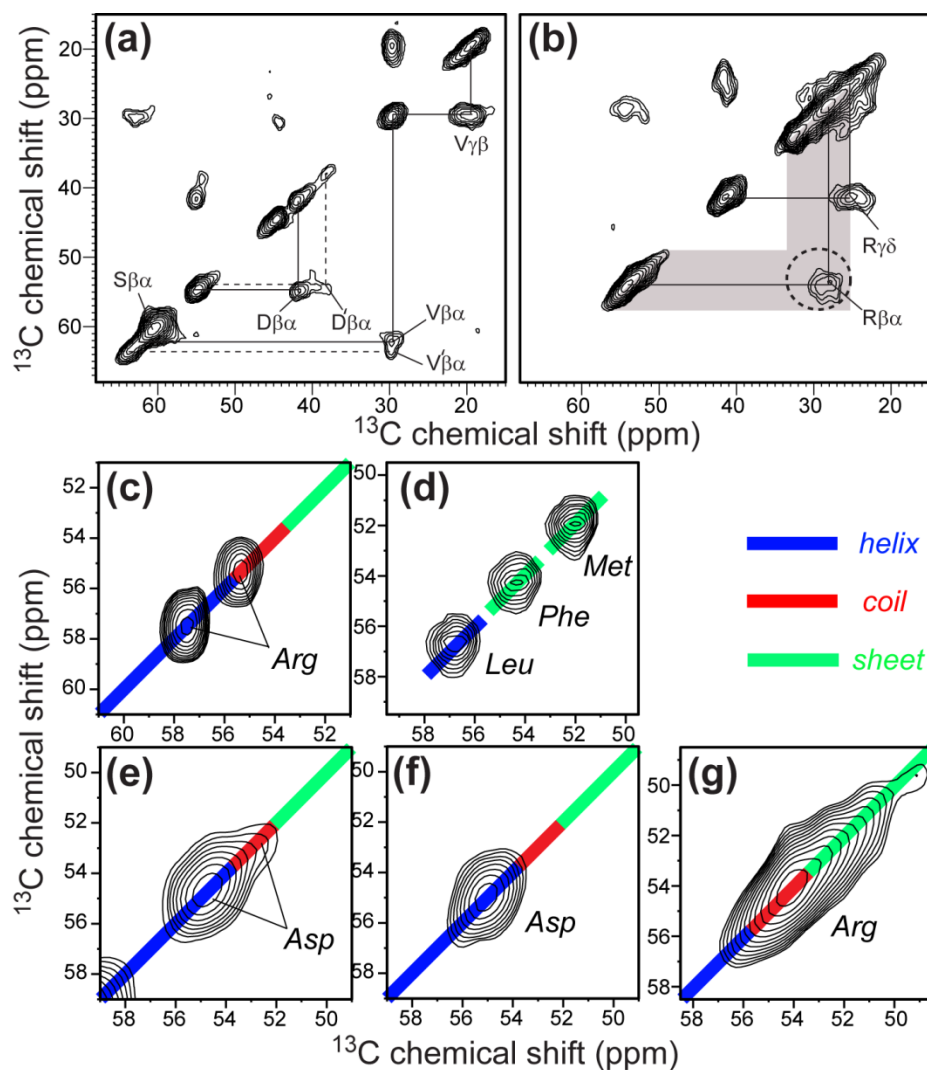


Fig. S7.1. Conformational dispersion of membrane-bound peptides revealed by 2D DQ filtered correlation spectra. (a) VSGD-M2TM in DMPC membrane at 238 K. (b) Arg8-labeled TAT in POPE/POPG membranes at 238 K. (c) $\text{C}\alpha$ region of Arg · HCl at 296 K. (d) f-MLF-OH at 296 K. (e) VSGD-M2TM in DMPC membranes at 238 K. (f) VSGD-M2TM in viral membranes at 273 K. (g) Arg8-labeled TAT in POPE/POPG lipids at 238 K. Colors indicate the chemical shift ranges of α -helix (blue), random-coil (red) and β -sheet (green) conformations.

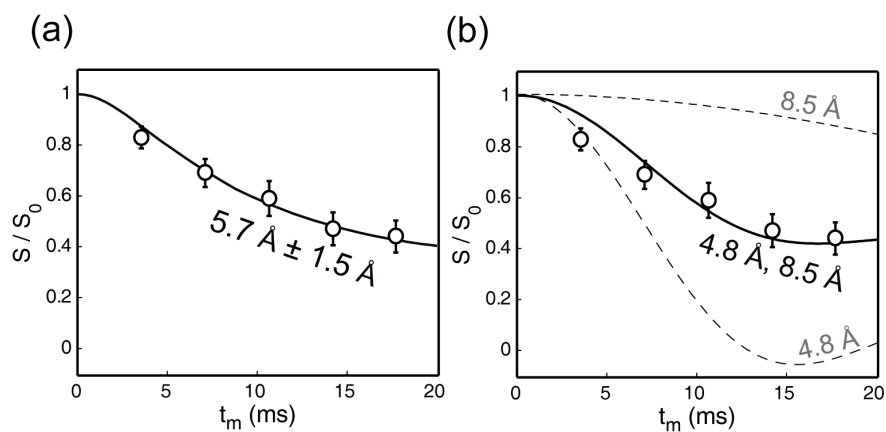


Fig. S7.2. ^{13}C - ^{31}P REDOR data for R4C ζ of PG-1 in POPE/POPG membranes. (a) Best fit assuming a Gaussian distribution gave a $5.7 \text{ \AA} \pm 1.5 \text{ \AA}$. (b) Best fit assuming two discrete distances, giving a 1:1 combination of 4.8 \AA and 8.5 \AA . Data were taken from ².

References

- (1) Su, Y.; Waring, A. J.; Ruchala, P.; Hong, M. *Biochemistry* **2010**, *49*, 6009-6020.
- (2) Tang, M.; Waring, A. J.; Hong, M. *J. Am. Chem. Soc.* **2007**, *129*, 11438-11446.

Chapter 8

Orientation, Dynamics, and Lipid Interaction of an Antimicrobial Arylamide Investigated by ^{19}F and ^{31}P Solid-State NMR spectroscopy

A paper published in Journal of American Chemical Society

2010, vol. 132(26), page 9197-9205

Yongchao Su ¹, William F. DeGrado ², Mei Hong ^{1,*}

¹ Department of Chemistry, Iowa State University, Ames, IA 50011

² Department of Biochemistry and Biophysics, University of Pennsylvania, Philadelphia, PA 19104-6059

8.1 Abstract

A number of arylamides have been synthesized and found to exhibit potent antimicrobial activities against a broad spectrum of Gram-positive and Gram-negative bacteria while exhibiting low toxicity toward eukaryotic cells. These facially amphiphilic foldamers have a relatively rigid intramolecular hydrogen-bonded arylamide as a framework, which places trifluormethyl versus positively charged amino and guanidino groups along opposite faces of the elongated molecule, facilitating interactions with lipid membranes. To better understand the mechanism of action of these antimicrobial foldamers, we have investigated the lipid interaction, depth of insertion, orientation, and dynamics of an arylamide, PMX30016, using ^{31}P and ^{19}F solid-state NMR spectroscopy. Static ^{31}P NMR line shapes of lipid membranes with a range of compositions indicate that PMX30016 does not disrupt the lamellar order of the lipid bilayer but perturbs the lipid headgroup conformation. This headgroup perturbation, manifested as systematic ^{31}P chemical shift anisotropy increases, is consistent with the well documented “electrometer” effect of lipid membranes in response to the addition of positive charges to membrane surfaces. Paramagnetic relaxation enhancement experiments indicate that the arylamide inserts into the membrane-water interface, just below the headgroup region. Measurement of ^{19}F - ^{19}F dipolar couplings within each CF_3 moiety revealed that PMX30016 is oriented with the molecular plane 20° and 30° from the membrane normal of neutral and anionic bilayers, respectively, and the long molecular axis lies parallel to the

membrane plane. Thus, this arylamide inserts into the bilayer in a knife-like fashion, consistent with previous vibrational spectroscopy results. Moreover, ^{19}F NMR line shapes indicate that this molecular knife undergoes fast uniaxial rotation around the bilayer normal. These results suggest that antimicrobial arylamides destabilize anionic lipid membranes primarily by altering the membrane electric potential profile, and the spinning molecular knife may additionally create transient defects in the lipid membrane. Compared to typical antimicrobial peptides, this arylamide has more subtle effects on and is less disruptive of the structure of lipid bilayers.

8.2 Introduction

Antimicrobial peptides (AMPs) have attracted much attention in the last two decades as potentially alternative antibiotics against drug-resistant bacteria (1). Many naturally occurring AMPs have been discovered that possess broad-spectrum and potent antimicrobial activities against many bacteria. However, despite the large number of AMPs studied, therapeutic applications have been limited by their relatively large size, toxicity and difficulties associated with large-scale synthesis of these molecules (1). Thus, it is important to design smaller and more structurally robust synthetic antimicrobial molecules with the essential structural requirements for potent antimicrobial activity and low toxicity. It is by now well known that AMP activities often correlate with their amphiphilic structures and high cationic charge densities, which enable them to selectively target and disrupt the negatively charged lipid membranes of microbial cells (2). Based on these considerations, short sequences of synthetic antimicrobial foldamers have been designed that contain arylamide (3), phenylene ethynylene (4, 5), polynorbornene (6,7) and polymethacrylate (8) backbones. The arylamide series has been particularly well studied. The arylamide backbone is decorated with basic guanidinium sidechains and hydrophobic moieties, and the molecules are conformationally rigid by virtue of thioether-based intramolecular hydrogen bonds and amide groups (9, 10). Structure-activity relationship studies revealed that the amphiphilicity and conformational rigidity of these arylamide foldamers are essential for their high antimicrobial potency and low toxicity, and members of this class of foldamers have been found to have low minimum

inhibitory concentrations (MICs) but high EC_{50} or HC_{50} values towards eukaryotic cells (9, 11).

While the antimicrobial activities of arylamide foldamers have been extensively studied, the physical mechanism of their interaction with the lipid membrane is still not well understood. Determining the three-dimensional structure and topology of these antimicrobial molecules in the lipid bilayer is essential for elucidating their mechanisms of action. So far, sum frequency generation (SFG) vibrational spectroscopy (12, 13) and molecular dynamics (MD) simulations (14, 15) have been used to deduce the topological structure and dynamics of the arylamides in the membrane. These studies suggest that the arylamide oligomers insert into the membrane perpendicular to the bilayer surface, and do not cause the formation of water pores in the membrane. However, high-resolution orientational constraints, depth of insertion, and the mobility of the arylamides have not been reported.

The chemical structure of one of the arylamide foldamers, PMX30016, is shown in **Fig.8.1**. The molecule consists of a central pyrimidine ring flanked by two phenylene diamine units. A thioether moiety allows the attachment of basic groups and forms intramolecular hydrogen bonds with neighboring amides. The phenylene diamine rings are also decorated with a trifluoromethyl group and a terminal guanidine-pentanoyl sidechain that increases the positive charge density of the molecule. PMX30016 was found to have excellent therapeutic indices: its MICs are 0.1 μM against Gram-negative *E. coli*, 0.2 μM against Gram-positive tetracyclin- and streptomycin-resistant *S. aureus*, and its HC_{50} against red blood cells is 440 μM (9,10).

In this work, we use ^{31}P and ^{19}F solid-state NMR spectroscopy to determine the lipid interaction and membrane topology of this arylamide foldamer in lipid bilayers of varying compositions. ^{31}P NMR is a sensitive probe of the membrane morphology and disorder induced by antimicrobial molecules (16-18). ^{19}F NMR is a highly sensitive and background-free indicator of membrane-active molecules, and has been used extensively for determining the orientation (19, 20) and quaternary structure (21-23) of oligomeric membrane peptides and proteins. While the three ^{19}F spins of a trifluoromethyl group are chemically equivalent, dipolar couplings among the three spins are observable and depend on the orientation of the C-CF₃ bond with respect to the membrane normal (24). We used a simple 2D di-

polar-chemical-shift correlation technique to resolve the orientation-dependent ^{19}F - ^{19}F dipolar coupling from the ^{19}F chemical shift pattern. Combined with paramagnetic relaxation enhancement experiments, we have determined both the orientation and the depth of insertion of PMX30016 in lipid bilayers, and propose its membrane disruptive mechanism.

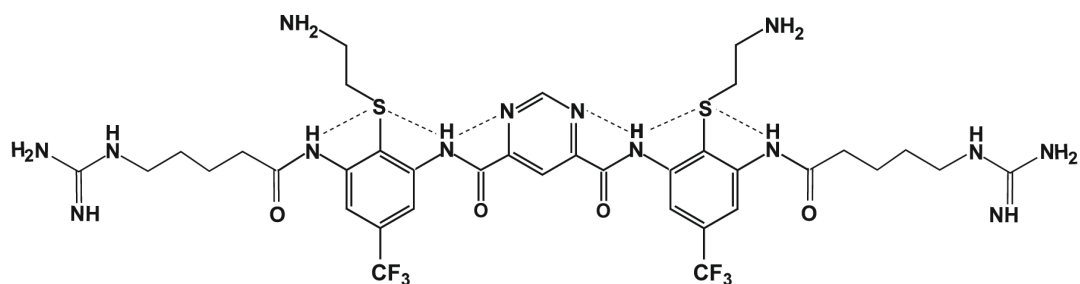


Figure 8.1 Molecular structure of PMX30016. Dash lines indicate the intra-molecular hydrogen bonds.

8.3 Materials and Methods

Lipids and arylamide compound

All lipids, including 1-palmitoyl -2-oleoyl-*sn*-glycero-3-phosphatidylcholine (POPC), 1-palmitoyl-2-oleoyl-*sn*-glycero-3-phosphatidylglycerol (POPG), palmitoyl-2-oleoyl-*sn*-glycero-3-phosphatidylserine (POPS), 1,2-dimyristoyl-*sn*-glycero-3-phosphocholine (DMPC), 1,2-dimyristoyl-*sn*-glycero-3-phosphatidylglycerol (DMPG), dihexylphosphatidylcholine (6-O-PC) and cholesterol were purchased from Avanti Polar Lipids (Alabaster, AL) and used without further purification. PMX30016 was synthesized by PolyMedix (Radnor, PA).

Membrane sample preparation

Glass-plate oriented lipid membranes containing varying concentrations of PMX30016 were prepared using a naphthalene-incorporated method 25. After co-dissolving PMX30016, lipids and naphthalene at desired molar ratios in MeOH/ CHCl_3 (1:2, v/v), the solution was deposited drop-wise onto 6 x 12 mm glass plates (Marienfeld, Germany). After drying overnight in a lyophilizer, the lipid films were hydrated first by directly applying 5 μl

water on each plate, followed by incubation in a 97% humidity chamber containing saturated K_2SO_4 solution at 20°C for 4-5 days. Finally, the glass plates were stacked and wrapped with parafilm for static ^{31}P NMR experiments. We prepared four membrane series with different lipid compositions: POPE/POPG (3 : 1), POPC/POPG (3 : 1), POPC/POPS (4.5 : 1), and POPC/POPS/cholesterol (4.5 : 1 : 2.4). The bicelle samples for orientation determination were prepared using published protocols 26. Briefly, the zwitterionic lipid DMPC was mixed with the ether lipid 6-O-PC at a DMPC/6-O-PC molar ratio of $q = 3.2$ to a total lipid concentration of 35% (w/v) in pH 7.0 phosphate buffer. The mixture was vortexed, heated to 42°C and cooled to 5°C until a clear, homogeneous and viscous solution was obtained. Static ^{31}P NMR spectra confirmed that the lipid mixture was well aligned in the membrane with the bilayer normal perpendicular to the magnetic field at 306 K. PMX30016 was added to the bicelle solution to a drug : lipid molar ratio of 1 : 15, then subjected to another round of vortexing, heating and cooling cycles, and the alignment of the resulting bicelle was again checked by ^{31}P NMR.

Unoriented PMX30016-containing lipid membranes were prepared by mixing PMX30016 with DMPC/DMPG (3:1) vesicles at a molar ratio of 1:15. The solution was incubated overnight and then spun down to obtain a hydrated membrane pellet. UV-VIS spectroscopy showed that >96% of PMX30016 was bound to the lipids. For paramagnet relaxation enhancement (PRE) experiments, 5 mol% Mn^{2+} relative to the total molar amount of lipids were added to hydrated DMPC/DMPG vesicles containing PMX30016. In general, Mn^{2+} ions added to a lipid vesicle solution cannot cross a lipid bilayer that is free of any defects or pores. Thus, all Mn^{2+} ions should be distributed on the outer surface of the bilayer, as demonstrated by NMR (27). However, freeze-thawing a one-sided Mn^{2+} -bound membrane sample redistributes the ions to both surfaces of the membrane due to the fragmentation of the bilayer by ice. We prepared both one-sided and two-sided Mn^{2+} -bound membrane samples containing PMX30016 to assess the depth and polarity of insertion of the arylamide compound.

Solid-state NMR experiments

All solid-state NMR experiments were carried out on a Bruker DSX-400 spectrometer (Karlsruhe, Germany) operating at a resonance frequency 376.8 MHz for ^{19}F and 162.1 MHz for ^{31}P . Typical radiofrequency (rf) pulse lengths were 5 μs for ^1H and ^{31}P and 6 μs for ^{19}F . ^{31}P chemical shifts were referenced to the liquid phosphoric acid peak at 0 ppm for the oriented membrane experiments, and to the isotropic signal of hydroxyapatite at +2.73 ppm on the phosphoric acid scale for unoriented membrane experiments. The ^{19}F chemical shifts were referenced to the Teflon isotropic ^{19}F signal at -122 ppm. A double-resonance probe equipped with a custom-designed $6 \times 12 \times 5$ mm rectangular coil was used for the ^{31}P NMR experiments on glass-plate oriented samples. The samples were positioned in the magnet with the alignment axis parallel to the magnetic field. The ^{31}P spectra were measured at 296 K by single pulse excitation. A $^1\text{H}/^{19}\text{F}/\text{X}$ magic-angle-spinning (MAS) probe was used for all ^{19}F experiments. Static 1D ^{31}P and ^{19}F spectra of bicelle samples were measured at 306 K, at which bicelle maintains good magnetic alignment. A 2D ^1H -decoupled correlation experiment (**Fig. 8.5a**) was implemented to correlate the ^{19}F - ^{19}F dipolar coupling with the ^{19}F chemical shift anisotropy. A dwell time of 20 μs and a total t_1 evolution time of 6.4 ms were used.

Orientation calculation and ^{19}F NMR lineshape analysis

The two C-CF₃ bonds lie mostly in the molecular plane formed by the centers of the three aromatic rings (**Fig. 8.6a**). The angle between the C-CF₃ bond and the long molecular axis, which is defined as the vector connecting the two carbons ortho to the nitrogen atoms of the pyrimidine ring, is 72°

For orientation calculations, we defined a molecule-fixed frame where the x-axis is the long molecular axis described above, the y-axis lies in the plane of the central aromatic ring, perpendicular to the ortho C-C vector, and the z-axis is perpendicular to the ring (**Fig. 8.6a**). The direction of the bilayer normal relative to the molecule is defined by a tilt angle τ from the z-axis and a rotation angle ρ between the x-axis and the projection of the bilayer normal onto the x-y plane. By rotating the bilayer normal through all combinations of (τ, ρ) from 0° to 360°, we can obtain the corresponding C-CF₃ bond orientations to the bilayer normal and thus calculate the ^{19}F - ^{19}F dipolar couplings as averaged by the CF₃ rotation

to be along the C-CF₃ bond.

The chemical shift anisotropy (CSA) tensor is defined by three principal values, $\delta_{xx}, \delta_{yy}, \delta_{zz}$, whose average is the isotropic shift $\delta_{iso} = (\delta_{xx} + \delta_{yy} + \delta_{zz})/3$. The anisotropy parameter δ is defined as $\delta = \delta_{zz} - \delta_{iso}$, and the asymmetry parameter η is defined as $\eta = (\delta_{yy} - \delta_{xx})/(\delta_{zz} - \delta_{iso})$. The δ_{yy} principal value is the closest to the isotropic chemical shift while δ_{zz} is the furthest. Powder patterns with $\eta = 0$ due to identical δ_{yy} and δ_{xx} frequencies are called uniaxial powder patterns. Another indicator of the size of the CSA is the span $\Delta\sigma = \delta_{zz} - \delta_{xx}$. For $\eta = 0$ CSA patterns, which are observed for all uniaxially diffusive molecules in lipid bilayers, the frequency position $\delta_{xx} = \delta_{yy}$ is called the 90° edge since they result from molecules whose bilayer normal is perpendicular to the magnetic field, while the δ_{zz} frequency is called the 0° edge.

8.4 Results

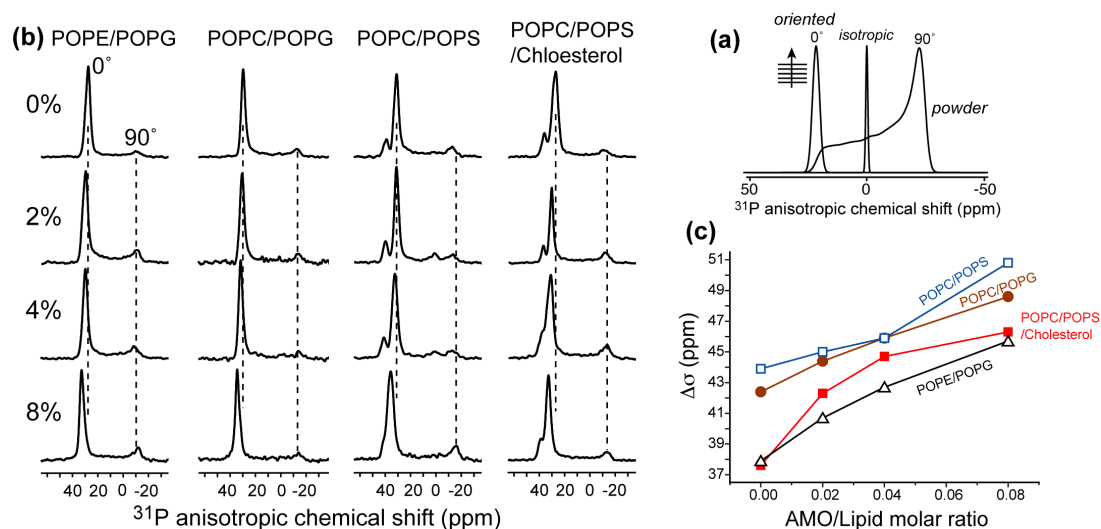


Figure 8.2. (a) Static ³¹P lineshapes of representative membrane morphologies. (b) Static ³¹P spectra of oriented lipid membranes of different compositions in the presence of PMX30016 at 296 K. The PMX30016 molar concentrations are 0%, 2%, 4% and 8% from top to bottom. The membrane compositions are POPE/POPG, POPC/POPG (brown), POPC/POPS (blue), and POPC/POPS/cholesterol (red). (c) ³¹P chemical shift anisotropy (CSA) change of different lipid membranes as a function of PMX30016 concentration.

The PMX30016 structure has a two-fold symmetry with respect to the central ring (Fig. 8.1). The pyrimidine-4,6-dicarboxylic center is connected to an m-phenylenediamine group on each side. A CF₃ group and a thioether group are attached to each

m-phenylenediamine to increase the amphiphilicity of the molecule. The molecule is terminated at the two ends by a hydrophilic guanidine-pentanoyl side chain. The aromatic rings, amide groups and hydrogen bonds create a highly rigid molecule, which was found to be important for antimicrobial potency and selectivity (10). The compound has a molecular weight of 1063 Da, which is smaller than that of most antimicrobial peptides, which have molecular weights of 2-5 kDa.

Membrane perturbation by PMX30016

Static ^{31}P NMR lineshapes of aligned lipid membranes are sensitive reporters of the types of lipid morphology caused by antimicrobial molecules. Both the anisotropic frequency and the intensity distribution reflect the membrane morphology and the lipid headgroup packing. Lamellar bilayers aligned with the bilayer normal parallel to the magnetic field exhibit a single narrow peak at ~ 30 ppm. Unoriented bilayers show a broad powder pattern with maximum intensity at about -12 ppm. Isotropic vesicles and micelles give a sharp isotropic signal near 0 ppm (**Fig. 8.2a**). Membranes whose orientational order is perturbed by antimicrobial peptides often exhibit residual powder patterns and intensities at the 90° edge. Thus the area fraction of the disordered region reflects the extent of the membrane disruption (16, 18).

Fig. 8.2b shows the static ^{31}P spectra of four series of oriented membranes in the presence of varying concentrations of PMX30016. Three series combine a zwitterionic lipid (POPE or POPC) with a negatively charged lipid (POPG or POPS) to mimic the bacterial cell membrane composition, while the fourth series contains cholesterol along with POPC and POPS to mimic the eukaryotic membrane composition. Interestingly, we did not observe any significant residual powder patterns nor isotropic intensities in these spectra up to a peptide molar concentration of 16%. The fractional disorder is 20-35% at 8% PMX30016, which is small compared to most antimicrobial peptides (16, 18). Thus, PMX30016 does not disrupt the overall lamellar morphology of the bilayer. However, in all four series the 0° ^{31}P peak shifted downfield (to larger chemical shifts) with increasing concentrations of PMX30016, indicating that the electronic environment of the ^{31}P was altered by the drug. Using the difference between the 0° and 90° edges of the powder pattern as an indicator of the magnitude

of the ^{31}P CSA, we found that the span increased by 6.2 – 8.7 ppm, or 15-23%, for the four membrane series between 0 and 8% arylamide (**Fig. 8.2c**). Upon addition of 16% PMX30016, the most bacteria-mimetic membrane, POPE/POPG, showed a span increase of 9.3 ppm (26%), while the most eukaryote-mimetic POPC/POPS/cholesterol membrane exhibited a span increase of 13.2 ppm (32%) (see **SI Figure 8.1**).

Binding of PMX30016 to the membrane-water interface

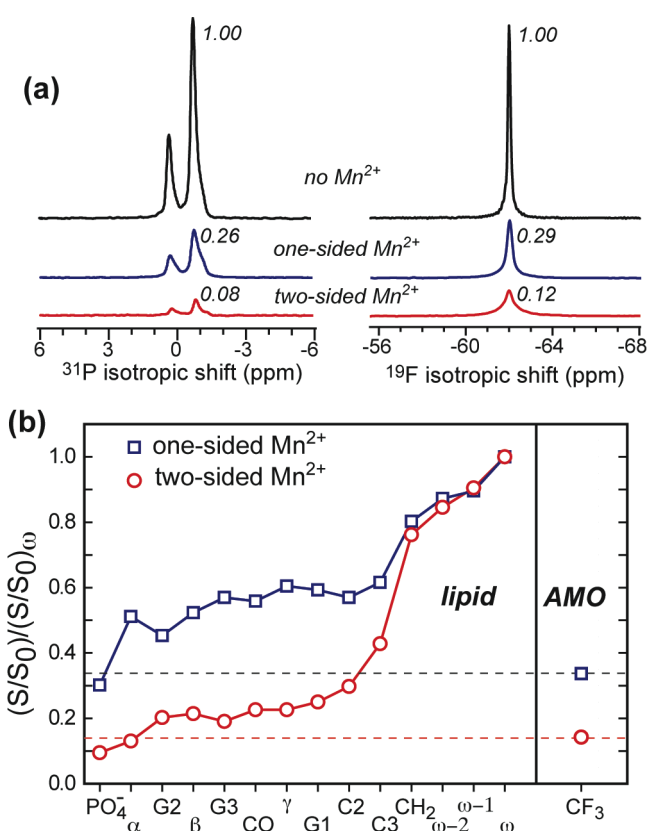


Figure 8.3. Depth of insertion of PMX30016 in lipid membranes from Mn^{2+} paramagnetic relaxation enhancement experiments. (a) ^{31}P and ^{19}F MAS spectra of PMX30016-containing DMPC/DMPG bilayers without Mn^{2+} (black), with Mn^{2+} on the outer membrane surface (blue), and with Mn^{2+} on both membrane surfaces. The intensities normalized to the Mn^{2+} -free samples are indicated. (b) PRE effects of PMX30016 in DMPC/DMPG (3:1) bilayers containing 5% Mn^{2+} . The ratio of the lipid ^{13}C intensities (not shown) between the Mn^{2+} -containing sample (S) and a Mn^{2+} -free control sample (S_0) is S/S_0 . This dephasing value was further normalized to the S/S_0 of the acyl-chain terminal methyl group ω . The ^{19}F intensity of PMX30016 is comparable to the glycerol and headgroup carbons, indicating that PMX30016 is associated to the membrane-water interface, close to the surface water.

To determine the depth of insertion of PMX30016 in lipid membranes, we carried out a paramagnetic resonance enhancement (PRE) experiment using Mn^{2+} ions. Mn^{2+} ions bind to the surfaces of lipid bilayers and enhance the T_2 relaxation rates of nuclear spins in a distance-dependent fashion. The closer the nuclear spins to the paramagnetic center, the broader and lower the signal intensities (28). The ratio of the peak height in the presence of Mn^{2+} to the full intensity in the absence of Mn^{2+} reflects the distance of the nuclear spins to the paramagnetic ions on the membrane surface. By comparing the PRE effect of the peptide signals with that of lipid functional groups, whose depths are known (29), we can thus determine the insertion depth of PMX30016.

Fig. 8.3a shows the single-pulse ^{31}P spectra of the DMPC/DMPG bilayer and ^{19}F spectra of PMX30016. Three spectra, without Mn^{2+} , with Mn^{2+} on the outer surface of the bilayer, and with Mn^{2+} on both surfaces of the bilayer, are compared. The one-side Mn^{2+} sample reduced the ^{31}P intensity to 26% and the ^{19}F signal of the arylamide to a similar level of 29%. The addition of Mn^{2+} to both surfaces of the bilayer further decreased the ^{31}P and ^{19}F signals. Again, the residual ^{19}F signal height (12%) is larger than the residual ^{31}P signal (8%), indicating that the CF_3 groups are buried more deeply than the phosphate group. The lower NMR signals of the one-side Mn^{2+} sample compared to the two-side Mn^{2+} sample indicates that the arylamide, just like the lipid, is bound to both leaflets of the bilayer rather than to only the outer leaflet, since the distance from the outer leaflet to the inner surface of the membrane is sufficiently large that purely outer-leaflet bound molecules would not experience sufficient PRE effect from Mn^{2+} ions on the inner membrane surface (27). The difference between the two spectra also clearly demonstrates that Mn^{2+} is not freely permeable to the inside of the vesicle, thus ruling out the possibility that the arylamide forms large stable pores.

To obtain more quantitative depth information, we compared the PRE effects of all lipid ^{13}C signals in the one-sided and two-sided Mn^{2+} samples with the ^{19}F PRE of PMX30016 (**Fig. 8.3b**). The lipid signals show the expected trend of increasing residual intensity (weaker PRE) with increasing distance from the membrane surface, and the two-side Mn^{2+} samples have lower residual intensities than the one-side Mn^{2+} sample. The ^{19}F intensities are comparable to that of the headgroup carbons for each sample, indicating that

PMX30016 is shallowly inserted into the membrane-water interface, between the phosphate groups and the glycerol backbone region.

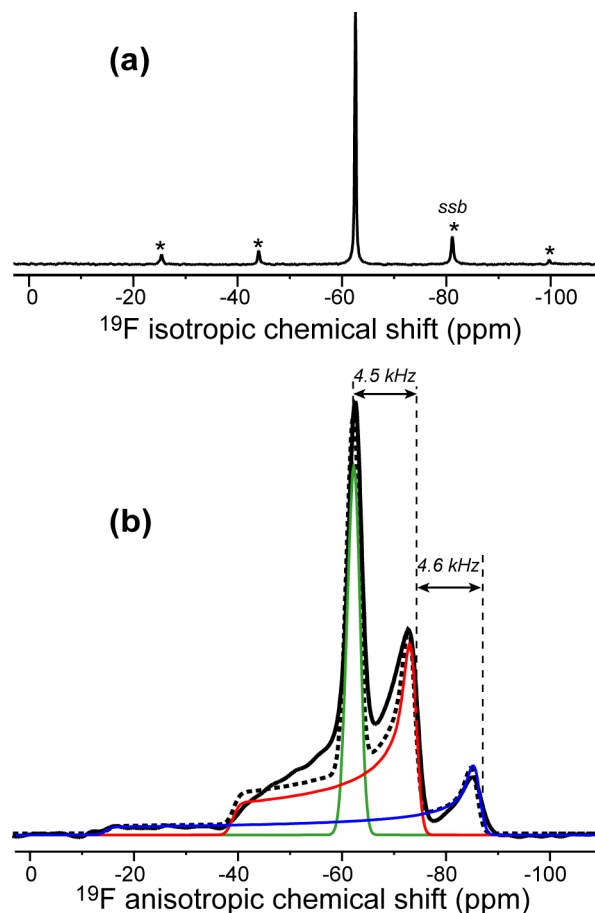


Figure 8.4. ^{19}F spectrum of PMX30016 in unoriented DMPC/DMPG (3:1) bilayers. (a) MAS spectrum. (b) Static spectrum (black line). Three simulated powder patterns corresponding to $\omega_{\text{CSA}} - \omega_{\text{D}}$ (green), ω_{CSA} (red), and $\omega_{\text{CSA}} + \omega_{\text{D}}$ (blue), at 1 : 2 : 1 area ratios are shown. The sum of the three simulated patterns is shown as dashed line. A line broadening of 10 ppm was used for each sub-spectrum. The 90° edges of the triplet are spaced by a ^{19}F - ^{19}F dipolar coupling of 4.5 kHz.

Orientation and uniaxial rotation of PMX30016 in lipid bilayers

The ^{19}F MAS spectrum of PMX30016 in DMPC/DMPG bilayers (**Fig. 8.4a**) shows only a single ^{19}F peak (-62.6 ppm), indicating that the two trifluoromethyl groups have the same chemical environment in lipid membranes. Under the static condition, the ^{19}F spectrum shows a triplet powder pattern with three distinct 90° edges at -62.6 ppm, -73.4 ppm and

-85.4 ppm (**Fig. 8.4b**). This triplet pattern is well known for CF_3 groups as resulting from ^{19}F - ^{19}F dipolar splitting of each ^{19}F by the two other fluorines in the trifluoromethyl group and has been explored extensively for orientation measurements of membrane peptides (19,20). The three components of the triplet correspond to the unperturbed chemical shift spectrum and the sum and difference of the anisotropic dipolar and chemical shift frequencies: $\omega_{\text{CSA}} - \omega_D$, ω_{CSA} , and $\omega_{\text{CSA}} + \omega_D$. Analogous to the C-H J-splitting of a CH_2 group, the integrated intensities of the three sub-spectra have the ratio of 1 : 2 : 1. **Fig. 8.4b** shows that the central component of the PMX30016 triplet has a uniaxial lineshape ($\eta = 0$), indicating that the molecule undergoes fast uniaxial rotation around the bilayer normal. This motion averages both the ^{19}F - ^{19}F dipolar coupling and the ^{19}F CSA to be uniaxial and collinear with the bilayer normal. As a result, the sum and difference spectra are particularly simple: they have $h = 0$ lineshapes and anisotropy parameters of $\bar{\delta}_{\text{CSA}} + \bar{\delta}_D$ and $\bar{\delta}_{\text{CSA}} - \bar{\delta}_D$. Since the central 90° edge of the triplet (-73.4 ppm) is 4.4 kHz from the two other 90° edges, the motionally averaged ^{19}F - ^{19}F dipolar coupling constant $\bar{\delta}_D$ is 4.4 kHz. **Fig. 8.4b** shows simulated ^{19}F spectrum based on a 1 : 2 : 1 superposition of three $\eta = 0$ powder patterns with motionally averaged anisotropy parameters of 0.5, 23.6, and 46.7 ppm, respectively. The simulation has excellent agreement with the experimental spectrum, confirming the nature of the triplet.

To better resolve the ^{19}F - ^{19}F dipolar coupling from the ^{19}F CSA, we implemented a 2D dipolar chemical-shift (DIPSHIFT) correlation experiment where a 180° pulse in the middle of the t_1 evolution period encodes pure ^{19}F - ^{19}F dipolar coupling in the indirect dimension and correlates it with the mixed CSA-dipolar spectrum in the direct dimension (**Fig. 8.5a**). Although the directly detected dimension is not a pure chemical shift spectrum, for simplicity we use the terminology of homonuclear DIPSHIFT to refer to this experiment. Pure ^{19}F dipolar spectra have been previously extracted mainly using the 1D Carr-Purcell-Meiboom-Gill (CPMG) experiment (30, 31), where the ^{19}F signals were detected in the windows of long multiple-pulse trains (19, 24, 32). Compared to the multiple-pulse experiment, this 2D Hahn-echo based homonuclear DIPSHIFT experiment has the benefits of a lower radio-frequency duty cycle and a simpler signal acquisition method, since windowed detection entails scaling of the spectral width and is sensitive to the cumulative effects of pulse imperfections.

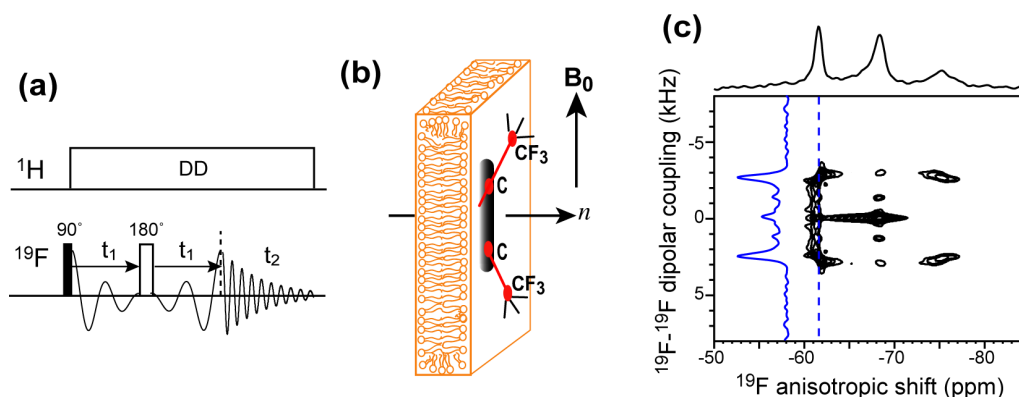


Figure 8.5. Orientation determination of PMX30016 in neutral lipid bilayers. (a) Static 2D ^{19}F dipolar chemical-shift correlation pulse sequence for measuring ^{19}F - ^{19}F dipolar couplings. (b) Geometry of magnetically oriented bicelles containing PMX30016. (c) Static 2D ^{19}F homonuclear DIPSHIFT spectrum of PMX30016 in aligned DMPC/6-O-PC bicelles. The dipolar cross section at -62 ppm is shown as a blue trace.

We first applied the static 2D homonuclear DIPSHIFT experiment to PMX30016 in magnetically aligned DMPC/6-O-PC bicelles. The alignment axis of the bicelle is perpendicular to the magnetic field, thus scaling all measured couplings by -0.5 (**Fig. 8.5b**). The 2D spectrum shows the expected correlation of the triplet pattern in the ω_2 dimension with ^{19}F - ^{19}F dipolar coupling in the ω_1 dimension. Both the most downfield (-61.5 ppm) and the most upfield (-75.3 ppm) ^{19}F peaks exhibit a doublet splitting of 5.2 kHz, as expected because these two ^{19}F peaks correlate with dipolar couplings with the same magnitude, $\bar{\delta}_{\text{CSA}} - \bar{\delta}_D$ and $\bar{\delta}_{\text{CSA}} + \bar{\delta}_D$, and the dipolar spectrum is sign-insensitive. Also as expected, the central ^{19}F peak (-68.5 ppm) does not exhibit a splitting because it corresponds to the unperturbed CSA, $\bar{\delta}_{\text{CSA}}$. The dipolar coupling constant of interest is half the splitting, which is thus 2.6 kHz.

We now consider the orientation dependence of the motionally averaged ^{19}F - ^{19}F dipolar coupling of the CF_3 group. For two ^{19}F spins separated by 2.09 Å as in a CF_3 group, the homonuclear ^{19}F - ^{19}F dipolar coupling in the absence of motion is 17.6 kHz. The three-site jumps of the CF_3 scales the coupling by a factor of $(3\cos^2 90^\circ - 1)/2 = -0.5$ due to the 90° angle between each F-F vector and the C- CF_3 axis. Thus, the ^{19}F - ^{19}F coupling of a rotating CF_3 group without any *other* motion is 8.8 kHz. If the C- CF_3 axis undergoes rotation around the bilayer normal, then the dipolar couplings will be scaled by an orientation-dependent

$$\text{factor } S_{CC,n} = \left(3\cos^2\theta_{CC,n} - 1\right)/2.$$

All lipids and peptides in aligned bicelles rotate around the bicelle normal, which is perpendicular to the magnetic field in our case. The bicelle normal usually exhibits a small degree of wobbling, as described by an order parameter $S_{bicelle}$. These two effects further reduce the dipolar coupling, so that the total measured ^{19}F - ^{19}F coupling is:

$$\overline{\omega}_D^{CF_3,bicelle} = 8.8 \text{ kHz} \times |(-0.5)|_{bicelle} \times S_{bicelle} \times S_{CC,n} = 3.9 \times S_{CC,n} \text{ kHz}. \quad (1)$$

In the above equation we have used a $S_{bicelle}$ value of 0.89, which was directly measured from the ^{31}P spectrum according to

$$S_{bicelle} = (\delta_{obs} - \delta_{iso}) / (\delta_{90^\circ} - \delta_{iso}), \quad (2)$$

where $\delta_{iso} = -0.9 \text{ ppm}$, $\delta_{90^\circ} = -14.9 \text{ ppm}$, $\delta_{obs} = -13.3 \text{ ppm}$. This $S_{bicelle}$ value is consistent with the literature range of 0.75 – 0.94, which depends on the q ratio, the hydration level and temperature of the bicelle (26, 33).

In unoriented membranes where the molecule of interest undergoes uniaxial diffusion, the observed ^{19}F - ^{19}F dipolar coupling constant is larger due to the lack of two scaling factors:

$$\overline{\delta}_D^{CF_3,powder} = 8.8 \times S_{CC,n} \text{ kHz} \quad (3)$$

Equations (1) and (3) show that the ^{19}F - ^{19}F dipolar coupling of the CF_3 group ultimately depends only on the angle between the C- CF_3 bond and the bilayer normal. Since the C- CF_3 bond is rigidly held to the rest of the arylamide ring plane, this vector orientation reveals the orientation of the rigid molecular plane with respect to the membrane normal. Thus, simulation of the ^{19}F - ^{19}F dipolar coupling can yield the orientation of PMX30016 in the lipid bilayer.

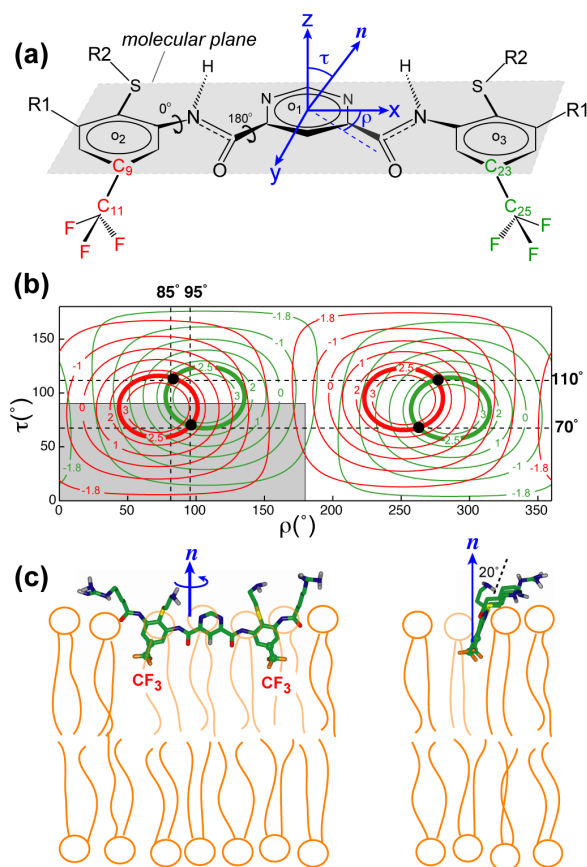


Figure 8.6. Extraction of the orientation of PMX30016 in neutral DMPC/6-O-PC bicelles. (a) Definitions of the molecular coordinate system and (τ, ρ) angles. (b) Calculated ^{19}F - ^{19}F dipolar couplings as a function of (τ, ρ) for the CF_3 groups associated with the C9-C11 bond (red) and the C23-C25 bond (green). Contour lines for the measured value of 2.6 kHz are bolded. The best-fit $(\tau, \rho) = (70^\circ, 95^\circ)$ and its degenerate solutions are indicated as black dots. The non-degenerate region of the orientation plot is shown in grey. (c) Front (left) and side (right) views of the orientation of PMX30016 in DMPC bilayers. The plane of PMX30016 is tilted by 20° from the bilayer normal, which corresponds to $\tau = 70^\circ$.

Fig. 8.6b shows the calculated ^{19}F - ^{19}F dipolar couplings as a function of the tilt angle and rotation angle of the arylamide with respect to the bilayer normal. A tilt angle of 0° and 90° means, respectively, that the normal of the molecular plane is parallel and perpendicular to the bilayer normal. A rotation angle of 0° and 90° corresponds to the long molecular axis being parallel and perpendicular to the bilayer normal, respectively. The observation of only one ^{19}F - ^{19}F dipolar coupling in the static spectrum indicates that the two C-CF₃ bonds have the same orientation with respect to the bilayer normal. The calculated dipolar couplings of

the two CF_3 groups are shown in red and green contour lines, and the contour lines corresponding to the observed 2.6 kHz coupling are bolded. Since both CF_3 groups exhibit the same coupling, only a single solution of $(\tau, \rho) = (70^\circ, 95^\circ)$ was identified within the non-degenerate quadrant of $0\text{-}180^\circ$ for ρ and $0^\circ\text{-}90^\circ$ for τ . All other solutions such as $(\tau, \rho) = (110^\circ, 85^\circ)$ are degenerate. **Fig. 8.6c** shows the $(\tau=70^\circ, \rho=95^\circ)$ orientation of PMX30016 in the DMPC bilayer. The molecular plane is almost perpendicular to the bilayer plane, reflecting the tilt angle, while the long axis of the molecule is nearly parallel to the bilayer surface, reflecting the rotation angle. This orientation corresponds to a knife-like insertion of the arylamide into the membrane, with the aromatic plane only 20° from the vertical bilayer normal.

To determine whether the orientation is affected by the presence of negatively charged lipids, we measured the 2D ^{19}F DIPSHIFT spectrum of PMX30016 in unoriented DMPC/DMPG bilayers. **Fig. 8.7a** shows a similar triplet pattern in the direct dimension, but it is now correlated with a larger dipolar splitting of 8.6 kHz due to the absence of two bicelle scaling factors (Equation 3). The dipolar coupling constant of 4.35 kHz was calculated to yield a unique orientation solution of $(\tau=60^\circ, \rho=99^\circ)$ (**Fig. 8.7b**), indicating that now the molecular plane is moderately more tilted from the bilayer normal (30°) than the case in the neutral DMPC bilayer, but the long molecular axis remains largely parallel to the membrane plane. Overall, the knife-like insertion motif is maintained, as shown in **Fig. 8.7c**.

8.5 Discussion

The above solid-state NMR data provides the most comprehensive information to date about the lipid interaction, depth of insertion, orientation, and dynamics of an arylamide oligomer. We first discuss the membrane topology of this arylamide foldamer. In both neutral DMPC bilayers and anionic DMPC/DMPG bilayers, the long molecular backbone lies parallel to the bilayer surface, as reflected by $\rho \approx 90^\circ$. Our ^{19}F NMR method allows precise measurement of the orientation of the phenyl rings of the arylamide molecule. We did not measure the orientation of the central pyrimidyl ring, but previous studies showed it to be constrained to lie coplanar with the phenyl rings through the formation of an extended hy-

drogen-bonded network (Fig. 8.1) (9). The two phenyl groups are oriented with their rigid aryl planes nearly perpendicular to the membrane surface ($\tau = 60^\circ, 70^\circ$). The phenyl ring's deviation from perpendicularity is 20° for the neutral bilayer and 30° for the anionic bilayer. This orientation resembles a knife cutting into the bilayer, which makes perfect sense because it matches the amphiphilic structure of the arylamide with the amphiphilic structure of the lipid bilayer, by pointing the basic guanidinium and the amino-ethyl thioether substituents to the aqueous surface of the membrane while the hydrophobic groups towards the lipid chains.

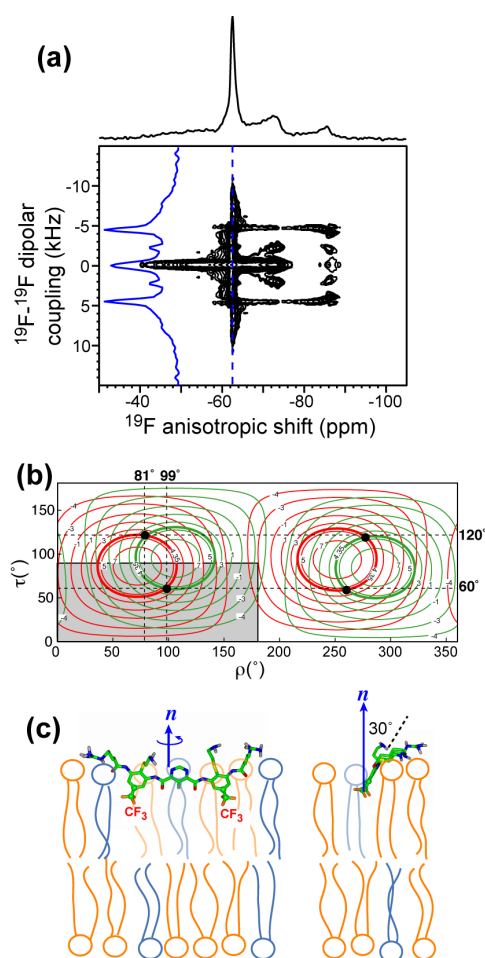


Figure 8.7. Orientation of PMX30016 in unoriented DMPC/DMPG membranes. (a) 2D ^{19}F homonuclear DIPSHIFT spectrum of PMX30016 in DMPC/DMPG (3:1) membranes. (b) Calculated ^{19}F - ^{19}F dipolar couplings as a function of (τ, ρ) angles. The intercepts of the two CF_3 groups' couplings at 4.35 kHz give the best-fit orientation, which is $(\tau, \rho) = (60^\circ, 99^\circ)$. The non-degenerate region of the orientation plot is shown in grey. (c) Best-fit orientation of PMX30016 in anionic lipid membranes.

The parallel orientation of the long molecular axis with the membrane plane satisfies the two-fold symmetry of the molecule and maintains the same intermolecular potentials for the two sides of the pyrimidine ring, which are chemically identical. The moderate difference in the tilt angle between the neutral and anionic membranes can be understood by the fact that the less vertical molecular plane enables the positively charged guanidinium groups to interact more strongly with the negatively charged DMPG headgroups on the membrane surface (Fig. 8.7c). In other words, competition between water and the negative charge density of the membrane surface may cause small modulation of the tilt angle of the arylamide plane.

The knife-like orientation of PMX30016 obtained here is in excellent agreement with the results of SFG vibrational spectra of an analogous arylamide (12). There, analysis of the symmetric and asymmetric stretching modes of tert-butyl sidechains adsorbed onto DPPG bilayers concluded an angle of $0^\circ - 35^\circ$ for the three-fold axis of the tert-butyl. This orientation, while of the limiting nature, is consistent with the ^{19}F NMR result for the DMPC/DMPG-bound PMX30016, where the molecular plane is 30° from the bilayer normal (Fig. 8.7c). Since the two arylamide molecules differ in their basic sidechains and the hydrophobic functional groups, the similarity of the results indicates that the facial amphiphilicity and restrained backbone structure of the molecules are sufficient to determine their orientations. The ^{19}F NMR constraints obtained here have higher angular resolution and more complete information than the SFG results, since as long as the arylamide plane is not exactly perpendicular to the bilayer plane, a second angle defining the long axis direction is necessary to fully describe the molecular orientation.

Paramagnetic relaxation enhancement data indicate that the knife-like arylamide inserts only shallowly into the membrane, just below the phosphate headgroups and not reaching into the acyl chain region (Fig. 8.3). The shallow depth was obtained at a drug : lipid molar ratio of 1 : 15, at which the arylamide was already distributed into both leaflets of the bilayer. Direct comparisons of the drug : lipid molar ratios in the hydrated pastes of the solid-state NMR samples versus the aqueous solutions of antimicrobial assays are fraught with uncertainties. Nevertheless, we believe at higher arylamide concentrations the equilibrium structure is unlikely to be a deeper transmembrane insertion, and the mechanism of ac-

tion of the arylamide should be considered in the context of the observed shallow depth and knife-like orientation. This topology should be combined with the fact that the drug undergoes fast uniaxial diffusion at rates greater than 10^5 s^{-1} . Thus, the rigid arylamide knife is by no means static, but spins around the membrane normal with its full extended length, which has the potential to perturb and destabilize a large area of the membrane.

The topology and dynamics of PMX30016 in the lipid bilayer are inconsistent with the three main classical antimicrobial structural models, namely, the barrel-stave (34, 35), the toroidal pore (36, 37), and the carpet models (38). The arylamide foldamer is not transmembrane, and does not cause lipid orientational disorders of the toroidal type. The knife-like topology is also distinct from the carpet model, since the arylamide does not aggregate into extended immobile assemblies.

One of the most intriguing aspects of the arylamide interaction with the lipid membrane is the increased ^{31}P CSA and the nearly complete absence of orientational disorder as the concentration of the foldamer increases. These features indicate that the doubly charged molecule influences the headgroup conformation of the phospholipids without causing large-scale orientational disorder of the bilayer. It is well known that the polar lipid headgroups act as molecular electrometers to membrane surface charges (39). The addition of positively charged metal ions, hydrophobic ions, amphiphiles, and peptides increases the magnitude of the ^{31}P CSA and the 2H quadrupolar coupling of the headgroup $\beta\text{-CD2}$, but decreases the ^2H coupling of the $\alpha\text{-CD2}$ (39-42). The addition of negatively charged species to the membrane surface creates the opposite effects. Based on analysis of the ^{31}P chemical shift tensor and ^2H quadrupolar couplings, it was proposed that cationic species change the lipid headgroup conformation such that the N^+ end of the $^-\text{P}-\text{N}^+$ dipole moves towards the water phase. The PMX30016-induced ^{31}P CSA increase is consistent with this electrometer effect both qualitatively and quantitatively. A cationic amphiphile, sodium dialkyl phosphate, was found to increase the ^{31}P CSA of POPC lipids by 8 ppm at 20 mol% amphiphile (40). Similarly, at 8 mol% arylamide, which corresponds to 16 mol% positive charge density, the ^{31}P CSA span of the POPE/POPG membrane increased by 7.8 ppm (**Fig. 8.2**).

The ^{19}F NMR results of the arylamide and the ^{31}P NMR spectra of the lipids, taken together, suggest that the antimicrobial arylamide disrupts the membrane barrier function of microbial

cells primarily by altering the membrane electric potential profile. While the spinning molecular knife would certainly perturb lipid packing on the molecular level, it appears to do so only transiently and leaves no long-lasting physical damages behind. The lack of permanent membrane disorder by PMX30016, manifested by the ^{31}P spectra, is in sharp contrast to many other antimicrobial peptides such as PG-1 (18, 43) and magainin (44). The absence of permanent disruption is more akin to tachyplesin, which, interestingly, also exhibits fast uniaxial rotation with an in-plane orientation (17, 45). Instead, the spinning arylamide knife, with its positively charged guanidinium groups, significantly alters the lipid headgroup conformation, an effect that is absent for tachyplesins. We propose that this perturbation of the lipid headgroup conformation changes the membrane surface potential and eventually leads to membrane permeabilization, possibly by interacting with protein components of bacterial membranes.

At higher drug concentrations than used in this study, it is possible that the spinning arylamide may increasingly cause more pronounced physical disruption of the membrane, so that a balance between the two effects –perturbation of the membrane potential versus the physical disruption – may be responsible for bacterial killing. Such a mixed mechanistic scenario has been suggested before for analogous antimicrobial arylamides based on the different concentrations and kinetics of membrane permeabilization and bacteria killing (10). The possibility of a mixture of mechanistic modes has also been gleaned for some antimicrobial peptides. For example, magainin showed clear signs of physical disruption of lipid membranes based on ^{31}P NMR spectra (44), but it also dissipates the electrical potential across lipid membranes and has been proposed to kill bacteria by decreasing the membrane potential and interfering with free-energy transduction in microbial cells (46).

The present study illustrates the robustness and utility of ^{19}F solid-state NMR for elucidating the topology and dynamics of pharmaceutical compounds. The high sensitivity and lack of background of ^{19}F spins, combined with the large chemical shift anisotropy and ^{19}F - ^{19}F dipolar couplings, make ^{19}F NMR exquisitely sensitive to molecular orientation and dynamics. The simple 2D ^{19}F homonuclear DIPSHIFT experiment, while analogous to several other NMR techniques (47-49), has not been employed before for determining orientation-dependent dipolar couplings, and promises to facilitate high-resolution structural analy-

sis of CF₃-containing pharmaceutical compounds.

8.6 Conclusion

The orientation, depth of insertion, mobility and lipid interaction of an antimicrobial arylamide has been determined using ¹⁹F and ³¹P solid-state NMR. The arylamide inserts into the lipid membrane just below the headgroups with the molecular plane nearly perpendicular to the bilayer surface and the long axis parallel to the bilayer. In this knife-like manner, the molecule undergoes fast uniaxial rotation around the bilayer normal. Interestingly, this spinning molecular knife does not directly cause permanent damage to the lamellar integrity of the lipid bilayer, but rather changes the lipid headgroup conformation, specifically, the P-N dipole orientation, through interaction of the positively charged guanidinium ions with the lipid phosphate groups. This conformational change, manifested as ³¹P chemical shift increases, was detected in all negatively charged lipid membranes studied here. We propose that the antimicrobial arylamide destroys the barrier function of microbial cell membrane mainly by altering its electrical potential, and the spinning molecular knife may further create transient defects in the membrane.

8.7 Acknowledgements

This work is funded by NIH grants GM66976 to M.H., AI75866 to W.F.D. and UL1RR024134 from the National Center For Research Resources.

8.8 References

1. Zasloff, M. (2002) Antimicrobial peptides of multicellular organisms, *Nature*, 389-395.
2. Epanand, R. M., and Vogel, H. J. (1999) Diversity of antimicrobial peptides and their mechanisms of action, *Biochim. Biophys. Acta* 1462, 11-28.
3. Tew, G. N., Liu, D., Chen, B., Doerksen, R. J., Kaplan, J., Carroll, P. J., Klein, M. L., and DeGrado, W. F. (2002) De novo design of biomimetic antimicrobial polymers, *Proc. Natl. Acad. Sci. U. S. A.* 99, 5110-5114.
4. Tew, G. N., Clements, D., Tang, H., Arnt, L., and Scott, R. W. (2006) Antimicrobial activity of an abiotic host defense peptide mimic, *Biochim. Biophys. Acta.* 1758, 1387-1392.
5. Yang, L., Gordon, V. D., Trinkle, D. R., Schmidt, N. W., Davis, M. A., DeVries, C., Som, A., Cronan, J. E., Tew, G. N., and Wong, G. C. (2008) Mechanism of a prototypical syn-

- thetic membrane-active antimicrobial: Efficient hole-punching via interaction with negative intrinsic curvature lipids, *Proc. Natl. Acad. Sci. U. S. A.* 105, 20595-20600.
6. Gabriel, G. J., Pool, J. G., Som, A., Dabkowski, J. M., Coughlin, E. B., Muthukumar, M., and Tew, G. N. (2008) Interactions between Antimicrobial Polynorbornenes and Phospholipid Vesicles Monitored by Light Scattering and Microcalorimetry, *Langmuir* 24, 12489-12495.
 7. Som, A., Vemparala, S., Ivanov, I., and Tew, G. N. (2008) Synthetic mimics of antimicrobial peptides, *Biopolymers* 90, 83-93.
 8. Kuroda, K., and DeGrado, W. F. (2005) Amphiphilic Polymethacrylate Derivatives as Antimicrobial Agents, *J. Am. Chem. Soc.* 127, 4128-4129.
 9. Tew, G. N., Scott, R. W., Klein, M. L., and DeGrado, W. F. (2010) De novo design of antimicrobial polymers, foldamers, and small molecules: from discovery to practical applications, *Acc. Chem. Res.* 43, 30-39.
 10. Choi, S., Isaacs, A., Clements, D., Liu, D., Kim, H., Scott, R. W., Winkler, J. D., and DeGrado, W. F. (2009) De novo design and in vivo activity of conformationally restrained antimicrobial arylamide foldamers, *Proc. Natl. Acad. Sci. U. S. A.* 106, 6968-6973.
 11. Scott, R. W., DeGrado, W. F., and Tew, G. N. (2008) De novo designed synthetic mimics of antimicrobial peptides, *Curr. Opin. Biotechnol.* 19, 620-627.
 12. Chen, X., Tang, H., Even, M. A., Wang, J., Tew, G. N., and Chen, Z. (2006) Observing a Molecular Knife at Work, *J. Am. Chem. Soc.* 128, 2711-2714.
 13. Avery, C. W., Som, A., Xu, Y., Tew, G. N., and Chen, Z. (2009) Dependence of Antimicrobial Selectivity and Potency on Oligomer Structure Investigated Using Substrate Supported Lipid Bilayers and Sum Frequency Generation Vibrational Spectroscopy, *Anal. Chem.* 81, 8365-8372.
 14. Lopez, C. F., Nielsen, S. O., Srinivas, G., DeGrado, W. F., and Klein, M. L. (2006) Probing Membrane Insertion Activity of Antimicrobial Polymers via Coarse-Grain Molecular Dynamics, *J. Chem. Theory. Comput.* 2, 649-655.
 15. Liu, D., Choi, S., Chen, B., Doerksen, R. J., Clements, D. J., Winkler, J. D., Klein, M. L., and DeGrado, W. F. (2004) Nontoxic Membrane-Active Antimicrobial Arylamide Oligomers, *Angew. Chem. Int. Ed. Engl.* 43, 1033.
 16. Buffy, J. J., McCormick, M. J., Wi, S., Waring, A. J., Lehrer, R. I., and Hong, M. (2004) Solid-State NMR Investigation of the Selective Perturbation of Lipid Bilayers by the Cyclic Antimicrobial Peptide RTD-1, *Biochemistry* 43, 9800-9812.
 17. Doherty, T., Waring, A. J., and Hong, M. (2006) Peptide-lipid interactions of the β -hairpin antimicrobial peptide tachyplesin and its linear derivatives from solid-state NMR, *Biochim. Biophys. Acta.*, 1285-1291.
 18. Mani, R., Buffy, J. J., Waring, A. J., Lehrer, R. I., and Hong, M. (2004) Solid-State NMR Investigation of the Selective Disruption of Lipid Membranes by Protegrin-1, *Biochemis-*

- try 43, 13839-13848.
19. Ulrich, A. S. (2005) Solid state ^{19}F NMR methods for studying biomembranes, *Prog. Nucl. Magn. Reson. Spectrosc.*, 1-21.
 20. Glaser, R. W., Sachse, C., Dürr, U. H., Wadhvani, P., Afonin, S., Strandberg, E., and Ulrich, A. S. (2005) Concentration-Dependent Realignment of the Antimicrobial Peptide PGLa in Lipid Membranes Observed by Solid-State ^{19}F -NMR, *Biophys. J.* 88, 3392-3397.
 21. Luo, W., and Hong, M. (2006) Determination of the Oligomeric Number and Intermolecular Distances of Membrane Protein Assemblies by Anisotropic ^1H -Driven Spin Diffusion NMR Spectroscopy, *J. Am. Chem. Soc.*, 7242-7251.
 22. Luo, W., Mani, R., and Hong, M. (2007) Sidechain conformation and gating of the M2 transmembrane peptide proton channel of influenza A virus from solid-state NMR, *J. Phys. Chem.* 111, 10825-10832.
 23. Hong, M. (2007) Structure, Topology, and Dynamics of Membrane Peptides and Proteins from Solid-State NMR Spectroscopy, *J. Phys. Chem. B.*, 10340-10351.
 24. Grage, S. L., and Ulrich, A. S. (2000) Orientation-Dependent ^{19}F Dipolar Couplings within a Trifluoromethyl Group Are Revealed by Static Multipulse NMR in the Solid State, *J. Magn. Reson.*, 81-88.
 25. Hallock, K. J., Henzler-Wildman, K. A., Lee, D. K., and Ramamoorthy, A. (2002) Sublimable solids can be used to mechanically align lipid bilayers for solid-state NMR studies, *Biophys. J.*, 2499-2503
 26. De Angelis, A., and Opella, S. J. (2007) Bicelle samples for solid-state NMR of membrane proteins, *Nat. Protoc.* 2, 2332-2338.
 27. Su, Y., Mani, R., and Hong, M. (2008) Asymmetric insertion of membrane proteins in lipid bilayers by solid-state NMR paramagnetic relaxation enhancement: a cell-penetrating Peptide example, *J. Am. Chem. Soc.* 130, 8856-8864.
 28. Buffy, J. J., Hong, T., Yamaguchi, S., Waring, A. J., Lehrer, R. I., and Hong, M. (2003) Solid-State NMR Investigation of the Depth of Insertion of Protegin-1 in Lipid Bilayers Using Paramagnetic Mn^{2+} , *Biophys. J.* 85, 2363-2373.
 29. Wiener, M. C., and White, S. H. (1992) Structure of a fluid DOPC bilayer determined by joint refinement of x-ray and neutron diffraction data III Complete structure, *Biophys. J.* 61, 434-447.
 30. Carr, H. Y., and Purcell, E. M. (1954) Effects of diffusion on free precession in nuclear magnetic resonance experiments, *Phys. Rev.* 94, 630-638.
 31. Meiboom, S., and Gill, D. (1958) Modified spin-echo method for measuring nuclear relaxation times, *Rev. Sci. Instrum.* 29, 688-691.
 32. Grage, S. L., and Ulrich, A. S. (1999) Structural Parameters from ^{19}F Homonuclear Dipolar Couplings, Obtained by Multipulse Solid-State NMR on Static and Oriented Systems, *J. Magn. Reson.*, 98-106.

33. Yamamoto, K., Soong, R., and Ramamoorthy, A. (2009) Comprehensive Analysis of Lipid Dynamics Variation with Lipid Composition and Hydration of Bicelles Using Nuclear Magnetic Resonance (NMR) Spectroscopy, *Langmuir* 25, 7012-7018.
34. Baumann, G., and Mueller, P. (1974) A molecular model of membrane excitability, *J. Supramol. Struct.* 2, 538-557.
35. He, K., Ludtke, S. J., Worcester, D. L., and Huang, H. W. (1996) Neutron scattering in the plane of membranes: structure of alamethicin pores, *Biophys. J.* 70, 2659-2666.
36. Ludtke, S. J., He, K., Heller, W. T., Harroun, T. A., Yang, L., and Huang, H. W. (1996) Membrane Pores Induced by Magainin, *Biochemistry* 35, 13723-13728.
37. Matsuzaki, K., Murase, O., Fujii, N., and Miyajima, K. (1996) An antimicrobial peptide, magainin 2, induced rapid flip-flop of phospholipids coupled with pore formation and peptide translocation, *Biochemistry* 35, 11361-11368.
38. Pouny, Y., Rapaport, D., Mor, A., Nicolas, P., and Shai, Y. (1992) Interaction of antimicrobial dermaseptin and its fluorescently labeled analogs with phospholipid membranes, *Biochemistry* 31, 12416-12423.
39. Seelig, J., MacDonald, P. M., and Scherer, P. G. (1987) Phospholipid head groups as sensors of electric charge in membranes, *Biochemistry* 26, 7535-7541.
40. Scherer, P. G., and Seelig, J. (1989) Electric charge effects on phospholipid headgroups. Phosphatidylcholine in mixtures with cationic and anionic amphiphiles, *Biochemistry* 28, 7720-7728.
41. MacDonald, P. M., Leisen, J., and Marassi, F. M. (1991) Response of phosphatidylcholine in the gel and liquid-crystalline states to membrane surface charges, *Biochemistry* 30, 3558-3566.
42. Ziegler, A., Blatter, X. L., Seelig, A., and J., S. (2003) Protein Transduction Domains of HIV-1 and SIV TAT Interact with Charged Lipid Vesicles. Binding Mechanism and Thermodynamic Analysis, *Biochemistry* 42, 9185-9194.
43. Yamaguchi, S., Waring, A., Hong, T., Lehrer, R., and Hong, M. (2002) Solid-State NMR Investigations of Peptide-Lipid Interaction and Orientation of a beta-Sheet Antimicrobial Peptide, *Protegrin*, *Biochemistry* 41, 9852-9862.
44. Bechinger, B. (2005) Detergent-like properties of magainin antibiotic peptides: A 31P solid-state NMR spectroscopy study, *Biochim. Biophys. Acta.* 1712, 101-108.
45. Doherty, T., Waring, A. J., and Hong, M. (2008) Dynamic structure of disulfide-removed linear analogs of tachyplesin-I in the lipid bilayer from solid-state NMR, *Biochemistry* 47, 1105-1116.
46. Westerhoff, H. V., Juretić, D., Hendler, R. W., and Zasloff, M. (1989) Magainins and the disruption of membrane-linked free-energy transduction, *Proc. Natl. Acad. Sci. U. S. A.* 86, 6597-6601.
47. Bennett, A. E., Becerra, L. R., and Griffin, R. G. (1994) Frequency selective heteronuclear recoupling in rotating solids, *J. Chem. Phys.* 100, 812-814.

48. Wu, C. H., Ramamoorthy, A., and Opella, S. J. (1994) High-resolution heteronuclear dipolar solid-state NMR spectroscopy, *J. Magn. Reson.* 109, 270-272.
49. Munowitz, M. G., Griffin, R. G., Bodenhausen, G., and Huang, T. H. (1981) Two-dimensional rotational spin-echo NMR in solids: correlation of chemical shift and dipolar interactions, *J. Am. Chem. Soc.* 103, 2529-2533.

8.9 Supporting Information.

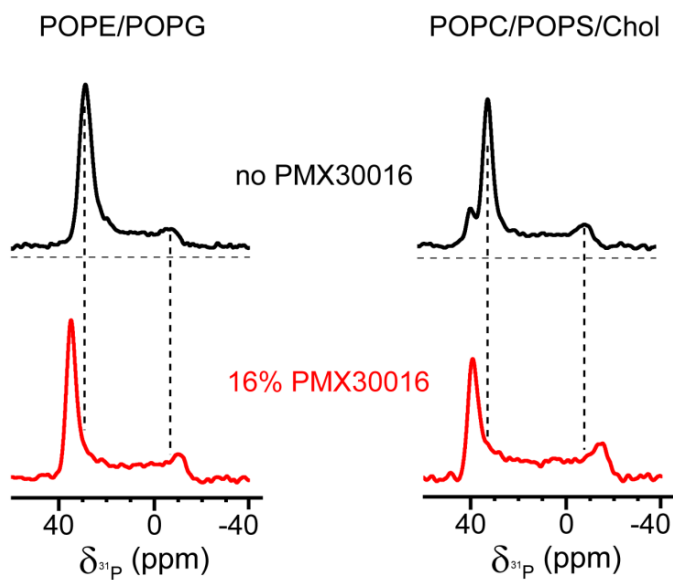


Figure S8.1. Static ^{31}P spectra of oriented lipid membranes of POPE/POPG (3:1) and POPC/POPS/cholesterol (4.5:1:2.4) without (black) and with (red) 16% PMX30016.

Chapter 9

Solid-State NMR Study of β -hairpin Antimicrobial Peptides in Lipopolysaccharide Incorporated Lipid Membranes: Mechanism of Gram-Selectivity

*A paper published in **Biochemistry***

2011, vol. 50(12), page 642-252

Yongchao Su ¹, Alan J. Waring ^{2,3}, Piotr Ruchala ², and Mei Hong ^{1*}

¹ Department of Chemistry, Iowa State University, Ames, IA 50011;

² Department of Medicine, David Geffen School of Medicine, University of California at Los Angeles, Los Angeles, CA 90095;

³ Department of Physiology and Biophysics, School of Medicine, University of California, Irvine, Irvine, CA 92697-4560

9.1 Abstract

The structural basis for the Gram selectivity of two disulfide-bonded β -hairpin antimicrobial peptides (AMPs) is investigated using solid-state NMR spectroscopy. The hexa-arginine PG-1 exhibits potent activities against both Gram-positive and Gram-negative bacteria, while a mutant of PG-1 with only three cationic residues maintains Gram-positive activity but is 30-fold less active against Gram-negative bacteria. We determined the topological structure and lipid interactions of these two peptides in a lipopolysaccharide (LPS)-rich membrane that mimics the outer membrane of Gram-negative bacteria and in the POPE/POPG membrane, which mimics the membrane of Gram-positive bacteria. ³¹P NMR lineshapes indicate that both peptides cause less orientational disorder to the LPS-rich membrane than to the POPE/POPG membrane. ¹³C chemical shifts and ¹³C-¹H dipolar couplings show that both peptides maintain their β -hairpin conformation in these membranes and are largely immobilized, but the mutant exhibited noticeable intermediate-timescale motion in the LPS membrane at physiological temperature, suggesting shallow insertion. Indeed, ¹H spin diffusion from lipid chains to the peptides showed that PG-1 fully inserted into the LPS-rich membrane whereas the mutant did not. The ¹³C-³¹P distances between the most hydrophobically embedded Arg of PG-1 and the lipid ³¹P are significantly longer in the LPS membrane than in the POPE/POPG membrane, indicating that PG-1 does not cause toroidal pore defects in the LPS membrane, in contrast to its behavior in the POPE/POPG membrane.

Taken together, these data indicate that PG-1 causes transmembrane pores of the barrel-stave type in the LPS membrane, thus allowing further translocation of the peptide into the inner membrane of Gram-negative bacteria to kill the cells. In comparison, the less cationic mutant cannot fully cross the LPS membrane due to weaker electrostatic attractions, thus causing weaker antimicrobial activities. Therefore, strong electrostatic attraction between the peptide and the membrane surface, ensured by having a sufficient number of Arg residues, is essential for potent antimicrobial activities against Gram-negative bacteria. The data provide a rational basis for controlling Gram selectivity of AMPs by adjusting the charge densities.

Abbreviations: AMP: antimicrobial peptide; POPE, 1-palmitoyl-2-oleoyl-*sn*-glycero-3-phosphoethanolamine; POPG, 1-palmitoyl-2-oleoyl-*sn*-glycero-3-phosphatidylglycerol; LPS: lipopolysaccharide; DEPE: 1,2-dielaidoyl-*sn*-glycero-3-phosphoethanolamine; MAS, magic-angle spinning; CP, cross-polarization; DARR, dipolar-assisted rotational resonance DIPSHIFT, dipolar-chemical-shift correlation; REDOR, rotational-echo double-resonance.

9.2 Introduction

As a consequence of evolution, a large number of bacterial strains have developed resistance to conventional antibiotics, urging the design of new antimicrobial molecules (1, 2). Antimicrobial peptides (AMPs), small cationic peptides of the innate immune systems of many animals and plants, have attracted much attention as potential antibiotics because of their potent and broad-spectrum activities (3, 4). The mechanisms of action of AMPs have been extensively investigated using biophysical and biochemical methods (5-8). These studies showed that a large number of AMPs kill bacteria by disrupting the membrane integrity (6) or altering the membrane potential (9, 10) of the microbial cells. Thus, the structures of the protective layers of bacterial cells traversed and disrupted by AMPs are relevant for understanding AMP's mechanisms of action. Gram-positive bacteria are coated by a thick peptidoglycan layer of several tens of nanometers and an inner phospholipid bilayer, while Gram-negative bacteria are protected by a lipopolysaccharide (LPS)-rich outer membrane, a thin periplasmic peptidoglycan layer, and an inner phospholipid bilayer (**Fig. 9.1**) (11). The outer membrane of Gram-negative bacteria is compositionally asymmetric: LPS molecules cover ~90% of the outer membrane surface while phospholipids compose the inner leaflet (12). It is known that the activity of many AMPs that target Gram-negative bacteria is con-

current upon permeabilization of the inner phospholipid bilayer rather than the outer membrane. This is true, for example, for the β -sheet-rich and disulfide-bonded protegrin-1 (PG-1) and human β -defensins (9, 13). Thus, these AMPs must first bind to and cross the LPS-rich outer membrane before reaching their target phospholipid bilayer. As a corollary, AMPs that are active against Gram-positive bacteria but not Gram-negative bacteria must be discriminated by the LPS membrane. Therefore, elucidating the structure and lipid interactions of AMPs in the LPS-rich membrane is important for understanding the mechanism of Gram selectivity.

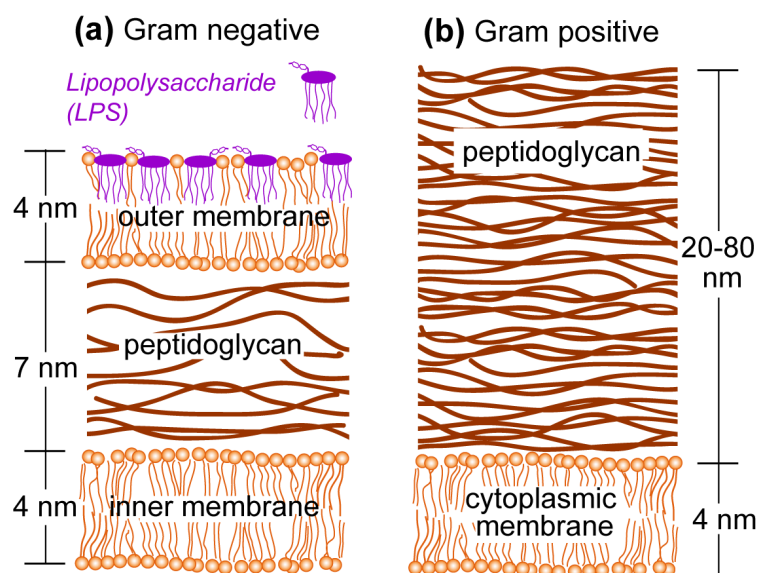


Fig. 9.1. Schematics of the different membrane structure of bacteria. (a) Gram-negative bacteria have a lipopolysaccharide (LPS)-rich outer membrane, a thin peptidoglycan layer, and an inner phospholipid membrane. (b) Gram-positive bacteria have a thick peptidoglycan layer and a cytoplasmic membrane. The main phospholipids in both bacteria are phosphatidylethanolamine (PE) and phosphatidylglycerol (PG) (79). LPS is about 10 mol% of the phospholipid amount in *E. coli* cells (38). The long O-antigen chain of LPS is shortened for simplicity.

LPS is a negatively charged complex glycolipid that can be divided into three structural regions: the hydrophobic lipid A that anchors LPS to the membrane, an oligosaccharide core, and an O-antigen polysaccharide (11, 14). The lipid A moiety consists of four to seven acyl chains attached to a di-glucosamine diphosphate, and is responsible for the severe host

inflammatory responses triggered by LPS (11, 15). The oligosaccharide core can be divided into the inner core, which contains a Kdo (3-deoxy-D-manno-oct-2-ulosonic acid) disaccharide and heptoses, and a structurally diverse outer core. The LPS derived from the *E. coli* deep rough mutant, ReLPS (Fig. 9.2b), contains only lipid A and two Kdo units, yet retains most of the endotoxin activity of native LPS (16). This structurally homogeneous ReLPS is thus an appealing molecule for investigating AMP-LPS interactions.

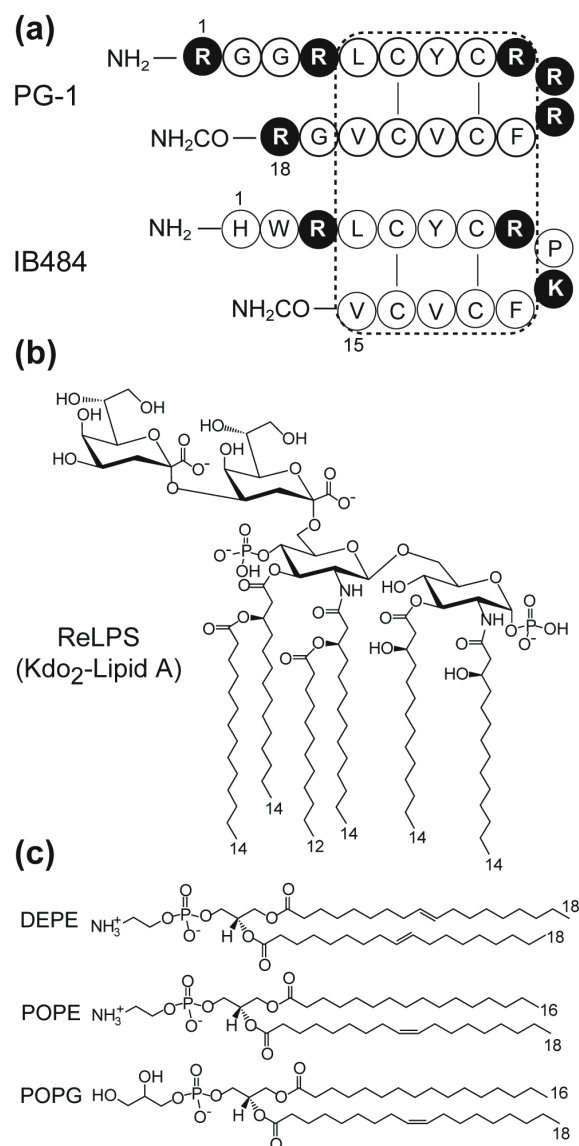


Fig. 9.2. Chemical structures of the peptides and lipids used in this study. (a) Amino acid sequences of disulfide-bonded PG-1 and IB-484. (b) Chemical structure of ReLPS. (c) Chemical structures of DEPE, POPE and POPG.

A number of biophysical and biochemical studies have probed the interactions of AMPs with LPS (14, 17-22). Most of these studies indicate that strong binding of AMPs to LPS is necessary for potent antimicrobial activities. For example, transmission electron and atomic force microscopies were used to study the effects of NK-lysin peptides on the morphology of different Gram-negative bacteria. The results suggested that electrostatic interaction with LPS was the decisive factor that correlated with bacteria killing (18), while subsequent outer-membrane intercalation and permeabilization are mostly independent of the chemical structure of the LPS oligosaccharides. Several solution NMR studies gave high-resolution structures of AMPs bound to LPS micelles and showed favorable electrostatic interactions between the cationic residues of the peptides and the anionic phosphates and Kdo units of LPS (14, 17). However, the biochemical studies used vesicles or real cells and had low structural resolution, while high-resolution solution NMR studies used LPS micelles or monolayers, which do not represent the bilayer nature of outer membranes well.

Here, we investigate two protegrin peptides, PG-1 and a charge-reduced mutant, IB484, to understand the structural basis underlying the Gram selectivity of β -hairpin AMPs. PG-1 is a porcine-derived 18-residue disulfide-bonded AMP containing six Arg residues (**Fig. 9.2a**). It is active against both Gram-positive and Gram-negative bacteria, with minimum inhibitory concentrations (MICs) of 0.3 – 3.0 μ M (23, 24). The mutant IB484 contains the same disulfide bonds but only three cationic residues, two Arg and one Lys (**Fig. 9.2a**). Its activity against the Gram-positive methicillin-resistant *Staphylococcus aureus* (MRSA) is comparable to PG-1 but its activity against the Gram-negative *Pseudomonas aeruginosa* is more than 30-fold weaker than PG-1 (25). The MIC values of PG-1 and IB484 are tabulated in **Table 9.1**. Our previous solid-state NMR studies showed that PG-1 disrupts anionic POPE/POPG membranes by forming transmembrane (TM) oligomeric β -barrels. Some of the lipid molecules around these β -barrels embed their phosphate groups into the hydrophobic middle of the membrane, thus connecting the two membrane leaflets (6, 26-33). The formation of these toroidal pores explains the antimicrobial activity of PG-1 against Gram-positive bacteria. However, how PG-1 interacts with the LPS membrane of Gram-negative bacteria has not been studied. Further, the topological structures of the Gram-selective IB484 in the two types of lipid membranes are completely unknown.

Table 9.1. Minimum inhibitory concentrations (MICs) of PG-1 and IB484 against two types of bacteria. The MIC values were normalized to those of PG-1, which are 1-4 $\mu\text{g/ml}$ against MRSA and 0.2-2 $\mu\text{g/ml}$ against *P. aeruginosa*. The data are quoted from reference (25).

Peptide	MRSA (Gram positive)	<i>P. aeruginosa</i> (Gram negative)
PG-1	1	1
IB484	2	32

In this study, we use solid-state NMR spectroscopy to determine the structure and lipid interaction of PG-1 and IB484 in lipid membranes that mimic the Gram-positive and Gram-negative bacteria cell surfaces. ^{31}P NMR was used to examine the nature and extent of membrane disorder caused by these peptides. The peptide conformation and dynamics were characterized by two-dimensional (2D) ^{13}C - ^{13}C correlation and dipolar-chemical-shift (DIP-SHIFT) correlation experiments. We then determined the depth of insertion of PG-1 and IB484 in the two types of membranes using ^1H spin diffusion and ^{13}C - ^{31}P distance measurements. From the observed structural differences, we propose mechanistic models for the Gram selectivity of the charge-reduced mutant as well as the interaction of wild-type PG-1 with the LPS membrane of Gram-negative bacteria.

9.3 Materials and Methods

Lipids and peptides

All lipids, including 1-palmitoyl-2-oleoyl-*sn*-glycero-3-phosphoethanolamine (POPE), 1-palmitoyl-2-oleoyl-*sn*-glycero-3-phosphatidylglycerol (POPG), 1,2-dielaidoyl-*sn*-glycero-3-phosphoethanolamine (DEPE) (**Fig. 9.2c**), and the deep rough mutant ReLPS isolated from the *E. coli* strain WBB06, were purchased from Avanti Polar Lipids (Alabaster, AL). ReLPS (Kdo₂-Lipid A) has comparable endotoxin activity as native LPS and can now be obtained with high purity in large scale (34). Fmoc-protected ^{13}C , ^{15}N -labeled Val was prepared in-house while backbone and sidechain protected ^{13}C , ^{15}N -labeled Arg was purchased from Cambridge Isotope Laboratories.

PG-1 (RGGRLCYCRRRFCVVCVGR-CONH₂) and IB484 (HWRL-CYCRPKFCVVCV-CONH₂) were synthesized using Fmoc solid-phase synthesis protocols and purified by reversed-phase HPLC. The peptides were oxidized and folded as described before (29) to yield the correct disulfide linkages. The disulfide connectivity pattern is the

same between synthetic and natural protegrin peptides based on sequential enzyme digestion combined with mass spectrometry analysis (35) and solution NMR studies (36, 37). The PG-1 sample contained labeled Arg4 while the IB484 sample contained labeled Arg3 and Val13.

Membrane sample preparation

POPE and POPG were mixed at 3 : 1 molar ratio in chloroform, dried under nitrogen gas, redissolved in cyclohexane and lyophilized overnight. The homogeneous dry powder was suspended in 2 ml phosphate buffer (10 mM, pH 7.0) and freeze-thawed 6 times to obtain a translucent vesicle solution. About 5.5 mg peptide was dissolved in 0.5 ml phosphate buffer. The lipid vesicle solution was added to the peptide solution, which immediately caused precipitation, indicating membrane binding of the peptides. The solution was incubated overnight at 4°C, followed by ultracentrifugation at 55,000 rpm at 6°C for 3 hours to obtain a membrane pellet. UV-VIS analysis indicated >95% binding of the peptide to the membrane. The water content of the pellet was adjusted to 40% (w/w) by slow evaporation of the samples in a desiccator. The pellet was center-packed into a 4 mm NMR rotor.

The LPS membrane contained ReLPS and DEPE at 1 : 5 molar ratio (about 3 : 5 mass ratio) to mimic the outer membrane composition of Gram-negative bacteria (38). The two lipids were codissolved in chloroform/methanol (4:1, v/v) and subjected to the same procedure as above to produce the proteoliposomes. All peptide-containing membranes had a peptide/lipid molar ratio of 1 : 12.5.

Solid-state NMR spectroscopy

NMR experiments were conducted on a 9.4 Tesla wide-bore Bruker DSX-400 spectrometer (Karlsruhe, Germany) operating at a resonance frequency of 162.12 MHz for ^{31}P , 100.72 MHz for ^{13}C and 40.58 MHz for ^{15}N . 4 mm magic-angle spinning (MAS) probes tuned to triple resonance $^1\text{H}/^{13}\text{C}/^{31}\text{P}$ or double-resonance $^1\text{H}/\text{X}$ ($\text{X} = ^{13}\text{C}$ or ^{15}N) were used. Low temperatures were achieved using a Kinetics Thermal System XR air-jet sample cooler (Stone Ridge, NY). Typical ^1H , ^{13}C and ^{31}P 90° pulse lengths were 4.0, 5.0 and 4.5 μs , respectively. ^{13}C , ^{15}N and ^{31}P chemical shifts were referenced to the ^{13}C signal of the α -Gly CO at 176.49 ppm on the TMS scale, the ^{15}N signal of ^{15}N -acetyl-valine (NAV) at 122.0 ppm on

the liquid ammonia scale, and the ^{31}P signal of hydroxylapatite at 2.73 ppm on the phosphoric acid scale, respectively.

^1H - ^{13}C cross polarization (CP) was achieved using spin-lock fields of 50 kHz. ^{13}C chemical shifts were assigned using 1D double-quantum (DQ) filtered experiments and 2D ^{13}C - ^{13}C DARR correlation experiments (39). DQ excitation and reconversion were achieved using the SPC-5 sequence (40) under 4.5-5.5 kHz MAS. The DARR experiments used a mixing time of 40 ms to establish through-space correlation peaks.

^{13}C - ^1H dipolar couplings were measured using the DIPSHIFT experiment under spinning speeds of 3.5-5.0 kHz (41, 42). ^1H homonuclear decoupling was achieved using the MREV-8 sequence with a ^1H 105° pulse length of 4.0 μs (43). Fitting the t_1 curve gave the apparent C-H dipolar coupling, which was divided by the MREV-8 scaling factor of 0.47 to give the true dipolar coupling. The ratio of the true coupling to the rigid-limit value, 22.7 kHz, gave the order parameter S_{CH} . The model tripeptide, ^{13}C , ^{15}N labeled N-formyl-Met-Leu-Phe-OH (f-MLF), was used to verify the MREV-8 scaling factor.

Semi-quantitative distances from the peptide to the center of the lipid membrane and to water were measured using the 2D ^{13}C -detected ^1H spin diffusion experiment. This approach has been used extensively to determine the depth of insertion and water accessibility of membrane peptides and proteins (26, 44-49). The experiment selects the ^1H magnetization of mobile lipid chains and water using a ^1H T_2 filter of 0.8-1.0 ms. The selected ^1H magnetization is then transferred to the rigid peptide and protein during a mixing period (t_m). The transfer rate depends on the intermolecular distances. The result of ^1H spin diffusion to the protein is detected via ^{13}C after a ^1H - ^{13}C CP step. The buildup of the cross peak intensities as a function of t_m is fit to give semi-quantitative distances. We carried out the ^1H spin diffusion experiments under 5 kHz MAS at 308 K for the ReLPS/DEPE samples and 288 K for the POPE/POPG samples. Both temperatures were 3°C below the phase transitions of each membrane and thus give comparable spin diffusion coefficients. For the POPE/POPG samples, a buildup curve was also measured at 298 K, 7°C above the phase transition temperature, to compare with previous PG-1 data measured at 298 K and to validate the interfacial diffusion coefficient used for distance fitting at 288 K.

^{13}C - ^{31}P distances between the peptide and the lipid phosphates were measured using the rotational-echo double-resonance (REDOR) experiment (50, 51). For $\text{C}\alpha$ - ^{31}P distances, a 1 ms ^{13}C 180° Gaussian pulse on resonance with the $\text{C}\alpha$ peak was applied in the middle of the REDOR mixing period to refocus the ^{13}C chemical shift and eliminate the ^{13}C - ^{13}C scalar couplings (51). Arg $\text{C}\zeta$ does not have a directly bonded ^{13}C , thus a non-selective 180° pulse was used. A pair of experiments without (S_0) and with (S) ^{31}P pulses was measured for each mixing time. A ^1H decoupling field strength of 71 kHz was used during the REDOR period, and the experiments were conducted at 233-237 K under 4.0 or 4.5 kHz MAS. The decay of S/S_0 as a function of mixing time was fit using the SIMPSON software (52) to obtain the distances. Two-spin (^{13}C - ^{31}P) simulations were used for all distance fitting. We have shown before (27) that, for ^{13}C - ^{31}P distances shorter than 5 Å, two-spin simulations accurately represent the ^{13}C distance to the nearest ^{31}P , since the average ^{31}P - ^{31}P separation in membrane bilayers is much larger, ~ 10 Å. For apparent two-spin distances greater than 7 Å, the two-spin distance closely represents, and only slightly over-estimates, the vertical distance of the ^{13}C spin to the ^{31}P plane.

9.4 Results

In our study, the POPE/POPG membrane was used to mimic the Gram-positive bacterial membrane as well as the inner membrane of Gram-negative bacteria, whereas the ReLPS/DEPE membrane was used to mimic the outer membrane of Gram-negative bacteria. ReLPS and DEPE mix homogeneously because of their similar phase transition temperatures (36°C for ReLPS (34) and 38°C for DEPE (53)) and the strong hydrogen-bonding capability of the PE headgroup (54, 55).

Membrane disorder caused by PG-1 and IB484

We first measured the static ^{31}P spectra of the two types of lipid membranes to assess the membrane disorder caused by IB484. ^{31}P chemical shift anisotropy (CSA) is highly sensitive to the membrane morphology (32, 56-62). Unoriented liquid-crystalline lamellar bilayers exhibit a powder pattern with a uniaxial lineshape, whose maximal intensity (90° edge) appears between -12 and -17 ppm. Correspondingly the span of the powder pattern is

38-50 ppm. In comparison, small isotropic vesicles, micelles and cubic-phase lipids give rise to an isotropic ^{31}P peak at about 0 ppm due to lateral diffusion of the lipids over the curved surface of these morphologies or fast tumbling of the vesicles when they are highly hydrated. Finally, hexagonal-phase lipids exhibit a uniaxial lineshape that is mirror-symmetric with that of the lamellar bilayer around the isotropic shift, with the maximal intensity at about +8 ppm.

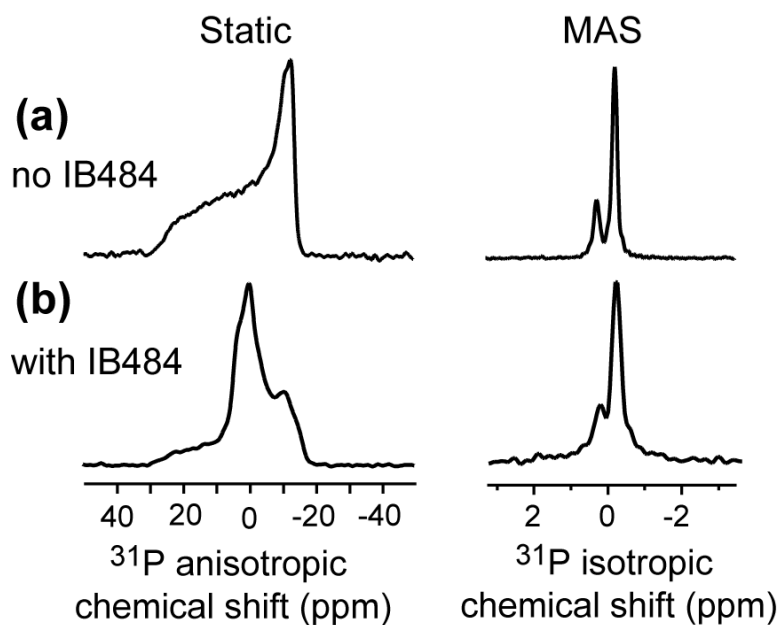


Fig. 9.3. ^{31}P static (left) and MAS (right) spectra of POPE/POPG membranes at 303 K. (a) Without peptide. (b) With 8 mol% IB484.

Fig. 9.3 shows the static and MAS ^{31}P spectra of the POPE/POPG membrane without and with IB484. While the peptide-free spectrum is characteristic of liquid-crystalline lamellar bilayers, the static spectrum of IB484-containing POPE/POPG membranes exhibits a high 0-ppm isotropic peak superimposed with residual powder intensities, indicating that the bilayer is significantly disrupted by the peptide to form high-curvature isotropic phases. The MAS spectra show that IB484 binding broadened the ^{31}P linewidths so that the two lipid signals are no longer well resolved. Thus, IB484 strongly disrupts the POPE/POPG membrane, similar to PG-1 (29, 32), consistent with the similar antimicrobial activities of the two peptides towards Gram-positive bacteria (**Table 9.1**).

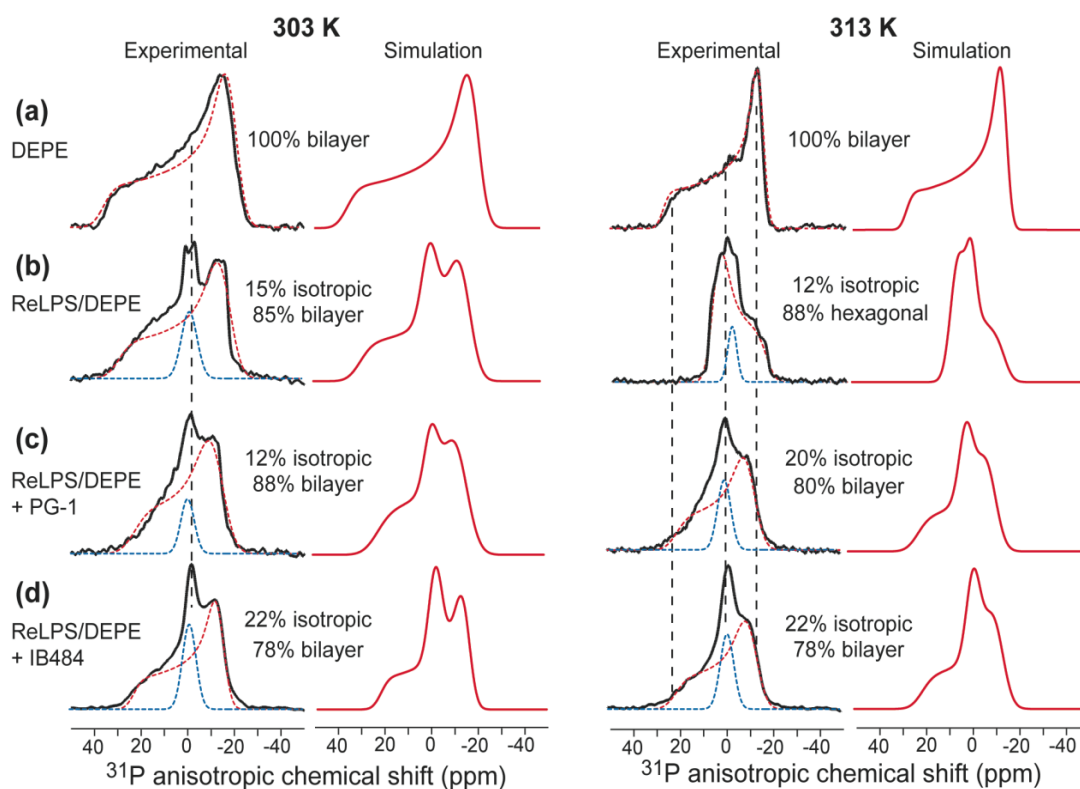


Fig. 9.4. Experimental (black) and simulated (red and blue) static ^{31}P spectra of ReLPS-containing membranes without and with peptides. The spectra were measured at 303 K and 313 K. (a) DEPE spectra. (b) ReLPS/DEPE spectra. (c) Spectra of ReLPS/DEPE membranes containing 8 mol% PG-1. (d) Spectra of ReLPS/DEPE membranes containing 8 mol% IB484. Best-fit simulations yield the percentages of each component.

Fig. 9.4 shows static ^{31}P spectra of ReLPS/DEPE membranes in the absence and presence of the peptides and their best-fit simulations to identify the membrane morphologies under the various conditions. The spectra were measured at 303 K and 313 K, which are slightly below and above the phase transition temperature of the membrane. The spectra of pure DEPE membranes (**Fig. 9.4a**) show lamellar powder patterns at both temperatures. In contrast, the ReLPS/DEPE (1:5) membrane exhibits a clear isotropic peak ($\sim 15\%$) in addition to a bilayer powder pattern (**Fig. 9.4b**) at 303 K, indicating that a small fraction of lipids assembled into small vesicles, micelles, or cubic phases. When the temperature increased to 313 K, the bilayer pattern was replaced by a hexagonal-phase powder pattern, which accounted for $\sim 88\%$ of the total intensity. This hexagonal phase formation suggests that the

LPS acyl chains experience larger disorder relative to the headgroup in the liquid-crystalline phase, thus causing negative curvature strain to the membrane. The result is consistent with previous X-ray diffraction and NMR studies of LPS-related membranes. For example, X-ray diffraction of lipid A membranes detected inverse hexagonal phase in the liquid-crystalline state under a wide range of hydration levels and Mg^{2+} concentrations (63, 64) X-ray diffraction of LPS molecules with varying acyl chain numbers and headgroup sizes (65) showed that whether LPS molecules have cylindrical or conical conformations strongly influences the packing and phase behavior of mixed LPS-phospholipid membranes.

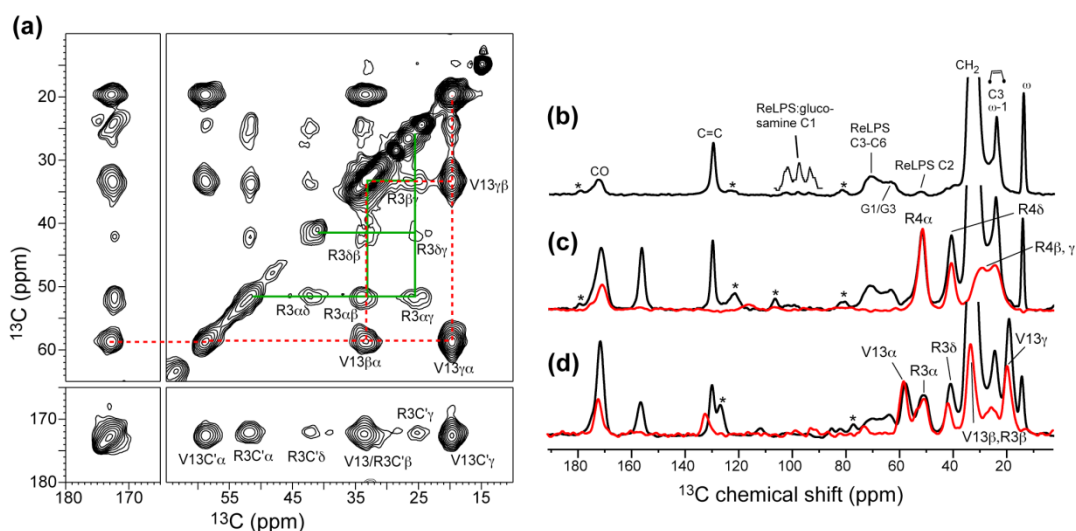


Fig. 9.5. ^{13}C chemical shifts of PG-1 and IB484 in ReLPS/DEPE membranes. (a) Representative 2D ^{13}C - ^{13}C DARR spectrum (40 ms mixing) of Arg3, Val13-labeled IB484 in POPE/POPG membranes at 263 K. The 2D spectrum was measured in 19 hrs with a maximum t_1 evolution time of 6 ms, 218 t_1 slices and 160 scans per slice. (b) 1D ^{13}C CP-MAS spectra of ReLPS/DEPE membranes. Asterisks indicate spinning sidebands. (c) ^{13}C CP-MAS spectrum (black) and ^{13}C DQ filtered spectrum (red) of PG-1 in ReLPS/DEPE membranes. (d) ^{13}C CP-MAS spectrum (black) and ^{13}C DQ filtered spectrum (red) of IB484 in ReLPS/DEPE membranes. The 1D spectra were measured between 237 and 253 K under 4-5 kHz MAS. The 1D DQ filtered spectra were acquired with 2560 scans.

A previous ^{31}P NMR analysis of ReLPS mixtures with phospholipids found that ReLPS forms lamellar bilayers with PE lipids more readily than with phosphocholine (PC) lipids due to the shape complementarity of LPS and PE (55), and that at 10 mol% ReLPS, only a small isotropic ^{31}P peak was present at 40°C. However, small- and wide-angle X-ray scattering indicated that the amount of the isotropic phase increases with the LPS concentra-

tion and becomes dominant in equimolar mixtures of ReLPS with DPPE/DPPG lipids (66). The ReLPS/DEPE membrane used here contains 20 mol% ReLPS, thus the significant but not dominant ^{31}P isotropic peak in the 313 K spectrum is qualitatively consistent with the previous results obtained at 10% and 50% LPS.

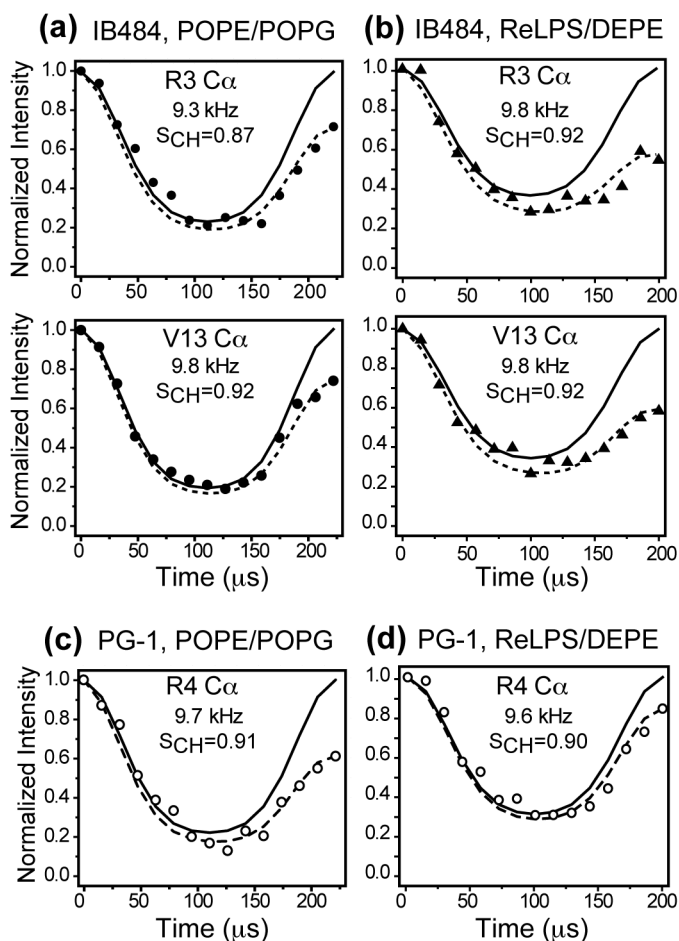


Fig. 9.6. C-H order parameters of IB484 and PG-1 in different membranes by 2D DIPSHIFT experiments. (a) IB484 in POPE/POPG membranes at 298 K under 4.5 kHz MAS. (b) IB484 in ReLPS/DEPE membranes at 308 K under 5 kHz MAS. (c) PG-1 in POPE/POPG membranes at 298 K under 4.5 kHz MAS. (d) PG-1 in ReLPS/DEPE membrane at 308 K under 5.0 kHz MAS. Solid and dashed lines are best-fit simulations without and with the T_2 decays, respectively.

Adding PG-1 and IB484 to the LPS membrane removed the hexagonal phase and stabilized the bilayer phase to about $\sim 80\%$ of the total intensity (**Fig. 9.4c, d**) (67). Thus, PG-1 and IB484 counter the negative curvature strain of the LPS-rich membrane. At 303 K, the bilayer powder patterns are ~ 9 ppm narrower than those of the peptide-free LPS mem-

branes, suggesting that the lipid headgroup conformation may be moderately affected by the peptides to give a different motionally averaged CSA (57, 68). The ^{31}P powder patterns in the presence of the peptides also show less defined edges, even though the same ^1H decoupling field (50 kHz) was applied. We attribute this effect to peptide-induced changes of the lipid diffusion rates, which cause intermediate-timescale broadening of the spectra. Finally, for both PG-1 and IB484, the isotropic peak of the ReLPS/DEPE membrane is smaller than that of the POPE/POPG membrane (**Fig. 9.3b**) (31), and the difference between the spectra of PG-1 and IB484 containing ReLPS/DEPE membranes is modest compared to the 30-fold MIC difference against Gram-negative bacteria. Thus, we turned to other observables to understand the origin of the different interactions of these two peptides with the LPS membrane.

Conformation and dynamics of PG-1 and IB484 in bacteria-mimic membranes

We determined the conformation of PG-1 and IB484 in the two lipid membranes by measuring ^{13}C chemical shifts of site-specifically labeled residues. The 2D ^{13}C correlation spectrum of IB484 in POPE/POPG membranes resolved all intra-residue cross peaks of Arg3 and Val13 (**Fig. 9.5a**). For the ReLPS/DEPE samples, 1D ^{13}C spectrum in the absence of the peptides (**Fig. 9.5b**) showed weak carbohydrate signals in the 60-100 ppm range as expected. The addition of PG-1 and IB484 gave rise to clear peptide ^{13}C signals that were confirmed by DQ filtered spectra (red), which suppressed all natural abundance ^{13}C signals of the lipids. These 1D and 2D spectra readily yielded $\text{C}\alpha$, $\text{C}\beta$, CO and $\text{N}\alpha$ chemical shifts of the labeled residues, and confirmed the β -sheet conformation of the two peptides in the ReLPS/DEPE membrane. Moreover, no chemical shift or linewidth changes were observed from 243 K to 308 K, and the 308 K ^{13}C spectra showed $\sim 85\%$ of the intensities of the 243 K spectra (data now shown). Thus, PG-1 and IB484 are mostly immobilized in the LPS membranes at physiological temperature.

To quantify the dynamics of IB484 in the two lipid membranes, we measured C-H dipolar couplings. **Fig. 9.6** shows the DIPSHIFT data of IB484 in POPE/POPG membranes at 298 K, which is above the phase transition temperature (291 K), and in ReLPS/DEPE membranes at 308 K, slightly below the phase transition temperature (311 K).

In both membranes, the C α sites of Arg3 and Val13 exhibit fast dephasing in the first half of the rotor period, indicating strong C-H dipolar couplings. The best-fit couplings gave C-H order parameters of ~ 0.9 , indicating that IB484 does not undergo fast motions at these temperatures in the two membranes. The POPE/POPG result was also reproduced at 288 K (data not shown), confirming the lack of fast peptide motion at 298 K. However, the time signals of IB484 showed varying extents of asymmetry between the first and second half of the rotor period: the intensities at the end of the rotor period was $\sim 72\%$ of the first time point for the POPE/POPG sample at 298 K and $\sim 54\%$ for the ReLPS/DEPE sample at 308 K. This asymmetry is known to be caused by intermediate-timescale motion that interferes with ^{13}C - ^1H and ^1H - ^1H dipolar couplings and MAS (69). The larger intensity reduction in the ReLPS/DEPE membrane suggests that IB484 may bind more superficially to this membrane or may be less oligomerized compared to its behavior in the POPE/POPG membrane. Comparison with reported DIPSHIFT curves for various motional rates and amplitudes (69) suggests that the intermediate-timescale motion of IB484 may occur in the 2-10 kHz regime, although the exact rates and amplitudes depend on the motional geometry and are outside the scope of this study.

Interestingly, the POPE/POPG-bound PG-1 also exhibited noticeable intensity asymmetry in the DIPSHIFT data (**Fig. 9.6c**), indicating that intermediate-timescale motion was already present in the wild-type peptide. **Table S9.1** summarizes the C-H order parameters and the apparent T_2 decay constants (T_2^*) of the four peptide-lipid combinations. In the ReLPS/DEPE membrane, PG-1 has a much longer T_2^* (1.45 ms) or much less DIPSHIFT asymmetry (**Fig. 9.6d**) than IB484 (0.34 ms), suggesting that the wild-type peptide binds more tightly to the LPS membrane than the mutant.

Depth of insertion from ^{13}C -detected ^1H spin diffusion

To determine the depth of insertion of the two peptides, we conducted 2D ^{13}C -detected ^1H spin diffusion experiments. The spin diffusion spectra were measured for POPE/POPG samples at 288 K and ReLPS/DEPE samples at 308 K, $\sim 3^\circ\text{C}$ below the corresponding phase transition temperatures. The similar reduced temperatures make ^1H spin diffusion coefficients similar so that buildup curves can be compared between the two types of

membranes. Based on previous calibrations we used the following diffusion coefficients to extract lipid-protein and water-protein distances: $D_L = 0.012 \text{ nm}^2/\text{ms}$ for the lipid phase, $D_W = 0.03 \text{ nm}^2/\text{ms}$ for water, and $D_P = 0.3 \text{ nm}^2/\text{ms}$ for the peptides (26, 45, 48). For the lipid-protein interface, we used a D_{int} of $0.005 \text{ nm}^2/\text{ms}$, as verified below.

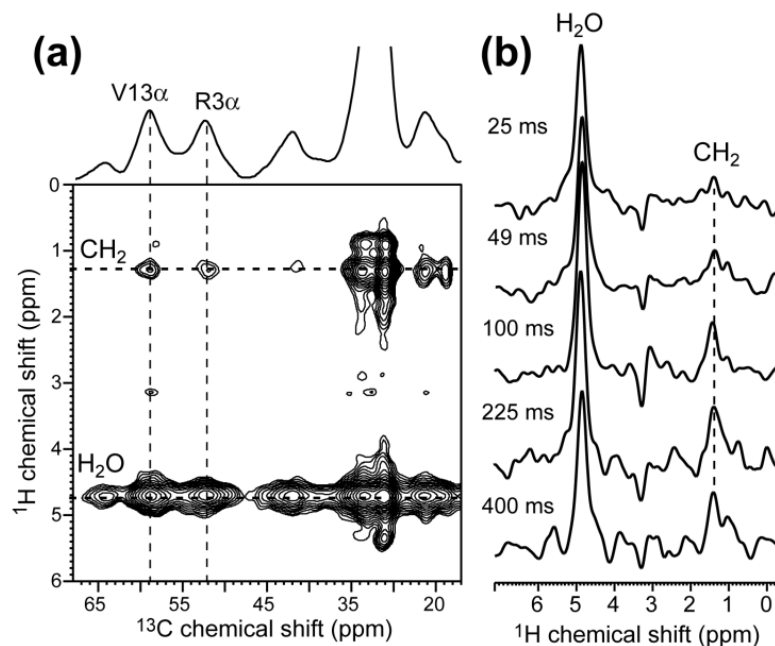


Fig. 9.7. 2D ^{13}C -detected ^1H spin diffusion spectra of IB484 in the ReLPS/DEPE membrane to determine the peptide's depth of insertion. (a) Representative 2D spectrum, measured with a 100 ms mixing time. (b) Sum of the Arg3 and Val13 $\text{C}\alpha$ ^1H cross sections as a function of mixing time.

Fig. 9.7a shows a representative 2D ^{13}C - ^1H correlation spectrum of IB484 in ReLPS/DEPE membranes. With a 100 ms mixing time, peptide- CH_2 and peptide-water cross peaks were clearly observed at ^1H chemical shifts of 1.3 ppm and 4.8 ppm, respectively. The sum of the ^1H cross sections of Arg3 $\text{C}\alpha$ and Val13 $\text{C}\alpha$ as a function of mixing time is shown in **Fig. 9.7b**. The cross peak intensity buildup as a function of mixing time is shown in **Fig. 9.8a** for IB484 in the two membranes. The lipid CH_2 buildup curve rises much more slowly in the ReLPS/DEPE membrane than in the POPE/POPG membrane. The latter curve is best fit to a 2 \AA distance, indicating that IB484 is inserted into the center of the POPE/POPG membrane. The lipid chain CH_3 buildup curve (not shown) is similar to the CH_2 curve (44),

confirming that the mutant is fully inserted across the membrane. Water spin diffusion to IB484 is also fast in the POPE/POPG membrane. Since the IB484 length (~ 26 Å) is shorter than the POPE/POPG P-P thickness (~ 40 Å), fast spin diffusion from both water and lipid acyl chains suggest water permeation into the membrane. In comparison, the CH₂ buildup curve for the ReLPS/DEPE membrane is best fit to a distance of 7 Å, indicating that IB484 is only partly inserted into the LPS membrane. At the same time, the water buildup curve is also slower in the ReLPS/DEPE membrane than in the POPE/POPG membrane, corresponding to a ~ 5 Å distance.

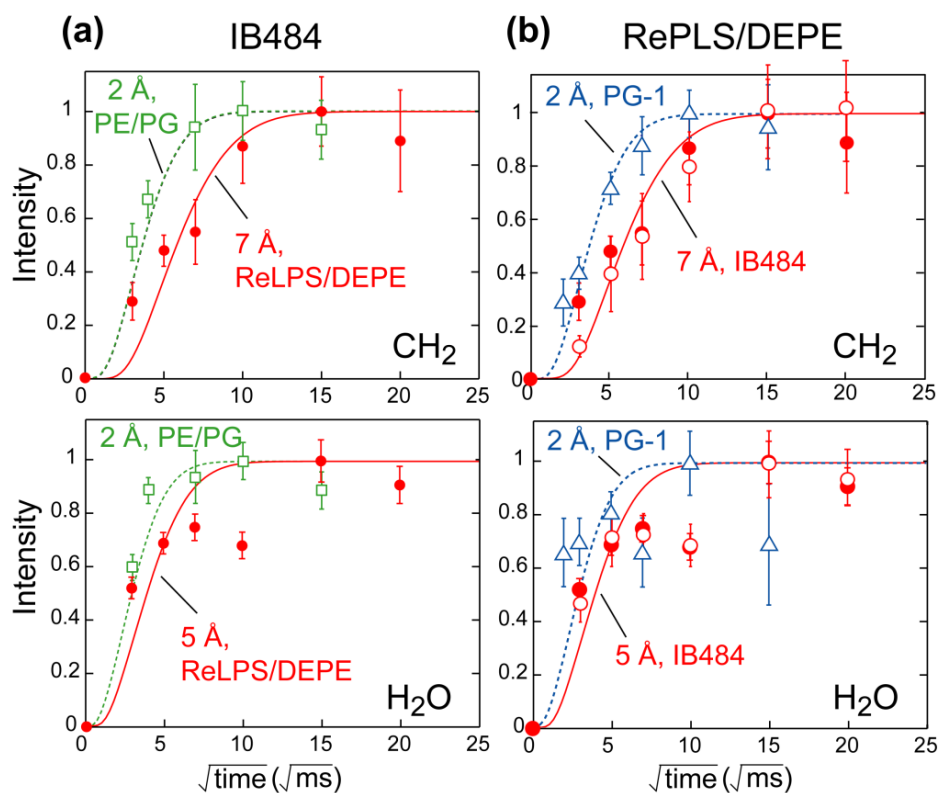


Fig. 9.8. Analysis of ^1H spin diffusion data of PG-1 and IB484 in two lipid membranes. **(a)** Buildup curves of IB484 in ReLPS/DEPE (filled circles) and POPE/POPG membranes (open squares), measured at 308 K and 288 K, respectively. The intensity is the sum of the Arg3 and Val13 C α ^1H cross sections. Top: Spin diffusion from lipid CH₂ protons to the peptide. Bottom: Spin diffusion from water to the peptide. **(b)** Buildup curves of IB484 (circles) and PG-1 (triangles) in ReLPS/DEPE membranes at 308 K. For the IB484 data, the sum of the Arg3 and Val13 C α intensity is shown as filled circles, while the Arg3 C α intensity is shown as open circles.

The ^1H spin diffusion curves of PG-1 and IB484 in the ReLPS/DEPE membrane are compared in **Fig. 9.8b**. Spin diffusion from both lipid CH_2 and water to PG-1 is rapid (2 \AA), indicating TM insertion of the peptide. The lipid CH_2 buildup curve is clearly faster for PG-1 than for IB484, supporting deeper insertion of the more cationic PG-1. Water spin diffusion to PG-1 is modestly faster than to IB484 in the LPS membrane. Since the PG-1 buildup curves were extracted from the $\text{C}\alpha$ signal of Arg4, which contains labile sidechain protons that can readily exchange with water, we analyzed the water spin diffusion curve to IB484 using only the Arg3 $\text{C}\alpha$ intensity. The resulting buildup curve (open circles) is the same as that obtained using the combined Arg3 and Val13 intensities (filled circles, **Fig. 9.8b**), confirming that IB484 is further away from water than PG-1.

The above spin diffusion buildup curves were fit using an interfacial diffusion coefficient of $0.005 \text{ nm}^2/\text{ms}$, which is larger than the value of $0.002 \text{ nm}^2/\text{ms}$ used before for liquid-crystalline membranes (45). This interfacial diffusion coefficient is a sensitive parameter in the distance fitting, and is only semi-quantitatively estimated based on ^1H - ^1H dipolar couplings (48). Although the higher D_{int} was consistent with the moderate gel-phase nature (3°C below the phase transition temperature) of the membranes in our experiments, we further verified the interfacial diffusion coefficient by repeating the spin diffusion experiment for the POPE/POPG-bound IB484 at 298 K. **Fig. S9.1a** compares the CH_2 buildup curves of IB484 and PG-1 at 298 K in the POPE/POPG membrane (26). The two curves superimpose well, indicating that the two peptides have similar distances to the center of the POPE/POPG membrane. Using a D_{int} of $0.00175 \text{ nm}^2/\text{ms}$, which was previously estimated for PG-1, we obtained the 2 \AA distance for IB484, which is identical to the result at 288 K. **Fig. S9.1b** compares the buildup curves of IB484 at 288 K and 298 K in the POPE/POPG membrane. As expected, higher temperature slowed down ^1H spin diffusion due to the lower membrane viscosity, but the intrinsic depth of the peptide is the same within this narrow temperature range. Thus, the choice of $0.005 \text{ nm}^2/\text{ms}$ for D_{int} at 288 K is consistent with the higher D_{int} value for liquid-crystalline POPE/POPG membranes, and IB484 is inserted into the hydrophobic center of this membrane.

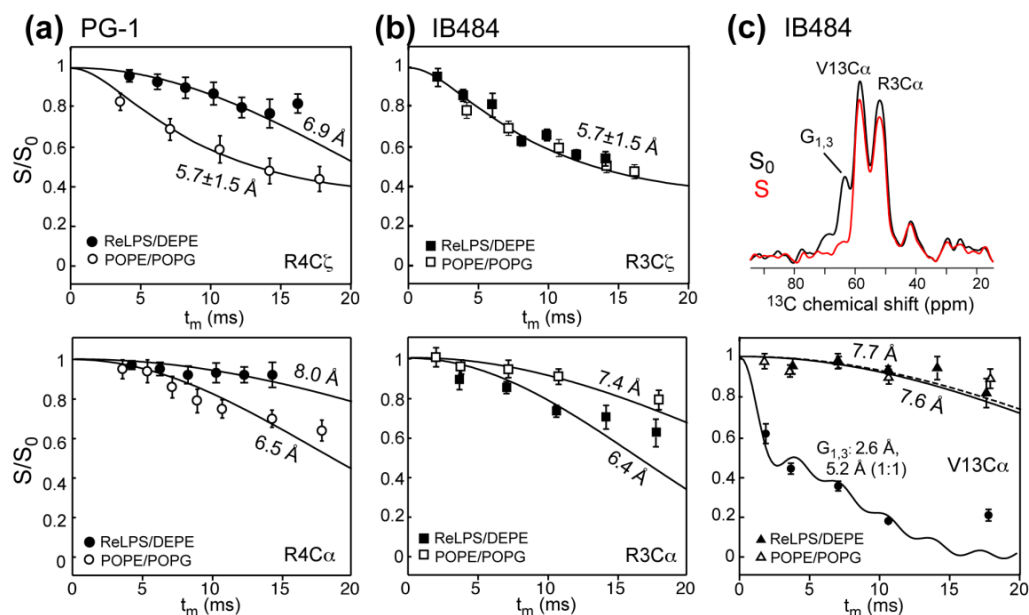


Fig. 9.9. ^{13}C - ^{31}P REDOR data of PG-1 and IB484. (a) PG-1 Arg4 C α and C ζ distances to ^{31}P in the ReLPS/DEPE membrane (filled symbols). The POPE/POPG data (open symbols) are superimposed (27). (b) IB484 Arg3 C α , C ζ and Val13 C α data in the ReLPS/DEPE membrane (filled symbols) versus the POPE/POPG membrane (open symbols). (c) Representative REDOR S_0 and S spectra of IB484 in the POPE/POPG membrane. Mixing time: 10.7 ms. The REDOR experiments were carried out at 233-237 K under 4.0 or 4.5 kHz MAS.

Guanidinium-phosphate ^{13}C - ^{31}P distances

To understand how Arg residues in the two peptides interact with the lipids, we measured ^{13}C - ^{31}P distances in both the LPS and regular phospholipid membranes. **Fig. 9.9a** shows the REDOR data of PG-1 in ReLPS/DEPE membranes and compares them with the previously reported POPE/POPG results (27). In the POPE/POPG membrane, Arg4 has a short C ζ -P distance of 5.7 Å indicative of guanidinium-phosphate complexation and a C α -P distance of 6.5 Å (27). These distances suggest toroidal pore formation by PG-1 in POPE/POPG membranes (26, 27). In the ReLPS/DEPE membrane, the Arg4 C ζ -P distance increased to 6.9 Å while the C α -P distance increased to 8.0 Å. Thus, guanidinium-phosphate salt bridge no longer exists in the LPS-bound PG-1. Since the ^1H spin diffusion data indicates TM insertion of PG-1 in this membrane, the lack of short ^{13}C - ^{31}P distances suggests that there are fewer or no lipid headgroups in the center of the membrane, which is consistent with the

limited isotropic intensity in the static ^{31}P spectrum of PG-1 containing LPS membrane (**Fig. 9.4c**).

Fig. 9.9b show the REDOR curves of IB484 in POPE/POPG (open symbols) and ReLPS/DEPE membranes (filled symbols), and a representative pair of REDOR spectra is shown in **Fig. 9.9c**. The Arg3 C ζ -P dephasing in both membranes are well fit by a Gaussian distribution of distances centered at 5.7 Å with a half width of 1.5 Å. Thus, on average Arg3 has close contact with the lipid phosphates in both membranes. For the backbone atoms, Arg3 shows a C α -P distance of 6.4 Å in the LPS membrane and 7.4 Å in the POPE/POPG membrane, while Val13 has a C α -P distance of 7.6-7.7 Å in both membranes. The accuracy of the REDOR experiment is verified by the rapid dephasing of the lipid glycerol G1 and G3 peak (63.5 ppm), which fit to a 1:1 combination of a 2.6 Å and 5.2 Å distance, consistent with the short intramolecular distances of these carbons to ^{31}P . All measured ^{13}C - ^{31}P distances are summarized in **Table 9.2**.

Table 9.2. ^{13}C - ^{31}P distances of PG-1 and IB484 in POPE/POPG and ReLPS/DEPE membranes.

Peptide	Residue	Site	POPE/POPG	ReLPS/DEPE
PG-1	Arg4	C ζ	5.7 ± 1.5 Å (27)	6.9 Å
		C α	6.5 Å (27)	8.0 Å
IB484	Arg3	C ζ	5.7 ± 1.5 Å	5.7 ± 1.5 Å
		C α	7.4 Å	6.4 Å
	Val13	C α	7.6 Å	7.7 Å

Although short guanidinium-phosphate distances were found for IB484 in both lipid membranes, the different depths of the peptide obtained from the ^1H spin diffusion experiment indicate different reasons for the short ^{13}C - ^{31}P distances. The mutant is shallowly inserted into the ReLPS/DEPE membrane and is thus in close proximity with the phosphate groups on the membrane surface. In contrast, the peptide is fully inserted across the POPE/POPG membrane, thus the relatively short C ζ -P distance of Arg3 must result from phosphate groups embedded in the hydrophobic region of the membrane, as in toroidal pores. The 1.3 Å difference in the Arg3 and Val13 C α distances to ^{31}P in the LPS membrane suggests that the C-terminus may be more deeply inserted into the membrane than the

N-terminus, due to the more hydrophobic nature of the C-terminal strand compared to the N-terminal strand (**Fig. 9.2a**).

9.5 Discussion

Understanding the Gram selectivity of AMPs is important for designing new antibiotics that selectively targets resistant bacteria. Previous studies of AMPs in LPS micelles or intact Gram-negative bacteria suggested the lack of peptide insertion to be the cause for the weaker antimicrobial activities of Gram-negative-inactive AMPs (17-19). However, molecular structures of AMPs in LPS-containing lipid bilayers have not been reported so far. The current study addresses the mechanism of Gram-selectivity by comparing the structures of PG-1 and a mutant in Gram-positive and Gram-negative mimetic lipid membranes. Based on our data, we propose four structural models (**Fig. 9.10 and Table S9.2**) that explain the different antimicrobial activities of the two peptides.

Both PG-1 and IB484 adopt a robust β -hairpin fold due to the disulfide bond constraints. Previous solid-state NMR data and MD simulations showed that the wild-type β -hairpins assemble into oligomeric TM β -barrels in POPE/POPG membranes (26, 70, 71), which lead to toroidal pore defects (**Fig. 9.10a**) (27). The current data show that the charge-reduced mutant is similarly inserted into the POPE/POPG membrane and also exhibits short Arg C ζ -P distances that are diagnostic of toroidal pores (**Fig. 9.10c**). The membrane disorder is consistent with the ^{31}P NMR lineshape of mutant-bound POPE/POPG membranes, which exhibited a high isotropic peak (**Fig. 9.3b**). It is also consistent with the similar antimicrobial activities of IB484 and PG-1 against Gram-positive bacteria (**Table 9.1**).

Guanidinium-phosphate salt bridges have now been observed for many cationic membrane peptides, including the antimicrobial peptides PG-1 (27) and human α -defensin 1 (72), the cell-penetrating peptides penetratin (73, 74) and HIV TAT (75), and the S4 helix of the KvAP potassium channel (76). Solid-state NMR provided the most direct means of identifying the existence of guanidinium-phosphate complexation through distance measurements between the Arg C ζ and lipid ^{31}P . In addition to interaction with the lipid phosphates, the guanidinium ion can also H-bond with water (77, 78). Both interactions shield the positive charge from the hydrophobic lipid chains, thus facilitating membrane insertion of these pep-

tides. IB484 exhibits clear guanidinium-phosphate interactions in POPE/POPG membranes, suggesting that even with only two Arg residues, the peptide is able to cause some phospholipids to reorient to lower the free energy barrier of peptide insertion into the hydrophobic region of the membrane.

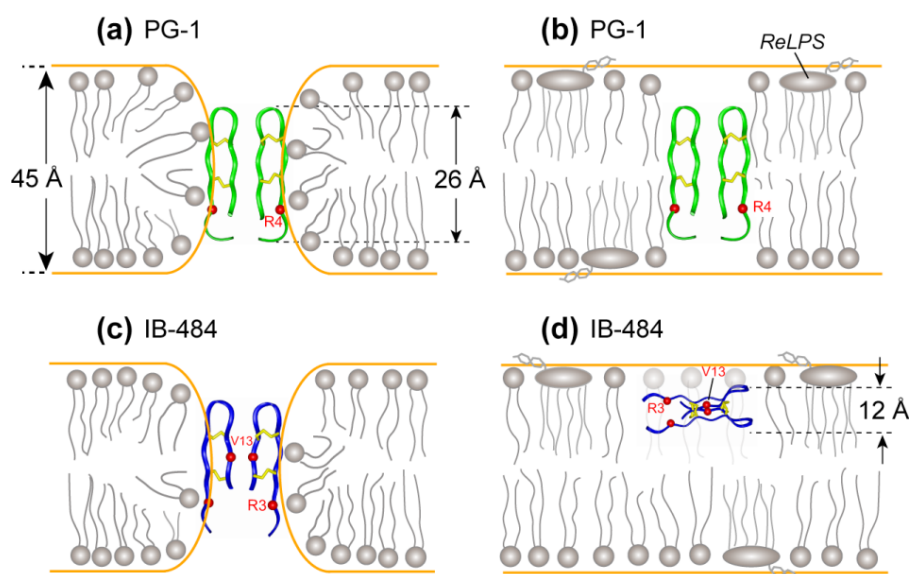


Fig. 9.10. Structural models of PG-1 and IB484 in ReLPS/DEPE and POPE/POPG membranes. (a) In the POPE/POPG membrane, PG-1 is TM and causes toroidal pores with strong orientational disorder (26, 27). (b) In the ReLPS/DEPE membrane, PG-1 is TM and causes barrel-stave pores with little lipid orientational disorder. (c) In the POPE/POPG membrane, IB484 is TM and causes toroidal pores with moderate lipid disorder. (d) In the ReLPS/DEPE membrane, IB484 is partially inserted without causing lipid disorder. The peptide cannot subsequently cross into the cytoplasmic membrane, thus explaining its weak antimicrobial activity against Gram-negative bacteria.

While both PG-1 and IB484 induce toroidal pores in the POPE/POPG membrane, they show different Arg C α -P distances: IB484 Arg3 C α exhibited a 1-Å longer distance (7.4 Å) than the corresponding Arg4 C α in PG-1 (6.5 Å). This difference suggests that fewer phosphate groups may reorient to contact the Arg in the mutant, as a result of the weaker electrostatic interaction of the membrane with the +3 charged mutant compared to the +6 charged PG-1. The distance difference is consistent with the 2-fold weaker antimicrobial activity of IB484 than PG-1 towards Gram-positive MRSA (**Table 9.1**).

In ReLPS/DEPE membranes, ^1H spin diffusion data indicate that PG-1 lies close to both water and lipid chains and is thus inserted in a TM fashion (26). However, the peptide

exhibits much longer Arg4 distances to ^{31}P compared to the distances in the POPE/POPG membrane. Although only Arg4 is measured in the present study, distances from other Arg's to ^{31}P will not provide additional information about the peptide-lipid interaction, because the other five Arg's in PG-1 are located at the hairpin tip and at the N- and C-termini, thus they are close to the lipid ^{31}P regardless of whether the peptide adopts a TM or a surface-bound structure. Among the six Arg's, Arg4 is closest to the hydrophobic middle of the β -hairpin, and is thus most sensitive to the absence or presence of toroidal pore defects. The combination of ^1H spin diffusion and ^{13}C - ^{31}P distance data indicate that PG-1 causes TM pores of the barrel-stave type in the ReLPS/DEPE membrane (**Fig. 9.10b**), where the lipid molecules maintain their regular orientation parallel to the membrane normal. The relative lack of orientational disorder is confirmed by the ^{31}P spectra (**Fig. 9.4c**). These TM pores, presumably filled with water, shield the Arg residues from the hydrophobic lipid chains, and at the same time provide a conduit for translocation of more PG-1 molecules into the cytoplasmic membrane, where actual cell killing occurs. The phase behavior of the ReLPS/DEPE membrane is complex in the absence of the peptide, and has not been fully explored as a function of temperature and composition (55, 66). Nevertheless, the ^{31}P spectra in **Fig. 9.4** clearly show that the ReLPS/DEPE membrane has significant curvature strain in the liquid-crystalline phase that is reduced in the gel phase. Thus, chain disorder plays a significant role in the lipid packing of the ReLPS/DEPE membrane. Binding of either peptide to the LPS membrane restored the lamellar bilayer at high temperature, which may proceed by chain rigidification or by the peptides counteracting the negative curvature strain of the lipids.

The biggest difference between the mutant and wild-type PG-1 lies in their depths of insertion in the ReLPS/DEPE membrane. The mutant cannot insert into the center of the LPS membrane, as shown by the slower ^1H spin diffusion from the lipid CH_2 , thus it cannot cross further into the cytoplasmic membrane. The shallow insertion of IB484 in the LPS membrane, in contrast to its TM orientation in the POPE/POPG membrane, may result from a combination of the large oligosaccharide moiety, the presence of six acyl chains, and the divalent cations that neutralize the LPS negative charges. These structural features serve to make the LPS-rich membrane more rigid and less permeable than regular phospholipid membranes (**Fig. 9.2**). The fact that wild-type PG-1 still inserts into the ReLPS/DEPE membrane, despite

the high membrane viscosity and impermeability, must then be attributed to the higher charge of the wild-type peptide and the stronger electrostatic interaction. But the more rigid LPS molecules cannot reorient to neutralize the Arg's of the inserted PG-1, thus no toroidal pores are observed. For IB484, the smaller number of cationic residues (2 Arg and 1 Lys) weakens the electrostatic attraction with the membrane, hence abolishing TM insertion. In the asymmetric outer membrane of real Gram-negative bacterial cells, the LPS molecules are almost exclusively located in the outer leaflet. Therefore, resistance against peptide insertion may be stronger and a higher cationicity may be required for potent antimicrobial activities.

In conclusion, the solid-state NMR data obtained here indicate that Gram selectivity among β -hairpin AMPs is largely the result of different insertion depths, which depend on the degree of peptide binding to the membrane, which is in turn determined by the Arg density of the peptides. Having a sufficient number of Arg residues facilitates peptide binding to and translocation across the LPS membrane of Gram-negative bacteria, allowing subsequent disruption of the inner cytoplasmic membrane.

9.6 Acknowledgement

This work was supported by grant GM066976 from the National Institutes of Health (to M.H.).

9.7 Reference

1. Fischbach, M. A., and Walsh, C. T. (2009) Antibiotics for emerging pathogens, *Science* 325, 1089-1093.
2. Levy, S. B., and Marshall, B. (2004) Antibacterial resistance worldwide: causes, challenges and responses, *Nat. Med.* 10, S122-S129.
3. Hancock, R. E., and Sahl, H. G. (2006) Antimicrobial and host-defense peptides as new anti-infective therapeutic strategies, *Nat. Biotechnol.* 24, 1551-1557.
4. Zasloff, M. (2002) Antimicrobial peptides of multicellular organisms, *Nature* 415, 389-395.
5. Brogden, K. A. (2005) Antimicrobial peptides: pore formers or metabolic inhibitors in bacteria?, *Nat. Rev. Microbiol.* 3, 238-250.
6. Tang, M., and Hong, M. (2009) Structure and mechanism of beta-hairpin antimicrobial peptides in lipid bilayers from solid-state NMR spectroscopy, *Mol. Biosyst.* 5, 317-322.

7. Epanand, R. M., and Vogel, H. J. (1999) Diversity of antimicrobial peptides and their mechanisms of action, *Biochim. Biophys. Acta* 1462, 11-28.
8. Huang, H. W. (2000) Action of antimicrobial peptides: two-state model., *Biochemistry* 39, 8347-8352.
9. Kagan, B. L., Selsted, M. E., Ganz, T., and Lehrer, R. I. (1990) Antimicrobial defensin peptides form voltage-dependent ion-permeable channels in planar lipid bilayer membranes, *Proc. Natl. Acad. Sci. U.S.A.* 87, 210-214.
10. Westerhoff, H. V., Juretić, D., Hendler, R. W., and Zasloff, M. (1989) Magainins and the disruption of membrane-linked free-energy transduction, *Proc. Natl. Acad. Sci. U. S. A.* 86, 6597-6601.
11. Sperandio, P., Dehò, G., and Polissi, A. (2009) The lipopolysaccharide transport system of Gram-negative bacteria, *Biochim Biophys Acta* 1791, 594-602.
12. Rosenfeld, Y., and Shai, Y. (2006) Lipopolysaccharide (Endotoxin)-host defense antibacterial peptides interactions: role in bacterial resistance and prevention of sepsis, *Biochim. Biophys. Acta.* 1758, 1513-1522.
13. Lehrer, R. I., Barton, A., Daher, K. A., Harwig, S. S., Ganz, T., and Selsted, M. E. (1989) Interaction of human defensins with *Escherichia coli*. Mechanism of bactericidal activity, *J. Clin. Invest.* 84, 553-561.
14. Mares, J., Kumaran, S., Gobbo, M., and Zerbe, O. (2009) Interactions of lipopolysaccharide and polymyxin studied by NMR spectroscopy., *J. Biol. Chem.* 284, 11498-11506.
15. Hancock, R. E., and Scott, M. G. (2000) The role of antimicrobial peptides in animal defenses, *Proc. Natl. Acad. Sci. U. S. A.* 97, 8856-8861.
16. Raetz, C. R., Garrett, T. A., Reynolds, C. M., Shaw, W. A., Moore, J. D., Smith, D. C., Ribeiro, A. A., Murphy, R. C., Ulevitch, R. J., Fearn, C., Reichart, D., Glass, C. K., Benner, C., Subramaniam, S., Harkewicz, R., Bowers-Gentry, R. C., Buczynski, M. W., Cooper, J. A., Deems, R. A., and Dennis, E. A. (2006) Kdo2-Lipid A of *Escherichia coli*, a defined endotoxin that activates macrophages via TLR-4, *J. Lipid Res.* 47, 1097-1111.
17. Bhunia, A., Domadia, P. N., Torres, J., Hallock, K. J., Ramamoorthy, A., and Bhattacharjya, S. (2010) NMR structure of pardaxin, a pore-forming antimicrobial peptide, in lipopolysaccharide micelles: mechanism of outer membrane permeabilization., *J. Biol. Chem.* 285, 3883-3895.
18. Hammer, M. U., Brauser, A., Olak, C., Brezesinski, G., Goldmann, T., Gutschmann, T., and Andrä, J. (2010) Lipopolysaccharide interaction is decisive for the activity of the antimicrobial peptide NK-2 against *Escherichia coli* and *Proteus mirabilis*, *Biochem. J.* Epub ahead of print.
19. Rosenfeld, Y., Barra, D., Simmaco, M., Shai, Y., and Mangoni, M. L. (2006) A synergism between temporins toward Gram-negative bacteria overcomes resistance imposed by the lipopolysaccharide protective layer, *J. Biol. Chem.* 281, 28565-28574.

20. Zhang, L., Scott, M. G., Yan, H., Mayer, L. D., and Hancock, R. E. (2000) Interaction of polyphemusin I and structural analogs with bacterial membranes, lipopolysaccharide, and lipid monolayers, *Biochemistry* 39, 14504-14514.
21. Lienkamp, K., Kumar, K. N., Som, A., Nüsslein, K., and Tew, G. N. (2009) "Doubly selective" antimicrobial polymers: how do they differentiate between bacteria?, *Chem.–Eur. J.* 15, 11710-11714.
22. Böhring, A., Hagge, S. O., Roes, S., Podschun, R., Sahly, H., Harder, J., Schröder, J. M., Grötzinger, J., Seydel, U., and Gutschmann, T. (2006) Lipid-specific membrane activity of human beta-defensin-3, *Biochemistry* 45, 5663-5670.
23. Bellm, L., Lehrer, R. I., and Ganz, T. (2000) Protegrins: new antibiotics of mammalian origin, *Expert Opin. Investig. Drugs.* 9, 1731-1742.
24. Tam, J. P., Wu, C., and Yang, J. L. (2000) Membranolytic selectivity of cysteine-stabilized cyclic protegrins., *Eur. J. Biochem.* 267, 3289-3300.
25. Chen, J., Falla, T. J., Liu, H., Hurst, M. A., Fujii, C. A., Mosca, D. A., Embree, J. R., Loury, D. J., Radel, P. A., Cheng, C. C., Gu, L., and Fiddes, J. C. (2000) Development of protegrins for the treatment and prevention of oral mucositis: structure-activity relationships of synthetic protegrin analogues, *Biopolymers* 55, 88-98.
26. Mani, R., Cady, S. D., Tang, M., Waring, A. J., Lehrer, R. I., and Hong, M. (2006) Membrane-dependent oligomeric structure and pore formation of a beta-hairpin antimicrobial peptide in lipid bilayers from solid-state NMR, *Proc. Natl. Acad. Sci. U S A.* 103, 16242-16247.
27. Tang, M., Waring, A. J., and Hong, M. (2007) Phosphate-Mediated Arginine Insertion into Lipid Membranes and Pore Formation by a Cationic Membrane Peptide from Solid-State NMR, *J. Am. Chem. Soc.* 129, 11438-11446.
28. Mani, R., Tang, M., Wu, X., Buffy, J. J., Waring, A. J., Sherman, M. A., and Hong, M. (2006) Membrane-bound dimer structure of a b-hairpin antimicrobial peptide from rotational-echo double-resonance solid-state NMR, *Biochemistry* 45, 8341-8349.
29. Yamaguchi, S., Hong, T., Waring, A., Lehrer, R. I., and Hong, M. (2002) Solid-state NMR investigations of peptide-lipid interaction and orientation of a beta-sheet antimicrobial peptide, protegrin, *Biochemistry* 41, 9852-9862.
30. Buffy, J. J., Waring, A. J., Lehrer, R. I., and Hong, M. (2003) Immobilization and aggregation of the antimicrobial peptide protegrin-1 in lipid bilayers investigated by solid-state NMR, *Biochemistry* 42, 13725-13734.
31. Mani, R., Buffy, J. J., Waring, A. J., Lehrer, R. I., and Hong, M. (2004) Solid-state NMR investigation of the selective disruption of lipid membranes by protegrin-1, *Biochemistry* 43, 13839-13848.
32. Mani, R., Waring, A. J., Lehrer, R. I., and Hong, M. (2005) Membrane-disruptive abilities of beta-hairpin antimicrobial peptides correlate with conformation and activity: a 31P and 1H NMR study, *Biochim Biophys Acta.* 1716, 11-18.

33. Wi, S., and Kim, C. (2008) Pore structure, thinning effect, and lateral diffusive dynamics of oriented lipid membranes interacting with antimicrobial peptide protegrin-1: P-31 and H-2 solid-state NMR study, *J. Phys. Chem. B* 112, 11402-11414.
34. Sasaki, H., and White, S. H. (2008) Aggregation Behavior of an Ultra-Pure Lipopolysaccharide that Stimulates TLR-4 Receptors, *Biophys. J.* 95, 986-993.
35. Harwig, S. S., Swiderek, K. M., Lee, T. D., and Lehrer, R. I. (1995) Determination of disulphide bridges in PG-2, an antimicrobial peptide from porcine leukocytes, *J. Pept. Sci.* 1, 207-215.
36. Aumelas, A., Mangoni, M., Roumestand, C., Chiche, L., Despaux, E., Grassy, G., Calas, B., and Chavanieu, A. (1996) Synthesis and solution structure of the antimicrobial peptide protegrin-1, *Eur. J. Biochem.* 237, 575-583.
37. Fahrner, R. L., Dieckmann, T., Harwig, S. S., Lehrer, R. I., Eisenberg, D., and Feigon, J. (1996) Solution structure of protegrin-1, a broad-spectrum antimicrobial peptide from porcine leukocytes, *Chem. & Biol.* 3, 543-550.
38. Raetz, C. R., and Whitfield, C. (2002) Lipopolysaccharide Endotoxins, *Annu. Rev. Biochem.* 71, 635-700.
39. Takegoshi, K., Nakamura, S., and Terao, T. (2001) ^{13}C - ^1H dipolar-assisted rotational resonance in magic-angle spinning NMR, *Chem. Phys. Lett.* 344, 631-637.
40. Hohwy, M., Rienstra, C. M., Jaroniec, C. P., and Griffin, R. G. (1999) Fivefold symmetric homonuclear dipolar recoupling in rotating solids: Application to double quantum spectroscopy, *J. Chem. Phys.* 110, 7983-7992.
41. Munowitz, M. G., Griffin, R. G., Bodenhausen, G., and Huang, T. H. (1981) Two-dimensional rotational spin-echo nuclear magnetic resonance in solids: correlation of chemical shift and dipolar interactions, *J. Am. Chem. Soc.*, 2529-2533.
42. Hong, M., Gross, J. D., Rienstra, C. M., Griffin, R. G., Kumashiro, K. K., and Schmidt-Rohr, K. (1997) Coupling Amplification in 2D MAS NMR and Its Application to Torsion Angle Determination in Peptides, *J. Magn. Reson.* 129, 85-92.
43. Rhim, W. K., Elleman, D. D., and Vaughan, R. W. (1973) Analysis of multiple pulse NMR in solids, *J. Chem. Phys.* 59, 3740-3749.
44. Tang, M., Waring, A. J., and Hong, M. (2009) Effects of arginine density on the membrane-bound structure of a cationic antimicrobial peptide from solid-state NMR, *Biochim. Biophys. Acta.* 1788, 514-521.
45. Luo, W., and Hong, M. (2010) Conformational changes of an ion channel detected through water-protein interactions using solid-state NMR spectroscopy, *J. Am. Chem. Soc.* 132, 2378-2384.
46. Ader, C., Schneider, R., Seidel, K., Etzkorn, M., Becker, S., and Baldus, M. (2009) Structural rearrangements of membrane proteins probed by water-edited solid-state NMR spectroscopy, *J. Am. Chem. Soc.* 131, 170-176.

47. Hong, M. (2006) Solid-State NMR Studies of the Structure and Dynamics of Disordered and Membrane-Bound Peptides and Proteins, *Acct. Chem. Res.* 39, 176-183.
48. Huster, D., Yao, X. L., and Hong, M. (2002) Membrane Protein Topology Probed by ^1H Spin Diffusion from Lipids Using Solid-State NMR Spectroscopy, *J. Am. Chem. Soc.* 124, 874-883.
49. Kumashiro, K. K., Schmidt-Rohr, K., Murphy, O. J., Ouellette, K. L., Cramer, W. A., and Thompson, L. K. (1998) A novel tool for probing membrane protein structure: solid-state NMR with proton spin diffusion and X-nucleus detection, *J. Am. Chem. Soc.* 120, 5043-5051.
50. Gullion, T., and Schaefer, J. (1989) Rotational-echo double-resonance NMR, *J. Magn. Reson.* 81, 196-200.
51. Jaroniec, C. P., Tounge, B. A., Herzfeld, J., and Griffin, R. G. (2001) Frequency selective heteronuclear dipolar recoupling in rotating solids: accurate (^{13}C) - (^{15}N) distance measurements in uniformly (^{13}C) , (^{15}N) -labeled peptides, *J. Am. Chem. Soc.* 123, 3507-3519.
52. Bak, M., Rasmussen, T., and Nielsen, N. C. (2000) SIMPSON: A General Simulation Program for Solid-State NMR Spectroscopy, *J. Magn. Reson.* 147, 296-330.
53. Prenner, E. J., Lewis, R. N., Neuman, K. C., Gruner, S. M., Kondejewski, L. H., Hodges, R. S., and McElhaney, R. N. (1997) Nonlamellar phases induced by the interaction of gramicidin S with lipid bilayers. A possible relationship to membrane-disrupting activity, *Biochemistry* 36, 7906-7916.
54. Fried, V. A., and Rothfield, L. I. (1978) Interactions between lipopolysaccharide and phosphatidylethanolamine in molecular monolayers, *Biochim. Biophys. Acta.* 514, 69-82.
55. Nomura, K., Inaba, T., Morigaki, K., Brandenburg, K., Seydel, U., and Kusumoto, S. (2008) Interaction of Lipopolysaccharide and Phospholipid in Mixed Membranes: Solid-State ^{31}P -NMR Spectroscopic and Microscopic Investigations, *Biophys. J.* 95, 1226-1238.
56. Seelig, J. (1978) ^{31}P nuclear magnetic resonance and the headgroup structure of phospholipids in membranes, *BIOCHIM. BIOPHYS. ACTA.* 515, 105-140.
57. Su, Y., DeGrado, W. F., and Hong, M. (2010) Orientation, dynamics, and lipid interaction of an antimicrobial arylamide investigated by ^{19}F and ^{31}P solid-state NMR spectroscopy, *J. Am. Chem. Soc.* 132, 9197-9205.
58. Doherty, T., Waring, A. J., and Hong, M. (2006) Peptide-lipid interactions of the beta-hairpin antimicrobial peptide tachyplesin and its linear derivatives from solid-state NMR, *Biochim. Biophys. Acta* 1758, 1285-1291.
59. Yamaguchi, S., Huster, D., Waring, A., Lehrer, R. I., Tack, B. F., Kearney, W., and Hong, M. (2001) Orientation and Dynamics of an Antimicrobial Peptide in the Lipid Bilayer by Solid-State NMR, *Biophys. J.* 81, 2203-2214.

60. Buffy, J. J., McCormick, M. J., Wi, S., Waring, A., Lehrer, R. I., and Hong, M. (2004) Solid-State NMR Investigation of the Selective Perturbation of Lipid Bilayers by the Cyclic Antimicrobial Peptide RTD-1, *Biochemistry* 43, 9800-9812.
61. Aisenbrey, C., Bertani, P., and Bechinger, B. (2010) Solid-state NMR investigations of membrane-associated antimicrobial peptides, *Methods Mol. Biol.* 618, 209-233.
62. Auger, M. (2009) Structural and Dynamics Studies of Lipids by Solid-State NMR.
63. Brandenburg, K., Koch, M. H., and Seydel, U. (1990) Phase diagram of lipid A from *Salmonella minnesota* and *Escherichia coli* rough mutant lipopolysaccharide, *J. Struct. Biol.* 105, 11-21.
64. Nomura, K., Maeda, M., Sugase, K., and Kusumoto, S. (2010) Lipopolysaccharide induces raft domain expansion in membrane composed of a phospholipid-cholesterol-sphingomyelin ternary system, *Innate Immun.*, [Epub ahead of print].
65. Schromm, A. B., Brandenburg, K., Loppnow, H., Zähringer, U., Rietschel, E. T., Carroll, S. F., Koch, M. H., Kusumoto, S., and Seydel, U. (1998) The charge of endotoxin molecules influences their conformation and IL-6-inducing capacity, *J. Immunol.* 161, 5464-5471.
66. Urbán, E., Bóta, A., and Kocsis, B. (2006) Non-bilayer formation in the DPPE-DPPG vesicle system induced by deep rough mutant of *Salmonella minnesota* R595 lipopolysaccharide, *Colloids Surf. B Biointerfaces* 48, 106-111.
67. Brandenburg, K., Koch, M. H., and Seydel, U. (1998) Biophysical characterisation of lysozyme binding to LPS Re and lipid A, *Eur. J. Biochem.* 258, 686-695.
68. Seelig, J., MacDonald, P. M., and Scherer, P. G. (1987) Phospholipid head groups as sensors of electric charge in membranes, *Biochemistry* 26, 7535-7541.
69. deAzevedo, E. R., Saalwachter, K., Pascui, O., de Souza, A. A., Bonagamba, T. J., and Reichert, D. (2008) Intermediate motions as studied by solid-state separated local field NMR experiments, *J. Chem. Phys.* 128, 104505.
70. Jang, H., Ma, B., Lal, R., and Nussinov, R. (2008) Models of Toxic beta-Sheet Channels of Protegrin-1 Suggest a Common Subunit Organization Motif Shared with Toxic Alzheimer beta-Amyloid Ion Channels *Biophys. J.* 95, 4631-4642.
71. Langham, A. A., Ahmad, A. S., and Kaznessis, Y. N. (2008) On the nature of antimicrobial activity: a model for protegrin-1 pores, *J. Am. Chem. Soc.* 130, 4338-4346.
72. Zhang, Y., Lu, W., and Hong, M. (2010) The Membrane-Bound Structure and Topology of a Human α -Defensin Indicate a Dimer Pore Mechanism for Membrane Disruption, *Biochemistry* 49, 9770-9782.
73. Su, Y., Doherty, T., Waring, A. J., Ruchala, P., and Hong, M. (2009) Roles of Arginine and Lysine Residues in the Translocation of a Cell-Penetrating Peptide from 13C, 31P, and 19F Solid-State NMR, *Biochemistry* 48, 4587-4595.

74. Su, Y., Mani, R., and Hong, M. (2008) Asymmetric insertion of membrane proteins in lipid bilayers by solid-state NMR paramagnetic relaxation enhancement: a cell-penetrating Peptide example, *J. Am. Chem. Soc.* 130, 8856-8864.
75. Su, Y., Waring, A. J., Ruchala, P., and Hong, M. (2010) Membrane-bound dynamic structure of an arginine-rich cell-penetrating peptide, the protein transduction domain of HIV TAT, from solid-state NMR, *Biochemistry* 49, 6009-6020.
76. Doherty, T., Su, Y., and Hong, M. (2010) High-resolution orientation and depth of insertion of the voltage-sensing S4 helix of a potassium channel in lipid bilayers, *J. Mol. Biol.* 401, 642-652.
77. Freites, J. A., Tobias, D. J., von Heijne, G., and White, S. H. (2005) Interface connections of a transmembrane voltage sensor, *Proc. Natl. Acad. Sci. U. S. A.* 102, 15059-15064.
78. Li, S., Su, Y., Luo, W., and Hong, M. (2010) Water-protein interactions of an arginine-rich membrane peptide in lipid bilayers investigated by solid-state nuclear magnetic resonance spectroscopy, *J. Phys. Chem. B* 114, 4063-4069.
79. Raetz, C. R. (1978) Enzymology, Genetics, and Regulation of Membrane Phospholipid Synthesis in *Escherichia coli*, *Microbiol. Rev.* 42, 614-659.

9.8 Supporting Information

Table S9.1. C-H order parameters (S_{CH}) and the apparent T_2^* of IB484 and PG-1 in different lipid membranes. T_2^* is the apparent decay constant in the DIPSHIFT time data due to intermediate time-scale motion, and was measured as the decay of the last data point compared to the first data point.

Peptide	POPE/POPG			ReLPS/DEPE		
	Temp	S_{CH}	T_2^* (ms)	Temp	S_{CH}	T_2^* (ms)
IB484 Arg3 C α	288 K	0.87	0.48	308 K	0.92	0.34
	298 K	0.87	0.66			
PG-1 Arg4 C α	288 K	0.91	0.40	308 K	0.90	1.45
	298 K	0.91	0.94			

Table S9.2. Experimental constraints for the topologies of PG-1 and IB484 in POPE/POPG and ReLPS/DEPE membranes.

Peptide	Membrane	Insertion model	^1H spin diffusion		^{13}C - ^{31}P distances	
			Lipid CH ₂	Water	Backbone	Arg C ζ
PG-1	POPE/POPG	β -barrel toroidal pore	2 Å	2 Å	5.5-6.5 Å	4.0-5.7 Å
	ReLPS/DEPE	Barrel-stave pores	2 Å	2 Å	8.0 Å	6.9 Å
IB484	POPE/POPG	Toroidal pore	2 Å	2 Å	7.4-7.6 Å	5.7 Å
	ReLPS/DEPE	Partial insertion	7 Å	5 Å	6.4-7.7 Å	5.7 Å

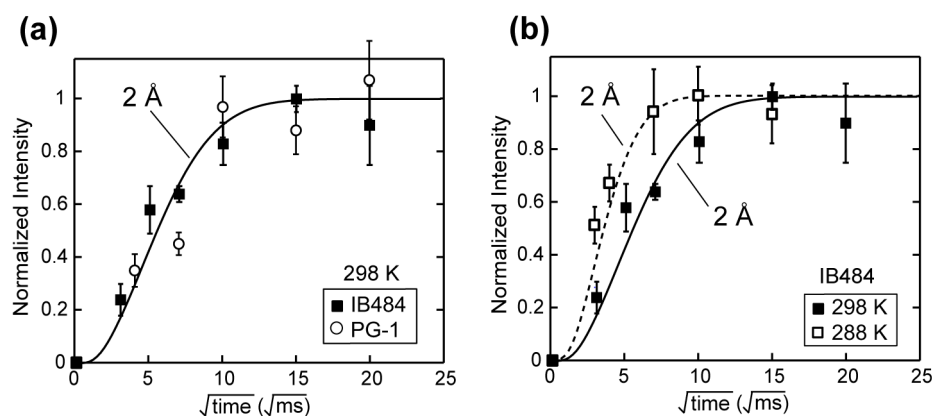


Figure S9.1. Comparison of lipid-peptide ^1H spin diffusion curves at different temperatures for POPE/POPG-bound peptides. (a) Buildup curves of PG-1 (open circles) and IB484 (filled squares) at 298 K. A D_{int} of $0.00175 \text{ nm}^2/\text{ms}$ was used for distance fitting. (b) Buildup curves of IB484 at 298 K (filled squares) and 288 K (open squares). D_{int} was $0.00175 \text{ nm}^2/\text{ms}$ for 298 K and $0.005 \text{ nm}^2/\text{ms}$ for 288 K.

Chapter 10

High-Resolution Orientation and Depth of Insertion of the Voltage-Sensing S4 Helix of a Potassium Channel in Lipid Bilayers[†]

A paper published in Journal of Molecular Biology

2010 vol. 401 pp. 642-252

Tim Doherty*, Yongchao Su* and Mei Hong (* indicates equal contribution)

Department of Chemistry, Iowa State University, Ames, IA 50011

[†] *A preliminary form of this article is included in Dr. Tim Doherty's thesis.*

10.1 Abstract

The opening and closing of voltage-gated potassium (Kv) channels are controlled by several conserved Arg residues in the S4 helix of the voltage-sensing domain. The interaction of these positively charged Arg's with the lipid membrane has been of intense interest for understanding how membrane proteins fold to allow charged residues to insert into lipid bilayers against free energy barriers. We have now determined the orientation and insertion depth of the S4 peptide of the KvAP channel in lipid bilayers using solid-state NMR. 2D ¹⁵N correlation experiments of macroscopically oriented S4 peptide in phospholipid bilayers revealed a tilt angle of 40°, and two possible rotation angles differing by 180° around the helix axis. Remarkably, the tilt angle and one of the two rotation angles are identical to those of the S4 helix in the intact voltage-sensing domain, suggesting that interactions between the S4 segment and other helices of the voltage-sensing domain is not essential for the membrane topology of the S4 helix. ¹³C-³¹P distances between the S4 backbone and the lipid ³¹P indicate a ~9 Å local thinning and 2 Å average thinning of the DMPC/DMPG bilayer, consistent with neutron diffraction data. Moreover, a short distance of 4.6 Å from the guanidinium Cζ of the second Arg to ³¹P indicates the existence of guanidinium-phosphate hydrogen bonding and salt bridge. These data suggest that the structure of the Kv gating helix is mainly determined by protein-lipid interactions instead of inter-helical protein-protein interactions, and the S4 amino acid sequence encodes sufficient information for the membrane topology of this crucial gating helix.

10.2 Introduction

Voltage-activated potassium (Kv) channels are important for electrical signaling by neurons and muscle cells. The Kv voltage-sensing domain, which contains four helices designated S1 to S4, drives the opening and closing of the potassium-conducting pore in response to changes in the membrane potential (1, 2). Most of the gating charges are located on the S4 helix, which contains several conserved arginine residues (Arg) at every third position (3). High-resolution crystal structures (4-6) and avidin accessibility measurements (7) suggested that the S3b-S4 segment, which forms a helix-turn-helix motif called the voltage-sensing paddle, moves by as much as 15 Å during channel activation under depolarizing membrane voltages. Since positively charged Arg residues incur a high free energy cost to insert into the low-dielectric hydrophobic core of lipid bilayers (8), there has been intense interest in understanding how the Arg-rich S4 helix is structured in the lipid bilayer in the resting and activated states of the protein. The paddle model proposes that the gating Arg's interact directly with the lipids (5), while the canalculi model proposes that the Arg's are shielded by acidic residues in other transmembrane (TM) helices (9). Molecular dynamics (MD) simulations of the S4 helix alone (10) and of the entire voltage-sensing domain (11, 12) suggested that Arg-phosphate salt bridges, water clusters near the guanidinium moieties deep in the membrane, and membrane thinning, contribute to the stabilization of the S4 Arg's in the lipid membrane. Conductivity measurements showed that voltage sensing requires phosphate groups in lipid membranes (13, 14), also supporting the notion that the voltage-sensing domain interacts strongly with the lipid headgroups. Neutron diffraction of the KvAP S1-S4 domain in POPC/POPG bilayers showed that the voltage sensor is fully embedded in the lipid bilayer and does not cause strong perturbations of the membrane structure (15). Despite this increasing body of evidence, atomic-level structural information of the Kv voltage-sensing paddle and the Arg residues therein, measured directly in phospholipid bilayers, remains scarce.

Solid-state NMR spectroscopy has contributed significantly to the understanding of the structural basis for the function of Arg-rich membrane peptides such as antimicrobial peptides (16, 17) and cell-penetrating peptides (18, 19). These studies demonstrated the feasibility of measuring inter-atomic distances between Arg residues and lipid phosphates in

multilamellar lipid membranes. In addition, due to the intrinsic orientation dependence of NMR frequencies, solid-state NMR spectroscopy is a sensitive probe of the orientation of membrane proteins in lipid bilayers. Here, we combine static oriented-membrane solid-state NMR techniques with magic-angle spinning experiments to determine the orientation, depth of insertion, and Arg-phosphate interaction of the Kv S4 peptide in phospholipid bilayers. We compare these results with the structure of the S4 helix in the intact voltage sensor to infer the importance of lipid-protein versus protein-protein interactions for channel gating.

10.3 Results

S4 backbone conformation in the lipid bilayer

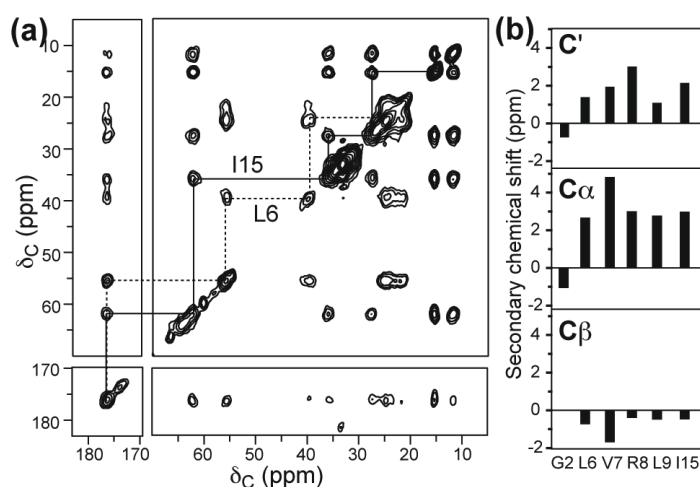


Figure 10.1. ^{13}C isotropic chemical shifts of the KvAP S4 peptide in DMPC/DMPG bilayers. (a) 2D ^{13}C - ^{13}C correlation spectrum of Leu₆, Ile₁₅ labeled S4 at 263 K, with a spin diffusion mixing time of 30 ms. (b) Secondary chemical shifts of CO, C α and C β of labeled residues, using random coil chemical shifts of reference (21) (**Table S10.1**).

Before determining the S4 peptide orientation, we first measured the backbone conformation of the KvAP S4 peptide (residues 113-130) to determine if this segment is α -helical in the lipid membrane in the absence of the other helices of the voltage-sensing domain. For this purpose we measured the ^{13}C isotropic chemical shifts of six labeled residues distributed throughout the segment: Gly₂, Leu₆, Val₇, Arg₈, Leu₉ and Ile₁₅. A representative 2D ^{13}C - ^{13}C DARR (20) correlation spectrum is shown in **Fig. 10.1a**. The difference

of the $C\alpha$, $C\beta$, and CO isotropic chemical shifts from the random coil values gives information on the protein secondary structure (21). **Fig. 10.1b** shows that most residues exhibit positive CO and $C\alpha$ secondary shifts and negative $C\beta$ secondary shifts, which are characteristic of the α -helical conformation. The only exception is the N-terminal Gly₂, which is consistent with the fact that the corresponding Gly residue in the intact voltage sensor is part of the turn between the S3b and S4 helices (4).

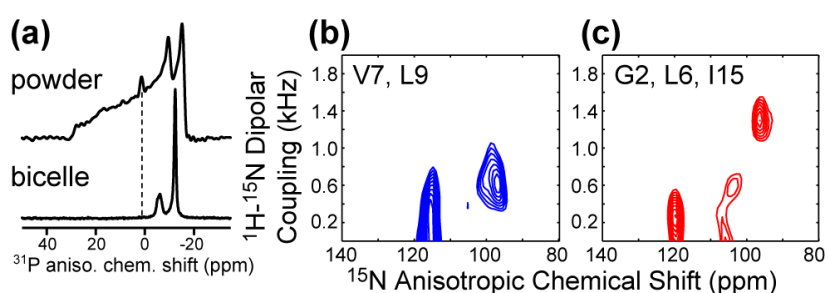


Figure 10.2. Measured orientation-dependent spectra of KvAP S4. (a) ^{31}P spectra of S4-containing unoriented DMPC/DMPG membranes (top) and magnetically aligned DMPC/6-O-PC bicelles (bottom). The minor peak at 0 ppm (top) is the phosphate buffer signal. (b-c) 2D N-H dipolar and ^{15}N CSA correlation spectra of bicelle aligned S4 peptide. (b) With Val₇, Leu₉ ^{15}N labels. (c) With Gly₂, Leu₆, and Ile₁₅ ^{15}N labels.

S4 helix orientation in the lipid bilayer

The S4 helix orientation was determined using a 2D ^{15}N NMR experiment that correlates the ^{15}N - ^1H dipolar coupling with the ^{15}N CSA of uniaxially aligned peptides (22). Due to the periodic orientation distribution of the backbone N-H bonds with respect to the helix axis and the relative orientation of the ^{15}N chemical shift tensor to the N-H bond, these 2D spectra exhibit wheel-like patterns (23, 24) whose position and size indicate the tilt angle of the helix from the bilayer normal. The position of individual resonances on these “PISA” wheel indicates the directions of the sidechains around the helical axis.

We oriented the S4 peptide using magnetically aligned DMPC/6-O-PC bicelles. Static ^{31}P spectra show sharp peaks at frequencies consistent with well-aligned bicelles whose bilayer normal is perpendicular to the magnetic field (**Fig. 10.2a**). No isotropic ^{31}P peak was observed in the bicelle spectrum, and the unoriented spectrum of S4-containing DMPC/DMPG bilayers which also shows a uniaxial powder pattern except for a phosphate

buffer peak, indicating that the peptide does not perturb the bilayer integrity. The absence of strong membrane perturbation is consistent with neutron diffraction data of the S1-S4 domain in POPC/POPG membranes (15). **Fig. 10.2b, c** show the 2D ^{15}N correlation spectra of the oriented S4 peptide: the Val₇, Leu₉-labeled sample shows an N-H dipolar splitting of 1.2 kHz (read as twice the value from the zero-frequency axis) for one residue and nearly vanishing coupling for the other (**b**), while the triply Gly₂, Leu₆, Ile₁₅-labeled sample shows a maximum N-H splitting of 2.8 kHz (**c**). The latter spectrum can be partially assigned on the basis of the ^{15}N -labeled positions: Leu₆ and Ile₁₅ should differ in their ρ angles by 180° since every consecutive residue in an α -helix increments the ρ angle by 100° . Thus Leu₆ and Ile₁₅ peaks should appear on opposite sides of the PISA wheel. As a result, the 120 ppm and 95 ppm peaks in **Fig. 10.2c** must be assigned to Leu₆ and Ile₁₅, while the weak signal at 106 ppm can be assigned to Gly₂. Its nearly vanishing coupling is consistent with the unstructured nature of Gly₂ obtained from the ^{13}C isotropic chemical shifts. Since Gly₂ is not part of the α -helix, we do not consider its ^{15}N frequencies in the following orientation analysis.

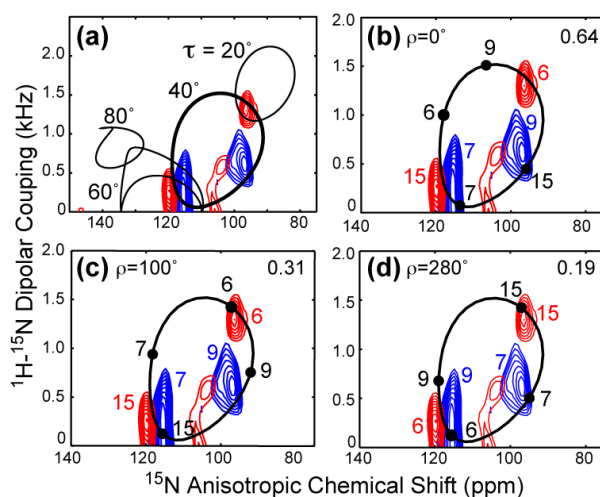


Figure 10.3. Simulated orientation-dependent spectra of KvAP S4. (a) Simulated 2D ^{15}N - ^1H dipolar and ^{15}N CSA correlation spectra (black lines) overlaid with the sum of the two experimental spectra of **Fig. 10.2b, c**. Best fit is $\tau=40^\circ \pm 5^\circ$. Simulated spectra are scaled from the rigid-limit values as shown in **Fig. S10.4** (57). (b-d) Simulated 2D spectra for $\tau = 40^\circ$ and different ρ . (b) $\rho = 0^\circ$. (c) $\rho = 100^\circ$. (d) $\rho = 280^\circ$. The assignment in the simulated spectra is annotated in black, while the assignment for the experimental spectrum is shown in color. The RMSD between the calculated and measured spectra is indicated in the upper right corner of each panel.

Fig. 10.3a superimposed the sum of the two experimental spectra with simulated 2D PISA wheel spectra for an ideal α -helix with tilt angles of 0° to 90° . The best-fit τ is found at 40° , where the position and size of the wheel are in excellent agreement with the experimental peak distribution. The spectral linewidths are 4 – 5 ppm for the ^{15}N anisotropic chemical shift dimension and 0.4 – 0.5 kHz for the dipolar dimension. These linewidths allow the tilt angle to be determined with a precision better than 5° , as shown in **Fig. S10.1**. A survey of published oriented membrane protein spectra shows that the ^{15}N anisotropic chemical shift linewidths range from 2.5 ppm to 9 ppm, while the N-H dipolar coupling dimension has linewidths of 0.3 to 1.2 kHz. This large linewidth variation reflects the intrinsic conformational distribution and dynamic disorder of the different membrane proteins (25-30).

To extract the ρ angle, we require that not only should the individual resonance positions on the $\tau=40^\circ$ wheel have minimal deviations from the measured frequencies, but also the order of peaks around the PISA wheel should follow the intrinsic orientation relationships of the N-H bonds. Excluding Gly₂, the order of the four residues in the clockwise direction should be Leu₆, Leu₉, Ile₁₅, and Val₇. **Fig. 10.3b-d** show simulated spectra for several ρ angles, where the RMSD between the simulated and measured spectra is indicated. The $\rho=0^\circ$ spectrum is an example of poor fit with large RMSD, while $\rho=100^\circ\pm 20^\circ$ and $280^\circ\pm 20^\circ$ show good agreement with the experimental spectra and correspond to the two RMSD minima in the full 360° range (**Fig. S10.2**). Moreover, the peak assignments are consistent with the known ^{15}N -labeled positions in the two samples. The difference of 180° in the two ρ solutions is not coincidental, since Leu₆ and Ile₁₅ differ in ρ by 180° while Val₇ and Leu₉ differ in ρ by 200° , thus the two assignments are nearly degenerate. Although the RMSD values indicate that $\rho=280^\circ$ agrees better with the experimental spectra, due to the near degeneracy we consider both orientations in the subsequent analysis that combines the insertion depth and the peptide orientation.

Depth of insertion of S4 residues and Arg - phosphate interaction

We probed the insertion depth of the S4 helix through ^{13}C - ^{31}P distances between the peptide and the lipid. C α -P distances indicate the backbone immersion depths while the Arg

C ζ distance to ^{31}P identify possible salt bridges and snorkeling (31). The ^{31}P atoms lie in lamellar planes in our membrane samples based on the lack of isotropic peaks in the static ^{31}P spectra of both oriented bicelles and unoriented liposomes (Fig. 10.2). Fig. 10.4 shows representative ^{13}C - ^{31}P REDOR data. Arg $_8$ guanidinium C ζ shows the shortest ^{13}C - ^{31}P distance of 5.5 Å when fit with a single distance. When the slower dephasing at long mixing times were taken into account, then a 1:1 combination of a 4.6 Å distance and a 7.8 Å distance was found to best reproduce the data. Thus, at least 50% of the Arg $_8$ guanidinium lies within hydrogen-bonding distance to the lipid phosphate headgroups.

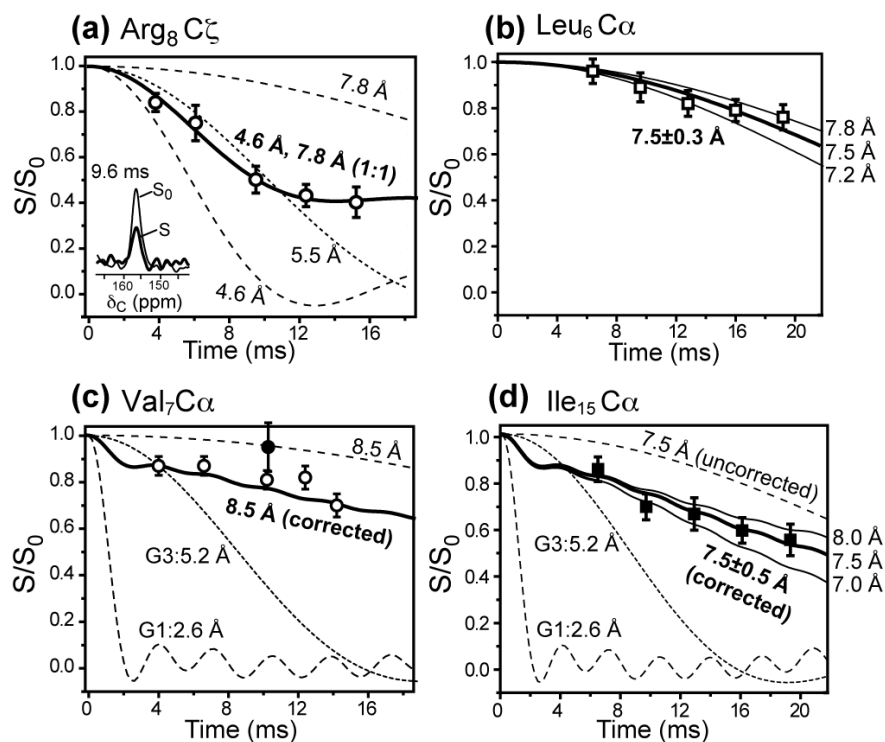


Figure 10.4. Representative ^{13}C - ^{31}P REDOR data of DMPC/DMPG membrane-bound S4. (a) Arg $_8$ C ζ data. Best fit involves a 1:1 combination of a short distance of 4.6 ± 0.2 Å and a long distance of 7.8 ± 0.5 Å. The single-distance best fit gives an average distance of 5.5 Å. Representative control (S_0 , thin line) and dephased spectra (S , thick line) are shown in the inset. (b) Leu $_6$ C α , with a best-fit distance of 7.5 ± 0.3 Å. (c) Val $_7$ C α , with a best-fit distance of 8.5 ± 1.0 Å. (d) Ile $_{15}$ C α , with a best-fit distance of 7.5 ± 0.5 Å. For (c) and (d), the simulated REDOR decay curves (solid lines) were corrected for lipid G1 and G3 intensities, whose distances to ^{31}P are fixed (dashed lines). In (c), a double-quantum REDOR data point (filled circle) falls on the uncorrected REDOR curve for 8.5 Å, thus confirming the single-quantum corrected REDOR distance simulation. All simulated REDOR curves

are two-spin distances, which reflect the vertical distance of the ^{13}C to the ^{31}P -containing membrane plane for distances within 7 – 9 Å (16).

Compared to Arg₈, the hydrophobic residues all exhibit longer distances to ^{31}P . Leu₆ and Ile₁₅ C α are 7.5 Å from the ^{31}P plane, while Val₇ has an even longer C α -P distance of 8.5±1.0 Å. These distances were obtained using two-spin REDOR simulations. For fast REDOR dephasing such as that of Arg₈ C ζ , only one ^{31}P atom can approach the peptide ^{13}C closely due to the average 10 Å ^{31}P - ^{31}P separation in the plane of the membrane. For slower REDOR dephasing that corresponds to a nominal two-spin distance of 7 Å or longer, multiple ^{31}P atoms can interact with each ^{13}C spin. In this case, we have previously shown by multi-spin REDOR simulations that although the individual ^{13}C - ^{31}P distances are longer than the nominal value obtained from two-spin simulations, the *vertical* distance between the ^{13}C atom and the ^{31}P plane (16), which is the relevant parameter for reporting membrane protein depths, approaches the nominal two-spin distance. Thus, the two-spin simulated distances here can be used to reflect the depth of the ^{13}C spins to the membrane plane.

Val₇ and Ile₁₅ C α signals overlap with the lipid glycerol G3 and G1 carbons, which have short distances to ^{31}P . Thus, in the REDOR simulation, we corrected for the lipid intensity contribution using the equation $(S/S_0)_{\text{observed}} = 0.76(S/S_0)_{\text{peptide}} + 0.12(S/S_0)_{\text{G1}} + 0.12(S/S_0)_{\text{G3}}$, where the coefficients were based on the lipid/peptide molar ratio. This natural-abundance correction was confirmed by a double-quantum filtered REDOR experiment (19) on the Val₇ labeled S4 peptide, which removed the lipid ^{13}C signals (Fig. S10.5). The resulting REDOR S/S_0 value supports the natural-abundance corrected REDOR distance of 8.5 Å (Fig. 10.4c).

10.4 Discussion

The ^{13}C isotropic chemical shifts indicate that most labeled residues in the S4 peptide exhibit the α -helical conformation in lipid bilayers (21), consistent with the conformation of this domain in the intact protein (4, 6). The only non-helical residue is the N-terminus Gly₂, which is also consistent with the turn conformation of the corresponding Gly₁₁₄ between S3b and S4 helices in the intact KvAP voltage sensor.

The 2D ^{15}N anisotropic correlation spectra indicate that the S4 helix deviates significantly from the limiting cases of a fully TM orientation ($\tau = 0^\circ$) or a fully in-plane orientation ($\tau = 90^\circ$). Spectral simulations yielded a tilt angle of $40 \pm 5^\circ$ and two ρ angles differing by 180° around the helix axis (**Fig. 10.5**). The data does not allow unambiguous determination of which ρ is adopted by the peptide, and it is possible that both are populated in the absence of other TM helices of the voltage sensor. Although not all residues of the peptide were ^{15}N -labeled, the inclusion of residues 6 and 15 among the labeled sites suggests that the tilt angle is valid for the central majority of the helix. Additional simulations show that the best-fit spectrum agrees with the experimental spectra to within $\pm 5^\circ$ for the tilt angle (**Fig. S10.1**). It has been shown that PISA wheels are sensitive not only to helix orientation but also to backbone (ϕ, ψ) angles (32). Non-idealities greater than $\pm 4^\circ$ of the torsion angles produce significant distortions in the PISA wheel pattern. Thus, the good agreement between the best-fit and experimental spectra of the S4 peptide suggests that the conformation of the C-terminal half of the peptide, although only labeled at Ile₁₅ in this study, may not differ significantly from the α -helical structure. Interestingly, the crystal structure of the paddle-chimaera channel showed residues 297 to 306 to be a 3_{10} helix. However, detailed examination of the conformation of membrane proteins in available crystal and solid-state NMR structures by Cross and coworkers suggests that the low dielectric and anhydrous environment of the lipid bilayer disfavors the formation of 3_{10} helices, since 3_{10} helices increase the exposure of the partial negative charge of the carbonyl oxygens to the lipid membrane compared to α -helices (32). Moreover, due to their significantly different (ϕ, ψ) angles, 3_{10} helices have distinct 2D ^{15}N spectral patterns from the PISA wheels for α -helices (33) (**Fig. S10.1**). Additional ^{15}N -labeling of the C-terminal residues will be useful for verifying the exact conformation of the C-terminal portion of the S4 peptide in the lipid bilayer.

To compare the NMR-determined orientation of the isolated S4 peptide with that in the intact voltage sensor, we show the 2.4 Å crystal structure of the voltage-sensing domain of the paddle-chimaera channel in **Fig. 10.5c, d**. The tetramer structure was taken from PDB (accession code: 2R9R) (6), where the S4 helix and the S4-S5 linker helix were colored to guide the eye, and the pore helices S5 and S6 were removed from view for clarity. The

structure was solved using crystals grown in a mixture of detergents and phospholipids (6), where the S4 helix was that of the Kv2.1 potassium channel with a different amino acid sequence. The S3b-S4 voltage-sensor paddle has been shown to be transferrable among voltage sensors of different origins (34), and three of the four Arg residues are conserved between KvAP and Kv2.1, thus the S4 helix is expected to be comparable between the crystal structure construct and the NMR sample studied here. We extracted the tilt angle of the S4 helix by comparing the average N-H bond orientation of each helix with the orientation of the four-fold symmetry axis of the tetramer, and found the tilt angle to be 43° for all four helices. Within experimental uncertainty, the NMR-determined $40 \pm 5^\circ$ tilt angle of the isolated S4 peptide is identical to the 43° tilt of the S4 helix in the intact voltage sensor. Even more strikingly, **Fig. 10.5** shows that one of the two rotation angle solutions, $\rho=100^\circ$, agrees very well with the sidechain directions of the S4 in the intact voltage sensor (6). Using the hydrophobic Leu₁₃ between the third and fourth Arg (Arg₁₁ and Arg₁₄) as a point of reference, since the Leu rotameric state is relatively well defined (35), we found that the Leu₁₃ sidechain in the isolated peptide has a similar orientation to the corresponding Leu₂₉₈ in the intact voltage sensor. The remarkable similarities in τ and ρ angles indicate that the isolated S4 helix, bound to the lipid bilayer, already adopts its final orientation in the intact S1-S4 domain. This in turn suggests that the S4 structure in the membrane is mainly dictated by the lipid-protein interaction and the S4 amino acid sequence, and is only minimally affected by interactions with the other helices in the voltage sensor. In the crystal structure, the two C-terminal Arg's of the S4 helix interact with glutamate residues in the S1 and S2 helices while the two N-terminal Arg's interact mainly with lipid phosphates and water (6). The preservation of the S4 orientation in the absence of the acidic residues suggests that the two lipid-interacting Arg residues may be largely sufficient for determining the global topology of the membrane-bound S4 helix.

Since the S4 peptide is mostly hydrophobic, the non-Arg residues are not expected to interact significantly with the polar lipid headgroups. If the Arg residues were not present, we suspect that the peptide orientation will be less tilted, like the WALP peptides (36), to better match the thickness of the lipid bilayer. We speculate that the tendency of Arg residues

to interact with the lipid phosphates and snorkel their sidechains to the membrane surface may be an important driving force for the observed tilted orientation of the S4 helix.

The short 4.6 Å distance between the C ζ of the second Arg and the lipid ^{31}P provides the first direct distance constraint for Arg-phosphate interactions in the Kv voltage sensor. Since the guanidinium C ζ is surrounded by N-H groups while the ^{31}P is surrounded by oxygen atoms, the 4.6 Å C ζ -P distance suggests N-H to O-P hydrogen bonding. This Arg-phosphate interaction is fully consistent with biochemical data that voltage gating is inhibited when the phosphate groups of lipids are enzymatically removed (13, 14). In either orientation of **Fig. 10.5a, b**, all four Arg residues can adopt well-populated rotamers to bring their sidechains towards the membrane surface ^{31}P . For example, in the $\rho=280^\circ$ orientation, excellent Arg-headgroup contacts are established if Arg₅, Arg₈, Arg₁₁ and Arg₁₄ adopt the mtm-85, ttp180, tpt85 and tpt85 rotamers, respectively, where t, p, and m represent 180° , $+60^\circ$, and -60° (**Fig. 10.5a**). For $\rho=100^\circ$, guanidinium contacts with the membrane surfaces can be established if all four Arg's adopt the mtt180 state, which is the second most populated Arg rotamer in α -helices (35) (**Fig. 10.5b**). Modeling shows that more than one rotameric state can allow guanidinium snorkeling to the bilayer surface. In fact, the thermal disorder of the lipids and interactions with other helices of the voltage sensor may induce multiple rotamers for each Arg while still maintaining the salt bridge with the lipid phosphates.

The measured C α - P distances confirm the implicit assumption of **Fig. 10.5** that the S4 peptide is fully immersed in the lipid bilayer. Specifically, Ile₁₅ has a similar C α -P distance (7.5 Å) to Leu₆ and Val₇ C α (7.5 and 8.5 Å), which are 8 and 9 residues apart. These distances rule out a half inserted model (**Fig. S10.3**), since the vertical separation between Ile₁₅ and Leu₆ C α or between Ile₁₅ and Val₇ C α is too short compared to the combined C α -P distances of ~ 16 Å: the separation is 8-10 Å for $\rho=100^\circ$ and 12-13 Å for $\rho=280^\circ$, which is 2-8 Å shorter than the sum of the C α -P distances. Thus the S4 peptide must be fully inserted into the bilayer, in agreement with neutron diffraction data of deuterated S1-S4 domain in POPC/POPG bilayers (15). For the fully inserted helix, combining the Val₇-Ile₁₅ C α -C α vertical distance of 10 Å, the Val₇ C α -P distance of 8.5 Å, and the Ile₁₅ C α -P distance of 7.5 Å, we obtain a P-P separation of 26 Å between the two membrane planes (**Fig. 10.6a**). This dis-

tance is 9 Å shorter than the unperturbed DMPC/DMPG bilayer thickness of 35 Å (37). Thus, the distance and orientation data suggest that the DMPC/DMPG bilayer is thinned by about 9 Å at the site of S4 insertion. If residues Phe₁₂ to Ile₁₅ adopt the more extended 3₁₀ conformation rather than the α -helical conformation, then the vertical separation between Val₇ and Ile₁₅ C α would increase to about 13 Å, which would still indicate membrane thinning, but by about 6 Å.

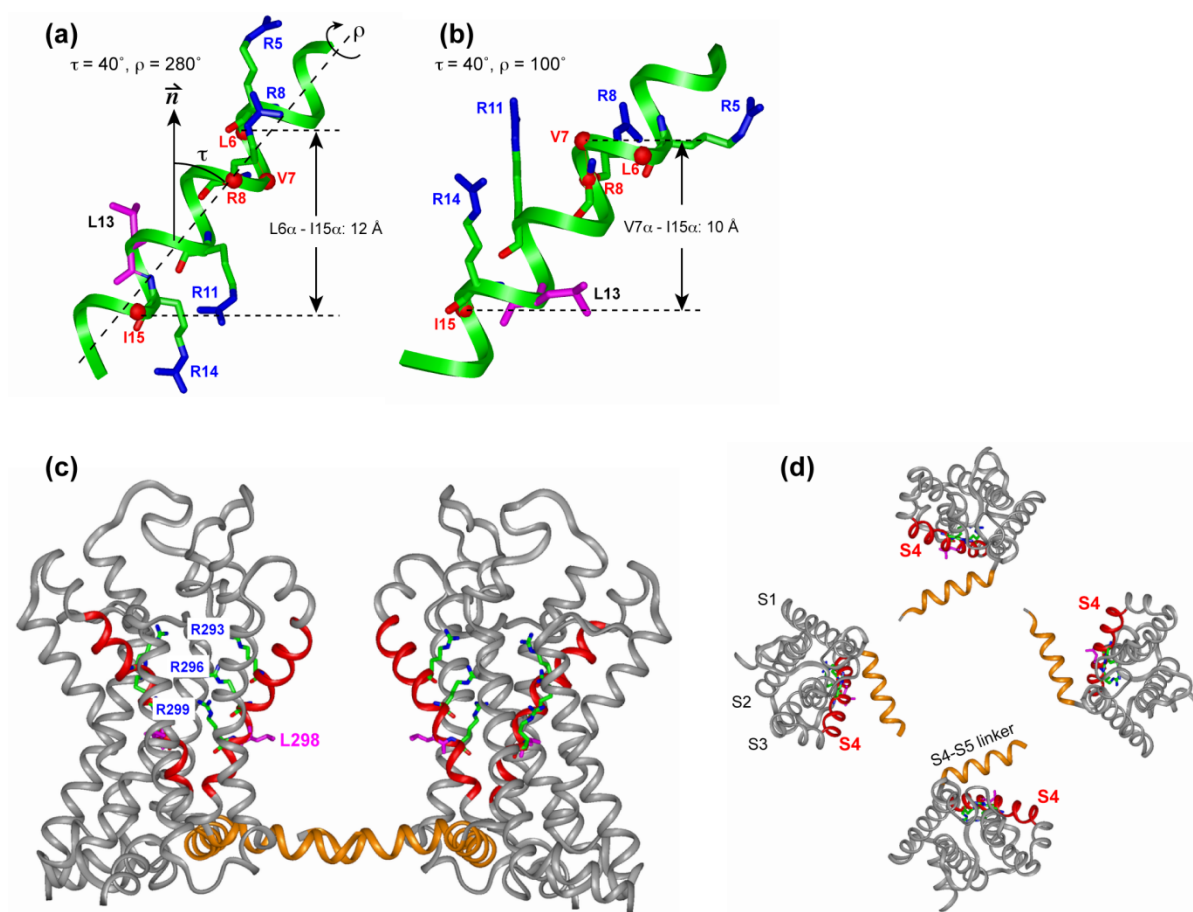


Figure 10.6. Proposed membrane topology of the KvAP S4 peptide in lipid bilayers. (a) Orientation and depth of insertion of the peptide. S4 is fully inserted and causes a 9 Å thinning of the membrane at the site of peptide binding. (b) Helical wheel diagram of the S4 peptide, with hydrophobic residues in red and Arg's in blue. The peptide has little amphiphilicity, supporting a TM motif.

Local thinning of phospholipid bilayers has been frequently observed before (38-41), and is often associated with the function of membrane-active peptides (42). Mem-

brane thinning has also been seen in MD simulations of the S4 helix (10, 11). A thinning of 9 Å may appear large at first. However, at the 1 : 5 peptide/lipid mass ratio used in the NMR samples, the 9 Å local thinning translates to a modest ~ 2 Å thinning averaged over the entire membrane, which is in excellent agreement with neutron diffraction data of the S1-S4 domain (15). This membrane thinning is almost certainly driven by the Arg-phosphate attraction, similar to what has been reported for Arg-rich antimicrobial peptides and cell-penetrating peptides (16, 19). The membrane thinning would better allow the central two Arg's, Arg₈ and Arg₁₁, to reach the membrane surfaces to establish guanidinium-phosphate contacts, which would lead to a reduction of the free energy of insertion.

How does the S4 amino acid sequence dictate the membrane-bound topology of the S4 helix? The helical wheel diagram (**Fig. 10.6b**) shows that the S4 peptide is actually quite hydrophobic despite the presence of four Arg residues, and lacks a clear polar/non-polar separation. The calculated hydrophobic moment (μ_H) of the peptide is only 2.0 (43), which is comparable to the μ_H of hydrophobic membrane peptides such as the influenza A M2 TM domain (44). In contrast, surface-bound membrane peptides such as magainin-2 and melittin have much higher μ_H values of 5-7. Thus, a TM topology of the S4 helix is actually not so surprising. Its significant tilt angle allows the four Arg residues to reach the membrane surface more readily than a helix that is completely parallel to the bilayer normal, since the latter backbone may cause steric conflicts with the Arg sidechains.

The fact that the isolated S4 peptide adopts the same orientation as in the intact voltage-sensing domain suggests that S4 interactions with acidic residues in the rest of the voltage-sensing domain may not affect the global structural topology of this domain in the membrane, even though they may influence local structural features such as the sidechain conformations. Phospholipids and the intrinsic amino acid sequence appear to be sufficient for determining the membrane-bound orientation and depth of this important gating helix. The NMR data here thus supports the model that the paddle directly interacts with the lipid bilayer during channel activation and deactivation. Perhaps it is not so surprising that the helix carrying the gating residues of the Kv channels has an intrinsic orientation that is not easily perturbed by the rest of the protein. The Kv voltage-sensing domain may have evolved to preserve the core structure and function of the S4 helix, making it dependent on the ubiqui-

tous and less variable phospholipids of the cell membrane rather than the easily mutated protein residues.

10.5 Materials and Methods

Peptide and lipids

The segment corresponding to residues 113–130 of the voltage-sensing domain of KvAP, which is an archaebacterial Kv channel from *Aeropyrum pernix*, was synthesized and purified using Fmoc chemistry (PrimmBiotech, Cambridge, MA). The amino acid sequence is LGLFRLVRLR RFLRILLI. The corresponding amino acid sequence of the Kv2.1 segment in the paddle-chimaera crystal structure is residues 286–303 --VVQIFRIM RILIRFKL (6). Except for the first Arg, the second to fourth Arg residues were conserved between the two sequences. Four KvAP S4 peptides were synthesized, incorporating a total of six ¹³C, ¹⁵N-labeled residues: Gly₂, Leu₆, Val₇, Arg₈, Leu₉ and Ile₁₅. The four samples were Gly₂, Leu₆, Ile₁₅-labeled S4, Val₇, Leu₉-labeled S4, Val₇, Arg₈-labeled S4, and Leu₆, Ile₁₅-labeled S4.

DMPC (1,2-dimyristoyl-*sn*-glycero-3-phosphocholine), DMPG (1,2-dimyristoyl-*sn*-glycero-3-phosphatidylglycerol), and 6-O-PC (1,2-di-O-hexyl-*sn*-glycero-3-phosphocholine) were purchased from Avanti Polar Lipids.

Unoriented and oriented membrane samples

Unoriented hydrated proteoliposomes were prepared by mixing the peptide and lipids in organic solvents (3 : 1 chloroform : methanol) or in aqueous solution. A DMPC: DMPG (3 : 1) lipid mixture and a peptide/lipid molar ratio of 1:16 were used for all unoriented samples for magic-angle-spinning (MAS) experiments. For organic-solvent mixed samples, the peptide-lipid mixture were lyophilized and rehydrated to 35 wt% using a 10 mM pH 7 phosphate buffer. For the aqueous-phase mixed samples, the peptide was dissolved in 2 mL of 30–60 mg/mL octyl- β -glucoside (OG) solution, mixed with the lipid vesicle solution at pH 7, then dialyzed against the buffer for 3 days to remove the detergent (45). The proteoliposome solution was centrifuged at 150,000 g at 6 °C to yield a homogeneous pellet. Ex-

cess water was removed by vacuum drying and the powder was then rehydrated to 35% water for MAS experiments.

Oriented DMPC/6-O-PC bicelles containing the peptide were prepared as described before (46-49). The lipid mixture was suspended in a 25 mM pH 7 HEPES buffer to make a 35% (w/v) solution. The mixture was thermocycled between 0 and 42°C three times and incubated at 4°C overnight. The resulting homogenous solution was viscous at 42°C but fluid at 0°C, characteristic of bicelles. The degree of alignment of the bicelle in the magnetic field was examined by ^{31}P NMR. 2.5 mg of KvAP S4 was mixed with 75 μL of the bicelle solution, subjected to several thermocycles, and incubated at 4°C until a homogenous solution was obtained.

Solid-State NMR experiments

Magic-angle-spinning experiments were carried out on a Bruker DSX-400 (9.4 Tesla) spectrometer at Larmor frequencies of 100.70 MHz for ^{13}C and 162.1 MHz for ^{31}P , using a triple-resonance 4 mm MAS probe. ^{13}C and ^{31}P chemical shifts were referenced to the α -glycine CO resonance at 176.49 ppm on the TMS scale and the hydroxyapatite ^{31}P signal at 2.73 ppm on the phosphoric acid scale. Conformation-dependent ^{13}C chemical shifts were measured using 2D ^{13}C - ^{13}C DARR correlation experiments and a double-quantum (DQ) filtered experiment (50) that removed the lipid ^{13}C signals. The 2D experiments were conducted at 233-263 K under moderate spinning rates of 5.0 and 5.5 kHz. Low temperatures were achieved using a Kinetics Thermal Systems XR air-jet sample cooler (Stone Ridge, NY). Thermocouple-indicated temperatures were reported here. The actual sample temperature for both the moderate spinning MAS experiments and the static bicelle experiments is expected to be within 1-2°C of the reported value.

A frequency-selective REDOR experiment (51, 52) was used to measure peptide-lipid ^{13}C - ^{31}P distances. A selective ^{13}C Gaussian pulse (0.8 – 1.0 ms) in the center of the REDOR period removed ^{13}C - ^{13}C J couplings in the uniformly ^{13}C -labeled residues, thus allowing ^{13}C - ^{31}P REDOR effects to be observed at long mixing times. The experiments were carried out at 228 K, well below the phase transition temperature of the DMPC/DMPG membrane, to freeze lipid and peptide motions. Spinning speeds were 4.5 kHz to 5.5 kHz.

Static ^{31}P and ^{15}N NMR spectra for orientation determination were measured on a 600 MHz spectrometer (14.1 Tesla). The static probe contained a solenoid coil whose axis is perpendicular to the magnetic field. ^{15}N chemical shifts were externally referenced to the N-acetylvaline signal at 122 ppm on the NH_3 scale, and ^{31}P chemical shifts were referenced to 85% H_3PO_4 at 0 ppm. The sample temperature was carefully chosen between 302 and 310 K to optimize bicelle alignment. For the 2D ^1H - ^{15}N dipolar-chemical-shift correlation (DIPSHIFT) experiment (22), the N-H evolution period followed the ^1H - ^{15}N cross polarization (CP), and ^1H - ^1H homonuclear decoupling was achieved using the FSLG sequence (53), whose scaling factor was directly measured on model compounds to be 0.54. During ^{15}N detection, ^{13}C decoupling at 5 kHz removed the one-bond ^{15}N - ^{13}C dipolar coupling. This 2D experiment differs from the PISEMA experiment in the way the ^{15}N magnetization evolves during t_1 , but produces the same 2D spectral patterns as the PISEMA experiment (54). Similar to PISEMA spectra, the static 2D DIPSHIFT spectra were plotted to show only half of the symmetric dipolar dimension, and simulated PISA wheels that cross over to the other half of the dipolar dimension were reflected back to the unique half.

Orientation calculation

Orientation-dependent 2D N-H/ ^{15}N correlation spectra were calculated for an ideal α -helix with $(\phi, \psi) = (-64^\circ, -40^\circ)$ as described before (22). Briefly, we defined a molecule-fixed frame whose z-axis was the helix axis, which was calculated as the average N-H vector orientation of 18 residues of the peptide. The y-z plane was defined as the common plane containing the helix axis and the CO-N vector between residues Leu₃ and Phe₄. The tilt angle τ was the angle between the helix axis and the bilayer normal, while the rotation angle ρ was the angle between the bilayer normal and the y-z plane of the molecular frame. $\rho = 0^\circ$ corresponds to the case when the bilayer normal lies in the y-z plane. In the Rose convention of Euler angles $\Omega(\alpha, \beta, \gamma)$, the rotation angle, which is uniquely determined by the protein sequence, corresponds to the azimuthal angle α (55, 56) of the bilayer normal in the molecule-fixed frame. It differs from the azimuthal angle γ of the helix axis in a bilayer-fixed frame. The angle γ generally assumes all values, but for oriented samples whose alignment axis is parallel to the magnetic field, the NMR frequency is independent of γ . For oriented

samples whose alignment axis is not coincident with the magnetic field, the different γ angles will lead to different anisotropic frequencies. However, bicelles undergo fast uniaxial rotation around the bicelle normal, thus averaging the γ angle and making the frequency only dependent on the tilt angle τ ($=\beta$) and the rotation angle ρ ($=\alpha$).

We simulated 2D spectra for τ between 0° and 90° in 5° steps and ρ between 0° and 360° in 20° steps. To obtain the best-fit orientation angles, we minimized the root-mean-square deviation (RMSD) between the calculated and experimental 2D spectra using (22):

$$RMSD = \sqrt{\sum_i \left[\left(\frac{\omega_{NH\ i}^{obs} - \omega_{NH\ i}^{sim}}{\delta_{NH}^{max}} \right)^2 + \left(\frac{\omega_{CSA\ i}^{obs} - \omega_{CSA\ i}^{sim}}{\delta_{CSA}^{max}} \right)^2 \right]}, \quad (1)$$

where the maximum N-H coupling δ_{NH}^{max} and ^{15}N chemical shift anisotropy (CSA)

δ_{CSA}^{max} are:

$$\delta_{NH}^{max} = -\delta_{NH}^{rigid} \cdot 0.5 \cdot 0.8 \cdot 0.54 = 2.16 \text{ kHz} \quad (2)$$

$$\delta_{CSA}^{max} = -\left(\delta_{zz}^{rigid} - \delta_{iso} \right) \cdot 0.5 \cdot 0.8 + \delta_{iso} = 80 \text{ ppm} \quad (3)$$

In the above equations, we used a rigid-limit N-H coupling δ_{NH}^{rigid} of 10.0 kHz, ^{15}N z-principal value δ_{zz}^{rigid} of 227 ppm, and a ^{15}N isotropic shift δ_{iso} of 122 ppm. The factor of -0.5 is due to the 90° orientation of the bicelle axis from the magnetic field. The factor of 0.8 accounts for the wobble of the bicelle axis, and was estimated from the ^{31}P CSA of the bicelles, which was 82-88% of the ^{31}P CSA of lipid bilayers (**Table S10.3**) (47, 57, 58). This value was confirmed by simulations of the measured 2D ^{15}N spectra (**Fig. S10.4**). The scaling factor of 0.54 accounts for the homonuclear decoupling sequence of FSLG.

To visualize the peptide orientation, we affixed the best-fit bilayer normal to the molecule-fixed coordinate system defined above. The assembly of the peptide and the Carte-

sian system was then rotated such that the bilayer normal is vertical on the screen. The bilayer normal coordinates were inputted as $(x = r \sin \theta \cos \phi, y = r \sin \theta \sin \phi, z = r \cos \theta)$, where $\theta = \tau$ and $\phi = \rho + 90^\circ$.

To extract the orientation of the S4 helix in the crystal structure of the paddle-chimaera channel, we calculated the S4 helix axis as the average N-H bond orientation for eleven consecutive residues from 286 to 296. The choice of eleven residues was to complete three turns of the α -helix while not involving residues in the 3_{10} helix (from residue 297). Since the tetramer is symmetric, the channel axis orientation was the average orientation of the four S4 helix axes. The scalar product between the channel axis and each S4 helix axis gives the tilt angle.

10.6 Acknowledgement

T. D. is the grateful recipient of a Roy J. Carver Trust pre-doctoral training fellowship. This work is supported by NIH grant GM-066976.

10.7 Reference

1. Borjesson, S. I., and Elinder, F. (2008) Structure, Function, and Modification of the Voltage Sensor in Voltage-Gated Ion Channels, *Cell Biochem. Biophys.* 52, 149-174.
2. Swartz, K. J. (2008) Sensing voltage across lipid membranes, *Nature* 456, 891-897.
3. Seoh, S. A., Sigg, D., Papazian, D. M., and Bezanilla, F. (1996) Voltage-sensing residues in the S2 and S4 segments of the Shaker K⁺ channel, *Neuron* 16, 1159-1167.
4. Jiang, Y., Lee, A., Chen, J., Ruta, V., Cadene, M., Chait, B. T., and MacKinnon, R. (2003) X-ray Structure of a Voltage Dependent K⁺ Channel, *Nature* 423, 33-41.
5. Jiang, Y., Ruta, V., Chen, J., Lee, A., and MacKinnon, R. (2003) The Principle of Gating Charge Movement in a Voltage-Dependent K⁺ Channel, *Nature* 423, 42-48.
6. Long, S. B., Tao, X., Campbell, E. B., and MacKinnon, R. (2007) Atomic Structure of a Voltage-Dependent K⁺ Channel in a Lipid Membrane-Like Environment, *Nature* 450, 376-383.
7. Ruta, V., Chen, J., and MacKinnon, R. (2005) Calibrated measurement of gating-charge arginine displacement in the KvAP voltage-dependent K⁺ channel, *Cell* 123, 463-475.
8. Hessa, T., Kim, H., Bihlmaier, K., Lundin, C., Boekel, J., Andersson, H., Nilsson, I., White, S. H., and von Heijne, G. (2005) Recognition of transmembrane helices by the endoplasmic reticulum translocon, *Nature* 433, 377-381.

9. Cuello, L. G., Cortes, D. M., and Perozo, E. (2004) Molecular Architecture of the KvAP Voltage-Dependent K⁺ Channel in a Lipid Bilayer, *Science* 306, 491-495.
10. Freites, J. A., Tobias, D. J., von Heijne, G., and White, S. H. (2005) Interface Connections of a Transmembrane Voltage Sensor, *Proc. Natl. Acad. Sci. U. S. A.* 102, 15059-15064.
11. Sands, Z. A., and Sansom, M. S. P. (2007) How Does a Voltage Sensor Interact with a Lipid Bilayer? Simulations of a Potassium Channel Domain, *Structure* 15, 235-244.
12. Jogini, V., and Roux, B. (2007) Dynamics of the Kv1.2 voltage-gated K⁺ channel in a membrane environment, *Biophys. J.* 93, 3070-3082.
13. Schmidt, D., Jiang, Q., and MacKinnon, R. (2006) Phospholipids and the Origin of Cationic Gating Charges in Voltage Sensors, *Nature* 444, 775-779.
14. Xu, Y., Ramu, Y., and Lu, Z. (2008) Removal of phospho-head groups of membrane lipids immobilizes voltage sensors of K⁺ channels, *Nature* 451, 826-829.
15. Krepkiy, D., Mihailescu, M., Freites, J. A., Schow, E. V., Worcester, D. L., Gawrisch, K., Tobias, D. J., White, S. H., and Swartz, K. J. (2009) Structure and hydration of membranes embedded with voltage-sensing domains, *Nature* 462, 473-479.
16. Tang, M., Waring, A. J., and Hong, M. (2007) Phosphate-Mediated Arginine Insertion Into Lipid Membranes and Pore Formation by a Cationic Membrane Peptide from Solid-State NMR, *J. Am. Chem. Soc.* 129, 11438-11446.
17. Tang, M., Waring, A. J., Lehrer, R. I., and Hong, M. (2008) Effects of Guanidinium-Phosphate Hydrogen Bonding on the Membrane-Bound Structure and Activity of an Arginine-Rich Membrane Peptide from Solid-State NMR, *Angew. Chem. Int. Ed. Engl.* 47, 3202-3205.
18. Su, Y., Mani, R., and Hong, M. (2008) Asymmetric Insertion of Membrane Proteins in Lipid Bilayers by Solid-State NMR Paramagnetic Relaxation Enhancement: a Cell-Penetrating Peptide Example, *J. Am. Chem. Soc.* 130, 8856-8864.
19. Su, Y., Doherty, T., Waring, A. J., Ruchala, P., and Hong, M. (2009) Roles of arginine and lysine residues in the translocation of a cell-penetrating peptide from (13)C, (31)P, and (19)F solid-state NMR, *Biochemistry* 48, 4587-4595.
20. Takegoshi, K., Nakamura, S., and Terao, T. (2001) C-13-H-1 dipolar-assisted rotational resonance in magic-angle spinning NMR, *Chem. Phys. Lett.* 344, 631-637.
21. Wang, Y., and Jardetzky, O. (2002) Probability-based protein secondary structure identification using combined NMR chemical-shift data., *Protein Sci.* 11, 852-861.
22. Tang, M., Waring, A., Lehrer, R., and Hong, M. (2006) Orientation of a Beta-Hairpin Antimicrobial Peptide in Lipid Bilayers from Two-Dimensional Dipolar Chemical-Shift Correlation NMR, *Biophys. J.* 90, 3616-3624.
23. Marassi, F. M., and Opella, S. J. (2000) A Solid-State NMR Index of Helical Membrane Protein Structure and Topology, *J. Magn. Reson.* 144, 150-155.

24. Wang, J., Denny, J., Tian, C., Kim, S., Mo, Y., Kovacs, F., Song, Z., Nishimura, K., Gan, Z., Fu, R., Quine, J. R., and Cross, T. A. (2000) Imaging membrane protein helical wheels, *J. Magn. Reson.* 144, 162-167.
25. Hoffmann, A., Kane, A., Nettels, D., Hertzog, D. E., Baumgärtel, P., Lengefeld, J., Reichardt, G., Horsley, D. A., Seckler, R., Bakajin, O., and Schuler, B. (2007) Mapping protein collapse with single-molecule fluorescence and kinetic synchrotron radiation circular dichroism spectroscopy, *Proc. Natl. Acad. Sci. U. S. A.* 104, 105-110.
26. Li, C., Qin, H., Gao, F. P., and Cross, T. A. (2007) Solid-state NMR characterization of conformational plasticity within the transmembrane domain of the influenza A M2 proton channel, *Biochim. Biophys. Acta* 1768, 3162-3170.
27. Wang, J., Kim, S., Kovacs, F., and Cross, T. A. (2001) Structure of the the transmembrane region of the M2 protein H⁺ channel, *Prot. Sci.* 10, 2241-2250.
28. Park, S. H., Mrse, A. A., Nevzorov, A. A., Mesleh, M. F., Oblatt-Montal, M., Montal, M., and Opella, S. J. (2003) Three-dimensional structure of the channel-forming trans-membrane domain of virus protein "u" (Vpu) from HIV-1, *J. Mol. Biol.* 333, 409-424.
29. Thiriot, D. S., Nevzorov, A. A., Zagayanskiy, L., Wu, C. H., and Opella, S. J. (2004) Structure of the coat protein in Pf1 bacteriophage determined by solid-state NMR spectroscopy, *J. Mol. Biol.* 341, 869-879.
30. Zeri, A. C., Mesleh, M. F., Nevzorov, A. A., and Opella, S. J. (2003) Structure of the coat protein in fd filamentous bacteriophage particles determined by solid-state NMR spectroscopy, *Proc. Natl. Acad. Sci. U. S. A.* 100, 6458-6463.
31. Segrest, J. P., De Loof, H., Dohlman, J. G., Brouillette, C. G., and Anantharamaiah, G. M. (1990) Amphipathic helix motif: classes and properties, *Proteins* 8, 103-117.
32. Page, R. C., Kim, S., and Cross, T. A. (2008) Transmembrane helix uniformity examined by spectral mapping of torsion angles, *Structure* 16, 787-797.
33. Kim, S., and Cross, T. A. (2004) 2D Solid-State NMR Spectral Simulation of 310, a, and p-helices, *J. Magn. Reson.* 168, 187-193.
34. Alabi, A. A., Bahamonde, M. I., Jung, H. J., Kim, J. I., and Swartz, K. J. (2007) Portability of paddle motif function and pharmacology in voltage sensors, *Nature* 450, 370-375.
35. Lovell, S. C., Word, J. M., Richardson, J. S., and Richardson, D. C. (2000) The Penultimate Rotamer Library, *Proteins: Struct., Funct., Genet.* 40, 389-408.
36. Strandberg, E., Morein, S., Rijkers, D. T. S., Liskamp, R. M. J., vanderWel, P. C. A., and Killian, J. A. (2002) Lipid dependence of membrane anchoring properties and snorkeling behavior of aromatic and charged residues in transmembrane peptides, *Biochemistry* 41, 7190-7198.
37. Kucerka, N., Liu, Y., Chu, N., Petrache, H. I., Tristram-Nagle, S., and Nagle, J. F. (2005) Structure of fully hydrated fluid phase DMPC and DLPC lipid bilayers using

- X-ray scattering from oriented multilamellar arrays and from unilamellar vesicles, *Biophys. J.* 88, 2626-2637.
38. Heller, W. T., Waring, A. J., Lehrer, R. I., Harroun, T. A., Weiss, T. M., Yang, L., and Huang, H. W. (2000) Membrane-thinning effect of the β -sheet antimicrobial protegrin., *Biochemistry* 39, 139-145.
 39. Yamaguchi, S., Huster, D., Waring, A., Lehrer, R. I., Tack, B. F., Kearney, W., and Hong, M. (2001) Orientation and Dynamics of an Antimicrobial Peptide in the Lipid Bilayer by Solid-State NMR, *Biophys. J.* 81, 2203-2214.
 40. Buffy, J., Hong, T., Yamaguchi, S., Waring, A., Lehrer, R., and Hong, M. (2003) Solid-State NMR Investigation of the Depth of Insertion of Protegrin-1 in Lipid Bilayers Using Paramagnetic Mn^{2+} , *Biophys. J.* 85, 2363-2373.
 41. Mecke, A., Lee, D. K., Ramamoorthy, A., Orr, B. G., and Banaszak Holl, M. M. (2005) Membrane thinning due to antimicrobial peptide binding: an atomic force microscopy study of MSI-78 in lipid bilayers, *Biophys. J.* 89, 4043-4050.
 42. Huang, H. W. (2006) Molecular mechanism of antimicrobial peptides: the origin of cooperativity, *Biochim. Biophys. Acta* 1758, 1292-1302.
 43. Jaysinghe, S., Hristova, K., Wimley, W., Snider, C., and White, S. H. (2008) <http://blanco.biomol.uci.edu/mpex>.
 44. Cady, S. D., Luo, W. B., Hu, F., and Hong, M. (2009) Structure and function of the influenza M2 proton channel, *Biochemistry* 48, 7356-7364.
 45. Luo, W., Mani, R., and Hong, M. (2007) Side-Chain Conformation of the M2 Transmembrane Peptide Proton Channel of Influenza A Virus from 19F Solid-State NMR.
 46. DeAngelis, A., and Opella, S. (2007) Bicelle samples for solid-state NMR of membrane proteins, *Nature Protocols* 2, 2332-2338.
 47. Marcotte, I., and Auger, M. (2005) Bicelles as Model Membranes for Solid-State and Solution-State NMR Studies of Membrane Peptides and Proteins, *Concept Magn. Reson. A* 24a, 17-37.
 48. Prosser, R. S., Evanics, F., Kitevski, J. L., and Al-Abdul-Wahid, M. S. (2006) Current applications of bicelles in NMR studies of membrane-associated amphiphiles and proteins., *Biochemistry* 45, 8453-8465.
 49. Aussenac, F., Lavigne, B., and Dufourc, E. (2005) Toward bicelle stability with ether-linked phospholipids: temperature, composition, and hydration diagrams by 2H and ^{31}P solid-state NMR., *Langmuir* 21, 7129-7135.
 50. Hohwy, M., Jakobsen, H. J., Eden, M., Levitt, M. H., and Nielsen, N. C. (1998) Broad-band dipolar recoupling in the nuclear magnetic resonance of rotating solids: a compensated $C7$ pulse sequence., *J. Chem. Phys.* 108, 2686-2694.
 51. Gullion, T., and Schaefer, J. (1989) Rotational Echo Double Resonance NMR, *J. Magn. Reson.* 81, 196-200.

52. Jaroniec, C. M., Tounge, B. A., Rienstra, C. M., Herzfeld, J., and Griffin, R. G. (1999) Measurement of C-13-N-15 Distances in Uniformly C-13 Labeled Biomolecules: J-Decoupled REDOR, *J. Am. Chem. Soc.* 121, 10237-10238.
53. Bielecki, A., Kolbert, A. C., de Groot, H. J. M., Griffin, R. G., and Levitt, M. H. (1990) Frequency-switched Lee-Goldberg sequences in solids, *Advances in Magnetic Resonance* 14, 111-124.
54. Wu, C. H., Ramamoorthy, A., and Opella, S. J. (1994) High-resolution heteronuclear dipolar solid-state NMR spectroscopy, *J. Magn. Reson.* 109, 270-272.
55. Schmidt-Rohr, K., and Spiess, H. W. (1994) *Multidimensional Solid-State NMR and Polymers*, 1st ed., Academic Press, San Diego.
56. Rose, M. E. (1957) *Elementary Theory of Angular Momentum*, Wiley, New York.
57. Park, S., DeAngelis, A., Nevzorov, A., Wu, C., and Opella, S. (2006) Three-Dimensional Structure of the Transmembrane Domain of Vpu from HIV-1 in Aligned Phospholipid Bicelles, *Biophys. J.* 91, 3032-3042.
58. DeAngelis, A., Howell, S., Nevzorov, A., and Opella, S. (2006) Structure Determination of a Membrane Protein with Two Trans-membrane Helices in Aligned Phospholipid Bicelles by Solid-State NMR Spectroscopy, *J. Am. Chem. Soc.* 128, 12256-12267.

10.8 Supplementary Material

Table S10.1. ^{13}C isotropic chemical shifts (ppm) of labeled residues in KvAP S4 in DMPC/DMPG bilayers. Secondary chemical shifts were calculated by subtracting the experimental shifts by the random coil (rc) chemical shifts ¹. The chemical shifts are relative to TMS.

Residue	Site	$\delta_{\text{expt}}^{\text{KvAP}}$	δ^{rc}	$\delta_{\text{expt}}^{\text{KvAP}} - \delta^{\text{rc}}$
G2	CO	171.9	172.6	-0.7
	C α	42.6	43.6	-1.0
L6	CO	176.3	174.9	1.4
	C α	55.9	53.2	2.7
	C β	39.4	40.2	-0.8
V7	CO	176.0	174.1	1.9
	C α	64.9	60.1	4.8
	C β	29.3	31.0	-1.7
R8	CO	177.2	174.2	3.0
	C α	57.4	54.3	3.1
	C β	28.5	28.8	-0.3
L9	CO	176	174.9	1.1
	C α	56.0	53.2	2.8
	C β	39.7	40.2	-0.5
I15	CO	175.9	173.8	2.1
	C α	61.9	58.9	3.0
	C β	36.1	36.6	-0.5

Table S10.2. TALOS ² predicted (ϕ, ψ) torsion angles for Val₇ and Arg₈ of the S4 helix, obtained using DSS-referenced ^{13}C chemical shifts.

Residue	(ϕ, ψ)
Val ₇	(-61 \pm 5 $^\circ$, -48 \pm 9 $^\circ$)
Arg ₈	(-61 \pm 4 $^\circ$, -43 \pm 8 $^\circ$)

Table S10.3. Observed ^{31}P anisotropic chemical shift δ_{obs} of DMPC lipids in DMPC/6-O-PC bicelles containing the KvAP S4 peptide. The order parameter was calculated using $S_{\text{bicelle}} = (\delta_{\text{obs}} - \delta_{\text{iso}}) / (\delta_{90^\circ} - \delta_{\text{iso}})$ ³, where the input chemical shifts were $\delta_{\text{iso}} = -0.8 \text{ ppm}$ and $\delta_{90^\circ} = -14.9 \text{ ppm}$.

Sample	δ_{obs} (ppm)	S_{bicelle}
G2, L6, I15-labeled S4	-12.4	0.82
V7, L9-labeled S4	-13.2	0.88

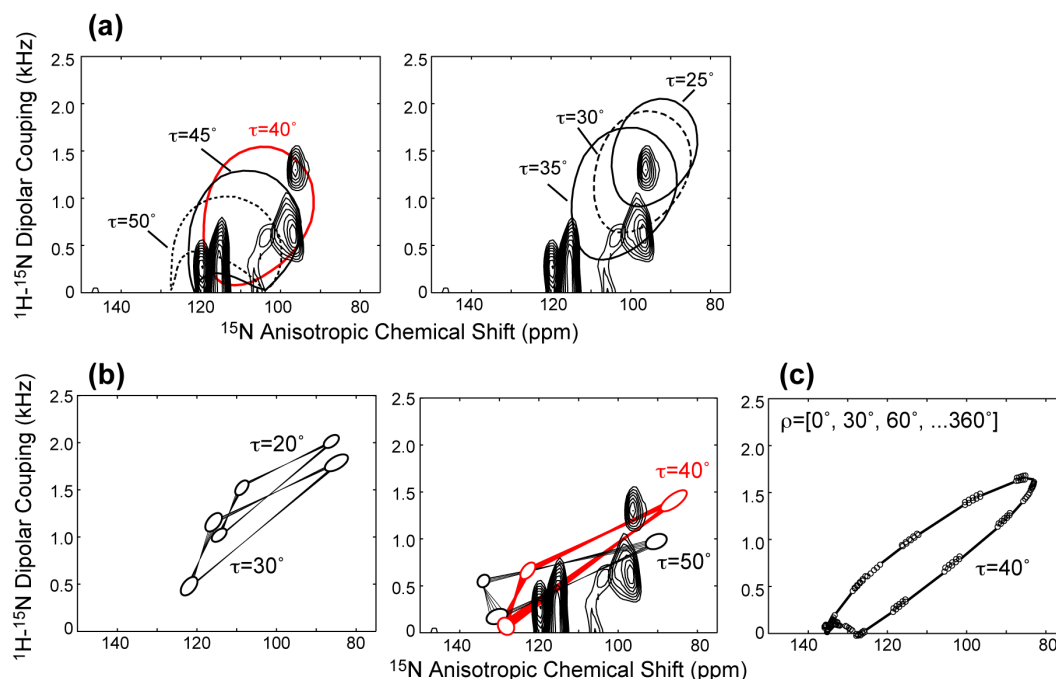


Fig. S10.1. Simulated 2D ^{15}N - ^1H dipolar and ^{15}N chemical shift correlation spectra to estimate the precision and accuracy of the S4 helix orientation. (a) Simulated spectra for α -helices with tilt angles of 25° to 50° at 5° steps. An 18-residue ideal α -helix with (ϕ, ψ) angles of $(-64^\circ, -40^\circ)$ was used as the input. The 40° PISA wheel (red) best fit the experimental spectrum, with a precision of better than 5° . (b) Simulated 2D ^{15}N spectra for 3_{10} helices with tilt angles from 20° to 50° at 10° steps and an arbitrary rotation angle. A 15-residue 3_{10} helix with (ϕ, ψ) angles of $(-49^\circ, -26^\circ)$ were used as the input. Circles indicate the simulated peak positions. Lines connect the peak positions of consecutive residues but do not indicate possible peak positions. Due to the 3-residue per turn geometry of the 3_{10} helix, the spectral patterns have an approximate 3-residue periodicity, and the peaks for each unique (τ, ρ) pair are clustered at three positions, leaving most of the spectral region empty. (c) When multiple rotation angles (at 30° steps) are combined for a tilt angle ($\tau=40^\circ$ as an example), an elliptical pattern emerges. Since a functional transmembrane helix has unique rotation angles (within $< 10^\circ$ uncertainty), most of the positions of each ellipse are not populated, in contrast to an α -helix.

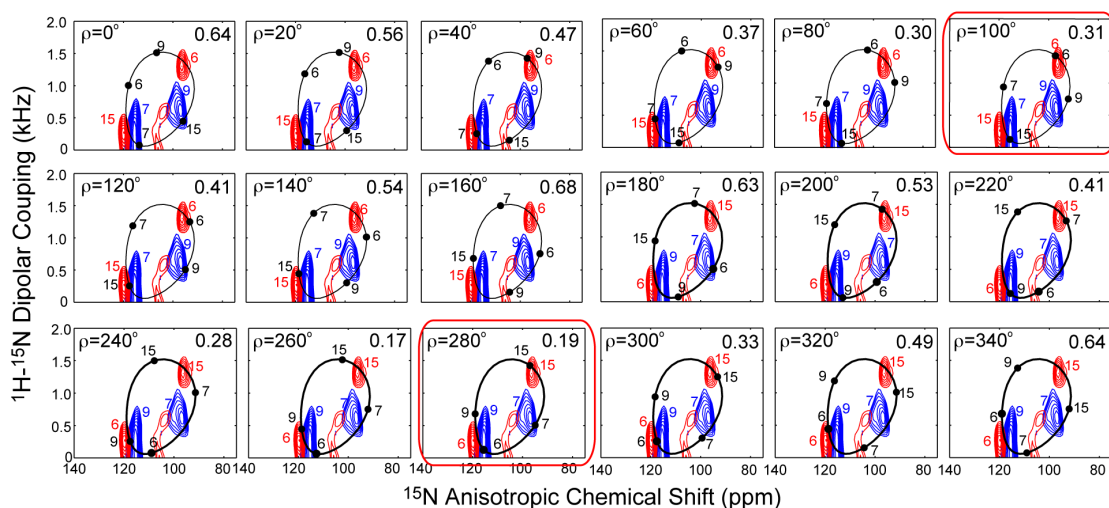


Fig. S10.2. Simulated 2D ^{15}N anisotropic correlation spectra for $\tau = 40^\circ$ and ρ from 0° to 340° . The assignment for each simulation is indicated in black and the closest experimental assignment is indicated in blue and red. Two degenerate best fits to the experimental spectrum are found at $\rho = 100^\circ \pm 20^\circ$ and $280^\circ \pm 20^\circ$.

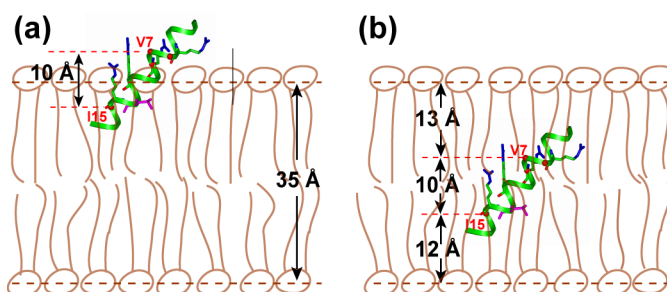


Fig. S10.3. Two alternative membrane topology models of KvAP S4 that can be ruled out based on solid-state NMR constraints. The S4 peptide is shown to scale with a 35 Å thick DMPC bilayer⁴. The vertical separation between V7 C α and I15 C α , which depends on the helical conformation and the peptide orientation, is 10 Å. (a) Half insertion model. If this model were correct, then the sum of the Val₇ and Ile₁₅ $^{13}\text{C}\alpha$ - ^{31}P distance should be equal to 10 Å. However, the measured sum of $^{13}\text{C}\alpha$ - ^{31}P distances is 16 Å, thus ruling out this model. (b) Full insertion model without membrane thinning. This model would require Val₇ and Ile₁₅ C α to be 12-13 Å from the ^{31}P plane, which does not agree with the measured distance of 7.5 Å and 8.5 Å.

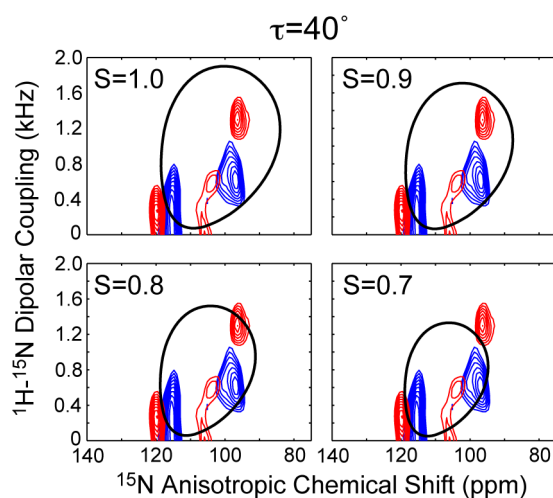


Fig. S10.4. Simulated 2D ^{15}N anisotropic correlation spectra to verify the bicelle wobble order parameter. A tilt angle of $\tau = 40^\circ$ was simulated using a generalized order parameter S from 1.0 to 0.7. Best fit was found for $S = 0.8$, consistent with the ^{31}P spectra and previous literature evidence for this bicelle composition⁵⁻⁷.

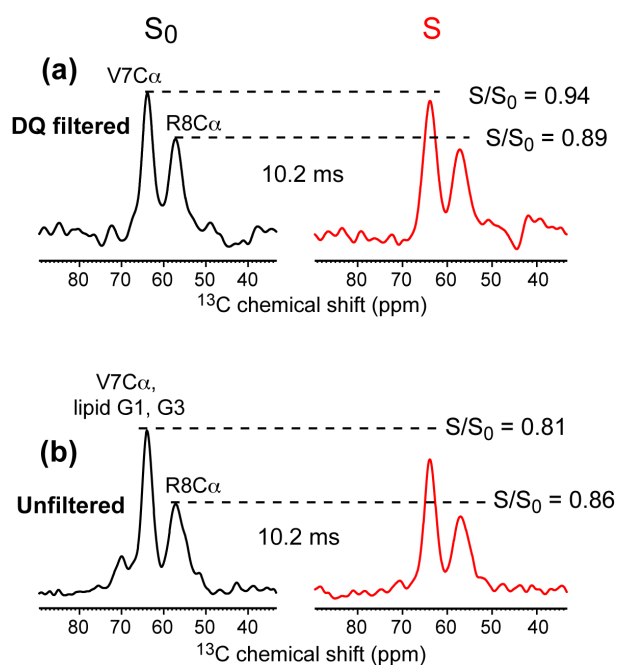


Fig. S10.5. ^{13}C double-quantum filtered ^{13}C - ^{31}P REDOR data of Val₇ C α and Arg₈ C α in DMPC/DMPG-bound S4 helix. The lipid natural-abundance glycerol G1 and G3 peaks, which overlap with the Val₇ C α peak, were removed by the DQ filter. (a) Double-quantum filtered REDOR S_0 and S spectra at a mixing time of 10.2 ms. (b) Unfiltered ^{13}C - ^{31}P REDOR spectra at the same mixing time. The regular REDOR spectra show lower S/S_0 values for the Val₇ C α peak due to the influence of the glycerol G3 and G1 carbons, which are close to the phosphate group.

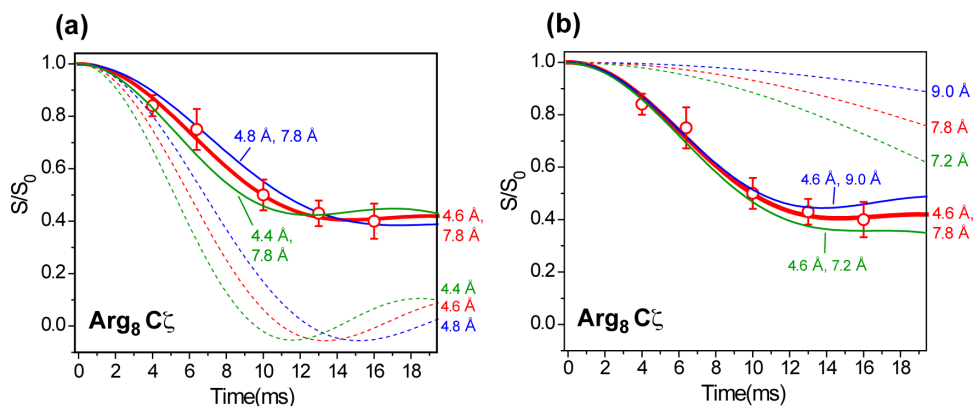


Figure S10.6. Distance uncertainty for the $\text{Arg}_8 \text{C}\zeta$ - ^{31}P REDOR data. (a) Uncertainty of the short component of the dual-distance fit. The 4.6 Å fit is distinguishably better than 4.4 Å and 4.8 Å, indicating an error bar of 0.2 Å. (b) Uncertainty of the long component of the dual-distance fit. The 7.8 Å has an uncertainty of +1.2 Å and -0.6 Å, consistent with the larger difficulty of measuring longer distances with high precision.

References

1. Wang, Y. & Jardetzky, O. (2002). Probability-based protein secondary structure identification using combined NMR chemical-shift data. *Protein Sci.* 11, 852-861.
2. Cornilescu, G., Delaglio, F. & Bax, A. (1999). Protein backbone angle restraints from searching a database for chemical shift and sequence homology. *J. Biomol. NMR* 13, 289-302.
3. Yamamoto, K., Soong, R. & Ramamoorthy, A. (2009). Comprehensive Analysis of Lipid Dynamics Variation with Lipid Composition and Hydration of Bicelles Using Nuclear Magnetic Resonance (NMR) Spectroscopy. *Langmuir*.
4. Kucerka, N., Liu, Y., Chu, N., Petrache, H. I., Tristram-Nagle, S. & Nagle, J. F. (2005). Structure of fully hydrated fluid phase DMPC and DLPC lipid bilayers using X-ray scattering from oriented multilamellar arrays and from unilamellar vesicles. *Biophys. J.* 88, 2626-2637.
5. Park, S., DeAngelis, A., Nevzorov, A., Wu, C. & Opella, S. (2006). Three-Dimensional Structure of the Transmembrane Domain of Vpu from HIV-1 in Aligned Phospholipid Bicelles. *Biophys. J.* 91, 3032-3042.
6. Marcotte, I. & Auger, M. (2005). Bicelles as Model Membranes for Solid-State and Solution-State NMR Studies of Membrane Peptides and Proteins. *Concept Magn. Reson. A* 24a, 17-37.
7. DeAngelis, A., Howell, S., Nevzorov, A. & Opella, S. (2006). Structure Determination of a Membrane Protein with Two Trans-membrane Helices in Aligned Phospholipid Bicelles by Solid-State NMR Spectroscopy. *J. Am. Chem. Soc.* 128, 12256-12267.

Chapter 11

General conclusion

Solid-state NMR is among the most important analytical techniques to provide atomic-level structural and dynamic information of chemical and biological systems. Due to the insoluble and non-crystalline nature of most membrane peptides and proteins, SSNMR is particularly powerful to investigate their conformations, dynamics, domain assembly, oligomerization, and the characteristic structural properties in lipid bilayers including insertion orientation and depth, residue-lipid interaction, and membrane perturbation. Our research is to collect structural and dynamic information and correlate it with biological functions to elucidate the structure-bioactivity relation. In my PhD projects, we have successfully applied various SSNMR techniques to study many interesting membrane peptides including the cell-penetrating peptide (CPP), antimicrobial peptides (AMP), antimicrobial oligomer (AMO), gating helix of K⁺ channel (KvAP) and transmembrane ¹H channel of influenza M2 protein (M2TM). Their biological functions and structures are concisely summarized in **Table 1.2** on page 14. We also developed a novel paramagnetic-ion-membrane bound paramagnetic relaxation enhancement (PRE) method to provide quantitative long-range distance constrain (~20 Å) in membrane-active biosystems and applied the method to obtain high-resolution residue-specific insertion depth of two membrane peptides, penetratin and M2TM.

One main category of my research topics is the cationic membrane peptide. On the one hand, phospholipid membranes have highly hydrophobic interiors that cannot accommodate charged species, while on the other hand, cationic peptides need to insert or translocate across the membrane to conduct biological functions. So, we are motivated to uncover the structural basis of the membrane insertion and translocation. With this motivation, we have studied two kinds of cationic bio-macromolecules, including CPP and AMP. We have experimentally proved that all these Arg-rich peptides generally have strong guanidinium-phosphate ($Gdn-PO_4^-$) interaction with the phospholipids. This charge-charge interaction causes headgroup reorientation and allows the peptide to insert. For CPPs, the $Gdn-PO_4^-$ ion pair helps to stabilize the unstructured peptide in the membrane-water interface. The observed peptide-water interaction further minimizes the peptide polarity and

makes it more membrane-soluble. We find that two representative CPPs, penetratin and TAT, have highly dynamic and plastic conformations, proposed to facilitate the movement within the membrane. In the penetratin study, the one-side Mn^{2+} -bound PRE method has been developed and applied to study the peptide-concentration dependent insertion depth and symmetry in the outer and inner leaflets of the POPC/POPG bilayer. Another important kind of cationic membrane peptides is AMP. Taking PG-1 and its charge reduced mutant IB484 as model AMPs, we have studied the antimicrobial mechanism, and for the first time, provided high-resolution structural information to elucidate the bacterial Gram-selectivity. We find that the $Gdn - PO_4^-$ interaction manifests the manner of peptide insertion in terms of orientation and depth, which in turn determined the antimicrobial ability in gram positive and negative bacterial membranes. The antimicrobial mechanism of a guanidinium-rich AMO, PMX30016, has also been investigated. The finding of drug-concentration dependant lipid ^{31}P CSA change and the fast uniaxial motion in the interfacial membrane region suggest a subtle and combined antimicrobial mechanism of membrane potential perturbation and in-plane disruption.

Another category of my research topics is the transmembrane ion-conductive channel study, including the gating mechanism of a K^+ channel (KvAP) and the blocking mechanism of the M2TM 1H channel by the metal ion inhibitor (Cu^{2+}). We have determined the topology of an isolated gating helix (S4) of KvAP and compared the orientation with that of an intact K^+ channel, Kv1.2-Kv2.1 paddle chimera. The identical tilted and rotational angles of the S4 helix in the isolated form and intact protein, and the observed $Gdn - PO_4^-$ interaction suggest the channel gating might be manifested by the peptide-lipid interaction rather than the interaction among different helical domains. Finally, we applied PRE techniques to study the Cu^{2+} -inhibited M2TM channel and obtained high resolution Cu^{2+} binding structure and long-range distance constraints for the binding structure refinement.

Appendix A

Preparation of oriented samples: glass-plate aligned samples and bicelle

A.1. Glass-plate aligned sample preparation:

Sample to prepare: The peptide-incorporated POPC/POPG oriented sample

Apparatus and materials: 10 μ l, 200 μ l and 1 ml glass syringes, 6 \times 12 mm² or 4 mm round glass plates, humidity chamber, etc.; e-pure water, chloroform, POPC, POPG, etc.

Preparation procedures using naphthalene-incorporated method:

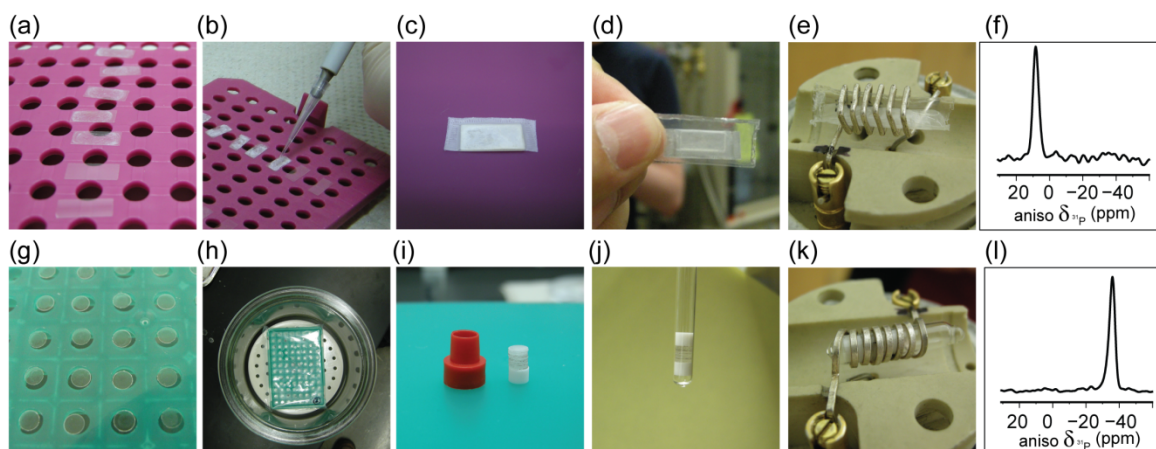


Figure A.1. Preparation of square (a-f) and round (g-i) glass-plate supported lipid bilayers. (a) Dry lipid film spread on glass plates after evaporating the organic solvent in hood. (b) Direct hydration of lipids on glass plates after overnight lyophilization. (c) Parafilm-wrapped glass plates. (d) The glass plate sample sealed in a plastic bag. (e) The glass-plate sample in a square coil. (f) the ³¹P spectrum of oriented POPC lipids prepared in (a-e). (g) Lipid-coated round-glass plates. (h) Indirect hydration in the humidity chamber. (i) Stacked glass plates on top of a spacer. (j) Glass plates packed in a glass tube with top and bottom spacers. (k) The round glass-plate sample in a 5-mm round coil. (l) the ³¹P spectrum, of oriented POPC lipids prepared in (g-k). Note: *These samples are prepared by Frank Lange and Yongchao Su together for the pulsed-field-gradient (PFG) NMR study of the transmembrane M2 ¹H channel.*

- (1) Weigh peptides and lipids at a desired molar ratio. Weigh naphthalene at a 1: 1 molar ratio to lipids.

Note: total amount of lipid/peptide film on each plate is ~1 mg for 6 × 12 mm² glass plates, or 0.01-0.02 mg/mm².

- (2) Co-dissolve all compounds in CHCl₃.

Note: if the peptide cannot be dissolved in CHCl₃, other organic solvent can be used, such as methanol, TFE, etc.

- (3) The solution is deposited dropwise onto six to twelve 6 × 12 mm² glass plates (**Figure A.1.a**).

- (4) Evaporate the solvent in hood for 1-2 hrs and then lyophilize-dry overnight to remove any residual naphthalene and organic solvent.

- (5) Hydrate the lipid films by directly dropping 1 μL of water on each plate, giving a hydration level of ~50% (**Figure A.1.b**).

*Note: for samples with much less total lipid mass on each plate, e.g. 0.1 mg on each plate for the small round glass-plate sample shown in the bottom row of **Figure A.1.**, direct hydrate using a small amount of water can be achieved via spray but is not highly recommended since it makes the hydration hard to quantify. Instead, the sample can be indirectly hydrated in a humidity chamber as shown in **Figure A.1.h**.*

- (6) Incubate the glass plates in a 97% humidity chamber containing a saturated K₂SO₄ solution for 3-4 days.

Note: keep the humidity chamber in an incubator to maintain a temperature above the lipid phase transition temperature.

- (7) Finally, the glass plates are stacked and wrapped with parafilm for NMR experiments (**Figure A.1.c**).

Note: to prevent the sample from dehydration, the parafilm-wrapped glass plates can be sealed in a polyethylene bag (Figure A.1.d).

- (8) Load the wrapped oriented sample in a square coil for static NMR measurements. (**Figure A.1.e**)

Reference

1. Hallock, K. J., Henzler Wildman, K., Lee, D. K., and Ramamoorthy, A. An innovative procedure using a sublimable solid to align lipid bilayers for solid-state NMR studies. *Biophys. J.* 82, 2499–2503 (2002)
2. Aisenbrey, C., Bertani, P., and Bechinger, B. Solid-state NMR investigations of membrane-associated antimicrobial peptides. *Methods Mol. Biol.* 618, 209–233. (2010)
3. R. Mani, J.J. Buffy, A.J. Waring, R.I. Lehrer, and M. Hong, Solid-State NMR Investigation of the Selective Disruption of Lipid Membranes by Protegrin-1, *Biochemistry*, 43, 13839-48 (2004)
4. Y. Su, W.F. DeGrado and M. Hong, Orientation, dynamics and lipid interaction of an antimicrobial arylamide in lipid bilayers investigated by ¹⁹F and ³¹P solid-state NMR, *J. Am. Chem. Soc.* 132, 9197-9205 (2010)
5. Y. Su, A.J. Waring, P. Ruchala, and M. Hong, Membrane-bound dynamic structure of an Arginine-rich cell-penetrating peptide, the protein transduction domain of HIV TAT, from solid-state NMR, *Biochemistry*, 49, 6009-6020 (2010).

A.2. Bicelle (magnetically aligned) sample preparation:

The bicelle sample is prepared using published protocols (see references). Brief procedures to prepare DMPC/6-O-PC bicelle-incorporated protein samples are listed here:

- (1) Weigh the zwitterionic lipid DMPC and the ether lipid 6-O-PC at a molar ratio of $q = 3.2$.
- (2) Mix the lipids in pH 7.0 phosphate buffer (or HEPES buffer) to a total lipid concentration of 35% (w/v).
- (3) Vortex the mixture, heat to 42 °C, and cool to 5 °C. Keep the vortexing, thawing and

cooling cycle till a clear homogeneous and viscous solution is obtained.

- (4) The mixture is then incubated at 4 °C overnight. The resulting homogenous solution should be viscous at 42 °C but fluid at 0 °C, which is the characteristic of bicelles.
- (5) The bicelle alignment in the magnetic field is examined by ^{31}P NMR. A well aligned bicelle sample should have only sharp peaks, as shown in the bottom spectrum in **Figure A.2**. The 90° peaks should appear at negative ppm since the bilayer normal is perpendicular to the magnetic field, which is different from the glass plate-aligned sample.
- (6) The protein (or drug) is added to the bicelle solution to a desired molar ratio and the solution is then subjected to another round of vortexing as well as heating and cooling cycles. The alignment of the protein-incorporated bicelle is again checked by ^{31}P NMR.

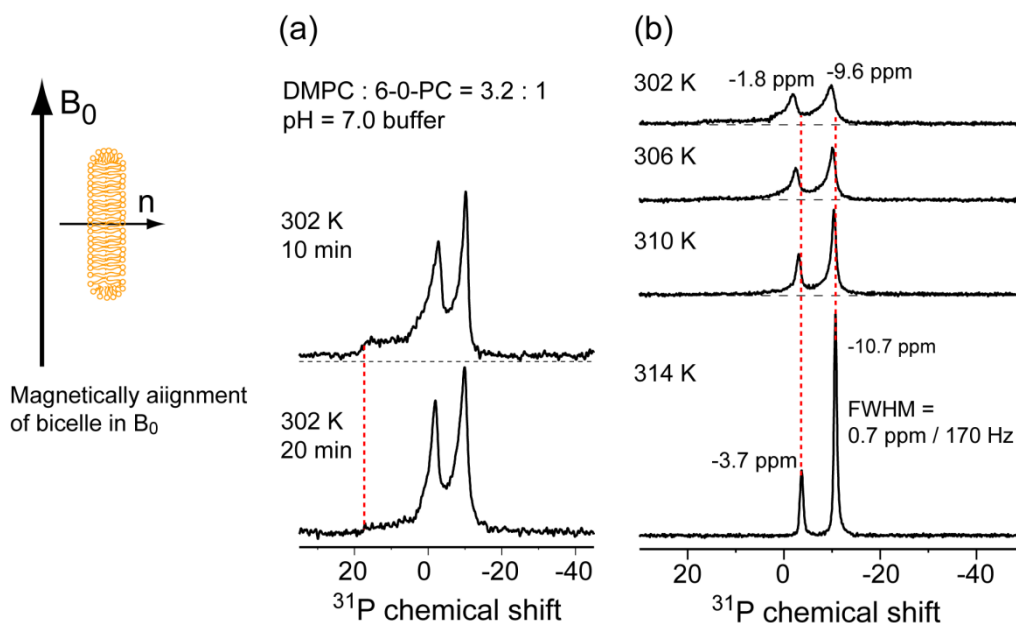


Figure A.2. Bicelle alignment checking using static ^{31}P NMR. (a) Time dependence of bicelle alignment. It takes at least 20 min to get better alignment in the 600 MHz static field. (b) Temperature dependence of bicelle alignment. The best alignment is found at 314 K. The FWHM is 0.7 ppm at 50 ^1H kHz decoupling.

Storage of bicelle samples

The peptide-containing bicelle sample can be stored in 4 °C or -25 °C freezer. The alignment can be well maintained for at least 6 months from my experience.

Reference

1. DeAngelis, A. & Opella, S. Bicelle samples for solid-state NMR of membrane proteins. *Nat. Protoc.* 2, 2332–2338. (2007)
2. Marcotte, I. & Auger, M. Bicelles as model membranes for solid-state and solution-state NMR studies of membrane peptides and proteins. *Concept. Magn. Reson. A*, 24, 17–37. (2005).
3. Prosser, R. S., Evanics, F., Kitevski, J. L. & Al-Abdul-Wahid, M. S. Current applications of bicelles in NMR studies of membrane-associated amphiphiles and proteins. *Biochemistry*, 45, 8453–8465. (2006)
4. Aussenac, F., Lavigne, B. & Dufourc, E. Toward bicelle stability with ether-linked phospholipids: temperature, composition, and hydration diagrams by ²H and ³¹P solid-state NMR. *Langmuir*, 21, 7129–7135. (2005)
5. T. Doherty, Y. Su and M. Hong, “High-Resolution Orientation and Depth of Insertion of the Voltage-Sensing S4 Helix of a Potassium Channel in Lipid Bilayers”, *J. Mol. Biol.* 401, 642-652 (2010).
6. Y. Su, W.F. DeGrado and M. Hong, “Orientation, dynamics and lipid interaction of an antimicrobial arylamide in lipid bilayers investigated by ¹⁹F and ³¹P solid-state NMR”, *J. Am. Chem. Soc.* 132, 9197-9205 (2010)

Appendix B

Paramagnetic Relaxation Enhancement (PRE) membrane-bound peptide sample preparation: applications of Mn(II) and Cu(II) ions

B.1. One-side and two-side PRE (Mn^{2+}) membrane-bound peptide sample

The unoriented lipid membrane sample for magic-angle spinning (MAS) experiments is prepared by an aqueous-phase mixing protocol. Mn^{2+} ions are added in two different ways. Taking peptide-containing POPC/POPG sample for example:

- (1) Weigh and mix POPC/POPG lipid in $CHCl_3$ at a desired molar ratio.
- (2) Blow dry the lipid solution in hood using dry N_2 gas. Then dissolve the lipid film in cyclohexane and lyophilize overnight.

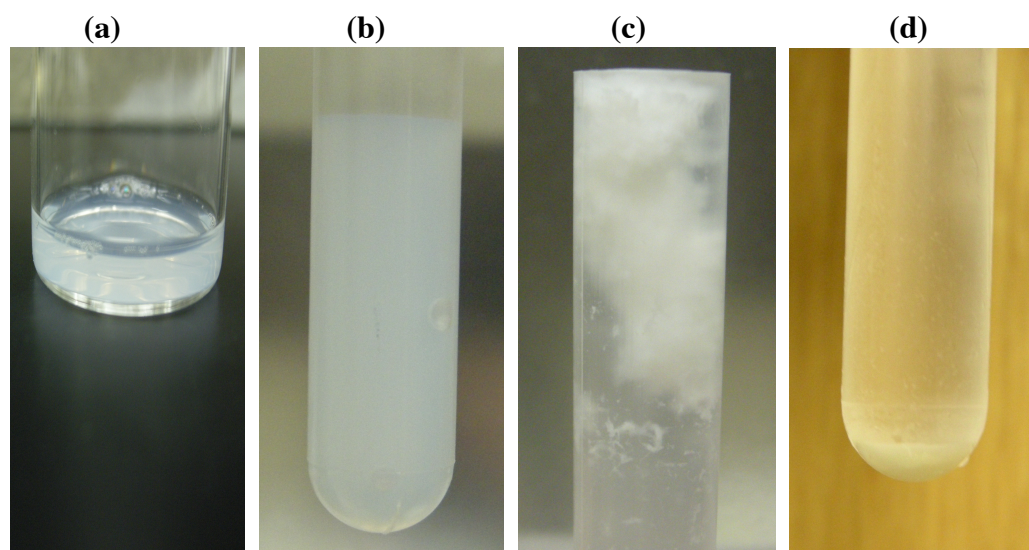


Figure B.1. (a) The translucent lipid solution after extraction through $0.1\mu m$ filter. (b) The POPE/POPG lipid vesicle solution after freeze-thawing thermocycles. (c) Precipitate after adding the cationic peptide IB549. Clear precipitation can be seen in cases of penetratin, TAT, KvAP S4, PG-1, IB484 and IB549. (d) Pellet at the bottom after ultracentrifugation. The sample is prepared together with Byungsu Kwon for the antimicrobial mechanism study of the lysine-mutant IB549 of PG-1.

- (3) The dry lipid mixtures are suspended in buffer and then freeze-thawed eight times to make multilamellar vesicles. It will usually look like a homogenous system (**Figure B.1**). To make smaller lipid vesicles, extraction can be done.

- (4) The lipid suspension is then gone through the extrusion process. It is first extruded through first 0.4 mm and then 0.1 mm filters to produce large unilamellar vesicles (LUVs). The final extruded lipid solution looks extremely homogeneous and translucent. *Make sure that the lipid concentration is not too high to cause vesicle fusion.*
- (5) Add the lipid solution into peptide solution to reach the desired peptide/lipid molar ratio (P/L) and allow overnight binding. One should expect clear white precipitate after cationic peptide-lipid binding (**Figure B.1**)
- (6) The membrane mixtures are ultracentrifuged above the phase transition temperature to obtain pellets. The wet pellet is then packed as the SSNMR sample.

Addition of Mn^{2+} (in form of $MnCl_2$) for one-side PRE sample

There are two methods to incorporate Mn^{2+} into the lipid membrane sample.

- (1) Add right before ultracentrifugation. This method allows a small metal ion concentration. The metal ion binds to the membrane surface via free partition. The unbound ions will stay in the supernatant.
- (2) Add Mn^{2+} into the rotor directly after packing. This makes it easy to quantify the Mn^{2+} amount. We found 8% (molar ratio) Mn^{2+} of total lipid gave reasonable dephasing to detect the insertion depth of peptides.

It's crucial to prepare and store one-side PRE samples at a stable temperature above the lipid phase transition temperature (T_m) to avoid the bilayer reassemble.

Converting one-side sample to two-side PRE sample

The two-side PRE sample is prepared by thoroughly freezing and thawing the one-side Mn^{2+} sample. This thermocycle will reassemble the bilayer and make the metal ions distribute on both sides of the lipid bilayer. One should also note that the converted sample is highly likely a multilamellar sample.

Checking of one-side or two-side binding of Mn^{2+} by ^{31}P NMR

The static ^{31}P spectrum acquired using direct polarization is a quantitative method to check the sidedness of Mn^{2+} on the membrane surface. For the one-side sample, one expects half of the intensity (by area integration), while for the two-side sample, no ^{31}P signal will retain due to the PRE T_2 effect to ^{31}P spins on inner and outer membrane surfaces.

B.2. Cu(II)-bound membrane sample (in case of M2TM peptide)

Membrane sample preparation for insoluble peptides

The lipid vesicle preparation is similar to the protocol described in **B.1**, while the incorporation of the M2 transmembrane peptide is different because the peptide cannot be dissolved in water. Thus, the M2TM-bound membrane sample is prepared in ways of either organic mixing or OG-assisted preparation. The latter method can yield a more homogeneous sample. After the peptide-lipid mixing, dialysis helps to remove small OG molecules. I have used this method to prepare the V7, R8-labeled KvAP S4 incorporated DMPC/DMPG sample and the GHI-labeled M2TM incorporated viral membrane plus (VM^+) sample. **Figure B.1** shows the peptide-membrane precipitate after 3-day dialysis.

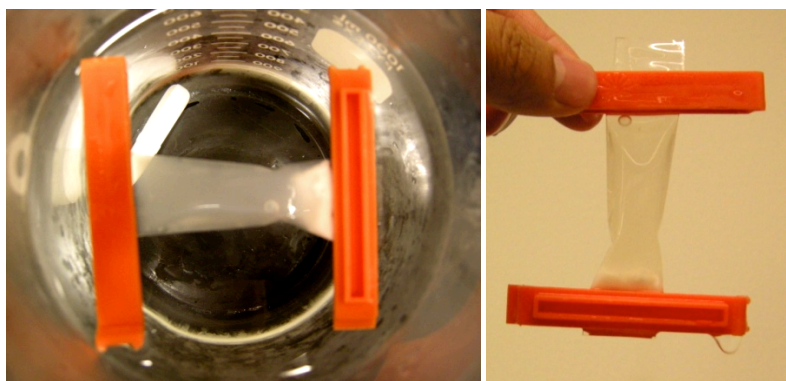


Figure B.1. The G34, H37, I42-labeled M2TM incorporated VM^+ sample in the dialysis bag after 3-day dialysis.

Cu^{2+} addition and concentration

Cu^{2+} is added to the NMR rotor directly in the form of $CuCl_2$ solution. Our pep-

tide-free POPC test shows that 6% Cu^{2+} is enough to see a reasonable PRE T_1 effect for carbons inside the membrane.

Reference

1. J. Buffy, T. Hong, A. Waring, R. I. Lehrer, and M. Hong, "Solid-State NMR Investigation of the Depth of Insertion of PG-1 in DLPC Using Paramagnetic Mn^{2+} ", *Biophys. J.* 85, 2363-2373 (2003)
2. Y. Su, R. Mani, and M. Hong, Asymmetric Insertion of Membrane Proteins in Lipid Bilayers by Solid-State NMR Paramagnetic Relaxation Enhancement: a Cell-Penetrating Peptide Example, *J. Am. Chem. Soc.* 130(27), 8856-8864 (2008)
3. Y. Su, F. Hu and M. Hong, "Binding Structure of Cu(II) Inhibition of Influenza A/M2 Proton Channels from Solid-State NMR", in preparation (2011)

Appendix C

Simulation codes of the separated-local-field (SLF) experiment for orientation determination of a body-rigid molecule

MATLAB (version: R2007b) simulation codes for Su et al, JACS, 2010

```

% -----
% calculate dipolar couplings of C-CF3 bond of a
% rigid molecule, AMO
% written by Y. Su and M. Hong, 2010
% -----

clear

% 1st C-CF3 bond, C1C2
a14=[-8.267 6.006 2.789];
a16=[-8.739 7.493 2.775];
c9c11=a16-a14;
nor_c9c11=c9c11/norm(c9c11);

% 2nd C-CF3 bond, C3C4
a35=[5.624 6.022 2.571];
a37=[6.081 7.505 2.755];
c23c25=a37-a35;
nor_c23c25=c23c25/norm(c23c25);

% x-axis, molecular axis, connect a4_a6 vector of
% the central ring
c4=[-2.529 3.981 2.693];
c6=[-0.101 3.964 2.584];
molx=c4-c6;

% y-axis, along the C-H bond of the central ring
% normal to the a4-a6 vector; a5=C2; a67=H2;
a5=[-1.311 4.705 2.675];
a67=[-1.302 5.785 2.721];
moly=a67-a5;

% define z-axis, an axis perpendicular to xy-plane
molz=cross(molx,moly);

% normalization of x, y, z axis (unit vectors)

nor_x=molx/norm(molx);
nor_y=moly/norm(moly);
nor_z=molz/norm(molz);

new_c9c11(1)=nor_c9c11(1)*nor_x(1)+nor_c9c11(2)
)*nor_x(2)+nor_c9c11(3)*nor_x(3);
new_c9c11(2)=nor_c9c11(1)*nor_y(1)+nor_c9c11(2)
)*nor_y(2)+nor_c9c11(3)*nor_y(3);
new_c9c11(3)=nor_c9c11(1)*nor_z(1)+nor_c9c11(2)
)*nor_z(2)+nor_c9c11(3)*nor_z(3);

new_c23c25(1)=nor_c23c25(1)*nor_x(1)+nor_c23c
25(2)*nor_x(2)+nor_c23c25(3)*nor_x(3);
new_c23c25(2)=nor_c23c25(1)*nor_y(1)+nor_c23c
25(2)*nor_y(2)+nor_c23c25(3)*nor_y(3);
new_c23c25(3)=nor_c23c25(1)*nor_z(1)+nor_c23c2
5(2)*nor_z(2)+nor_c23c25(3)*nor_z(3);

% define bilayer normal and calculate the angle theta
%between bilayer normal & each of the C-CF3 bond

%tau=input('tau value = ')*(180/3.1415926);
%rou=input('rou value = ')*(180/3.1415926);
%ml=input('number of tau = ');
%n1=input('number of rou = ');

tau=[0:1:360]*(pi/180);
rou=[0:1:360]*(pi/180);
ntau=361;
nrrou=361;
taudeg=[0:1:360];
roudeg=[0:1:360];

for i=1:ntau
    for j=1:nrrou

```

```

        cos_theta_c9c11(i,j) =
(new_c9c11(1))*sin(tau(i))*cos(rou(j))+(new_c9c11(
2))*sin(tau(i))*sin(rou(j))+((new_c9c11(3)))*cos(tau
(i));
    end
end

% calculate dipolar coupling strength of C1C2
% scaled_dipolar_limit=input('scaled dipolar cou-
pling rigid limit = ')

% scaled dipolar couplinig limit for bicelle sample
scaled_dipolar_limit=3.9;

for i=1:ntau
    for j=1:nrou

wd_c9c11(i,j)=0.5*(3*cos_theta_c9c11(i,j)*cos_thet
a_c9c11(i,j)-1)*scaled_dipolar_limit;
        end
    end

for i=1:ntau
    for j=1:nrou

cos_theta_c23c25(i,j)=(new_c23c25(1))*sin(tau(i))*
cos(rou(j))+(new_c23c25(2))*sin(tau(i))*sin(rou(j))+
((new_c23c25(3)))*cos(tau(i));
        end
    end

% calculate dipolar coupling strength of C3C4
for i=1:ntau
    for j=1:nrou

wd_c23c25(i,j)=0.5*(3*cos_theta_c23c25(i,j)*cos_t
heta_c23c25(i,j)-1)*scaled_dipolar_limit;
        end
    end

% rmsd of C1C2 and C3C4, seperately
for i=1:ntau
    for j=1:nrou

rmsd_c9c11(i,j)=abs(abs(wd_c9c11(i,j))-2.54);

rmsd_c23c25(i,j)=abs(abs(wd_c23c25(i,j))-2.54);
        end
    end

% rmsd of C1C2 and C3C4 together

for i=1:ntau
    for j=1:nrou

rmsd_c9c11_c23c25(i,j)=sqrt((abs(wd_c23c25(i,j))-2
.54)^2+(abs(wd_c9c11(i,j))-2.54)^2);
        end
    end

% to plot the contour level

figure
v=[-4:1:4,2.54,-1.8];
[C1,h1] = contour (roudeg, taudeg, wd_c9c11,v);
set(h1,'ShowText','on','TextStep'.get(h1,'LevelStep')*
2)
colormap jet

figure
[C2,h2] = contour (roudeg, taudeg, wd_c23c25,v);
set(h2,'ShowText','on','TextStep'.get(h2,'LevelStep')*
2)
colormap jet

figure
[C1,h1] = contour (roudeg, taudeg, wd_c9c11,v,'r');
set(h1,'ShowText','on','TextStep'.get(h1,'LevelStep')*
2)
hold
[C2,h2] = contour (roudeg, taudeg, wd_c23c25,v,'b');
set(h2,'ShowText','on','TextStep'.get(h2,'LevelStep')*
2)

figure
[C1,h1] = contour (roudeg, taudeg, wd_c9c11,v,'r');
hold
[C2,h2] = contour (roudeg, taudeg, wd_c23c25,v,'b');

% figure
% contour(roudeg, taudeg,rmsd_c9c11)

```

```
figure  
contour (roudeg, taudeg, wd_c9c11,2.54,'r')  
hold  
contour (roudeg, taudeg, wd_c23c25,2.54,'b')
```

```
figure
```

```
contour(roudeg,taudeg,rmsd_c9c11_c23c25)  
%[C3,h3] = con-  
tour(roudeg,taudeg,rmsd_c9c11_c23c25)  
%set(h3,'ShowText','on','TextStep'.get(h3,'LevelStep'  
)*2)  
%colormap jet
```

Appendix D

Spin diffusion coefficients consolidated from previous studies

Table D.1. Experimentally established spin diffusion coefficients in membrane proteins.

Reference	Membrane	T (K)	diffusion coefficients (nm ² /ms)*		
			D _{pp}	D _{wp}	D _{lp}
Kumashiro et al, 1998	DLPG/DLPC (2:3)	~ 240	0.4	0.025 and 0.050	-
Huster et al, 2002	POPC/POPG (3:1)	293	0.3	0.0025	0.0025
Gallagher et al, 2004	DMPC	~245	0.375	0.025	-
Mani et al, 2006	POPE/POPG (3:1)	298	0.3	0.00125	0.00125
Ader et al, 2008	DMPC	280	0.3	0.008	-
Tang et al, 2009	POPC	295	0.3	-	0.0005
Tang et al, 2009	POPG	295	0.3	-	0.0012
Luo et al, 2010	viral membrane	293	0.3	0.008	-
Zhang et al, 2010	DMPC/DMPG (3:1)	303	0.3	0.0025	0.0025
Su et al, 2011	ReLPS/DEPE (1:5)	308	0.3	0.005	0.005
Su et al, 2011	POPE/POPG (3:1)	288	0.3	0.005	0.005
Su et al, 2011	POPE/POPG (3:1)	298	0.3	0.00175	0.00175

* D_{pp}: diffusion coefficient within peptide; D_{wp}: water-to-peptide diffusion coefficient; D_{lp}: lipid-to-peptide diffusion coefficient.

Reference

1. Kumashiro, K. K.; Schmidt-Rohr, K.; Murphy, O. J.; Ouellette, K. L.; Cramer, W. A.; Thompson, L. K. A Novel Tool for Probing Membrane Protein Structure: Solid-State NMR with Proton Spin Diffusion and X-Nucleus Detection, *J. Am. Chem. Soc.* 120, 5043–5051.(1998)
2. D. Huster, X.L. Yao and M. Hong, "Membrane Protein Topology Probed by ¹H Spin Diffusion from Lipids Using Solid-State NMR Spectroscopy", *J. Am. Chem. Soc.* 124, 874-883 (2002)
3. Gallagher, G. J.; Hong, M.; Thompson, L. K. , Solid-state NMR spin diffusion for measurement of membrane-bound peptide structure: Gramicidin A. *Biochemistry* 43,7899–

7906. (2004)

4. R. Mani, S.D. Cady, M. Tang, A.J. Waring, R.I. Lehrer, and M. Hong, "Membrane-dependent oligomeric structure and pore formation of a β -hairpin antimicrobial peptide in lipid bilayers from solid-state NMR", *Proc. Natl. Acad. Sci. U.S.A.*, 103, 16242-16247 (2006)
5. Ader, C.; Schneider, R.; Seidel, K.; Eitzkorn, M.; Becker, S.; Baldus, M. , Structural rearrangements of membrane proteins probed by water-edited solid-state NMR spectroscopy. *J. Am. Chem. Soc.* 131, 170–176 (2009)
6. M. Tang, A.J. Waring and M. Hong, "Effects of Arginine Density on the Membrane-Bound Structure of a Cationic Antimicrobial Peptide from Solid-State NMR", *Biochim. Biophys. Acta*, 1788, 514-521 (2009)
7. W. Luo and M. Hong, "Conformational Changes of an Ion Channel Detected Through Water-Protein Interactions Using Solid-State NMR", *J. Am. Chem. Soc.* 132, 2378-2384 (2010)
8. Y. Zhang and M. Hong, "Membrane-bound structure and topology of a human alpha-defensin indicates dimer pore as the mechanism of antimicrobial activity", *Biochemistry*, 49, 9770-9782 (2010)
9. Y. Su, A. J. Waring, P. Ruchala, and M. Hong, "Structure of b-hairpin Antimicrobial Peptides in Lipopolysaccharide Membranes: Mechanism of Gram Selectivity Obtained from Solid-State NMR", *Biochemistry*, 50, 2072-2083 (2011)